Springer Handbook of Nano-technology

CD-ROM

Bhushan
Editor

3rd Edition

Bharat Bhushan (Ed.)

3rd revised and extended edition
With DVD-ROM, 1577 Figures and 127 Tables

Editor
Professor Bharat Bhushan
Nanoprobe Laboratory
for Bio- and Nanotechnology and Biomimetics (NLB^2)
Ohio State University
201 W. 19th Avenue
Columbus, OH 43210-1142
USA

ISBN: 978-3-642-02524-2 e-ISBN: 978-3-642-02525-9
DOI 10.1007/978-3-642-02525-9
Springer Heidelberg Dordrecht London New York

Library of Congress Control Number: 2010921002

Production and typesetting: le-tex publishing services GmbH, Leipzig
Senior Manager Springer Handbook: Dr. W. Skolaut, Heidelberg
Typography and layout: schreiberVIS, Seeheim
Illustrations: Hippmann GbR, Schwarzenbruck
Cover design: eStudio Calamar S.L., Spain/Germany
Cover production: WMXDesign GmbH, Heidelberg
Printing and binding: Stürtz GmbH, Würzburg

Printed on acid free paper

Springer is part of Springer Science+Business Media (www.springer.com)

62/3180/YL 5 4 3 2 1 0

Mehran Mehregany
Case Western Reserve University
Department of Electrical Engineering
and Computer Science
Cleveland, OH 44106, USA
e-mail: *mxm31@cwru.edu*

Etienne Menard
Semprius, Inc.
4915 Prospectus Dr.
Durham, NC 27713, USA
e-mail: *etienne.menard@semprius.com*

Ernst Meyer
University of Basel
Institute of Physics
Basel, Switzerland
e-mail: *ernst.meyer@unibas.ch*

Robert Modliñski
Baolab Microsystems
Terrassa 08220, Spain
e-mail: *rmodlinski@gmx.com*

Mohammad Mofrad
University of California, Berkeley
Department of Bioengineering
Berkeley, CA 94720, USA
e-mail: *mofrad@berkeley.edu*

Marc Monthioux
CEMES – UPR A-8011 CNRS
Carbones et Matériaux Carbonés,
Carbons and Carbon-Containing Materials
29 Rue Jeanne Marvig
31055 Toulouse 4, France
e-mail: *monthiou@cemes.fr*

Markus Morgenstern
RWTH Aachen University
II. Institute of Physics B and JARA-FIT
52056 Aachen, Germany
e-mail: *mmorgens@physik.rwth-aachen.de*

Seizo Morita
Osaka University
Department of Electronic Engineering
Suita-City
Osaka, Japan
e-mail: *smorita@ele.eng.osaka-u.ac.jp*

Koichi Mukasa
Hokkaido University
Nanoelectronics Laboratory
Sapporo, Japan
e-mail: *mukasa@nano.eng.hokudai.ac.jp*

Bradley J. Nelson
Swiss Federal Institute of Technology (ETH)
Institute of Robotics and Intelligent Systems
8092 Zurich, Switzerland
e-mail: *bnelson@ethz.ch*

Michael Nosonovsky
University of Wisconsin-Milwaukee
Department of Mechanical Engineering
3200 N. Cramer St.
Milwaukee, WI 53211, USA
e-mail: *nosonovs@uwm.edu*

Hiroshi Onishi
Kanagawa Academy of Science and Technology
Surface Chemistry Laboratory
Kanagawa, Japan
e-mail: *oni@net.ksp.or.jp*

Alain Peigney
Centre Inter-universitaire de Recherche
sur l'Industrialisation des Matériaux (CIRIMAT)
Toulouse 4, France
e-mail: *peigney@chimie.ups-tlse.fr*

Oliver Pfeiffer
Individual Computing GmbH
Ingelsteinweg 2d
4143 Dornach, Switzerland
e-mail: *oliver.pfeiffer@gmail.com*

Haralampos Pozidis
IBM Zurich Research Laboratory
Storage Technologies
Rüschlikon, Switzerland
e-mail: *hap@zurich.ibm.com*

Robert Puers
Katholieke Universiteit Leuven
ESAT/MICAS
Leuven, Belgium
e-mail: *bob.puers@esat.kuleuven.ac.be*

Calvin F. Quate
Stanford University
Edward L. Ginzton Laboratory
450 Via Palou
Stanford, CA 94305-4088, USA
e-mail: *quate@stanford.edu*

Oded Rabin
University of Maryland
Department of Materials Science and Engineering
College Park, MD, USA
e-mail: *oded@umd.edu*

Françisco M. Raymo
University of Miami
Department of Chemistry
1301 Memorial Drive
Coral Gables, FL 33146-0431, USA
e-mail: *fraymo@miami.edu*

Manitra Razafinimanana
University of Toulouse III (Paul Sabatier)
Centre de Physique des Plasmas
et leurs Applications (CPPAT)
Toulouse, France
e-mail: *razafinimanana@cpat.ups-tlse.fr*

Ziv Reich
Weizmann Institute of Science Ha'Nesi Ha'Rishon
Department of Biological Chemistry
Rehovot 76100, Israel
e-mail: *ziv.reich@weizmann.ac.il*

John A. Rogers
University of Illinois
Department of Materials Science and Engineering
Urbana, IL, USA
e-mail: *jrogers@uiuc.edu*

Cosmin Roman
ETH Zurich
Micro and Nanosystems Department of Mechanical
and Process Engineering
8092 Zurich, Switzerland
e-mail: *cosmin.roman@micro.mavt.ethz.ch*

Marina Ruths
University of Massachusetts Lowell
Department of Chemistry
1 University Avenue
Lowell, MA 01854, USA
e-mail: *marina_ruths@uml.edu*

Ozgur Sahin
The Rowland Institute at Harvard
100 Edwin H. Land Blvd
Cambridge, MA 02142, USA
e-mail: *sahin@rowland.harvard.edu*

Akira Sasahara
Japan Advanced Institute
of Science and Technology
School of Materials Science
1-1 Asahidai
923-1292 Nomi, Japan
e-mail: *sasahara@jaist.ac.jp*

Helmut Schift
Paul Scherrer Institute
Laboratory for Micro- and Nanotechnology
5232 Villigen PSI, Switzerland
e-mail: *helmut.schift@psi.ch*

André Schirmeisen
University of Münster
Institute of Physics
Wilhelm-Klemm-Str. 10
48149 Münster, Germany
e-mail: *schirmeisen@uni-muenster.de*

Christian Schulze
Beiersdorf AG
Research & Development
Unnastr. 48
20245 Hamburg, Germany
e-mail: *christian.schulze@beiersdorf.com;*
christian.schulze@uni-leipzig.de

Alexander Schwarz
University of Hamburg
Institute of Applied Physics
Jungiusstr. 11
20355 Hamburg, Germany
e-mail: *aschwarz@physnet.uni-hamburg.de*

Udo D. Schwarz
Yale University
Department of Mechanical Engineering
15 Prospect Street
New Haven, CT 06520-8284, USA
e-mail: *udo.schwarz@yale.edu*

Philippe Serp
Ecole Nationale Supérieure d'Ingénieurs
en Arts Chimiques et Technologiques
Laboratoire de Chimie de Coordination (LCC)
118 Route de Narbonne
31077 Toulouse, France
e-mail: *philippe.serp@ensiacet.fr*

Huamei (Mary) Shang
GE Healthcare
4855 W. Electric Ave.
Milwaukee, WI 53219, USA
e-mail: *huamei.shang@ge.com*

Susan B. Sinnott
University of Florida
Department of Materials Science and Engineering
154 Rhines Hall
Gainesville, FL 32611-6400, USA
e-mail: *ssinn@mse.ufl.edu*

Anisoara Socoliuc
SPECS Zurich GmbH
Technoparkstr. 1
8005 Zurich, Switzerland
e-mail: *socoliuc@nanonis.com*

Olav Solgaard
Stanford University
E.L. Ginzton Laboratory
450 Via Palou
Stanford, CA 94305-4088, USA
e-mail: *solgaard@stanford.edu*

Dan Strehle
University of Leipzig
Institute of Experimental Physics I
Division of Soft Matter Physics
Linnéstr. 5
04103 Leipzig, Germany
e-mail: *dan.strehle@uni-leipzig.de*

Carsten Stüber
University of Leipzig
Institute of Experimental Physics I
Division of Soft Matter Physics
Linnéstr. 5
04103 Leipzig, Germany
e-mail: *stueber@rz.uni-leipzig.de*

Yu-Chuan Su
ESS 210
Department of Engineering and System Science 101
Kuang-Fu Road
Hsinchu, 30013, Taiwan
e-mail: *ycsu@ess.nthu.edu.tw*

Kazuhisa Sueoka
Graduate School of Information Science
and Technology
Hokkaido University
Nanoelectronics Laboratory
Kita-14, Nishi-9, Kita-ku
060-0814 Sapporo, Japan
e-mail: *sueoka@nano.isthokudai.ac.jp*

Yasuhiro Sugawara
Osaka University
Department of Applied Physics
Yamada-Oka 2-1, Suita
565-0871 Osaka, Japan
e-mail: *sugawara@ap.eng.osaka-u.ac.jp*

Benjamin Sullivan
TearLab Corp.
11025 Roselle Street
San Diego, CA 92121, USA
e-mail: *bdsulliv@TearLab.com*

Paul Swanson
Nexogen, Inc.
Engineering
8360 C Camino Santa Fe
San Diego, CA 92121, USA
e-mail: *pswanson@nexogentech.com*

Yung-Chieh Tan
Washington University School of Medicine
Department of Medicine
Division of Dermatology
660 S. Euclid Ave.
St. Louis, MO 63110, USA
e-mail: *ytanster@gmail.com*

Shia-Yen Teh
University of California at Irvine
Biomedical Engineering Department
3120 Natural Sciences II
Irvine, CA 92697-2715, USA
e-mail: *steh@uci.edu*

W. Merlijn van Spengen
Leiden University
Kamerlingh Onnes Laboratory
Niels Bohrweg 2
Leiden, CA 2333, The Netherlands
e-mail: *spengen@physics.leidenuniv.nl*

Peter Vettiger
University of Neuchâtel
SAMLAB
Jaquet-Droz 1
2002 Neuchâtel, Switzerland
e-mail: *peter.vettiger@unine.ch*

Franziska Wetzel
University of Leipzig
Institute of Experimental Physics I
Division of Soft Matter Physics
Linnéstr. 5
04103 Leipzig, Germany
e-mail: *franziska.wetzel@uni-leipzig.de*

Heiko Wolf
IBM Research GmbH
Zurich Research Laboratory
Säumerstr. 4
8803 Rüschlikon, Switzerland
e-mail: *hwo@zurich.ibm.com*

Darrin J. Young
Case Western Reserve University
Department of EECS, Glennan 510
10900 Euclid Avenue
Cleveland, OH 44106, USA
e-mail: *djy@po.cwru.edu*

Babak Ziaie
Purdue University
Birck Nanotechnology Center
1205 W. State St.
West Lafayette, IN 47907-2035, USA
e-mail: *bziaie@purdue.edu*

Christian A. Zorman
Case Western Reserve University
Department of Electrical Engineering
and Computer Science
10900 Euclid Avenue
Cleveland, OH 44106, USA
e-mail: *caz@case.edu*

Jim V. Zoval
Saddleback College
Department of Math and Science
28000 Marguerite Parkway
Mission Viejo, CA 92692, USA
e-mail: *jzoval@saddleback.edu*

Contents

List of Abbreviations

μCP	microcontact printing
1-D	one-dimensional
18-MEA	18-methyl eicosanoic acid
2-D	two-dimensional
2-DEG	two-dimensional electron gas
3-APTES	3-aminopropyltriethoxysilane
3-D	three-dimensional

A

a-BSA	anti-bovine serum albumin
a-C	amorphous carbon
A/D	analog-to-digital
AA	amino acid
AAM	anodized alumina membrane
ABP	actin binding protein
AC	alternating-current
AC	amorphous carbon
ACF	autocorrelation function
ADC	analog-to-digital converter
ADXL	analog devices accelerometer
AFAM	atomic force acoustic microscopy
AFM	atomic force microscope
AFM	atomic force microscopy
AKD	alkylketene dimer
ALD	atomic layer deposition
AM	amplitude modulation
AMU	atomic mass unit
AOD	acoustooptical deflector
AOM	acoustooptical modulator
AP	alkaline phosphatase
APB	actin binding protein
APCVD	atmospheric-pressure chemical vapor deposition
APDMES	aminopropyldimethylethoxysilane
APTES	aminopropyltriethoxysilane
ASIC	application-specific integrated circuit
ASR	analyte-specific reagent
ATP	adenosine triphosphate

B

BAP	barometric absolute pressure
BAPDMA	behenyl amidopropyl dimethylamine glutamate
bcc	body-centered cubic
BCH	brucite-type cobalt hydroxide
BCS	Bardeen–Cooper–Schrieffer
BD	blu-ray disc
BDCS	biphenyldimethylchlorosilane
BE	boundary element
BFP	biomembrane force probe
BGA	ball grid array
BHF	buffered HF
BHPET	1,1'-(3,6,9,12,15-pentaoxapentadecane-1,15-diyl)bis(3-hydroxyethyl-1H-imidazolium-1-yl) di[bis(trifluoromethanesulfonyl)imide]
BHPT	1,1'-(pentane-1,5-diyl)bis(3-hydroxyethyl-1H-imidazolium-1-yl) di[bis(trifluoromethanesulfonyl)imide]
BiCMOS	bipolar CMOS
bioMEMS	biomedical microelectromechanical system
bioNEMS	biomedical nanoelectromechanical system
BMIM	1-butyl-3-methylimidazolium
BP	bit pitch
BPAG1	bullous pemphigoid antigen 1
BPT	biphenyl-4-thiol
BPTC	cross-linked BPT
BSA	bovine serum albumin
BST	barium strontium titanate
BTMAC	behentrimonium chloride

C

CA	constant amplitude
CA	contact angle
CAD	computer-aided design
CAH	contact angle hysteresis
cAMP	cyclic adenosine monophosphate
CAS	Crk-associated substrate
CBA	cantilever beam array
CBD	chemical bath deposition
CCD	charge-coupled device
CCVD	catalytic chemical vapor deposition
CD	compact disc
CD	critical dimension
CDR	complementarity determining region
CDW	charge density wave
CE	capillary electrophoresis
CE	constant excitation
CEW	continuous electrowetting
CG	controlled geometry
CHO	Chinese hamster ovary
CIC	cantilever in cantilever
CMC	cell membrane complex
CMC	critical micelle concentration
CMOS	complementary metal–oxide–semiconductor
CMP	chemical mechanical polishing

CNF	carbon nanofiber
CNFET	carbon nanotube field-effect transistor
CNT	carbon nanotube
COC	cyclic olefin copolymer
COF	chip-on-flex
COF	coefficient of friction
COG	cost of goods
CoO	cost of ownership
COS	CV-1 in origin with SV40
CP	circularly permuted
CPU	central processing unit
CRP	C-reactive protein
CSK	cytoskeleton
CSM	continuous stiffness measurement
CTE	coefficient of thermal expansion
Cu-TBBP	Cu-tetra-3,5 di-tertiary-butyl-phenyl porphyrin
CVD	chemical vapor deposition

D

DBR	distributed Bragg reflector
DC-PECVD	direct-current plasma-enhanced CVD
DC	direct-current
DDT	dichlorodiphenyltrichloroethane
DEP	dielectrophoresis
DFB	distributed feedback
DFM	dynamic force microscopy
DFS	dynamic force spectroscopy
DGU	density gradient ultracentrifugation
DI FESP	digital instrument force modulation etched Si probe
DI TESP	digital instrument tapping mode etched Si probe
DI	digital instrument
DI	deionized
DIMP	diisopropylmethylphosphonate
DIP	dual inline packaging
DIPS	industrial postpackaging
DLC	diamondlike carbon
DLP	digital light processing
DLVO	Derjaguin–Landau–Verwey–Overbeek
DMD	deformable mirror display
DMD	digital mirror device
DMDM	1,3-dimethylol-5,5-dimethyl
DMMP	dimethylmethylphosphonate
DMSO	dimethyl sulfoxide
DMT	Derjaguin–Muller–Toporov
DNA	deoxyribonucleic acid
DNT	2,4-dinitrotoluene
DOD	Department of Defense
DOE	Department of Energy
DOE	diffractive optical element
DOF	degree of freedom
DOPC	1,2-dioleoyl-sn-glycero-3-phosphocholine
DOS	density of states
DP	decylphosphonate
DPN	dip-pen nanolithography
DRAM	dynamic random-access memory
DRIE	deep reactive ion etching
ds	double-stranded
DSC	differential scanning calorimetry
DSP	digital signal processor
DTR	discrete track recording
DTSSP	3,3'-dithio-bis(sulfosuccinimidylproprionate)
DUV	deep-ultraviolet
DVD	digital versatile disc
DWNT	double-walled CNT

E

EAM	embedded atom method
EB	electron beam
EBD	electron beam deposition
EBID	electron-beam-induced deposition
EBL	electron-beam lithography
ECM	extracellular matrix
ECR-CVD	electron cyclotron resonance chemical vapor deposition
ED	electron diffraction
EDC	1-ethyl-3-(3-diamethylaminopropyl) carbodiimide
EDL	electrostatic double layer
EDP	ethylene diamine pyrochatechol
EDTA	ethylenediamine tetraacetic acid
EDX	energy-dispersive x-ray
EELS	electron energy loss spectra
EFM	electric field gradient microscopy
EFM	electrostatic force microscopy
EHD	elastohydrodynamic
EO	electroosmosis
EOF	electroosmotic flow
EOS	electrical overstress
EPA	Environmental Protection Agency
EPB	electrical parking brake
ESD	electrostatic discharge
ESEM	environmental scanning electron microscope
EU	European Union
EUV	extreme ultraviolet
EW	electrowetting
EWOD	electrowetting on dielectric

F

F-actin	filamentous actin
FA	focal adhesion
FAA	formaldehyde–acetic acid–ethanol
FACS	fluorescence-activated cell sorting

FAK	focal adhesion kinase
FBS	fetal bovine serum
FC	flip-chip
FCA	filtered cathodic arc
fcc	face-centered cubic
FCP	force calibration plot
FCS	fluorescence correlation spectroscopy
FD	finite difference
FDA	Food and Drug Administration
FE	finite element
FEM	finite element method
FEM	finite element modeling
FESEM	field emission SEM
FESP	force modulation etched Si probe
FET	field-effect transistor
FFM	friction force microscope
FFM	friction force microscopy
FIB-CVD	focused ion beam chemical vapor deposition
FIB	focused ion beam
FIM	field ion microscope
FIP	feline coronavirus
FKT	Frenkel–Kontorova–Tomlinson
FM	frequency modulation
FMEA	failure-mode effect analysis
FP6	Sixth Framework Program
FP	fluorescence polarization
FPR	*N*-formyl peptide receptor
FS	force spectroscopy
FTIR	Fourier-transform infrared
FV	force–volume

G

GABA	γ-aminobutyric acid
GDP	guanosine diphosphate
GF	gauge factor
GFP	green fluorescent protein
GMR	giant magnetoresistive
GOD	glucose oxidase
GPCR	G-protein coupled receptor
GPS	global positioning system
GSED	gaseous secondary-electron detector
GTP	guanosine triphosphate
GW	Greenwood and Williamson

H

HAR	high aspect ratio
HARMEMS	high-aspect-ratio MEMS
HARPSS	high-aspect-ratio combined poly- and single-crystal silicon
HBM	human body model
hcp	hexagonal close-packed
HDD	hard-disk drive
HDT	hexadecanethiol
HDTV	high-definition television
HEK	human embryonic kidney 293
HEL	hot embossing lithography
HEXSIL	hexagonal honeycomb polysilicon
HF	hydrofluoric
HMDS	hexamethyldisilazane
HNA	hydrofluoric-nitric-acetic
HOMO	highest occupied molecular orbital
HOP	highly oriented pyrolytic
HOPG	highly oriented pyrolytic graphite
HOT	holographic optical tweezer
HP	hot-pressing
HPI	hexagonally packed intermediate
HRTEM	high-resolution transmission electron microscope
HSA	human serum albumin
HtBDC	hexa-*tert*-butyl-decacyclene
HTCS	high-temperature superconductivity
HTS	high throughput screening
HUVEC	human umbilical venous endothelial cell

I

IBD	ion beam deposition
IC	integrated circuit
ICA	independent component analysis
ICAM-1	intercellular adhesion molecules 1
ICAM-2	intercellular adhesion molecules 2
ICT	information and communication technology
IDA	interdigitated array
IF	intermediate filament
IF	intermediate-frequency
IFN	interferon
IgG	immunoglobulin G
IKVAV	isoleucine–lysine–valine–alanine–valine
IL	ionic liquid
IMAC	immobilized metal ion affinity chromatography
IMEC	Interuniversity MicroElectronics Center
IR	infrared
ISE	indentation size effect
ITO	indium tin oxide
ITRS	International Technology Roadmap for Semiconductors
IWGN	Interagency Working Group on Nanoscience, Engineering, and Technology

J

JC	jump-to-contact
JFIL	jet-and-flash imprint lithography
JKR	Johnson–Kendall–Roberts

K

KASH	Klarsicht, ANC-1, Syne Homology
KPFM	Kelvin probe force microscopy

L

LA	lauric acid
LAR	low aspect ratio
LB	Langmuir–Blodgett
LBL	layer-by-layer
LCC	leadless chip carrier
LCD	liquid-crystal display
LCoS	liquid crystal on silicon
LCP	liquid-crystal polymer
LDL	low-density lipoprotein
LDOS	local density of states
LED	light-emitting diode
LFA-1	leukocyte function-associated antigen-1
LFM	lateral force microscope
LFM	lateral force microscopy
LIGA	Lithographie Galvanoformung Abformung
LJ	Lennard-Jones
LMD	laser microdissection
LMPC	laser microdissection and pressure catapulting
LN	liquid-nitrogen
LoD	limit-of-detection
LOR	lift-off resist
LPC	laser pressure catapulting
LPCVD	low-pressure chemical vapor deposition
LSC	laser scanning cytometry
LSN	low-stress silicon nitride
LT-SFM	low-temperature scanning force microscope
LT-SPM	low-temperature scanning probe microscopy
LT-STM	low-temperature scanning tunneling microscope
LT	low-temperature
LTM	laser tracking microrheology
LTO	low-temperature oxide
LTRS	laser tweezers Raman spectroscopy
LUMO	lowest unoccupied molecular orbital
LVDT	linear variable differential transformer

M

MALDI	matrix assisted laser desorption ionization
MAP	manifold absolute pressure
MAPK	mitogen-activated protein kinase
MAPL	molecular assembly patterning by lift-off
MBE	molecular-beam epitaxy
MC	microcantilever
MC	microcapillary
MCM	multi-chip module
MD	molecular dynamics
ME	metal-evaporated
MEMS	microelectromechanical system
MExFM	magnetic exchange force microscopy
MFM	magnetic field microscopy
MFM	magnetic force microscope
MFM	magnetic force microscopy
MHD	magnetohydrodynamic
MIM	metal–insulator–metal
MIMIC	micromolding in capillaries
MLE	maximum likelihood estimator
MOCVD	metalorganic chemical vapor deposition
MOEMS	microoptoelectromechanical system
MOS	metal–oxide–semiconductor
MOSFET	metal–oxide–semiconductor field-effect transistor
MP	metal particle
MPTMS	mercaptopropyltrimethoxysilane
MRFM	magnetic resonance force microscopy
MRFM	molecular recognition force microscopy
MRI	magnetic resonance imaging
MRP	molecular recognition phase
MscL	mechanosensitive channel of large conductance
MST	microsystem technology
MT	microtubule
mTAS	micro total analysis system
MTTF	mean time to failure
MUMP	multiuser MEMS process
MVD	molecular vapor deposition
MWCNT	multiwall carbon nanotube
MWNT	multiwall nanotube
MYD/BHW	Muller–Yushchenko–Derjaguin/Burgess–Hughes–White

N

NA	numerical aperture
NADIS	nanoscale dispensing
NASA	National Aeronautics and Space Administration
NC-AFM	noncontact atomic force microscopy
NEMS	nanoelectromechanical system
NGL	next-generation lithography
NHS	*N*-hydroxysuccinimidyl
NIH	National Institute of Health
NIL	nanoimprint lithography
NIST	National Institute of Standards and Technology
NMP	no-moving-part
NMR	nuclear magnetic resonance
NMR	nuclear mass resonance
NNI	National Nanotechnology Initiative

NOEMS	nanooptoelectromechanical system
NP	nanoparticle
NP	nanoprobe
NSF	National Science Foundation
NSOM	near-field scanning optical microscopy
NSTC	National Science and Technology Council
NTA	nitrilotriacetate
nTP	nanotransfer printing

O

ODA	octadecylamine
ODDMS	*n*-octadecyldimethyl(dimethylamino)silane
ODMS	*n*-octyldimethyl(dimethylamino)silane
ODP	octadecylphosphonate
ODTS	octadecyltrichlorosilane
OLED	organic light-emitting device
OM	optical microscope
OMVPE	organometallic vapor-phase epitaxy
OS	optical stretcher
OT	optical tweezers
OTRS	optical tweezers Raman spectroscopy
OTS	octadecyltrichlorosilane
oxLDL	oxidized low-density lipoprotein

P

P–V	peak-to-valley
PAA	poly(acrylic acid)
PAA	porous anodic alumina
PAH	poly(allylamine hydrochloride)
PAPP	*p*-aminophenyl phosphate
Pax	paxillin
PBC	periodic boundary condition
PBS	phosphate-buffered saline
PC	polycarbonate
PCB	printed circuit board
PCL	polycaprolactone
PCR	polymerase chain reaction
PDA	personal digital assistant
PDMS	polydimethylsiloxane
PDP	2-pyridyldithiopropionyl
PDP	pyridyldithiopropionate
PE	polyethylene
PECVD	plasma-enhanced chemical vapor deposition
PEEK	polyetheretherketone
PEG	polyethylene glycol
PEI	polyethyleneimine
PEN	polyethylene naphthalate
PES	photoemission spectroscopy
PES	position error signal
PET	poly(ethyleneterephthalate)
PETN	pentaerythritol tetranitrate
PFDA	perfluorodecanoic acid
PFDP	perfluorodecylphosphonate
PFDTES	perfluorodecyltriethoxysilane
PFM	photonic force microscope
PFOS	perfluorooctanesulfonate
PFPE	perfluoropolyether
PFTS	perfluorodecyltricholorosilane
PhC	photonic crystal
PI3K	phosphatidylinositol-3-kinase
PI	polyisoprene
PID	proportional–integral–differential
PKA	protein kinase
PKC	protein kinase C
PKI	protein kinase inhibitor
PL	photolithography
PLC	phospholipase C
PLD	pulsed laser deposition
PMAA	poly(methacrylic acid)
PML	promyelocytic leukemia
PMMA	poly(methyl methacrylate)
POCT	point-of-care testing
POM	polyoxy-methylene
PP	polypropylene
PPD	*p*-phenylenediamine
PPMA	poly(propyl methacrylate)
PPy	polypyrrole
PS-PDMS	poly(styrene-b-dimethylsiloxane)
PS/clay	polystyrene/nanoclay composite
PS	polystyrene
PSA	prostate-specific antigen
PSD	position-sensitive detector
PSD	position-sensitive diode
PSD	power-spectral density
PSG	phosphosilicate glass
PSGL-1	P-selectin glycoprotein ligand-1
PTFE	polytetrafluoroethylene
PUA	polyurethane acrylate
PUR	polyurethane
PVA	polyvinyl alcohol
PVD	physical vapor deposition
PVDC	polyvinylidene chloride
PVDF	polyvinyledene fluoride
PVS	polyvinylsiloxane
PWR	plasmon-waveguide resonance
PZT	lead zirconate titanate

Q

QB	quantum box
QCM	quartz crystal microbalance
QFN	quad flat no-lead
QPD	quadrant photodiode
QWR	quantum wire

R

RBC	red blood cell
RCA	Radio Corporation of America
RF	radiofrequency
RFID	radiofrequency identification
RGD	arginine–glycine–aspartic
RH	relative humidity
RHEED	reflection high-energy electron diffraction
RICM	reflection interference contrast microscopy
RIE	reactive-ion etching
RKKY	Ruderman–Kittel–Kasuya–Yoshida
RMS	root mean square
RNA	ribonucleic acid
ROS	reactive oxygen species
RPC	reverse phase column
RPM	revolutions per minute
RSA	random sequential adsorption
RT	room temperature
RTP	rapid thermal processing

S

SAE	specific adhesion energy
SAM	scanning acoustic microscopy
SAM	self-assembled monolayer
SARS-CoV	syndrome associated coronavirus
SATI	self-assembly, transfer, and integration
SATP	(*S*-acetylthio)propionate
SAW	surface acoustic wave
SB	Schottky barrier
SCFv	single-chain fragment variable
SCM	scanning capacitance microscopy
SCPM	scanning chemical potential microscopy
SCREAM	single-crystal reactive etching and metallization
SDA	scratch drive actuator
SEcM	scanning electrochemical microscopy
SEFM	scanning electrostatic force microscopy
SEM	scanning electron microscope
SEM	scanning electron microscopy
SFA	surface forces apparatus
SFAM	scanning force acoustic microscopy
SFD	shear flow detachment
SFIL	step and flash imprint lithography
SFM	scanning force microscope
SFM	scanning force microscopy
SGS	small-gap semiconducting
SICM	scanning ion conductance microscopy
SIM	scanning ion microscope
SIP	single inline package
SKPM	scanning Kelvin probe microscopy
SL	soft lithography
SLIGA	sacrificial LIGA
SLL	sacrificial layer lithography
SLM	spatial light modulator
SMA	shape memory alloy
SMM	scanning magnetic microscopy
SNOM	scanning near field optical microscopy
SNP	single nucleotide polymorphisms
SNR	signal-to-noise ratio
SOG	spin-on-glass
SOI	silicon-on-insulator
SOIC	small outline integrated circuit
SoS	silicon-on-sapphire
SP-STM	spin-polarized STM
SPM	scanning probe microscope
SPM	scanning probe microscopy
SPR	surface plasmon resonance
sPROM	structurally programmable microfluidic system
SPS	spark plasma sintering
SRAM	static random access memory
SRC	sampling rate converter
SSIL	step-and-stamp imprint lithography
SSRM	scanning spreading resistance microscopy
STED	stimulated emission depletion
SThM	scanning thermal microscope
STM	scanning tunneling microscope
STM	scanning tunneling microscopy
STORM	statistical optical reconstruction microscopy
STP	standard temperature and pressure
STS	scanning tunneling spectroscopy
SUN	Sad1p/UNC-84
SWCNT	single-wall carbon nanotube
SWCNT	single-walled carbon nanotube
SWNT	single wall nanotube
SWNT	single-wall nanotube

T

TA	tilt angle
TASA	template-assisted self-assembly
TCM	tetracysteine motif
TCNQ	tetracyanoquinodimethane
TCP	tricresyl phosphate
TEM	transmission electron microscope
TEM	transmission electron microscopy
TESP	tapping mode etched silicon probe
TGA	thermogravimetric analysis
TI	Texas Instruments
TIRF	total internal reflection fluorescence
TIRM	total internal reflection microscopy
TLP	transmission-line pulse
TM	tapping mode
TMAH	tetramethyl ammonium hydroxide
TMR	tetramethylrhodamine
TMS	tetramethylsilane

TMS	trimethylsilyl
TNT	trinitrotoluene
TP	track pitch
TPE-FCCS	two-photon excitation fluorescence cross-correlation spectroscopy
TPI	threads per inch
TPMS	tire pressure monitoring system
TR	torsional resonance
TREC	topography and recognition
TRIM	transport of ions in matter
TSDC	thermally stimulated depolarization current
TTF	tetrathiafulvalene
TV	television

U

UAA	unnatural AA
UHV	ultrahigh vacuum
ULSI	ultralarge-scale integration
UML	unified modeling language
UNCD	ultrananocrystalline diamond
UV	ultraviolet
UVA	ultraviolet A

V

VBS	vinculin binding site
VCO	voltage-controlled oscillator
VCSEL	vertical-cavity surface-emitting laser
vdW	van der Waals
VHH	variable heavy–heavy
VLSI	very large-scale integration
VOC	volatile organic compound
VPE	vapor-phase epitaxy
VSC	vehicle stability control

X

XPS	x-ray photon spectroscopy
XRD	x-ray powder diffraction

Y

YFP	yellow fluorescent protein

Z

Z-DOL	perfluoropolyether

1. Introduction to Nanotechnology

Bharat Bhushan

A biological system can be exceedingly small. Many of the cells are very tiny, but they are very active; they manufacture various substances; they walk around; they wiggle; and they do all kinds of marvelous things – all on a very small scale. Also, they store information. Consider the possibility that we too can make a thing very small which does what we want – that we can manufacture an object that maneuvers at that level.

(From the talk *There's Plenty of Room at the Bottom*, delivered by Richard P. Feynman at the annual meeting of the American Physical Society at the California Institute of Technology; Pasadena, December 29, 1959).

1.1 Nanotechnology – Definition and Examples

Nanotechnology literally means any technology on a nanoscale that has applications in the real world. Nanotechnology encompasses the production and application of physical, chemical, and biological systems at scales ranging from individual atoms or molecules to submicron dimensions, as well as the integration of the resulting nanostructures into larger systems. Nanotechnology is likely to have a profound impact on our economy and society in the early 21st century, comparable to that of semiconductor technology, information technology, or cellular and molecular biology. Science and technology research in nanotechnology promises breakthroughs in areas such as materials and manufacturing, nanoelectronics, medicine and healthcare, energy, biotechnology, information technology, and national security. It is widely felt that nanotechnology will be the next Industrial Revolution.

Nanometer-scale features are mainly built up from their elemental constituents. Examples include chemical synthesis, spontaneous self-assembly of molecular clusters (molecular self-assembly) from simple reagents in solution, biological molecules (e.g., DNA) used as building blocks for production of three-dimensional nanostructures, and quantum dots (nanocrystals) of arbitrary diameter (about $10–10^5$ atoms). The definition of a nanoparticle is an aggregate of atoms bonded together with a radius between 1 and 100 nm. It typically consists of $10–10^5$ atoms. A variety of vacuum deposition and nonequilibrium-plasma chemistry techniques are used to produce layered nanocomposites and nanotubes. Atomically controlled structures are produced using molecular-beam epitaxy and organometallic vapor-phase epitaxy. Micro- and nanosystem components are fabricated using top-down lithographic and nonlithographic fabrication techniques and range in size from micro- to nanometers. Continued improvements in lithography for use in the production of nanocomponents have resulted in line widths as small as 10 nm in experimental prototypes. The nanotechnology field, in addition to the fabrication of nanosystems, provides

impetus for the development of experimental and computational tools.

The discovery of novel materials, processes, and phenomena at the nanoscale and the development of new experimental and theoretical techniques for research provide fresh opportunities for the development of innovative nanosystems and nanostructured materials. The properties of materials at the nanoscale can be very different from those at a larger scale. When the dimension of a material is reduced from a large size, the properties remain the same at first, then small changes occur, until finally when the size drops below 100 nm, dramatic changes in properties can occur. If only one length of a three-dimensional nanostructure is of nanodimension, the structure is referred to as a quantum well; if two sides are of nanometer length, the structure is referred to as a quantum wire. A quantum dot has all three dimensions in the nano range. The term *quantum* is associated with these three types of nanostructures because the changes in properties arise from the quantum-mechanical nature of physics in the domain of the ultrasmall. Materials can

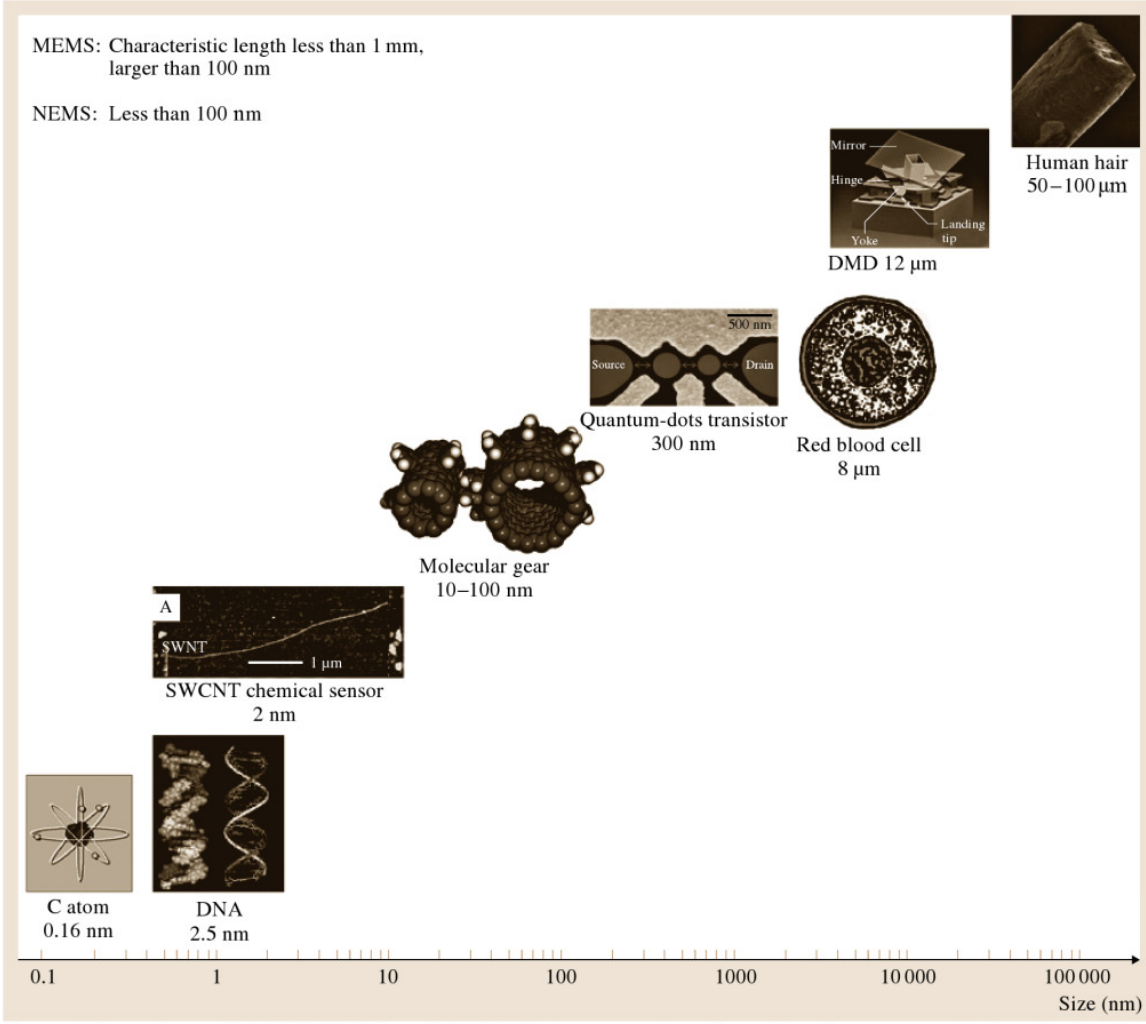

Fig. 1.1 Dimensions of MEMS/NEMS and BioNEMS in perspective. Examples shown are a single-walled carbon nanotube (SWCNT) chemical sensor [1.1], molecular dynamic simulations of carbon-nanotube-based gears [1.2], quantum-dot transistor obtained from [1.3], and digital microdevice (DMD) obtained from www.dlp.com. For comparison, dimensions and weights of various biological objects found in nature are also presented

Table 1.1 Characteristic dimensions and weights in perspective

Characteristic dimensions in perspective	
NEMS characteristic length	< 100 nm
MEMS characteristic length	< 1 mm and > 100 nm
SWCNT chemical sensor	≈ 2 nm
Molecular gear	≈ 10 nm
Quantum-dot transistor	300 nm
Digital micromirror	12 000 nm
Individual atoms	Typically a fraction of a nm in diameter
DNA molecules	≈ 2.5 nm wide
Biological cells	In the range of thousands of nm in diameter
Human hair	≈ 75 000 nm in diameter
Weight in perspective	
NEMS built with cross-sections of about 10 nm	As low as 10^{-20} N
Micromachine silicon structure	As low as 1 nN
Eyelash	≈ 100 nN
Water droplet	≈ 10 μN

be nanostructured for new properties and novel performance. This field is opening new avenues in science and technology.

Micro- and nanosystems include micro/nanoelectromechanical systems (MEMS/NEMS). MEMS refers to microscopic devices that have a characteristic length of less than 1 mm but more than 100 nm and that combine electrical and mechanical components. NEMS refers to nanoscopic devices that have a characteristic length of less than 100 nm and that combine electrical and mechanical components. In mesoscale devices, if the functional components are on the micro- or nanoscale, they may be referred to as MEMS or NEMS, respectively. These are referred to as intelligent miniaturized systems, comprising sensing, processing, and/or actuating functions and combining electrical and mechanical components. The acronym MEMS originated in the USA. The term commonly used in Europe is *microsystem technology* (MST), and in Japan the term *micromachines* is used. Another term generally used is micro/nanodevices. The terms MEMS/NEMS are also now used in a broad sense and include electrical, mechanical, fluidic, optical, and/or biological function. MEMS/NEMS for optical applications are referred to as micro/nanooptoelectromechanical systems (MOEMS/NOEMS). MEMS/NEMS for electronic applications are referred to as radiofrequency MEMS/NEMS (RF-MEMS/RF-NEMS). MEMS/NEMS for biological applications are referred to as bioMEMS/bioNEMS.

To put the dimensions of MEMS/NEMS and BioNEMS in perspective, see Fig. 1.1 and Table 1.1. Individual atoms are typically a fraction of a nanometer in diameter, DNA molecules are about 2.5 nm wide, biological cells are in the range of thousands of nm in diameter, and human hair is about 75 μm in diameter. The smallest length of BioNEMS shown in the figure is about 2 nm, NEMS ranges in size from 10 to 300 nm, and the size of MEMS is 12 000 nm. The mass of a micromachined silicon structure can be a low as 1 nN, and NEMS can be built with mass as low as 10^{-20} N with cross-sections of about 10 nm. In comparison, the mass

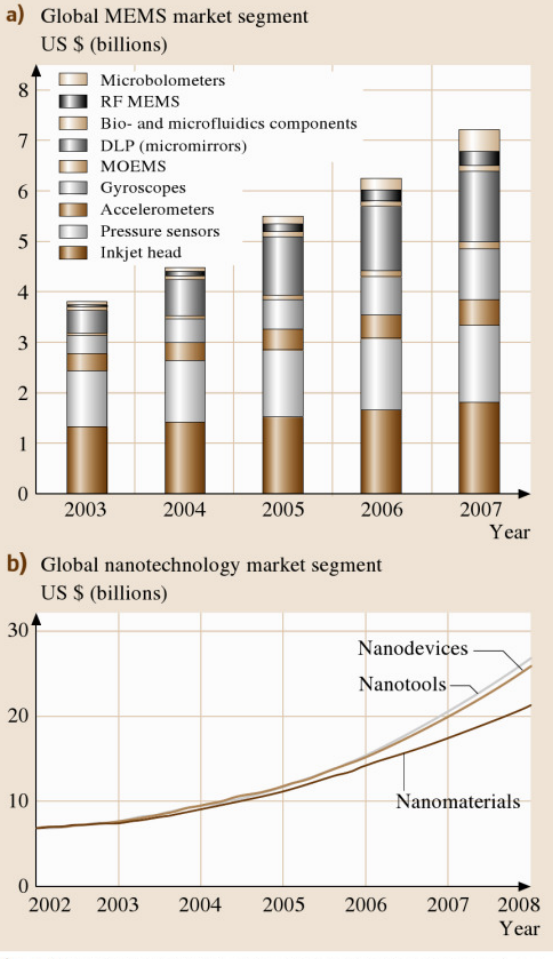

Fig. 1.2 Global MEMS and nanotechnology market segments (DLP – digital light processing)

of a drop of water is about 10 μN, and the mass of an eyelash is about 100 nN.

MEMS/NEMS and BioMEMS/BioNEMS are expected to have a major impact on our lives, comparable to that of semiconductor technology, information technology, or cellular and molecular biology [1.4, 5]. MEMS/NEMS and BioMEMS/BioNEMS are used in electromechanical, electronics, information/communication, chemical, and biological applications. The MEMS industry in 2004 was worth about US$ 4.5 billion, with a projected annual growth rate of 17% (Fig. 1.2) [1.6]. The NEMS industry was worth about US$ 10 billion in 2004, mostly in nanomaterials (Fig. 1.2) [1.7]. Growth of Si-based MEMS/NEMS may slow down and that of nonsilicon MEMS may pick up during the next decade. It is expected to expand in this decade, for nanomaterials and biomedical applications as well as nanoelectronics or molecular electronics. For example, miniaturized diagnostics could be implanted for early diagnosis of illness. Targeted drug-delivery devices are under development. Due to the enabling nature of these systems and because of the significant impact they can have on both commercial and defense applications, industry as well as federal governments have taken special interest in seeing growth in this field nurtured. MEMS/NEMS and BioMEMS/BioNEMS are the next logical step in the *silicon revolution*.

1.2 Background and Research Expenditures

On December 29, 1959 at the California Institute of Technology, Nobel Laureate *Richard P. Feynman* gave a talk at the Annual Meeting of the American Physical Society that has become one of the 20th century's classic science lectures, entitled *There's Plenty of Room at the Bottom* [1.8]. He presented a technological vision of extreme miniaturization in 1959, several years before the word *chip* became part of the lexicon. He talked about the problem of manipulating and controlling things on a small scale. Extrapolating from known physical laws, Feynman envisioned a technology using the ultimate toolbox of nature, building nanoobjects atom by atom or molecule by molecule. Since the 1980s, many inventions and discoveries in the fabrication of nanoobjects have been testaments to his vision. In recognition of this reality, the National Science and Technology Council (NSTC) of the White House created the Interagency Working Group on Nanoscience, Engineering, and Technology (IWGN) in 1998. In a January 2000 speech at the same institute, President W. J. Clinton talked about the exciting promise of *nanotechnology* and the importance of expanding research in nanoscale science and technology more broadly. Later that month, he announced in his State of the Union Address an ambitious US$ 497 million federal, multiagency National Nanotechnology Initiative (NNI) in the fiscal year 2001 budget, and made the NNI a top science and technology priority [1.9, 10]. The objective of this initiative was to form a broad-based coalition in which academia, the private sector, and local, state, and federal governments work together to push the envelop of nanoscience and nanoengineering to reap nanotechnology's potential social and economic benefits.

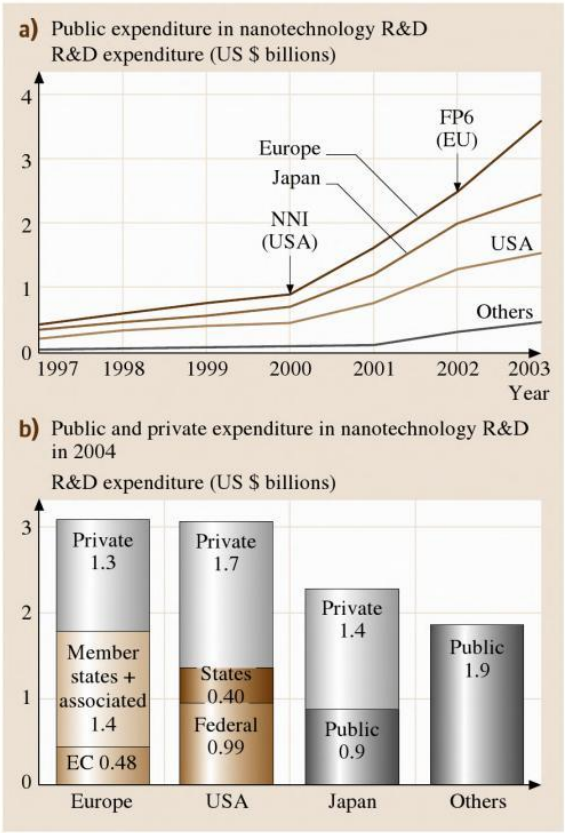

Fig. 1.3a,b Breakdown of expenditure in nanotechnology R&D (**a**) around the world (source: European Commission, 2003), and (**b**) by public and private resources in 2004 (source: European Commission, 2005; figures for private sources based upon data from Lux Research)

Funding in the USA has continued to increase. In January 2003, the US Senate introduced a bill to establish a National Nanotechnology Program. On December 3, 2003, President George W. Bush signed into law the 21st Century Nanotechnology Research and Development Act. This legislation put into law programs and activities supported by the National Nanotechnology Initiative. The bill gave nanotechnology a permanent home in the federal government and authorized US$ 3.7 billion to be spent in the 4 year period beginning in October 2005 for nanotechnology initiatives at five federal agencies. The funds would provide grants to researchers, coordinate research and development (R&D) across five federal agencies [the National Science Foundation (NSF), the Department of Energy (DOE), the National Aeronautics and Space Administration (NASA), the National Institute of Standards and Technology (NIST), and the Environmental Protection Agency (EPA)], establish interdisciplinary research centers, and accelerate technology transfer into the private sector. In addition, the Departments of Defense (DOD), Homeland Security, Agriculture, and Justice as well as the National Institutes of Health (NIH) also fund large R&D activities. They currently account for more than one-third of the federal budget for nanotechnology.

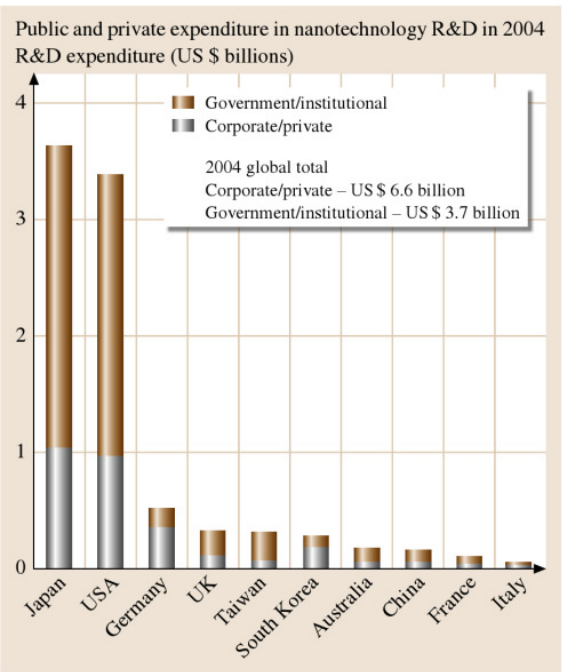

Fig. 1.4 Breakdown of public and private expenditures in nanotechnology R&D in 2004 in various countries (after [1.7])

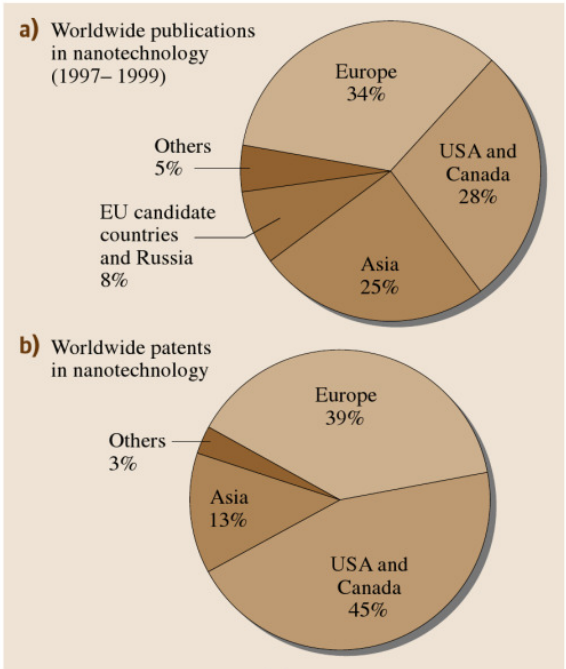

Fig. 1.5a,b Breakdown of (**a**) worldwide publications and (**b**) worldwide patents (source: European Commission, 2003)

The European Union (EU) made nanosciences and nanotechnologies a priority in the Sixth Framework Program (FP6) in 2002 for the period 2003–2006. There were also small dedicated funds in FP4 and FP5 before. FP6 was tailored to help better structure European research and to cope with the strategic objectives set out in Lisbon in 2000. Japan identified nanotechnology as one of its main research priorities in 2001. The funding levels increased sharply from US$ 400 million in 2001 to around US$ 950 million in 2004. In 2003, South Korea embarked upon a 10 year program with around US$ 2 billion of public funding, and Taiwan has committed around US$ 600 million of public funding over 6 years. Singapore and China are also investing on a large scale. Russia is well funded as well.

Figure 1.3a shows the public expenditure breakdown of nanotechnology R&D around the world, with about US$ 5 billion in 2004, coming approximately equally from the USA, Japan, and Europe. Next we compare public expenditure on a per-capita basis. The average expenditures per capita for the USA, the EU-

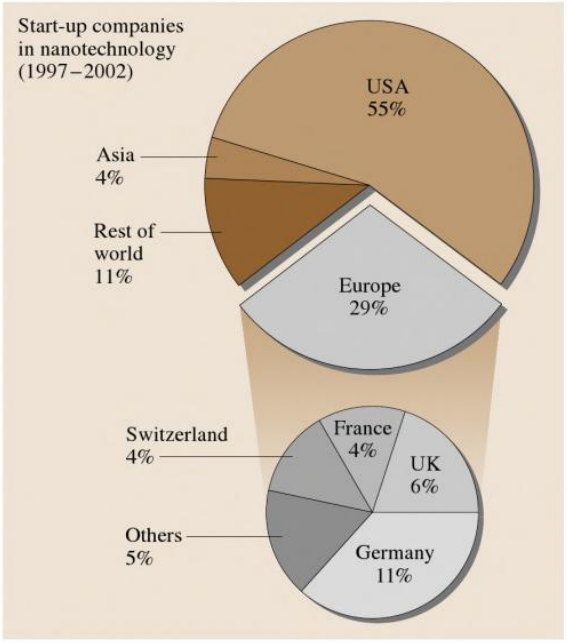

Fig. 1.6 Breakdown of start-up companies around the world (1997–2002) (source: CEA, Bureau d'Etude Marketing) ▶

25, and Japan are about US$ 3.7 billion, US$ 2.4 billion, and US$ 6.2 billion, respectively [1.11]. Figure 1.3b shows the breakdown of expenditure in 2004 by public and private sources, with more than US$ 10 billion spent in nanotechnology research. Two-thirds of this came from corporate and private funding. Private expenditure in the USA and Japan was slightly larger than that from public sources, whereas in Europe it was about one-third. Figure 1.4 shows the public and private expenditure breakdown in 2004 in various countries. Japan and USA had the largest expenditure, followed by Germany, Taiwan, South Korea, the UK, Australia, China, France, and Italy. Figure 1.5 shows a breakdown of worldwide publications and patents. USA and Canada led, followed by Europe and Asia. Figure 1.6 shows the breakdown in start-up companies around the world (1997–2002). Entrepreneurship in USA is clearly evident, followed by Europe.

1.3 Lessons from Nature (Biomimetics)

The word nanotechnology is a relatively new word, but it is not an entirely new field. Nature has gone through evolution over the 3.8 billion years since life is estimated to have appeared on Earth. Nature has many materials, objects, and processes which function from the macroscale to nanoscale [1.9]. Understanding the functions provided by these objects and processes can guide us to imitate and produce nanomaterials, nanodevices, and processes. Biologically inspired design, adaptation or derivation from nature is referred to as *biomimetics*, a term coined by the polymath Otto Schmitt in 1957. Biomimetics is derived from the Greek word *biomimesis*. Other terms used include bionics, biomimicry, and biognosis. The term biomimetics is relatively new; however, our ancestors looked to nature for inspiration and the development of various materials and devices many centuries ago [1.12, 13]. There are a large number of objects, including bacteria, plants, land and aquatic animals, seashells, and spider web, with properties of commercial interest. Figure 1.7 provides an overview of various objects from nature and their selected functions. Figure 1.8 shows a montage of some examples from nature, which serve as the inspiration for various technological developments.

The flagella of bacteria rotate at over 10 000 rpm [1.14]. This is an example of a biological molecular machine. The flagella motor is driven by the proton flow caused by the electrochemical potential differences across the membrane. The diameter of the bearing is about 20–30 nm, with an estimated clearance of ≈ 1 nm.

Several billions years ago, molecules began organizing into complex structures that could support life. Photosynthesis harnesses solar energy to support plant life. Molecular ensembles present in plant leaves, which include light-harvesting molecules such as chlorophyll, arranged within the cells (on the nanometer to micrometer scales), capture light energy and convert it into the chemical energy that drives the biochemical machinery of plant cells. Live organs use chemical energy in the body. This technology is being exploited for solar energy applications.

Some natural surfaces, including the leaves of water-repellent plants such as lotus, are known to be superhydrophobic and self-cleaning due to hierarchical roughness (microbumps superimposed with nanostructure) and the presence of a wax coating [1.15–19]. Roughness-induced superhydrophobic

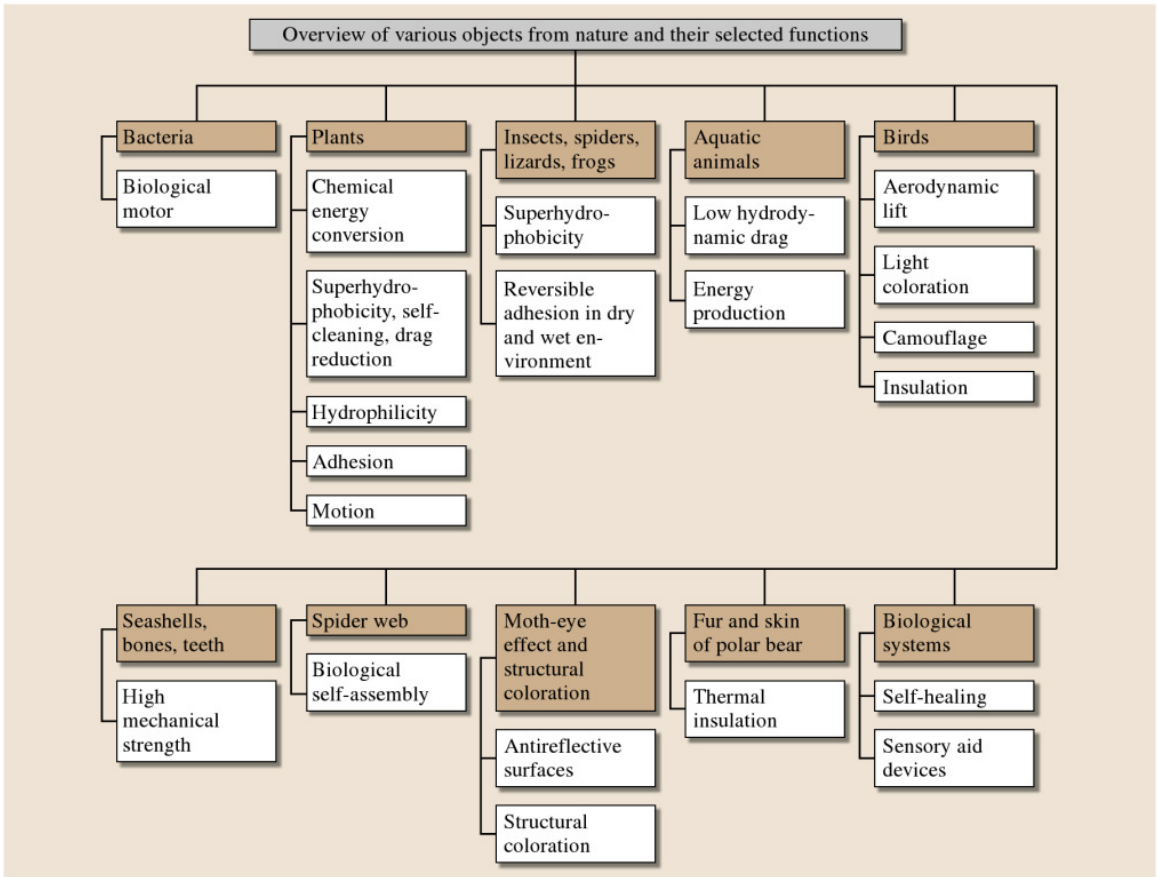

Fig. 1.7 Overview of various objects from nature and their selected function (after [1.13])

and self-cleaning surfaces are of interest in various applications, including self-cleaning windows, windshields, exterior paints for buildings and navigation ships, utensils, roof tiles, textiles, and applications requiring a reduction of drag in fluid flow, e.g., in micro/nanofluidics. Superhydrophobic surfaces can also be used for energy conversion and conservation [1.20]. Nonwetting surfaces also reduce stiction at contacting interfaces in machinery [1.21,22].

The leg attachment pads of several creatures, including many insects (e.g., beetles and flies), spiders, and lizards (e.g., geckoes), are capable of attaching to a variety of surfaces and are used for locomotion [1.23]. Biological evolution over a long period of time has led to the optimization of their leg attachment systems. The attachment pads have the ability to cling to different smooth and rough surfaces and detach at will [1.24,25]. This dynamic attachment ability is referred to as reversible adhesion or smart adhesion. Replication of the characteristics of gecko feet would enable the development of a superadhesive polymer tape capable of clean, dry adhesion which is reversible [1.25–27]. (It should be noted that common manmade adhesives such as tape or glue involve the use of wet adhesives that permanently attach two surfaces.) The reusable gecko-inspired adhesives have the potential for use in everyday objects such as tapes, fasteners, and toys, and in high technology such as microelectronic and space applications. Replication of the dynamic climbing and peeling ability of geckoes could find use in the treads of wall-climbing robots. Incidentally, *Velcro* was invented based on the action of the hooked seeds of the burdock plant [1.28].

Many aquatic animals can move in water at high speeds with low energy input. Drag is a major hindrance to movement. Most shark species move through water with high efficiency and maintain buoyancy. Through its ingenious design, their skin turns out to be an essen-

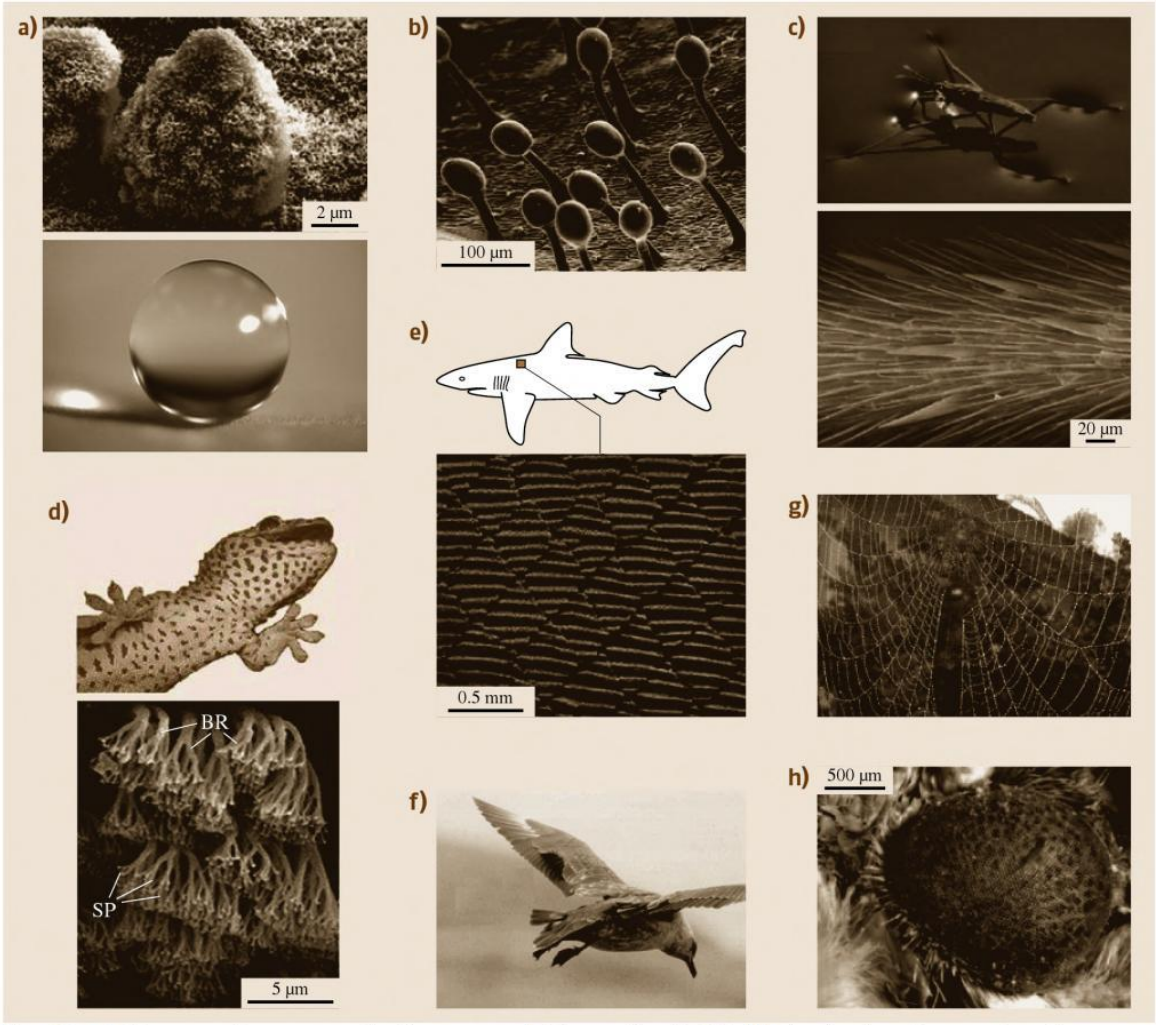

Fig. 1.8a–h Montage of some examples from nature: (**a**) lotus effect [1.30], (**b**) glands of carnivorous plant that secrete adhesive to trap insects [1.17], (**c**) water strider walking on water [1.31], (**d**) gecko foot exhibits reversible adhesion [1.32] (BR – branch, SP – spatula), (**e**) scale structure of shark reduces drag [1.33], (**f**) wings of a bird in landing approach, (**g**) spider web made of silk material [1.12], (**h**) moth's eyes are antireflective [1.34]

tial aid to this behavior by reducing friction drag and autocleaning ectoparasites from their surface [1.29]. The very small individual tooth-like scales of shark skin, called dermal denticles, are ribbed with longitudinal grooves, which result in water moving very efficiently over their surface. The scales also minimize the collection of barnacles and algae. Speedo created the whole-body swimsuit called Fastskin, modeled on shark skin, for elite swimming. Boat, ship, and aircraft manufacturers are trying to mimic shark skin to reduce friction drag and minimize the attachment of organisms to their bodies. In addition, mucus on the skin of aquatic animals, including sharks, acts as an osmotic barrier against the salinity of seawater and protects the creature from parasites and infections. It also acts as a drag-reducing agent. Artificial derivatives of fish mucus (polymer additives) are used to propel crude oil in the Alaska pipeline. The compliant skin of dolphins allows them to swim at high speed. By interacting with the water flowing over the body's surface it stabilizes the flow and delays the transition to turbulence. Dolphins possess an optimum shape for drag reduc-

tion of submerged bodies. Submarines use the shape of dolphins. The streamlined form of boxfish (*Ostracion meleagris*) has inspired Mercedes Benz's bionic concept car with low aerodynamic drag. The beak of the kingfisher was used to model the nose cone of the Japanese Shinkansen bullet train. Power is generated by the scalloped edges of a humpback whale, and this design is exploited for wind turbine blades.

Bird feathers make the body water repellant, and movable flaps create wing and tail for aerodynamic lift during flying [1.29]. Birds and butterflies create brilliant hues by refracting light through millions of repeated structures that bend light to make certain colors. Seashells are natural nanocomposites with a laminated structure and exhibit superior mechanical properties. Spider web consists of silk fiber which is very strong. The materials and structures used in these objects have led to the development of various materials and fibers with high mechanical strength. Moth eyes have a multifaceted surface on the nanoscale and are structured to reduce reflection. This antireflective design led to the discovery of antireflective surfaces [1.35].

A remarkable property of biological tissues is their ability for self-healing. In biological systems, chemical signals released at the site of a fracture initiate a systemic response that transports repair agents to the site of an injury and promotes healing. Various artificial self-healing materials are being developed [1.36]. Human skin is sensitive to impact, leading to purple-colored marks in areas that are hit. This idea has led to the development of coatings indicating impact damage [1.12]. Another interesting and promising idea involves the application of an array of sensors to develop an *artificial nose* or an *artificial tongue*.

Other lessons from nature include the wings of flying insects, abalone shell with high-impact ceramic properties, strong spider silk, ultrasonic detection by bats, infrared detection by beetles, and silent flying of owls because of frayed feathers on the edges of their wings.

1.4 Applications in Different Fields

Science and technology continue to move forward in making the fabrication of micro/nanodevices and systems possible for a variety of industrial, consumer, and biomedical applications [1.37, 38]. A variety of MEMS devices have been produced, and some are in commercial use [1.39–48]. A variety of sensors are used in industrial, consumer, defense, and biomedical applications. Various micro/nanostructures and micro/nanocomponents are used in microinstruments and other industrial applications such as micromirror arrays. The largest *killer* MEMS applications include accelerometers (some 90 million units installed in vehicles in 2004), silicon-based piezoresistive pressure sensors for manifold absolute pressure sensing for engines and for disposable blood pressure sensors (about 30 million and 25 million units, respectively), capacitive pressure sensors for tire pressure measurements (about 37 million units in 2005), thermal inkjet printheads (about 500 million units in 2004), micromirror arrays for digital projection displays (about US$ 700 million revenue in 2004), and optical cross-connections in telecommunications. Other applications of MEMS devices include chemical/biosensors and gas sensors, microresonators, infrared detectors and focal-plane arrays for Earth observation, space science, and missile defense applications, picosatellites for space applications, fuel cells, and many hydraulic, pneumatic, and other consumer products. MEMS devices are also being pursued for use in magnetic storage systems [1.49], where they are being developed for supercompact and ultrahigh-recording-density magnetic disk drives.

NEMS are produced by nanomachining in a typical top–down approach and bottom–up approach, largely relying on nanochemistry [1.50–56]. Examples of NEMS include microcantilevers with integrated sharp nanotips for scanning tunneling microscopy (STM) and atomic force microscopy (AFM), quantum corrals formed using STM by placing atoms one by one, AFM cantilever arrays for data storage, AFM tips for nanolithography, dip-pen lithography for printing molecules, nanowires, carbon nanotubes, quantum wires (QWRs), quantum boxes (QBs), quantum-dot transistors, nanotube-based sensors, biological (DNA) motors, molecular gears formed by attaching benzene molecules to the outer walls of carbon nanotubes, devices incorporating nm-thick films [e.g., in giant magnetoresistive (GMR) read/write magnetic heads and magnetic media] for magnetic rigid disk drives and magnetic tape drives, nanopatterned magnetic rigid disks, and nanoparticles (e.g., nanoparticles in magnetic tape substrates and magnetic particles in magnetic tape coatings).

Nanoelectronics can be used to build computer memory using individual molecules or nanotubes to

store bits of information, molecular switches, molecular or nanotube transistors, nanotube flat-panel displays, nanotube integrated circuits, fast logic gates, switches, nanoscopic lasers, and nanotubes as electrodes in fuel cells.

BioMEMS/BioNEMS are increasingly used in commercial and defense applications [1.57–63]. They are used for chemical and biochemical analyses (biosensors) in medical diagnostics (e.g., DNA, RNA, proteins, cells, blood pressure and assays, and toxin identification) [1.63, 64], tissue engineering [1.65], and implantable pharmaceutical drug delivery [1.66, 67]. Biosensors, also referred to as biochips, deal with liquids and gases. There are two types of biosensors. A large variety of biosensors are based on micro/nanofluidics. Micro/nanofluidic devices offer the ability to work with smaller reagent volumes and shorter reaction times, and perform analyses multiple times at once. The second type of biosensors includes micro/nanoarrays which perform one type of analysis thousands of times. Micro/nanoarrays are a tool used in biotechnology research to analyze DNA or proteins to diagnose diseases or discover new drugs. Also called DNA arrays, they can identify thousands of genes simultaneously [1.60]. They include a microarray of silicon nanowires, roughly a few nm in size, to selectively bind and detect even a single biological molecule, such as DNA or protein, by using nanoelectronics to detect the slight electrical charge caused by such binding, or a microarray of carbon nanotubes to electrically detect glucose.

After the tragedy of September 11, 2001, concern about biological and chemical warfare has led to the development of handheld units with bio- and chemical sensors for detection of biological germs, chemical or nerve agents, and mustard agents, and chemical precursors to protect subways, airports, water supplies, and the population at large [1.68].

BioMEMS/BioNEMS are also being developed for minimal invasive surgery, including endoscopic surgery, laser angioplasty, and microscopic surgery. Other applications include implantable drug-delivery devices (micro/nanoparticles with drug molecules encapsulated in functionalized shells for site-specific targeting applications) and a silicon capsule with a nanoporous membrane filled with drugs for long-term delivery.

1.5 Various Issues

There is an increasing need for a multidisciplinary, system-oriented approach to the manufacture of micro/nanodevices which function reliably. This can only be achieved through the cross-fertilization of ideas from different disciplines and the systematic flow of information and people among research groups. Common potential failure mechanisms for MEMS/NEMS requiring relative motion that need to be addressed in order to increase their reliability are: adhesion, friction, wear, fracture, fatigue, and contamination [1.21, 22, 69, 70]. Surface micro/nanomachined structures often include smooth and chemically active surfaces. Due to the large surface area to volume ratio in MEMS/NEMS, they are particularly prone to stiction (high static friction) as part of normal operation. Fracture occurs when the load on a microdevice is greater than the strength of the material. Fracture is a serious reliability concern, particularly for brittle materials used in the construction of these components, since it can immediately or would eventually lead to catastrophic failures. Additionally, debris can be formed from the fracturing of microstructures, leading to other failure processes. For less brittle materials, repeated loading over a long period of time causes fatigue that can also lead to the breaking and fracturing of the device. In principle, this failure mode is relatively easy to observe and simple to predict. However, the materials properties of thin films are often not known, making fatigue predictions error prone.

Many MEMS/NEMS devices operate near their thermal dissipation limit. They may encounter hot spots that may cause failures, particularly in weak structures such as diaphragms or cantilevers. Thermal stressing and relaxation caused by thermal variations can create material delamination and fatigue in cantilevers. When exposed to large temperature changes, as experienced in the space environment, bimetallic beams will also experience warping due to mismatched coefficients of thermal expansion. Packaging has been a big problem. The contamination that probably happens in packaging and during storage also can strongly influence the reliability of MEMS/NEMS. For example, a dust particle that lands on one of the electrodes of a comb drive can cause catastrophic failure. There are no MEMS/NEMS fabrications standards, which make it difficult to transfer fabrication steps in MEMS/NEMS between foundries.

Obviously, studies of the determination and suppression of active failure mechanisms affecting this new and promising technology are critical to high reliability of MEMS/NEMS and are determining factors for successful practical application.

Adhesion between a biological molecular layer and the substrate, referred to as *bioadhesion*, and reduction of friction and wear of biological layers, biocompatibility, and biofouling for BioMEMS/BioNEMS are important.

Mechanical properties are known to exhibit a dependence on specimen size. Mechanical property evaluation of nanoscale structures is carried out to help design reliable systems since good mechanical properties are of critical importance in such applications. Some of the properties of interest are: Young's modulus of elasticity, hardness, bending strength, fracture toughness, and fatigue life. Finite-element modeling is carried out to study the effects of surface roughness and scratches on stresses in nanostructures. When nanostructures are smaller than a fundamental physical length scale, conventional theory may no longer apply, and new phenomena emerge. Molecular mechanics is used to simulate the behavior of a nanoobject.

The societal, ethical, political, and health/safety implications of nanotechnology are also attracting major attention [1.11]. One of the prime reasons is to avoid some of the public skepticism that surrounded the debate over biotechnology advances such as genetically modified foods, while at the same time dispelling some of the misconceptions the public may already have about nanotechnology. Health/safety issues need to be addressed as well. For example, one key question is what happens to nanoparticles (such as buckyballs or nanotubes) in the environment and whether they are toxic in the human body, if digested.

1.6 Research Training

With the decreasing number of people in Western countries going into science and engineering and the rapid progress being made in nanoscience and nanotechnology, the problem of ensuring a trained workforce is expected to become acute. Education and training are essential to produce a new generation of scientists, engineers, and skilled workers with the flexible and interdisciplinary R&D approach necessary for rapid progress in the nanosciences and nanotechnology [1.71]. The question is being asked: is the traditional separation of academic disciplines into physics, chemistry, biology, and various engineering disciplines meaningful at the nanolevel? Generic skills and entrepreneurship are needed to transfer scientific knowledge into products. Scientists and engineers in cooperation with relevant experts should address the societal, ethical, political, and health/safety implications of their work for society at large.

To increase the pool of students interested in science and technology, science needs to be projected to be exciting at the high-school level. Interdisciplinary curricula relevant for nanoscience and nanotechnology need to be developed. This requires the revamping of education, the development of new courses and course material including textbooks [1.47, 56, 70, 72–74] and instruction manuals, and the training of new instructors.

1.7 Organization of the Handbook

This Handbook integrates knowledge from the fabrication, mechanics, materials science, and reliability points of view. Organization of the Handbook is straightforward. The Handbook is divided into nine parts. The first part of the book includes an introduction to nanostructures, micro/nanofabrication, methods, and materials. The second part introduces various MEMS/NEMS and BioMEMS/BioNEMS devices. The third part introduces scanning probe microscopy. The fourth part provides an overview of bio/nanotribology and bio/nanomechanics, which will prepare the reader to understand the interface reliability in industrial applications. The fifth part provides an overview of molecularly thick films for lubrication. The sixth part focuses on the emerging field of biomimetics, in which one mimics nature to develop products and processes of interest. The seventh part focuses on industrial applications, and the eighth part focuses on micro/nanodevice reliability. The final part focuses on technological convergence from the nanoscale as well as social, ethical, and political implications of nanotechnology.

References

1.1 R.J. Chen, H.C. Choi, S. Bangsaruntip, E. Yenilmex, X. Tang, Q. Wang, Y.L. Chang, H. Dai: An investigation of the mechanisms of electrode sensing of protein adsorption on carbon nanotube devices, J. Am. Chem. Soc. **126**, 1563–1568 (2004)

1.2 D. Srivastava: Computational nanotechnology of carbon nanotubes. In: *Carbon Nanotubes: Science and Applications*, ed. by M. Meyyappan (CRC, Boca Raton 2004) pp. 25–36

1.3 W.G. van der Wiel, S. De Franceschi, J.M. Elzerman, T. Fujisawa, S. Tarucha, L.P. Kauwenhoven: Electron transport through double quantum dots, Rev. Mod. Phys. **75**, 1–22 (2003)

1.4 Anonymous: *Microelectromechanical Systems: Advanced Materials and Fabrication Methods* (National Academy Press, Washington 1997), NMAB-483

1.5 M. Roukes: Nanoelectromechanical systems face the future, Phys. World **14**, 25–31 (2001)

1.6 J.C. Eloy: *Status of the MEMS Industry* (Yole Developpement, Lyon 2005), presented at SPIE Photonics West, San Jose (2005)

1.7 S. Lawrence: Nanotech grows up, Technol. Rev. **108**(6), 31 (2005)

1.8 R.P. Feynman: There's plenty of room at the bottom, Eng. Sci. **23**, 22–36 (1960), http://www.zyvex.com/nanotech/feynman.html

1.9 I. Amato: *Nanotechnology* (2000), http://www.ostp.gov/nstc/html/iwgn/iwgn.public.brochure/welcome.htm or http://www.nsf.gov/home/crssprgm/nano/nsfnnireports.htm

1.10 Anonymous: *National Nanotechnology Initiative* (2000), http://www.ostp.gov/nstc/html/iwgn.fy01budsuppl/nni.pdf or http://www.nsf.gov/home/crssprgm/nano/nsfnnireports.htm

1.11 Anonymous: *Towards a European Strategy for Nanotechnology* (European Commission Research Directorate General, Brussels 2004)

1.12 Y. Bar-Cohen (Ed.): *Biomimetics – Biologically Inspired Technologies* (CRC, Boca Raton 2005)

1.13 B. Bhushan: Biomimetics: Lessons from nature – An overview, Philos. Trans. R. Soc. Lond. Ser. A **367**, 1445–1486 (2009)

1.14 C.J. Jones, S. Aizawa: The bacterial flagellum and flagellar motor: Structure, assembly, and functions, Adv. Microb. Physiol. **32**, 109–172 (1991)

1.15 B. Bhushan, Y.C. Jung: Wetting, adhesion and friction of superhydrophobic and hydrophilic leaves and fabricated micro-/nanopatterned surfaces, J. Phys. D **20**, 225010 (2008)

1.16 K. Koch, B. Bhushan, W. Barthlott: Diversity of structure, morphology, and wetting of plant surfaces, Soft Matter **4**, 1943–1963 (2008)

1.17 K. Koch, B. Bhushan, W. Barthlott: Multifunctional surface structures of plants: An inspiration for biomimetics (invited), Prog. Mater. Sci. **54**, 137–178 (2009)

1.18 M. Nosonovsky, B. Bhushan: *Multiscale Dissipative Mechanisms and Hierarchical Surfaces: Friction, Superhydrophobicity, and Biomimetics* (Springer, Berlin, Heidelberg 2008)

1.19 M. Nosonovsky, B. Bhushan: Roughness-induced superhydrophobicity: A way to design non-adhesive surfaces, J. Phys. D **20**, 225009 (2008)

1.20 M. Nosonovsky, B. Bhushan: Multiscale effects and capillary interactions in functional biomimetic surfaces for energy conversion and green engineering, Philos. Trans. R. Soc. Lond. Ser. A **367**, 1511–1539 (2009)

1.21 B. Bhushan: *Principles and Applications of Tribology* (Wiley, New York 1999)

1.22 B. Bhushan (Ed.): *Introduction to Tribology* (Wiley, New York 2002)

1.23 S. Gorb (Ed.): *Attachment Devices of Insect Cuticle* (Kluwer, Dordrecht 2001)

1.24 K. Autumn, Y.A. Liang, S.T. Hsieh, W. Zesch, W.P. Chan, T.W. Kenny, R. Fearing, R.J. Full: Adhesive force of a single gecko foot-hair, Nature **405**, 681–685 (2000)

1.25 B. Bhushan: Adhesion of multi-level hierarchical attachment systems in gecko feet, J. Adhes. Sci. Technol. **21**, 1213–1258 (2007)

1.26 A.K. Geim, S.V. Dubonos, I.V. Grigorieva, K.S. Novoselov, A.A. Zhukov, S.Y. Shapoval: Microfabricated adhesive mimicking gecko foot-hair, Nat. Mater. **2**, 461–463 (2003)

1.27 B. Bhushan, R.A. Sayer: Surface characterization and friction of a bio-inspired reversible adhesive tape, Microsyst. Technol. **13**, 71–78 (2007)

1.28 S.A. Velcro: Improvements in or relating to a method and a device for producing velvet type fabric, Switzerland Patent 721338 (1995)

1.29 D.W. Bechert, M. Bruse, W. Hage, R. Meyer: Fluid mechanics of biological surfaces and their technological application, Naturwissenschaften **87**, 157–171 (2000)

1.30 B. Bhushan, Y.C. Jung, K. Koch: Micro-, nano-, and hierarchical structures for superhydrophobicity, self-cleaning, and low adhesion, Philos. Trans. R. Soc. Lond. Ser. A **367**, 1631–1672 (2009)

1.31 X.F. Gao, L. Jiang: Biophysics: Water-repellent legs of water striders, Nature **432**, 36 (2004)

1.32 H. Gao, X. Wang, H. Yao, S. Gorb, E. Arzt: Mechanics of hierarchical adhesion structures of geckos, Mech. Mater. **37**, 275–285 (2005)

1.33 W.E. Reif: *Squamation and Ecology of Sharks*, Courier Forschungsinst. Senckenberg, Vol. 78 (Schweizerbart, Stuttgart 1985)

1.34 J. Genzer, K. Efimenko: Recent developments in superhydrophobic surfaces and their relevance to

marine fouling: A review, Biofouling **22**, 339–360 (2006)
1.35 C.G. Bernhard, W.H. Miller, A.R. Möller: The insect corneal nipple array: A biological, broad-band impedance transformer that acts as a antireflection coating, Acta Physiol. Scand. **63**, 1–79 (1965)
1.36 J.P. Youngblood, N.R. Sottos: Bioinspired materials for self-cleaning and self-healing, MRS Bulletin **33**, 732–738 (2008)
1.37 Anonymous: *Small Tech 101 – An Introduction to Micro and Nanotechnology* (Small Times, 2003)
1.38 M. Schulenburg: *Nanotechnology – Innovation for Tomorrow's World* (European Commission Research Directorate General, Brussels 2004)
1.39 R.S. Muller, R.T. Howe, S.D. Senturia, R.L. Smith, R.M. White: *Microsensors* (IEEE, New York 1991)
1.40 I. Fujimasa: *Micromachines: A New Era in Mechanical Engineering* (Oxford Univ. Press, Oxford 1996)
1.41 W.S. Trimmer (Ed.): *Micromachines and MEMS, Classical and Seminal Papers to 1990* (IEEE, New York 1997)
1.42 B. Bhushan: *Tribology Issues and Opportunities in MEMS* (Kluwer, Dordrecht 1998)
1.43 G.T.A. Kovacs: *Micromachined Transducers Sourcebook* (WCB McGraw-Hill, Boston 1998)
1.44 M. Elwenspoek, R. Wiegerink: *Mechanical Microsensors* (Springer, Berlin Heidelberg 2001)
1.45 S.D. Senturia: *Microsystem Design* (Kluwer, Boston 2000)
1.46 T.R. Hsu: *MEMS and Microsystems: Design and Manufacture* (McGraw-Hill, Boston 2002)
1.47 M. Madou: *Fundamentals of Microfabrication: The Science of Miniaturization*, 2nd edn. (CRC, Boca Raton 2002)
1.48 A. Hierlemann: *Integrated Chemical Microsensor Systems in CMOS Technology* (Springer, Berlin Heidelberg 2005)
1.49 B. Bhushan: *Tribology and Mechanics of Magnetic Storage Devices*, 2nd edn. (Springer, Berlin Heidelberg 1996)
1.50 K.E. Drexler: *Nanosystems: Molecular Machinery, Manufacturing and Computation* (Wiley, New York 1992)
1.51 G. Timp (Ed.): *Nanotechnology* (Springer, New York 1999)
1.52 M.S. Dresselhaus, G. Dresselhaus, P. Avouris: *Carbon Nanotubes – Synthesis, Structure, Properties, and Applications* (Springer, Berlin Heidelberg 2001)
1.53 E.A. Rietman: *Molecular Engineering of Nanosystems* (Springer, Berlin, Heidelberg 2001)
1.54 W.A. Goddard, D.W. Brenner, S.E. Lyshevski, G.J. Iafrate (Eds.): *Handbook of Nanoscience, Engineering,and Technology* (CRC, Boca Raton 2002)
1.55 H.S. Nalwa (Ed.): *Nanostructured Materials and Nanotechnology* (Academic, San Diego 2002)
1.56 C.P. Poole, F.J. Owens: *Introduction to Nanotechnology* (Wiley, New York 2003)
1.57 A. Manz, H. Becker (Eds.): *Microsystem Technology in Chemistry and Life Sciences*, Top. Curr. Chem., Vol. 194 (Springer, Berlin, Heidelberg 1998)
1.58 J. Cheng, L.J. Kricka (Eds.): *Biochip Technology* (Harwood, Philadephia 2001)
1.59 M.J. Heller, A. Guttman (Eds.): *Integrated Microfabricated Biodevices* (Marcel Dekker, New York 2001)
1.60 C. Lai Poh San, E.P.H. Yap (Eds.): *Frontiers in Human Genetics* (World Scientific, Singapore 2001)
1.61 C.H. Mastrangelo, H. Becker (Eds.): *Microfluidics and BioMEMS*, Proc. SPIE, Vol. 4560 (SPIE, Bellingham 2001)
1.62 H. Becker, L.E. Locascio: Polymer microfluidic devices, Talanta **56**, 267–287 (2002)
1.63 A. van der Berg (Ed.): *Lab-on-a-Chip: Chemistry in Miniaturized Synthesis and Analysis Systems* (Elsevier, Amsterdam 2003)
1.64 P. Gravesen, J. Branebjerg, O.S. Jensen: Microfluidics – A review, J. Micromech. Microeng. **3**, 168–182 (1993)
1.65 R.P. Lanza, R. Langer, J. Vacanti (Eds.): *Principles of Tissue Engineering*, 2nd edn. (Academic, San Diego 2000)
1.66 K. Park (Ed.): *Controlled Drug Delivery: Challenges and Strategies* (American Chemical Society, Washington 1997)
1.67 P.Å. Öberg, T. Togawa, F.A. Spelman: *Sensors in Medicine and Health Care* (Wiley, New York 2004)
1.68 M. Scott: MEMS and MOEMS for national security applications, Proc. SPIE **4980**, xxxvii–xliv (2003)
1.69 B. Bhushan: *Handbook of Micro/Nanotribology* (CRC, Boca Raton 1999)
1.70 B. Bhushan (Ed.): *Nanotribology and Nanomechanics – An Introduction*, 2nd edn. (Springer, Berlin, Heidelberg 2008)
1.71 Anonymous: Current status and future needs, Proc. Workshop Res. Train. Nanosci. Nanotechnol. (European Commission Research Directorate General, Brussels 2005)
1.72 M. Di Ventra, S. Evoy, J.R. Heflin: *Introduction to Nanoscale Science and Technology* (Springer, Berlin Heidelberg 2004)
1.73 A. Hett: *Nanotechnology – Small Matter, Many Unknowns* (Swiss Reinsurance Company, Zurich 2004)
1.74 M. Köhler, W. Fritzsche: *Nanotechnology* (Wiley, New York 2004)

Part A Nanostructures, Micro-/Nanofabrication and Materials

2. Nanomaterials Synthesis and Applications: Molecule-Based Devices

Françisco M. Raymo

The constituent components of conventional devices are carved out of larger materials relying on physical methods. This top-down approach to engineered building blocks becomes increasingly challenging as the dimensions of the target structures approach the nanoscale. Nature, on the other hand, relies on chemical strategies to assemble nanoscaled biomolecules. Small molecular building blocks are joined to produce nanostructures with defined geometries and specific functions. It is becoming apparent that nature's bottom-up approach to functional nanostructures can be mimicked to produce artificial molecules with nanoscaled dimensions and engineered properties. Indeed, examples of artificial nanohelices, nanotubes, and molecular motors are starting to be developed. Some of these fascinating chemical systems have intriguing electrochemical and photochemical properties that can be exploited to manipulate chemical, electrical, and optical signals at the molecular level. This tremendous opportunity has led to the development of the molecular equivalent of conventional logic gates. Simple logic operations, for example, can be reproduced with collections of molecules operating in solution. Most of these chemical systems, however, rely on bulk addressing to execute combinational and sequential logic operations. It is essential to devise methods to reproduce these useful functions in solid-state configurations and, eventually, with single molecules. These challenging objectives are stimulating the design of clever devices that interface small assemblies of organic molecules with macroscaled and nanoscaled electrodes. These strategies have already produced rudimentary examples of diodes, switches, and transistors based on functional molecular components. The rapid and continuous progress of this exploratory research will, we hope, lead to an entire generation of molecule-based devices that might ultimately find useful applications in a variety of fields, ranging from biomedical research to information technology.

2.1 Chemical Approaches to Nanostructured Materials

The fabrication of conventional devices relies on the assembly of macroscopic building blocks with specific configurations. The shapes of these components are carved out of larger materials by exploiting physical methods. This top-down approach to engineered building blocks is extremely powerful and can deliver effectively and reproducibly microscaled objects. This strategy becomes increasingly challenging, however, as the dimensions of the target structures approach the nanoscale. Indeed, the physical fabrication of nanosized features with subnanometer precision is a formidable technological challenge.

2.1.1 From Molecular Building Blocks to Nanostructures

Nature efficiently builds nanostructures by relying on chemical approaches. Tiny molecular building blocks are assembled with a remarkable degree of structural control in a variety of nanoscaled materials with defined shapes, properties, and functions. In contrast to the top-down physical methods, small components are connected to produce larger objects in these bottom-up chemical strategies. It is becoming apparent that the limitations of the top-down approach to artificial nanostructures can be overcome by mimicking nature's bottom-up processes. Indeed, we are starting to see emerge beautiful and ingenious examples of molecule-based strategies to fabricate chemically nanoscaled building blocks for functional materials and innovative devices.

2.1.2 Nanoscaled Biomolecules: Nucleic Acids and Proteins

Nanoscaled macromolecules play a fundamental role in biological processes [2.1]. Nucleic acids, for example, ensure the transmission and expression of genetic information. These particular biomolecules are linear polymers incorporating nucleotide repeating units (Fig. 2.1a). Each nucleotide has a phosphate bridge and a sugar residue. Chemical bonds between the phosphate of one nucleotide and the sugar of the next ensures the propagation of a polynucleotide strand from the 5′ to the 3′ end. Along the sequence of alternating sugar and phosphate fragments, an extended chain of robust covalent bonds involving carbon, oxygen, and phosphorous atoms forms the main backbone of the polymeric strand.

Every single nucleotide of a polynucleotide strand carries one of the four heterocyclic bases shown in Fig. 2.1b. For a strand incorporating 100 nucleotide repeating units, a total of 4^{100} unique polynucleotide sequences are possible. It follows that nature can fabricate a huge number of closely related nanostructures relying only on four building blocks. The heterocyclic bases appended to the main backbone of alternating phosphate and sugar units can sustain hydrogen bonding and $[\pi \cdots \pi]$ stacking interactions. Hydrogen bonds, formed between [N−H] donors and either N or O acceptors, encourage the pairing of adenine (A) with thymine (T) and of guanine (G) with cytosine (C). The stacking interactions involve attractive contacts between the extended π-surfaces of heterocyclic bases.

In the *B* conformation of deoxyribonucleic acid (DNA), the synergism of hydrogen bonds and $[\pi \cdots \pi]$ stacking glues pairs of complementary polynucleotide strands in fascinating double helical supermolecules (Fig. 2.1c) with precise structural control at the subnanometer level. The two polynucleotide strands wrap around a common axis to form a right-handed double helix with a diameter of ≈ 2 nm. The hydrogen bonded and $[\pi \cdots \pi]$ stacked base pairs lie at the core of the helix with their π-planes perpendicular to the main axis of the helix. The alternating phosphate and sugar units define the outer surface of the double helix. In *B*-DNA, ≈ 10 base pairs define each helical turn corresponding to a rise per turn or helical pitch of ≈ 3 nm. Considering that these molecules can incorporate up to $\approx 10^{11}$ base pairs, extended end-to-end lengths spanning from only few nanometers to hundreds of meters are possible.

Nature's operating principles to fabricate nanostructures are not limited to nucleic acids. Proteins are also built joining simple molecular building blocks, the amino acids, by strong covalent bonds [2.1]. More precisely, nature relies on 20 amino acids differing in their side chains to assemble linear polymers, called polypeptides, incorporating an extended backbone of robust [C−N] and [C−C] bonds (Fig. 2.2a). For a single polymer strand of 100 repeating amino acid units, a total of 20^{100} unique combinations of polypeptide sequences are possible. Considering that proteins can incorporate more than one polypetide chain with over 4000 amino acid residues each, it is obvious that nature can assemble an enormous number of different biomolecules relying on the same fabrication strategy and a relatively small pool of building blocks.

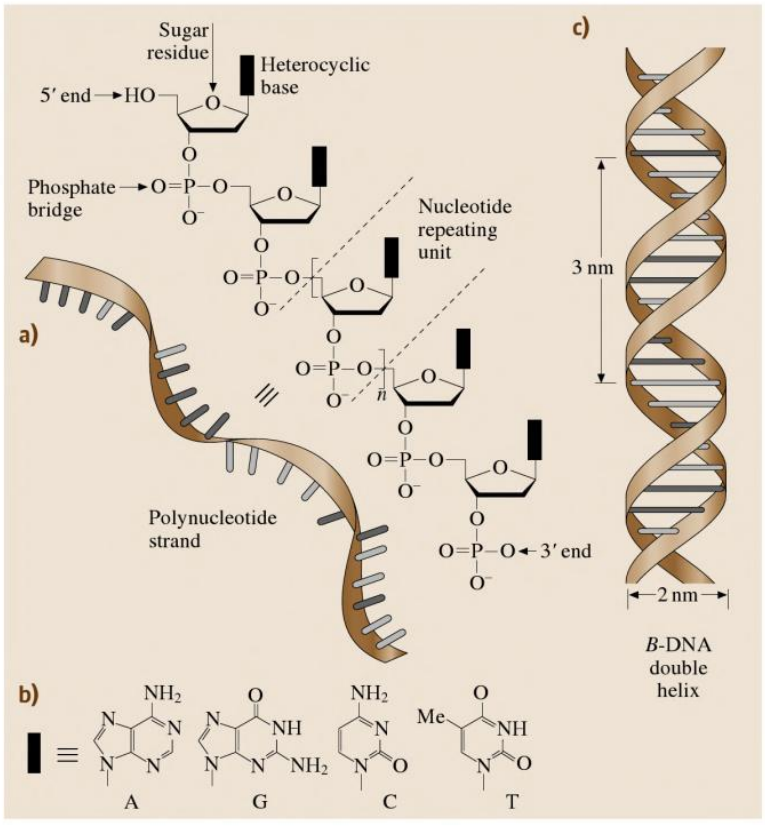

Fig. 2.1a–c A polynucleotide strand (**a**) incorporates alternating phosphate and sugar residues joined by covalent bonds. Each sugar carries one of four heterocyclic bases (**b**). Noncovalent interactions between complementary bases in two independent polynucleotide strands encourage the formation of nanoscaled double helixes (**c**)

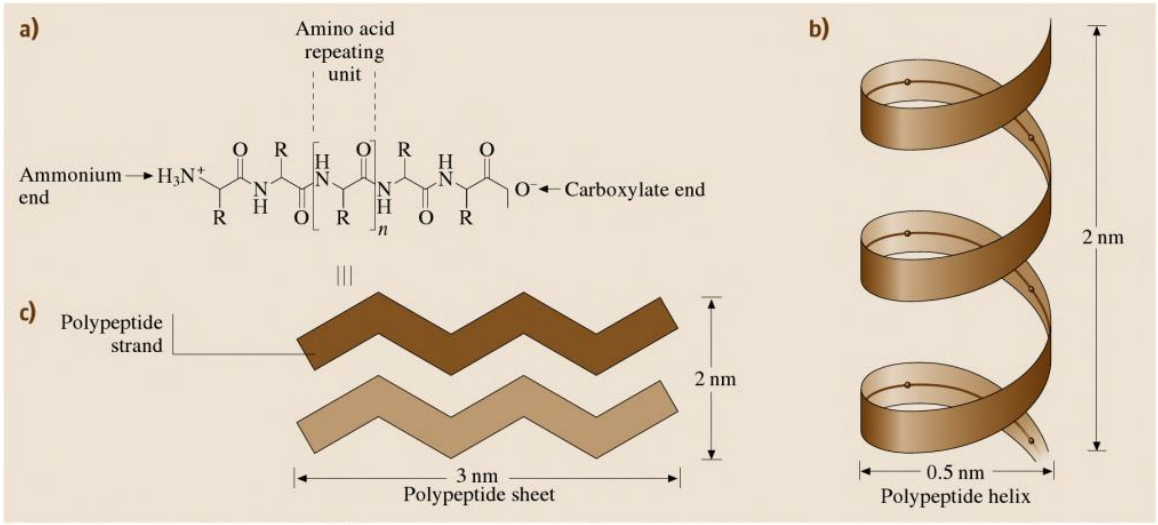

Fig. 2.2a–c A polypeptide strand (**a**) incorporates amino acid residues differing in their side chains and joined by covalent bonds. Hydrogen bonding interactions curl a single polypeptide strand into a helical arrangement (**b**) or lock pairs of strands into nanoscaled sheets (**c**)

The covalent backbones of the polypeptide strands form the main skeleton of a protein molecule. In addition, a myriad of secondary interactions, involving noncovalent contacts between portions of the amino acid residues, control the arrangement of the individual polypeptide chains. Intrastrand hydrogen bonds curl single polypeptide chains around a longitudinal axis in a helical fashion to form tubular nanostructures $\approx 0.5\,\text{nm}$ wide and $\approx 2\,\text{nm}$ long (Fig. 2.2b). Similarly, interstrand hydrogen bonds can align from 2 up to 15 parallel or antiparallel polypeptide chains to form nanoscaled sheets with average dimensions of $2 \times 3\,\text{nm}^2$ (Fig. 2.2c). Multiple nanohelices and/or nanosheets combine into a unique three-dimensional arrangement dictating the overall shape and dimensions of a protein.

2.1.3 Chemical Synthesis of Artificial Nanostructures

Nature fabricates complex nanostructures relying on simple criteria and a relatively small pool of molecular building blocks. Robust chemical bonds join the basic components into covalent scaffolds. Noncovalent interactions determine the three-dimensional arrangement and overall shape of the resulting assemblies. The multitude of unique combinations possible for long sequences of chemically connected building blocks provides access to huge libraries of nanoscaled biomolecules.

Modern chemical synthesis has evolved considerably over the past few decades [2.2]. Experimental procedures to join molecular components with structural control at the picometer level are available. A multitude of synthetic schemes to encourage the formation of chemical bonds between selected atoms in reacting molecules have been developed. Furthermore, the tremendous progress of crystallographic and spectroscopic techniques has provided efficient and reliable tools to probe directly the structural features of artificial inorganic and organic compounds. It follows that designed molecules with engineered shapes and dimensions can be now prepared in a laboratory relying on the many tricks of chemical synthesis and the power of crystallographic and spectroscopic analyses.

The high degree of sophistication reached in this research area translates into the possibility of mimicking the strategies successfully employed by nature to fabricate chemically nanostructures [2.3]. Small molecular building blocks can be synthesized and joined covalently following routine laboratory procedures. It is even possible to design the stereoelectronic properties of the assembling components in order to shape the geometry of the final product with the assistance of noncovalent interactions. For example, five bipyridine building blocks (Fig. 2.3) can be connected in five synthetic steps to produce an oligobipyridine strand [2.4]. The five repeating units are bridged by C−O bonds and can chelate metal cations in the bay regions defined by their two nitrogen atoms. The spontaneous assembly of two organic strands in a double helical arrangement occurs in the presence of inorganic cations. In the resulting helicate, the two oligobipyridine strands wrap around an axis defined by five Cu(I) centers. Each inorganic cation coordinates two bipyridine units with a tetrahedral geometry imposing a diameter of $\approx 0.6\,\text{nm}$ on the nanoscaled helicate [2.5]. The overall length from one end of the helicate to the other is $\approx 3\,\text{nm}$ [2.6]. The analogy between this artificial double helix and the *B*-DNA double helix shown in Fig. 2.1c is obvious. In both instances, a supramolecular glue combines two independent molecular strands into nanostructures with defined shapes and dimensions.

The chemical synthesis of nanostructures can borrow nature's design criteria as well as its molecular building blocks. Amino acids, the basic components of proteins, can be assembled into artificial macrocycles. In the example of Fig. 2.4, eight amino acid residues are joined through the formation of C−N bonds in multiple synthetic steps [2.7]. The resulting covalent backbone defines a circular cavity with a diameter of $\approx 0.8\,\text{nm}$ [2.8]. In analogy to the polypeptide chains of proteins, the amino acid residues of this artificial oligopeptide can sustain hydrogen bonding interactions. It follows that multiple macrocycles can pile on top of each other to form tubular nanostructures. The walls of the resulting nanotubes are maintained in position by the cooperative action of at least eight primary hydrogen bonding contacts per macrocycle. These noncovalent interactions maintain the mean planes of independent macrocycles in an approximately parallel arrangement with a plane-to-plane separation of $\approx 0.5\,\text{nm}$.

2.1.4 From Structural Control to Designed Properties and Functions

The examples in Figs. 2.3 and 2.4 demonstrate that modular building blocks can be assembled into target compounds with precise structural control at the picometer level through programmed sequences of synthetic steps. Indeed, modern chemical synthesis offers access to complex molecules with nanoscaled dimensions and, thus, provides cost-effective strategies for the pro-

duction and characterization of billions of engineered nanostructures in parallel. Furthermore, the high degree of structural control is accompanied by the possibility of designing specific properties into the target nanostructures. Electroactive and photoactive components can be integrated chemically into functional molecular machines [2.9]. Extensive electrochemical investigations have demonstrated that inorganic and organic compounds can exchange electrons with macroscopic electrodes [2.10]. These studies have unraveled the processes responsible for the oxidation and reduction of numerous functional groups and indicated viable design criteria to adjust the ability of molecules to accept or donate electrons [2.11]. Similarly, detailed photochemical and photophysical investigations have elucidated the mechanisms responsible for the absorption and emission of photons at the molecular level [2.12]. The vast knowledge established on the interactions between light and molecules offers the opportunity to engineer chromophoric and fluorophoric functional groups with defined absorption and emission properties [2.11, 13].

The power of chemical synthesis to deliver functional molecules is, perhaps, better illustrated by the molecular motor shown in Fig. 2.5. The preparation of this [2]rotaxane requires 12 synthetic steps starting from known precursors [2.14]. This complex molecule incorporates a Ru(II)-trisbipyridine stopper bridged to a linear tetracationic fragment by a rigid triaryl spacer. The other end of the tetracationic portion is terminated by a bulky tetraarylmethane stopper. The bipyridinium unit of this dumbbell-shaped compound is encircled by a macrocyclic polyether. No covalent bonds join the macrocyclic and linear components. Rather, hydrogen bonding and $[\pi \cdots \pi]$ stacking interactions maintain the

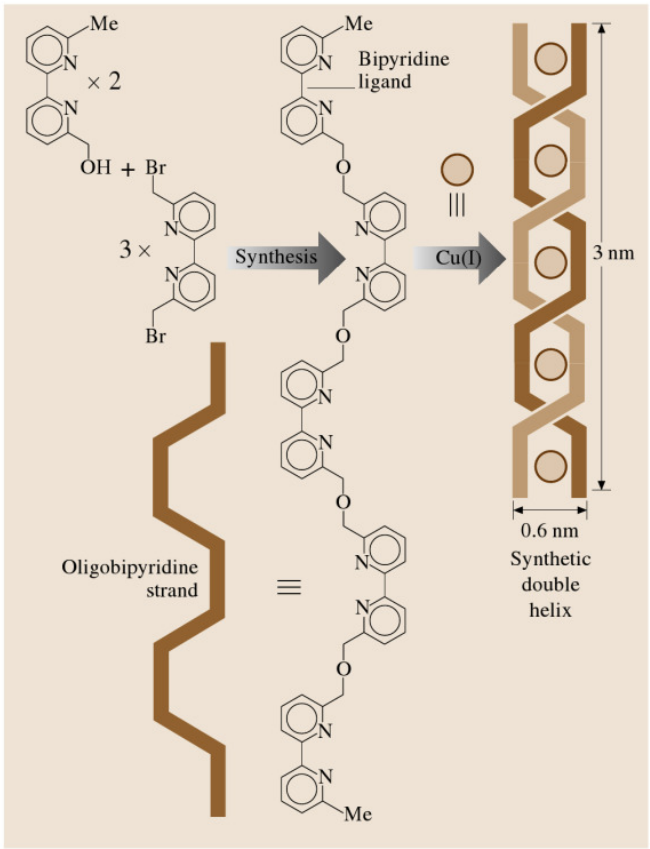

Fig. 2.3 An oligobipyridine strand can be synthesized joining five bipyridine subunits by covalent bonds. The tetrahedral coordination of pairs of bipyridine ligands by Cu(I) ions encourages the assembly two oligobipyridine strands into a double helical arrangement

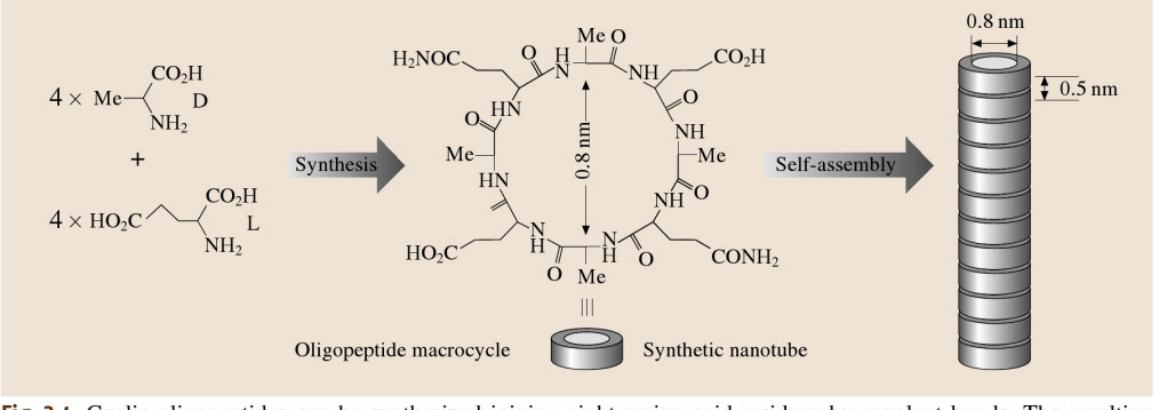

Fig. 2.4 Cyclic oligopeptides can be synthesized joining eight amino acid residues by covalent bonds. The resulting macrocycles self-assemble into nanoscaled tubelike arrays

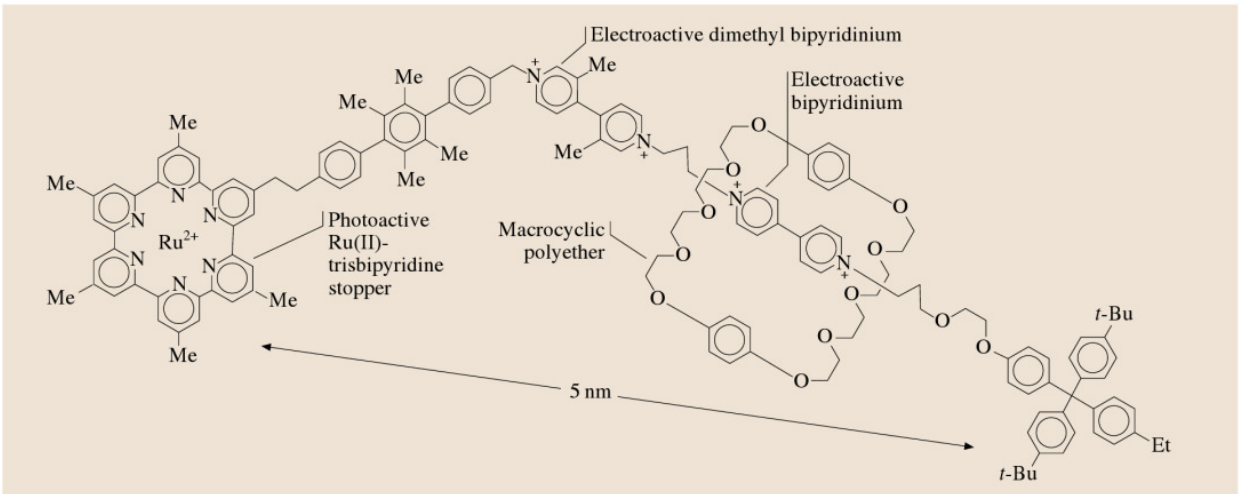

Fig. 2.5 This nanoscaled [2]rotaxane incorporates a photoactive Ru(II)-trisbipyridine stopper and two electroactive bipyridinium units. Photoinduced electron transfer from the photoactive stopper to the encircled electroactive unit forces the macrocyclic polyether to shuttle to the adjacent bipyridinium dication

macrocyclic polyether around the bipyridinium unit. In addition, mechanical constrains associated with the bulk of the two terminal stoppers prevent the macrocycle to slip off the thread. The approximate end-to-end distance for this [2]rotaxane is ≈ 5 nm.

The bipyridinium and the 3,3′-dimethyl bipyridinium units within the dumbbell-shaped component undergo two consecutive and reversible monoelectronic reductions [2.14]. The two methyl substituents on the 3,3′-dimethyl bipyridinium dication make this electroactive unit more difficult to reduce. In acetonitrile, its redox potential is ≈ 0.29 V more negative than that of the unsubstituted bipyridinium dication. Under irradiation at 436 nm in degassed acetonitrile, the excitation of the Ru(II)-trisbipyridine stopper is followed by electron transfer to the unsubstituted bipyridinium unit. In the presence of a sacrificial electron donor (triethanolamine) in solution, the photogenerated hole in the photoactive stopper is filled, and undesired back electron transfer is suppressed. The permanent and light-induced reduction of the dicationic bipyridinium unit to a radical cation depresses significantly the magnitude of the noncovalent interactions holding the macrocyclic polyether in position. As a result, the macrocycle shuttles from the reduced unit to the adjacent dicationic 3,3′-dimethyl bipyridinum. After the diffusion of molecular oxygen into the acetonitrile solution, oxidation occurs restoring the dicationic form of the bipyridinium unit and its ability to sustain strong noncovalent bonds. As a result, the macrocyclic polyether shuttles back to its original position. This amazing example of a molecular shuttle reveals that dynamic processes can be controlled reversibly at the molecular level relying on the clever integration of electroactive and photoactive fragments into functional and nanoscaled molecules.

2.2 Molecular Switches and Logic Gates

Everyday, we routinely perform dozens of switching operations. We turn on and off our personal computers, cellular phones, CD players, radios, or simple light bulbs at a click of a button. Every single time, our finger exerts a mechanical stimulation on a control device, namely a switch. The external stimulus changes the physical state of the switch closing or opening an electric circuit and enabling or preventing the passage of electrons. Overall, the switch transduces a mechanical input into an electrical output.

2.2.1 From Macroscopic to Molecular Switches

The use of switching devices is certainly not limited to electric circuits. For example, a switch at the junction

of a railroad can divert trains from one track to another. Similarly, a faucet in a lavatory pipe can block or release the flow of water. Of course, the nature of the control stimulations and the character of the final outcome vary significantly from case to case, but the operating principle behind each switching device is the same. In all cases, input stimulations reach the switch changing its physical state and producing a specific output.

The development of nanoscaled counterparts to conventional switches is expected to have fundamental scientific and technological implications. For instance, one can envisage practical applications for ultraminiaturized switches in areas ranging from biomedical research to information technology. The major challenge in the quest for nanoswitches, however, is the identification of reliable design criteria and operating principles for these innovative and fascinating devices. Chemical approaches to implement molecule-sized switches appear to be extremely promising. The intrinsically small dimensions of organic molecules coupled with the power of chemical synthesis are the main driving forces behind these exploratory investigations.

Certain organic molecules adjust their structural and electronic properties when stimulated with chemical, electrical, or optical inputs. Generally, the change is accompanied by an electrochemical or spectroscopic response. Overall, these nanostructures transduce input stimulations into detectable outputs and, appropriately, are called molecular switches [2.15, 16]. The chemical transformations associated with these switching processes are often reversible. The chemical system returns to the original state when the input signal is turned off. The interconverting states of a molecular switch can be isomers, an acid and its conjugated base, the oxidized and reduced forms of a redox active molecule, or even the complexed and uncomplexed forms of a receptor [2.9, 13, 15, 16]. The output of a molecular switch can be a chemical, electrical, and/or optical signal that varies in intensity with the interconversion process. For example, changes in absorbance, fluorescence, pH, or redox potential can accompany the reversible transformation of a molecular switch.

2.2.2 Digital Processing and Molecular Logic Gates

In present computer networks, data are elaborated electronically by microprocessor systems [2.17] and are exchanged optically between remote locations [2.18]. Data processing and communication require the encoding of information in electrical and optical signals in the form of binary digits. Using arbitrary assumptions, logic thresholds can be established for each signal and, then, 0 and 1 digits can be encoded following simple conventions. Sequences of electronic devices manipulate the encoded bits executing logic functions as a result of basic switching operations.

The three basic AND, NOT, and OR operators combine binary inputs into binary outputs following precise logic protocols [2.17]. The NOT operator converts an input signal into an output signal. When the input is 0, the output is 1. When the input is 1, the output is 0. Because of the inverse relationship between the input and output values, the NOT gate is often called *inverter* [2.19]. The OR operator combines two input signals into a single output signal. When one or both inputs are 1, the output is 1. When both inputs are 0, the output is 0. The AND gate also combines two input signals into one output signal. In this instance, however, the output is 1 only when both inputs are 1. When at least one input is 0, the output is 0.

The output of one gate can be connected to one of the inputs of another operator. A NAND gate, for example, is assembled connecting the output of an AND operator to the input of a NOT gate. Now the two input signals are converted into the final output after two consecutive logic operations. In a similar fashion, a NOR gate can be assembled connecting the output of an OR operator to the input of a NOT gate. Once again, two consecutive logic operations determine the relation between two input signals and a single output. The NAND and NOR operations are termed universal functions because any conceivable logic operation can be implemented relying only on one of these two gates [2.17]. In fact, digital circuits are fabricated routinely interconnecting exclusively NAND or exclusively NOR operators [2.19].

The logic gates of conventional microprocessors are assembled interconnecting transistors, and their input and output signals are electrical [2.19]. But the concepts of binary logic can be extended to chemical, mechanical, optical, pneumatic, or any other type of signal. First it is necessary to design devices that can respond to these stimulations in the same way transistors respond to electrical signals. Molecular switches respond to a variety of input stimulations producing specific outputs and can, therefore, be exploited to implement logic functions [2.13, 20, 21].

2.2.3 Molecular AND, NOT, and OR Gates

More than a decade ago, researchers proposed a potential strategy to execute logic operations at the molecular level [2.22]. Later, the analogy between molecular switches and logic gates was recognized in a seminal article [2.23], in which it was demonstrated that AND, NOT, and OR operations can be reproduced with fluorescent molecules. The pyrazole derivative **1** (Fig. 2.6) is a molecular NOT gate. It imposes an inverse relation between a chemical input (concentration of H^+) and an optical output (emission intensity). In a mixture of methanol and water, the fluorescence quantum yield of **1** is 0.13 in the presence of only 0.1 equivalents of H^+ [2.23]. The quantum yield drops to 0.003 when the equivalents of H^+ are 1000. Photoinduced electron transfer from the central pyrazoline unit to the pendant benzoic acid quenches the fluorescence of the protonated form. Thus, a change in H^+ concentration (I) from a low to a high value switches the emission intensity (O) from a high to a low value. The inverse relationship between the chemical input I and the optical output O translates into the truth table of a NOT operation if a positive logic convention (low = 0, high = 1) is applied to both signals. The emission intensity is high (O = 1) when the concentration of H^+ is low (I = 0). The emission intensity is low (O = 0) when the concentration of H^+ is high (I = 1).

The anthracene derivative **2** (Fig. 2.6) is a molecular OR gate. It transduces two chemical inputs (concentrations of Na^+ and K^+) into an optical output (emission intensity). In methanol, the fluorescence quantum yield is only 0.003 in the absence of metal cations [2.23]. Photoinduced electron transfer from the nitrogen atom of the azacrown fragment to the anthracene fluorophore quenches the emission. After the

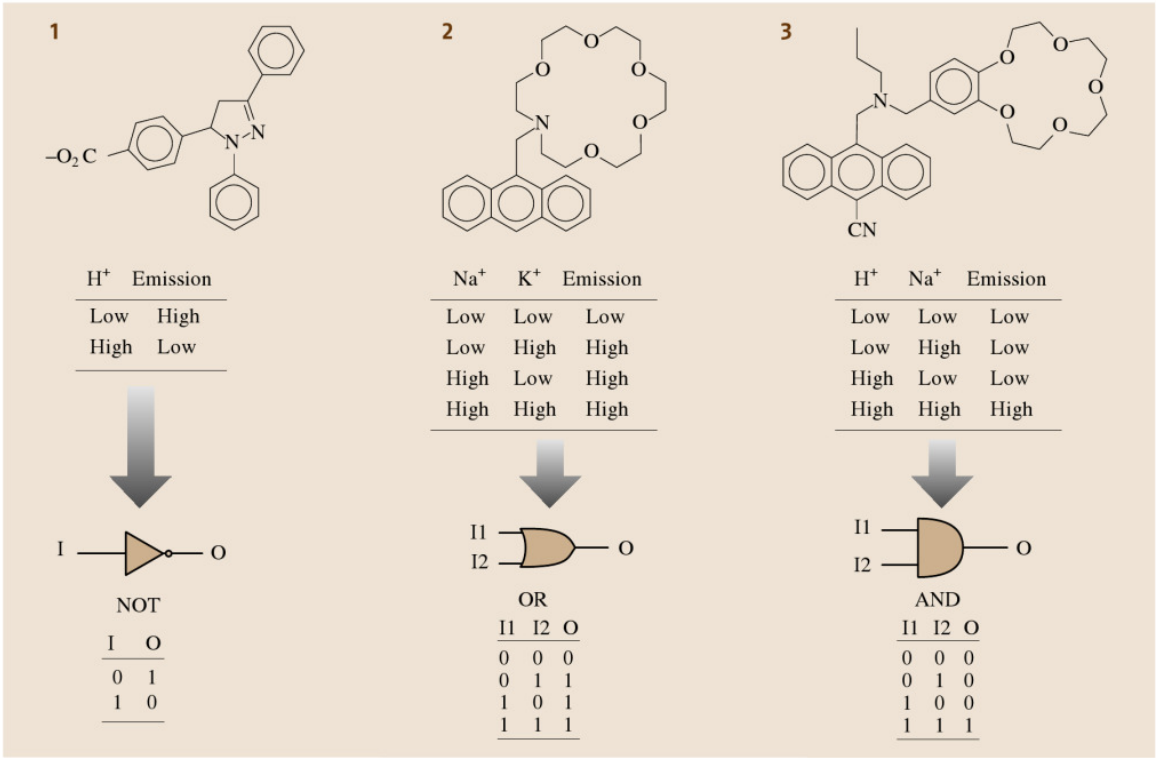

Fig. 2.6 The fluorescence intensity of the pyrazoline derivative **1** is high when the concentration of H^+ is low, and vice versa. The fluorescence intensity of the anthracene derivative **2** is high when the concentration of Na^+ and/or K^+ is high. The emission is low when both concentrations are low. The fluorescence intensity of the anthracene **3** is high only when the concentrations of H^+ and Na^+ are high. The emission is low in the other three cases. The signal transductions of the molecular switches **1**, **2**, and **3** translate into the truth tables of NOT, OR, and AND gates, respectively, if a positive logic convention is applied to all inputs and outputs (low = 0, high = 1)

addition of 1000 equivalents of either Na^+ or K^+, the quantum yield raises to 0.053 and 0.14, respectively. Similarly, the quantum yield is 0.14 when both metal cations are present in solution. The complexation of one of the two metal cations inside the azacrown receptor depresses the efficiency of the photoinduced electron transfer enhancing the fluorescence. Thus, changes in the concentrations of Na^+ (I1) and/or K^+ (I2) from low to high values switch the emission intensity (O) from a low to a high value. The relationship between the chemical inputs I1 and I2 and the optical output O translates into the truth table of an OR operation if a positive logic convention (low = 0, high = 1) is applied to all signals. The emission intensity is low (O = 0) only when the concentration of Na^+ and K^+ are low (I1 = 0, I2 = 0). The emission intensity is high (O = 1) for the other three input combinations.

The anthracene derivative **3** (Fig. 2.6) is a molecular AND gate. It transduces two chemical inputs (concentrations of H^+ and Na^+) into an optical output (emission intensity). In a mixture of methanol and *iso*-propanol, the fluorescence quantum yield is only 0.011 in the absence of H^+ or Na^+ [2.23]. Photoinduced electron transfer from either the tertiary amino group or the catechol fragment to the anthracene fluorophore quenches the emission. After the addition of either 100 equivalents of H^+ or 1000 equivalents of Na^+, a modest change of the quantum yield to 0.020 and 0.011, respectively, is observed. Instead, the quantum yield increases to 0.068 when both species are present in solution. The protonation of the amino group and the insertion of the metal cation in the benzocrown ether receptor depress the efficiency of the photoinduced electron transfer processes enhancing the fluorescence. Thus, changes in the concentrations of H^+ (I1) and Na^+ (I2) from low to high values switch the emission intensity (O) from a low to a high value. The relationship between the chemical inputs I1 and I2 and the optical output O translates into the truth table of an AND operation if a positive logic convention (low = 0, high = 1) is applied to all signals. The emission intensity is high (O = 1) only when the concentration of H^+ and Na^+ are high (I1 = 1, I2 = 1). The emission intensity is low (O = 0) for the other three input combinations.

2.2.4 Combinational Logic at the Molecular Level

The fascinating molecular AND, NOT, and OR gates illustrated in Fig. 2.6 have stimulated the design of related chemical systems able to execute the three basic logic operations and simple combinations of them [2.13, 20,21]. Most of these molecular switches convert chemical inputs into optical outputs. But the implementation of logic operations at the molecular level is not limited to the use of chemical inputs. For example, electrical signals and reversible redox processes can be exploited to modulate the output of a molecular switch [2.24]. The supramolecular assembly **4** (Fig. 2.7) executes a XNOR function relying on these operating principles. The π-electron rich tetrathiafulvalene (TTF) guest threads the cavity of a π-electron deficient bipyridinium (BIPY) host. In acetonitrile, an absorption band associated with the charge-transfer interactions between the complementary π-surfaces is observed at 830 nm. Electrical stimulations alter the redox state of either the TTF or the BIPY units encouraging the separation of the two components of the complex and the disappearance of the charge-transfer band. Electrolysis at a potential of +0.5 V oxidizes the neutral TTF unit to a monocationic state. The now cationic guest is expelled from the cavity of the tetracationic host as a result of electrostatic repulsion. Consistently, the absorption band at 830 nm disappears. The charge-transfer band, however, is restored after the exhaustive back reduction of the TTF unit at a potential of 0 V. Similar changes in the absorption properties can be induced addressing the BIPY units. Electrolysis at −0.3 V reduces the dicationic BIPY units to their monocationic forms encouraging the separation of the two components of the complex and the disappearance of the absorption band. The original absorption spectrum is restored after the exhaustive back oxidation of the BIPY units at a potential of 0 V. Thus, this supramolecular system responds to electrical stimulations producing an optical output. One of the electrical inputs (I1) controls the redox state of the TTF unit switching between 0 and +0.5 V. The other (I2) determines the redox state of the bipyridinium units switching between −0.3 and 0 V. The optical output (O) is the absorbance of the charge-transfer band. A positive logic convention (low = 0, high = 1) can be applied to the input I1 and output O. A negative logic convention (low = 1, high = 0) can be applied to the input I2. The resulting truth table corresponds to that of a XNOR circuit (Fig. 2.7). The charge-transfer absorbance is high (O = 1) only when one voltage input is low and the other is high (I1 = 0, I2 = 0) or vice versa (I1 = 1, I2 = 1). It is important to note that the input string with both I1 and I2 equal to 1 implies that input potentials of +0.5 and −0.3 V are applied simultaneously to a solution containing the supramolecular assembly **4** and not to an individual complex. Of course,

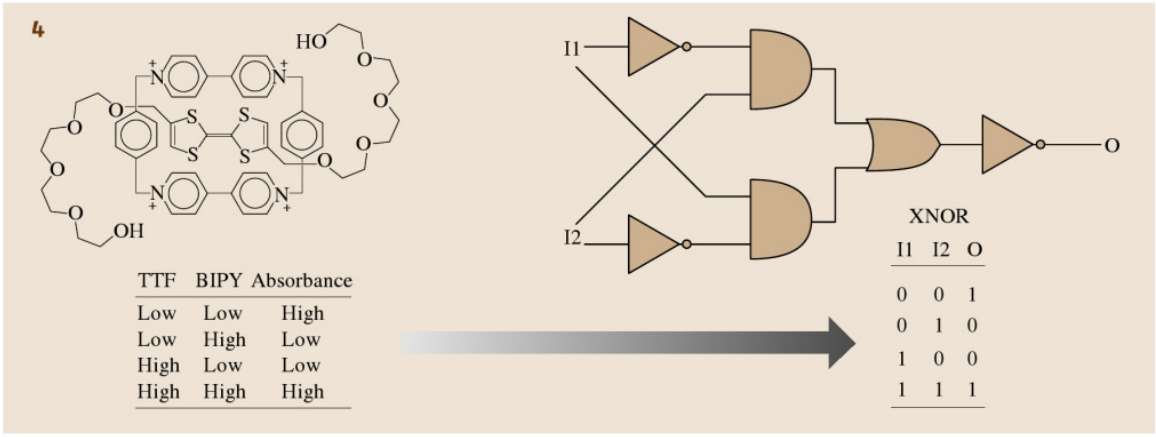

Fig. 2.7 The charge-transfer absorbance of the complex **4** is high when the voltage input addressing the tetrathiafulvalene (TTF) unit is low and that stimulating the bipyridinium (BIPY) units is high and vice versa. If a positive logic convention is applied to the TTF input and to the absorbance output (low = 0, high = 1) while a negative logic convention is applied to the BIPY input (low = 0, high = 1), the signal transduction of **4** translates into the truth table of a XNOR circuit

the concomitant oxidation of the TTF guest and reduction of the BIPY units in the very same complex would be unrealistic. In bulk solution, instead, some complexes are oxidized while others are reduced, leaving the average solution composition unaffected. Thus, the XNOR operation executed by this supramolecular system is a consequence of bulk properties and not a result of unimolecular signal transduction.

Optical inputs can be employed to operate the three-state molecular switch of Fig. 2.8 in acetonitrile solution [2.25]. This chemical system responds to three inputs producing two outputs. The three input stimulations are ultraviolet light (I1), visible light (I2), and the concentration of H^+ (I3). One of the two optical outputs is the absorbance at 401 nm (O1), which is high when the molecular switch is in the yellow-green state **6** and low in the other two cases. The other optical output is the absorbance at 563 nm (O2), which is high when the molecular switch is in the purple state **7** and low in the other two cases. The colorless spiropyran state **5** switches to the merocyanine form **7** upon irradiation with ultraviolet light. It switches to the protonated merocyanine from **6** when treated with H^+. The colored state **7** isomerizes back to **5** in the dark or upon irradiation with visible light. Alternatively, **7** switches to **6** when treated with H^+. The colored state **6** switches to **5**, when irradiated with visible light, and to **7**, after the removal of H^+. In summary, this three-state molecular switch responds to two optical inputs (I1 and I2) and one chemical input (I3) producing two optical outputs (O1 and O2). Binary digits can be encoded on each signal applying positive logic conventions (low = 0, high = 1). It follows that the three-state molecular switch converts input strings of three binary digits into output strings of two binary digits. The corresponding truth table (Fig. 2.8) reveals that the optical output O1 is high (O1 = 1) when only the input I3 is applied (I1 = 0, I2 = 0, I3 = 1), when only the input I2 is not applied (I1 = 1, I2 = 0, I3 = 0), or when all three inputs are applied (I1 = 1, I2 = 0, I3 = 0). The optical output O2 is high (O2 = 1) when only the input I1 is applied (I1 = 1, I2 = 0, I3 = 0) or when only the input I3 is not applied (I1 = 1, I2 = 0, I3 = 0). The combinational logic circuit (Fig. 2.8) equivalent to this truth table shows that all three inputs determine the output O1, while only I1 and I3 control the value of O2.

2.2.5 Intermolecular Communication

The combinational logic circuits in Figs. 2.7 and 2.8 are arrays of interconnected AND, NOT, and OR operators. The digital communication between these basic logic elements ensures the execution of a sequence of simple logic operations that results in the complex logic function processed by the entire circuit. It follows that the logic function of a given circuit can be adjusted altering the number and type of basic gates and their interconnection protocol [2.17]. This modular approach to combinational logic circuits is extremely powerful. Any logic function can be implemented connecting the appropriate combination of simple AND, NOT, and OR gates.

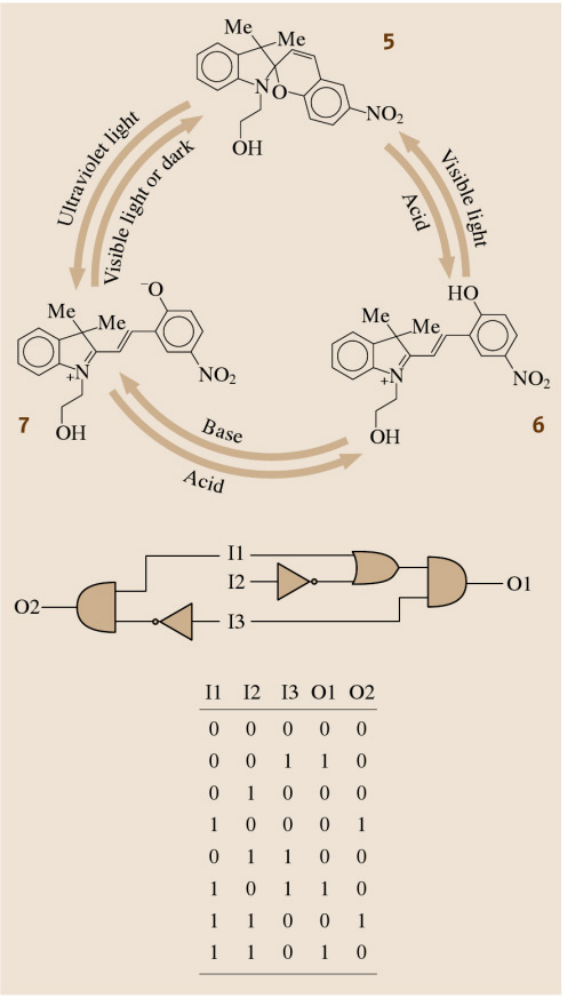

I1	I2	I3	O1	O2
0	0	0	0	0
0	0	1	1	0
0	1	0	0	0
1	0	0	0	1
0	1	1	0	0
1	0	1	1	0
1	1	0	0	1
1	1	0	1	0

Fig. 2.8 Ultraviolet light (I1), visible light (I2), and H^+ (I3) inputs induce the interconversion between the three states **5**, **6**, and **7**. The colorless state **5** does not absorb in the visible region. The yellow-green state **6** absorbs at 401 nm (O1). The purple state **7** absorbs at 563 nm (O2). The truth table illustrates the conversion of input strings of three binary digits (I1, I2, and I3) into output strings of two binary digits (O1 and O2) operated by this three-state molecular switch. A combinational logic circuit incorporating nine AND, NOT, and OR operators correspond to this particular truth table

The strategies followed so far to implement complex logic functions with molecular switches are based on the careful design of the chemical system and on the judicious choice of the inputs and outputs [2.13, 20, 21]. A specific sequence of AND, NOT, and OR operations is programmed in a single molecular switch. No digital communication between distinct gates is needed since they are built in the same molecular entity. Though extremely elegant, this strategy does not have the same versatility of a modular approach. A different molecule has to be designed, synthesized, and analyzed every single time a different logic function has to be realized. In addition, the degree of complexity that can be achieved with only one molecular switch is fairly limited. The connection of the input and output terminals of independent molecular AND, NOT, and OR operators, instead, would offer the possibility of assembling any combinational logic circuit from three basic building blocks.

In digital electronics, the communication between two logic gates can be realized connecting their terminals with a wire [2.19]. Methods to transmit binary data between distinct molecular switches are not so obvious and must be identified. Recently we developed two strategies to communicate signals between compatible molecular components. In one instance, a chemical signal is communicated between two distinct molecular switches [2.26]. They are the three-state switch illustrated in Fig. 2.8 and the two-state switch of Fig. 2.9. The merocyanine form **7** is a photogenerated base. Its *p*-nitrophenolate fragment, produced upon irradiation of the colorless state **5** with ultraviolet light, can abstract a proton from an acid present in the same solution. The resulting protonated form **6** is a photoacid. It releases a proton upon irradiation with visible light and can protonate a base co-dissolved in the same medium. The orange azopyridine **8** switches to the red-purple azopyridinium **9** upon protonation. This process is reversible, and the addition of a base restores the orange state **8**. It follows that photoinduced proton transfer can be exploited to communicate a chemical signal from **6** to **8** and from **9** to **7**. The two colored states **8** and **9** have different absorption properties in the visible region. In acetonitrile, the orange state **8** absorbs at 422 nm, and the red-purple state **9** absorbs at 556 nm. The changes in absorbance of these two bands can be exploited to monitor the photoinduced exchange of protons between the two communicating molecular switches.

The three-state molecular switch and the two-state molecular switch can be operated sequentially when dissolved in the same acetonitrile solution. In the presence of one equivalent of H^+, the two-state molecular switch is in state **9** and the absorbance at 556 nm is high (O = 1). Upon irradiation with ultraviolet light (I1 = 0), **5** switches to **7**. The photogenerated base deprotonates **9** producing **8** and **6**. As a result, the absorbance at 556 nm decreases (O = 0). Upon irradiation

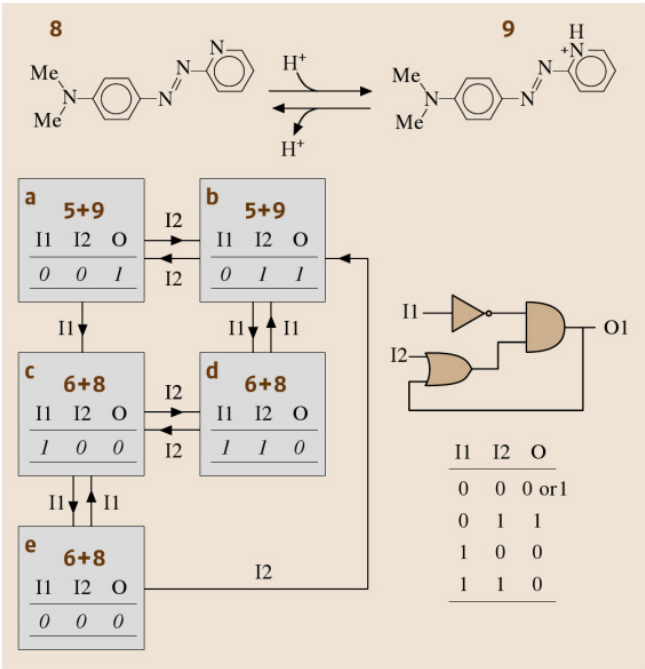

Fig. 2.9 The concentration of H^+ controls the reversible interconversion between the two states **8** and **9**. In response to ultraviolet (I1) and visible (I2) inputs, the three-state molecular switch in Fig. 2.7 modulates the ratio between these two forms and the absorbance (O) of **9** through photoinduced proton transfer. The truth table and sequential logic circuit illustrate the signal transduction behavior of the two communicating molecular switches. The interconversion between the five three-digit strings of input (I1 and I2) and output (O) data is achieved varying the input values in steps ◀

with visible light (I2 = 1), **6** switches to **5** releasing H^+. The result is the protonation of **8** to form **9** and restore the high absorbance at 556 nm (O = 1). In summary, the three-state molecular switch transduces two optical inputs (I1 = ultraviolet light, I2 = visible light) into a chemical signal (proton transfer) that is communicated to the two-state molecular switch and converted into a final optical output (O = absorbance at 556 nm).

The logic behavior of the two communicating molecular switches is significantly different from those of the chemical systems illustrated in Figs. 2.6–2.8 [2.26]. The truth table in Fig. 2.9 lists the four possible combinations of two-digit input strings and the corresponding one-digit output. The output digit O for the input strings 01, 10, and 11 can take only one value. In fact, the input string 01 is transduced into a 1, and the input strings 10 and 11 are converted into 0. Instead, the output digit O for the input string 00 can be either 0 or 1. The sequence of events leading to the input string 00 determines the value of the output. The boxes **a**–**e** in Fig. 2.9 illustrates this effect. They correspond to the five three-digit input/output strings. The transformation of one box into any of the other four is achieved in one or two steps by changing the values of I1 and/or I2. In two instances (**a** and **b**), the two-state molecular switch is in state **9**, and the output signal is high (O = 1). In the other three cases (**c**, **d**, and **e**), the two-state molecular switch is in state **8**, and the output signal is low (O = 0). The strings 000 (**e**) and 001 (**a**) correspond to the first entry of the truth table. They share the same input digits but differ in the output value. The string 000 (**e**) can be obtained only from the string 100 (**c**) varying the value of I1. Similarly, the string 001 (**a**) can be accessed only from the string 011 (**b**) varying the value of I2. In both transformations, the output digit remains unchanged. Thus, the value of O1 in the parent string is memorized and maintained in the daughter string when both inputs become 0. This memory effect is the fundamental operating principle of sequential logic circuits [2.17], which are used extensively to assemble the memory elements of modern microprocessors. The sequential logic circuit equivalent to the truth table of the two communicating molecular switches is also shown in Fig. 2.9. In this circuit, the input data I1 and I2 are combined through NOT, OR, and AND operators. The output of the AND gate O is also an input of the OR gate and controls, together with I1 and I2, the signal transduction behavior.

The other strategy for digital transmission between molecules is based on the communication of optical signals between the three-state molecular switch (Fig. 2.8) and fluorescent compounds [2.27]. In the optical network of Fig. 2.10, three optical signals travel from an excitation source to a detector after passing through two quartz cells. The first cell contains an equimolar acetonitrile solution of naphthalene, anthracene, and tetracene. The second cell contains an acetonitrile solution of the three-state molecular switch. The excitation source sends three consecutive monochromatic light beams to the first cell stimulating the emission of the three fluorophores. The light emitted in the direction perpendicular to the exciting beam reaches the second cell. When the molecular switch is in state **5**, the naphthalene emission at 335 nm is absorbed and a low intensity output (O1) reaches the detector. Instead, the anthracene and tetracene emissions at 401 and 544 nm,

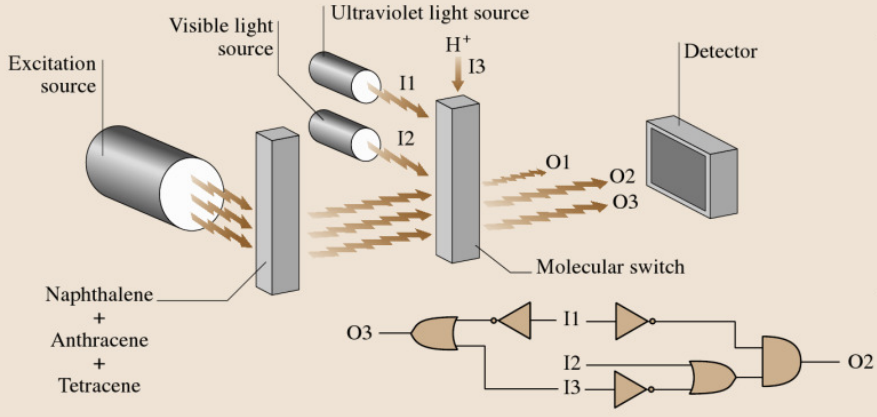

I1	I2	I3	O1	O2	O3
0	0	0	0	1	1
0	0	1	0	0	1
0	1	0	0	1	1
1	0	0	0	0	0
0	1	1	0	1	1
1	0	1	0	0	1
1	1	0	0	0	0
1	1	1	0	0	1

Fig. 2.10 The excitation source sends three monochromatic light beams (275, 357, and 441 nm) to a quartz cell containing an equimolar acetonitrile solution of naphthalene, anthracene and tetracene. The three fluorophores absorb the exciting beams and reemit at 305, 401, and 544 nm, respectively. The light emitted in the direction perpendicular to the exciting beams passes through another quartz cell containing an acetonitrile solution of the three-state molecular switch shown in Fig. 2.7. Ultraviolet (I1), visible (I2), and H^+ (I3) inputs control the interconversion between the three states of the molecular switch. They determine the intensity of the optical outputs reaching the detector and correspond to the naphthalene (O1), anthracene (O2), and tetracene (O3) emissions. The truth table and equivalent combinational logic illustrate the relation between the three inputs and the three outputs. The output O1 is always 0, and it is not influenced by the three inputs. Only two inputs determine the value of O3, while all of them control the output O2

respectively, pass unaffected and high intensity outputs (O2 and O3) reach the detector. When the molecular switch is in state **6**, the naphthalene and anthracene emissions are absorbed and only the tetracene emission reaches the detector (O1 = 0, O2 = 0, O3 = 1). When the molecular switch is state **7**, the emission of all three fluorophores is absorbed (O1 = 0, O2 = 0, O3 = 0). The interconversion of the molecular switch between the three states is induced addressing the second cell with ultraviolet (I1), visible (I2) and H^+ (I3) inputs. Thus, three independent optical outputs (O1, O2 and O3) can be modulated stimulating the molecular switch with two optical and one chemical input. The truth table in Fig. 2.10 illustrates the relation between the three inputs (I1, I2 and I3) and the three outputs (O1, O2 and O3), when positive logic conventions are applied to all signals. The equivalent logic circuit shows that all three inputs control the anthracene channel O2, but only I1 and I3 influence the tetracene channel O3. Instead, the intensity of the naphthalene channel O1 is always low, and it is not affected by the three inputs.

The operating principles of the optical network in Fig. 2.10 can be simplified to implement all-optical logic gates. The chemical input inducing the formation of the protonated form **6** of the molecular switch can be eliminated. The interconversion between the remaining two states **5** and **7** can be controlled relying exclusively on ultraviolet inputs. Indeed, ultraviolet irradiation induces the isomerization of the colorless form **5** to the colored species **7**, which reisomerizes to the original state in the dark. Thus, a single ultraviolet source is sufficient to control the switching from **5** to **7** and vice versa. On the basis of these considerations, all-optical NAND, NOR, and NOT gates can be implemented operating sequentially or in parallel from one to three independent switching elements [2.28]. For example, the all-optical network illustrated in Fig. 2.11 is a three-input NOR gate. A monochromatic optical signal travels from a visible source to a detector. Three switching elements are aligned along the path of the traveling light. They are quartz cells containing an acetonitrile solution of the molecular switch shown in Fig. 2.8. The interconversion of the colorless form **5** into the purple isomer **7** is induced stimulating the cell with an ultraviolet input. The reisomerization from **7** to **5** occurs spontaneously, as the ultraviolet sources is turned off. Using three distinct ultraviolet sources, the three switching elements can be controlled independently.

The colorless form **5** does not absorb in the visible region, while the purple isomer **7** has a strong absorption band at 563 nm. Thus, a 563 nm optical signal leaving the visible source can reach the detector

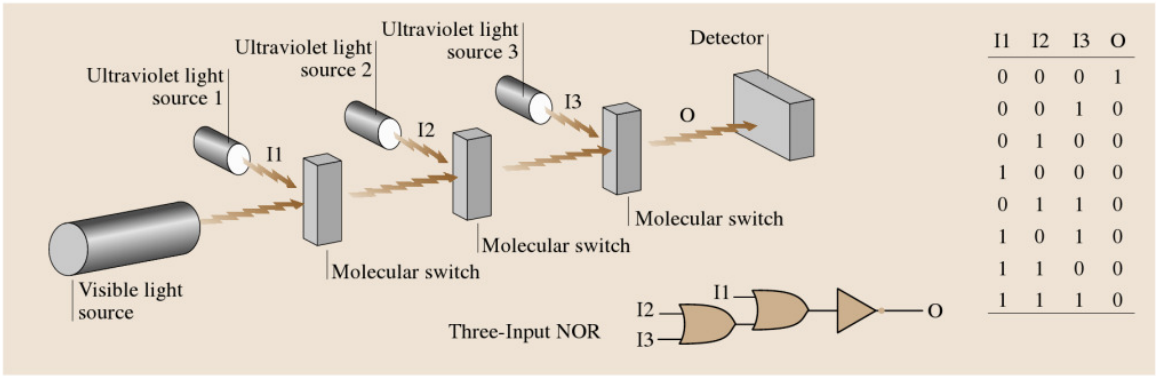

I1	I2	I3	O
0	0	0	1
0	0	1	0
0	1	0	0
1	0	0	0
0	1	1	0
1	0	1	0
1	1	0	0
1	1	1	0

Fig. 2.11 The visible source sends a monochromatic beam (563 nm) to the detector. The traveling light is forced to pass through three quartz cells containing the molecular switch illustrated in Fig. 2.7. The three switching elements are operated by independent ultraviolet inputs. When at least one of them is on, the associated molecular switch is in the purple form **7**, which can absorb and block the traveling light. The truth table and equivalent logic circuit illustrate the relation between the three inputs I1, I2, and I3 and the optical output O

unaffected only if all three switching elements are in the nonabsorbing state **5**. If one of the three ultraviolet inputs I1, I2, or I3 is turned on, the intensity of the optical output O drops to 3–4% of its original value. If two or three ultraviolet inputs are turned on simultaneously, the optical output drops to 0%. Indeed, the photogenerated state **7** absorbs and blocks the traveling light. Applying positive logic conventions to all signals, binary digits can be encoded in the three optical inputs and in the optical output. The resulting truth table is illustrated in Fig. 2.11. The output O is 1 only if all three inputs I1, I2, or I3 are 0. The output O is 0 if at least one of the three inputs I1, I2, or I3 is 1. This signal transduction corresponds to that executed by a three-input NOR gate, which is a combination of one NOT and two OR operators.

2.3 Solid State Devices

The fascinating chemical systems illustrated in Figs. 2.6–2.11 demonstrate that logic functions can be implemented relying on the interplay between designed molecules and chemical, electrical and/or optical signals [2.13, 20, 21].

2.3.1 From Functional Solutions to Electroactive and Photoactive Solids

These molecular switches, however, are operated exclusively in solution and remain far from potential applications in information technology at this stage. The integration of liquid components and volatile organic solvents in practical digital devices is hard to envisage. Furthermore, the logic operations executed by these chemical systems rely on bulk addressing. Although the individual molecular components have nanoscaled dimensions, macroscopic collections of them are employed for digital processing. In some instances, the operating principles cannot even be scaled down to the unimolecular level. Often bulk properties are responsible for signal transduction. For example, a single fluorescent compound **2** cannot execute an OR operation. Its azacrown appendage can accommodate only one metal cation. As a result, an individual molecular switch can respond to only one of the two chemical inputs. It is a collection of numerous molecular switches dissolved in an organic solvent that responds to both inputs enabling an OR operation.

The development of miniaturized molecule-based devices requires the identification of methods to transfer the switching mechanisms developed in solution to the solid state [2.29]. Borrowing designs and fabrication strategies from conventional electronics, researchers are starting to explore the integration of molecular components into functional circuits and devices [2.30–33]. Generally, these strategies combine lithography and surface chemistry to assemble nanometer-thick organic films on the surfaces of microscaled or nanoscaled

electrodes. Two main approaches for the deposition of organized molecular arrays on inorganic supports have emerged so far. In one instance, amphiphilic molecular building blocks are compressed into organized monolayers at air/water interfaces. The resulting films can be transferred on supporting solids employing the Langmuir–Blodgett technique [2.34]. Alternatively, certain molecules can be designed to adsorb spontaneously on the surfaces of compatible solids from liquid or vapor phases. The result is the self-assembly of organic layers on inorganic supports [2.35].

2.3.2 Langmuir–Blodgett Films

Films of amphiphilic molecules can be deposited on a variety of solid supports employing the Langmuir–Blodgett technique [2.34]. This method can be extended to electroactive compounds incorporating hydrophilic and hydrophobic groups. For example, the amphiphile **10** (Fig. 2.12) has a hydrophobic hexadecyl tail attached to a hydrophilic bipyridinium dication [2.36, 37]. This compound dissolves in mixtures of chloroform and methanol, but it is not soluble in moderately concentrated aqueous solutions of sodium perchlorate. Thus the spreading of an organic solution of **10** on an aqueous sodium perchlorate subphase affords a collection of disorganized amphiphiles floating on the water surface (Fig. 2.12), after the organic solvent has evaporated. The molecular building blocks can be compressed into a monolayer with the aid of a moving barrier. The hydrophobic tails align away from the aqueous phase. The hydrophilic dicationic heads and the accompanying perchlorate counterions pack to form an organized monolayer at the air/water interface. The compression process can be monitored recording the surface pressure (π)-area per molecule (A) isotherm, which indicates a limiting molecular area of $\approx 50\,\text{Å}^2$. This value is larger than the projected area of an oligomethylene chain. It correlates reasonably, however, with the overall

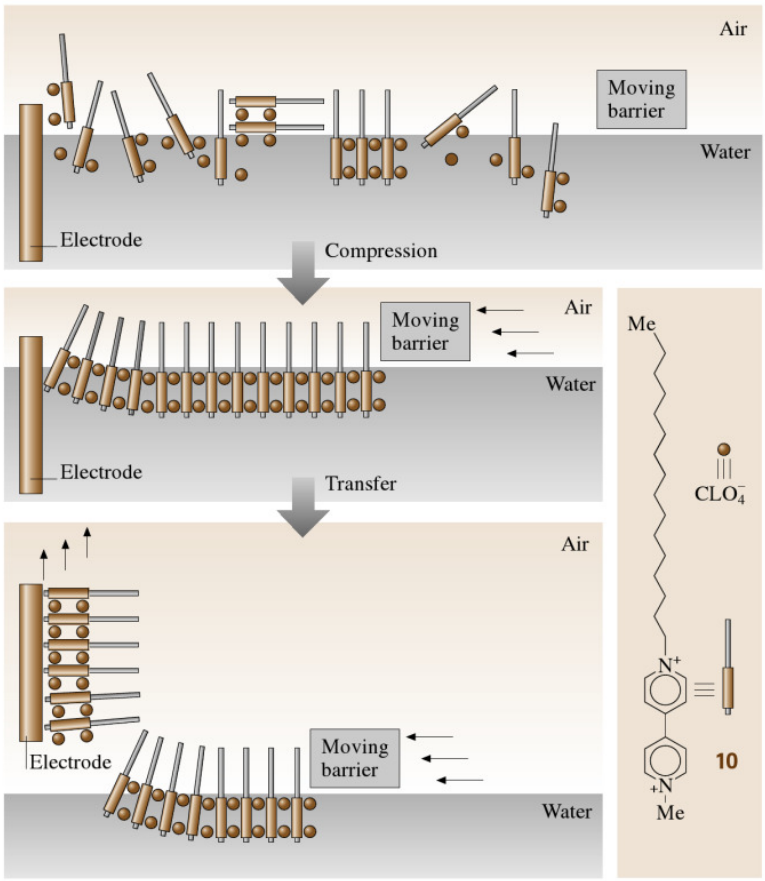

Fig. 2.12 The compression of the amphiphilic dication **10** with a moving barrier results in the formation of a packed monolayer at the air/water interface. The lifting of an electrode pre-immersed in the aqueous subphase encourages the transfer of part of the monolayer on the solid support

area of a bipyridinium dication plus two perchlorate anions.

The monolayer prepared at the air/water interface (Fig. 2.12) can be transferred on the surface of a indium-tin oxide electrode pre-immersed in the aqueous phase. The slow lifting of the solid support drags the monolayer away from the aqueous subphase. The final result is the coating of the electrode with an organic film containing electroactive bipyridinium building blocks. The modified electrode can be integrated in a conventional electrochemical cell to probe the redox response of the electroactive layer. The resulting cyclic voltammograms reveal the characteristic waves for the first reduction process of the bipyridinium dications, confirming the successful transfer of the electroactive amphiphiles from the air/water interface to the electrode surface. The integration of the redox waves indicates a surface coverage of $\approx 4 \times 10^{10}$ mol cm^{-2}. This value corresponds to a molecular area of ≈ 40 Å^2 and is in excellent agreement with the limiting molecular area of the π–A isotherm.

These seminal experiments demonstrate that electroactive amphiphiles can be organized into uniform monolayers at the air/water interface and then transferred efficiently on the surface of appropriate substrates to produce electrode/monolayer junctions. The resulting electroactive materials can become the functional components of molecule-based devices. For example, bipyridinium-based photodiodes can be fabricated following this approach [2.38,39]. Their operating principles rely on photoinduced electron transfer from chromophoric units to bipyridinium acceptors. The electroactive and photoactive amphiphile **11** (Fig. 2.13) incorporates hydrophobic ferrocene and pyrene tails and a hydrophilic bipyridinium head. Chloroform solutions of **11** containing ten equivalents of arachidic acid can be spread on an aqueous calcium chloride subphase in a Langmuir trough. The amphiphiles can be compressed into a mixed monolayer, after the evaporation of the organic solvent. Pronounced steps in the corresponding π–A isotherm suggest that the bulky ferrocene and pyrene groups are squeezed away from the water surface. In the final arrangement, both photoactive groups align above the hydrophobic dication.

A mixed monolayer of **11** and arachidic acid can be transferred from the air/water interface to the surface of a transparent gold electrode following the methodology illustrated for the system in Fig. 2.12. The coated electrode can be integrated in a conventional electrochemical cell. Upon irradiation at 330 nm under an inert atmosphere, an anodic photocurrent of ≈ 2 nA develops at a potential of 0 V relative to a saturated calomel electrode. Indeed, the illumination of the electroactive monolayer induces the electron transfer from the pyrene appendage to the bipyridinium acceptor and then from the reduced acceptor to the electrode. A second intramolecular electron transfer from the ferrocene donor to the oxidized pyrene fills its photogenerated hole. Overall, a unidirectional flow of electrons across the monolayer/electrode junction is established under the influence of light.

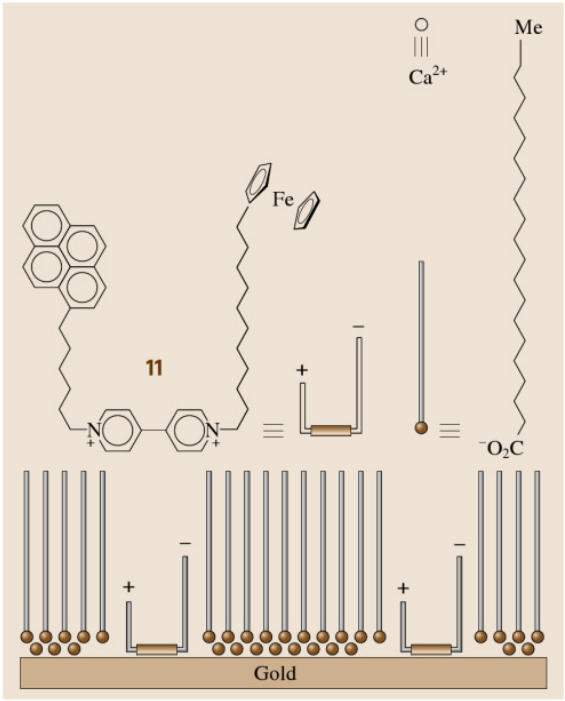

Fig. 2.13 Mixed monolayers of the amphiphile **11** and arachidic acid can be transferred from the air/water interface to the surface of an electrode to generate a molecule-based photodiode

The ability to transfer electroactive monolayers from air/water interfaces to electrode surfaces can be exploited to fabricate molecule-based electronic devices. In particular, arrays of interconnected electrode/monolayer/electrode tunneling junctions can be assembled combining the Langmuir–Blodgett technique with electron beam evaporation [2.33]. Figure 2.14 illustrates a schematic representation of the resulting devices. Initially, parallel fingers are patterned on a silicon wafer with a silicon dioxide overlayer by electron beam evaporation. The bottom electrodes deposited on the support can be either aluminum wires

covered by an aluminum oxide or *n*-doped silicon lines with silicon dioxide overlayers. Their widths are ≈ 6 or 7 μm, respectively. The patterned silicon chip is immersed in the aqueous subphase of a Langmuir trough prior to monolayer formation. After the compression of electroactive amphiphiles at the air/water interface, the substrate is pulled out of the aqueous phase to encourage the transfer of the molecular layer on the parallel bottom electrodes as well as on the gaps between them. Then, a second set of electrodes orthogonal to the first is deposited through a mask by electron beam evaporation. They consist of a titanium underlayer plus an aluminum overlayer. Their thicknesses are ≈ 0.05 and 1 μm, respectively, and their width is ≈ 10 μm. In the final assembly, portions of the molecular layer become sandwiched between the bottom and top electrodes. The active areas of these electrode/monolayer/electrode junctions are ≈ 60–70 μm^2 and correspond to ≈ 10^6 molecules.

The [2]rotaxane **12** (Fig. 2.14) incorporates a macrocyclic polyether threaded onto a bipyridinium-based backbone [2.40, 41]. The two bipyridinium dications are bridged by a *m*-phenylene spacer and terminated by tetraarylmethane appendages. These two bulky groups trap mechanically the macrocycle preventing its dissociation from the tetracationic backbone. In addition, their hydrophobicity complements the hydrophilicity of the two bipyridinium dications imposing amphiphilic character on the overall molecular assembly. This compound does not dissolve in aqueous solutions and can be compressed into organized monolayers at air/water interfaces. The corresponding π–A isotherm reveals a limiting molecular area of ≈ 130 $Å^2$. This large value is a consequence of the bulk associated with the hydrophobic tetraarylmethane tails and the macrocycle encircling the tetracationic backbone.

Monolayers of the [2]rotaxane **12** can be transferred from the air/water interface to the surfaces of the bottom aluminum/aluminum oxide electrodes of a patterned silicon chip with the hydrophobic tetraarylmethane groups pointing away from the supporting substrate. The subsequent assembly of a top titanium/aluminum electrode

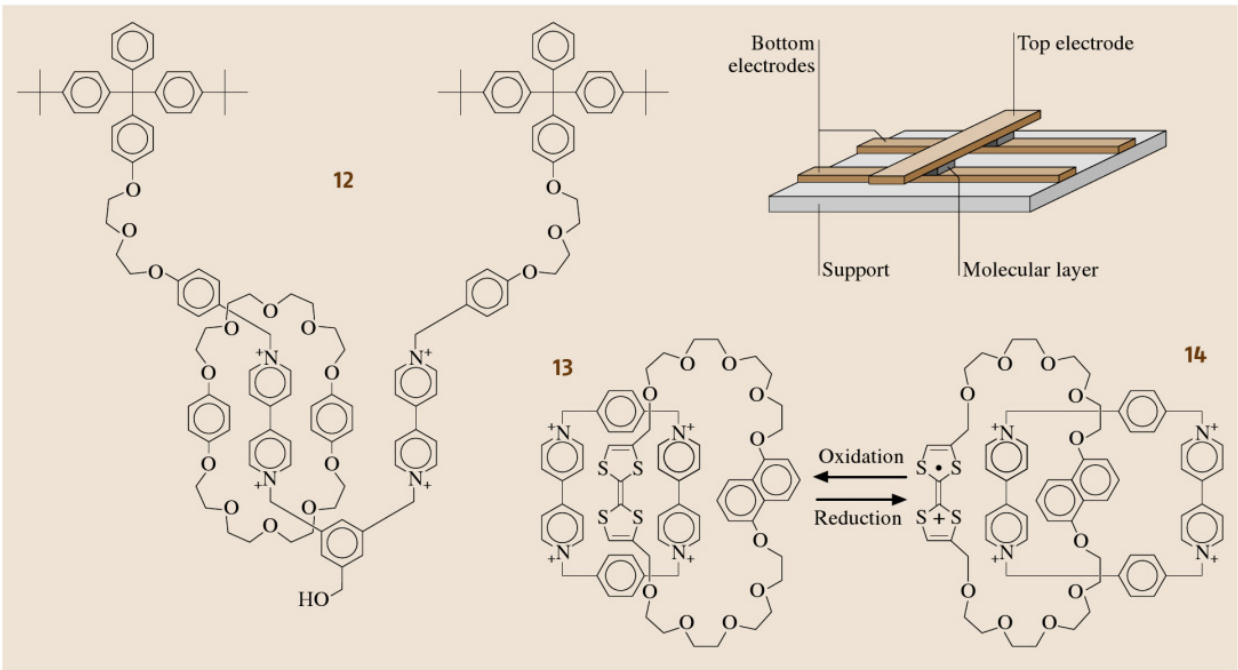

Fig. 2.14 The [2]rotaxane **12** and the [2]catenane **13** can be compressed into organized monolayers at air/water interfaces. The resulting monolayers can be transferred on the bottom electrodes of a patterned silicon support. After the deposition of a top electrode, electrode/monolayer/electrode junctions can be assembled. Note that only the portion of the monolayer sandwiched between the top and bottom electrodes is shown in the diagram. The oxidation of the tetrathiafulvalene unit of the [2]catenane **13** is followed by the circumrotation of the macrocyclic polyether to afford the [2]catenane **14**. The process is reversible, and the reduction of the cationic tetrathiafulvalene unit restores the original state

affords electrode/monolayer/electrode junctions. Their current/voltage signature can be recorded grounding the top electrode and scanning the potential of the bottom electrode. A pronounced increase in current is observed when the potential is lowered below -0.7 V. Under these conditions, the bipyridinium-centered LUMOs mediate the tunneling of electrons from the bottom to the top electrode leading to a current enhancement. A similar current profile is observed if the potential is returned to 0 and then back to -2 V. Instead, a modest increase in current in the opposite direction is observed when the potential is raised above $+0.7$ V. Presumably, this trend is a result of the participation of the phenoxy-centered HOMOs in the tunneling process. After a single positive voltage pulse, however, no current can be detected if the potential is returned to negative values. In summary, the positive potential scan suppresses irreversibly the conducting ability of the electrode/molecule/electrode junction. The behavior of this device correlates with the redox response of the [2]rotaxane **12** in solution. Cyclic voltammograms reveal reversible monoelectronic reductions of the bipyridinium dications. But they also show two irreversible oxidations associated, presumably, with the phenoxy rings of the macrocycle and tetraarylmethane groups. These observations suggest that a positive voltage pulse applied to the electrode/monolayer/electrode junction oxidizes irreversibly the sandwiched molecules suppressing their ability to mediate the transfer of electrons from the bottom to the top electrode under a negative bias.

The device incorporating the [2]rotaxane **13** can be exploited to implement simple logic operations [2.40]. The two bottom electrodes can be stimulated with voltage inputs (I1 and I2) while measuring a current output (O) at the common top electrode. When at least one of the two inputs is high (0 V), the output is low (< 0.7 nA). When both inputs are low (-2 V), the output is high (≈ 4 nA). If a negative logic convention is applied to the voltage inputs (low $= 1$, high $= 0$) and a positive logic convention is applied to the current output (low $= 0$, high $= 1$), the signal transduction behavior translates into the truth table of an AND gate. The output O is 1 only when both inputs are 1. Instead, an OR operation can be executed if the logarithm of the current is considered as the output. The logarithm of the current is -12 when both voltage inputs are 0 V. It raises to ≈ -9 when one or both voltage inputs are lowered to -2 V. This signal transduction behavior translates into the truth table of an OR gate if a negative logic convention is applied to the voltage inputs (low $= 1$, high $= 0$) and a positive logic convention is applied to the current output (low $= 0$, high $= 1$). The output O is 1 when at least one of the two inputs is 1.

The [2]catenane **13** (Fig. 2.14) incorporates a macrocyclic polyether interlocked with a tetracationic cyclophane [2.42, 43]. Organic solutions of the hexafluorophosphate salt of this [2]catenane and six equivalents of the sodium salt of dimyristoylphosphatidic acid can be co-spread on the water surface of a Langmuir trough [2.44]. The sodium hexafluorophosphate formed dissolves in the supporting aqueous phase, while the hydrophilic bipyridinium cations and the amphiphilic anions remain at the interface. Upon compression, the anions align their hydrophobic tails away from the water surface forming a compact monolayer above the cationic bipyridinium derivatives. The corresponding π–A isotherm indicates limiting molecular areas of ≈ 125 Å^2. This large value is a consequence of the bulk associated with the two interlocking macrocycles.

Monolayers of the [2]catenane **13** can be transferred from the air/water interface to the surfaces of the bottom n-doped silicon/silicon dioxide electrodes of a patterned silicon chip with the hydrophobic tails of the amphiphilic anions pointing away from the supporting substrate [2.45, 46]. The subsequent assembly of a top titanium/aluminum electrode affords electrode/monolayer/electrode arrays. Their junction resistance can be probed grounding the top electrode and maintaining the potential of the bottom electrode at $+0.1$ V. If a voltage pulse of $+2$ V is applied to the bottom electrode before the measurement, the junction resistance probed is ≈ 0.7 GΩ. After a pulse of -2 V applied to the bottom electrode, the junction resistance probed at $+0.1$ V drops ≈ 0.3 GΩ. Thus, alternating positive and negative voltage pulses can switch reversibly the junction resistance between high and low values. This intriguing behavior is a result of the redox and dynamic properties of the [2]catenane **13**.

Extensive spectroscopic and crystallographic studies [2.42, 43] demonstrated that the tetrathiafulvalene unit resides preferentially inside the cavity of the tetracationic cyclophane of the [2]catenane **13** (Fig. 2.14). Attractive $[\pi \cdots \pi]$ stacking interactions between the neutral tetrathiafulvalene and the bipyridinium dications are responsible for this co-conformation. Oxidation of the tetrathiafulvalene generates a cationic form that is expelled from the cavity of the tetracationic cyclophane. After the circumrotation of the macrocyclic polyether, the oxidized tetrathiafulvalene is exchanged with the neutral 1,5-dioxynaphthalene producing the [2]catenane **14** (Fig. 2.14). The reduction of the tetrathiafulvalene back to its neutral state

is followed by the circumrotation of the macrocyclic polyether, which restores the original state **14**. The voltage pulses applied to the bottom electrode of the electrode/monolayer/junction oxidize and reduce the tetrathiafulvalene unit inducing the interconversion between the forms **13** and **14**. The difference in the stereoelectronic properties of these two states translates into distinct current/voltage signatures. Indeed, their ability to mediate the tunneling of electrons across the junction differs significantly. As a result, the junction resistance probed at a low voltage after an oxidizing pulse is significantly different from that determined under the same conditions after a reducing pulse.

2.3.3 Self-Assembled Monolayers

In the examples illustrated in Figs. 2.12–2.14, monolayers of amphiphilic and electroactive derivatives are assembled at air/water interfaces and then transferred on the surfaces of appropriate substrates. An alternative strategy to coat electrodes with molecular layers relies on the ability of certain compounds to adsorb spontaneously on solid supports from liquid or vapor phases [2.35]. In particular, the affinity of certain sulfurated functional groups for gold can be exploited to encourage the self-assembly of organic molecules on microscaled and nanoscaled electrodes.

The electrode/monolayer/electrode junction in Fig. 2.15 incorporates a molecular layer between two gold electrodes mounted on a silicon nitride support. This device can be fabricated combining chemical vapor deposition, lithography, anisotropic etching, and self-assembly [2.47]. Initially, a silicon wafer is coated with a 50 nm thick layer of silicon nitride by low pressure chemical vapor deposition. Then, a square of $400 \times 400\,\mu m^2$ is patterned on one side of the coated wafer by optical lithography and reactive ion etching. Anisotropic etching of the exposed silicon up to the other side of the wafer leaves a suspended silicon nitride membrane of $40 \times 40\,\mu m^2$. Electron beam lithography and reactive ion etching can be used to carve a bowl-shaped hole (diameter = 30–50 nm) in the membrane. Evaporation of gold on the membrane fills the pore producing a bowl-shaped electrode. Immersion of the substrate in a solution of the thiol **15** results in the self-assembly of a molecular layer on the narrow part of the bowl-shaped electrode. The subsequent evaporation of a gold film on the organic monolayer produces an electrode/monolayer/electrode junction (Fig. 2.15) with a contact area of less than $2000\,nm^2$ and ≈ 1000 molecules.

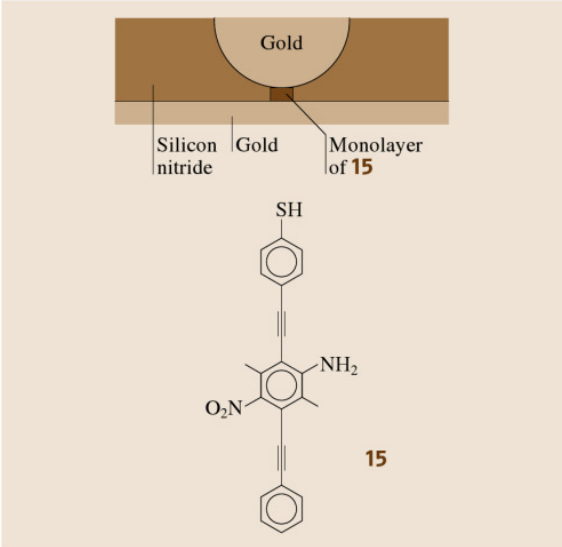

Fig. 2.15 A monolayer of the thiol **15** is embedded between two gold electrodes maintained in position by a silicon nitride support

Under the influence of voltage pulses applied to one of the two gold electrodes in Fig. 2.15, the conductivity of the sandwiched monolayer switches reversibly between low and high values [2.48]. In the initial state, the monolayer is in a low conducting mode. A current output of only 30 pA is detected, when a probing voltage of +0.25 V is applied to the bowl-shaped electrode. If the same electrode is stimulated with a short voltage pulse of +5 V, the monolayer switches to a high conducting mode. Now a current output of 150 pA is measured at the same probing voltage of +0.25 V. Repeated probing of the current output at various intervals of time indicates that the high conducting state is memorized by the molecule-based device, and it is retained for more than 15 min. The low conducting mode is restored after either a relatively long period of time or the stimulation of the bowl-shaped electrode with a reverse voltage pulse of −5 V. Thus the current output switches from a low to a high value, if a high voltage input is applied. It switches from a high to a low value, under the influence of a low voltage pulse. This behavior offers the opportunity to store and erase binary data in analogy to a conventional random access memory [2.17]. Binary digits can be encoded on the current output of the molecule-based device applying a positive logic convention (low = 0, high = 1). It follows that a binary 1 can be stored in the molecule-based device applying a high voltage

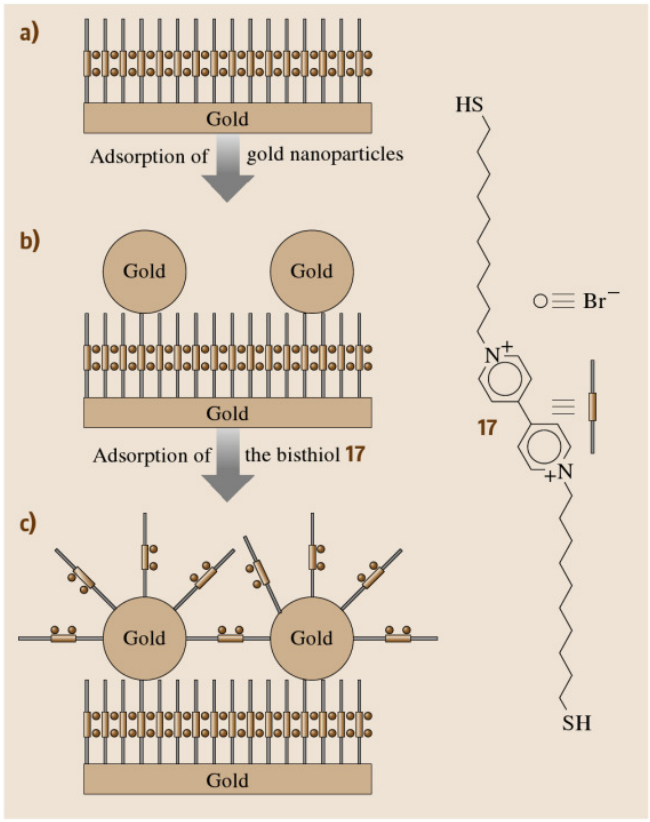

Fig. 2.16 (**a**) The bisthiol **16** self-assembles on gold electrodes as a result of thiolate–gold bond formation. (**b**) Gold nanoparticles adsorb spontaneously on the molecular layer. (**c**) Exposure of the composite assembly to a solution of **16** results in the formation of an additional molecular layer on the surface of the gold nanoparticles

input, and it can be erased applying a low voltage input [2.48].

The ability of thiols to self-assemble on the surface of gold can be exploited to fabricate nanocomposite materials integrating organic and inorganic components. For example, the bisthiol **16** forms monolayers (Fig. 2.16a) on gold electrodes with surface coverages of $\approx 4.1 \times 10^{10}$ mol cm^2 [2.49, 50]. The formation of a thiolate–gold bond at one of the two thiol ends of **16** is responsible for adsorption. The remaining thiol group points away from the supporting surface and can be exploited for further functionalization. Gold nanoparticles adsorb on the molecular layer (Fig. 2.16b), once again, as a result of thiolate–gold bond formation. The immersion of the resulting material in a methanol solution of **16** encourages the adsorption of an additional organic layer (Fig. 2.16c) on the composite material. Following these procedures, up to ten alternating organic and inorganic layers can be deposited on the electrode surface. The resulting assembly can mediate the unidirectional electron transfer from the supporting electrode to redox active species in solution. For example, the cyclic voltammogram of the $[Ru(NH_3)_6]^{3+/2+}$ couple recorded with a bare gold electrode reveals a reversible reduction process. In the presence of ten alternating molecular and nanoparticle layers on the electrode surface, the reduction potential shifts by ≈ -0.2 V and the back oxidation wave disappears. The pronounced potential shift indicates that $[Ru(NH_3)_6]^{3+}$ accepts electrons only after the surface-confined bipyridinium dications have been reduced. The lack of reversibility indicates that the back oxidation to the bipyridinium dications inhibits the transfer of electrons from the $[Ru(NH_3)_6]^{2+}$ to the electrode. Thus the electroactive multilayer allows the flow of electrons in one direction only in analogy to conventional diodes.

The current/voltage behavior of individual nanoparticles in Fig. 2.16b can be probed by scanning tunneling spectroscopy in an aqueous electrolyte under an inert atmosphere [2.51]. The platinum-iridium tip of a scanning tunneling microscope is positioned above one of the gold particles. The voltage of the gold substrate relative to the tip is maintained at -0.2 V while that relative to a reference electrode immersed in the same electrolyte is varied to control the redox state of the electroactive units. Indeed, the bipyridinium dications in the molecular layer can be reduced reversibly to a monocationic state. The resulting monocations can be reduced further and, once again, reversibly to a neutral form. Finally, the current flowing from the gold support to the tip of the scanning tunneling microscope is monitored as the tip–particle distance increases. From the distance dependence of the current, inverse length decays of ≈ 16 and 7 nm^{-1} for the dicationic and monocationic states, respectively, of the molecular spacer can be determined. The dramatic decrease indicates that the reduction of the electroactive unit facilitates the tunneling of electrons through the gold/molecule/nanoparticle/tip junction. In summary, a change in the redox state of the bipyridinium components can be exploited to gate reversibly the current flowing through this nanoscaled device.

Similar nanostructured materials, combining molecular and nanoparticles layers, can be prepared on layers on indium-tin oxide electrodes following multistep procedures [2.52]. The hydroxylated surfaces of indium-tin oxide supports can be functionalized with 3-ammoniumpropylsilyl groups and then exposed to

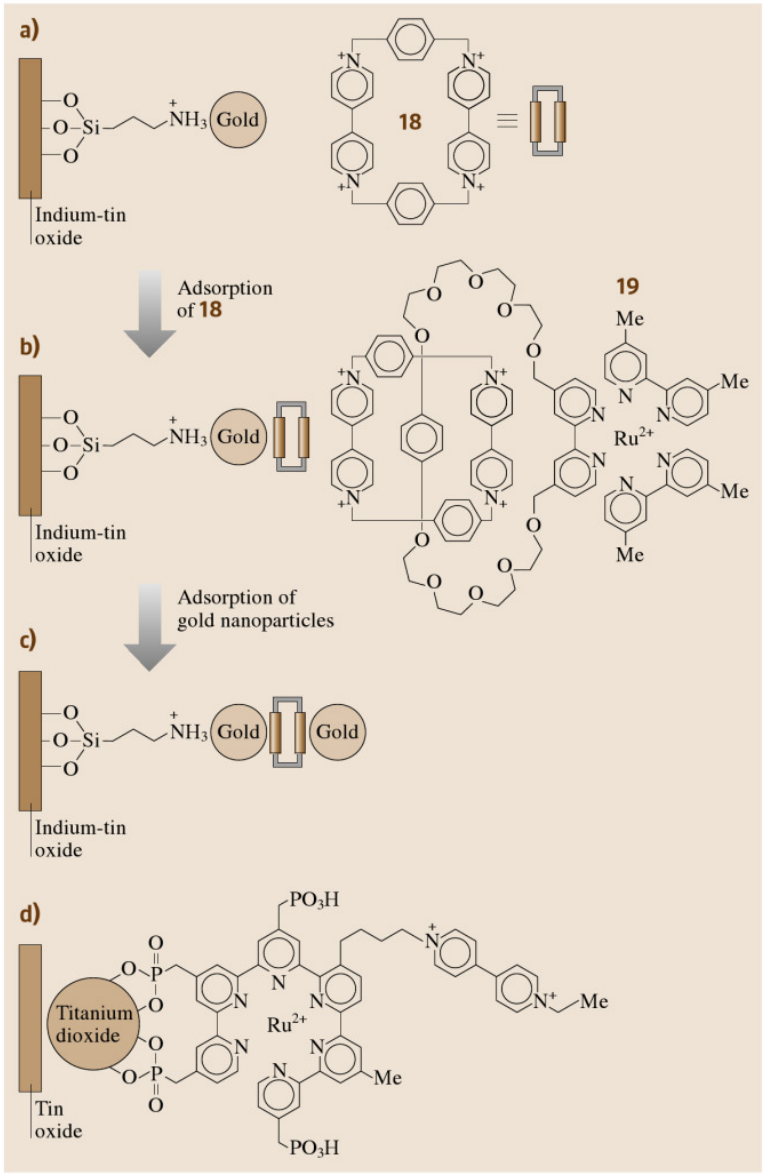

Fig. 2.17 (**a**) Gold nanoparticles assemble spontaneously on pre-functionalized indium-tin oxide electrodes. (**b**) Electrostatic interactions encourage the adsorption of the tetracationic cyclophane **17** on the surface-confined nanoparticles. (**c**) An additional layer of nanoparticles assembles on the cationic organic coating. Similar composite films can be prepared using the tetracationic [2]catenane **18** instead of the cyclophane **17**. (**d**) Phosphonate groups can be used to anchor molecular building blocks to titanium dioxide nanoparticles

gold nanoparticles having a diameter of ≈ 13 nm [2.53, 54]. Electrostatic interactions promote the adsorption of the nanoparticles on the organic layer (Fig. 2.17a). The treatment of the composite film with the bipyridinium cyclophane **17** produces an organic layer on the gold nanoparticles (Fig. 2.18b). Following this approach, alternating layers of inorganic nanoparticles and organic building blocks can be assembled on the indium-tin oxide support. Cyclic voltammograms of the resulting materials show the oxidation of the gold nanoparticles and the reduction of the bipyridinium units. The peak current for both processes increases with the number of alternating layers. Comparison of these values indicates that the ratio between the number of tetracationic cyclophanes and that of the nanoparticles is ≈ 100 : 1.

The tetracationic cyclophane **17** binds dioxyarenes in solution [2.55, 56]. Attractive supramolecular forces between the electron deficient bipyridinium units and the electron rich guests are responsible for complexation. This recognition motif can be exploited to probe

the ability of the composite films in Fig. 2.17b,c to sense electron rich analytes. In particular, hydroquinone is expected to enter the electron deficient cavities of the surface-confined cyclophanes. Cyclic voltammograms consistently reveal the redox waves associated with the reversible oxidation of hydroquinone even when very small amounts of the guest ($\approx 1 \times 10^{-5}$ M) are added to the electrolyte solution [2.53, 54]. No redox response can be detected with a bare indium-tin oxide electrode under otherwise identical conditions. The supramolecular association of the guest and the surface confined cyclophanes increases the local concentration of hydroquinone at the electrode/solution interface enabling its electrochemical detection.

Following a related strategy, the [2]catenane **18** (Fig. 2.17) can be incorporated into similar composite arrays [2.57, 58]. This interlocked molecule incorporates a Ru(II)/trisbipyridine sensitizer and two bipyridinium acceptors. Upon irradiation of the composite material at 440 nm, photoinduced electron transfer from the sensitizer to the appended acceptors occurs. The photogenerated hole in the sensitizer is filled after the transfer of an electron from a sacrificial electron donor present in the electrolyte solution. Under a positive voltage bias applied to the supporting electrode, an electron flow from the bipyridinium acceptors to the indium-tin oxide support is established. The resulting current switches between high and low values as the light source is turned on and off.

Another photoresponsive device, assembled combining inorganic nanoparticles with molecular building blocks, is illustrated in Fig. 2.17d. Phosphonate groups can be used to anchor a Ru(II)/trisbipyridine complex with an appended bipyridinium dication to titanium dioxide nanoparticles deposited on a doped tin oxide electrode [2.59, 60]. The resulting composite array can be integrated in a conventional electrochemical cell filled with an aqueous electrolyte containing triethanolamine. Under a bias voltage of -0.45 V and irradiation at 532 nm, 95% of the excited ruthenium centers transfer electrons to the titanium dioxide nanoparticles. The other 5% donate electrons to the bipyridinium dications. All the electrons transferred to the bipyridinium acceptors return to the ruthenium centers, while only 80% of those accepted by the nanoparticles return to the transition metal complexes. The remaining 15% reach the bipyridinium acceptors, while electron transfer from sacrificial triethanolamine donors fills the photogenerated holes left in the ruthenium sensitizers. The photoinduced reduction of the bipyridinium dication is accompanied by the appearance of the characteristic band of the radical cation in the absorption spectrum. This band persists for hours under open circuit conditions. But it fades in ≈ 15 s under a voltage bias of $+1$ V, as the radical cation is oxidized back to the dicationic form. In summary, an optical stimulation accompanied by a negative voltage bias reduces the bipyridinium building block. The state of the photogenerated form can be read optically, recording the absorption spectrum in the visible region, and erased electrically, applying a positive voltage pulse.

2.3.4 Nanogaps and Nanowires

The operating principles of the electroactive and photoactive devices illustrated in Figs. 2.12–2.17 exploit the ability of small collections of molecular components to manipulate electrons and photons. Designed molecules are deposited on relatively large electrodes and can be addressed electrically and/or optically by controlling the voltage of the support and/or illuminating its surface. The transition from devices relying on collections of molecules to unimolecular devices requires the identification of practical methods to contact single molecules. This fascinating objective demands the rather challenging miniaturization of contacting electrodes to the nanoscale.

A promising approach to unimolecular devices relies on the fabrication of nanometer-sized gaps in metallic features followed by the insertion of individual molecules between the terminals of the gap. This strategy permits the assembly of nanoscaled three-terminal devices equivalent to conventional transistors [2.61–63]. A remarkable example is illustrated in Fig. 2.18a [2.61]. It incorporates a single molecule in the nanogap generated between two gold electrodes. Initially electron beam lithography is used to pattern a gold wire on a doped silicon wafer covered by an insulating silicon dioxide layer. Then the gold feature is broken by electromigration to generate the nanogap. The lateral size of the separated electrodes is ≈ 100 nm and their thickness is ≈ 15 nm. Scanning electron microcopy indicates that the facing surfaces of the separated electrodes are not uniform and that tiny gaps between their protrusions are formed. Current/voltage measurements suggest that the size of the smallest nanogap is ≈ 1 nm. When the breakage of the gold feature is preceded by the deposition of a dilute toluene solution of C_{60} (**19**), junctions with enhanced conduction are obtained. This particular molecule has a diameter of ≈ 0.7 nm and can insert in the nanogap facilitating the flow of electrons across the junction.

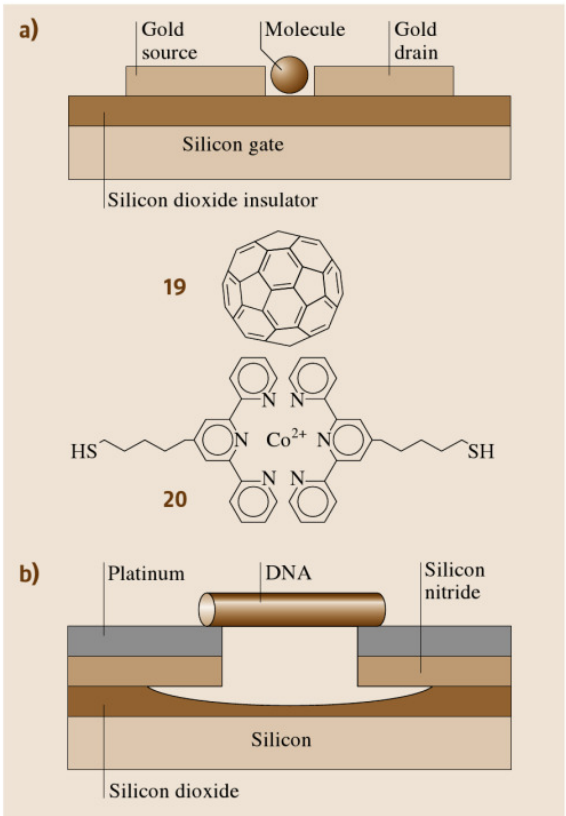

Fig. 2.18 (**a**) Nanoscaled transistors can be fabricated inserting a single molecule (**19** or **20**) between source and drain electrodes mounted on a silicon/silicon dioxide support. (**b**) A DNA nanowire can bridge nanoelectrodes suspended above a silicon dioxide support

The unique configuration of the molecule-based device in Fig. 2.18a can reproduce the functions of a conventional transistor [2.19] at the nanoscale. The two gold terminals of the junction are the drain and source of this nanotransistor, and the underlying silicon wafer is the gate. At a temperature of 1.5 K, the junction conductance is very small, when the gate bias is low, and increases in steps at higher voltages [2.61]. The conductance gap is a consequence of the finite energy required to oxidize/reduce the single C_{60} positioned in the junction. It is interesting that the zero-conductance window also changes with the gate voltage and can be opened and closed reversibly adjusting the gate bias.

A similar strategy can be employed to fabricate a nanoscaled transistor incorporating the Co(II) complex **20** shown in Fig. 2.18 [2.63]. In this instance, a silicon dioxide layer with a thickness of ≈ 30 nm is grown thermally on a doped silicon substrate. Then a gold wire with a width of ≈ 200 nm and a thicknesses of $\approx 10-15$ nm is patterned on the silicon dioxide overlayer by electron beam lithography. After extensive washing of the substrate with acetone and methylene chloride and cleaning with oxygen plasma, the gold wire is exposed to a solution of the bisthiol **20**. The formation of thiolate–gold bonds promotes the self-assembly of the molecular building block on the gold surface. At this point, electromigration-induced breakage produces a gap of 1–2 nm in the gold wire. The surface-confined bisthiol **20** is only 0.24 nm long and, therefore, it can insert in the nanogap producing an electrode/molecule/electrode junction.

The cobalt center in **20** can be oxidized/reduced reversibly between Co(II) and Co(III) [2.63]. When this electroactive molecule is inserted in a nanogap (Fig. 2.18a), its ability to accept and donate electrons dictates the current/voltage profile of the resulting electrode/molecule/electrode junction. More precisely, no current flows across the junction below a certain voltage threshold. As the source voltage is raised above this particular value, the drain current increases in steps. The threshold associated with the source voltage varies in magnitude with the gate voltage. This intriguing behavior is a consequence of the finite energy necessary to oxidize/reduce the cobalt center and of a change in the relative stabilities of the oxidized and reduced forms Co(II) and Co(III) with the gate voltage. In summary, the conduction of the electrode/molecule/electrode junction can be tuned adjusting the voltage of the silicon support. The behavior of this molecule-based nanoelectronic device is equivalent to that of a conventional transistor [2.19]. In both instances, the gate voltage regulates the current flowing from the source to the drain.

The electromigration-induced breakage of preformed metallic features successfully produces nanogaps by moving apart two fragments of the same wire. Alternatively, nanogaps can be fabricated reducing the separation of the two terminals of much larger gaps. For example, gold electrodes separated by a distance of 20–80 nm can be patterned on a silicon/silicon dioxide substrate by electron beam lithography [2.64]. The relatively large gap between them can be reduced significantly by the electrochemical deposition of gold on the surfaces of both electrodes. The final result is the fabrication of two nanoelectrodes separated by ≈ 1 nm and with a radius of curvature of 5–15 nm. The two terminals of this nanogap can be *contacted* by organic nanowires grown between them [2.65]. In particular, the

electropolymerization of aniline produces polyaniline bridges between the gold nanoelectrodes. The conductance of the resulting junction can be probed immersing the overall assembly in an electrolyte solution. Employing a bipotentiostat, the bias voltage of the two terminals of the junction can be maintained at 20 mV, while their potentials are scanned relative to that of a silver/silver chloride reference electrode. Below ≈ 0.15 V, the polymer wire is in an insulating state and the current flowing across the junction is less than 0.05 nA. At this voltage threshold, however, the current raises abruptly to ≈ 30 nA. This value corresponds to a conductivity for the polymer nanojunction of $10-100\ \mathrm{S\,cm^{-1}}$. When the potential is lowered again below the threshold, the current returns back to very low values. The abrupt decrease in current in the backward scan is observed at a potential that is slightly more negative than that causing the abrupt current increase in the forward scan. In summary, the conductance of this nanoscaled junction switches on and off as a potential input is switched above and below a voltage threshold.

It is interesting to note that the influence of organic bridges on the junction conductance can be exploited for chemical sensing. Nanogaps fabricated following a similar strategy but lacking the polyaniline bridge alter their conduction after exposure to dilute solutions of small organic molecules [2.66]. Indeed, the organic analytes dock into the nanogaps producing a marked decrease in the junction conductance. The magnitude of the conductance drop happens to be proportional to the analyte–nanoelectrode binding strength. Thus the presence of the analyte in solution can be detected probing the current/voltage characteristics of the nanogaps.

Nanogaps between electrodes patterned on silicon/silicon dioxide supports can be bridged also by DNA double strands [2.67,68]. The device in Fig. 2.18b has a 10.4 nm long poly(G)–poly(C) DNA oligomer suspended between two nanoelectrodes. It can be fabricated patterning a 30 nm wide slit in a silicon nitride overlayer covering a silicon/silicon dioxide support by electron beam evaporation. Underetching the silicon dioxide layer leaves a silicon nitride finger, which can be sputtered with a platinum layer and chopped to leave a nanogap of 8 nm. At this point, a microdroplet of a dilute solution of DNA is deposited on the device and a bias of 5 V is applied between the two electrodes. Electrostatic forces encourage the deposition of a single DNA wire on top of the nanogap. As soon as the nanowire is in position, current starts to flow across the junction. The current/voltage signature of the electrode/DNA/electrode junction shows currents below 1 pA at low voltage biases. Under these conditions, the DNA nanowire is an insulator. Above a certain voltage threshold, however, the nanowire becomes conducting and currents up to 100 nA can flow across the junction through a single nanowire. Assuming that direct tunneling from electrode to electrode is extremely unlikely for a relatively large gap of 8 nm, the intriguing current/voltage behavior has to be a consequence of the participation of the molecular states in the electron transport process. Two possible mechanisms can be envisaged. Sequential hopping of the electrons between states localized in the DNA base pairs can allow the current flow above a certain voltage threshold. But this mechanism would presumably result in a Coulomb blockade voltage gap that is not observed experimentally. More likely, electronic states delocalized across the entire length of the DNA nanowire are producing a molecular conduction band. The off-set between the molecular conduction band and the Fermi levels of the electrodes is responsible for the insulating behavior at low biases. Above a certain voltage threshold, the molecular band and one of the Fermi levels align facilitating the passage of electrons across the junction.

Carbon nanotubes are extremely versatile building blocks for the assembly of nanoscaled electronic devices. They can be used to bridge nanogaps [2.69–72] and assemble nanoscaled cross junctions [2.73–75]. In Fig. 2.19a, a single-wall carbon nanotube crosses over another one in an orthogonal arrangement [2.73]. Both nanotubes have electrical contacts at their ends. The fabrication of this device involves three main steps. First, alignment marks for the electrodes are patterned on a silicon/silicon dioxide support by electron beam lithography. Then the substrate is exposed to a dichloromethane suspension of single-wall SWNT carbon nanotubes. After washing with isopropanol, crosses of carbon nanotubes in an appropriate alignment relative to the electrode marks are identified by tapping mode atomic force microscopy. Finally chromium/gold electrodes are fabricated on top of the nanotube ends, again, by electron beam lithography. The conductance of individual nanotubes can be probed by exploiting the two electric contacts at their ends. These two-terminal measurements reveal that certain nanotubes have metallic behavior, while others are semiconducting. It follows that three distinct types of cross junctions differing in the nature of their constituent nanotubes can be identified on the silicon/silicon dioxide support. Four terminal current/voltage measurements indicate that junctions formed by two metallic nanotubes have high conductance and ohmic behavior.

Similarly, high junction conductance and ohmic behavior is observed when two semiconducting nanotubes cross. The current/voltage signature of junctions formed when a metallic nanotube crosses a semiconducting one are, instead, completely different. The metallic nanotube depletes the semiconducting one at the junction region producing a nanoscaled Schottky barrier with a pronounced rectifying behavior.

Similar fabrication strategies can be exploited to assemble nanoscaled counterparts of conventional transistors. The device in Fig. 2.19b is assembled patterning an aluminum finger on a silicon/silicon dioxide substrate by electron beam lithography [2.75]. After exposure to air, an insulating aluminum oxide layer forms on the aluminum finger. Then a dichloromethane suspension of single-wall carbon nanotubes is deposited on the resulting substrate. Atomic force microscopy can be used to select carbon nanotubes with a diameter of ≈ 1 nm positioned on the aluminum finger. After registering their coordinates relative to alignment markers, gold contacts can be evaporated on their ends by electron beam lithography. The final assembly is a nanoscaled three-terminal device equivalent to a conventional field effect transistor [2.19]. The two gold contacts are the source and drain terminals, while the underlying aluminum finger reproduces the function of the gate. At a source to drain bias of ≈ -1.3 V, the drain current jumps from ≈ 0 to ≈ 50 nA when the gate voltage is lowered from -1.0 to -1.3 V. Thus moderate changes in the gate voltage vary significantly the current flowing through the nanotube-based device in analogy to a conventional enhancement mode p-type field effect transistor [2.19].

The nanoscaled transistor in Fig. 2.18a has a microscaled silicon gate that extends under the entire chip [2.61, 63]. The configuration in Fig. 2.19b, instead, has nanoscaled aluminum gates for every single carbon nanotube transistor fabricated on the same support [2.75]. It follows that multiple nanoscaled transistors can be fabricated on the same chip and operated independently following this strategy. This unique feature offers the possibility of fabricating nanoscaled digital circuits by interconnecting the terminals of independent nanotube transistors. The examples in Fig. 2.19c,d illustrate the configurations of nanoscaled NOT and NOR gates implemented using one or two nanotube transistors. In Fig. 2.19c, an off-chip bias resistor is connected to the drain terminal of a single transistor while the source is grounded. A voltage input applied to the gate modulates the nanotube conductance altering the voltage output probed at the drain terminal. In particular, a voltage input of -1.5 V lowers the nanotube resistance (26 MΩ) below that of the bias resistor (100 MΩ). As a result, the voltage output drops to 0 V. When the voltage input is raised to 0 V, the nanotube resistance increases above that of the bias resistor and the voltage output becomes -1.5 V. Thus

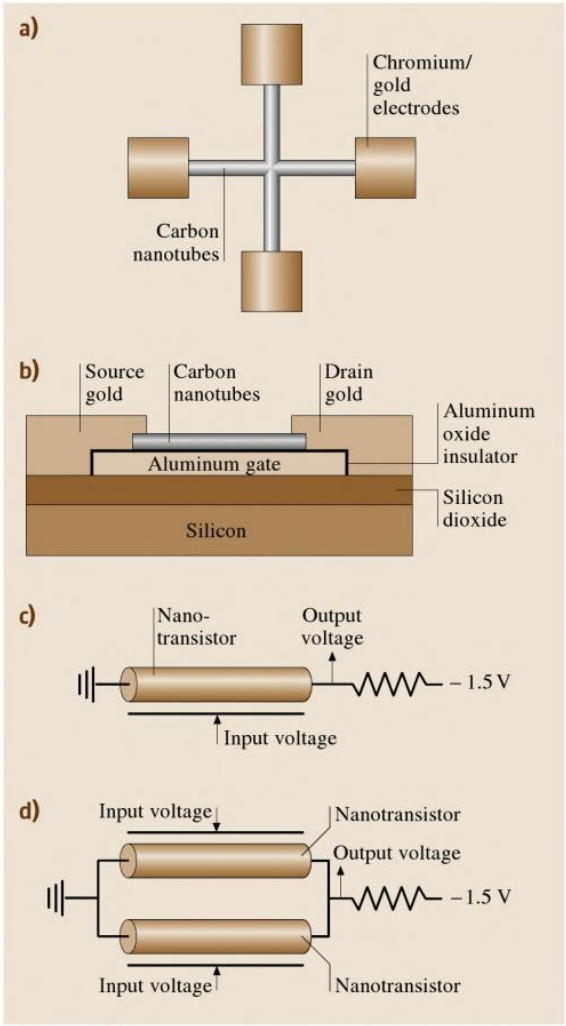

Fig. 2.19 (**a**) Nanoscaled junctions can be assembled on silicon/silicon dioxide supports crossing pairs of orthogonally arranged single-wall carbon nanotubes with chromium/gold electrical contacts at their ends. (**b**) Nanotransistors can be fabricated contacting the two ends of a single-wall carbon nanotube deposited on an aluminum/aluminum oxide gate with gold sources and drain. One or two nanotube transistors can be integrated into nanoscaled NOT (**c**) and NOR (**d**) logic gates

the output of this nanoelectronic device switches from a high (0 V) and to a low (− 1.5 V) level as the input shifts from a low (− 1.5 V) to a high (0 V) value. The inverse relation between input and output translates into a NOT operation if a negative logic convention (low = 1, high = 0) is applied to both signals.

In Fig. 2.15d, the source terminals of two independent nanotube transistors fabricated on the same chip are connected by a gold wire and grounded [2.75]. Similarly, the two drain terminals are connected by another gold wire and contacted to an off-chip bias resistors. The gate of each nanotube can be stimulated with a voltage input and the voltage output of the device can be probed at their interconnected drain terminals. When the resistance of at least one of the two nanotubes is below that of the resistor, the output is 0 V. When both nanotubes are in a nonconducting mode, the output voltage is − 1.5 V. Thus if a low voltage input − 1.5 V is applied to one or both transistors, the output is high (0 V). When both voltage inputs are high (0 V), the output is low (− 1.5 V). If a negative logic convention (low = 1, high = 0) is applied to all signals, the signal transduction behavior translates in to a NOR operation.

2.4 Conclusions and Outlook

Nature builds nanostructured biomolecules relying on a highly modular approach [2.1]. Small building blocks are connected by robust chemical bonds to generate long strands of repeating units. The synergism of a multitude of attractive supramolecular forces determines the three-dimensional arrangement of the resulting polymeric chains and controls the association of independent strands into single and well-defined entities. Nucleic acids and proteins are two representative classes of biomolecules assembled with subnanometer precision through the subtle interplay of covalent and noncovalent bonds starting from a relatively small pool of nucleotide and amino acid building blocks.

The power of chemical synthesis [2.2] offers the opportunity of mimicking nature's modular approach to nanostructured materials. Following established experimental protocols, small molecular building blocks can be joined together relying on the controlled formation of covalent bonds between designed functional groups. Thus artificial molecules with nanoscaled dimensions can be assembled piece by piece with high structural control. Indeed, helical, tubular, interlocked, and highly branched nanostructures have been all prepared already exploiting this general strategy and the synergism of covalent and noncovalent bonds [2.3].

The chemical construction of nanoscaled molecules from modular building blocks also offers the opportunity for engineering specific properties in the resulting assemblies. In particular, electroactive and photoactive fragments can be integrated into single molecules. The ability of these functional subunits to accept/donate electrons and photons can be exploited to design nanoscaled electronic and photonic devices. Indeed, molecules that respond to electrical and optical stimulations producing detectable outputs have been designed already [2.16]. These chemical systems can be employed to control the interplay of input and output signals at the molecular level. Their conceptual analogy with the signal transduction operated by conventional logic gates in digital circuits is evident. In fact, electroactive and photoactive molecules able to reproduce AND, NOT, and OR operations as well as simple combinational of these basic logic functions are already a reality [2.13, 20, 21].

Most of the molecular switches for digital processing developed so far rely on bulk addressing. In general, relatively large collections of functional molecules are addressed simultaneously in solution. The realization of molecule-based devices with reduced dimensions as well as practical limitations associated with liquid phases in potential applications are encouraging a transition from the solution to the solid state. The general strategy followed so far relies on the deposition of functional molecules on the surfaces of appropriate electrodes following either the Langmuir–Blodgett methodology [2.34] or self-assembly processes [2.35]. The combination of these techniques with the nanofabrication of insulating, metallic, and semiconducting features on appropriate supports has already allowed the realization of fascinating molecule-based devices [2.30–33, 52]. The resulting assemblies integrate inorganic and organic components and, in some instances, even biomolecules to execute specific functions. They can convert optical stimulations into electrical signals. They can execute irreversible and reversible switching operations. They can sense qualitatively and quantitatively specific analytes. They can reproduce the functions of conventional rectifiers and transistors. They can be

integrated within functioning nanoelectronic devices capable of simple logic operations.

The remarkable examples of molecule-based materials and devices now available demonstrate the great potential and promise for this research area. At this stage, the only limit left to the design of functional molecules is the imagination of the synthetic chemist. All sort of molecular building blocks with tailored dimensions, shapes, and properties are more or less accessible with the assistance of modern chemical synthesis. Now, the major challenges are (1) to master the operating principles of the molecule-based devices that have been and continue to be assembled and (2) to expand and improve the fabrication strategies available to incorporate molecules into reliable device architectures. As we continue to gather further insights in these directions, design criteria for a wide diversity of molecule-based devices will emerge. It is not unrealistic to foresee the evolution of an entire generation of nanoscaled devices, based on engineered molecular components, that will find applications in a variety of fields ranging from biomedical research to information technology. Perhaps nature can once again illuminate our path, teaching us not only how to synthesize nanostructured molecules but also how to use them. After all, nature is replete with examples of extremely sophisticated molecule-based devices. From tiny bacteria to higher animals, we are all a collection of molecule-based devices.

References

2.1 D. Voet, J.G. Voet: *Biochemistry* (Wiley, New York 1995)

2.2 K.C. Nicolau, E.C. Sorensen: *Classics in Total Synthesis* (VCH, Weinheim 1996)

2.3 J.-M. Lehn: *Supramolecular Chemistry: Concepts and Perspectives* (VCH, Weinheim 1995)

2.4 M.M. Harding, U. Koert, J.-M. Lehn, A. Marquis-Rigault, C. Piguet, J. Siegel: Synthesis of unsubstituted and 4,4′-substituted oligobipyridines as ligand strands for helicate self-assembly, Helv. Chim. Acta **74**, 594–610 (1991)

2.5 J.-M. Lehn, A. Rigault, J. Siegel, B. Harrowfield, B. Chevrier, D. Moras: Spontaneous assembly of double-stranded helicates from oligobipyridine ligands and copper(I) cations: Structure of an inorganic double helix, Proc. Natl. Acad. Sci. USA **84**, 2565–2569 (1987)

2.6 J.-M. Lehn, A. Rigault: Helicates: Tetra- and pentanuclear double helix complexes of Cu(I) and poly(bipyridine) strands, Angew. Chem. Int. Ed. Engl. **27**, 1095–1097 (1988)

2.7 J.D. Hartgerink, J.R. Granja, R.A. Milligan, M.R. Ghadiri: Self-assembling peptide nanotubes, J. Am. Chem. Soc. **118**, 43–50 (1996)

2.8 M.R. Ghadiri, J.R. Granja, R.A. Milligan, D.E. McRee, N. Khazanovich: Self-assembling organic nanotubes based on a cyclic peptide architecture, Nature **366**, 324–327 (1993)

2.9 V. Balzani, A. Credi, F.M. Raymo, J.F. Stoddart: Artificial molecular machines, Angew. Chem. Int. Ed. **39**, 3348–3391 (2000)

2.10 A.J. Bard, L.R. Faulkner: *Electrochemical Methods: Fundamentals and Applications* (Wiley, New York 2000)

2.11 V. Balzani (Ed.): *Electron Transfer in Chemistry* (Wiley-VCH, Weinheim 2001)

2.12 J.D. Coyle: *Principles and Applications of Photochemistry* (Wiley, New York 1988)

2.13 V. Balzani, M. Venturi, A. Credi: *Molecular Devices and Machines* (Wiley-VCH, Weinheim 2003)

2.14 P.R. Ashton, R. Ballardini, V. Balzani, A. Credi, K.R. Dress, E. Ishow, C.J. Kleverlaan, O. Kocian, J.A. Preece, N. Spencer, J.F. Stoddart, M. Venturi, S. Wenger: A photochemically driven molecular-level abacus, Chem. Eur. J. **6**, 3558–3574 (2000)

2.15 M. Irié (Ed.): Photochromism: memories and switches, Chem. Rev. **100**, 1683–1890 (2000)

2.16 B.L. Feringa (Ed.): *Molecular Switches* (Wiley-VCH, Weinheim 2001)

2.17 R.J. Mitchell: *Microprocessor Systems: An Introduction* (Macmillan, London 1995)

2.18 D.R. Smith: *Digital Transmission Systems* (Van Nostrand Reinhold, New York 1993)

2.19 S. Madhu: *Electronics: Circuits and Systems* (SAMS, Indianapolis 1985)

2.20 F.M. Raymo: Digital processing and communication with molecular switches, Adv. Mater. **14**, 401–414 (2002)

2.21 A.P. de Silva: Molecular computation – Molecular logic gets loaded, Nat. Mater. **4**, 15–16 (2005)

2.22 A. Aviram: Molecules for memory, logic and amplification, J. Am. Chem. Soc. **110**, 5687–5692 (1988)

2.23 A.P. de Silva, H.Q.N. Gunaratne, C.P. McCoy: A molecular photoionic AND gate based on fluorescent signaling, Nature **364**, 42–44 (1993)

2.24 M. Asakawa, P.R. Ashton, V. Balzani, A. Credi, G. Mattersteig, O.A. Matthews, M. Montalti, N. Spencer, J.F. Stoddart, M. Venturi: Electrochemically induced molecular motions in pseudorotaxanes: A case of dual-mode (oxidative and reductive) dethreading, Chem. Eur. J. **3**, 1992–1996 (1997)

2.25 F.M. Raymo, S. Giordani, A.J.P. White, D.J. Williams: Digital processing with a three-state molecular switch, J. Org. Chem. **68**, 4158–4169 (2003)

2.26 F.M. Raymo, S. Giordani: Signal communication between molecular switches, Org. Lett. **3**, 3475–3478 (2001)

2.27 F.M. Raymo, S. Giordani: Multichannel digital transmission in an optical network of communicating molecules, J. Am. Chem. Soc. **124**, 2004–2007 (2002)

2.28 F.M. Raymo, S. Giordani: All-optical processing with molecular switches, Proc. Natl. Acad. Sci. USA **99**, 4941–4944 (2002)

2.29 A.J. Bard: *Integrated Chemical Systems: A Chemical Approach to Nanotechnology* (Wiley, New York 1994)

2.30 C. Joachim, J.K. Gimzewski, A. Aviram: Electronics using hybrid-molecular and mono-molecular devices, Nature **408**, 541–548 (2000)

2.31 J.M. Tour: Molecular electronics. Synthesis and testing of components, Acc. Chem. Res. **33**, 791–804 (2000)

2.32 A.R. Pease, J.O. Jeppesen, J.F. Stoddart, Y. Luo, C.P. Collier, J.R. Heath: Switching devices based on interlocked molecules, Acc. Chem. Res. **34**, 433–444 (2001)

2.33 R.M. Metzger: Unimolecular electrical rectifiers, Chem. Rev. **103**, 3803–3834 (2003)

2.34 M.C. Petty: *Langmuir–Blodgett Films: An Introduction* (Cambridge Univ. Press, Cambridge 1996)

2.35 A. Ulman: *An Introduction to Ultrathin Organic Films* (Academic, Boston 1991)

2.36 C. Lee, A.J. Bard: Comparative electrochemical studies of *N*-methyl-*N*′-hexadecyl viologen monomolecular films formed by irreversible adsorption and the Langmuir–Blodgett method, J. Electroanal. Chem. **239**, 441–446 (1988)

2.37 C. Lee, A.J. Bard: Cyclic voltammetry and Langmuir film isotherms of mixed monolayers of *N*-docosoyl-*N*′-methyl viologen with arachidic acid, Chem. Phys. Lett. **170**, 57–60 (1990)

2.38 M. Fujihira, K. Nishiyama, H. Yamada: Photoelectrochemical responses of optically transparent electrodes modified with Langmuir–Blodgett films consisting of surfactant derivatives of electron donor, acceptor and sensitizer molecules, Thin Solid Films **132**, 77–82 (1985)

2.39 M. Fujihira: Photoelectric conversion with Langmuir–Blodgett films. In: *Nanostructures Based on Molecular Materials*, ed. by W. Göpel, C. Ziegler (VCH, Weinheim 1992) pp. 27–46

2.40 C.P. Collier, E.W. Wong, M. Belohradsky, F.M. Raymo, J.F. Stoddart, P.J. Kuekes, R.S. Williams, J.R. Heath: Electronically configurable molecular-based logic gates, Science **285**, 391–394 (1999)

2.41 E.W. Wong, C.P. Collier, M. Belohradsky, F.M. Raymo, J.F. Stoddart, J.R. Heath: Fabrication and transport properties of single-molecule-thick electrochemical junctions, J. Am. Chem. Soc. **122**, 5831–5840 (2000)

2.42 M. Asakawa, P.R. Ashton, V. Balzani, A. Credi, C. Hamers, G. Mattersteig, M. Montalti, A.N. Shipway, N. Spencer, J.F. Stoddart, M.S. Tolley, M. Venturi, A.J.P. White, D.J. Williams: A chemically and electrochemically switchable [2]catenane incorporating a tetrathiafulvalene unit, Angew. Chem. Int. Ed. **37**, 333–337 (1998)

2.43 V. Balzani, A. Credi, G. Mattersteig, O.A. Matthews, F.M. Raymo, J.F. Stoddart, M. Venturi, A.J.P. White, D.J. Williams: Switching of pseudorotaxanes and catenanes incorporating a tetrathiafulvalene unit by redox and chemical inputs, J. Org. Chem. **65**, 1924–1936 (2000)

2.44 M. Asakawa, M. Higuchi, G. Mattersteig, T. Nakamura, A.R. Pease, F.M. Raymo, T. Shimizu, J.F. Stoddart: Current/voltage characteristics of monolayers of redox-switchable [2]catenanes on gold, Adv. Mater. **12**, 1099–1102 (2000)

2.45 C.P. Collier, G. Mattersteig, E.W. Wong, Y. Luo, K. Beverly, J. Sampaio, F.M. Raymo, J.F. Stoddart, J.R. Heath: A [2]catenane based solid-state electronically reconfigurable switch, Science **289**, 1172–1175 (2000)

2.46 C.P. Collier, J.O. Jeppesen, Y. Luo, J. Perkins, E.W. Wong, J.R. Heath, J.F. Stoddart: Molecular-based electronically switchable tunnel junction devices, J. Am. Chem. Soc. **123**, 12632–12641 (2001)

2.47 J. Chen, M.A. Reed, A.M. Rawlett, J.M. Tour: Large on-off ratios and negative differential resistance in a molecular electronic device, Science **286**, 1550–1552 (1999)

2.48 M.A. Reed, J. Chen, A.M. Rawlett, D.W. Price, J.M. Tour: Molecular random access memory cell, Appl. Phys. Lett. **78**, 3735–3737 (2001)

2.49 D.I. Gittins, D. Bethell, R.J. Nichols, D.J. Schiffrin: Redox-controlled multilayers of discrete gold particles: A novel electroactive nanomaterial, Adv. Mater. **9**, 737–740 (1999)

2.50 D.I. Gittins, D. Bethell, R.J. Nichols, D.J. Schiffrin: Diode-like electron transfer across nanostructured films containing a redox ligand, J. Mater. Chem. **10**, 79–83 (2000)

2.51 D.I. Gittins, D. Bethell, D.J. Schiffrin, R.J. Nichols: A nanometer-scale electronic switch consisting of a metal cluster and redox-addressable groups, Nature **408**, 67–69 (2000)

2.52 A.N. Shipway, M. Lahav, I. Willner: Nanostructured gold colloid electrodes, Adv. Mater. **12**, 993–998 (2000)

2.53 A.N. Shipway, M. Lahav, R. Blonder, I. Willner: Bis-bipyridinium cyclophane receptor–Au nanoparticle superstructure for electrochemical sensing applications, Chem. Mater. **11**, 13–15 (1999)

2.54 M. Lahav, A.N. Shipway, I. Willner, M.B. Nielsen, J.F. Stoddart: An enlarged bis-bipyridinum cyclophane–Au nanoparticle superstructure for selective electrochemical sensing applications, J. Electroanal. Chem. **482**, 217–221 (2000)

2.55 R.E. Gillard, F.M. Raymo, J.F. Stoddart: Controlling self-assembly, Chem. Eur. J. **3**, 1933–1940 (1997)

2.56 F.M. Raymo, J.F. Stoddart: From supramolecular complexes to interlocked molecular compounds, Chemtracts Org. Chem. **11**, 491–511 (1998)

2.57 M. Lahav, T. Gabriel, A.N. Shipway, I. Willner: Assembly of a Zn(II)-porphyrin-bipyridinium dyad and Au-nanoparticle superstructures on conductive surfaces, J. Am. Chem. Soc. **121**, 258–259 (1999)

2.58 M. Lahav, V. Heleg-Shabtai, J. Wasserman, E. Katz, I. Willner, H. Durr, Y. Hu, S.H. Bossmann: Photoelectrochemistry with integrated photosensitizer-electron acceptor Au-nanoparticle arrays, J. Am. Chem. Soc. **122**, 11480–11487 (2000)

2.59 G. Will, S.N. Rao, D. Fitzmaurice: Heterosupramolecular optical write-read-erase device, J. Mater. Chem. **9**, 2297–2299 (1999)

2.60 A. Merrins, C. Kleverlann, G. Will, S.N. Rao, F. Scandola, D. Fitzmaurice: Time-resolved optical spectroscopy of heterosupramolecular assemblies based on nanostructured TiO_2 films modified by chemisorption of covalently linked ruthenium and viologen complex components, J. Phys. Chem. B **105**, 2998–3004 (2001)

2.61 H. Park, J. Park, A.K.L. Lim, E.H. Anderson, A.P. Alivisatos, P.L. McEuen: Nanomechanical oscillations in a single C_{60} transistor, Nature **407**, 57–60 (2000)

2.62 W. Liang, M.P. Shores, M. Bockrath, J.R. Long, H. Park: Kondo resonance in a single-molecule transistor, Nature **417**, 725–729 (2002)

2.63 J. Park, A.N. Pasupathy, J.I. Goldsmith, C. Chang, Y. Yaish, J.R. Petta, M. Rinkoski, J.P. Sethna, H.D. Abruna, P.L. McEuen, D.C. Ralph: Coulomb blockade and the Kondo effect in single-atom transistors, Nature **417**, 722–725 (2002)

2.64 C.Z. Li, H.X. He, N.J. Tao: Quantized tunneling current in the metallic nanogaps formed by electrodeposition and etching, Appl. Phys. Lett. **77**, 3995–3997 (2000)

2.65 H. He, J. Zhu, N.J. Tao, L.A. Nagahara, I. Amlani, R. Tsui: A conducting polymer nanojunction switch, J. Am. Chem. Soc. **123**, 7730–7731 (2001)

2.66 A. Bogozi, O. Lam, H. He, C. Li, N.J. Tao, L.A. Nagahara, I. Amlani, R. Tsui: Molecular adsorption onto metallic quantum wires, J. Am. Chem. Soc. **123**, 4585–4590 (2001)

2.67 A. Bezryadin, C.N. Lau, M. Tinkham: Quantum suppression of superconductivity in ultrathin nanowires, Nature **404**, 971–974 (2000)

2.68 D. Porath, A. Bezryadin, S. de Vries, C. Dekker: Direct measurement of electrical transport through DNA molecules, Nature **403**, 635–638 (2000)

2.69 S.J. Tans, M.H. Devoret, H. Dai, A. Thess, E.E. Smalley, L.J. Geerligs, C. Dekker: Individual single-wall carbon nanotubes as quantum wires, Nature **386**, 474–477 (1997)

2.70 A.F. Morpurgo, J. Kong, C.M. Marcus, H. Dai: Gate-controlled superconducting proximity effect in carbon nanotubes, Nature **286**, 263–265 (1999)

2.71 J. Nygård, D.H. Cobden, P.E. Lindelof: Kondo physics in carbon nanotubes, Nature **408**, 342–346 (2000)

2.72 W. Liang, M. Bockrath, D. Bozovic, J.H. Hafner, M. Tinkham, H. Park: Fabry–Perot interference in a nanotube electron waveguide, Nature **411**, 665–669 (2001)

2.73 M.S. Fuhrer, J. Nygård, L. Shih, M. Forero, Y.-G. Yoon, M.S.C. Mazzoni, H.J. Choi, J. Ihm, S.G. Louie, A. Zettl, P.L. McEuen: Crossed nanotube junctions, Science **288**, 494–497 (2000)

2.74 T. Rueckes, K. Kim, E. Joselevich, G.Y. Tseng, C.-L. Cheung, C.M. Lieber: Carbon nanotube-based nonvolatile random access memory for molecular computing, Science **289**, 94–97 (2000)

2.75 A. Bachtold, P. Hadley, T. Nakanishi, C. Dekker: Logic circuits with carbon nanotube transistors, Science **294**, 1317–1320 (2001)

3. Introduction to Carbon Nanotubes

Marc Monthioux, Philippe Serp, Emmanuel Flahaut, Manitra Razafinimanana, Christophe Laurent, Alain Peigney, Wolfgang Bacsa, Jean-Marc Broto

Carbon nanotubes are remarkable objects that look set to revolutionize the technological landscape in the near future. Tomorrow's society will be shaped by nanotube applications, just as silicon-based technologies dominate society today. Space elevators tethered by the strongest of cables; hydrogen-powered vehicles; artificial muscles: these are just a few of the technological marvels that may be made possible by the emerging science of carbon nanotubes.

Of course, this prediction is still some way from becoming reality; we are still at the stage of evaluating possibilities and potential. Consider the recent example of fullerenes – molecules closely related to nanotubes. The anticipation surrounding these molecules, first reported in 1985, resulted in the bestowment of a Nobel Prize for their discovery in 1996. However, a decade later, few applications of fullerenes have reached the market, suggesting that similarly enthusiastic predictions about nanotubes should be approached with caution.

There is no denying, however, that the expectations surrounding carbon nanotubes are very high. One of the main reasons for this is the anticipated application of nanotubes to electronics. Many believe that current techniques for miniaturizing microchips are about to reach their lowest limits, and that nanotube-based technologies are the best hope for further miniaturization. Carbon nanotubes may therefore provide the building blocks for further technological progress, enhancing our standards of living.

In this chapter, we first describe the structures, syntheses, growth mechanisms and properties of carbon nanotubes. Then we discuss nanotube-related nano-objects, including those formed by reactions and associations of all-carbon nanotubes with foreign atoms, molecules and compounds, which may provide the path to hybrid materials with even better properties than *pristine* nanotubes. Finally, we will describe the most important current and potential applications of carbon nanotubes, which suggest that the future for the carbon nanotube industry looks very promising indeed.

Carbon nanotubes have long been synthesized as products of the action of a catalyst on the gaseous species originating from the thermal decomposition of hydrocarbons (Sect. 3.2) [3.1]. The first evidence that the nanofilaments produced in this way were actually nanotubes – that they exhibited an inner cavity – can be found in the transmission electron microscope micrographs published by *Radushkevich* and *Lukyanovich* in 1952 [3.2]. This was of course related to and made possible by the progress in transmission electron microscopy. It is then likely that the carbon filaments prepared by *Hughes* and *Chambers* in 1889 [3.3], which is probably the first patent ever deposited in the field, and whose preparation method was also based on the catalytically enhanced thermal cracking of hydrocarbons, were already carbon nanotube-related morphologies. The preparation of vapor-grown carbon fibers was actually reported over a century ago [3.4, 5]. Since then, the interest in carbon nanofilaments/nanotubes has been recurrent, though within a scientific area almost limited to the carbon material scientist community. The reader is invited to consult the review published by *Baker* and *Harris* [3.6] regarding the early works. Worldwide enthusiasm came unexpectedly in 1991, after the catalyst-free formation of nearly perfect concentric multiwall carbon nanotubes (c-MWNTs, Sect. 3.1) was reported [3.7] as by-products of the formation of fullerenes via the electric-arc technique. But the real breakthrough occurred two years later, when attempts to fill the nanotubes in situ with various metals (Sect. 3.5) led to the discovery – again unexpected – of single-wall carbon nanotubes (SWNTs) simultaneously by *Iijima* and *Ichihashi* [3.8] and *Bethune* et al. [3.9]. Single-wall carbon nanotubes were really new nano-objects with properties and behaviors that are often quite specific (Sect. 3.4). They are also beautiful objects for fundamental physics as well as unique molecules for experimental chemistry, although they are still somewhat mysterious since their formation mechanisms are the subject of controversy and are still debated (Sect. 3.3). Potential applications seem countless, although few have reached marketable status so far (Sect. 3.6). Consequently, about five papers a day are currently published by research teams from around the world with carbon nanotubes as the main topic, an illustration of how extraordinarily active – and highly competitive – this field of research is. It is an unusual situation, similar to that for fullerenes, which, by the way, are again carbon nano-objects structurally closely related to nanotubes.

This is not, however, only about scientific exaltation. Economic aspects are leading the game to a greater and greater extent. According to experts, the world market was estimated to be more than 430 million dollars in 2004 and it is predicted to grow to several billion dollars before 2009. That is serious business, and it will be closely related to how scientists and engineers deal with the many challenges found on the path from the beautiful, ideal molecule to the reliable – and it is hoped, cheap – manufactured product.

3.1 Structure of Carbon Nanotubes

It is relatively easy to imagine a single-wall carbon nanotube (SWNT). Ideally, it is enough to consider a perfect graphene sheet (graphene is a polyaromatic monoatomic layer consisting of sp^2-hybridized carbon atoms arranged in hexagons; genuine graphite consists of layers of this graphene) and to roll it into a cylinder (Fig. 3.1), making sure that the hexagonal rings placed in contact join coherently. Then the tips of the tube are sealed by two caps, each cap being a hemi-fullerene of the appropriate diameter (Fig. 3.2a–c).

3.1.1 Single-Wall Nanotubes

Geometrically, there is no restriction on the tube diameter. However, calculations have shown that collapsing the single-wall tube into a flattened two-layer ribbon is energetically more favorable than maintaining the tubular morphology beyond a diameter value of ≈ 2.5 nm [3.10]. On the other hand, it is easy to grasp intuitively that the shorter the radius of curvature, the higher the stress and the energetic cost, although

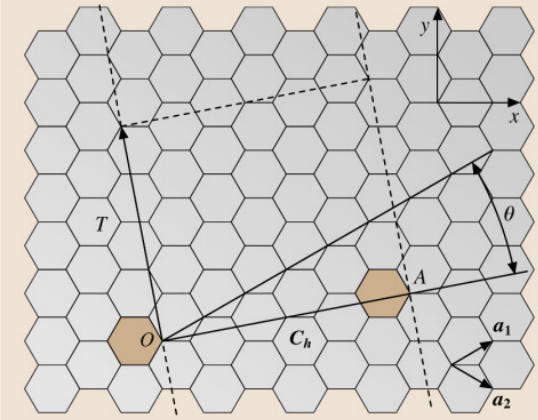

Fig. 3.1 Sketch of the way to make a single-wall carbon nanotube, starting from a graphene sheet (adapted from [3.12])

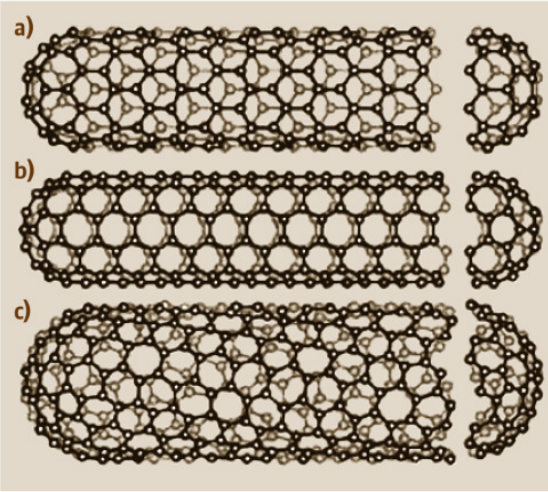

Fig. 3.2a–c Sketches of three different SWNT structures that are examples of (**a**) a zigzag-type nanotube, (**b**) an armchair-type nanotube, (**c**) a helical nanotube (adapted from [3.13])

SWNTs with diameters as low as 0.4 nm have been synthesized successfully [3.11]. A suitable energetic compromise is therefore reached for ≈ 1.4 nm, the most frequent diameter encountered regardless of the synthesis technique (at least for those based on solid carbon sources) when conditions ensuring high SWNT yields are used. There is no such restriction on the nanotube length, which only depends on the limitations of the preparation method and the specific conditions used for the synthesis (thermal gradients, residence time, and so on). Experimental data are consistent with these statements, since SWNTs wider than 2.5 nm are only rarely reported in the literature, whatever the preparation method, while the length of the SWNTs can be in the micrometer or the millimeter range. These features make single-wall carbon nanotubes a unique example of single molecules with huge aspect ratios.

Two important consequences derive from the SWNT structure as described above:

1. All carbon atoms are involved in hexagonal aromatic rings only and are therefore in equivalent positions, except at each nanotube tip, where $6 \times 5 = 30$ atoms are involved in pentagonal rings (considering that adjacent pentagons are unlikely) – though not more, not less, as a consequence of Euler's rule that also governs the fullerene structure. For ideal SWNTs, chemical reactivity will therefore be highly favored at the tube tips, at the locations of the pentagonal rings.
2. Although carbon atoms are involved in aromatic rings, the C=C bond angles are not planar. This means that the hybridization of carbon atoms is not pure sp^2; it has some degree of the sp^3 character, in a proportion that increases as the tube radius of curvature decreases. The effect is the same as for the C_{60} fullerene molecules, whose radius of curvature is 0.35 nm, and whose bonds therefore have 10% sp^3 character [3.14]. On the one hand, this is believed to make the SWNT surface a bit more reactive than regular, planar graphene, even though it still consists of aromatic ring faces. On the other hand, this somehow induces variable overlapping of energy bands, resulting in unique and versatile electronic behavior (Sect. 3.4).

As illustrated by Fig. 3.2, there are many ways to roll a graphene into a single-wall nanotube, with some of the resulting nanotubes possessing planes of symmetry both parallel and perpendicular to the nanotube axis (such as the SWNTs from Fig. 3.2a,b), while others do not (such as the SWNT from Fig. 3.2c). Similar to the terms used for molecules, the latter are commonly called *chiral* nanotubes, since they are unable to be superimposed on their own image in a mirror. *Helical* is however sometimes preferred (see below). The various ways to roll graphene into tubes are therefore mathematically defined by the vector of helicity $\boldsymbol{C}_h$, and the angle of helicity θ, as follows (referring to Fig. 3.1)

$$\boldsymbol{OA} = \boldsymbol{C}_h = n\boldsymbol{a}_1 + m\boldsymbol{a}_2$$

with

$$\boldsymbol{a}_1 = \frac{a\sqrt{3}}{2}\boldsymbol{x} + \frac{a}{2}\boldsymbol{y} \quad \text{and} \quad \boldsymbol{a}_2 = \frac{a\sqrt{3}}{2}\boldsymbol{x} - \frac{a}{2}\boldsymbol{y}\,,$$

where $a = 2.46\,\text{Å}$

and

$$\cos\theta = \frac{2n+m}{2\sqrt{n^2+m^2+nm}}\,,$$

where n and m are the integers of the vector $\boldsymbol{OA}$ considering the unit vectors $\boldsymbol{a}_1$ and $\boldsymbol{a}_2$.

The vector of helicity $\boldsymbol{C}_\text{h}(= \boldsymbol{OA})$ is perpendicular to the tube axis, while the angle of helicity θ is taken with respect to the so-called zigzag axis: the vector of helicity that results in nanotubes of the *zigzag* type (see below). The diameter D of the corresponding nanotube is related to $\boldsymbol{C}_\text{h}$ by the relation

$$D = \frac{|\boldsymbol{C}_\text{h}|}{\pi} = \frac{a_{\text{CC}}\sqrt{3(n^2+m^2+nm)}}{\pi}\,,$$

where

$$\underset{\text{(graphite)}}{1.41\,\text{Å}} \leq a_{\text{C=C}} \leq \underset{(\text{C}_{60})}{1.44\,\text{Å}}\,.$$

The C−C bond length is actually elongated by the curvature imposed by the structure; the average bond length in the C_{60} fullerene molecule is a reasonable upper limit, while the bond length in flat graphene in genuine graphite is the lower limit (corresponding to an infinite radius of curvature). Since $\boldsymbol{C}_\text{h}$, θ, and D are all expressed as a function of the integers n and m, they are sufficient to define any particular SWNT by denoting them (n, m). The values of n and m for a given SWNT can be simply obtained by counting the number of hexagons that separate the extremities of the $\boldsymbol{C}_\text{h}$ vector following the unit vector $\boldsymbol{a}_1$ first and then $\boldsymbol{a}_2$ [3.12]. In the example of Fig. 3.1, the SWNT that is obtained by rolling the graphene so that the two shaded aromatic cycles can be superimposed exactly is a (4, 2) chiral nanotube. Similarly, SWNTs from Fig. 3.2a–c are (9, 0), (5, 5), and (10, 5) nanotubes respectively, thereby providing examples of zigzag-type SWNT (with an angle of helicity = 0°), armchair-type SWNT (with an angle of helicity of 30°) and a chiral SWNT, respectively. This also illustrates why the term *chiral* is sometimes inappropriate and should preferably be replaced with *helical*. Armchair (n, n) nanotubes, although definitely achiral from the standpoint of symmetry, exhibit a nonzero *chiral angle*. *Zigzag* and *armchair* qualifications for achiral nanotubes refer to the way that the carbon atoms are displayed at the edge of the nanotube cross section (Fig. 3.2a,b). Generally speaking, it is clear from Figs. 3.1 and 3.2a that having the vector of helicity perpendicular to any of the three overall C=C bond directions will provide zigzag-type SWNTs, denoted $(n, 0)$, while having the vector of helicity parallel to one of the three C=C bond directions will provide armchair-type SWNTs, denoted (n, n). On the other hand, because of the sixfold symmetry of the graphene sheet, the angle of helicity θ for the chiral (n, m) nanotubes is such that $0 < \theta < 30°$. Figure 3.3 provides two examples of what chiral SWNTs look like, as seen via atomic force microscopy.

Fig. 3.3 Image of two neighboring chiral SWNTs within a SWNT bundle as seen using high-resolution scanning tunneling microscopy (courtesy of Prof. Yazdani, University of Illinois at Urbana, USA)

The graphenes in graphite have π electrons which are accommodated by the stacking of graphenes, al-

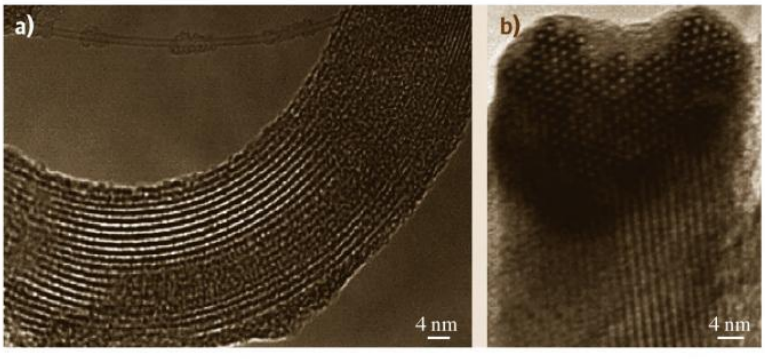

Fig. 3.4a,b High-resolution transmission electron microscopy images of a SWNT rope. **(a)** Longitudinal view. An isolated single SWNT also appears at the top of the image. **(b)** Cross-sectional view (from [3.15])

lowing van der Waals forces to develop. Similar reasons make fullerenes gather and order into fullerite crystals and SWNTs into SWNT ropes (Fig. 3.4a). Provided the SWNT diameter distribution is narrow, the SWNTs in ropes tend to spontaneously arrange into hexagonal arrays, which correspond to the highest compactness achievable (Fig. 3.4b). This feature brings new periodicities with respect to graphite or turbostratic polyaromatic carbon crystals. Turbostratic structure corresponds to graphenes that are stacked with random rotations or translations instead of being piled up following sequential *ABAB* positions, as in graphite structure. This implies that no lattice atom plane exists other than the graphene planes themselves (corresponding to the (001) atom plane family). These new periodicities give specific diffraction patterns that are quite different to those of other sp^2-carbon-based crystals, although *hk* reflections, which account for the hexagonal symmetry of the graphene plane, are still present. On the other hand, 00*l* reflections, which account for the stacking sequence of graphenes in regular, *multilayered* polyaromatic crystals (which do not exist in SWNT ropes) are absent. This hexagonal packing of SWNTs within the ropes requires that SWNTs exhibit similar diameters, which is the usual case for SWNTs prepared by electric arc or laser vaporization processes. SWNTs prepared using these methods are actually about 1.35 nm wide (diameter of a (10, 10) tube, among others), for reasons that are still unclear but are related to the growth mechanisms specific to the conditions provided by these techniques (Sect. 3.3).

3.1.2 Multiwall Nanotubes

Building multiwall carbon nanotubes is a little bit more complex, since it involves the various ways graphenes can be displayed and mutually arranged within filamentary morphology. A similar versatility can be expected to the usual textural versatility of polyaromatic solids. Likewise, their diffraction patterns are difficult to differentiate from those of anisotropic polyaromatic solids. The easiest MWNT to imagine is the concentric type (c-MWNT), in which SWNTs with regularly increasing diameters are coaxially arranged (according to a Russian-doll model) into a multiwall nanotube (Fig. 3.5). Such nanotubes are generally formed either by the electric arc technique (without the need for a catalyst), by catalyst-enhanced thermal cracking of gaseous hydrocarbons, or by CO disproportionation (Sect. 3.2). There can be any number of walls (or coaxial tubes), from two upwards. The intertube distance is approximately the same as the intergraphene distance in turbostratic, polyaromatic solids, 0.34 nm (as opposed to 0.335 nm in genuine graphite), since the increasing radius of curvature imposed on the concentric graphenes prevents the carbon atoms from being arranged as in graphite, with each of the carbon atoms from a graphene facing either a ring center or a carbon atom from the neighboring graphene. However, two cases allow a nanotube to reach – totally or partially – the 3-D crystal periodicity of graphite. One is to consider a high number of concentric graphenes: concentric graphenes with a long radius of curvature. In this case, the shift in the relative positions of carbon atoms from superimposed graphenes is so small with respect to that in graphite that some commensurability is possible.

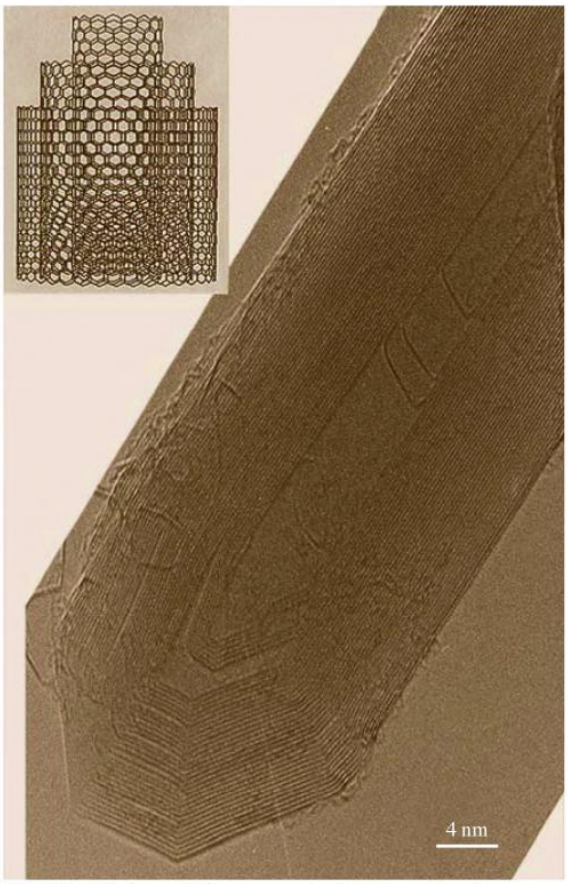

Fig. 3.5 High-resolution transmission electron microscopy image (longitudinal view) of a concentric multiwall carbon nanotube (c-MWNT) prepared using an electric arc. The *insert* shows a sketch of the Russian doll-like arrangement of graphenes

This may result in MWNTs where both structures are associated; in other words they have turbostratic cores and graphitic outer parts [3.16]. The other case occurs for c-MWNTs exhibiting faceted morphologies, originating either from the synthesis process or more likely from subsequent heat treatment at high temperature (such as 2500 °C) in inert atmosphere. Facets allow the graphenes to resume a flat arrangement of atoms (except at the junction between neighboring facets) which allows the specific stacking sequence of graphite to develop.

Another frequent inner texture for multiwall carbon nanotubes is the so-called herringbone texture (h-MWNTs), in which the graphenes make an angle with respect to the nanotube axis (Fig. 3.6). The angle value varies upon the processing conditions (such as the catalyst morphology or the composition of the atmosphere), from 0 (in which case the texture becomes that of a c-MWNT) to 90° (in which case the filament is no longer a tube, see below), and the inner diameter varies so that the tubular arrangement can be lost [3.20], meaning that the latter are more accurately called nanofibers rather than nanotubes. h-MWNTs are exclusively obtained by processes involving catalysts, generally catalyst-enhanced thermal cracking of hydrocarbons or CO disproportionation. One long-time debated question was whether the herringbone texture, which actually describes the texture projection rather than the overall three-dimensional texture, originates from the scrolllike spiral arrangement of a single graphene ribbon or from the stacking of independent truncated conelike graphenes in what is also called a *cup-stack* texture. It is now demonstrated that both exist [3.21, 22].

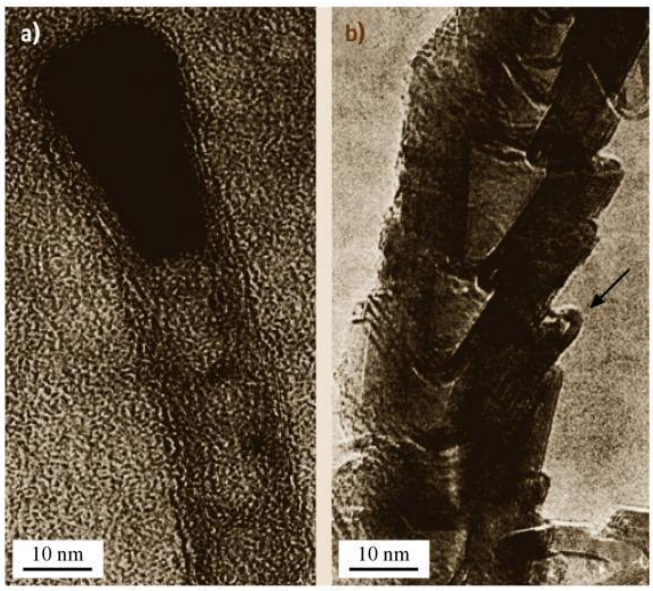

Fig. 3.6a,b Some of the earliest high-resolution transmission electron microscopy images of a herringbone (and bamboo) multiwall nanotube (bh-MWNT, longitudinal view) prepared by CO disproportionation on Fe-Co catalyst. **(a)** As-grown. The nanotube surface is made of free graphene edges. **(b)** After 2900 °C heat treatment. Both the herringbone and the bamboo textures have become obvious. Graphene edges from the surface have buckled with their neighbors (*arrow*), closing off access to the intergraphene space (adapted from [3.17])

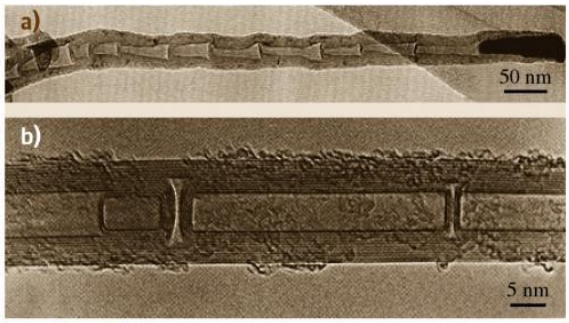

Fig. 3.7a,b Transmission electron microscopy images from bamboo multiwall nanotubes (longitudinal views). **(a)** Low magnification of a bamboo-herringbone multiwall nanotube (bh-MWNT) showing the nearly periodic nature of the texture, which occurs very frequently. (from [3.18]); **(b)** high-resolution image of a bamboo-concentric multiwall nanotube (bc-MWNT) (modified from [3.19])

Another common feature is the occurrence, to some degree, of a limited amount of graphenes oriented perpendicular to the nanotube axis, thus forming a *bamboo* texture. This is not a texture that can exist on its own; it affect either the c-MWNT (bc-MWNT) or the h-MWNT (bh-MWNT) textures (Figs. 3.6 and 3.7). The question is whether such filaments, although hollow, should still be called nanotubes, since the inner cavity is no longer open all the way along the filament as it is for a genuine tube. These are therefore sometimes referred as *nanofibers* in the literature too.

One nanofilament that definitely cannot be called a nanotube is built from graphenes oriented perpendicular to the filament axis and stacked as piled-up plates. Although these nanofilaments actually correspond to h-MWNTs with a graphene/MWNT axis angle of 90°, an inner cavity is no longer possible, and such filaments are therefore often referred to as *platelet nanofibers* in the literature [3.20].

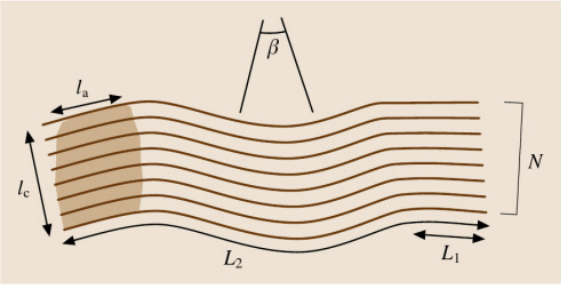

Fig. 3.8 Sketch explaining the various parameters obtained from high-resolution (lattice fringe mode) transmission electron microscopy, used to quantify nanotexture: L_1 is the average length of perfect (distortion-free) graphenes of coherent areas; N is the number of piled-up graphenes in coherent (distortion-free) areas; L_2 is the average length of continuous though distorted graphenes within graphene stacks; β is the average distortion angle. L_1 and N are related to the l_a and l_c values obtained from x-ray diffraction

Unlike SWNTs, whose aspect ratios are so high that it is almost impossible to find the tube tips, the aspect ratios for MWNTs (and carbon nanofibers) are generally lower and often allow one to image tube ends by transmission electron microscopy. Aside from c-MWNTs derived from electric arc (Fig. 3.5), which grow in a catalyst-free process, nanotube tips are frequently found to be associated with the catalyst crystals from which they were formed.

The properties of the MWNT (Sect. 3.4) will obviously largely depend on the perfection and the orientation of the graphenes in the tube (for example, the spiral angles of the nanotubes constituting c-MWNTs has little importance). Graphene orientation is a matter of texture, as described above. Graphene perfection is a matter of nanotexture, which is commonly used to describe other polyaromatic carbon materials, and which is quantified by several parameters preferably obtained from high-resolution transmission electron microscopy (Fig. 3.8). Both texture and nanotexture depend on the processing conditions. While the texture type is a permanent, intrinsic feature which can only be completely altered upon a severe degradation treatment (such as oxidation), the nanotexture can be improved by subsequent thermal treatments at high temperatures (such as $> 2000\,^{\circ}\mathrm{C}$) and potentially degraded by chemical treatments (such as slightly oxidizing conditions).

3.2 Synthesis of Carbon Nanotubes

Producing carbon nanotubes so that the currently planned applications currently planned become marketable will require solving some problems that are more or less restrictive depending on the case. Examples include specifically controlling the configuration (chirality), the purity, or the structural quality of SWNTs, and adapting the production capacity to the application. One objective would be to understand the mechanism of nanotube nucleation and growth perfectly, and this remains a controversial subject despite an intense, worldwide experimental effort. This problem is partly due to our lack of knowledge regarding several parameters controlling the conditions during synthesis. For instance, the exact and accurate role of the catalysts in nanotube growth is often unknown. Given the large number of experimental parameters and considering the large range of conditions that the synthesis techniques correspond to, it is quite legitimate to think of more than one mechanism intervening during nanotube formation.

3.2.1 Solid Carbon Source-Based Production Techniques for Carbon Nanotubes

Among the different SWNT production techniques, the four processes (laser ablation, solar energy, dc electric arc, and three-phase ac arc plasma) presented in this section have at least two points in common: a high-temperature ($1000\,\mathrm{K} < T < 6000\,\mathrm{K}$) medium and the fact that the carbon source originates from the erosion of solid graphite. Despite these common points, the morphologies of the carbon nanostructures and the SWNT yields can differ notably with respect to the experimental conditions.

Before being utilized for carbon nanotube synthesis, these techniques permitted the production of fullerenes. Laser vaporization of graphite was actually the very first method to demonstrate the existence of fullerenes, including the most common one (because it is the most stable and therefore the most abundant), C_{60} [3.23]. On the other hand, the electric arc technique was (and still is) the first method of producing fullerenes in

relatively large quantities [3.24–26]. Unlike fullerene formation, which requires the presence of carbon atoms in high-temperature media and the absence of oxygen, the utilization of these techniques for the synthesis of nanotubes (of SWNT type at least) requires an additional condition: the presence of catalysts in either the electrode or the target.

The different mechanisms (such as carbon molecule dissociation and atom recombination processes) involved in these high-temperature techniques take place at different time scales, from nanoseconds to microseconds and even milliseconds. The formation of nanotubes and other graphene-based products occurs afterward with a relatively long delay.

The methods of laser ablation, solar energy, and electric arc are all based on one essential mechanism: the energy transfer resulting from the interaction between either the target material and an external radiation source (a laser beam or radiation emanating from solar energy) or the electrode and the plasma (in case of an electric arc). This interaction causes target or anode erosion, leading to the formation of a plasma: an electrically neutral ionized gas, composed of neutral atoms, charged particles (molecules and ionized species) and electrons. The ionization degree of this plasma, defined by the ratio $(n_e/(n_e+n_o))$, where n_e and n_o are the electron and that of neutral atom densities respectively, highlights the importance of energy transfer between the plasma and the material. The characteristics of this plasma and notably the ranges in temperature and concentrations of the various species present in the plasma thereby depend not only on the nature and composition of the target or the electrode but also on the energy transferred.

One of the advantages of these synthesis techniques is the ability to vary a large number of parameters that modify the composition of the high-temperature medium and consequently allow the most relevant parameters to be determined so that the optimal conditions for the control of carbon nanotube formation can be obtained. However, a major drawback of these techniques – and of any other technique used to produce SWNTs – is that the SWNTs formed are not pure: they are associated with other carbon phases and remnants of the catalyst. Although purification processes have been proposed in the literature and by some commercial companies for removing these undesirable phases, they are all based on oxidation (such as acid-based) processes that are likely to significantly affect the SWNT structure [3.15]. Subsequent thermal treatments at $\approx 1200\,^{\circ}\mathrm{C}$ under inert atmosphere, however, succeed in recovering structural quality somewhat [3.29].

Laser Ablation

After the first laser was built in 1960, physicists immediately made use of it as a means of concentrating a large quantity of energy inside a very small volume within a relatively short time. The consequence of this energy input naturally depends upon the characteristics of the device employed. During the interaction between the laser beam and the material, numerous phenomena occur at the same time and/or follow each other within the a certain time period, and each of these processes are sensitive to different parameters such as the characteristics of the laser beam, the incoming power density (also termed the *fluence*), the nature of the target, and the environment surrounding it. For instance, the solid target can merely heat up, melt or vaporize depending on the power provided.

While this technique was successfully used to synthesize fullerene-related structures for the very first time [3.23], the synthesis of SWNTs by laser ablation took another ten years of research [3.27].

Laser Ablation – Experimental Devices

Two types of laser devices are currently utilized for carbon nanotube production: lasers operating in pulsed mode and lasers operating in continuous mode, with the latter generally providing a smaller fluence.

An example of the layout of a laser ablation device is given in Fig. 3.9. A graphite pellet containing the catalyst is placed in the middle of a quartz tube filled with inert gas and placed in an oven maintained at a temperature of 1200 °C [3.27,28]. The energy of the laser beam focused on the pellet permits it to vaporize and sublime the graphite by uniformly bombarding its surface. The carbon species, swept along by a flow of neutral gas, are then deposited as soot in different regions: on the con-

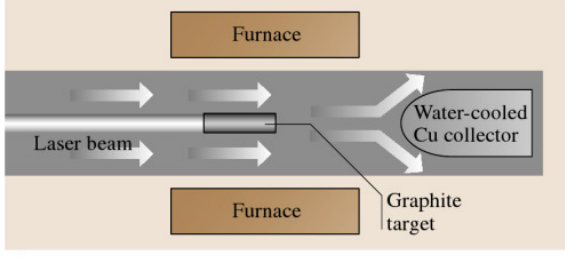

Fig. 3.9 Sketch of an early laser vaporization apparatus (adapted from [3.27, 28])

ical water-cooled copper collector, on the quartz tube walls, and on the backside of the pellet.

Various improvements have been made to this device in order to increase the production efficiency. For example, *Thess* et al. [3.31] employed a second pulsed laser that follows the initial impulsion but at a different frequency in order to ensure a more complete and efficient irradiation of the pellet. This second impulsion vaporizes the coarse aggregates issued from the first ablation, causing them to participate in the active carbon feedstock involved in nanotube growth. Other modifications were suggested by *Rinzler* et al. [3.29], who inserted a second quartz tube of a smaller diameter coaxially inside the first one. This second tube reduces the vaporization zone and so permits an increased amounts of sublimed carbon to be obtained. They also arranged the graphite pellet on a revolving system so that the laser beam uniformly scans its whole surface.

Other groups have realized that, where the target contains both the catalyst and the graphite, the latter evaporates first and the pellet surface becomes more and more metal-rich, resulting in a decrease in the efficiency of nanotube formation during the course of the process. To solve this problem, *Yudasaka* et al. [3.32] utilized two pellets facing each other, one made entirely from the graphite powder and the other from an alloy of transition metals (catalysts), and irradiated them simultaneously.

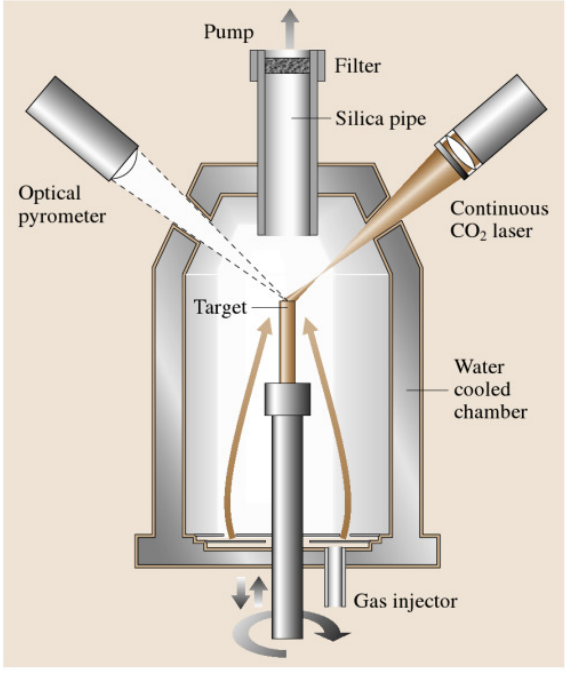

Fig. 3.10 Sketch of a synthesis reactor with a continuous CO_2 laser device (adapted from [3.30])

A sketch of a synthesis reactor based on the vaporization of a target at a fixed temperature by a continuous CO_2 laser beam ($\lambda = 10.6\,\mu m$) is shown in Fig. 3.10 [3.30]. The power can be varied from 100 to 1600 W. The temperature of the target is measured with an optical pyrometer, and these measurements are used to regulate the laser power to maintain a constant vaporization temperature. The gas, heated by contact with the target, acts as a local furnace and creates an extended hot zone, making an external furnace unnecessary. The gas is extracted through a silica pipe, and the solid products formed are carried away by the gas flow through the pipe and then collected on a filter. The synthesis yield is controlled by three parameters: the cooling rate of the medium where the active, secondary catalyst particles are formed, the residence time, and the temperature (in the range 1000–2100 K) at which SWNTs nucleate and grow [3.33].

However, devices equipped with facilities to gather data such as the target temperature in situ are scarce and, generally speaking, this is one of the numerous variables of the laser ablation synthesis technique. The parameters that have been studied the most are the nature of the target, the nature and concentration of the catalyst, the nature of the neutral gas flow, and the temperature of the outer oven.

Laser Ablation – Results

In the absence of catalysts in the target, the soot collected mainly contains multiwall nanotubes (c-MWNTs). Their lengths can reach 300 nm. Their quantity and structural quality are dependent on the oven temperature. The best quality is obtained for an oven temperature set at 1200 °C. At lower oven temperatures, the structural quality decreases, and the nanotubes start presenting many defects [3.27]. As soon as small quantities (a few percent or less) of transition metal (Ni, Co) catalysts are incorporated into the graphite pellet, the products yielded undergo significant modifications, and SWNTs are formed instead of MWNTs. The yield of SWNTs strongly depends on the type of metal catalyst used and is seen to increase with the furnace temperature, among other factors. The SWNTs have remarkably uniform diameters and they self-organize into ropelike crystallites 5–20 nm in diameter and tens to hundreds of micrometers in length (Fig. 3.11). The ends of all of the SWNTs appear to be perfectly closed with hemispherical end-caps that show no evidence of any

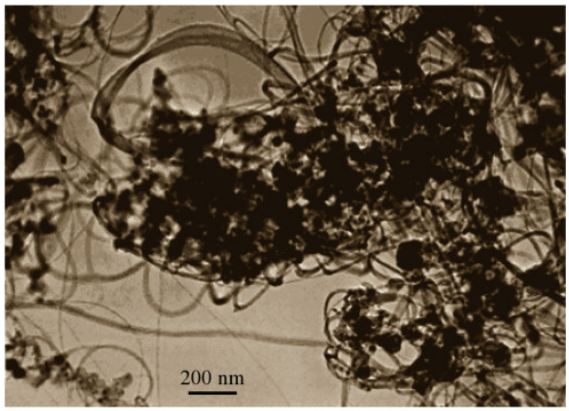

Fig. 3.11 Low-magnification TEM images of a typical raw SWNT material obtained using the laser vaporization technique. The fibrous structures are SWNT bundles, and the dark particles are remnants of the catalyst. Raw SWNT materials obtained from an electric arc exhibit similar features (from [3.15])

associated metal catalyst particle, although, as pointed out in Sect. 3.1, finding the two tips of a SWNT is rather challenging, considering the huge aspect ratio of the nanotube and their entangled nature. Another feature of the SWNTs produced with this technique is that they are supposedly *cleaner* than those produced using other techniques; in other words they associated with smaller amounts of the amorphous carbon that either coats the SWNTs or is gathered into nanoparticles. This advantage, however, only occurs for synthesis conditions designed to ensure high-quality SWNTs. It is not true when high-yield conditions are preferred; in this case SWNTs from an electric arc may appear cleaner than SWNTs from laser vaporization [3.15].

The laser vaporization technique is one of the three methods currently used to prepare SWNTs as commercial products. SWNTs prepared this way were first marketed by Carbon Nanotechnologies Inc. (Houston, USA), with prices as high as 1000 $/g (raw materials) until December 2002. Probably because lowering the amount of impurities in the raw materials using this technique is impossible, they have recently decided to focus on fabricating SWNTs using the HiPCo technique (Sect. 3.2.2). Laser-based methods are generally not considered to be competitive in the long term for the low-cost production of SWNTs compared to CCVD-based methods (Sect. 3.2.2). However, prices as low as 0.03 $/g of raw high concentration have been estimated possible from a pre-industrial project study (Acolt S.A., Yverdon, Switzerland).

Electric Arc Method

Electric arcs between carbon electrodes have been studied as light sources and radiation standards for a very long time. They have however received renewed attention more recently due to their use in the production of new fullerene-related molecular carbon nanostructures, such as genuine fullerenes or nanotubes. This technique was first brought to light by *Krätschmer* et al. [3.24] who utilized it to achieve the production of fullerenes in macroscopic quantities. In the course of investigating other carbon nanostructures formed along with the fullerenes, and more particularly the solid carbon deposit that formed on the cathode, *Iijima* [3.7] discovered the catalyst-free formation of perfect c-MWNT-type carbon nanotubes. Then, as mentioned in the *Introduction*, the catalyst-promoted formation of SWNTs was accidentally discovered after some amounts of transition metals were introduced into the anode in an attempt to fill the c-MWNTs with metals during growth [3.8, 9]. Since then, a lot of work has been carried out by many groups using this technique in order to understand the mechanisms of nanotube growth as well as the role played by the catalysts (if any) in the synthesis of MWNTs and/or SWNTs [3.34–46].

Electric Arc Method – Experimental Devices

The principle of this technique is to vaporize carbon in the presence of catalysts (iron, nickel, cobalt, yttrium, boron, gadolinium, cerium, and so forth) in a reduced atmosphere of inert gas (argon or helium). After triggering an arc between two electrodes, a plasma is formed consisting of the mixture of carbon vapor, the rare gas (helium or argon), and the catalyst vapors. The vaporization is the consequence of energy transfer from the arc to the anode made of graphite doped with catalysts. The importance of the anode erosion rate depends on the power of the arc and also on other experimental conditions. It is worth noting that a high anode erosion does not necessarily lead to a high carbon nanotube production.

An example of a reactor layout is shown in Fig. 3.12. It consists of a cylinder about 30 cm in diameter and about 1 m in height, equipped with diametrically opposed sapphire windows located so that they face the plasma zone, observing the arc. The reactor possesses two valves, one for performing the primary evacuation (0.1 Pa) of the chamber, the other for filling it with a rare gas up to the desired working pressure.

Contrary to the solar energy technique, SWNTs are deposited (provided appropriate catalysts are used) in different regions of the reactor:

1. The collaret, which forms around the cathode
2. The weblike deposits found above the cathode
3. The soot deposited all around the reactor walls and the bottom.

On the other hand, MWNTs are formed in a hard deposit adherent to the cathode whether catalysts are used or not. The cathode deposits form under the cathode. The formation of collaret and web is not systematic and depends on the experimental conditions, as indicated in Table 3.1, as opposed to the cathode deposit and soot, which are obtained consistently.

Two graphite rods of few millimeters in diameter constitute the electrodes between which a potential difference is applied. The dimensions of these electrodes vary according to the authors. In certain cases, the cathode has a greater diameter than the anode in order to facilitate their alignment [3.37, 47]. Other authors utilize electrodes of the same diameter [3.46]. The whole device can be designed horizontally [3.38, 46] or vertically [3.39, 41–43]. The advantage of the latter is the symmetry brought by the verticality with respect to gravity, which facilitates computer modeling (regarding convection flows, for instance).

Two types of anode can be utilized when catalysts are introduced:

1. A graphite anode containing a coaxial hole several centimeters in length into which a mixture of the catalyst and the graphite powder is placed.

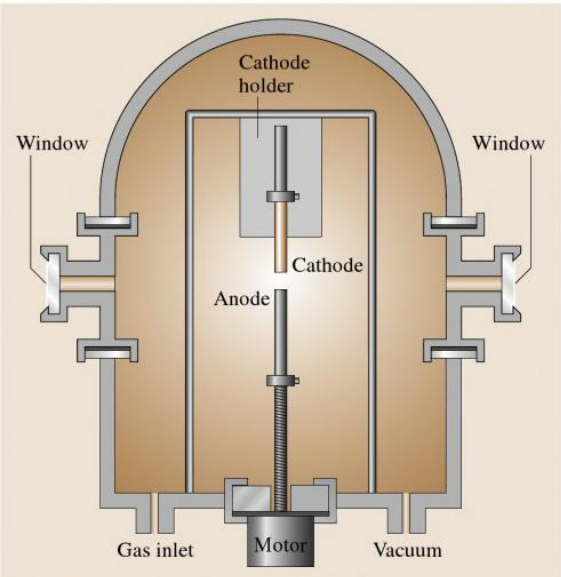

Fig. 3.12 Sketch of an electric arc reactor

2. A graphite anode within which the catalysts are homogeneously dispersed [3.48].

The former are by far the most popular, due to their ease of fabrication.

Optimizing the process in terms of the nanotube yield and quality is achieved by studying the roles of various parameters such as the type of doped anode (homogeneous or heterogeneous catalyst dispersion), the nature as well as the concentration of the catalyst, the nature of the plasmagen gas, the buffer gas pressure, the arc current intensity, and the distance between electrodes. Investigating the influences of these parameters on the type and amount of carbon nanostructures formed is, of course, the preliminary work that has been done. Although electric arc reactors equipped with the facilities to perform such investigations are scarce (Fig. 3.12), investigating the missing link (the effect of varying the parameters on the plasma characteristics – the species concentrations and temperature) is likely to provide a more comprehensive understanding of the phenomena involved during nanotube formation. This has been recently performed using atomic and molecular optical emission spectroscopy [3.39, 41–44, 46].

Finally, we should mention attempts to create an electric arc in liquid media, such as liquid nitrogen [3.49] or water [3.50, 51]. The goal here is to make processing easier, since such systems should not require pumping devices or a closed volume and so they are more likely to allow continuous synthesis. This adaptation has not, however, reached the stage of mass production.

Electric Arc Method – Results

In view of the numerous results obtained with this electric arc technique, it is clear that both the morphology and the production efficiency of nanotubes strongly depends upon the experimental conditions used and, in particular, upon the nature of the catalysts. It is worth noting that the products obtained do not consist solely of carbon nanotubes. Nontubular forms of carbon, such as nanoparticles, fullerenelike structures including C_{60}, poorly organized polyaromatic carbons, nearly amorphous nanofibers, multiwall shells, single-wall nanocapsules, and amorphous carbon have all been obtained, as reported in Table 3.1 [3.40, 42, 43]. In addition, remnants of the catalyst are found all over the place – in the soot, the collaret, the web and the cathode deposit – in various concentrations. Generally, at a helium pressure of about 600 mbar, for an arc current of 80 A and for an electrode gap of 1 mm, the synthesis of

Table 3.1 Different carbon morphologies obtained by changing the type of anode, the type of catalyst and the pressure in a series of arc discharge experiments (electrode gap = 1 mm)

Catalyst (at. %) Arc conditions	**0.6Ni + 0.6Co (homogeneous anode) $P \approx 60$ kPa $I \approx 80$ A**	**0.6Ni + 0.6Co (homogeneous anode) $P \approx 40$ kPa $I \approx 80$ A**	**0.5Ni + 0.5Co $P \approx 60$ kPa $I \approx 80$ A**	**4.2Ni + 1Y $P \approx 60$ kPa $I \approx 80$ A**
Soot	• MWNT + **MWS** + **POPAC** or **Cn** ± catalysts $\phi \approx 3$–35 nm • NANF + catalysts • AC particles + catalysts • [*DWNT*], [*SWNT*], ropes or isolated, + POPAC	• **POPAC** and AC particles + **catalysts** $\phi \approx 2$–20 nm • NANF + catalysts $\phi \approx 5$–20 nm + MWS • [*SWNT*] $\phi \approx 1$–1.4 nm, distorted or damaged, isolated or ropes + Cn	• AC and POPAC particles + catalysts $\phi \approx 3$–35 nm • **NANF** + catalysts $\phi \approx 4$–15 nm • [*SWNT*] $\phi \approx 1.2$ nm, isolated or ropes	• **POPAC** and AC + particles + catalysts $\phi \leq 30$ nm • SWNT $\phi \approx 1.4$ nm, clean + Cn, short with tips, [*damaged*], isolated or ropes $\phi \leq 25$ nm • [*SWNC*] particles
Web	• [*MWNT*], **DWNT**, ϕ 2.7 – **4** – 5.7 nm SWNT ϕ 1.2–1.8 nm, isolated or **ropes** $\phi < 15$ nm, + POPAC ± **Cn** • AC particles + catalysts $\phi \approx 3$–40 nm + MWS • [*NANF*]	None	None	• **SWNT**, $\phi \approx 1.4$ nm, isolated or **ropes** $\phi \leq 20$ nm, + AC • POPAC and AC particles + catalysts $\phi \approx 3$ – **10** – 40 nm + MWS
Collaret	• **POPAC** and **SWNC** particles • Catalysts $\phi \approx 3$–250 nm, < **50** nm + MWS • SWNT ϕ 1–1.2 nm, [*opened*], **distorted**, isolated or **ropes** $\phi < 15$ nm, + **Cn** • [*AC*] particles	• AC and **POPAC** particles + catalysts $\phi \approx 3$–25 nm • SWNT $\phi \approx 1$–1.4 nm clean + Cn, [*isolated*] or ropes $\phi < 25$ nm • Catalysts $\phi \approx 5$–50 nm + MWS, • [SWNC]	• **Catalysts** $\phi \approx 3$–170 nm + MWS • AC or POPAC particles + **catalysts** $\phi \approx 3$–50 nm • SWNT $\phi \approx 1.4$ nm clean + Cn isolated or ropes $\phi < 20$ nm	• **SWNT** $\phi \approx 1.4$–2.5 nm, clean + Cn, [*damaged*], isolated or **ropes** $\phi < 30$ nm • POPAC or AC particles + catalysts $\phi \approx 3$–30 nm • [*MWS*] + catalysts or catalyst-free
Cathode deposit	• **POPAC** and SWNC particles • **Catalysts** $\phi \approx 5$–300 nm MWS • MWNT $\phi < 50$ nm • [*SWNT*] $\phi \approx 1.6$ nm clean + Cn, isolated or ropes	• **POPAC** and **SWNC** particles + Cn • Catalysts $\phi \approx 20$–100 nm + MWS	• **MWS**, catalyst-free • **MWNT** $\phi < 35$ nm • POPAC and PSWNC particles • [*SWNT*], isolated or ropes • [*Catalysts*] $\phi \approx 3$–30 nm	•**SWNT** $\phi \approx 1.4$–4.1 nm, clean + **Cn**, short with tips, isolated or ropes $\phi \leq 20$ nm. • **POPAC** or **AC** particles + catalysts $\phi \approx 3$–30 nm • MWS + catalysts $\phi < 40$ nm or catalyst-free • [*MWNT*]

Abundant – Present – [*Rare*]

Glossary: AC: amorphous carbon; POPAC: poorly organized polyaromatic carbon; Cn: fullerenelike structure, including C_{60}; NANF: nearly amorphous nanofiber; MWS: multiwall shell; SWNT: single-wall nanotube; DWNT: double-wall nanotube, MWNT: multiwall nanotube; SWNC: single-wall nanocapsule.

SWNTs is favored by the use of Ni/Y as coupled catalysts [3.8, 38, 52]. In these conditions, which give high SWNT yields, SWNT concentrations are highest in the collaret (50–70%), then in the web (≈ 50% or less) and then in the soot. On the other hand, c-MWNTs are found in the cathode deposit. SWNT lengths are micrometric and, typical outer diameters are around 1.4 nm. Using the latter conditions (Table 3.1, column 4), Table 3.1 illustrates the consequence of changing the parameters. For instance (Table 3.1, column 3), using Ni/Co instead of Ni/Y as catalysts prevents the formation of SWNTs. But when the Ni/Co catalysts are homogeneously dispersed in the anode (Table 3.1, column 1), the formation of nanotubes is promoted again, but

MWNTs with two or three walls prevail over SWNTs, among which DWNTs (double-wall nanotubes) dominate. However, decreasing the ambient pressure from 60 to 40 kPa (Table 3.1, column 2) again suppresses nanotube formation.

Based on works dealing with the influence of the granulometry of the graphite powders which are mixed with the catalyst powder and placed in hollow-type graphite anodes, recent studies have demonstrated that one of the control keys for growing SWNTs with enhanced purity and yield is for the anode to exhibit a high thermal conductivity with as more limited radial and longitudinal variations as possible [3.53, 54]. This explains why similar results (i. e., enhanced purity and yield) were previously obtained when replacing the graphite powder by diamond powder [3.44, 45] in spite of the low electrical conductivity of diamond, since graphite and diamond powders lead to the same plasma composition once vaporized at high temperatures (> 4000 K).

A comparison of the plasma characteristics (i. e., radial temperature profiles and CI/NiI concentration ratio) obtained for anodes with different filler material features (i. e., 1/ 100 μm granulometry and sp^2/sp^3 carbon) is presented in Fig. 3.13a,b respectively. The whole plasma temperature radial profiles obtained using either the Ni/Y/graphite ($\phi \approx 1$ μm) anode or the Ni/Y/diamond ($\phi \approx 1$ μm) anode is much smoother than with the standard Ni/Y/graphite ($\phi \approx 100$ μm) anode, meanwhile exhibiting less extreme temperatures (≈ 6200 K for the highest as opposed to ≈ 8000 K respectively for the standard anode). From 1 mm from the arc axis, temperature is maintained at a constant value at about 4000 K. The absence of large temperature fluctuations is consistent with the fact that the plasma is continuously fed by a rather constant ratio of [carbon]/[catalysts] resulting from the steadier erosion of the anode and a better powder mixture homogenization. In this regard, it might be significant that the smoothest temperature profile over the longest radial distance is obtained for the Ni/Y/graphite ($\varphi \approx 1$ μm) anode, which has resulted in the highest yield [3.53,54]. Likewise, the CI/NiI concentration ratio profiles related to either the Ni/Y/graphite ($\phi \approx 1$ μm) anode or the Ni/Y/diamond anode show a dramatic difference with respect to the Ni/Y/graphite ($\phi \approx 100$ μm) anode (Fig. 3.13b). They exhibit a fluctuation-free regime along the whole radial profile, with a unique maximum at ≈ 1.3–1.5 mm from the arc axis. The average ratio is low ($\approx 5 \times 10^5$) due to a relatively low distribution of carbon concentration leading to a higher plasma temperature. This makes a perfect sense, since carbon species are very emissive in the range 4500–6000 K, inducing that radiative losses are more significant when plasmas are enriched in carbon species, leading to colder plasma temperatures, and vice versa. Such a feature is again consistent with the steady erosion of high thermal conductivity anodes. It is also worth noting that, again, area where CI/NiI ratios exhibit

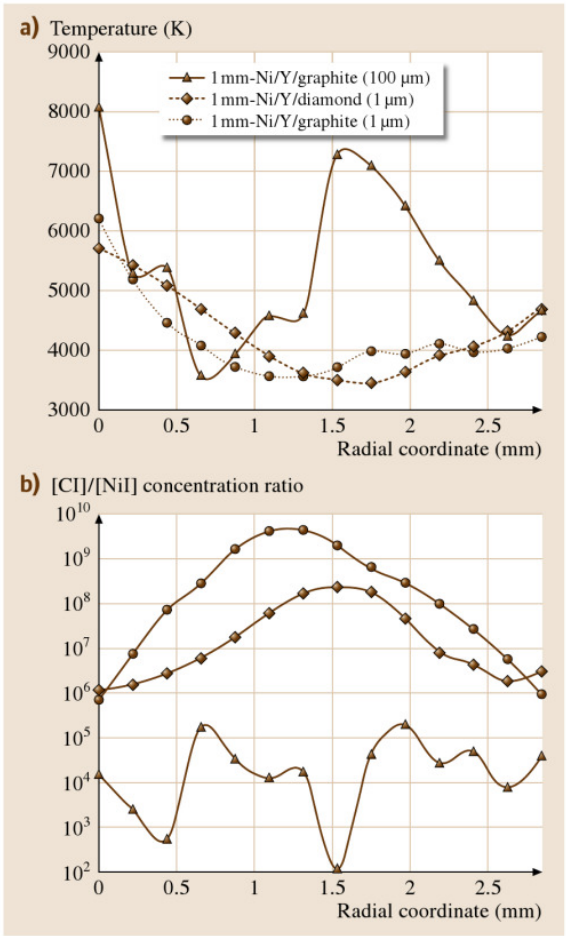

Fig. 3.13a,b Radial temperature profiles (**a**) and radial [CI]/[NiI] concentration ratio (**b**) as obtained by emission spectroscopy for hollowed-type anodes with various thermal behaviours. The thermal behaviour was varied by varying the grain size (1 or 100 μm) and the carbon type (sp^2 – graphite, or sp^3 – diamond) of the carbon powder which the hollow core of the anode is filled with (along with yttrium and nickel catalyst powder). Smaller grain size results in better compaction, hence in higher thermal conductivity

maximum values in Fig. 3.13b relate to area of minimum temperature values in Fig. 3.13a. In addition, the CI/NiI concentration ratio is up to about 3–5 orders of magnitude higher for the fine-grain graphite-containing anode and the diamond-containing anode than for the large-grain graphite-containing anode. Moreover, the CI/NiI concentration ratio is even higher as ≈ 1.5 orders of magnitude for the fine-grain graphite-containing anode than for the diamond-containing anode.

Highly and homogeneously thermally conductive anodes lead to a steadier anode erosion, hence to steadier plasma characteristics, hence to a more constant variety of the carbon phase formed (SWNTs), finally resulting in an enhanced purity and yield of the latter. Such experiments have revealed, as in the comparison between the results from using homogeneous instead of heterogeneous anodes, that the physical phenomena (charge and heat transfers) that occur in the anode during the arc are of the utmost importance, a factor which was neglected before this.

It is clear that while the use of a rare earth element (such as Y) as a single catalyst does not provide the right conditions to grow SWNTs, associating it with a transition metal (Ni/Y for instance) seems to lead to the best combinations that give the highest SWNT yields [3.47]. On the other hand, using a single rare earth element may lead to unexpected results, such as the closure of graphene edges from a c-MWNT wall with the neighboring graphene edges from the same wall side, leading to the preferred formation of telescopelike and open c-MWNTs that are able to contain nested Gd crystals [3.41, 43]. The effectiveness of bimetallic catalysts is believed to be due to the transitory formation of nickel particles coated with yttrium carbide, which has a lattice constant that is somewhat commensurable with that of graphene [3.55].

Figure 3.14 illustrates other interesting features of the plasma. A common feature is that a huge vertical gradient (≈ 500 K/mm) rapidly establishes (≈ 0.5 mm from the center in the radial direction) from the bottom to the top of the plasma, probably due to convection phenomena (Fig. 3.14a). The zone of actual SWNT formation is beyond the limit of the volume analyzable in the radial direction, corresponding to colder areas. The C_2 concentration increases dramatically from the anode to the cathode and decreases dramatically in the radial direction (Fig. 3.14b). This demonstrates that C_2 moieties are secondary products resulting from the recombination of primary species formed from the anode. It also suggests that C_2 moieties may be the building blocks for MWNTs (formed at the cathode) but not for SWNTs [3.43, 45].

Although many aspects of it still need to be understood, the electric arc method is one of the three methods currently used to produce SWNTs as commercial products. Though not selling bare nanotubes anymore, Nanoledge S.A. (Montpellier, France), for instance, had a current production that reached several tens of kilograms per year (raw SWNTs, in other words unpurified), with a market price of ≈ 65 €/g in 2005, which was much cheaper than any other production method. However, the drop of prices for raw SWNTs

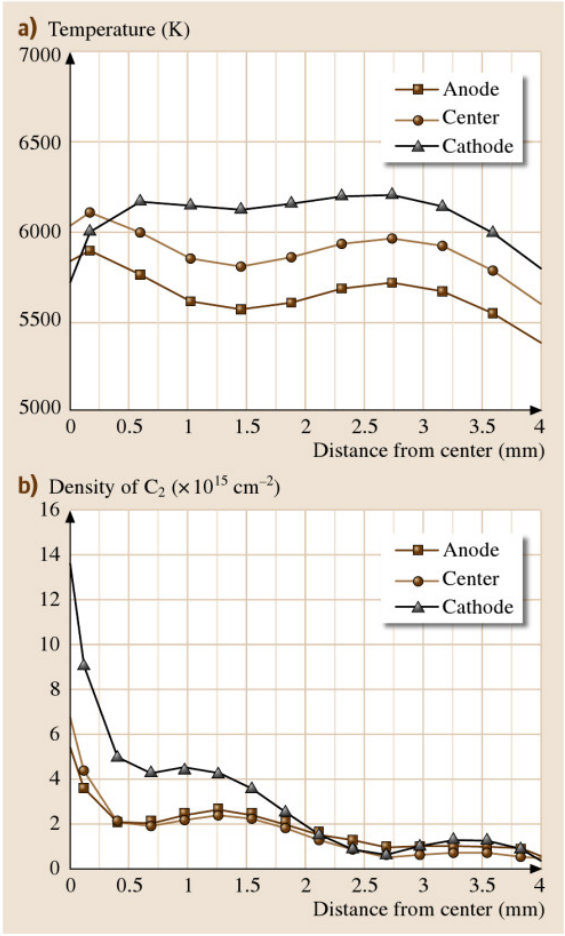

Fig. 3.14a,b Typical temperature (**a**) and C_2 concentration (**b**) profiles for plasma at the anode surface (*squares*), at the center of the plasma (*dots*), and at the cathode surface (*triangles*) at *standard* conditions (see text). Gradients are similar whichever catalyst is used, although absolute values may vary

down to 2–5 €/g which was anticipated for 2007 has not been possible. Actually, Bucky USA (Houston, Texas, USA) are still supplying raw SWNTs derived from electric arcs at a market price of 250 $/g in 2006 (which is, however, a 75% decrease in two years), which is barely lower than the ≈ 350 $/g proposed for 70–90%-purified SWNTs from Nanocarblab (Moscow, Russia).

Three-Phase AC Arc Plasma

An original semi-industrial three-phase AC plasma technology has been developed for the processing of carbon nanomaterials [3.57, 58]. The technology has been specially developed for the treatment of liquid, gaseous or dispersed materials. An electric arc is established between three graphite electrodes. The system is powered by a three-phase AC power supply operated at 600 Hz and at arc currents of 250–400 A. Carbon precursors, gaseous, liquid or solid, are injected at the desired (variable) position into the plasma zone. The reactive mixture can be extracted from the reaction chamber at different predetermined positions. After cooling down to room temperature, the aerosol passes through a filtering system. The main operating parameters, which are freely adjustable, include the arc current,

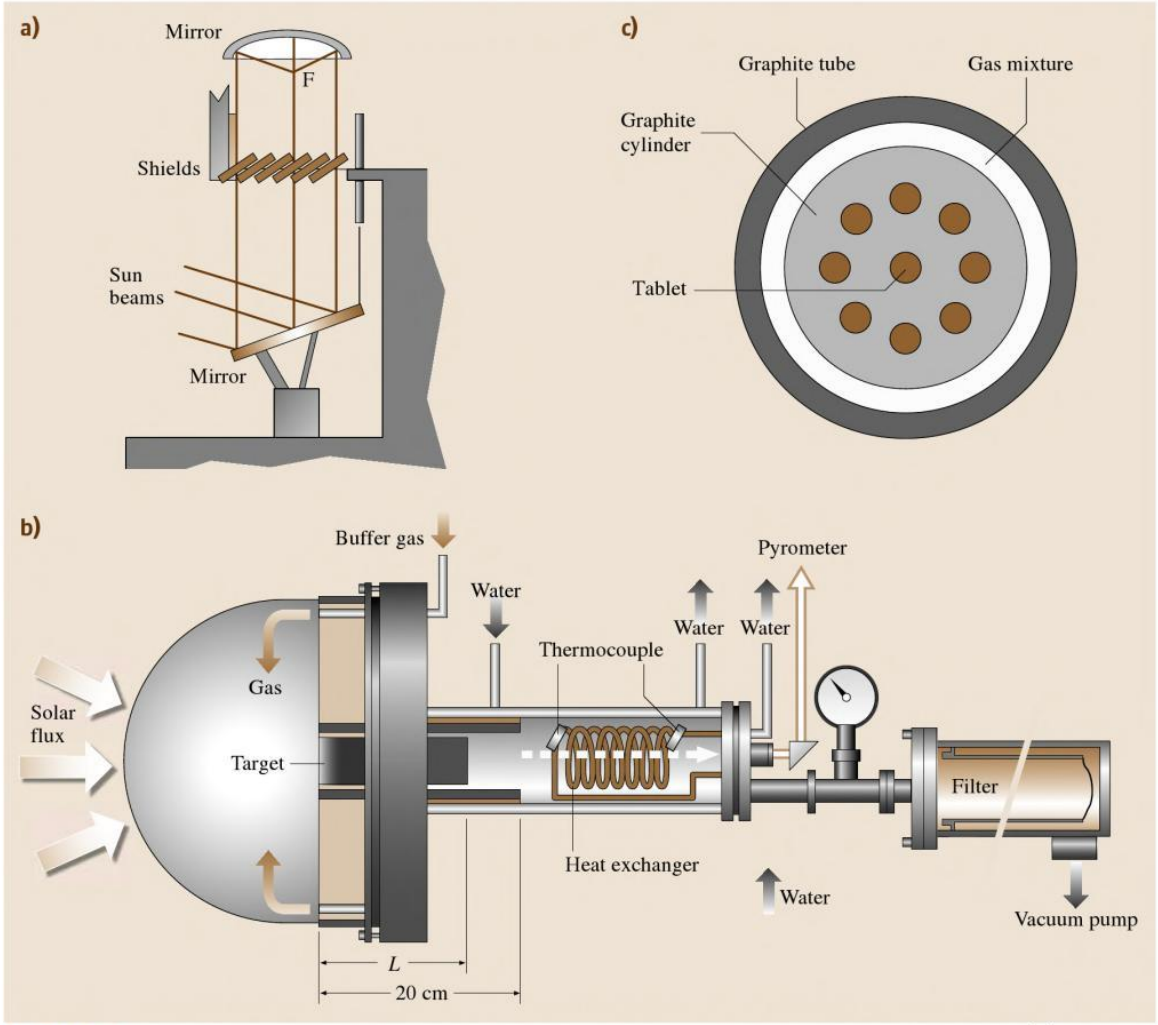

Fig. 3.15a–c Sketch of a solar energy reactor in use in the PROMES-CNRS Laboratory, Odeilho (France). (**a**) Gathering of sun rays, focused at F; (**b**) side view of the experimental set-up at the focus of the 1 MW solar furnace; (**c**) top view of the target graphite rod (adapted from [3.56])

the flow rate and the nature of the plasma gas (N_2, Ar, H_2, He, and so on), the carbon precursor (gaseous, liquid, solid, up to 3 kg/h), the injection and extraction positions, and the quenching rate. This plasma technology has shown very high versatility and it has been demonstrated that it can be used to produce a wide range of carbon nanostructures ranging from carbon blacks to carbon nanotubes over fullerenes with a high product selectivity.

Solar Furnace

Solar furnace devices were originally utilized by several groups to produce fullerenes [3.59–61]. *Heben* et al. [3.62] and *Laplaze* et al. [3.63] later modified their original devices to achieve carbon nanotube production. This modification consisted mainly of using more powerful ovens [3.64, 65].

Solar Furnace – Experimental Devices

The principle of this technique is again based on the sublimation of a mixture of graphite powder and catalysts placed in a crucible in an inert gas. An example of such a device is shown in Fig. 3.15. The solar rays are collected by a plain mirror and reflected toward a parabolic mirror that focuses them directly onto a graphite pellet in a controlled atmosphere (Fig. 3.15a). The high temperature of about 4000 K causes both the carbon and the catalysts to vaporize. The vapors are then dragged by the neutral gas and condense onto the cold walls of the thermal screen. The reactor consists of a brass support cooled by water circulation, upon which Pyrex chambers of various shapes can be fixed (Fig. 3.15b). This support contains a watertight passage permitting the introduction of the neutral gas and a copper rod onto which the target is mounted. The target is a graphite rod that includes pellets containing the catalysts, which is surrounded by a graphite tube (Fig. 3.15c) that acts as both a thermal screen to reduce radiation losses (very important in the case of graphite) and a duct to lead carbon vapors to a filter, which stops soot from being deposited on the Pyrex chamber wall. The graphite rod target replaces the graphite crucible filled with powdered graphite (for fullerene synthesis) or the mixture of graphite and catalysts (for nanotube synthesis) that were used in the techniques we have discussed previously.

These studies primarily investigated the target composition, the type and concentration of catalyst, the flow-rate, the composition and pressure of the plasmagenic gas inside the chamber, and the oven power. The objectives were similar to those of the works associated with the other solid carbon source-based processes. When possible, specific in situ diagnostics (pyrometry, optical emission spectroscopy, and so on) are also performed in order to investigate the roles of various parameters (temperature measurements at the crucible surface, along the graphite tube acting as thermal screen, C_2 radical concentration in the immediate vicinity of the crucible).

Solar Furnace – Results

Some of the results obtained by different groups concerning the influence of the catalyst can be summarized as follows. With Ni/Co, and at low pressure, the sample collected contains mainly MWNTs with bamboo texture, carbon shells, and some bundles of SWNTs [3.64]. At higher pressures, only bundles of SWNTs are obtained, with fewer carbon shells. Relatively long bundles of SWNTs are observed with Ni/Y and at a high pressure. Bundles of SWNTs are obtained in the soot with Co; the diameters of the SWNTs range from 1 to 2 nm. *Laplaze* et al. [3.64] observed very few nanotubes but a large quantity of carbon shells.

In order to proceed to large-scale synthesis of single-wall carbon nanotubes, which is still a challenge for chemical engineers, *Flamant* et al. [3.56] and *Luxembourg* et al. [3.66] recently demonstrated that solar energy-based synthesis is a versatile method for obtaining SWNTs that can be scaled up from 0.1–0.2 to 10 g/h and then to 100 g/h productivity using existing solar furnaces. Experiments performed on a medium scale produced about 10 g/h of SWNT-rich material using various mixtures of catalysts (Ni/Co, Ni/Y, Ni/Ce). A numerical reactor simulation was performed in order to improve the quality of the product, which was subsequently observed to reach 40% SWNT in the soot [3.67].

3.2.2 Gaseous Carbon Source-Based Production Techniques for Carbon Nanotubes

As mentioned in the *Introduction*, the catalysis-enhanced thermal cracking of a gaseous carbon source (hydrocarbons, CO) – commonly referred to as catalytic chemical vapor deposition (CCVD) – has long been known to produce carbon nanofilaments [3.4], so reporting on all of the works published in the field since the beginning of the century is almost impossible. Until the 1990s, however, carbon nanofilaments were mainly produced to act as a core substrate for the subsequent growth of larger (micrometric) carbon fibers – so-called

vapor-grown carbon fibers – via thickening in catalyst-free CVD processes [3.68, 69]. We are therefore going to focus instead on more recent attempts to prepare genuine carbon nanotubes.

The synthesis of carbon nanotubes (either single- or multiwalled) by CCVD methods involves the catalytic decomposition of a carbon-containing source on small metallic particles or clusters. This technique involves either an heterogeneous process if a solid substrate is involved or an homogeneous process if everything takes place in the gas phase. The metals generally used for these reactions are transition metals, such as Fe, Co and Ni. It is a rather low-temperature process compared to arc discharge and laser ablation methods, with the formation of carbon nanotubes typically occurring between 600 and 1000 °C. Because of the low temperature, the selectivity of the CCVD method is generally better for the production of MWNTs with respect to graphitic particles and amorphouslike carbon, which remain an important part of the raw arc discharge SWNT samples, for example. Both homogeneous and heterogeneous processes appear very sensitive to the nature and the structure of the catalyst used, as well as to the operating conditions [3.70]. Carbon nanotubes prepared by CCVD methods are generally much longer (a few tens to hundreds of micrometers) than those obtained by arc discharge (a few micrometers). Depending on the experimental conditions, it is possible to grow dense arrays of nanotubes. It is a general statement that MWNTs from CCVD contain more structural defects (exhibit a lower nanotexture) than MWNTs from arc discharge, due to the lower temperature of the reaction, which does not allow any structural rearrangements. These defects can be removed by subsequently applying heat treatments in vacuum or inert atmosphere to the products. Whether such a discrepancy is also true for SWNTs remains questionable. CCVD SWNTs are generally gathered into bundles that are generally of smaller diameter (a few tens of nm) than their arc discharge and laser ablation counterparts (around 100 nm in diameter). Specifically when performed in fluidized-bed reactor [3.71], CCVD provides reasonably good perspectives on large-scale and low-cost processes for the mass production of carbon nanotubes, a key point for their application at the industrial scale.

A final word concerns the nomenclature. Because work in the field started more than a century ago, the names of the carbon objects prepared by this method have changed with time with the authors, research areas, and fashions. These same objects have been called vapor-grown carbon fibers, nanofilaments, nanofibers and nanotubes. For multilayered fibrous morphologies (since single-layered fibrous morphologies can only be SWNT anyway), the exact name should be vapor-grown carbon nanofilaments (VGCNF). Whether or not the filaments are tubular is a matter of textural description, which should go with other textural features such as bamboo, herringbone and concentric (Sect. 3.1.2). In the following, we will therefore use MWNTs for any hollowed nanofilament, whether they contain graphene walls oriented transversally or not. Any other nanofilament will be termed a *nanofiber*.

Heterogeneous Processes

Heterogeneous CCVD processes simply involve passing a gaseous flow containing a given proportion of a hydrocarbon (mainly CH_4, C_2H_2, C_2H_4, or C_6H_6, usually as a mixture with either H_2 or an inert gas such as Ar) over small transition metal particles (Fe, Co, Ni) in a furnace. The particles are deposited onto an inert substrate, by spraying a suspension of the metal particles on it or by another method. The reaction is chemically defined as catalysis-enhanced thermal cracking

$$C_xH_y \rightarrow x\,C + \tfrac{y}{2}\,H_2\,.$$

Catalysis-enhanced thermal cracking was used as long ago as the late nineteenth century. Extensive works on this topic published before the 1990s include those by *Baker* et al. [3.6, 72], or *Endo* et al. [3.73, 74]. Several review papers have been published since then, such as [3.75], in addition to many regular papers.

CO can be used instead of hydrocarbons; the reaction is then chemically defined as catalysis-enhanced disproportionation (the so-called the Boudouard equilibrium)

$$2\,CO \rightleftharpoons C + CO_2\,.$$

Heterogeneous Processes – Experimental Devices

The ability of catalysis-enhanced CO disproportionation to make carbon nanofilaments was reported by *Davis* et al. [3.76] as early as 1953, probably for the first time. Extensive follow-up work was performed by *Boehm* [3.77], *Audier* et al. [3.17, 78–80], and *Gadelle* et al. [3.81–84].

Although formation mechanisms for SWNTs and MWNTs can be quite different (Sect. 3.3, or refer to a review article such as [3.85]), many of the catalytic process parameters play similar and important roles in the type of nanotubes formed: the temperature, the duration of the treatment, the gas composition and flow rate,

and of course the catalyst nature and size. At a given temperature, depending mainly on the nature of both the catalyst and the carbon-containing gas, the catalytic decomposition will take place at the surfaces of the metal particles, followed by mass transport of the freshly produced carbon by surface or volume diffusion until the carbon concentration reaches the solubility limit, and the precipitation starts.

It is now agreed that CCVD carbon nanotubes form on very small metal particles, typically in the nanometer range [3.85]. These catalytic metal particles are prepared mainly by reducing transition metal compounds (salts, oxides) by H_2 prior to the nanotube formation step (where the carbon containing gas is required). It is possible, however, to produce these catalytic metal particles in situ in the presence of the carbon source, allowing for a one-step process [3.88]. Because controlling the metal particle size is the key issue (they have to be nanosized), coalescence is generally avoided by placing them on an inert support such as an oxide (Al_2O_3, SiO_2, zeolites, $MgAl_2O_4$, MgO) or more rarely on graphite. A low concentration of the catalytic metal precursor is required to limit the coalescence of the metal particles, which can happen during the reduction step. The supported catalysts can be used as a static phase placed within the gas flow, but can also be used as a fine powder suspended into and by the gas phase, in a so-called fluidised bed process. In the latter, the reactor has to be vertical so that to compensate the effect of gravity by the suspending effect of the gas flow.

There are two main ways to prepare the catalyst:

1. The impregnation of a substrate with a solution of a salt of the desired transition metal catalyst
2. The preparation of a solid solution of an oxide of the chosen catalytic metal in a chemically inert and thermally stable host oxide.

The catalyst is then reduced to form the metal particles on which the catalytic decomposition of the carbon source will lead to carbon nanotube growth. In most cases, the nanotubes can then be separated from the catalyst (Fig. 3.16).

Heterogeneous Processes – Results with CCVD Involving Impregnated Catalysts

A lot of work had been done in this area even before the discovery of fullerenes and carbon nanotubes, but although the formation of tubular carbon structures by catalytic processes involving small metal particles was clearly identified, the authors did not focus on the preparation of SWNTs orMWNTs with respect to the other carbon species. Some examples will be given here to illustrate the most striking improvements obtained.

With the impregnation method, the process generally involves four different and successive steps:

1. Impregnation of the support by a solution of a salt (nitrate, chloride) of the chosen metal catalyst
2. Drying and calcination of the supported catalyst to get the oxide of the catalytic metal
3. Reduction in a H_2-containing atmosphere to make the catalytic metal particles
4. The decomposition of a carbon-containing gas over the freshly prepared metal particles that leads to nanotube growth.

For example, *Ivanov* et al. [3.89] prepared nanotubes through the decomposition of C_2H_2 (pure or mixed with H_2) on well-dispersed transition metal par-

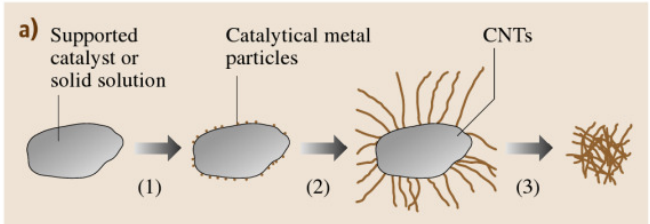

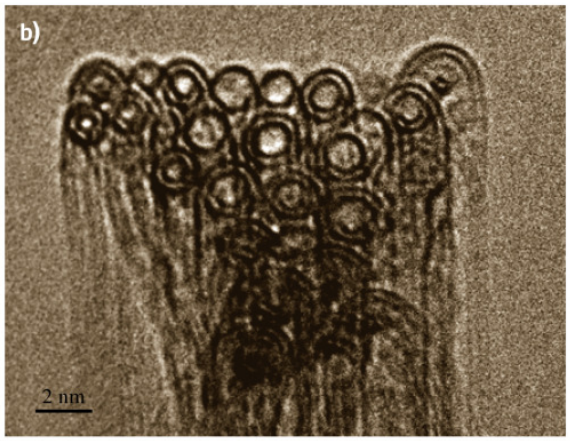

Fig. 3.16 (a) Formation of nanotubes via the CCVD-based impregnation technique. (1) Formation of catalytic metal particles by reduction of a precursor; (2) Catalytic decomposition of a carbon-containing gas, leading to the growth of carbon nanotubes; (3) Removal of the catalyst to recover the nanotubes (from [3.86]). (b) Example of a bundle of double-wall nanotubes (DWNTs) prepared this way (from [3.87])

ticles (Fe, Co, Ni, Cu) supported on graphite or SiO_2. Co-SiO_2 was found to be the best catalyst/support combination for the preparation of MWNTs, but most of the other combinations led to carbon filaments, sometimes covered with amorphouslike carbon. The same authors have developed a precipitation-ion-exchange method that provides a better dispersion of metals on silica compared to the classical impregnation technique. The same group then proposed the use of a zeolite-supported Co catalyst [3.90, 91], resulting in very finely dispersed metal particles (from 1 to 50 nm in diameter). They observed MWNTs with a diameter around 4 nm and only two or three walls only on this catalyst. *Dai* et al. [3.92] have prepared SWNTs by CO disproportionation on nanosized Mo particles. The diameters of the nanotubes obtained are closely related to those of the original particles and range from 1 to 5 nm. The nanotubes obtained by this method are free of an amorphous carbon coating. They also found that a synergetic effect occurs for the alloy instead of the components alone, and one of the most striking examples is the addition of Mo to Fe [3.93] or Co [3.94].

Heterogeneous Processes – Results with CCVD Involving Solid Solution–Based Catalysts

A solid solution of two metal oxides is formed when ions of one metalmix with ions of the other metal. For example, Fe_2O_3 can be prepared in solid solution in Al_2O_3 to give a $Al_{2-2x}Fe_{2x}O_3$ solid solution. The use of a solid solution allows a perfectly homogeneous dispersion of one oxide in the other to be obtained. These solid solutions can be prepared in different ways, but coprecipitation of mixed oxalates and combustion synthesis are the most common methods used to prepare nanotubes. The synthesis of nanotubes by the catalytic decomposition of CH_4 over an $Al_{2-2x}Fe_{2x}O_3$ solid solution was originated by *Peigney* et al. [3.88] and then studied extensively by the same group using different oxides such as spinel-based solid solutions ($Mg_{1-x}M_xAl_2O_4$ with M = Fe, Co, Ni, or a binary alloy [3.86, 95]) or magnesia-based solid solutions [3.86, 96] ($Mg_{1-x}M_xO$, with M = Fe, Co or Ni). Because of the very homogeneous dispersion of the catalytic oxide, it is possible to produce very small catalytic metal particles at the high temperature required for the decomposition of CH_4 (which was chosen for its greater thermal stability compared to other hydrocarbons). The method proposed by these authors involves the heating of the solid solution from room temperature to a temperature of between 850 and 1050 °C in a mixture of H_2 and CH_4, typically containing 18 mol % of CH_4. The nanotubes obtained clearly depend upon the nature of both the transition metal (or alloy) used and the inert oxide (matrix); the latter because the Lewis acidity seems to play an important role [3.97]. For example, in the case of solid solutions containing around 10 wt % of Fe, the amount of carbon nanotubes obtained decreases in the following order depending on the matrix oxide: $MgO > Al_2O_3 > MgAl_2O_4$ [3.86]. In the case of MgO-based solid solutions, the nanotubes can be very easily separated from the catalyst by dissolving it (in diluted HCl for example) [3.96]. The nanotubes obtained are typically gathered into small-diameter bundles (less than 15 nm) with lengths of up to 100 µm. The nanotubes are mainly SWNTs and DWNTs, with diameters of between 1 and 3 nm.

Obtaining pure nanotubes by the CCVD method requires, as for all the other techniques, the removal of the catalyst. When a catalyst supported (impregnated) in a solid solution is used, the supporting – and catalytically inactive – oxide is the main impurity, both in weight and volume. When oxides such as Al_2O_3 or SiO_2 (or even combinations) are used, aggressive treatments involving hot caustic solutions (KOH, NaOH) for Al_2O_3 or the use of HF for SiO_2 are required. These treatments have no effect, however, on other impurities such as other forms of carbon (amorphouslike carbon, graphitized carbon particles and shells, and so on). Oxidizing treatments (air oxidation, use of strong oxidants such as HNO_3, $KMnO_4$, H_2O_2) are thus required and permit the removal of most unwanted forms of carbon, but they result in a low final yield of carbon nanotubes, which are often quite damaged. *Flahaut* et al. [3.96] were the first to use a MgCoO solid solution to prepare SWNTs and DWNTs that could be easily separated without incurring any damage via fast and safe washing with an aqueous HCl solution.

In most cases, only very small quantities of catalyst (typically less than 500 mg) are used, and most claims of *high-yield* productions of nanotubes are based on laboratory experimental data, without taking into account all of the technical problems related to scaling up to a laboratory-scale CCVD reactor. At the present time, although the production of MWNTs is possible on an industrial scale, the production of affordable SWNTs is still a challenge, and controlling the arrangement of and the number of walls in the nanotubes is also problematic. For example, adding small amounts of molybdenum to the catalyst [3.98] can lead to drastic modifications of the nanotube type (from regular nanotubes to carbon nanofibers – Sect. 3.1). *Flahaut* et al.have recently shown that the method used to pre-

pare a particular catalyst can play a very important role [3.99]. Double-walled carbon nanotubes (DWNTs) represent a special case: they are at the frontier between single- (SWNTs) and multiwalled nanotubes (MWNTs). Because they are the MWNTs with the lowest possible number of walls, their structures and properties are very similar to those of SWNTs. Any subsequent functionalization, which is often required to improve the compatibility of nanotubes with their external environment (composites) or to give them new properties (solubility, sensors), will partially damage the external wall, resulting in drastic modifications in terms of both electrical and mechanical properties. This is a serious drawback for SWNTs. In the case of DWNTs, the outer wall can be modified (functionalized) while retaining the structure of the inner tube. DWNTs have been recently synthesised on a gram-scale by CCVD [3.87], with a high purity and a high selectivity (around 80% DWNTs) (Fig. 3.16b).

Homogeneous Processes

The homogenous route, also called the *floating catalyst method,* differs from the other CCVD-based methods because it uses only gaseous species and does not require the presence of any solid phase in the reactor. The basic principle of this technique, similar to the other CCVD processes, is to decompose a carbon source (ethylene, xylene, benzene, carbon monoxide, and so on) on nanosized transition metal (generally Fe, Co, or Ni) particles in order to obtain carbon nanotubes. The catalytic particles are formed directly in the reactor, however, and are not introduced before the reaction, as occurs in supported CCVD for instance.

Homogeneous Processes – Experimental Devices

The typical reactor used in this technique is a quartz tube placed in an oven into which the gaseous feedstock, containing the metal precursor, the carbon source, some hydrogen and a vector gas (N_2, Ar, or He), is passed. The first zone of the reactor is kept at a lower temperature, and the second zone, where the formation of tubes occurs, is heated to 700–1200 °C. The metal precursor is generally a metal-organic compound, such as a zerovalent carbonyl compound like $[Fe(CO)_5]$ [3.100], or a metallocene [3.101–103] such as ferrocene, nickelocene or cobaltocene. The use of metal salts, such as cobalt nitrate, has also been reported [3.104]. It may be advantageous to make the reactor vertical, so that gravity acts symmetrically on the gaseous volume inside the furnace.

Homogeneous Processes – Results

The metal-organic compound decomposes in the first zone of the reactor, generating nanosized metallic particles that can catalyze nanotube formation. In the second part of the reactor, the carbon source is decomposed to atomic carbon, which is then responsible for the formation of nanotubes.

This technique is quite flexible and SWNTs [3.105], DWNTs [3.106] and MWNTs [3.107] have been obtained, in proportions depending on the carbon feedstock gas. The technique has also been exploited for some time in the production of vapor-grown carbon nanofibers [3.108].

The main drawback of this type of process is again that it is difficult to control the size of the metal nanoparticles, and thus nanotube formation is often accompanied by the production of undesired carbon forms (amorphous carbon or polyaromatic carbon phases found as various phases or as coatings). In particular, encapsulated forms have been often found as the result of the formation of metal particles that are too large to promote nanotube growth (and so they can end up being totally covered with graphene layers instead).

The same kind of parameters have to be controlled as for heterogeneous processes in order to finely tune this process and selectively obtain the desired morphology and structure of the nanotubes formed, such as: the choice of the carbon source; the reaction temperature; the residence time; the composition of the incoming gaseous feedstock, with particular attention paid to the role played by the proportion of hydrogen, which can influence the orientation of the graphene with respect to the nanotube axis, thus switching from c-MWNT to h-MWNT [3.82]; and the ratio of the metallorganic precursor to the carbon source [3.101]. In an independent study [3.109], it was shown that the general tendency is:

1. To synthesize SWNTs when the ferrocene/benzene molar ratio is high, typically ≈ 15%
2. To produce MWNTs when the ferrocene/benzene molar ratio is between ≈ 4 and ≈ 9%
3. To synthesize carbon nanofibers when the ferrocene/benzene molar ratio is below ≈ 4%.

As recently demonstrated, the overall process can be improved by adding other compounds such as ammonia or sulfur-containing species to the reactive gas phase. The former allows aligned nanotubes and mixed C-N nanotubes [3.110] to be obtained, while the latter results in a significant increase in productivity [3.108, 111].

An interesting result is the increase in yield and purity brought about by a small input of oxygen, as achieved by using alcohol vapors instead of hydrocarbons as feedstock [3.112]. It is assumed that the oxygen preferably burns the poorly organized carbon out into CO_2, thereby enhancing the purity, and prevents the catalyst particles from being encapsulated in the carbon shells too early, making them inactive, thereby enhancing the nanotube yield. Moreover, it was found to promote the formation of SWNTs over MWNTs, since suppressing carbon shell formation suppresses MWNT formation too.

It should be emphasized that only small amounts have been produced so far, and scale-up to industrial levels seems quite difficult due to the large number of parameters that must be considered. A critical one is to be able to increase the quantity of metallorganic compound that is used in the reactor, in order to increase production, without obtaining particles that are too big. This problem has not yet been solved. An additional problem inherent in the process is the possibility of clogging the reactor due to the deposition of metallic nanoparticles on the reactor walls followed by carbon deposition. An interesting alternative could be the injection, into the vertical floating reactor, of a supported catalyst powder instead of an organometallic compound. This approach has allowed the continuous production of single-walled carbon nanotubes with scaling capability up to 220 g/h [3.114].

A significant breakthrough concerning this technique could be the HiPCo process developed at Rice University, which produces SWNTs of very high purity [3.115, 116]. This gas phase catalytic reaction uses carbon monoxide to produce, from $[Fe(CO)_5]$, a SWNT material that is claimed to be relatively free of by-products. The temperature and pressure conditions required are applicable to industrial plants. Upon heating, the $[Fe(CO)_5]$ decomposes into atoms which condense into larger clusters, and SWNT nucleate and grow on these particles in the gas phase via CO disproportionation (the Boudouard reaction, see *Heterogeneous Processes* in Sect. 3.1.2):

The company Carbon Nanotechnologies Inc. (Houston, USA) currently sells raw SWNT materials prepared in this way, at a market price of 375 $/g, or 500 $/g if purified (2005 data). Other companies that specialize in MWNTs include Applied Sciences Inc. (Cedarville, USA), currently has a production facility of $\approx$ 40 tons/year of $\approx$ 100 nm large MWNTs (Pyrograf-III), and Hyperion Catalysis (Cambridge, USA), which makes MWNT-based materials. Though prepared in a similar way by CCVD-related processes, MWNTs remain far less expensive than SWNTs, reaching prices as low as 0.055 $/g (current ASI fares for Pyrograf-III grade).

Templating

Another interesting technique, although one that is definitely not suitable for mass production (and so we only touch on it briefly here), is the templating technique. It is the only other method aside from the electric arc technique that is able to synthesize carbon nanotubes without any catalyst. Any other work reporting the catalyst-free formation of nanotubes is actually likely to have involved the presence of catalytic metallic impurities in the reactor or some other factors that caused a chemical gradient in the system. Another useful aspect of this approach is that it allows aligned nanotubes to be obtained naturally, without the help of any subsequent alignment procedure. However, the template must be removed (dissolved) to recover the nanotubes, in which case the alignment of the nanotubes is lost.

Templating – Experimental Devices

The principle of this technique is to deposit the solid carbon coating obtained from the CVD method onto the walls of a porous substrate whose pores are arranged in parallel channels. The feedstock is again a hydrocarbon, such as a common source of carbon. The substrate can be alumina or zeolite for instance, which present natural channel pores, while the whole system is heated to a temperature that cracks the hydrocarbon selected as the carbon source (Fig. 3.17).

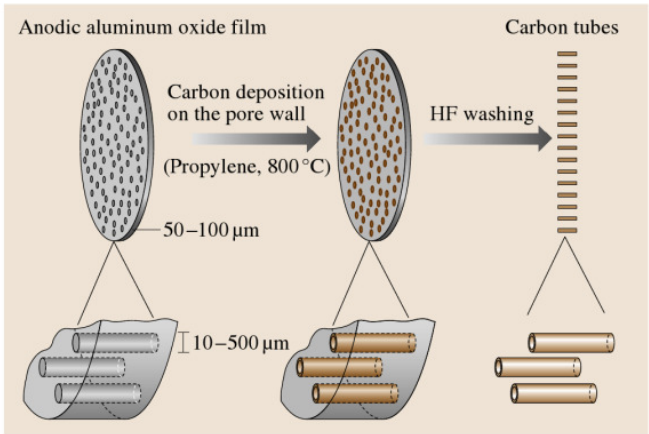

Fig. 3.17 Principle of the templating technique used in the catalyst-free formation of single-walled or concentric-type multiwalled carbon nanotubes (from [3.113])

Templating – Results

Provided the chemical vapor deposition mechanism (which is actually better described as a chemical vapor infiltration mechanism) is well controlled, synthesis results in the channel pore walls being coated with a variable number of graphenes. Both MWNTs (exclusively concentric type) and SWNTs can be obtained. The smallest SWNTs (diameters ≈ 0.4 nm) ever obtained (Sect. 3.1) were actually been synthesized using this technique [3.11]. The nanotube lengths are directly determined by the channel lengths; in other words by the thickness of the substrate plate. One main advantage of the technique is the purity of the tubes (no catalyst remnants, and few other carbon phases). On the other hand, the nanotube structure is not closed at both ends, which can be an advantage or a drawback depending on the application. For instance, the porous matrix must be dissolved using one of the chemical treatments previously cited in order to recover the tubes. The fact that the tubes are open makes them even more sensitive to attack from acids.

3.2.3 Miscellaneous Techniques

In addition to the major techniques described in Sects. 3.2.1 and 3.2.2, many attempts to produce nanotubes in various ways, often with a specific goal in mind, such as looking for a low-cost or a catalyst-free production process, can be found in the literature. As yet, none has been convincing enough to be presented as a serious alternative to the major processes described previously. Some examples are provided in the following.

Hsu et al. [3.117] have succeeded in preparing MWNTs (including coiled MWNTs, a peculiar morphology resembling a spring) by a catalyst-free (although Li was present) electrolytic method, by running a 3–5 A current between two graphite electrodes (the anode was a graphite crucible and the cathode a graphite rod). The graphite crucible was filled with lithium chloride, while the whole system was heated in air or argon at $\approx 600\,^{\circ}$C. As with many other techniques, by-products such as encapsulated metal particles, carbon shells, amorphous carbon, and so on, are formed.

Cho et al. [3.118] have proposed a pure chemistry route to nanotubes, using the polyesterification of citric acid onto ethylene glycol at $50\,^{\circ}$C, followed by polymerization at $135\,^{\circ}$C and then carbonization at $300\,^{\circ}$C under argon, followed by oxidation at $400\,^{\circ}$C in air. Despite the latter oxidation step, the solid product contains short MWNTs, although they obviously have poor nanotextures. By-products such as carbon shells and amorphous carbon are also formed.

Li et al. [3.119] have also obtained short MWNTs through a catalyst-free (although Si is present) pyrolytic method which involves heating silicon carbonitride nanograins in a BN crucible to $1200–1900\,^{\circ}$C in nitrogen within a graphite furnace. No details are given about the possible occurrence of by-products, but they are likely considering the complexity of the chemical system (Si-C-B-N) and the high temperatures involved.

Terranova et al. [3.120] have investigated the catalyzed reaction between a solid carbon source and atomic hydrogen. Graphite nanoparticles (≈ 20 nm) are sent with a stream of H_2 onto a Ta filament heated at $2200\,^{\circ}$C. The species produced, whatever they are, then hit a Si polished plate warmed to $900\,^{\circ}$C that supports transition metal particles. The whole chamber is kept in a dynamic vacuum of 40 Torr. SWNTs are supposed to form according to the authors, although their images are not very convincing. One major drawback of the method, besides its complexity compared to the others, is that it is difficult to recover the *nanotubes* from the Si substrates to which they seem to be firmly bonded.

The final example is an attempt to prepare nanotubes by diffusion flame synthesis [3.121]. A regular gaseous hydrocarbon source (ethylene, ...) along with ferrocene vapor is passed into a laminar diffusion flame derived from air and CH_4 of temperature $500–1200\,^{\circ}$C. SWNTs are formed, together with encapsulated metal particles, soot, and so on. In addition to a low yield, the SWNT structure is quite poor.

3.2.4 Synthesis of Carbon Nanotubes with Controlled Orientation

Several applications (such as field emission-based displays Sect. 3.6) require that carbon nanotubes grow as highly aligned bunches, in highly ordered arrays, or that they are located at specific positions. In this case, the purpose of the process is not mass production but controlled growth and purity, with subsequent control of nanotube morphology, texture and structure. Generally speaking, the more promising methods for the synthesis of aligned nanotubes are based on CCVD processes, which involve the use of molecular precursors as carbon sources, and the method of thermal cracking assisted by the catalytic activity of transition metal (Co, Ni, Fe) nanoparticles deposited onto solid supports. Although this approach initially produced mainly MWNTs, DWNT [3.122] and SWNT [3.123] arrays can be selectively obtained today. Generally speaking,

SWNTs and DWNTs nucleate at higher temperatures than MWNTs [3.124].

However, the catalyst-free templating methods related to those described in Sect. 3.2.2 are not considered here, due to the lack of support after the template is removed, which means that the previous alignment is not maintained.

During the CCVD growth, nanotubes can self-assemble into nanotube bunches aligned perpendicular to the substrate if the catalyst film on the substrate has a critical thickness [3.127, 128]. The driving forces for this alignment are the van der Waals interactions between the nanotubes, which allow them to grow perpendicularly to the substrates. If the catalyst nanoparticles are deposited onto a mesoporous substrate, the mesoscopic pores may also have an effect on the alignment when the growth starts, thus controlling the growth direction of the nanotubes. Two kinds of substrates have been used so far for this purpose: mesoporous silica [3.129, 130] and anodic alumina [3.131].

Different methods of depositing metal particles onto substrates have been reported in the literature:

1. Deposition of a thin film on alumina substrates using metallic salt precursor impregnation followed by oxidation/reduction steps [3.132].
2. Embedding catalyst particles in mesoporous silica by sol–gel processes [3.129].
3. Thermal evaporation of Fe, Co, Ni or Co-Ni metal alloys on SiO_2 or quartz substrates under high vacuum [3.133, 134].
4. Photolithographic patterning of metal-containing photoresist polymer using conventional black and white films as a mask [3.135] or photolithography and the inductive plasma deep etching technique [3.136].
5. Electrochemical deposition into pores in anodic aluminum oxide templates [3.131].
6. Deposition of colloidal suspensions of catalyst particles with tailored diameters on a support [3.137–141], by spin-coating for instance.
7. Stamping a catalyst precursor over a patterned silicon wafer is also possible and has been used to grow networks of nanotubes parallel to the substrate (Fig. 3.18a), or more generally to localize the growth of individual CNTs [3.142].

A technique that combines the advantages of electron beam lithography and template methods has also been reported for the large-scale production of ordered MWNTs [3.143] or AFM tips [3.144].

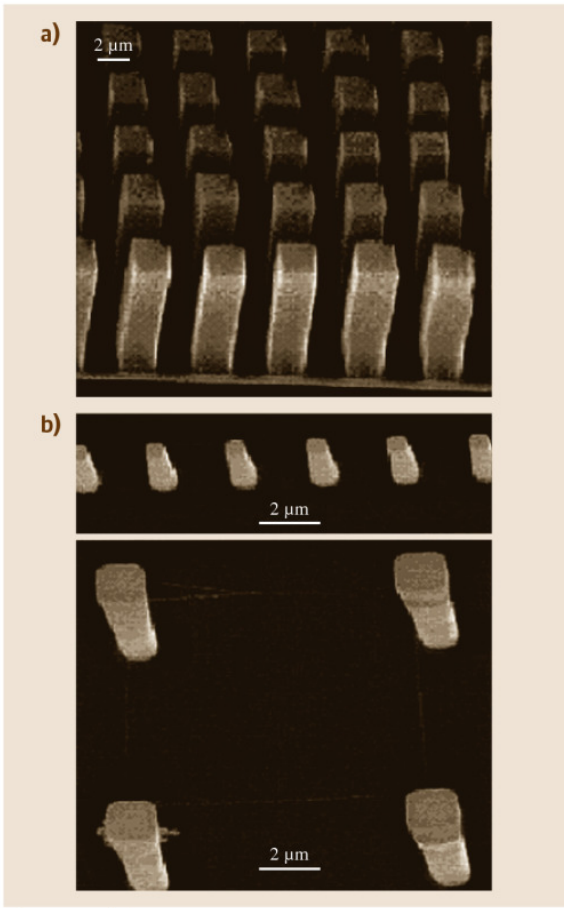

Fig. 3.18 (a) Example of a controlled network of nanotubes grown parallel to the substrate [3.125]; (b) example of a free-standing MWNT array obtained from the pyrolysis of a gaseous carbon source over catalyst nanoparticles previously deposited onto a patterned substrate. Each square-base rod is a bunch of MWNTs aligned perpendicular to the surface (from [3.126])

Depositing the catalyst nanoparticles onto a prepatterned substrate allows one to control the frequency of local occurrence and the arrangement of the nanotube bunches formed. The materials produced mainly consist of arrayed, densely packed, freestanding, aligned MWNTs (Fig. 3.18b), which are quite suitable for field emission-based applications for instance [3.126]. SWNTs have also been produced, and it was reported that the introduction of water vapor during the CVD process allows impurity-free SWNTs to be synthesized [3.145], due to a mechanism related to that

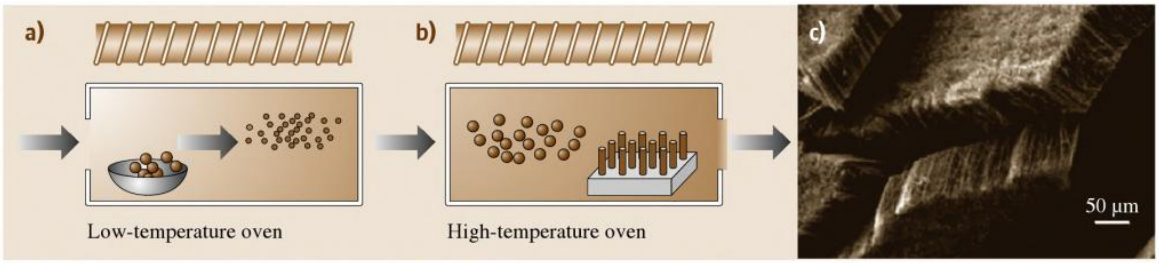

Fig. 3.19a–c Sketch of a double-furnace CCVD device used in the organometallic/hydrocarbon copyrolysis process. **(a)** Sublimation of the precursor. **(b)** Decomposition of the precursor and MWNT growth onto the substrate. **(c)** Example of the densely packed and aligned MWNT material obtained (from [3.146])

previously proposed for the effect of using alcohol instead of hydrocarbon feedstock [3.127].

When a densely packed coating of vertically aligned MWNTs is desired (Fig. 3.19c), another route is the pyrolysis of hydrocarbons in the presence of organometallic precursor molecules like metallocene or iron pentacarbonyl, operating in a dual furnace system (Fig. 3.19a,b). The organometallic precursor (such as ferrocene) is first sublimed at low temperature in the first furnace or injected as a solution along with the hydrocarbon feedstock, and then the whole system is pyrolyzed at higher temperature in the second furnace [3.105, 146–149]. The important parameters here are the heating or feeding rate of ferrocene, the flow rates of the vector gas (Ar or N_2) and the gaseous hydrocarbon, and the temperature of pyrolysis (650–1050 °C). Generally speaking, the codeposition process using [$Fe(CO)_5$] as the catalyst source results in thermal decomposition at elevated temperatures, producing atomic iron that deposits on the substrates in the hot zone of the reactor. Since nanotube growth occurs at the same time as the introduction of [$Fe(CO)_5$], the temperatures chosen for the growth depend on the carbon feedstock utilized; for example, they can vary from 750 °C for acetylene to 1100 °C for methane. Mixtures of [$FeCp_2$] and xylene or [$FeCp_2$] and acetylene have also been successfully used to produce freestanding MWNTs.

The nanotube yield and quality are directly linked to the amount and size of the catalyst particles, and since the planar substrates used do not exhibit high surface areas, the dispersion of the metal can be a key step in the process. It has been observed that an etching pretreatment of the surface of the deposited catalyst thin film with NH_3 may be critical to efficient nanotube growth of nanotubes since it provides the appropriate metal particle size distribution. It may also favor the alignment of MWNTs and prevent the formation of amorphous carbon due to the thermal cracking of acetylene [3.150]. The application of phthalocyanines of Co, Fe and Ni has also been reported, and in this case the pyrolysis of the organometallic precursors also produces the carbon for the vertically aligned MWNTs [3.151].

Densely packed coatings of vertically aligned MWNTs may also be produced over metal-containing deposits, such as iron oxides on aluminum [3.152], in which case MWNT synthesis takes place on small particles that are formed from the iron oxide deposit. Interestingly, it has been recently reported that well aligned MWNT arrays can be produced on a large scale on ceramic spheres using the floating catalyst techniques [3.153]. Finally, it has been recently reported that the Langmuir–Blodgett method can effectively be used to produce monolayers of aligned noncovalently functionalized SWNTs from organic solvent with dense packing [3.154]. This method seems valid for bulk materials with various diameters and offers the advantage that the SWNT monolayers are readily patterned for device integration by microfabrication.

3.3 Growth Mechanisms of Carbon Nanotubes

The growth mechanisms of carbon nanotubes are still the source of much debate. However, researchers have been impressively imaginative, and have come up with a number of hypotheses. One reason for the debate is that the conditions that allow carbon nanofilaments to grow are very diverse, which means that there are many related growth mechanisms. For a given set of conditions, the true mechanism is probably a combination of

or a compromise between some of the proposals. Another reason is that the phenomena that occur during growth are pretty rapid and difficult to observe in situ. It is generally agreed, however, that growth occurs such that the number of dangling bonds is minimized, for energetic reasons.

3.3.1 Catalyst-Free Growth

As already mentioned, in addition to the templating technique, which is merely a chemical vapor infiltration mechanism for pyrolytic carbon, the growth of c-MWNT as a deposit on the cathode in the electric arc method is a rare example of catalyst-free carbon nanofilament growth. The driving force is obviously related to the electric field; in other words to charge transfer from one electrode to the other via the particles contained in the plasma. It is not clear how the MWNT nucleus is formed, but once it has, it may include the direct incorporation of C_2 species into the primary graphene structure, as it was previously proposed for fullerenes [3.155]. This is supported by recent C_2 radical concentration measurements that reveal an increasing concentration of C_2 from the anode being consumed at the growing cathode (Fig. 3.14). This indicates that C_2 are only secondary species and that the C_2 species may actually actively participate in the growth of c-MWNTs in the arc method.

3.3.2 Catalytically Activated Growth

Growth mechanisms involving catalysts are more difficult to ascertain, since they are more diverse. Although it involves a more or less extensive contribution from a VLS (vapor–liquid–solid [3.156]) mechanism, it is quite difficult to find comprehensive and plausible explanations that are able to account for both the various conditions used and the various morphologies observed. What follows is an attempt to provide overall explanations of most of the phenomena, while remaining consistent with the experimental data. We do not consider any hypothesis for which there is a lack of experimental evidence, such as the moving nanocatalyst mechanism, which proposes that dangling bonds from a growing SWNT may be temporarily stabilized by a nanosized catalyst located at the SWNT tip [3.28], or the scooter mechanism, which proposes that dangling bonds are temporarily stabilized by a single catalyst atom which moves around the edge of the SWNT , allowing subsequent C atom addition [3.157].

From various results, it appears that the most important parameters are probably the thermodynamic ones (only temperature will be considered here), the catalyst particle size, and the presence of a substrate. Temperature is critical and basically corresponds to the discrepancy between CCVD methods and solid carbon source-based methods.

Low-Temperature Conditions

Low-temperature conditions are typical used in CCVD, where nanotubes are frequently found to grow far below 1000 °C. If the conditions are such that the catalyst is a crystallized solid, the nanofilament is probably formed via a mechanism similar to a VLS mechanism, in which three steps are defined:

1. Adsorption then decomposition of C-containing gaseous moieties at the catalyst surface
2. Dissolution then diffusion of the C species through the catalyst, thus forming a solid solution
3. Back-precipitation of solid carbon as nanotube walls. The texture is then determined by the orientation of the crystal faces relative to the filament axis (Fig. 3.20), as demonstrated beyond doubt by transmission electron microscopy images such as those in *Rodriguez* et al. [3.20].

This mechanism can therefore provide either c-MWNT, h-MWNT, or platelet nanofibers. The latter, however, are mainly formed in large particle sizes (> 100 nm for example). Platelet nanofibers with low diameters (< 40 nm) have never been observed. The reasons for this are related to graphene energetics, such as the need to reach the optimal ratio between the amount of edge carbon atoms (with dangling bonds) and inner carbon atoms (where all of the σ and π orbitals are satisfied).

If conditions are such that the catalyst is a liquid droplet, due to the use of high temperatures or because a catalyst that melts at a low temperature is employed, a mechanism similar to that described above can still occur, which is really VLS (vapor = gaseous C species, liquid = molten catalyst, S = graphenes), but there are obviously no crystal faces to orient preferentially with the rejected graphenes. Energy minimization requirements will therefore tend to make them concentric and parallel to the filament axis.

With large catalyst particles (or in the absence of any substrate), the mechanisms above will generally follow a *tip growth* scheme: the catalyst will move forward while the rejected carbon will form the nanotube behind, whether there is a substrate or not. In this case, there is a good chance that one end will be open. On

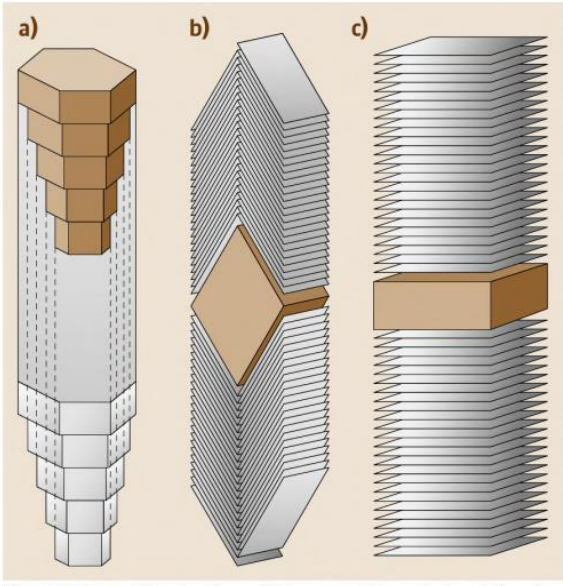

Fig. 3.20a–c Illustration of the possible relationships between the outer morphology of the catalyst crystal and the inner texture of the subsequent carbon nanofilament (adapted from [3.20]). In (**a**), a nanotube with graphenes making the wall arranged concentrically (*concentric MWNT*). In (**b**), a nanofibre with graphenes arranged so that they make an angle with respect to the nanofibre axis (*herringbone nanofibre*). In (**c**), a nanofibre with the graphenes piled up perpendicularly to the nanofibre axis (*platelet nanofibre*). Crystals are drawn with the projected plane perpendicular to the electron beam in a transmission electron microscope; the crystal morphologies and the subsequent graphene arrangements in the out-of-plane dimension are not intended to be accurate representations in these sketches (for example, the graphenes in the herringbone-type nanotubes or nanofibers in (**b**) cannot be arranged like a pile of open books, as sketched here, because it would leave too many dangling bonds)

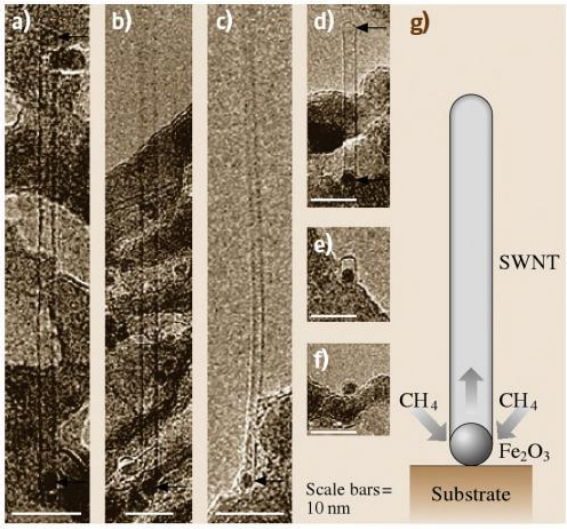

Fig. 3.21a–g High-resolution transmission electron microscopy images of several SWNTs grown from iron-based nanoparticles using the CCVD method, showing that particle sizes determine SWNT diameters in this case (adapted from [3.158]). Yet the catalyst crystal imaged (the *dark spot* at the bottom of each tube) is different for each figure, considering images backward from (**f**) to (**c**) illustrates what could be a sequence of growth of a SWNT from a single nanocrystal, as sketched in (**g**). (**a**) and (**b**) show additional examples of fully grown SWNTs, similar to (**c**)

the other hand, when the catalyst particles deposited onto the substrate are small enough (nanoparticles) to be held in place by interaction forces with the substrate, the growth mechanism will follow a *base growth* scheme, where the carbon nanofilament grows away from the substrate, leaving the catalyst nanoparticle attached to the substrate (Fig. 3.21).

The bamboo texture that affects both the herringbone and the concentric texture may reveal a distinguishing aspect of the dissolution-rejection mechanism: the periodic, discontinuous dynamics of the phenomenon. Once the catalyst has reached the saturation threshold in terms of its carbon content, it expels it quite suddenly. Then it becomes able to incorporate a given amount of carbon again without having any catalytic activity for a little while. Then over-saturation is reached again, and so on. An exhaustive study of this phenomenon has been carried out by *Jourdain* et al. [3.159].

Therefore, it is clear that 1 catalyst particle = 1 nanofilament in any of the mechanisms above. This explains why, although it is possible to make SWNTs by CCVD methods, controlling the catalyst particle size is critical, since it influences the nanofilament that grows from it. Achieving a really narrow size distribution in CCVD is quite challenging, particularly when nanosizes are required for the growth of SWNTs. Only particles < 2 nm are useful for this (Fig. 3.21), since larger SWNTs are not favored energetically [3.10]. Another distinguishing aspect of the CCVD method and its related growth mechanisms is that the process can occur all along the isothermal zone of the reactor furnace since it is continuously fed with a carbon-rich feedstock, which is generally in excess, with a constant composition at a given species time of flight. Roughly

Table 3.2 Guidelines indicating the relationships between possible carbon nanofilament morphologies and some basic synthesis conditions. Columns (1) and (2) mainly relate to CCVD-based methods; column (3) mainly relates to plasma-based methods

		Increasing temperature . . . → . . . and physical state of catalyst			Substrate		Thermal gradient	
		solid (crystallized) (1)	liquid from melting (2)	liquid from condensing atoms (3)	yes	no	low	high
Catalyst particle size	$\lesssim 3$ nm	SWNT	SWNT	?	base-growth	tip-growth	long length	short length
	$\gtrsim 3$ nm	MWNT (c,h,b) platelet nanofiber	c-MWNT	SWNT	tip-growth			
Nanotube diameter		(heterogeneous related to catalyst particle size)		homogeneous (independent from particle size)		(except for SWNTs growing from case (3) catalyst)		
Nanotube/particle		one nanotube/particle		several SWNTs/particle				

speaking, the longer the isothermal zone (in gaseous carbon excess conditions), the longer the nanotubes. This is why the lengths of the nanotubes can be much longer than those obtained using solid carbon source-based methods.

Table 3.2 provides an overview of the relationship between general synthesis conditions and some features of nanotube grown.

High-Temperature Conditions

High-temperature conditions are typical used in solid carbon source-based methods such as the electric arc method, laser vaporization, and the solar furnace method (Sect. 3.2). The huge temperatures involved (several thousands of °C) atomize both the carbon source and the catalyst. Of course, catalyst-based SWNTs do not form in the areas with the highest temperatures (contrary to c-MWNTs in the electric arc method); the medium is a mixture of atoms and radicals, some of which are likely to combine and condense into liquid droplets. At some distance from the atomization zone, the medium is therefore made of carbon metal alloy droplets and of secondary carbon species that range from C_2 to higher order molecules such as corannulene, which is made of a central pentagon surrounded by five hexagons. The preferred formation of such a molecule can be explained by the previous association of carbon atoms into a pentagon, because it is the fastest way to limit dangling bonds at low energetic cost, thereby providing a fixation site for other carbon atoms (or C_2) which also will tend to close into a ring, again to limit dangling bonds. Since adjacent pentagons are not energetically favored, these cycles will be hexagons. Such a molecule is thought to be a probable precursor for fullerenes. Fullerenes are actually always produced, even in conditions that produce SWNTs. The same saturation in C described in Sect. 3.3.2 occurs for the carbon-metal alloy droplet as well, resulting in the precipitation of excess C outside the particle due to the effect of the decreasing thermal gradient in the reactor, which decreases the solubility threshold of C in the metal [3.160]. Once the *inner* carbon atoms reach the surface of the catalyst particle, they meet the *outer* carbon species, including corannulene, that will contribute to capping the merging nanotubes. Once formed and capped, nanotubes can grow both from the inner carbon atoms (Fig. 3.22a), according to the VLS mechanism proposed by *Saito* et al. [3.160], and from the outer carbon atoms, according the adatom mechanism proposed by *Bernholc* et al. [3.161]. In the latter, carbon atoms from the surrounding medium in the reactor are attracted then stabilized by the carbon/catalyst interface

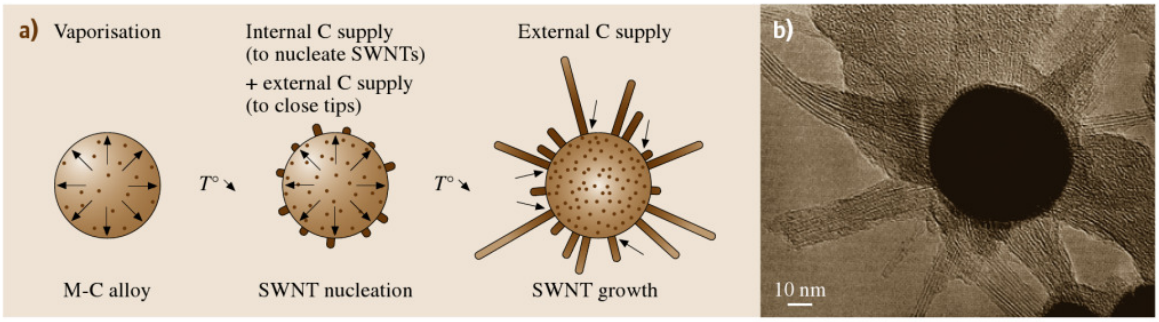

Fig. 3.22 (**a**) Mechanism proposed for SWNT growth (see text). (**b**) Transmission electron microscopy image of SWNT growing radially from the surface of a large Ni catalyst particle in an electric arc experiment. (Modified from [3.18])

at the nanotube/catalyst surface contact, promoting their subsequent incorporation at the tube base. The growth mechanism therefore mainly follows the base growth scheme. However, once the nanotubes are capped, any C_2 species that still remains in the medium that meets the growing nanotubes far from the nanotube/catalyst interface may still incorporate the nanotubes from both the side wall or the tip, thereby giving rise to some proportion of Stone–Wales defects [3.45]. The occurrence of a nanometer-thick surface layer of yttrium carbide (onto the main Ni-containing catalyst core), the lattice distance of which is commensurable with that of the C−C distance in graphene (as recently revealed by *Gavillet* et al. [3.55]), could possibly play a beneficial role in stabilizing the nanotube/catalyst interface, which could explain why the SWNT yield is enhanced by bimetallic alloys (as opposed to single metal catalysts).

A major difference from the low-temperature mechanisms described for CCVD methods is that many nanotubes are formed from a single, relatively large (≈ 10–50 nm) catalyst particle (Fig. 3.22b), whose size distribution is therefore not as critical as it is for the low-temperature mechanisms (particles that are too large, however, induce polyaromatic shells instead of nanotubes). This is why the diameters of SWNTs grown at high temperature are much more homogeneous than those associated with CCVD methods. The reason that the most frequent diameter is ≈ 1.4 nm is again a matter of energy balance. Single-wall nanotubes larger than ≈ 2.5 nm are not stable [3.10]. On the other hand, the strain on the C−C bond increases as the radius of curvature decreases. The optimal diameter (1.4 nm) should therefore correspond to the best energetic compromise. Another difference from the low-temperature mechanism for CCVD is that temperature gradients in high temperature methods are huge, and the gas phase composition surrounding the catalysts droplets is also subjected to rapid changes (as opposed to what could happen in a laminar flow of a gaseous feedstock whose carbon source is in excess). This explains why nanotubes from arcs are generally shorter than nanotubes from CCVD, and why mass production by CCVD is favored. In the latter, the metallic particle can act as a catalyst repeatedly as long as the conditions are maintained. In the former, the surrounding conditions change continuously, and the window for efficient catalysis can be very narrow. Decreasing the temperature gradients that occur in solid carbon source-based methods of producing SWNT, such as the electric arc reactor, should therefore increase the SWNT yield and length [3.162]. Amazingly, this is in opposition to what is observed during arc-based fullerene production.

3.4 Properties of Carbon Nanotubes

In previous sections, we noted that the normal planar configuration of graphene can, under certain growth conditions (Sect. 3.3), be changed into a tubular geometry. In this section, we take a closer look at the properties of these carbon nanotubes, which can depend on whether they are arranged as SWNTs or as MWNTs (Sect. 3.1).

3.4.1 Overview

The properties of MWNTs are generally similar to those of regular polyaromatic solids (which may exhibit graphitic, turbostratic or intermediate crystallographic structure). Variations are mainly due to different textural types of the MWNTs considered (concentric,

herringbone, bamboo) and the quality of the nanotexture (Sect. 3.1), both of which control the extent of anisotropy. Actually, for polyaromatic solids that consist of stacked graphenes, the bond strength varies significantly depending on whether the in-plane direction is considered (characterized by very strong covalent and therefore very short – 0.142 nm – bonds) or the direction perpendicular to it (characterized by very weak van der Waals and therefore very loose – ≈ 0.34 nm – bonds). Such heterogeneity is not found in single (isolated) SWNTs. However, the heterogeneity returns, along with the related consequences, when SWNTs associate into bundles. Therefore, the properties – and applicability – of SWNTs may also change dramatically depending on whether single SWNT or SWNT ropes are involved.

In the following, we will emphasize the properties of SWNTs, since their unique structures often lead to different properties to regular polyaromatic solids. However, we will also sometimes discuss the properties of MWNTs for comparison.

3.4.2 General Properties of SWNTs

The diameters of SWNT-type carbon nanotubes fall in the nanometer regime, but SWNTs can be hundreds of micrometers long. SWNTs are narrower in diameter than the thinnest line that can be obtained in electron beam lithography. SWNTs are stable up to 750 °C in air (but they are usually damaged before this temperature is reached due to oxidation mechanisms, as demonstrated by the fact that they can be filled with molecules (Sect. 3.5). They are stable up to ≈ 1500–1800 °C in inert atmosphere, beyond which they transform into regular, polyaromatic solids (phases built with stacked graphenes instead of single graphenes) [3.163]. They have half the mass density of aluminum. The properties of a SWNT, like any molecule, are heavily influenced by the way that its atoms are arranged. The physical and chemical behavior of a SWNT is therefore related to its unique structural features [3.164].

3.4.3 Adsorption Properties of SWNTs

An interesting feature of a SWNT is that it has the highest surface area of any molecule due to the fact that a graphene sheet is probably the only example of a sheetlike molecule that is energetically stable under normal conditions. If we consider an isolated SWNT with one open end (achieved through oxidation treatment for instance), the surface area is equal to that of a single, flat graphene sheet: $\approx 2700\,m^2/g$ (accounting for both sides).

In reality, nanotubes – specifically SWNTs – are usually associated with other nanotubes in bundles, fibers, films, papers, and so on, rather than as a single entity. Each of these associations has a specific range of porosities that determines its adsorption properties (this topic is also covered in Sect. 3.6.2 on applications). It is therefore more appropriate to discuss adsorption onto the outer or the inner surface of a bundle of SWNTs.

Furthermore, theoretical calculations have predicted that the adsorption of molecules onto the surface or inside of a nanotube bundle is stronger than that onto an individual tube. A similar situation exists for MWNTs, where adsorption can occur on or inside the tubes or between aggregated MWNTs. It has also been shown that the curvature of the graphene sheets constituting the nanotube walls results in a lower heat of adsorption compared to planar graphene (Sect. 3.1.1).

Accessible Specific Surface Area of CNTs

Various studies dealing with the adsorption of nitrogen onto MWNTs [3.165–167] and SWNTs [3.168] have highlighted the porous nature of these two materials. The pores in MWNTs can be divided mainly into hollow inner cavities with small diameters (with narrow size distributions, mainly 3–10 nm) and aggregated pores (with wide size distributions, 20–40 nm), formed by interactions between isolated MWNTs. It is also worth noting that the ultrastrong nitrogen capillarity in the aggregated pores dominates the total adsorption, indicating that the aggregated pores are much more important than the inner cavities of the MWNTs during adsorption. The determination of the space available between a bunch of closed MWNTs has been performed by grand canonical Monte Carlo simulation of nitrogen adsorption, resulting in a satisfactory description of the experimental N_2 adsorption and showing that the distance between nanotubes is in the 4–14 nm range [3.169]. Adsorption of N_2 has been studied on as-prepared and acid-treated SWNTs, and the results obtained highlight the microporous nature of SWNT materials, as opposed to the mesoporous nature of MWNT materials. Also, as opposed to isolated SWNTs (see above), surface areas that are well above $400\,m^2\,g^{-1}$ have been measured for SWNT-bundle-containing materials, with internal surface areas of $300\,m^2\,g^{-1}$ or higher.

The theoretical surface area of a carbon nanotube has a broad range, from 50 to $1315\,m^2\,g^{-1}$ depending on the number of walls, the diameter, and the number of

nanotubes in a bundle of SWNTs [3.170]. Experimentally, the surface area of a SWNT is often larger than that of a MWNT. The total surface area of as-grown SWNTs is typically between 400 and 900 $m^2\,g^{-1}$ (micropore volume 0.15–0.3 $cm^3\,g^{-1}$), whereas values of 200 and 400 $m^2\,g^{-1}$ for as-produced MWNTs are often reported. In the case of SWNTs, the diameters of the tubes and the number of tubes in the bundle will have the most effect on the BET value. It is worth noting that opening or closing the central canal significantly influences the adsorption properties of nanotubes. In the case of MWNTs, chemical treatments such as KOH or NaOH activation are useful for promoting microporosity, and surface areas as high as 1050 $m^2\,g^{-1}$ have been reported [3.171, 172]. An efficient two-step treatment (acid $+CO_2$ activation) has been reported to open both ends of MWNTs [3.173]. Therefore, it appears that opening or cutting carbon nanotubes, as well as chemically treating them (using purification steps for example) can considerably affect their surface area and pore structure.

Adsorption Sites and Binding Energy of the Adsorbates

An important problem to solve when considering adsorption onto nanotubes is to identify the adsorption sites. The adsorption of gases into a SWNT bundle can occur inside the tubes (internal sites), in the interstitial triangular channels between the tubes, on the outer surface of the bundle (external sites), or in the grooves formed at the contacts between adjacent tubes on the outside of the bundle (Fig. 3.23). Experimental adsorption studies on SWNT have confirmed the adsorption on internal, external and groove sites [3.175]. Modeling studies have pointed out that the convex surface of the SWNT is more reactive than the concave one and that this difference in reactivity increases as the tube diameter decreases [3.176]. Compared to the highly bent region in fullerenes, SWNTs are only moderately curved and are expected to be much less reactive towards dissociative chemisorption. Models have also predicted enhanced reactivity at the kink sites of bent SWNTs [3.177]. Additionally, it is worth noting that unavoidable imperfections, such as vacancies, Stone–Wales defects, pentagons, heptagons and dopants, are believed to play a role in tailoring the adsorption properties [3.178].

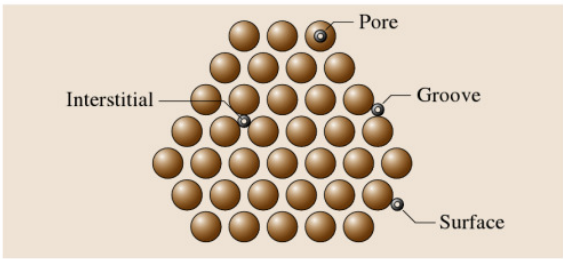

Fig. 3.23 Sketch of a SWNT bundle, illustrating the four different adsorption sites (adapted from [3.174])

Considering closed-end SWNTs first, simple molecules can be adsorbed onto the walls of the outer nanotubes of the bundle and preferably on the external grooves. In the first stages of adsorption (corresponding to the most attractive sites for adsorption), it seems that adsorption or condensation in the interstitial channels of the SWNT bundles depends on the size of the molecule (and/or on the SWNT diameters) and on their interaction energies [3.179–181]. Opening the tubes favors gas adsorption (including O_2, N_2 within the inner walls [3.182, 183]). It was found that the adsorption of nitrogen on open-ended SWNT bundles is three times larger than that on closed-ended SWNT bundles [3.184]. The significant influence that the external surface area of the nanotube bundle has on the character of the surface adsorption isotherm of nitrogen (type I, II or even IV of the IUPAC classification) has been demonstrated from theoretical calculations [3.185]. Additionally, it has been shown that the analysis of theoretical adsorption isotherms, determined from a simple model based on the formalism of *Langmuir* and *Fowler*, can help to experimentally determined the ratio of open to closed SWNTs in a sample [3.186]. For hydrogen and other small molecules like CO, computational methods have shown that, for open SWNTs, the pore, interstitial and groove sites are energetically more favorable than surface sites [3.187, 188]. In the case of carbon monoxide, aside from physisorbed CO, CO hydrogen bonds to hydroxyl functionalities created on the SWNTs by acid purification have been identified [3.188]. FTIR and temperature-programmed desorption (TPD) experiments have shown that NH_3 or NO_2 adsorb molecularly and that NO_2 is slightly more strongly bound than NH_3 [3.189]. For NO_2, the formation of nitrito (O-bonded) complexes is preferred to nitro (N-bonded) ones. For ozone, a strong oxidizing agent, theoretical calculations have shown that physisorption occurs on ideal, defect-free SWNT, whereas strong chemisorption occurs on Stone–Wales defects, highlighting the key role of defective sites in adsorption properties [3.190]. Finally, for acetone, TPD experiments have shown that this molecule chemisorbs on SWNT while physisorption occurs on graphite [3.191].

For MWNTs, adsorption can occur in the aggregated pores, inside the tube or on the external walls. In the latter case, the presence of defects, as incomplete graphene layers, must be taken into consideration. Although adsorption between the graphenes (intercalation) has been proposed in the case of hydrogen adsorption in h-MWNTs or platelet nanofibers [3.192], it is unlikely to occur for many molecules due to steric effects and should not prevail for small molecules due to the long diffusion paths involved. In the case of inorganic fluorides (BF_3, TiF_4, NbF_5 and WF_6), accommodation of the fluorinated species into the carbon lattice has been shown to result from intercalation and adsorption/condensation phenomena. In this case, doping-induced charge transfer has been demonstrated [3.193].

Only a few studies deal with adsorption sites in MWNTs, but it has been shown that butane adsorbs more onto MWNTs with smaller outside diameters, which is consistent with another statement that the strain on curved graphene surfaces affects sorption. Most of the butane adsorbs to the external surface of the MWNTs while only a small fraction of the gas condenses in the pores [3.194]. Comparative adsorption of krypton or of ethylene onto MWNTs or onto graphite has allowed scientists to determine the dependence of the adsorption and wetting properties of the nanotubes on their specific morphologies. Nanotubes were found to have higher condensation pressures and lower heats of adsorption than graphite [3.195]. These differences are mainly due to decreased lateral interactions between the adsorbed molecules, related to the curvature of the graphene sheets.

A limited number of theoretical as well as experimental studies on the binding energies of gases onto carbon nanotubes exist. While most of these studies report low binding energies on SWNTs, consistent with physisorption, some experimental results, in particular for hydrogen, are still controversial (Sect. 3.6.2). For platelet nanofibers, the initial dissociation of hydrogen on graphite edge sites, which constitute most of the nanofiber surface, has been proposed [3.196]. For carbon nanotubes, a mechanism that involves H_2 dissociation on the residual metal catalyst followed by H spillover and adsorption on the most reactive nanotube sites was envisaged [3.197]. Similarly, simply mixing carbon nanotubes with supported palladium catalysts increased the hydrogen uptake of the carbon by a factor of three, due to hydrogen spillover from the supported catalyst [3.198]. Doping nanotubes with alkali may enhance hydrogen adsorption, due to charge transfer from the alkali metal to the nanotube, which polarizes the H_2 molecule and induces dipole interactions [3.199].

Generally speaking, the adsorbates can be either charge donors or acceptors to the nanotubes. Trends in the binding energies of gases with different van der Waals radii suggest that the groove sites of SWNTs are the preferred low coverage adsorption sites due to their higher binding energies. Finally, several studies have shown that, at low coverage, the binding energy of the adsorbate on SWNT is between 25 and 75% higher than the binding energy on a single graphene. This discrepancy can be attributed to an increase of effective coordination at the binding sites, such as the groove sites, in SWNTs bundles [3.200, 201]. Representative results on the adsorption properties of SWNTs and MWNTs are summarized in Table 3.3.

3.4.4 Electronic and Optical Properties

The electronic states in SWNTs are strongly influenced by their one-dimensional cylindrical structures.

Table 3.3 Adsorption properties and sites of SWNTs and MWNTs. The letters in the *Absorption sites* column refer to Fig. 3.22. The data in the last two columns are from [3.174]

Type of nanotube	Porosity (cm^3g^{-1})	Surface area (m^2/g)	Binding energy of the adsorbate	Adsorption sites	Attractive potential per site (eV)	Surface area per site (m^2/g)
SWNT (bundle)	Microporous V_{micro}: 0.15–0.3	400–900	Low, mainly physisorption 25–75% > graphite	Surface (A) Groove (B) Pore (C) Interstitial (D)	0.049 0.089 0.062 0.119	483 22 783 45
MWNT	Mesoporous	200–400	Physisorption	Surface Pore Aggregated pores	–	–

One-dimensional subbands are formed that have strong singularities in the density of states (Van Hove singularities) [3.202]. By rolling the graphene sheet to form a tube, new periodic boundary conditions are imposed on the electronic wavefunctions, which give rise to one-dimensional subbands: $CnK = 2q$ where q is an integer. Cn is the roll-up vector $na1 + ma2$ which defines the helicity (chirality) and the diameter of the tube (Sect. 3.1). Much of the electronic band structure of CNTs can be derived from the electronic band structure of graphene by applying the periodic boundary conditions of the tube under consideration. The conduction and the valence bands of the graphene only touch at six corners (K points) of the Brillouin zone [3.203]. If one of these subbands passes through the K point, the nanotube is metallic; otherwise it is semiconducting. This is a unique property that is not found in any other one-dimensional system, which means that for certain orientations of the honeycomb lattice with respect to the tube axis (chirality), some nanotubes are semiconducting and others are metallic. The band gap for semiconducting tubes is found to be inversely proportional to the tube diameter. As pointed out in Sect. 3.1, knowing (n, m) allows us, in principle, to predict whether the tube is metallic or not. The energy gap decreases for larger tube diameters and MWNTs with larger diameter are found to have properties similar to other forms of regular, polyaromatic solids. It has been shown that electronic conduction mostly occurs through the external tube for MWNTs; even so, interactions with internal tubes often cannot be neglected and they depend upon the helicity of the neighboring tubes [3.204]. The electronic and optical properties of the tubes are considerably influenced by the environment [3.205]. Under externally applied pressure, the small interaction between the tube walls results in the internal tubes experiencing reduced pressure [3.206]. The electronic transition energies are in the infrared and visible spectral range. The one-dimensional Van Hove singularities have a large influence on the optical properties of CNTs. Visible light is selectively and strongly absorbed, which can lead to the spontaneous burning of agglomerated SWNTs in air at room temperature [3.207]. Strong Coulomb interaction in quasi-one dimension leads to the formation of excitons with very large binding energies in CNTs (200–400 meV), and degenerated states at the K, K' points lead to multiple exciton states with dipole allowed (bright) and dipole forbidden transitions (dark) [3.208,209]. Photoluminescence can be observed in individual SWNT aqueous suspensions stabilized by the addition of surfactants. Detailed photoexcitation maps provide information about the helicity (chirality)-dependent transition energies and the electronic band structures of CNTs [3.210]. Agglomeration of tubes into ropes or bundles influences the electronic states of CNTs. Photoluminescence signals are quenched for agglomerated tubes.

CNTs are model systems for the study of one-dimensional transport in materials. Apart from the singularities in the density of states, electron–electron interactions are expected to show drastic changes at the Fermi edge; the electrons in CNTs are not described by a Fermi liquid, but instead by a Luttinger liquid model [3.211] that describes electronic transport in one-dimensional systems. It is expected that the variation of electronic conductance vs. temperature follows a power law, with zero conductance at low temperatures. Depending on how L_ϕ (the coherence length) on the one hand and L_m (the electronic mean free path) on the other hand compare to L (the length of the nanotube), different conduction modes are observed: ballistic if $L \ll L_\phi$, $L \ll L_\mathrm{m}$, diffusive if $L_\phi \ll L_\mathrm{m} < L$ and localization if $L_\mathrm{m} \ll L_\phi \ll L$. Fluctuations in the conductance can be seen when $L \approx L_\phi$. For ballistic conduction (a small number of defects) [3.212–214], the predicted electronic conductance is independent of the tube length. The conductance value is twice the fundamental conductance unit $G_0 = 4\,\mathrm{e/h}$ due to the existence of two propagating modes. Due to the reduced electron scattering observed for metallic CNTs and their stability at high temperatures, CNTs can support high current densities (max. $10^9\,\mathrm{A/cm^2}$): about three orders of magnitude higher than Cu. Structural defects can, however, lead to quantum interference of the electronic wave function, which localizes the charge carriers in one-dimensional systems and increases resistivity [3.211, 215, 216]. Localization and quantum interference can be strongly influenced by applying a magnetic field [3.217]. At low temperatures, the discrete energy spectrum leads to a Coulomb blockade resulting in oscillations in the conductance as the gate voltage is increased [3.216]. In order to observe the different conductance regimes, it is important to consider the influence of the electrodes where Schottky barriers are formed. Palladium electrodes have been shown to form excellent junctions with nanotubes [3.218]. The influence of superconducting electrodes or ferromagnetic electrodes on electronic transport in CNTs due to spin polarization has also been explored [3.219, 220].

As a probable consequence of both the small number of defects (at least the kind of defects that oppose phonon transport) and the cylindrical topography,

SWNTs exhibit a large phonon mean free path, which results in a high thermal conductivity. The thermal conductivity of SWNTs is comparable to that of a single, isolated graphene layer or high purity diamond [3.221], or possibly higher ($\approx 6000\,\mathrm{W/(m\,K)}$).

3.4.5 Mechanical Properties

While tubular nanomorphology is also observed for many two-dimensional solids, carbon nanotubes are unique due to the particularly strong bonding between the carbons (sp^2 hybridization of the atomic orbitals) of the curved graphene sheet, which is stronger than in diamond (sp^3 hybridization), as revealed by the difference in C−C bond lengths (0.142 versus 0.154 nm for graphene and diamond respectively). This makes carbon nanotubes – SWNTs or c-MWNTs – particularly stable against deformations. The tensile strength of SWNTs can be 20 times that of steel [3.222] and has actually been measured as ≈ 45 GPa [3.223]. Very high tensile strength values are also expected for ideal (defect-free) c-MWNTs, since combining perfect tubes concentrically is not supposed to be detrimental to the overall tube strength, provided the tube ends are well capped (otherwise, concentric tubes could glide relative to each other, inducing high strain). Tensile strength values as high as ≈ 150 GPa have actually been measured for perfect MWNTs from an electric arc [3.224], although the reason for such a high value compared to that measured for SWNTs is not clear. It probably reveals the difficulties involved in carrying out such measurements in a reliable manner. The flexural modulus of perfect MWNTs should logically be higher than that for SWNTs [3.222], with a flexibility that decreases as the number of walls increases. On the other hand, measurements performed on defective MWNTs obtained from CCVD exhibit a range of 3–30 GPa [3.225]. Values of tensile modulus are also the highest values known, 1 TPa for MWNTs [3.226], and possibly even higher for SWNTs, up to 1.3 TPa [3.227, 228]. Figure 3.24 illustrates how defect-free carbon nanotubes could spectacularly revolutionize the field of high performance fibrous materials.

3.4.6 Reactivity

The chemical reactivities of graphite, fullerenes, and carbon nanotubes are similar in many ways. Like any small object, carbon nanotubes have a large surface to interact with their environment (Sect. 3.4.1). It is worth noting, however, that nanotube chemistry differs from

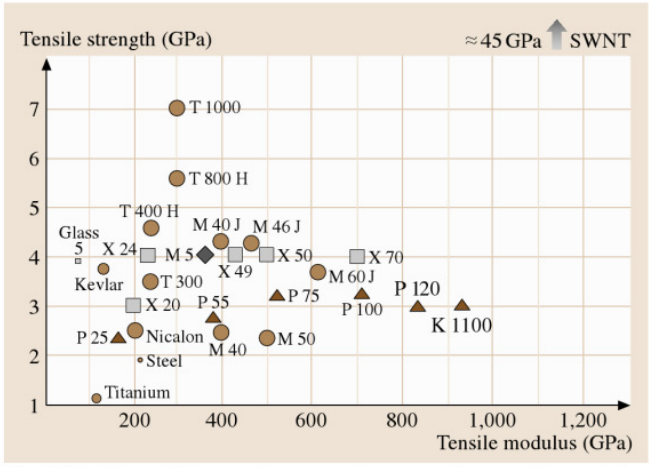

Fig. 3.24 Plot of the tensile strength versus the tensile modulus for various fibrous materials and SWNTs. *Large circles* are PAN-based carbon fibers, which include the fiber with the highest tensile strength available on the market (T1000 from Torayca); *Triangles* are pitch-based carbon fibers, which include the fiber with the highest tensile modulus on the market (K1100 from Amoco)

that observed for regular polyaromatic carbon materials due the unique shape of the nanotube, its small diameter, and its structural properties. Unlike graphite, perfect SWNTs have no (chemically active) dangling bonds (the reactions of polyaromatic solids is known to occur mainly at graphene edges). Unlike fullerenes, the ratio of *weak* sites (C−C bonds involved in heterocycles) to strong sites (C−C bonds between regular hexagons) is only deviates slightly from 0 for ideal tubes. For C_{60} fullerenes this ratio is 1 – C_{60} molecules have 12 pentagons (therefore accounting for $5\times12=30$ C−C bonds) and 20 hexagons, each of them with three C−C bonds not involved in an adjacent pentagon but shared with a neighboring hexagon (so $20\times3\times1/2=30$ C−C bonds are involved in hexagons only). Although graphene faces are chemically relatively inert, the radius of curvature imposed on the graphene in nanotubes causes the three normally planar C−C bonds caused by sp^2 hybridization to undergo distortions, resulting in bond angles that are closer to three of the four C−C bonds in diamond (characteristic of genuine sp^3 hybridization), as the radius of curvature decreases. Even though it is not enough to make the carbon atoms chemically reactive, one consequence of this is that either nesting sites are created at the concave surface, or strong physisorption sites are created above each carbon atom of the convex surface, both with a bonding efficiency that increases as the nanotube diameter decreases.

As already pointed out in Sect. 3.1, the chemical reactivities of SWNTs (and c-MNWTs) are believed to derive mainly from the caps, since they contain six pentagons each, as opposed to the tube body, which supposedly only contains hexagons. Indeed, applying oxidizing treatments to carbon nanotubes (air oxidation, wet-chemistry oxidation) selectively opens the nanotube tips [3.229]. However, that SWNTs can be opened by oxidation methods and then filled with foreign molecules such as fullerenes (Sect. 3.5) suggests the occurrence of side defects [3.15], whose identity and occurrence were discussed and then proposed to be an average of one Stone–Wales defect every 5 nm along the tube length, involving about 2% of the carbon atoms in a regular (10,10) SWNT [3.230]. A Stone–Wales defect is formed from four adjacent heterocycles, two pentagons and two heptagons, arranged in pairs opposite each other. Such a defect allows localized double bonds to form between the carbon atoms involved in the defect (instead of these electrons participating in the delocalized electron cloud above the graphene as usual, enhancing the chemical reactivity, for example toward chlorocarbenes [3.230]). This means that the overall chemical reactivity of carbon nanotubesshould depend strongly on how they are synthesized. For example, SWNTs prepared by the arc-discharge method are believed to contain fewer structural defects than CCVD-synthesized SWNTs, which are more chemically reactive. Of course, the reactivity of h-MWNT-type nanotubes is intrinsically higher, due to the occurrence of accessible graphene edges at the nanotube surface.

3.5 Carbon Nanotube-Based Nano-Objects

3.5.1 Heteronanotubes

It is possible to replace some or all of the carbon atoms in a nanotube with atoms of other elements without damaging the overall honeycomb lattice-based graphene structure. Nanotubes modified in this way are termed here *heteronanotubes*.

The elements used to replace carbon in this case are boron and/or nitrogen. Replacing carbon atoms in this way can result in new behavior (for example, BN nanotubes are electrical insulators), improved properties (resistance to oxidation for instance), or better control over such properties. For instance, one current challenge in carbon SWNT synthesis is to control the processing so that the desired SWNT structure (metallic or semiconductor) is formed selectively. In this regard, it was demonstrated that replacing some C atoms with N or B atoms leads to SWNTs with systematically metallic electrical behavior [3.231,232].

Some examples of heteronanotubes – mainly MWNTs – can be found in the literature. The heteroatom usually involved is nitrogen, due to the ease with which gaseous or solid nitrogen- and/or boron-containing species (such as N_2, NH_3, BN, HfB_2) can be passed into existing equipment for synthesizing MWNTs [3.231,233] until complete substitution of carbon occurs [3.234, 235]. An amazing result of such attempts to synthesize hetero-MWNTs is the subsequent formation of *multilayered* c-MWNTs: MWNTs made up of coaxial alternate carbon graphene tubes and boron nitride graphene tubes [3.236]. On the other hand, there are only a few examples of hetero-SWNTs. Syntheses of B- or N-containing SWNTs have recently been reported [3.232, 237], while just one successful synthesis of genuine BN-SWNTs has been reported so far [3.238].

3.5.2 Hybrid Carbon Nanotubes

Hybrid carbon nanotubes are defined here as carbon nanotubes, SWNTs or MWNTs that have inner cavities filled (partially or entirely) with foreign atoms, molecules, compounds or crystals. The terminology X@SWNT (or X@MWNT, if appropriate, where X is the atom, molecule and so on involved) is used for such structures [3.239].

Motivation

But why should we want to fill the cavities of carbon nanotubes [3.230]? The very small inner cavity of nanotubes is an amazing tool for preparing and studying the properties of confined nanostructures of any type, such as salts, metals, oxides, gases, or even discrete molecules like C_{60}, for example. Due to the almost one-dimensional structure of carbon nanotubes (particularly for SWNTs), we might expect that encapsulated material might have different physical and/or chemical properties to the unencapsulated material, and that the hybrid nanotube itself may behave differently to a *pure* nanotube. Indeed, if the volume available inside a carbon nanotube is small enough, the foreign material is largely *surface atoms* of reduced coordination. The

original motivation to create such hybrids was to obtain metal nanowires that are likely to of interest in electronics (as quantum wires). In this case, the nanotubes were considered to be nanomolds for the metal filler, and it was probably intended that the nanomold was to be removed afterwards. However, it is likely that this removal of the SWNT *container* to liberate the one-dimensional structure inside it may destroy or at least transform this structure due to the stabilizing effect of interactions with the nanotube wall.

Filling nanotubes while they grow (in situ filling) was one of the pioneering methods of nanotechnology. In most cases, however, the filling step is separate from nanotube synthesis. Three filling methods can then be distinguished: (a) wet chemistry procedures; capillarity-based physical procedures involving (b) a molten material or (c) a sublimated material.

Generally speaking, it is difficult to estimate the filling rate, and this is usually achieved through TEM observation, without obtaining any statistics on the number of tubes observed. Moreover, as far as SWNTs are concerned, the fact that the nanotubes are gathered into bundles makes it difficult to observe the exact number of filled tubes, as well as to estimate the filled length for each tube. It however seems that estimation of filling rates can now be reliably obtained from x-ray studies and Raman spectroscopy.

It is also possible to fill carbon nanotubes with materials that could not have been introduced directly. This is done by first filling the nanotubes with an appropriate precursor (one that is able to sublime, or melt or solubilize) that will later be transformed into the required material by chemical reaction or by a physical interaction, such as electron beam irradiation for example [3.240]. For secondary chemical transformation, reduction by H_2 is often used to obtain nanotubes filled with metals [3.241]. Sulfides can also be obtained if H_2S is used as a reducing agent [3.241].

Because the inner diameters of SWNTs are generally smaller than those of MWNTs, it is more difficult to fill them, and the driving forces involved in this phenomenon are not yet totally understood (see the review paper by *Monthioux* [3.230]). This field is therefore growing fairly rapidly, and so we have chosen to cite the pioneering works and then to focus on more recent works dealing with the more challenging topic of filling SWNTs.

In Situ Filling Method

Initially, most hybrid carbon nanotubes synthesized were based on MWNTs prepared using the electric arc method, and were obtained directly during processing. The filling materials were easily introduced in the system by drilling a central hole in the anode and filling it with the heteroelement. The first hybrid products obtained using this approach were all reported the same year [3.242–246] for heteroelements such as Pb, Bi, YC_2 and TiC. Later on, *Loiseau* and *Pascard* [3.247] showed that MWNTs could also be filled to several μm in length by elements such as Se, Sb, S, and Ge, but only with nanoparticles of elements such as Bi, B, Al and Te. Sulfur was suggested to play an important role during the in situ formation of filled MWNTs using arc discharge [3.248]. This technique is no longer the preferred one because it is difficult to control the filling ratio and yield and to achieve mass production.

Wet Chemistry Filling Method

The wet chemistry method requires that the nanotube tips are opened by chemical oxidation prior to the filling step. This is generally achieved by refluxing the nanotubes in dilute nitric acid [3.249–251], although other oxidizing liquid media may work as well, such as $[HCl + CrO_3]$ [3.252] or chlorocarbenes formed from the photolytic dissociation of $CHCl_3$ [3.230], a rare example of a nonacidic liquid route to opening SWNT tips. If a dissolved form (such as a salt or oxide) of the desired metal is introduced during the opening step, some of it will get inside the nanotubes. An annealing treatment (after washing and drying the treated nanotubes) may then lead to the oxide or to the metal, depending on the annealing atmosphere [3.229]. Although the wet chemistry method initially looked promising because a wide variety of materials can be introduced into nanotubes in this way and it operates at temperatures that are not much different from room temperature; however, close attention must be paid to the oxidation method that is used. The damage caused to nanotubes by severe treatments (such by using nitric acid) make them unsuitable for use with SWNTs. Moreover, the filling yield is not very good, probably due to the solvent molecules that also enter the tube cavity: the filled lengths rarely exceed 100 nm. *Mittal* et al. [3.252] have recently filled SWNTs with CrO_3 using wet chemistry with an average yield of $\approx 20\%$.

Molten State Filling Method

The physical filling method involving a liquid (molten) phase is more restrictive, firstly because some materials can decompose when they melt, and secondly because the melting point must be compatible with the nanotubes, so the thermal treatment temperature should

remain below the temperature of transformation or the nanotubes will be damaged. Because the filling occurs due to capillarity, the surface tension threshold of the molten material is 100–200 N/cm^2 [3.253], although this threshold was proposed for MWNTs, whose inner diameters (5–10 nm) are generally larger than those of SWNTs (1–2 nm). In a typical filling experiment, the MWNTs are closely mixed with the desired amount of filler by gentle grinding, and the mixture is then vacuum-sealed in a silica ampoule. The ampoule is then slowly heated to a temperature above the melting point of the filler and slowly cooled. This method does not require that the nanotubes are opened prior to the heat treatment. The mechanism of nanotube opening is yet to be clearly established, but it is certainly related to the chemical reactivities of the molten materials toward carbon, and more precisely toward defects in the tube structure (Sect. 3.4.4).

Most of the works involving the application of this method to SWNTs come from Oxford University [3.254–258], although other groups have followed the same procedure [3.249, 251, 259]. The precursors used to fill the nanotubes were mainly metal halides. Although little is known about the physical properties of halides crystallized within carbon nanotubes, the crystallization of molten salts within small-diameter SWNTs has been studied in detail, and the one-dimensional crystals have been shown to interact strongly with the surrounding graphene wall. For example, *Sloan* et al. [3.256] described two-layer 4 : 4 coordinated KI crystals that formed within SWNTs that were ≈ 1.4 nm in diameter. These two-layer crystals were *all surface* and had no *internal* atoms. Significant lattice distortions occurred compared to the bulk structure of KI, where the normal coordination is 6 : 6 (meaning that each ion is surrounded by six identical close neighbors). Indeed, the distance between two ions across the SWNT capillary is 1.4 times as much as the same distance along the tube axis. This suggests an accommodation of the KI crystal into the confined space provided by the inner nanotube cavity in the constrained crystal direction (across the tube axis). This implies that the interactions between the ions and the surrounding carbon atoms are strong. The volume available within the nanotubes thus somehow controls the crystal structures of inserted materials. For instance, the structures and orientations of encapsulated PbI_2 crystals inside their capillaries were found to differ for SWNTs and DWNTs, depending on the diameter of the confining nanotubes [3.254]. For SWNTs, most of the encapsulated one-dimensional PbI_2 crystals obtained exhibited a strong preferred orientation, with their (110) planes aligning at an angle of around 60° to the SWNT axes, as shown in Fig. 3.25a,b. Due to the extremely small diameters of the nanotube capillaries, individual crystallites are often only a few polyhedral layers thick, as outlined in Fig. 3.25d–h. Due to lattice terminations enforced by capillary confinement, the edging polyhedra must be of reduced coordination, as indicated in Fig. 3.25g,h. Similar crystal growth behavior was generally observed to occur for PbI_2 formed inside DWNTs in narrow nanotubes with diameters comparable to those of SWNTs. As the diameter of the encapsulating capillary increases, however, different preferred orientations are frequently observed (Fig. 3.26). In this example, the PbI_2 crystal is oriented with the [121] direction parallel to the direction of the electron beam (Fig. 3.26a–d). If the PbI_2@DWNT hybrid is viewed *side-on* (as indicated by the arrow in Fig. 3.26e), polyhedral slabs are seen to arrange along the capillary, oriented at an angle of around 45° with respect to the tubule axis. High-yield filling of CNTs by the capillary method is generally difficult but fillings of more than 60% have been reported for different halides, with filling lengths of up to a couple of hundreds of nm [3.260]. Results from the imaging

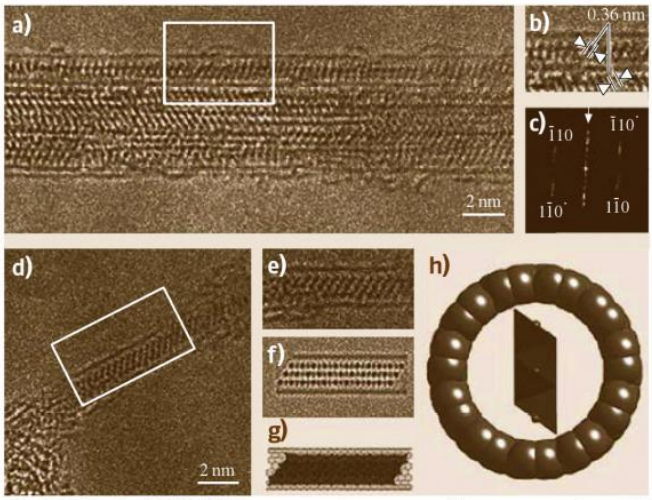

Fig. 3.25a–h HRTEM images and corresponding structural model for PbI_2 filled SWNTs. **(a)** Image of a bundle of SWNTs, all of them being filled with PbI_2. **(b)** Enlargement of the portion framed in **(a)**. **(c)** Fourier transform obtained from **(b)** showing the 110 distances at 0.36 nm of a single PbI_2 crystal. **(d)** Image of a single PbI_2-filled SWNT. **(e)** Enlargement of the portion framed in **(b)**. **(f)** Simulated HRTEM image, corresponding to **(e)**. **(g)** Structural model corresponding to **(f)**. **(h)** Structural model of a SWNT filled with a PbI_2 crystal as seen in cross section (from [3.254])

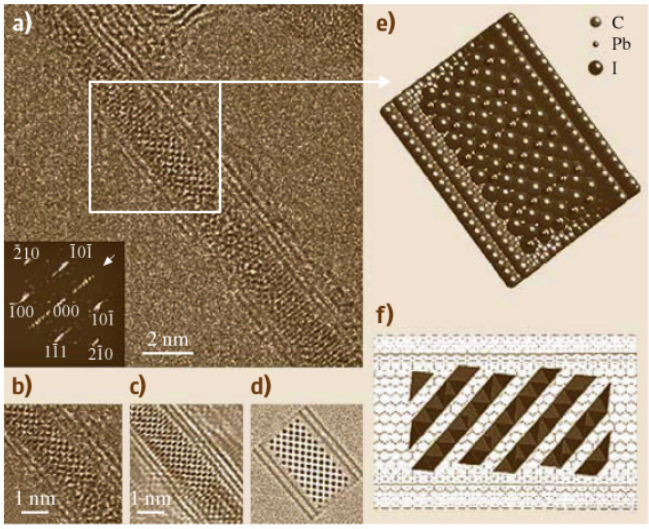

Fig. 3.26a–f HRTEM images (experimental and simulated) and corresponding structural model for a PbI_2-filled double-wall carbon nanotube. The larger inner cavity in DWNTs with respect to SWNTs (Fig. 3.25) makes the encapsulated PbI_2 crystal orientate differently. **(a)** Image of a single PbI_2-filled DWNT, with an insert showing the Fourier transform of the framed portion. **(b)** Enlargement of the portion framed in **(a)**. **(c)** Image reconstructed by a second Fourier transform of the inset in **(a)** (= filtered image). **(d)** Structural model corresponding to **(c)**. **(e)** and **(f)** Atom and structural models respectively, corresponding to **(d)** (from [3.254]) ▶

and characterization of individual molecules and atomically thin, effectively one-dimensional crystals of rock salt and other halides encapsulated within single-walled carbon nanotubes have recently been reviewed by *Sloan* et al. [3.261].

Sublimation Filling Method

This method is even more restrictive than the previous one, since it is only applicable to a very limited number of compounds due to the need for the filling material to sublimate within the temperature range of thermal stability of the nanotubes. Examples are therefore scarce. Actually, except for a few attempts to fill SWNTs with $ZrCl_4$ [3.257] or selenium [3.262], the first and most successful example published so far is the formation of C_{60}@SWNT (nicknamed *peapods*), reported for the first time in 1998 [3.263], where regular ≈ 1.4 nm-large SWNTs are filled with C_{60} fullerene molecule chains (Fig. 3.27a). Of course, the process requires that the SWNTs are opened by some method, as discussed previously; typically either acid attack [3.264] or heat treatment in air [3.265]. The opened SWNTs are then inserted into a glass tube together with fullerene powder, which is sealed and placed into a furnace heated above the sublimation temperature for fullerite ($\gtrsim 350\,^{\circ}C$). Since there are no filling limitations related to Laplace's law or the presence of solvent (only gaseous molecules are involved), filling efficiencies may actually reach $\approx 100\%$ for this technique [3.265].

C_{60}@SWNT has since been shown to possess remarkable behavior traits, such as the ability of the C_{60} molecules to move freely within the SWNT cavity (Fig. 3.27b,c) upon random ionization effects from electron irradiation [3.266], to coalesce into 0.7 nm-wide elongated capsules upon electron irradiation [3.267], or into a 0.7 nm-wide nanotube upon subsequent thermal treatment above $1200\,^{\circ}C$ under vacuum [3.266, 268]. Annealing C_{60}@SWNT material could therefore be

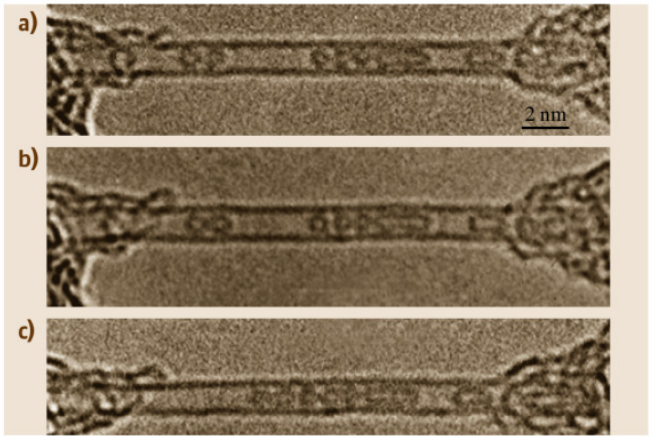

Fig. 3.27a–c HRTEM images of **(a)** an example of five regular C_{60} molecules encapsulated together with two higher fullerenes (C_{120} and C_{180}) as distorted capsules (*on the right*) within a regular 1.4 nm-diameter SWNT. **(a–c)** Example of the diffusion of the C_{60}-molecules along the SWNT cavity. The time between each image in the sequence is about 10 s. The fact that nothing occurs between **(a)** and **(b)** illustrates the randomness of the ionization events generated by the electron beam that are assumed to be responsible for the molecular displacement

an efficient way to produce DWNTs with constant inner (≈ 0.7 nm) and outer (≈ 1.4 nm) diameters. Using the coalescence of encapsulated fullerenes through both electron irradiation and thermal treatment, it appears to possible to control subsequent DWNT features (inner tube diameter, intertube distance) by varying the electron energy, flow and dose conditions, the temper-

ature, and the outer tube diameter [3.269]. The smallest MWNTs have been obtained in this way.

By synthesizing *endofullerenes* [3.13], it has been possible to use this process to synthesize more complex nanotube-based hybrid materials such as $La_2@C_{80}@SWNTs$ [3.270], $Gd@C_{82}@SWNTs$ [3.271], and $Er_xSc_{3-x}N@C_{80}@SWNT$ [3.272], among other examples. This suggests even more potential applications for peapods, although they are still speculative since the related properties are still being investigated [3.273–275].

The last example discussed here is the successful attempt to produce peapods by a related method, using accelerated fullerene ions (instead of neutral gaseous molecules) to force the fullerenes to enter the SWNT structure [3.276].

3.5.3 Functionalized Nanotubes

Noting the reactivity of carbon nanotubes (Sect. 3.4.6), nanotube functionalization reactions can be divided into two main groups. One is based on the chemical oxidation of the nanotubes (tips, structural defects) leading to carboxylic, carbonyl and/or hydroxyl functions. These functions are then used for additional reactions, to attach oligomeric or polymeric functional entities. The second group is based on direct addition to the graphiticlike surface of the nanotubes (without any intermediate step). Examples of the latter reactions include oxidation or fluorination (an important first step for further functionalization with other organic groups). The properties and applications of functionalized nanotubes have been reviewed in [3.277].

Oxidation of Carbon Nanotubes

Carbon nanotubes are often oxidized and therefore opened before chemical functionalization in order to increase their chemical reactivity (to create dangling bonds). The chemical oxidation of nanotubes is mainly performed using either wet chemistry or gaseous oxidants such as oxygen (typically air) or CO_2. Depending on the synthesis used, the oxidation resistance of nanotubes can vary. When oxidation is achieved using a gas phase, thermogravimetric analysis (TGA) is of great use for determining at which temperature the treatment should be applied. It is important to note that TGA accuracy increases as the heating rate diminishes, while the literature often provides TGA analyses obtained in unoptimized conditions, leading to overestimated oxidation temperatures. Differences in the presence of catalyst remnants (metals or, more rarely, oxides), the type of nanotubes used (SWNTs, c-MWNTs, h-MWNTs), the oxidizing agent used (air, O_2 is an inert gas, CO_2, and so on), as well as the flow rate used make it difficult to compare published results. It is generally agreed, however, that amorphous carbon burns first, followed by SWNTs and then multiwall materials (shells, MWNTs), even if TGA is often unable to separate the different oxidation steps clearly. Air oxidation (static or dynamic conditions) can however be used to prepare samples of very high purity – although the yield is generally low – as monitored by in situ Raman spectroscopy [3.278]. Aqueous solutions of oxidizing reagents are often used for nanotube oxidation. The main reagent is nitric acid, either concentrated or diluted (around 3 mol/l in most cases), but oxidants such as potassium dichromate ($K_2Cr_2O_7$), hydrogen peroxide (H_2O_2) or potassium permanganate ($KMnO_4$) are often used as well. HCl, like HF, does not damage nanotubes because it is not oxidizing.

Functionalization of Oxidized Carbon Nanotubes

The carboxylic groups located at the nanotube tips can be coupled to different chemical groups. Oxidized nanotubes are usually reacted with thionyl chloride ($SOCl_2$) to generate the acyl chloride, even if a direct reaction is theoretically possible with alcohols or amines, for example. The reaction of SWNTs with octadecylamine (ODA) was reported by *Chen* et al. [3.279] after reacting oxidized SWNTs with $SOCl_2$. The functionalized SWNTs are soluble in chloroform ($CHCl_3$), dichloromethane (CH_2Cl_2), aromatic solvents, and carbon bisulfide (CS_2). Many other reactions between functionalized nanotubes (after reaction with $SOCl_2$) and amines have been reported in the literature and will not be reviewed here. Noncovalent reactions between the carboxylic groups of oxidized nanotubes and octadecylammonium ions are possible [3.280], providing solubility in tetrahydrofuran (THF) and CH_2Cl_2. Functionalization by glucosamine using similar procedures [3.281] produced water soluble SWNTs, which is of special interest when considering biological applications of functionalized nanotubes. Functionalization with lipophilic and hydrophilic dendra (with long alkyl chains and oligomeric poly(ethyleneglycol) groups) has been achieved via amination and esterification reactions [3.282], leading to solubility of the functionalized nanotubes in hexane, chloroform, and water. It is interesting to note that, in the latter case, the functional groups could be removed simply by modifying the pH of the solution (base- and acid-catalyzed

hydrolysis reaction conditions, [3.283]). One last example is the possible interconnection of nanotubes via chemical functionalization. This has been recently achieved by *Chiu* et al. [3.284] using the acyl chloride method and a bifunctionalized amine to link the nanotubes through the formation of amide bonds. Finally, it has been discovered that imidazolium-ion-functionalized carbon nanotubes are highly dispersible in ionic liquids of analogous chemical structure and that mixtures of functionalized CNT and ionic liquids can form gels upon sonication [3.285] or waxes [3.286] that could find applications as soft composite materials for electrochemistry (sensors, capacitors, or actuators).

Sidewall Functionalization of Carbon Nanotubes

Covalent functionalization of nanotube walls is possible through fluorination reactions. It was first reported by *Mickelson* et al. [3.287], based on F_2 gas (the nanotubes can then be defluorinated, if required, with anhydrous hydrazine). As recently reviewed by *Khabashesku* et al. [3.288], it is then possible to use these fluorinated nanotubes to carry out subsequent derivatization reactions. Thus, sidewall-alkylated nanotubes can be prepared by nucleophilic substitution (Grignard synthesis or reaction with alkyllithium precursors [3.289]). These alkyl sidewall groups can be removed by air oxidation. Electrochemical addition of aryl radicals (from the reduction of aryl diazonium salts) to nanotubes has also been reported by *Bahr* et al. [3.290]. Functionalizations of the external wall of the nanotube by cycloaddition of nitrenes, addition of nuclephilic carbenes or addition of radicals have been described by *Holzinger* et al. [3.291]. Electrophilic addition of dichlorocarbene to SWNTs occurs via a reaction with the deactivated double bonds in the nanotube wall [3.292]. Silanization reactions are another way to functionalize nanotubes, although only tested with MWNTs. *Velasco-Santos* et al. [3.293] have reacted oxidized MWNTs with an organosilane ($RSiR_3$, where R is an organo functional group attached to silicon) and obtained nanotubes with organo functional groups attached via silanol groups.

The noncovalent sidewall functionalization of nanotubes is important because the covalent bonds are associated with changes from sp^2 hybridization to sp^3 carbon hybridization, which corresponds to loss of the graphitelike character. The physical properties of functionalized nanotubes, specifically SWNTs, can therefore be modified. One way to achieve the noncovalent functionalization of nanotubes is to wrap the nanotubes in a polymer [3.294], which permits solubilization (enhancing processing possibilities) while preserving the physical properties of the nanotubes. One reason to functionalize SWNTs is to make them soluble in regular solvents. A promising method to do this was found by *Pénicaud* et al., who made water-soluble by adding charges to SWNTs via the transient and reversible formation of a nanotube salt [3.295].

Finally, it is worth bearing in mind that none of these chemical reactions are specific to nanotubes and so they can affect most of the carbonaceous impurities present in the raw materials as well, making it difficult to characterize the functionalized samples. The experiments must therefore be performed with very pure carbon nanotube samples, which is unfortunately not always the case for the results reported in the literature. On the other hand, purifying the nanotubes to start with may also bias the functionalization experiments, since purification involves chemical treatment. However a demand for such products already exists, and purified then fluorinated SWNTs can be bought for 900 $/g (Carbon Nanotechnologies Inc., 2005).

3.6 Applications of Carbon Nanotubes

A carbon nanotube is inert, has a high aspect ratio and a high tensile strength, has low mass density, high heat conductivity, a large surface area, and a versatile electronic behavior, including high electron conductivity. However, while these are the main characteristics of individual nanotubes, many of them can form secondary structures such as ropes, fibers, papers and thin films with aligned tubes, all with their own specific properties. These properties make them ideal candidates for a large number of applications provided their cost is sufficiently low. The cost of carbon nanotubes depends strongly on both the quality and the production process. High-quality single-shell carbon nanotubes can cost 50–100 times more than gold. However, carbon nanotube synthesis is constantly improving, and sale prices are falling rapidly. The application of carbon nanotubes is therefore a very fast moving field, with new potential applications found every year, even several times per year. Therefore, creating an exhaustive list of these applications is not the aim of this section.

Instead, we will cover the most important applications, and divide them up according to whether they are *current* (Sect. 3.6.1) – they are already on the market, the application is possible in the near future, or because prototypes are currently being developed by profit-based companies – or *expected* applications (Sect. 3.6.2).

3.6.1 Current Applications

Near-Field Microscope Probes

The high mechanical strength of carbon nanotubes makes them almost ideal candidates for use as force sensors in scanning probe microscopy (SPM). They provide higher durability and the ability to image surfaces with a high lateral resolution, the latter being a typical limitation of conventional force sensors (based on ceramic tips). The idea was first proposed and tested by *Dai* et al. [3.92] using c-MWNTs. It was extended to SWNTs by *Hafner* et al. [3.297], since small-diameter SWNTs were believed to give higher resolution than MWNTs due to the extremely short radius of curvature of the tube end. However, commercial nanotube-based tips (such as those made by Piezomax, Middleton, WI, USA) use MWNTs for processing convenience. It is also likely that the flexural modulus of a SWNT is too low, resulting in artifacts that affect the lateral resolution when scanning a rough surface. On the other hand, the flexural modulus of a c-MWNT is believed to increase with the number of walls, although the radius of curvature of the tip increases at the same time. Whether based on SWNT or MWNT, such SPM tips also offer the potential to be functionalized, leading to the prospect of selective imaging based on chemical discrimination in *chemical force microscopy* (CFM). Chemical function imaging using functionalized nanotubes represents a huge step forward in CFM because the tip can be functionalized very specifically (ideally only at the very tip of the nanotube, where the reactivity is the highest), increasing the spatial resolution. The interaction between the chemical species present at the end of the nanotube tip and the surface containing chemical functions can be recorded with great sensitivity, allowing the chemical mapping of molecules [3.298, 299].

Current nanotube-based SPM tips are quite expensive; typically $\approx 450\,\$/\text{tip}$ (Nanoscience Co., 2005). This high cost is due to processing difficulties (it is necessary to grow or mount a single MWNT in the appropriate direction at the tip of a regular SPM probe; Fig. 3.28), and the need to individually control the tip quality. The market for nanotube SPM tips has been estimated at $\approx 20\,\text{M}\$/\text{year}$.

Field Emission-Based Devices

In a pioneering work by *de Heer* et al. [3.300], carbon nanotubes were shown to be efficient field emitters and this property is currently being used several applications, including flat panel displays for television sets and computers (the first prototype of such a display was exhibited by Samsung in 1999), and devices requiring an electron-producing cathode, such as x-ray sources. The principle of a field emission-based screen is demonstrated in Fig. 3.29a. Briefly, a potential difference is set up between the emitting tips and an extraction grid so that electrons are pulled from the tips onto an electron-sensitive screen layer. Replacing the glass support and protecting the screen using a polymer-based material should even permit the development of flexible screens. Unlike regular (metallic) electron-emitting tips, the structural perfection of carbon nanotubes allows higher electron emission stability, higher mechanical resistance, and longer lifetimes. Most importantly, using them saves energy since the tips operate at a lower heating temperature and require much lower threshold voltage than in other setups. For example, it is possible to produce a current density of $1\,\text{mA}/\text{cm}^2$ for a threshold voltage of $3\,\text{V}/\mu\text{m}$ with nanotubes, while it requires $20\,\text{V}/\mu\text{m}$ for graphite powder and $100\,\text{V}/\mu\text{m}$ for regular Mo or Si tips. The subsequent reductions in cost and energy consumption are estimated at 1/3 and 1/10 respectively. Generally speaking, the maximum current density that can be obtained ranges from 10^6 to $10^8\,\text{A}/\text{cm}^2$ depending on the nanotubes involved (SWNT or MWNT, opened or capped, aligned or not, and so on) [3.301–303]. Although the side walls of the nanotubes seem to emit as well as the tips, many

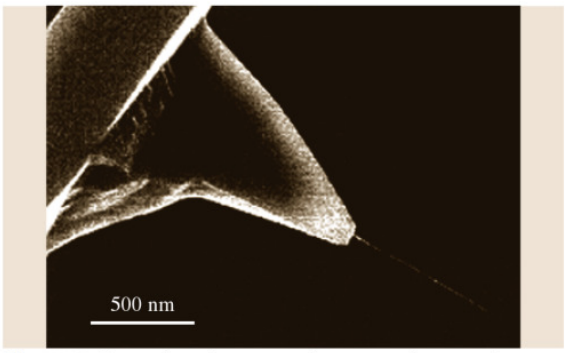

Fig. 3.28 Scanning electron microscopy image of a carbon nanotube (MWNT) mounted onto a regular ceramic tip as a probe for atomic force microscopy (modified from [3.296])

works have investigated the growth of nanotubes perpendicular to the substrate surface as regular arrays (Fig. 3.29b). Besides, it does not appear necessary to use SWNTs instead of MWNTs for many of these applications when they are used as bunches. On the other hand, when considering single, isolated nanotubes, SWNTs are generally less preferable since they permit much lower electron doses than MWNTs, although they often provide a more coherent source (an useful feature for devices such as electron microscopes or x-ray generators).

The market associated with this application is huge. With major companies involved, such as Motorola, NEC, NKK, Samsung, Thales and Toshiba, the first flat TV sets and computers using nanotube-based screens should enter the market in 2007 (Samsung data), once a problem with product lifetime (still only about half that required) is fixed. On the other hand, companies such as Oxford Instruments and Medirad are now commercializing miniature x-ray generators for medical applications that use nanotube-based cold cathodes developed by Applied Nanotech Inc.

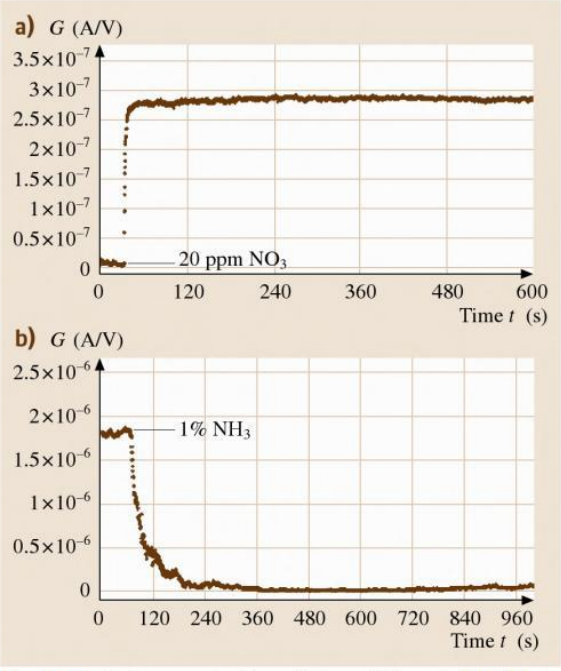

Fig. 3.30a,b Demonstration of the ability of SWNTs to detect trace molecules in inert gases. **(a)** Increase in the conductance of a single SWNT when 20 ppm of NO_2 are added to an argon gas flow. **(b)** Same, but with 1% NH_3 added to the argon gas flow (from [3.304])

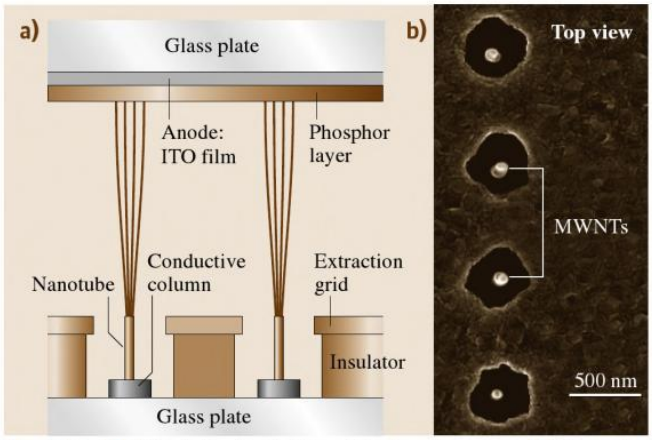

Fig. 3.29 **(a)** Principle of a field emitter-based screen. **(b)** Scanning electron microscope image of a nanotube-based emitter system (*top view*). *Round dots* are MWNT tips seen through the holes corresponding to the extraction grid. © *P. Legagneux* (Thales Research & Technology, Orsay, France)

Chemical Sensors

The electrical conductance of semiconductor SWNTs was recently demonstrated to be highly sensitive to changes in the chemical composition of the surrounding atmosphere at room temperature, due to charge transfer between the nanotubes and the molecules from the gases adsorbed onto SWNT surfaces. It has also been shown that there is a linear dependence between the concentration of the adsorbed gas and the change in electrical properties, and that the adsorption is reversible. First tries involved NO_2 or NH_3 [3.304] and O_2 [3.305]. SWNT-based chemical NO_2 and NH_3 sensors are characterized by extremely short response times (Fig. 3.30), unlike conventional sensors [3.304, 306]. The electrical response has been measured by exposing MWNT films to sub-ppm NO_2 concentrations (10–100 ppb in dry air) at different operating temperatures ranging between 25 and 215 °C [3.307]. For SWNTs, the sensor responses are linear for similar concentrations, with detection limits of 44 ppb for NO_2 and 262 ppb for nitrotoluene [3.308]. High sensitivity to water or ammonia vapor has been demonstrated on a SWNT-SiO_2 composite [3.309]. This study indicated the presence of p-type SWNTs dispersed among the predominantly metallic SWNTs, and that the chemisorption of gases on the surface of the semiconductor SWNTs is responsible for the sensing action. Determinations of CO_2 and O_2 concentrations on a SWNT-SiO_2 composite have also been reported [3.310]. By doping nanotubes with palladium

nanoparticles, *Kong* et al. [3.311] have also shown that the modified material can reveal the presence of hydrogen at levels of up to 400 ppm, whereas the as-grown material was totally ineffective. Miniaturized gas ionization sensors, which work by fingerprinting the ionization characteristics of distinct gases, have also been reported, with detection limits of 25 ppm for NH_3 [3.312].

Generally speaking, the sensitivities of these new nanotube-based sensors are three orders of magnitude higher than those of standard solid state devices. Another reason for using nanotubes instead of current sensors is their simplicity, the facts that they can be placed in very small systems and that they can operate at room temperature, as well as their selectivity. These advantages allow a limited number of sensor device architectures to be built for a variety of industrial purposes, while the current technology requires a large variety of devices based on mixed metal oxides, optomechanics, catalytic beads, electrochemistry, and so on. The market for such devices is expected to be $ 1.6 billion by 2006, including sensing applications in biological fields and the chemical industry. Nanotube-based sensors are currently being developed by large and small companies, such as Nanomix (Emeryville, USA), for example.

Catalyst Support

Carbon-based materials make good supports in heterogeneous catalytic processes due to their ability to be tailored to a specific need: indeed, activated carbons are already currently employed as catalyst supports due to their high surface areas, their stability at high temperatures (under nonoxidizing atmospheres), and the possibility of controlling both their porous structure and the chemical nature of their surfaces [3.313, 314]. Attention has focused on nanosized fibrous morphologies of carbon have appeared over the last decade, that show great potential for use as supports [3.315]. Carbon nanofibers (also incorrectly called graphite nanofibers) and carbon nanotubes have been successfully used in this area, and have been shown to provide, as catalyst-supporting materials, properties superior to those of such other regular catalyst-supports, such as activated carbon, soot or graphite [3.316–318]. The possibility to use MWNTs as nanoreactors, that means to deposit the active catalytic phase in the inner cavity of the nanotubes and to take advantage of the confinement effect to perform the catalytic reaction, also offers very exciting perspectives [3.319]. Various reactions have been studied [3.316–318]; hydrogenation reactions, Fischer–Tropsch, polymerization and even oxidation reactions, hydrocarbon decomposition and use as fuel cell electrocatalysts are among the most popular domains. The application of graphite nanofibers as direct catalysts for oxidative dehydrogenation [3.320, 321] or methane decomposition [3.322] has also been reported.

The morphology and size of the carbon nanotubes (particularly their aspect ratios), can play a significant role in catalytic applications due to their ability to disperse catalytically active metal particles. Their electronic properties are also of primary importance [3.323], since the conductive support may cause electronic perturbations as well as constraining the geometriies of the dispersed metal particles. A recent comparison between the interactions of transition metal atoms with carbon nanotube walls and their interactions with graphite has shown major differences in bonding sites, magnetic moments, and charge transfer direction [3.324]. Thus the possibility of a strong metal–support interaction must be taken into account. Their mechanical strength is also important, and this makes them resistant to attrition when recycled. Their external and internal surfaces are strongly hydrophobic and adsorb organic molecules strongly. For MWNT-based catalyst-supports, the relatively high surface area and the absence of microporosity (pores < 2 nm), associated with a high meso- and macropore volume (Sect. 3.4.3), result in significant improvements in catalytic activity for liquid phase reactions when compared to catalysts supported on activated carbon. With nanotube supports, the mass transfer of the reactants to the active sites is unlimited, due to the absence of microporosity, and the apparent contact time of the products with the catalyst is diminished, leading to more active and more selective catalytic effects. Finally, as for activated carbon, catalyst-forming is possible and porous granules of carbon nanotubes or electrodes based on carbon nanotubes can be obtained for catalysis or electrocatalysis respectively. Of course, the possibility of shaping these nanomaterials offers interesting perspectives, including for designing structured microreactors [3.325].

The technique usually used to prepare carbon nanotube-supported catalysts is incipient wetness impregnation, in which the purified support is impregnated with a solution of the metal precursor and then dried, calcinated and/or reduced in order to obtain metal particles dispersed on the support. Other techniques such as electrochemical deposition and the use of colloidal chemistry have also been investigated [3.326]. Chemical treatment and/or modification of the carbon nanotube surface were found to be useful ways

Table 3.4 Preparation and catalytic performances of some nanotube-supported catalysts

Catalyst	Preparation route	Catalytic reaction	Comments
Ru/MWNT + SWNT [3.315]	Liquid phase impregnation, no pretreatment of the tubes	Liquid phase cinnamaldehyde hydrogenation	A different kind of metal support interaction compared to activated carbon
Pt/MWNT electrodes [3.331]	Electrodeless plating with prefunctionalization of MWNT	Oxygen reduction for fuel cell applications	High electrocatalytic activity
Rh/MWNT [3.329]	Surface-mediated organometallic synthesis, prefunctionalization of MWNT	Liquid phase hydroformylation and hydrogenation	Higher activity of Rh/MWNT compared to Rh/activated carbon
Ru-alkali/MWNT [3.332]	Liquid phase impregnation, no pretreatment of the tubes	Ammonia synthesis, gas phase reaction	Higher activity with MWNT than with graphite
Rh-phosphine/MWNT [3.333]	Liquid phase grafting from $[RhH(CO)(PPh_3)_3]$	Liquid phase hydroformylation	Highly active and regioselective catalyst
Rh/MWNT (confined nanoparticles) [3.319]	Liquid phase impregnation of oxidized MWNTs	Conversion of CO and H_2 into ethanol	The overall formation rate of ethanol inside the nanotubes exceeds that on the outside of the nanotubes by more than one order of magnitude

of controlling its hydrophobic or hydrophilic character [3.327]. A strong metal/support interaction can thus be expected from the occurrence of functionalized groups created by the oxidation of the support surface, resulting in smaller particle sizes [3.328]. A more sophisticated technique for achieving the grafting of metal particles onto carbon nanotubes consists of functionalizing the outer surface of the tubes and then performing a chemical reaction with a metal complex, resulting in a good dispersion of the metallic particles (Fig. 3.31) [3.329]. The functionalization of noncovalent carbon nanotubes with polymer multilayers followed by the attachment of gold nanoparticles has also been reported [3.330].

Selected examples of some carbon nanotube-based catalysts together with related preparation routes and catalytic activities are listed in Table 3.4.

The market is important for this application, since it often concerns the heavy chemical industry. It implies and requires mass production of low-cost

Fig. 3.31 Transmission electron microscopy image showing rhodium nanoparticles supported on the surface of an MWNT (from [3.329]) ▶

nanotubes, processed by methods other than those based on solid carbon as the source (Sect. 3.2.1). Such an application also requires some surface reactivity, making the h-MWNT-type nanotubes, with poor nanotextures (Sect. 3.1.2), interesting candidates as starting material for preparing such catalyst supports. Catalysis-enhanced thermal cracking of gaseous carbon precursors is therefore preferred, and pilot plants are already being built by major chemical industrial companies (such as Arkema in France).

3.6.2 Expected Applications Related to Adsorption

Adsorptions of various gases, liquids or metals onto carbon nanotubes, and interactions between them, have attracted much attention recently. The applications resulting from the adsorptive properties of carbon nanotubes can be arbitrarily divided into two groups. The first group is based on the consequences of molecular adsorption on the electronic properties of nanotubes; the main application of this is chemical sensing (Sect. 3.6.1). The second group includes gas storage, gas separation, the use of carbon nanotubes as adsorbants, and results from morphological investigations of carbon nanotubes (surface areas, aspect ratios, and so forth). Among these latter potential applications, the possibility of storing gases – particularly hydrogen – on carbon nanotubes has received most attention.

Gas Storage – Hydrogen

The development of a lightweight and safe system for hydrogen storage is necessary for the widespead use of highly efficient H_2-air fuel cells in transportation vehicles. The US Department of Energy Hydrogen Plan has provided a commercially significant benchmark for the amount of reversible hydrogen adsorption required. This benchmark requires a system weight efficiency (the ratio of H_2 weight to system weight) of 6.5 wt % hydrogen, and a volumetric density of 63 kg H_2/m^3.

The failure to produce a practical storage system for hydrogen has prevented hydrogen from becoming one of the most important transportation fuels. The ideal hydrogen storage system needs to be light, compact, relatively inexpensive, safe, easy to use, and reusable without the need for regeneration. While research and development are continuing into such technologies as liquid hydrogen systems, compressed hydrogen systems, metal hydride systems, and superactivated carbon systems, all have serious disadvantages.

Therefore, there is still a great need for a material that can store hydrogen but is also light, compact, relatively inexpensive, safe, easy to use, and reusable without regeneration. Some recent articles and patents on the very high, reversible adsorption of hydrogen in carbon nanotubes or platelet nanofibers have aroused tremendous interest in the research community, stimulating much experimental and theoretical work. Most of the early works done on hydrogen adsorption on carbon nanotubes have been reviewed in [3.334–340], from the first report about the supposedly highly successful storage of hydrogen in carbon layered nanostructures at room temperature made by a group of Northeastern University [3.192,341], to the multiple yet vain attempts to reproduce this result that followed. Actually, in spite of a worldwide research effort, any work published since then claiming for a hydrogen storage in some nanotextured carbon material with an efficiency better than 1–2% at room temperature or close (and pressure below $\approx$ 300–500 bar may be regarded as suspicious. Modelling did not help, since it appeared that the calculations are closely constrained by the starting hypotheses. Actually, While considering the same (10,10) SWNT, calculations based on DFT predicted between 14.3 and 1 wt % storage [3.342,343], calculations based on a geometrical model predicted 3.3% [3.334], and calculations based on a quantum mechanical molecular dynamics model predicted 0.47% [3.344]. Therefore, neither experimental results, obviously often biased by procedure problems, nor theoretical results are yet able to demonstrate that an efficient storage of H_2 is possible for carbon nanotubes, whatever the type. However, a definitive statement of failure cannot yet be claimed. Attempts might have failed so far because they were considering by far too simplistic materials, i. e., plain nanotubes. Further efforts have to be made to enhance the adequation of the materials to this specific purpose, in particular:

1. By adjusting the surface properties, which can be modified by mechanical or chemical treatments, e.g. KOH [3.345]
2. By adjusting the texture of the material, such as the pore size [3.346] and possibly the curvature [3.347–349]
3. By complexifying the materials, e.g., by considering nanocomposites combining some host carbon materials and catalyst nanoparticles so as to promote the dissociation of hydrogen molecules to hydrogen atoms that can form bonds with the host [3.340, 350].

In this regard, whether the best carbon material for H_2 adsorption will still be nanotube-based is not ascertained.

Gas Storage – Gases Other than Hydrogen

Encouraged by the potential applications related to hydrogen adsorption, several research groups have tried to use carbon nanotubes as a means of stocking and transporting other gases such as oxygen, nitrogen, noble gases (argon and xenon) and hydrocarbons (methane, ethane, and ethylene). These studies have shown that carbon nanotubes could become the world's smallest gas cylinders, combining low weight, easy transportability and safe use with acceptable adsorbed quantities. Nanotubes may also be used in medicine, where it would be extremely useful to physically confine special gases (^{133}Xe for instance) prior to injection.

Kusnetzova et al. [3.351] conducted experiments with xenon and found that the storage capacities of nanotubes can be enhanced by a tremendous amount (a factor of 280, up to a molar ratio of $N_{Xe}/N_C = 0.045$) by opening the SWNT bundles via thermal activation at 800 °C. The gas can be adsorbed inside the nanotubes and the rates of adsorption are also increased using this treatment.

The possibility of storing argon in carbon nanotubes has been studied, with encouraging results, by *Gadd* et al. [3.352]. Their experiments show that large amounts of argon can be trapped in catalytically grown MWNTs (20–150 nm) by hot isostatic pressing (HIP-ing) for 48 h at 650 °C under an argon pressure of 1700 bar. Energy-dispersive x-ray spectroscopy was used to determine that the gas was located inside the tubes and not on the tube walls. Further studies determined the argon pressure inside the tubes at room temperature. The authors estimated this to be around 600 bar, indicating that equilibrium pressure was attained in the tubes during the HIP-ing and that MWNTs would be a convenient material for storing the gas.

Gas Separation

As SWNTs or MWNTs have regular geometries that can, to some extent, be controlled, they could be used to develop precise separation tools. If the sorption mechanisms are known, it should be possible to control sorption of various gases through particular combinations of temperature, pressure and nanotube morphology. Since the large-scale production of nanotubes is gradually progressing, and this should ultimately result in low costs, accurate separation methods based on carbon nanotubes are now being investigated.

A theoretical study has aimed to determine the effects of different factors such as tube diameter, density and type of the gas used on the flow of molecules inside nanotubes. An atomistic simulation with methane, ethane and ethylene [3.353] has shown that the molecular mobility decreases with decreasing tube for each of the three gases. Ethane and ethylene have smaller mobilities due to the stronger interactions they seem to have with the nanotube walls. In another theoretical study into the possibility of hydrocarbon mixture separation on SWNT bundles, the authors conclude that carbon nanotubes can be used to separate methane/*n*-butane and methane/isobutene mixtures [3.354] with an efficiency that increases as the average tube diameter decreases. Experimental work was also performed by the same group on the sorption of butane on MWNTs [3.194]. It has been also reported that the Fickian diffusivities of CH_4/H_2 mixtures in SWNT, like their pure component counterparts, are extraordinarily large when compared with adsorbed gases in other nanoporous materials [3.355].

Grand canonical Monte Carlo simulations of the separation of hydrogen and carbon monoxide by adsorption on SWNTs have also been reported [3.356]. In most of the situations studied, SWNTs were found to adsorb more CO than H_2, and excellent separation could again probably be obtained by varying the SWNT average diameter.

Adsorbents

Carbon nanotubes were found to be able to adsorb some toxic gases such as dioxins [3.357], fluoride [3.358], lead [3.359] and alcohols [3.360] better than adsorbent materials in common use, such as activated carbon. These pioneering works opened a new field of applications as cleaning filters for many industrial processes with hazardous by-products. The adsorption of dioxins, which are very common and persistent carcinogenic by-products of many industrial processes, is a good example of the potential of nanotubes in this field. Growing ecological awareness has resulted in the imposition of emission limits on dioxin-generating sources in many countries, but it is difficult to find materials that can act as effective filters, even at extremely low concentrations. *Long* and *Yang* [3.357] found that nanotubes can attract and trap more dioxins than activated carbons or other polyaromatic materials that are currently used as filters. This improvement is probably due to the stronger interaction forces that exist between dioxin molecules and the curved surfaces of nanotubes compared to those for flat graphene sheets.

MWNTs have also been used with success for the adsorption of other pollutants such as volatile organic compounds [3.361], reactive dyes [3.362], or natural organic matter in aqueous solutions [3.363]. MWNTs show also better performances than granular activated carbons for the adsorption of low molecular weight toxins [3.364].

The capacity of Al_2O_3/MWNT to adsorb fluoride from water has been reported to be 13.5 times that of activated carbon and four times that of Al_2O_3 [3.358]. The same group has also reported a capacity of MWNTs to adsorb lead from water that is higher than that for activated carbon [3.359]. The possibility of using graphite nanofibers to purify water from alcohols has also been explored [3.360]. MWNTs were found to be good adsorbents for the removal of dichlorobenzene from wastewaters over a wide range of pH. Typically, the nanotubes adsorb 30 mg of the organic molecule per gram of MWNTs from a 20 mg/l solution [3.365]. It has also been shown that SWNTs act as molecular sponges for molecules such as CCl_4; the nanotubes were in contact with a support surface which also adsorbs molecules, although more weakly than the nanotubes [3.366]. Finally, oxidized carbon nanotubes have been successfully used for the adsorption of heavy metal ions such as Zn(II) [3.367], Cu(II) [3.368], Pb(II) [3.369] or Th(IV) [3.370] from aqueous solutions. While an apolar surface might be more adapted for the adsorption of aromatic organic species, an oxidation of the CNTs that provides a polar and hydrophilic surface is highly desirable for the adsorption of heavy metal ions. These experimental results suggest that carbon nanotubes may be promising adsorbents for removing polluting agents from water.

Biosensors

Attaching molecules of biological interest to carbon nanotubes is an excellent way to produce nanometer-sized biosensors. The electrical conductivities of these functionalized nanotubes would depend on the interaction of the probe with the medium being studied, which would be affected by chemical changes or interactions with the target species. The science of attaching biomolecules to nanotubes is rather recent and was inspired by similar research in the fullerene area. Some results have already been patented, and so such systems may become available in the near future. Using the internal cavities of nanotubes to deliver drugs would be another amazing application, but little work has been carried out so far to investigate the toxicity of nanotubes in the human body. Comparison between the effects of nanotubes and asbestos was investigated by *Huczko* et al. [3.371] and they concluded that the tested samples were innocuous. However, a more recent work has shown that contact with nanotubes may lead to dermal toxicity [3.372] or induce lung lesions characterized by the presence of granulomas [3.373]. *Pantarotto* et al. [3.374] reported the translocation of water-soluble SWNT derivatives across cell membranes and have shown that cell death can be induced by functionalised nanotubes (bioactive peptides), depending upon their concentration in the media. Recent results also indicate that nanotubes may lead to an inflammatory response of the immune system by activating the complement system [3.375].

MWNTs have been used by *Mattson* et al. [3.376] as a substrate for neuronal growth. They have compared the activity of untreated MWNTs with that of MWNTs coated with a bioactive molecule (4-hydroxynonenal) and observed that neurons elaborated multiple neurites on these latter functionalized nanotubes. This is an important result that illustrates the feasibility of using nanotubes as a substrate for nerve cell growth.

Davis et al. [3.377] immobilized different proteins (metallothionein, cytochrome c and c_3, β-lactamase I) in MWNTs and checked whether these molecules were still catalytically active compared to the free ones. They have shown that confining a protein within a nanotube provides some protection for the external environment. Protein immobilization via noncovalent sidewall functionalization was proposed by *Chen* et al. [3.378] using a bifunctional molecule (1-pyrenebutanoic acid, succinimidyl ester). This molecule is tied to the nanotube wall by the pyrenyl group, and amine groups or biological molecules can react with the ester function to form amide bonds. This method was also used to immobilize ferritin and streptavidin onto SWNTs. Its main advantages are that it does not modify the SWNT wall and that it does not perturb the sp^2 structure, so the physical properties of the nanotubes are maintained. *Shim* et al. [3.379] have functionalized SWNTs with biotin and observed specific binding with streptavidin, suggesting biomolecular recognition possibilities. *Dwyer* et al. [3.380] have functionalized SWNTs by covalently coupling DNA strands to them using EDC (1-ethyl-3-(3-dimethylaminopropyl) carbodiimide hydrochloride) but did not test biomolecular recognition; other proteins such as bovine serum albumin (BSA) [3.381] have been attached to nanotubes using the same process (diimide-activated amidation with EDC) and most of the attached proteins remained

bioactive. Instead of working with individual nanotubes (or more likely nanotube bundles in the case of SWNTs), *Nguyen* et al. [3.382] have functionalized nanotubes arrayed with a nucleic acid, still using EDC as the coupling agent, in order to realize biosensors based on protein-functionalized nanotubes. *Azamian* et al. [3.383] have immobilized a series of biomolecules (cytochrome c, ferritin, and glucose oxidase) on SWNTs, and they observed that the use of EDC was not always necessary, indicating that the binding was predominantly noncovalent. In the case of glucose oxidase, they tested the catalytic activity of functionalized nanotubes immobilized on a glassy carbon electrode and observed a tenfold greater catalytic response compared to that seen in the absence of modified SWNTs.

Functionalization of nanotubes with biomolecules is still in its infancy, and their use as biosensors may lead to practical applications earlier than expected. For example, functionalized nanotubes can be used as AFM tips (Sect. 3.6.1), allowing single-molecule measurements to be taken using *chemical force microscopy* (CFM). Important improvements in the characterization of biomolecules have even been achieved with unfunctionalized nanotube-based tips (see the review by [3.297]). Nanotube-based biosensors have now been developed. They are based on either field effect transistors [3.384] involving functionalized CNTs (biomolecules) or on electrochemical detection [3.385].

3.6.3 Expected Applications Related to Composite Systems

Because of their exceptional morphological, electrical, thermal, and mechanical characteristics, carbon nanotubes make particularly promising reinforcement materials in composites with metals, ceramics or polymer matrices. Key issues to address include the good dispersion of the nanotubes, the control of the nanotube/matrix bonding, the densification of bulk composites and thin films, and the possibility of aligning the nanotubes. In addition, the nanotube type (SWNT, c-MWNT, h-MWNT, etc.) and origin (arc, laser, CCVD, etc.) are also important variables that control the structural perfection, surface reactivity and aspect ratio of the reinforcement.

The application of carbon nanotubes in this field is expected to lead to major advances in composites. The following sections will give overviews of current work on metal-, ceramic- and polymer-matrix composites containing nanotubes. Nanotubes coated with another material are not considered here. Filled nanotubes are discussed in Sect. 3.5.2.

Metal Matrix Composites

Nanotube-metal matrix composites are still rarely studied. Matrices include Al-, Cu-, Mg-, Ni-, Ni-P-, Ti-, WC-Co- and Zr-based bulk metallic glasses. The materials are generally prepared by standard powder metallurgy techniques, but in this case the nanotube dispersion is not optimal. Other techniques such as plasma spray forming [3.386], the so-called nanoscale-dispersion method [3.387], the rapid solidification technique [3.388] and CCVD [3.389], are being developed. The spark plasma sintering (SPS) technique is sometimes used to densify the composites whilst avoiding matrix-grain growth [3.390, 391]. The room-temperature electrical resistivity of hot-pressed CCVD MWNT-Al composites increases slightly upon increasing the MWNT volume fraction [3.392]. The tensile strengths and elongations of unpurified arc discharge MWNT-Al composites are only slightly affected by annealing at 873 K in contrast to those of pure Al [3.393]. The coefficient of thermal expansion (CTE) of 1 wt% MWNTs-Al composite fabricated by cold isostatic pressing and hot squeeze technique is 11% lower than to that of pure Al or 2024Al matrix, showing some promises as low-CTE materials. Associated to a high thermal conductivity, such materials would be interesting for applications such as packaging and space structures [3.394]. The Young's modulus of nonpurified arc discharge MWNTs-Ti composite is about 1.7 times that of pure Ti [3.395]. The formation of TiC, probably resulting from a reaction between amorphous carbon and the matrix, was observed, but the MWNTs themselves were not damaged. An increase in the Vickers hardness by a factor of 5.5 over that of pure Ti was associated with the suppression of coarsening of the Ti grains, TiC formation, and the addition of MWNTs. Purified nanotube-WC-Co nanocomposites exhibit better hardness-to-toughness relationships than pure nanocrystalline WC-Co [3.391]. Ni-plated MWNTs give better results than unplated MWNTs in strength tests. Indeed, nanotube coating is a promising way to improve the strength of bonding with the matrix [3.396]. Compressive testing of carbon nanotube-reinforced Zr-based bulk metallic glass composites [3.397] shows that the composites display a high fracture strength. In addition, the composites have strong ultrasonic attenuation characteristics and excellent ability to absorb waves. This implies that such composites may also be useful for shielding acous-

tic sound or environmental noise. CCVD MWNTs-Cu composites [3.398] also show a higher hardness and a lower friction coefficient and wear loss. Fifty to sixty percent deformation of the composites was observed. Carbon nanotube-Cu composite electrodes have been applied to the amperometric detection of carbohydrates, where they show an enhanced sensitivity compared to detectors based on Cu or nanotubes alone [3.399]. Hot-extruded nanotube-Mg nanocomposites showed a simultaneous increase in yield strength, ultimate tensile strength and ductility, until a threshold of 1.3 wt % was reached [3.400]. The yield strength of SWNT-Fe composites showed substantial enhancement relative to that of similarly treated pure iron materials [3.389]. The work hardening coefficient and the Vickers hardness coefficient also significantly increased in these composites. Composite films and coatings deposited by electroless or electrodeposition techniques on various substrates have also been studied. The addition of up to 15 vol. % purified SWNTs to nanocrystalline Al films reduces the coefficient of thermal expansion by as much as 65% and the resulting material could be a promising electronic packaging material [3.401]. Ni-carbon nanotube coatings deposited on carbon steel plate by electroless deposition show significantly increased resistance to corrosion [3.402] and higher Vickers microhardness, higher wear resistance, and lower friction coefficient than SiC-reinforced composite deposits [3.403]. Ni-P-SWNT coatings prepared by electroless plating show not only higher wear resistance but also a lower friction coefficient and a higher corrosion resistance compared to Ni-P coatings [3.404].

Ceramic Matrix Composites

Many different ceramic matrices have been studied over the years, although oxides (in particular alumina), are still the most studied [3.405]. There are three main methods for the preparation of CNT-ceramic nanocomposite powders. One is mechanical milling. It usually involves long times that could damage the nanotubes. Wet-milling is preferred but often requires the addition of organic additives to stabilize both the nanotubes and the ceramic powder. This also true for a second method, i. e., the in-situ synthesis of the matrix on preformed nanotubes. It can lead to a good adhesion between the nanotubes and the ceramic, but can be rather complex to implement. A third method is the in-situ synthesis of the nanotubes within the ceramic powder using procedures closely related to those described in Sect. 3.2.2. The densification of the nanocomposite powders is made difficult by the detrimental influence of the nanotubes. The most common method is hot-pressing (HP). Most of the works [3.406–413] report that increasing the nanotube content inhibits the densification of the material. It has been shown for a series of CNT-$MgAl_2O_4$ composites [3.413] that, for a low content (below 9 vol. %), CNTs favor the rearrangement of the grains, which is the first shrinkage step, probably owing to a lubricating role which facilitates the sliding at grain contacts or grain boundaries. By contrast, for higher contents, CNTs form a too rigid weblike structure, therefore inhibiting the rearrangement process. In the second sintering step, at higher temperatures, CNTs inhibit the shrinkage, all the more when their content is increased above 5.0 vol. % only, leading to decreasing densifications. Thus, composites in which the nanotubes are very homogeneously dispersed may be more difficult to densify. The spark-plasma sintering (SPS) technique has been reported as an efficient method to achieve the total densification of CNT-oxide composites without damaging the CNT [3.414–417]. Full densification can be reached with SPS at comparatively lower temperatures with substantial shorter holding time. However, the successful densification by SPS at a lower temperature than for HP supposes that matrix grains are non agglomerated and with size in the range few tens of nanometers.

The influence of the nanotube dispersion onto mechanical properties, in particular on toughness, has been controversial. Indeed, strong increases in toughness derived from the measure of Vickers indentation cracks have been reported [3.33], but they were shown to be probably widely overestimated because such materials are very resistant to contact damage [3.418, 419]. *Xia* et al. [3.420] reported microstructural investigations on MWNTs well-aligned in the pores of an alumina membrane. Different possible reinforcement mechanisms induced by the MWNTs have been evidenced, such as crack deflection, crack bridging, MWNT pulling-out, and MWNT collapsing in shear bands. Indeed, although so far neither SENB nor SEVNB result have evidenced that nanotubes can significantly reinforce alumina ceramics, this could be obtained with ceramic-matrix composites in which the nanotubes would have been properly organized. Enhanced wear resistance of composites has been reported [3.421–423]. The microhardness is found to either increase or decrease, and this depends greatly on the powder preparation route. As noted in [3.419], processing-induced changes in the matrix may have greater effects on the mechanical properties than the actual presence of nanotubes. Regarding the thermal properties, nanotube-ceramic

composites often show a lower thermal conductivity than the corresponding ceramics, probably caused by too high thermal contact resistances at nanotube-nanotube and nanotube-ceramic grain junctions [3.424, 425]. By contrast, nanotubes greatly increase the electrical conductivity of insulating ceramic nanocomposites [3.408, 411, 426–428], with a low percolation threshold (less than 1 vol. %) due to their very high aspect ratio [3.427]. The electrical conductivity can be tailored within several orders of magnitude directly by the CNTs quantity and is well fitted by the scaling law of the percolation theory with the exponent close to the theoretical value characteristic of a three-dimensional network [3.427]. An anisotropic conductivity is obtained when the nanotubes are aligned within the composite [3.429]. *Zhan* et al. [3.430] reported an increase of the thermoelectric power with increasing temperature for nanotube-zirconia composites.

Polymer Matrix Composites

Nanotube-polymer composites, first reported by *Ajayan* et al. [3.431], are now being intensively studied; especially epoxy- and polymethylmethacrylate (PMMA)-matrix composites. A review of the mechanical properties can be found in [3.432]. In terms of mechanical characteristics, the three key issues that affect the performance of a fiber-polymer composite are the strength and toughness of the fibrous reinforcement, its orientation, and good interfacial bonding, which is crucial to load transfer [3.433]. The ability of the polymer to form large-diameter helices around individual nanotubes favors the formation of a strong bond with the matrix [3.433]. Isolated SWNTs may be more desirable than MWNTs or bundles for dispersion in a matrix because of the weak frictional interactions between layers of MWNTs and between SWNTs in bundles [3.433]. The main mechanisms of load transfer are micromechanical interlocking, chemical bonding and van der Waals bonding between the nanotubes and the matrix. A high interfacial shear stress between the fiber and the matrix will transfer the applied load to the fiber over a short distance [3.434]. SWNTs longer than 10–100 μm would be needed for significant load-bearing ability in the case of nonbonded SWNT-matrix interactions, whereas the critical length for SWNTs cross-linked to the matrix is only 1 μm [3.435]. Defects are likely to limit the working length of SWNTs, however [3.436].

The load transfer to MWNTs dispersed in an epoxy resin was much higher in compression than in tension [3.434]. It was proposed that all of the walls of the MWNTs are stressed in compression, whereas only the outer walls are stressed in tension because all of the inner tubes are sliding within the outer tube. Mechanical tests performed on 5 wt % SWNT-epoxy composites [3.437] showed that SWNT bundles were pulled out of the matrix during the deformation of the material. The influence of the interfacial nanotube/matrix interaction was demonstrated by *Gong* et al. [3.438]. It was also reported that coating regular carbon fiber with MWNTs prior to their dispersion into an epoxy matrix improves the interfacial load transfer, possibly via local stiffening of the matrix near the interface [3.439]. DWNTs-epoxy composites prepared by a standard calendaring technique were shown to possess higher strength, Young's modulus and strain to failure at a nanotube content of only 0.1 wt % [3.440]. A significantly improved fracture toughness was also observed. The influence of the different types of nanotubes (SWNTs, DWNTs and MWNTs) on the mechanical properties of epoxy-matrix composites is discussed in [3.441]. The stiffness and damping properties of SWNT- and MWNT-epoxy composites were investigated for use in structural vibration applications [3.442]. It was shown that enhancement in damping ratio is more dominant than enhancement in stiffness, MWNTs making a better reinforcement than SWNTs. Indeed, up to 700% increase in damping ratio is observed for MWNT-epoxy beam as compared to the plain epoxy beam. Industrial epoxy loaded with 1 wt % unpurified CCVD-prepared SWNTs showed an increase in thermal conductivity of 70 and 125% at 40 K and at room temperature, respectively [3.443]. Also, the Vickers hardness rose by a factor of 3.5 with the SWNT loading up at 2 wt %. An increase in the amount of MWNTs led to an increase of the glass transition temperature of MWNT-epoxy-composites. The effect is stronger when using samples containing functionalized MWNTs [3.444]. *Pecastaings* et al. [3.445] have investigated the role of interfacial effects in carbon nanotube-epoxy nanocomposite behavior.

As for ceramic matrix composites, the electrical characteristics of SWNT- and MWNT-epoxy composites are described by the percolation theory. Very low percolation thresholds (much below 1 wt %) are often reported [3.446–448]. Thermogravimetric analysis shows that, compared to pure PMMA, the thermal degradation of PMMA films occurs at a slightly higher temperature when 26 wt % of MWNTs are added [3.449]. Improving the wetting between the MWNTs and the PMMA by coating the MWNTs with poly(vinylidene fluoride) prior to melt-blending

with PMMA resulted in an increased storage modulus [3.450]. The impact strength in aligned SWNT-PMMA composites increased significantly with only 0.1 wt % of SWNTs, possibly because of weak interfacial adhesion and/or of the high flexibility of the SWNTs and/or the pullout and sliding effects of individual SWNTs within bundles [3.451]. The transport properties of arc discharge SWNT-PMMA composite films (10 μm thick) were studied in great detail [3.452, 453]. The electrical conductivity increases by nine orders of magnitude from 0.1 to 8 wt % SWNTs. The room-temperature conductivity is again well described by the standard percolation theory, confirming the good dispersion of the SWNTs in the matrix. The rheological threshold of SWNT-PMMA composites is about 0.12 wt %, smaller than the percolation threshold of electrical conductivity, about 0.39 wt % [3.454]. This is understood in terms of the smaller nanotube–nanotube distance required for electrical conductivity compared to that required to impede polymer mobility. Furthermore, decreased SWNT alignment, improved SWNT dispersion and/or longer polymer chains increase the elastic response of the nanocomposite. The effects of small quantities of SWNTs (up to 1 wt %) in PMMA on its flammability properties were studied [3.455]. The formation of a continuous SWNTs network layer covering the entire surface without any cracks is critical for obtaining the lowest mass-loss rate of the nanocomposites. One of the most interesting development of nanotube-polymer composites is their use for the production of spun fibers, films and textiles with extraordinary mechanical and electrical properties [3.456–462].

Polymer composites with other matrices include CCVD-prepared MWNT-polyvinyl alcohol [3.463], arc-prepared MWNT-polyhydroxyaminoether [3.464], arc-prepared MWNT-polyurethane acrylate [3.465, 466], SWNT-polyurethane acrylate [3.467], SWNT-polycarbonate [3.468], MWNT-polyaniline [3.469], MWNT-polystyrene [3.470], CCVD double-walled nanotubes-polystyrene-polymethylacrylate [3.471], MWNT-polypropylene [3.472, 473], SWNT-polyethylene [3.474–476], SWNT-poly(vinyl acetate) [3.475,476], CCVD-prepared MWNT-polyacrylonitrile. [3.477], SWNT-polyacrylonitrile [3.478], MWNT-oxotitanium phthalocyanine [3.479], arc-prepared MWNT-poly(3-octylthiophene) [3.480], SWNT-poly(3-octylthiophene) [3.481] and CCVD MWNT-poly(3-hexylthiophene) [3.482]. These works deal mainly with films 100–200 μm thick, and aim to study the glass transition of the polymer, its mechanical and electrical characteristics, as well as the photoconductivity.

A great deal of work has also been devoted to the applications of nanotube-polymer composites as materials for molecular optoelectronics, using primarily poly(*m*-phenylenevinylene-co-2,5-dioctoxy-*p*-phenylenevinylene) (PmPV) as the matrix. This conjugated polymer tends to coil, forming a helical structure. The electrical conductivity of the composite films (4–36 wt % MWNTs) is increased by eight orders of magnitude compared to that of PmPV [3.483]. Using the MWNT-PmPV composites as the electron transport layer in light-emitting diodes results in a significant increase in brightness [3.484]. The SWNTs act as a hole-trapping material that blocks the holes in the composites; this is probably induced through long-range interactions within the matrix [3.485]. Similar investigations were carried out on arc discharge SWNT-polyethylene dioxythiophene (PEDOT) composite layers [3.486] and MWNT-polyphenylenevinylene composites [3.487].

To conclude, two critical issues must be considered when using nanotubes as components for advanced composites. One is to choose between SWNTs, DWNTs, and MWNTs. The former seem more beneficial to mechanical strengthening, provided that they are isolated or arranged into cohesive yarns so that the load can be conveniently transferred from one SWNT to another. Unfortunately, despite many advances [3.456–461], this is still a technical challenge. The other issue is to tailor the nanotube/matrix interface with respect to the matrix. In this case, DWNTs and MWNTs may be more useful than SWNTs.

Multifunctional Materials

One of the major benefits expected from incorporating carbon nanotubes into other solid or liquid materials is that they endow the material with some electrical conductivity while leaving other properties or behaviors unaffected. As already mentioned in the previous section, the percolation threshold is reached at very low nanotube loadings. Tailoring the electrical conductivity of a bulk material is then achieved by adjusting the nanotube volume fraction in the formerly insulating material while making sure that this fraction is not too large.As demonstrated by *Maruyama* [3.488], there are three areas of interest regarding the electrical conductivity:

1. Electrostatic discharge (for example, preventing fire or explosion hazards in combustible environments or perturbations in electronics, which requires an electrical resistivity of less than 10^{12} Ω cm)

Table 3.5 Applications of nanotube-based multifunctional materials (from [3.488]), © *B. Maruyama* (WPAFB, Dayton, Ohio) ([a] For electrostatic painting, to mitigate lightning strikes on aircraft, etc., [b] to increase service temperature rating of product, [c] to reduce operating temperatures of electronic packages, [d] reduces warping, [e] reduces microcracking damage in composites)

		Mechanical			Electrical			Thermal		Thermo-mechanical	
Fiber fraction	**Applications**	Strength/ stiffness	Specific strength	Through-thickness strength	Static dissipation	Surface conduction[a]	EMI shielding	Service[b] temperature	Conduction/ dissipation[c]	Dimensional stability[d]	CTE reduction[e]
Low volume fraction (fillers)											
Elastomers	Tires	×			×				×		
Thermoplastics	Chip package				×				×		
	Electronics/ housing	×					×	×	×		
Thermosets	Epoxy products	×	×	×		×				×	×
	Composites			×						×	
High volume fraction											
Structural composites	Space/aircraft components		×	×							
High conduction composites	Radiators	×							×	×	
	Heat exchangers	×						×	×		×
	EMI shield	×					×				

2. Electrostatic painting (which requires the material to be painted to have enough electrical conductivity – an electrical resistivity below $10^6\ \Omega\,\mathrm{cm}$ – to prevent the charged paint droplets from being repelled)
3. Electromagnetic interference shielding (which is achieved for an electrical resistivity of less than $10\ \Omega\,\mathrm{cm}$.

Materials are often required to be multifunctional; for example, to have both high electrical conductivity and high toughness, or high thermal conductivity and high thermal stability. An association of several materials, each of them bringing one of the desired features, generally meets this need. The exceptional features and properties of carbon nanotubes make them likely to be a perfect multifunctional material in many cases. For instance, materials used in satellites are often required to be electrical conductive, mechanically self-supporting, able to transport away excess heat, and often to be robust against electromagnetic interference, while being of minimal weight and volume. All of these properties should be possible with a single nanotube-containing composite material instead of complex multimaterials combining layers of polymers, aluminum, copper, and so on. Table 3.5 provides an overview of various fields in which nanotube-based multifunctional materials should find application.

Nanoelectronics

As reported in Sects. 3.1.1 and 3.4.4, SWNT nanotubes can be either metallic (with an electrical conductivity higher than that of copper), or semiconducting. This has inspired the design of several components for nanoelectronics. First, metallic SWNTs can be used as mere ballistic conductors. Moreover, as early as 1995, realizing a rectifying diode by joining one metallic SWNT to one semiconductor SWNT (hetero-junction) was proposed by *Lambin* et al. [3.489], then later by *Chico* et al. [3.490] and *Yao* et al. [3.491]. Also, field effect transistors (FET) can be built by attaching

a semiconductor SWNT across two electrodes (source and drain) deposited on an insulating substrate that serves as a gate electrode [3.492, 493]. The association of two such SWNT-based FETs makes a voltage inverter [3.494].

All of the latter developments are fascinating and provide promising outlets for nanotube-based electronics. However, progress is obviously needed before SWNT-based integrated circuits can be constructed on a routine basis. A key issue is the need to be able to selectively prepare either metallic or semiconductor nanotubes. Although a method of selectively destroying metallic SWNTs in bundles of undifferentiated SWNTs [3.496] has been proposed, the method is not scalable and selective synthesis would be preferable. Also, defect-free nanotubes are required. Generally speaking, this relates to another major challenge, which is to be able to fabricate integrated circuits including nanometer-size components (that only sophisticated imaging methods such as AFM are able to visualize) on an industrial scale. An overview of the issues related to the integration of carbon nanotubes into microelectronics systems has been written by *Graham* et al. [3.497].

Nanotools, Nanodevices and Nanosystems

Due to the ability of graphene to expand slightly when electrically charged, nanotubes have been found to act as actuators. *Kim* and *Lieber* [3.495] demonstrated this by designing *nanotweezers*, which are able to grab, manipulate and release nano-objects (the *nanobead* that was handled for the demonstration was actually closer to a micrometer in size than a nanometer), as well as to measure their electrical properties. This was made possible by simply depositing two nonintercon-

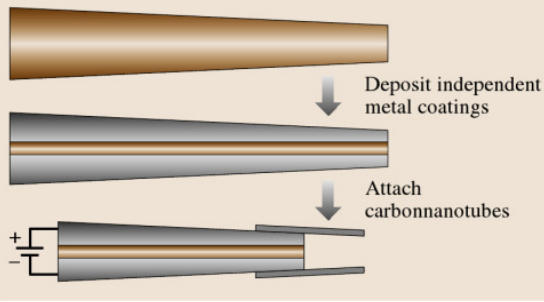

Fig. 3.32 Sketch explaining how the first nanotweezers were designed. The process involves modifying a glass micropipette (dark cone, *top*). Two Au coatings (in gray, *middle*) are deposited so that they are not in contact. Then a voltage is applied to the electrodes (from [3.495])

nected gold coatings onto a pulled glass micropipette (Fig. 3.32), and then attaching two MWNTs (or two SWNT-bundles) $\approx 20-50$ nm in diameter to each of the gold electrodes. Applying a voltage (0–8.5 V) between the two electrodes then makes the tube tips open and close reversibly in a controlled manner.

A similar experiment, again rather simple, was proposed by *Baughman* et al. the same year (1999) [3.498]. This consisted of mounting two SWNT-based paper strips (*bucky-paper*) on both sides of insulating double-sided tape. The two bucky-paper strips had been previously loaded with Na^+ and Cl^-, respectively. When 1 V was applied between the two paper strips, both of them expanded, but the strip loaded with Na^+ expanded a bit more, forcing the whole system to bend. Though performed in a liquid environment, this behavior has inspired the authors to predict a future use for their system in *artificial muscles*.

Another example of amazing nanotools is the nanothermometer proposed by *Gao* and *Bando* [3.499]. A single MWNT was used, which was partially filled with liquid gallium. Temperature variations in the range 50–500 °C cause the gallium to reversibly move up and down within the nanotube cavity at reproducible levels with respect to the temperature values applied.

Of course, nanotools such as nanotweezers or nanothermometers are hardly commercial enough to justify industrial investment. But such experiments are more than just amazing laboratory curiosities. They demonstrate the ability of carbon nanotubes to provide building blocks for future nanodevices, including nanomechanical systems.

Supercapacitors

Supercapacitors consist of two electrodes immersed in an electrolyte (such as 6 M KOH), separated by an insulating ion-permeable membrane. Charging the capacitors is achieved by applying a potential between the two electrodes, which makes the cations and the anions move toward the oppositely charged electrode. Suitable electrodes should exhibit high electrical conductivities and high surface areas, since the capacitance is proportional to these parameters. Actually, the surface area should consist of an appropriate combination of mesopores (to allow the electrolyte components to circulate well, which is related to the charging speed) and micropores (whose walls provide the attractive surfaces and fixation sites for the ions). Based on early work by *Niu* et al. [3.500], such a combination was found to be provided by the specific architecture offered by packed and entan-

gled h-MWNTs with poor nanotextures (Sect. 3.1.2). However, activation pretreatments were necessary. For instance, a capacitor made from nanotubes with a surface area of 220 m^2/g exhibited a capacitance of 20 F/g, which increased to 100 F/g after an activation treatment was applied to the nanotubes so that their surface area increased to 880 m^2/g [3.171]. Alternatively, again due to their remarkable architectures derived from their huge aspect ratios, nanotubes can also be used as supports for conductive polymer coatings, such as polypyrrole or polyaniline [3.501], or additives to regular carbon electrodes [3.502], which make the material more open, allowing easier circulation and penetration of ions. Supercapacitors built from such composites can survive more than 2000 charging cycles, with current densities as high as 350 mA/g [3.503]. Capacitors including nanotubes have already shown capacitances as high as 180–200 F/g, equivalent to those obtained with electrodes built from regular carbon materials, but they have the advantage of faster charging [3.171]. Current work in this area will certainly lead to further optimization of both the nanotube material architecture and the nanotube-supported conductive polymers, meaning that the outlook for the commercial use of nanotubes as components for supercapacitors is positive, and this is ignoring the potential application of second-generation nanotubes (such as nanotube-based nano-objects) in this field. A first attempt to use hybrid nanotubes (Sect. 3.5.2) has already resulted in improved properties with respect to genuine (undoped) nanotube-based systems [3.504].

3.7 Toxicity and Environmental Impact of Carbon Nanotubes

As the number of industrial applications of CNT increases constantly with the production capacity at the worldwide level (estimated to ca. a few hundreds of tons in 2007), it is reasonable to address the issue of their potential impact on both human health and environment. It is important to consider that the large variety of CNTs (SWNT, DWNT, MWNT, hetero-CNTs, hybrid CNTs, etc.) and of synthesis routes (arc-discharge, laser ablation, CCVD, ...) as well as the lack of standardized testing procedures make the investigation of the toxicity of CNTs very difficult, and the comparison of the already published results almost impossible [3.505]. CNTs are mostly found as bundles rather than as individual objects, or more likely as large micrometric agglomerates. All samples contain different levels of residual catalyst(s), depending on the synthesis route and purification steps that they may have undergone. Usual purification treatments involve the combination of acids and oxidising agents, which leads to partial functionalization of the outer wall, making the treated samples more hydrophilic. SWNTs and DWNTs usually form long and flexible bundles (typically hundreds of micrometers long) whereas MWNTs are generally shorter (tens of micrometers) and more rigid. MWNTs also have generally more surface defects, which enhances their chemical reactivity. The specific surface area can range from a few tens of squared metres per gram in the case of densely packed MWNTs to just below 1000 m^2/g in the case of SWNTs and DWNTs (the theoretical limit being ca. 1300 m^2/g in the case of individual closed SWNTs).

The main exposure routes for dry CNTs are inhalation and dermal contact (also possible in the case of suspensions). Ingestion is generally not considered (would be accidental), although it is in fact more or less related to inhalation. In the case of suspensions, the main issue concerns their stability. This question has been widely studied worldwide and the general approach is the addition of a surfactant in order to stabilise the CNT in the liquid. The main problem is that all commonly used surfactants are toxic to a certain extent and thus cannot be used in the presence of living cells or animals for in vivo or in vitro investigations, or at such low concentrations that they do not really play anymore the role they are supposed to play. Although a few natural surfactants have been investigated, the stability of the suspensions in the presence of living organisms is often very different (fast destabilisation leading to flocculation). Injection in the bloodstream is envisaged, but would not be accidental (biological applications such as imaging, targeted cell delivery, hyperthermia, etc.). After the CNTs have entered the body, they could travel following different routes depending on the entry point (movements from one organ to another are called translocation) but also mainly on their physicochemical characteristics. Objects recognised as non-self by the immune system usually end up in the liver or the kidneys if they can be transported there, and could possibly be excreted (eliminated) from the body. In the general case, CNTs will just accumulate (biopersistance). They are usually intercepted by macrophages (cells present in all tissues and which role is to phagocyte (engulf and

then digest) cellular debris and pathogens as well as to stimulate lymphocytes and other immune cells to respond to the pathogens). Taking into account the small size of macrophages as compared to that of agglomerates, bundles or even individual CNTs, macrophages usually do not manage to get rid of the CNTs by phagocytose. However, they try to do so and thus release reactive oxygen species (ROS), enzymes, cytokines (interferons (IFN)), etc. and agglomerate around them to isolate them from the body. Proteins present in the blood and most biological fluids (complement system – innate immunity) will play a similar role by *labelling* the CNTs (opsonisation) and possibly generating some inflammatory reactions. The complement system strongly interacts with the lymphocytes. These natural phenomena have deleterious consequences on the surrounding tissues: inflammation in a first instance, formation of granuloma (commonly observed in the lungs after exposure to CNTs). Each target organ has its own phagocyte cells (Kupffer cells in the liver, Langerhans cells in the skin, etc.).

Toxicity can be assessed both by in vitro and in vivo experiments. In the case of in vitro assays, cell cultures (usually immortalised cancer cells, but also primary cultures or even stem cells) are exposed to suspensions of CNTs. In the case of in vivo assays, the animals (mice, rats, worms, amphibians, fishes, etc.) are exposed either to aerosols (inhalation) or mainly again to suspensions of CNTs which will be administrated according to different protocols depending on the study (intra-tracheal instillation, injection, contact with the skin, etc.). Extrapolating the toxicity results from animals (or even worse, from cells) to humans is very delicate but the data are however very useful for the sake of comparison in a given system and with given experimental conditions. As soon as CNTs are in contact with a biological fluid, their surface chemistry is likely to be modified very quickly by adsorption of proteins (complement system [3.506], surfactants [3.507], etc.); this adsorption can be very specific [3.506, 507], and is likely to be dynamic and controlled by the affinity of the molecules for the surface of the CNTs (pristine or functionalised). It is thus obvious that the surface chemistry of the CNTs will play a very important role.

The potential use of CNTs in commercial products (Sect. 3.5) begs the question of their fate at the end of their lifecycle. If the impact of CNTs on human health is under investigation for already a few years now, it is noteworthy that the environmental impact has almost not been taken into account. Only a few publications (less than 15) are available to date and the concentration at which ecotoxic effects are evidenced is usually much higher than what could be reasonably found in the environment (unless very local and specific conditions). Due to the potentially very high specific surface area of CNTs, they could act as vectors for pollutants adsorbed on their surface (PAH, polycyclic aromatic hydrocarbons for example), even if themselves do not show any sign of toxicity.

There is currently no consensus about the toxicity of CNTs [3.505], although more than 500 papers have now been published already on this topic within the last 5 years. Despite the worldwide effort devoted to this field of research, the huge variety of CNT types, shapes, composition, etc. will make very difficult to answer this simple question: *are CNT toxic*? The *principle of precaution* should not stop all research in this area but only draw the attention to a more responsible attitude for people working on their synthesis or manipulating them, and industrials willing to include them in consumer products. Gloves should be worn at any time as well as an adapted (FFP3 type) disposable dust mask. Wearing a lab coat is recommended to limit contamination of clothes. CNT wastes should be burnt.

3.8 Concluding Remarks

Carbon nanotubes have been the focus of a lot of research work (and therefore a lot of funding) for nearly two decades now. Considering this investment of time and money, relatively few nanotube applications have reached the market yet. This may remind some of the disappointments associated with fullerene research, originally believed to be so promising, but which has resulted in no significant application after twenty years. However, nanotubes exhibit an extraordinary diversity of morphologies, textures, structures and nanotextures, far beyond that provided by fullerenes. Indeed, the properties of nanotubes are yet to be fully identified, and we should not forget the potential of hybrid nanotubes, heteronanotubes and nanotube-containing composites. The history of nanotubes has only just begun.

References

3.1 M. Monthioux, V.L. Kuznetsov: Who should be given the credit for the discovery of carbon nanotubes?, Carbon **44**, 1621–1623 (2006)

3.2 L.V. Radushkevich, V.M. Lukyanovich: O strukture ugleroda, obrazujucegosja pri termiceskom razlozenii okisi ugleroda na zeleznom kontakte, Zurn. Fis. Chim. **26**, 88–95 (1952), in Russian

3.3 T.V. Hughes, C.R. Chambers: Manufacture of Carbon Filaments, US Patent 405480 (1889)

3.4 P. Schützenberger, L. Schützenberger: Sur quelques faits relatifs à l'histoire du carbone, C. R. Acad. Sci. Paris **111**, 774–778 (1890), in French

3.5 C. Pélabon, H. Pélabon: Sur une variété de carbone filamenteux, C. R. Acad. Sci. Paris **137**, 706–708 (1903), in French

3.6 R.T.K. Baker, P.S. Harris: The formation of filamentous carbon. In: *Chemistry and Physics of Carbon*, Vol. 14, ed. by P.L. Walker Jr., P.A. Thrower (Dekker, New York 1978) pp. 83–165

3.7 S. Iijima: Helical microtubules of graphite carbon, Nature **354**, 56–58 (1991)

3.8 S. Iijima, T. Ichihashi: Single-shell carbon nanotubes of 1 nm diameter, Nature **363**, 603–605 (1993)

3.9 D.S. Bethune, C.H. Kiang, M.S. de Vries, G. Gorman, R. Savoy, J. Vazquez, R. Bayers: Cobalt-catalysed growth of carbon nanotubes with single-atomic-layer walls, Nature **363**, 605–607 (1993)

3.10 J. Tersoff, R.S. Ruoff: Structural properties of a carbon-nanotube crystal, Phys. Rev. Lett. **73**, 676–679 (1994)

3.11 N. Wang, Z.K. Tang, G.D. Li, J.S. Chen: Single-walled 4 Å carbon nanotube arrays, Nature **408**, 50–51 (2000)

3.12 N. Hamada, S.I. Sawada, A. Oshiyama: New one-dimensional conductors, graphite microtubules, Phys. Rev. Lett. **68**, 1579–1581 (1992)

3.13 M.S. Dresselhaus, G. Dresselhaus, P.C. Eklund: *Science of Fullerenes and Carbon Nanotubes* (Academic, San Diego 1995)

3.14 R.C. Haddon: Chemistry of the fullerenes: The manifestation of strain in a class of continuous aromatic molecules, Science **261**, 1545–1550 (1993)

3.15 M. Monthioux, B.W. Smith, B. Burteaux, A. Claye, J. Fisher, D.E. Luzzi: Sensitivity of single-wall nanotubes to chemical processing: An electron microscopy investigation, Carbon **39**, 1261–1272 (2001)

3.16 H. Allouche, M. Monthioux: Chemical vapor deposition of pyrolytic carbon onto carbon nanotubes. Part II – Structure and texture, Carbon **43**, 1265–1278 (2005)

3.17 M. Audier, A. Oberlin, M. Oberlin, M. Coulon, L. Bonnetain: Morphology and crystalline order in catalytic carbons, Carbon **19**, 217–224 (1981)

3.18 Y. Saito: Nanoparticles and filled nanocapsules, Carbon **33**, 979–988 (1995)

3.19 P.J.F. Harris: *Carbon Nanotubes and Related Structures* (Cambridge Univ. Press, Cambridge 1999)

3.20 N.M. Rodriguez, A. Chambers, R.T. Baker: Catalytic engineering of carbon nanostructures, Langmuir **11**, 3862–3866 (1995)

3.21 M. Monthioux, L. Noé, L. Dussault, J.-C. Dupin, N. Latorre, T. Ubieto, E. Romeo, C. Royo, A. Monzón, C. Guimon: Texturising and structurising mechanisms of carbon nanofilament during growth, J. Mater. Chem. **17**, 4611–4618 (2007)

3.22 J. Vera-Agullo, H. Varela-Rizo, J.A. Conesa, C. Almansa, C. Merino, I. Martin-Gullon: Evidence for growth mechanism and helix-spiral cone structure of stacked-cup carbon nanofibers, Carbon **45**, 2751–2758 (2007)

3.23 H.W. Kroto, J.R. Heath, S.C. O'Brien, R.F. Curl, R.E. Smalley: C_{60} Buckminsterfullerene, Nature **318**, 162–163 (1985)

3.24 W. Krätschmer, L.D. Lamb, K. Fostiropoulos, D.R. Huffman: Solid C_{60}: A new form of carbon, Nature **347**, 354–358 (1990)

3.25 L. Fulchieri, Y. Schwob, F. Fabry, G. Flamant, L.F.P. Chibante, D. Laplaze: Fullerene production in a 3-phase AC plasma process, Carbon **38**, 797–803 (2000)

3.26 K. Saidane, M. Razafinimanana, H. Lange, A. Huczko, M. Baltas, A. Gleizes, J.L. Meunier: Fullerene synthesis in the graphite electrode arc process: local plasma characteristics and correlation with yield, J. Phys. D Appl. Phys. **37**, 232–239 (2004)

3.27 T. Guo, P. Nikolaev, A.G. Rinzler, D. Tomanek, D.T. Colbert, R.E. Smalley: Self-assembly of tubular fullerenes, J. Phys. Chem. **99**, 10694–10697 (1995)

3.28 T. Guo, P. Nikolaev, A. Thess, D.T. Colbert, R.E. Smalley: Catalytic growth of single-walled nanotubes by laser vaporisation, Chem. Phys. Lett. **243**, 49–54 (1995)

3.29 A.G. Rinzler, J. Liu, H. Dai, P. Nikolaev, C.B. Huffman, F.J. Rodriguez-Macias, P.J. Boul, A.H. Lu, D. Heymann, D.T. Colbert, R.S. Lee, J.E. Fischer, A.M. Rao, P.C. Eklund, R.E. Smalley: Large scale purification of single wall carbon nanotubes: Process, product and characterization, Appl. Phys. A **67**, 29–37 (1998)

3.30 L.M. Chapelle, J. Gavillet, J.L. Cochon, M. Ory, S. Lefrant, A. Loiseau, D. Pigache: A continuous wave CO_2 laser reactor for nanotube synthesis, Proc. Electron. Prop. Nov. Mater. – XVI Int. Wintersch. – AIP Conf. Proc., ed. by H. Kuzmany, J. Fink, M. Mehring, S. Roth (Springer, Berlin Heidelberg 1999) pp. 237–240

3.31 A. Thess, R. Lee, P. Nikolaev, H. Dai, P. Petit, J. Robert, C. Xu, Y.H. Lee, S.G. Kim, D.T. Colbert, G. Scuseria, D. Tomanek, J.E. Fischer, R.E. Smalley: Crystalline ropes of metallic carbon nanotubes, Science **273**, 487–493 (1996)

3.32 M. Yudasaka, T. Komatsu, T. Ichihashi, S. Iijima: Single wall carbon nanotube formation by laser ablation using double targets of carbon and metal, Chem. Phys. Lett. **278**, 102–106 (1997)

3.33 M. Castignolles, A. Foutel-Richard, A. Mavel, J.L. Cochon, D. Pigache, A. Loiseau, P. Bernier: Combined experimental and numerical study of the parameters controlling the C-SWNT synthesis via laser vaporization, Proc. Electron. Prop. Nov. Mater. – XVI Int. Wintersch. – AIP Conf. Proc., ed. by H. Kuzmany, J. Fink, M. Mehring, S. Roth (Springer, Berlin Heidelberg 2002) pp. 385–389

3.34 T.W. Ebbesen, P.M. Ajayan: Large-scale synthesis of carbon nanotubes, Nature **358**, 220–221 (1992)

3.35 D. Ugarte: Morphology and structure of graphitic soot particles generated in arc-discharge C_{60} production, Chem. Phys. Lett. **198**, 596–602 (1992)

3.36 T.W. Ebbesen: Carbon nanotubes, Ann. Rev. Mater. Sci. **24**, 235–264 (1994)

3.37 T. Beltz, J. Find, D. Herein, N. Pfänder, T. Rühle, H. Werner, M. Wohlers, R. Schlögl: On the production of different carbon forms by electric arc graphite evaporation, Ber. Bunsen. Phys. Chem. **101**, 712–725 (1997)

3.38 C. Journet, W.K. Maser, P. Bernier, A. Loiseau, L.M. de la Chapelle, S. Lefrant, P. Deniard, R. Lee, J.E. Fischer: Large-scale production of single-walled carbon nanotubes by the electric-arc technique, Nature **388**, 756–758 (1997)

3.39 K. Saïdane, M. Razafinimanana, H. Lange, M. Baltas, A. Gleizes, J.J. Gonzalez: Influence of the carbon arc current intensity on fullerene synthesis, Proc. 24th Int. Conf. Phenom. Ioniz. Gases, ed. by P. Pisarczyk, T. Pisarczyk, J. Wotowski (Institute of Plasma Physics and Laser Microfusion, Warsaw 1999) pp. 203–204

3.40 H. Allouche, M. Monthioux, M. Pacheco, M. Razafinimanana, H. Lange, A. Huczko, T.P. Teulet, A. Gleizes, T. Sogabe: Physical characteristics of the graphite-electrode electric-arc as parameters for the formation of single-wall carbon nanotubes, Proc. Eurocarbon, Vol. 2 (Deutsche Keramische Gesellschaft, 2000) pp. 1053–1054

3.41 M. Razafinimanana, M. Pacheco, M. Monthioux, H. Allouche, H. Lange, A. Huczko, A. Gleizes: Spectroscopic study of an electric arc with Gd and Fe doped anodes for the carbon nanotube formation, Proc. 25th Int. Conf. Phenom. Ioniz. Gases, ed. by E. Goto (Nagoya Univ., Nagoya 2001) pp. 297–298

3.42 M. Razafinimanana, M. Pacheco, M. Monthioux, H. Allouche, H. Lange, A. Huczko, P. Teulet, A. Gleizes, C. Goze, P. Bernier, T. Sogabe: Influence of doped graphite electrode in electric arc for the formation of single wall carbon nanotubes, Proc. 6th Eur. Conf. Therm. Plasma Process. – Prog. Plasma Process. Mater., New York 2000, ed. by P. Fauchais (Begell House, New York 2001) pp. 649–654

3.43 M. Pacheco, H. Allouche, M. Monthioux, A. Razafinimanana, A. Gleizes: Correlation between the plasma characteristics and the morphology and structure of the carbon phases synthesised by electric arc discharge, Proc. 25th Bienn. Conf. Carbon, Lexington 2001, ed. by F. Derbyshire (American Carbon Society 2001), Extend. Abstr. (CD-ROM), Novel/14.1

3.44 M. Pacheco, M. Monthioux, M. Razafinimanana, L. Donadieu, H. Allouche, N. Caprais, A. Gleizes: New factors controlling the formation of single-wall carbon nanotubes by arc plasma, Proc. Carbon 2002 Int. Conf., Beijing 2002, ed. by H.-M. Cheng (Shanxi Chunqiu Audio-Visual Press, Beijing 2002), CD-ROM/Oral/I014

3.45 M. Monthioux, M. Pacheco, H. Allouche, M. Razafinimanana, N. Caprais, L. Donnadieu, A. Gleizes: New data about the formation of SWNTs by the electric arc method. In: *Electronic Properties of Molecular Nanostructures*, AIP Conf. Proc., ed. by H. Kuzmany, J. Fink, M. Mehring, S. Roth (Springer, Berlin Heidelberg 2002) pp. 182–185

3.46 H. Lange, A. Huczko, M. Sioda, M. Pacheco, M. Razafinimanana, A. Gleizes: Influence of gadolinium on carbon arc plasma and formation of fullerenes and nanotubes, Plasma Chem. Plasma Process **22**, 523–536 (2002)

3.47 C. Journet: La production de nanotubes de carbone. Ph.D. Thesis (University of Montpellier II, Montpellier 1998)

3.48 T. Sogabe, T. Masuda, K. Kuroda, Y. Hirohaya, T. Hino, T. Ymashina: Preparation of B_4C-mixed graphite by pressureless sintering and its air oxidation behavior, Carbon **33**, 1783–1788 (1995)

3.49 M. Ishigami, J. Cumings, A. Zettl, S. Chen: A simple method for the continuous production of carbon nanotubes, Chem. Phys. Lett. **319**, 457–459 (2000)

3.50 Y.L. Hsin, K.C. Hwang, F.R. Chen, J.J. Kai: Production and in-situ metal filling of carbon nanotube in water, Adv. Mater. **13**, 830–833 (2001)

3.51 H.W. Zhu, X.S. Li, B. Jiang, C.L. Xu, C.L. Zhu, Y.F. Zhu, D.H. Wu, X.H. Chen: Formation of carbon nanotubes in water by the electric arc technique, Chem. Phys. Lett. **366**, 664–669 (2002)

3.52 W.K. Maser, P. Bernier, J.M. Lambert, O. Stephan, P.M. Ajayan, C. Colliex, V. Brotons, J.M. Planeix, B. Coq, P. Molinie, S. Lefrant: Elaboration and characterization of various carbon nanostructures, Synth. Met. **81**, 243–250 (1996)

3.53 A. Mansour, M. Razafinimanana, M. Monthioux, M. Pacheco, A. Gleizes: A significant improvement of both yield and purity during SWCNT synthesis via the electric arc process, Carbon **45**, 1651–1661 (2007)

3.54 A. Mansour: Caractérisation expérimentale d'un plasma d'arc électrique en vue du contrôle de la synthèse des nanotubes de carbone monoparois. Ph.D. Thesis (University Paul Sabatier, Toulouse 2007)

3.55 J. Gavillet, A. Loiseau, J. Thibault, A. Maigné, O. Stéphan, P. Bernier: TEM study of the influence of the catalyst composition on the formation and growth of SWNT, Proc. Electron. Prop. Nov. Mater. –

XVI Int. Wintersch. – AIP Conf. Proc., ed. by H. Kuzmany, J. Fink, M. Mehring, S. Roth (Springer, Berlin Heidelberg 2002) pp. 202–206
3.56 G. Flamant, J.F. Robert, S. Marty, J.M. Gineste, J. Giral, B. Rivoire, D. Laplaze: Solar reactor scaling up. The fullerene synthesis case study, Energy **29**, 801–809 (2004)
3.57 T.M. Gruenberger, J. Gonzalez-Aguilar, F. Fabry, L. Fulchieri, E. Grivei, N. Probst, G. Flamant, H. Okuno, J.C. Charlier: Production of carbon nanotubes and other nanostructures via continuous 3-phase AC plasma processing, Fuller. Nanotub. Carbon Nanostruct. **12**, 571–581 (2004)
3.58 H. Okuno, E. Grivel, F. Fabry, T.M. Gruenberger, J.J. Gonzalez-Aguilar, A. Palnichenko, L. Fulchieri, N. Probst, J.C. Chalier: Synthesis of carbon nanotubes and nano-necklaces by thermal plasma process, Carbon **42**, 2543–2549 (2004)
3.59 L.P.F. Chibante, A. Thess, J.M. Alford, M.D. Diener, R.E. Smalley: Solar generation of the fullerenes, J. Phys. Chem. **97**, 8696–8700 (1993)
3.60 C.L. Fields, J.R. Pitts, M.J. Hale, C. Bingham, A. Lewandowski, D.E. King: Formation of fullerenes in highly concentrated solar flux, J. Phys. Chem. **97**, 8701–8702 (1993)
3.61 P. Bernier, D. Laplaze, J. Auriol, L. Barbedette, G. Flamant, M. Lebrun, A. Brunelle, S. Della-Negra: Production of fullerenes from solar energy, Synth. Met. **70**, 1455–1456 (1995)
3.62 M.J. Heben, T.A. Bekkedhal, D.L. Schultz, K.M. Jones, A.C. Dillon, C.J. Curtis, C. Bingham, J.R. Pitts, A. Lewandowski, C.L. Fields: Production of single wall carbon nanotubes using concentrated sunlight, Proc. Symp. Recent Adv. Chem. Phys. Fuller. Rel. Mater., Pennington 1996, ed. by K.M. Kadish, R.S. Ruoff (Electrochemical Society, Pennington 1996) pp. 803–811
3.63 D. Laplaze, P. Bernier, C. Journet, G. Vié, G. Flamant, E. Philippot, M. Lebrun: Evaporation of graphite using a solar furnace, Proc. 8th Int. Symp. Solar Conc. Technol., Köln 1996, ed. by M. Becker, M. Balmer (Müller, Heidelberg 1997) pp. 1653–1656
3.64 D. Laplaze, P. Bernier, W.K. Maser, G. Flamant, T. Guillard, A. Loiseau: Carbon nanotubes: The solar approach, Carbon **36**, 685–688 (1998)
3.65 T. Guillard, S. Cetout, L. Alvarez, J.L. Sauvajol, E. Anglaret, P. Bernier, G. Flamant, D. Laplaze: Production of carbon nanotubes by the solar route, Eur. Phys. J. **5**, 251–256 (1999)
3.66 D. Luxembourg, G. Flamant, A. Guillot, D. Laplaze: Hydrogen storage in solar produced single-walled carbon nanotubes, Mater. Sci. Eng. B **108**, 114–119 (2004)
3.67 G. Flamant, M. Bijeire, D. Luxembourg: Modelling of a solar reactor for single wall nanotubes synthesis, ASME J. Solar Energy Eng. **128**, 1–124 (2006)
3.68 G.G. Tibbetts, M. Endo, C.P. Beetz: Carbon fibers grown from the vapor phase: A novel material, SAMPE Journal **22**, 30 (1989)
3.69 R.T.K. Baker: Catalytic growth of carbon filaments, Carbon **27**, 315–323 (1989)
3.70 E. Lamouroux, P. Serp, P. Kalck: Catalytic chemical vapor deposition routes towards single-walled and double-walled carbon nanotubes, Catal. Rev. Sci. Eng. **49**, 341–405 (2007)
3.71 R. Philippe, A. Morançais, M. Corrias, B. Caussat, Y. Kihn, P. Kalck, D. Plee, P. Gaillard, D. Bernard, P. Serp: Catalytic production of carbon nanotubes by fluidized-bed CVD, Chem. Vap. Depos. **13**, 447–457 (2007)
3.72 R.T.K. Baker, P.S. Harris, R.B. Thomas, R.J. Waite: Formation of filamentous carbon from iron, cobalt, and chromium catalyzed decomposition of acetylene, J. Catal. **30**, 86–95 (1973)
3.73 T. Koyama, M. Endo, Y. Oyuma: Carbon fibers obtained by thermal decomposition of vaporized hydrocarbon, Jpn. J. Appl. Phys. **11**, 445–449 (1972)
3.74 M. Endo, A. Oberlin, T. Koyama: High resolution electron microscopy of graphitizable carbon fiber prepared by benzene decomposition, Jpn. J. Appl. Phys. **16**, 1519–1523 (1977)
3.75 N.M. Rodriguez: A review of catalytically grown carbon nanofibers, J. Mater. Res. **8**, 3233–3250 (1993)
3.76 W.R. Davis, R.J. Slawson, G.R. Rigby: An unusual form of carbon, Nature **171**, 756 (1953)
3.77 H.P. Boehm: Carbon from carbon monoxide disproportionation on nickel and iron catalysts; morphological studies and possible growth mechanisms, Carbon **11**, 583–590 (1973)
3.78 M. Audier, A. Oberlin, M. Coulon: Crystallographic orientations of catalytic particles in filamentous carbon; case of simple conical particles, J. Cryst. Growth **55**, 546–549 (1981)
3.79 M. Audier, M. Coulon: Kinetic and microscopic aspects of catalytic carbon growth, Carbon **23**, 317–323 (1985)
3.80 M. Audier, A. Oberlin, M. Coulon: Study of biconic microcrystals in the middle of carbon tubes obtained by catalytic disproportionation of CO, J. Cryst. Growth **57**, 524–534 (1981)
3.81 A. Thaib, G.A. Martin, P. Pinheiro, M.C. Schouler, P. Gadelle: Formation of carbon nanotubes from the carbon monoxide disproportionation reaction over Co/Al_2O_3 and Co/SiO_2 catalysts, Catal. Lett. **63**, 135–141 (1999)
3.82 P. Pinheiro, M.C. Schouler, P. Gadelle, M. Mermoux, E. Dooryhée: Effect of hydrogen on the orientation of carbon layers in deposits from the carbon monoxide disproportionation reaction over Co/Al_2O_3 catalysts, Carbon **38**, 1469–1479 (2000)
3.83 P. Pinheiro, P. Gadelle: Chemical state of a supported iron-cobalt catalyst during CO disproportion-

ation. I. Thermodynamic study, J. Phys. Chem. Solids **62**, 1015–1021 (2001)

3.84 P. Pinheiro, P. Gadelle, C. Jeandey, J.L. Oddou: Chemical state of a supported iron-cobalt catalyst during CO disproportionation. II. Experimental study, J. Phys. Chem. Solids **62**, 1023–1037 (2001)

3.85 C. Laurent, E. Flahaut, A. Peigney, A. Rousset: Metal nanoparticles for the catalytic synthesis of carbon nanotubes, New J. Chem. **22**, 1229–1237 (1998)

3.86 E. Flahaut: Synthèse par voir catalytique et caractérisation de composites nanotubes de carbone-metal-oxyde Poudres et matériaux denses. Ph.D. Thesis (Univers. Paul Sabatier, Toulouse 1999)

3.87 E. Flahaut, R. Bacsa, A. Peigney, C. Laurent: Gram-scale CCVD synthesis of double-walled carbon nanotubes, Chem. Commun., 1442–1443 (2003)

3.88 A. Peigney, C. Laurent, F. Dobigeon, A. Rousset: Carbon nanotubes grown in situ by a novel catalytic method, J. Mater. Res. **12**, 613–615 (1997)

3.89 V. Ivanov, J.B. Nagy, P. Lambin, A. Lucas, X.B. Zhang, X.F. Zhang, D. Bernaerts, G. Van Tendeloo, S. Amelinckx, J. Van Landuyt: The study of nanotubules produced by catalytic method, Chem. Phys. Lett. **223**, 329–335 (1994)

3.90 V. Ivanov, A. Fonseca, J.B. Nagy, A. Lucas, P. Lambin, D. Bernaerts, X.B. Zhang: Catalytic production and purification of nanotubules having fullerene-scale diameters, Carbon **33**, 1727–1738 (1995)

3.91 K. Hernadi, A. Fonseca, J.B. Nagy, D. Bernaerts, A. Fudala, A. Lucas: Catalytic synthesis of carbon nanotubes using zeolite support, Zeolites **17**, 416–423 (1996)

3.92 H. Dai, A.G. Rinzler, P. Nikolaev, A. Thess, D.T. Colbert, R.E. Smalley: Single-wall nanotubes produced by metal-catalysed disproportionation of carbon monoxide, Chem. Phys. Lett. **260**, 471–475 (1996)

3.93 A.M. Cassel, J.A. Raymakers, J. Kong, H. Dai: Large scale CVD synthesis of single-walled carbon nanotubes, J. Phys. Chem. B **109**, 6484–6492 (1999)

3.94 B. Kitiyanan, W.E. Alvarez, J.H. Harwell, D.E. Resasco: Controlled production of single-wall carbon nanotubes by catalytic decomposition of CO on bimetallic Co-Mo catalysts, Chem. Phys. Lett. **317**, 497–503 (2000)

3.95 A. Govindaraj, E. Flahaut, C. Laurent, A. Peigney, A. Rousset, C.N.R. Rao: An investigation of carbon nanotubes obtained from the decomposition of methane over reduced $Mg_{1-x}M_xAl_2O_4$ spinel catalysts, J. Mater. Res. **14**, 2567–2576 (1999)

3.96 E. Flahaut, A. Peigney, C. Laurent, A. Rousset: Synthesis of single-walled carbon nanotube-Co-MgO composite powders and extraction of the nanotubes, J. Mater. Chem. **10**, 249–252 (2000)

3.97 J. Kong, A.M. Cassel, H. Dai: Chemical vapor deposition of methane for single-walled carbon nanotubes, Chem. Phys. Lett. **292**, 567–574 (1998)

3.98 E. Flahaut, A. Peigney, W.S. Bacsa, R.R. Bacsa, C. Laurent: CCVD synthesis of carbon nanotubes from (Mg,Co, Mo)O catalysts: Influence of the proportions of cobalt and molybdenum, J. Mater. Chem. **14**, 646–653 (2004)

3.99 E. Flahaut, C. Laurent, A. Peigney: Catalytic CVD synthesis of double and triple-walled carbon nanotubes by the control of the catalyst preparation, Carbon **43**, 375–383 (2005)

3.100 R. Marangoni, P. Serp, R. Feurrer, Y. Kihn, P. Kalck, C. Vahlas: Carbon nanotubes produced by substrate free metalorganic chemical vapor deposition of iron catalyst and ethylene, Carbon **39**, 443–449 (2001)

3.101 R. Sen, A. Govindaraj, C.N.R. Rao: Carbon nanotubes by the metallocene route, Chem. Phys. Lett. **267**, 276–280 (1997)

3.102 Y.Y. Fan, H.M. Cheng, Y.L. Wei, G. Su, S.H. Shen: The influence of preparation parameters on the mass production of vapor grown carbon nanofibers, Carbon **38**, 789–795 (2000)

3.103 L. Ci, J. Wei, B. Wei, J. Liang, C. Xu, D. Wu: Carbon nanofibers and single-walled carbon nanotubes prepared by the floating catalyst method, Carbon **39**, 329–335 (2001)

3.104 M. Glerup, H. Kanzow, R. Almairac, M. Castignolles, P. Bernier: Synthesis of multi-walled carbon nanotubes and nano-fibres using aerosol method with metal-ions as the catalyst precursors, Chem. Phys. Lett. **377**, 293–298 (2003)

3.105 O.A. Nerushev, M. Sveningsson, L.K.L. Falk, F. Rohmund: Carbon nanotube films obtained by thermal vapour deposition, J. Mater. Chem. **11**, 1122–1132 (2001)

3.106 Z. Zhou, L. Ci, L. Song, X. Yan, D. Liu, H. Yuan, Y. Gao, J. Wang, L. Liu, W. Zhou, G. Wang, S. Xie: Producing cleaner double-walled carbon nanotubes in a floating catalyst system, Carbon **41**, 2607–2611 (2003)

3.107 F. Rohmund, L.K.L. Falk, F.E.B. Campbell: A simple method for the production of large arrays of aligned carbon nanotubes, Chem. Phys. Lett. **328**, 369–373 (2000)

3.108 G.G. Tibbetts, C.A. Bernardo, D.W. Gorkiewicz, R.L. Alig: Role of sulfur in the production of carbon fibers in the vapor phase, Carbon **32**, 569–576 (1994)

3.109 S. Bai, F. Li, Q.H. Yang, H.-M. Cheng, J.B. Bai: Influence of ferrocene/benzene mole ratio in the synthesis of carbon nanostructures, Chem. Phys. Lett. **376**, 83–89 (2003)

3.110 W.Q. Han, P. Kholer-Riedlich, T. Seeger, F. Ernst, M. Ruhle, N. Grobert, W.K. Hsu, B.H. Chang, Y.Q. Zhu, H.W. Kroto, M. Terrones, H. Terrones: Aligned CN_x nanotubes by pyrolysis of ferrocene under NH_3 atmosphere, Appl. Phys. Lett. **77**, 1807–1809 (2000)

3.111 L. Ci, Z. Rao, Z. Zhou, D. Tang, X. Yan, Y. Liang, D. Liu, H. Yuan, W. Zhou, G. Wang, W. Liu, S. Xie: Double wall carbon nanotubes promoted by sulfur in a floating iron catalyst CVD system, Chem. Phys. Lett. **359**, 63–67 (2002)

3.112 S. Maruyama, R. Kojima, Y. Miyauchi, S. Chiashi, M. Kohno: Low-temperature synthesis of high-purity single-walled carbon nanotubes from alcohol, Chem. Phys. Lett. **360**, 229–234 (2002)

3.113 T. Kyotani, L.F. Tsai, A. Tomita: Preparation of ultrafine carbon tubes in nanochannels of an anodic aluminum oxide film, Chem. Mater. **8**, 2109–2113 (1996)

3.114 E. Mora, T. Tokune, A.R. Harutyunyan: Continuous production of single-walled carbon nanotubes using a supported floating catalyst, Carbon **45**, 971–977 (2007)

3.115 R.E. Smalley, J.H. Hafner, D.T. Colbert, K. Smith: Catalytic growth of single-wall carbon nanotubes from metal particles, US Patent 19980601010903 (1998)

3.116 P. Nikolaev: Gas-phase production of single-walled carbon nanotubes from carbon monoxide: A review of the HiPco process, J. Nanosci. Nanotechnol. **4**, 307–316 (2004)

3.117 W.K. Hsu, J.P. Hare, M. Terrones, H.W. Kroto, D.R.M. Walton, P.J.F. Harris: Condensed-phase nanotubes, Nature **377**, 687 (1995)

3.118 W.S. Cho, E. Hamada, Y. Kondo, K. Takayanagi: Synthesis of carbon nanotubes from bulk polymer, Appl. Phys. Lett. **69**, 278–279 (1996)

3.119 Y.L. Li, Y.D. Yu, Y. Liang: A novel method for synthesis of carbon nanotubes: Low temperature solid pyrolysis, J. Mater. Res. **12**, 1678–1680 (1997)

3.120 M.L. Terranova, S. Piccirillo, V. Sessa, P. Sbornicchia, M. Rossi, S. Botti, D. Manno: Growth of single-walled carbon nanotubes by a novel technique using nano-sized graphite as carbon source, Chem. Phys. Lett. **327**, 284–290 (2000)

3.121 R.L. Vander Wal, T. Ticich, V.E. Curtis: Diffusion flame synthesis of single-walled carbon nanotubes, Chem. Phys. Lett. **323**, 217–223 (2000)

3.122 I. Gunjishima, T. Inoue, S. Yamamuro, K. Sumiyama, A. Okamoto: Synthesis of vertically aligned, double-walled carbon nanotubes from highly active Fe-V-O nanoparticles, Carbon **45**, 1193–1199 (2007)

3.123 G. Zhong, T. Iwasaki, J. Robertson, H. Kawarada: Growth kinetics of 0.5 cm vertically aligned single-walled carbon nanotubes, J. Phys. Chem. B **111**, 1907–1910 (2007)

3.124 H. Cui, G. Eres, J.Y. Howe, A. Puretzki, M. Varela, D.B. Geohegan, D.H. Lowndes: Growth behavior of carbon nanotubes on multilayered metal catalyst film in chemical vapor deposition, Chem. Phys. Lett. **374**, 222–228 (2003)

3.125 A.M. Cassel, N.R. Franklin, T.W. Tombler, E.M. Chan, J. Han, H. Dai: Directed growth of free-standing single-walled carbon nanotubes, J. Am. Chem. Soc. **121**, 7975–7976 (1999)

3.126 S. Fan, M. Chapline, N. Franklin, T. Tombler, A.M. Cassel, H. Dai: Self-oriented regular arrays of carbon nanotubes and their field emission properties, Science **283**, 512–514 (1999)

3.127 Y.Y. Wei, G. Eres, V.I. Merkulov, D.H. Lowdens: Effect of film thickness on carbon nanotube growth by selective area chemical vapor deposition, Appl. Phys. Lett. **78**, 1394–1396 (2001)

3.128 I.T. Han, B.K. Kim, H.J. Kim, M. Yang, Y.W. Jin, S. Jung, N. Lee, S.K. Kim, J.M. Kim: Effect of Al and catalyst thickness on the growth of carbon nanotubes and application to gated field emitter arrays, Chem. Phys. Lett. **400**, 139–144 (2004)

3.129 W.Z. Li, S.S. Xie, L.X. Qian, B.H. Chang, B.S. Zou, W.Y. Zhou, R.A. Zha, G. Wang: Large scale synthesis of aligned carbon nanotubes, Science **274**, 1701–1703 (1996)

3.130 F. Zheng, L. Liang, Y. Gao, J.H. Sukamto, L. Aardahl: Carbon nanotubes synthesis using mesoporous silica templates, Nano Lett. **2**, 729–732 (2002)

3.131 S.H. Jeong, O.-K. Lee, K.H. Lee, S.H. Oh, C.G. Park: Preparation of aligned carbon nanotubes with prescribed dimension: Template synthesis and sonication cutting approach, Chem. Mater. **14**, 1859–1862 (2002)

3.132 N.S. Kim, Y.T. Lee, J. Park, H. Ryu, H.J. Lee, S.Y. Choi, J. Choo: Dependence of vertically aligned growth of carbon nanotubes on catalyst, J. Phys. Chem. B **106**, 9286–9290 (2002)

3.133 C.J. Lee, D.W. Kim, T.J. Lee, Y.C. Choi, Y.S. Park, Y.H. Lee, W.B. Choi, N.S. Lee, G.-S. Park, J.M. Kim: Synthesis of aligned carbon nanotubes using thermal chemical vapor deposition, Chem. Phys. Lett. **312**, 461–468 (1999)

3.134 W.D. Zhang, Y. Wen, S.M. Liu, W.C. Tjiu, G.Q. Xu, L.M. Gan: Synthesis of vertically aligned carbon nanotubes on metal deposited quartz plates, Carbon **40**, 1981–1989 (2002)

3.135 S. Huang, L. Dai, A.W.H. Mau: Controlled fabrication of large scale aligned carbon nanofiber/nanotube patterns by photolithography, Adv. Mater. **14**, 1140–1143 (2002)

3.136 T. Sun, G. Wang, H. Liu, L. Feng, D. Zhu: Control over the wettability of an aligned carbon nanotube film, J. Am. Chem. Soc. **125**, 14996–14997 (2003)

3.137 Y. Huh, J.Y. Lee, J. Cheon, Y.K. Hong, J.Y. Koo, T.J. Lee, C.J. Lee: Controlled growth of carbon nanotubes over cobalt nanoparticles by thermal chemical vapor deposition, J. Mater. Chem. **13**, 2297–2300 (2003)

3.138 Y. Kobayashi, H. Nakashima, D. Takagi, Y. Homma: CVD growth of single-walled carbon nanotubes using size-controlled nanoparticle catalyst, Thin Solid Films **464/465**, 286–289 (2004)

3.139 C.L. Cheung, A. Kurtz, H. Park, C.M. Lieber: Diameter-controlled synthesis of carbon nanotubes, J. Phys. Chem. B **106**, 2429–2433 (2002)

3.140 Y. Huh, J.Y. Lee, J. Cheon, Y.K. Hong, J.Y. Koo, T.J. Lee, C.J. Lee: Controlled growth of carbon nanotubes over cobalt nanoparticles by thermal chemical vapor deposition, J. Mater. Chem. **13**, 2297–2300 (2003)

3.199 G.E. Froudakis: Why alkali-metal-doped carbon nanotubes possess high hydrogen uptake, Nano Lett. **1**, 531–533 (2001)

3.200 H. Ulbricht, G. Moos, T. Hertel: Physisorption of molecular oxygen on single-wall carbon nanotube bundles and graphite, Phys. Rev. B **66**, 075404–1–075404–7 (2002)

3.201 H. Ulbricht, J. Kriebel, G. Moos, T. Hertel: Desorption kinetics and interaction of Xe with single-wall carbon nanotube bundles, Chem. Phys. Lett. **363**, 252–260 (2002)

3.202 J.-C. Charlier, X. Blase, S. Roche: Electronic and transport properties of carbon nanotubes, Rev. Mod. Phys. **79**, 677–732 (2007)

3.203 R. Saito, G. Dresselhaus, M.S. Dresselhaus: *Physical Properties of Carbon Nanotubes* (Imperial College Press, London 1998)

3.204 A. Charlier, E. McRae, R. Heyd, M.F. Charlier, D. Moretti: Classification for double-walled carbon nanotubes, Carbon **37**, 1779–1783 (1999)

3.205 A. Charlier, E. McRae, R. Heyd, M.F. Charlier: Metal semi-conductor transitions under uniaxial stress for single- and double-walled carbon nanotubes, J. Phys. Chem. Solids **62**, 439–444 (2001)

3.206 P. Puech, H. Hubel, D. Dunstan, R.R. Bacsa, C. Laurent, W.S. Bacsa: Discontinuous tangential stress in double wall carbon nanotubes, Phys. Rev. Lett. **93**, 095506 (2004)

3.207 P.M. Ajayan, M. Terrrones, A. de la Guardia, V. Hue, N. Grobert, B.Q. Wei, H. Lezec, G. Ramanath, T.W. Ebbesen: Nanotubes in a flash – Ignition and reconstruction, Science **296**, 705 (2002)

3.208 H. Ajiki, T. Ando: Electronic states of carbon nanotubes, J. Phys. Soc. Jpn. **62**, 1255–1266 (1993)

3.209 T. Ando: Excitons in carbon nanotubes, J. Phys. Soc. Jpn. **66**, 1066 (1997)

3.210 S.M. Bachilo, M.S. Strano, C. Kittrell, R.H. Hauge, R.E. Smalley, R.B. Weisman: Structure-assigned optical spectra of single-walled carbon nanotubes, Science **298**, 2361 (2002)

3.211 M. Bockrath, D.H. Cobden, J. Lu, A.G. Rinzler, R.E. Smalley, L. Balents, P.L. McEuen: Luttinger liquid behaviour in carbon nanotubes, Nature **397**, 598–601 (1999)

3.212 C.T. White, T.N. Todorov: Carbon nanotubes as long ballistic conductors, Nature **393**, 240–242 (1998)

3.213 S. Frank, P. Poncharal, Z.L. Wang, W.A. de Heer: Carbon nanotube quantum resistors, Science **280**, 1744–1746 (1998)

3.214 W. Liang, M. Bockrath, D. Bozovic, J.H. Hafner, M. Tinkham, H. Park: Fabry–Perot interference in a nanotube electron waveguide, Nature **411**, 665–669 (2001)

3.215 L. Langer, V. Bayot, E. Grivei, J.-P. Issi, J.-P. Heremans, C.H. Olk, L. Stockman, C. van Haesendonck, Y. Buynseraeder: Quantum transport in a multiwalled carbon nanotube, Phys. Rev. Lett. **76**, 479–482 (1996)

3.216 K. Liu, S. Roth, G.S. Duesberg, G.T. Kim, D. Popa, K. Mukhopadhyay, R. Doome, J. B'Nagy: Antilocalization in multiwalled carbon nanotubes, Phys. Rev. B **61**, 2375–2379 (2000)

3.217 G. Fedorov, B. Lassagne, M. Sagnes, B. Raquet, J.M. Broto, F. Triozon, S. Roche, E. Flahaut: Gate-dependent magnetoresistance phenomena in carbon nanotubes, Phys. Rev. Lett. **94**, 66801–66804 (2005)

3.218 A. Javey, J. Guo, Q. Wang, M. Lundstrom, H. Dai: Ballistic carbon nanotube field-effect transistors, Nature **424**, 654–657 (2003)

3.219 Y.A. Kasumov, R. Deblock, M. Kociak, B. Reulet, H. Bouchiat, I.I. Khodos, Y.B. Gorbatov, V.T. Volkov, C. Journet, M. Burghard: Supercurrents through single-walled carbon nanotubes, Science **284**, 1508–1511 (1999)

3.220 B.W. Alphenaar, K. Tsukagoshi, M. Wagner: Magnetoresistance of ferromagnetically contacted carbon nanotubes, Phys. Eng. **10**, 499–504 (2001)

3.221 S. Berber, Y. Kwon, D. Tomanek: Unusually high thermal conductivity of carbon nanotubes, Phys. Rev. Lett. **84**, 4613–4616 (2000)

3.222 M.-F. Yu, O. Lourie, M.J. Dyer, K. Moloni, T.F. Kelley, R.S. Ruoff: Strength and breaking mechanism of multiwalled carbon nanotubes under tensile load, Science **287**, 637–640 (2000)

3.223 D.A. Walters, L.M. Ericson, M.J. Casavant, J. Liu, D.T. Colbert, K.A. Smith, R.E. Smalley: Elastic strain of freely suspended single-wall carbon nanotube ropes, Appl. Phys. Lett. **74**, 3803–3805 (1999)

3.224 B.G. Demczyk, Y.M. Wang, J. Cumings, M. Hetman, W. Han, A. Zettl, R.O. Ritchie: Direct mechanical measurement of the tensile strength and elastic modulus of multiwalled carbon nanotubes, Mater. Sci. Eng. A **334**, 173–178 (2002)

3.225 R.P. Gao, Z.L. Wang, Z.G. Bai, W.A. De Heer, L.M. Dai, M. Gao: Nanomechanics of individual carbon nanotubes from pyrolytically grown arrays, Phys. Rev. Lett. **85**, 622–625 (2000)

3.226 M.M.J. Treacy, T.W. Ebbesen, J.M. Gibson: Exceptionally high Young's modulus observed for individual carbon nanotubes, Nature **381**, 678–680 (1996)

3.227 N. Yao, V. Lordie: Young's modulus of single-wall carbon nanotubes, J. Appl. Phys. **84**, 1939–1943 (1998)

3.228 O. Lourie, H.D. Wagner: Transmission electron microscopy observations of fracture of single-wall carbon nanotubes under axial tension, Appl. Phys. Lett. **73**, 3527–3529 (1998)

3.229 S.C. Tsang, Y.K. Chen, P.J.F. Harris, M.L.H. Green: A simple chemical method of opening and filling carbon nanotubes, Nature **372**, 159–162 (1994)

3.230 M. Monthioux: Filling single-wall carbon nanotubes, Carbon **40**, 1809–1823 (2002)

3.231 W.K. Hsu, S.Y. Chu, E. Munoz-Picone, J.L. Boldu, S. Firth, P. Franchi, B.P. Roberts, A. Shilder, H. Terrones, N. Grobert, Y.Q. Zhu, M. Terrones,

M.E. McHenry, H.W. Kroto, D.R.M. Walton: Metallic behaviour of boron-containing carbon nanotubes, Chem. Phys. Lett. **323**, 572–579 (2000)
3.232 R. Czerw, M. Terrones, J.C. Charlier, X. Blasé, B. Foley, R. Kamalakaran, N. Grobert, H. Terrones, D. Tekleab, P.M. Ajayan, W. Blau, M. Rühle, D.L. Caroll: Identification of electron donor states, in N-doped carbon nanotubes, Nano Lett. **1**, 457–460 (2001)
3.233 O. Stephan, P.M. Ajayan, C. Colliex, P. Redlich, J.M. Lambert, P. Bernier, P. Lefin: Doping graphitic and carbon nanotube structures with boron and nitrogen, Science **266**, 1683–1685 (1994)
3.234 A. Loiseau, F. Willaime, N. Demoncy, N. Schramchenko, G. Hug, C. Colliex, H. Pascard: Boron nitride nanotubes, Carbon **36**, 743–752 (1998)
3.235 C.C. Tang, L.M. de la Chapelle, P. Li, Y.M. Liu, H.Y. Dang, S.S. Fan: Catalytic growth of nanotube and nanobamboo structures of boron nitride, Chem. Phys. Lett. **342**, 492–496 (2001)
3.236 K. Suenaga, C. Colliex, N. Demoncy, A. Loiseau, H. Pascard, F. Willaime: Synthesis of nanoparticles and nanotubes with well separated layers of boron-nitride and carbon, Science **278**, 653–655 (1997)
3.237 D. Golberg, Y. Bando, L. Bourgeois, K. Kurashima, T. Sato: Large-scale synthesis and HRTEM analysis of single-walled B- and N-doped carbon nanotube bundles, Carbon **38**, 2017–2027 (2000)
3.238 R.S. Lee, J. Gavillet, M. Lamy de la Chapelle, A. Loiseau, J.-L. Cochon, D. Pigache, J. Thibault, F. Willaime: Catalyst-free synthesis of boron nitride single-wall nanotubes with a preferred zig-zag configuration, Phys. Rev. B **64**, 121405.1–121405.4 (2001)
3.239 B. Burteaux, A. Claye, B.W. Smith, M. Monthioux, D.E. Luzzi, J.E. Fischer: Abundance of encapsulated C_{60} in single-wall carbon nanotubes, Chem. Phys. Lett. **310**, 21–24 (1999)
3.240 D. Ugarte, A. Châtelain, W.A. de Heer: Nanocapillarity and chemistry in carbon nanotubes, Science **274**, 1897–1899 (1996)
3.241 J. Cook, J. Sloan, M.L.H. Green: Opening and filling carbon nanotubes, Fuller. Sci. Technol. **5**, 695–704 (1997)
3.242 P.M. Ajayan, S. Iijima: Capillarity-induced filling of carbon nanotubes, Nature **361**, 333–334 (1993)
3.243 P.M. Ajayan, T.W. Ebbesen, T. Ichihashi, S. Iijima, K. Tanigaki, H. Hiura: Opening carbon nanotubes with oxygen and implications for filling, Nature **362**, 522–525 (1993)
3.244 S. Seraphin, D. Zhou, J. Jiao, J.C. Withers, R. Loufty: Yttrium carbide in nanotubes, Nature **362**, 503 (1993)
3.245 S. Seraphin, D. Zhou, J. Jiao, J.C. Withers, R. Loufty: Selective encapsulation of the carbides of yttrium and titanium into carbon nanoclusters, Appl. Phys. Lett. **63**, 2073–2075 (1993)
3.246 R.S. Ruoff, D.C. Lorents, B. Chan, R. Malhotra, S. Subramoney: Single-crystal metals encapsulated in carbon nanoparticles, Science **259**, 346–348 (1993)
3.247 A. Loiseau, H. Pascard: Synthesis of long carbon nanotubes filled with Se, S, Sb, and Ge by the arc method, Chem. Phys. Lett. **256**, 246–252 (1996)
3.248 N. Demoncy, O. Stephan, N. Brun, C. Colliex, A. Loiseau, H. Pascard: Filling carbon nanotubes with metals by the arc discharge method: The key role of sulfur, Eur. Phys. J. B **4**, 147–157 (1998)
3.249 C.H. Kiang, J.S. Choi, T.T. Tran, A.D. Bacher: Molecular nanowires of 1 nm diameter from capillary filling of single-walled carbon nanotubes, J. Phys. Chem. B **103**, 7449–7551 (1999)
3.250 Z.L. Zhang, B. Li, Z.J. Shi, Z.N. Gu, Z.Q. Xue, L.M. Peng: Filling of single-walled carbon nanotubes with silver, J. Mater. Res. **15**, 2658–2661 (2000)
3.251 A. Govindaraj, B.C. Satishkumar, M. Nath, C.N.R. Tao: Metal nanowires and intercalated metal layers in single-walled carbon nanotubes bundles, Chem. Mater. **12**, 202–205 (2000)
3.252 J. Mittal, M. Monthioux, H. Allouche: Room temperature filling of single-wall carbon nanotubes with chromium oxide in open air, Chem. Phys. Lett. **339**, 311–318 (2001)
3.253 E. Dujardin, T.W. Ebbesen, H. Hiura, K. Tanigaki: Capillarity and wetting of carbon nanotubes, Science **265**, 1850–1852 (1994)
3.254 E. Flahaut, J. Sloan, K.S. Coleman, V.C. Williams, S. Friedrichs, N. Hanson, M.L.H. Green: 1D p-block halide crystals confined into single walled carbon nanotubes, Proc. Mater. Res. Soc. Symp., Vol. 633 (2001) pp. A13.15.1–A13.15.6
3.255 J. Sloan, A.I. Kirkland, J.L. Hutchison, M.L.H. Green: Integral atomic layer architectures of 1D crystals inserted into single walled carbon nanotubes, Chem. Commun., 1319–1332 (2002)
3.256 J. Sloan, M.C. Novotny, S.R. Bailey, G. Brown, C. Xu, V.C. Williams, S. Friedrichs, E. Flahaut, R.L. Callender, A.P.E. York, K.S. Coleman, M.L.H. Green, R.E. Dunin-Borkowski, J.L. Hutchison: Two layer 4 : 4 co-ordinated KI crystals grown within single walled carbon nanotubes, Chem. Phys. Lett. **329**, 61–65 (2000)
3.257 G. Brown, S.R. Bailey, J. Sloan, C. Xu, S. Friedrichs, E. Flahaut, K.S. Coleman, J.L. Hutchinson, R.E. Dunin-Borkowski, M.L.H. Green: Electron beam induced in situ clusterisation of 1D $ZrCl_4$ chains within single-walled carbon nanotubes, Chem. Commun., 845–846 (2001)
3.258 J. Sloan, D.M. Wright, H.G. Woo, S. Bailey, G. Brown, A.P.E. York, K.S. Coleman, J.L. Hutchison, M.L.H. Green: Capillarity and silver nanowire formation observed in single walled carbon nanotubes, Chem. Commun., 699–700 (1999)
3.259 X. Fan, E.C. Dickey, P.C. Eklund, K.A. Williams, L. Grigorian, R. Buczko, S.T. Pantelides, S.J. Pennycook: Atomic arrangement of iodine atoms inside single-walled carbon nanotubes, Phys. Rev. Lett. **84**, 4621–4624 (2000)

3.260 G. Brown, S.R. Bailey, M. Novotny, R. Carter, E. Flahaut, K.S. Coleman, J.L. Hutchison, M.L.H. Green, J. Sloan: High yield incorporation and washing properties of halides incorporated into single walled carbon nanotubes, Appl. Phys. A **76**, 457–462 (2003)

3.261 J. Sloan, D.E. Luzzi, A.I. Kirkland, J.L. Hutchison, M.L.H. Green: Imaging and characterization of molecules and one-dimensional crystals formed within carbon nanotubes, Mater. Res. Soc. Bull. **29**, 265–271 (2004)

3.262 J. Chancolon, F. Archaimbault, A. Pineau, S. Bonnamy: Confinement of selenium into carbon nanotubes, Fuller. Nanotub. Carbon Nanostruct. **13**, 189–194 (2005)

3.263 B.W. Smith, M. Monthioux, D.E. Luzzi: Encapsulated C_{60} in carbon nanotubes, Nature **396**, 323–324 (1998)

3.264 B.W. Smith, D.E. Luzzi: Formation mechanism of fullerene peapods and coaxial tubes: A path to large scale synthesis, Chem. Phys. Lett. **321**, 169–174 (2000)

3.265 K. Hirahara, K. Suenaga, S. Bandow, H. Kato, T. Okazaki, H. Shinohara, S. Iijima: One-dimensional metallo-fullerene crystal generated inside single-walled carbon nanotubes, Phys. Rev. Lett. **85**, 5384–5387 (2000)

3.266 B.W. Smith, M. Monthioux, D.E. Luzzi: Carbon nanotube encapsulated fullerenes: A unique class of hybrid material, Chem. Phys. Lett. **315**, 31–36 (1999)

3.267 D.E. Luzzi, B.W. Smith: Carbon cage structures in single wall carbon nanotubes: A new class of materials, Carbon **38**, 1751–1756 (2000)

3.268 S. Bandow, M. Takisawa, K. Hirahara, M. Yudasoka, S. Iijima: Raman scattering study of double-wall carbon nanotubes derived from the chains of fullerenes in single-wall carbon nanotubes, Chem. Phys. Lett. **337**, 48–54 (2001)

3.269 Y. Sakurabayashi, M. Monthioux, K. Kishita, Y. Suzuki, T. Kondo, M. Le Lay: Tayloring double wall carbon nanotubes?. In: *Molecular Nanostructures*, Am. Inst. Phys. Conf. Proc., Vol. 685, ed. by H. Kuzmany, J. Fink, M. Mehring, S. Roth (Springer, Berlin Heidelberg 2003) pp. 302–305

3.270 B.W. Smith, D.E. Luzzi, Y. Achiba: Tumbling atoms and evidence for charge transfer in $La_2@C_{80}$@SWNT, Chem. Phys. Lett. **331**, 137–142 (2000)

3.271 K. Suenaga, M. Tence, C. Mory, C. Colliex, H. Kato, T. Okazaki, H. Shinohara, K. Hirahara, S. Bandow, S. Iijima: Element-selective single atom imaging, Science **290**, 2280–2282 (2000)

3.272 D.E. Luzzi, B.W. Smith, R. Russo, B.C. Satishkumar, F. Stercel, N.R.C. Nemes: Encapsulation of metallofullerenes and metallocenes in carbon nanotubes, Proc. Electron. Prop. Nov. Mater. – XVI Int. Winterssch. – AIP Conf. Proc., ed. by H. Kuzmany, J. Fink, M. Mehring, S. Roth (Springer, Berlin Heidelberg 2001) pp. 622–626

3.273 D.J. Hornbaker, S.-J. Kahng, S. Misra, B.W. Smith, A.T. Johnson, E.J. Mele, D.E. Luzzi, A. Yazdani: Mapping the one-dimensional electronic states of nanotube peapod structures, Science **295**, 828–831 (2002)

3.274 H. Kondo, H. Kino, T. Ohno: Transport properties of carbon nanotubes encapsulating C_{60} and related materials, Phys. Rev. B **71**, 115413 (2005)

3.275 S.H. Jhang, S.W. Lee, D.S. Lee, Y.W. Park, G.H. Jeong, T. Hirata, R. Hatakeyama, U. Dettlaff, S. Roth, M.S. Kabir, E.E.B. Campbell: Random telegraph noise in carbon nanotube peapod transistors, Fuller. Nanotub. Carbon Nanostruct. **13**, 195–198 (2005)

3.276 G.H. Jeong, R. Hatakeyama, T. Hirata, K. Tohji, K. Motomiya, N. Sato, Y. Kawazoe: Structural deformation of single-walled carbon nanotubes and fullerene encapsulation due to magnetized plasma ion irradiation, Appl. Phys. Lett. **79**, 4213–4215 (2001)

3.277 Y.P. Sun, K. Fu, Y. Lin, W. Huang: Functionalized carbon nanotubes: Properties and applications, Acc. Chem. Res. **35**, 1095–1104 (2002)

3.278 S. Osswald, E. Flahaut, H. Ye, Y. Gogotsi: Elimination of D-band in Raman spectra of double-wall carbon nanotubes by oxidation, Chem. Phys. Lett. **402**, 422–427 (2005)

3.279 J. Chen, M.A. Hamon, M. Hui, C. Yongsheng, A.M. Rao, P.C. Eklund, R.C. Haddon: Solution properties of single-walled carbon nanotubes, Science **282**, 95–98 (1998)

3.280 J. Chen, A.M. Rao, S. Lyuksyutov, M.E. Itkis, M.A. Hamon, H. Hu, R.W. Cohn, P.C. Eklund, D.T. Colbert, R.E. Smalley, R.C. Haddon: Dissolution of full-length single-walled carbon nanotubes, J. Phys. Chem. B **105**, 2525–2528 (2001)

3.281 F. Pompeo, D.E. Resasco: Water solubilization of single-walled carbon nanotubes by functionalization with glucosamine, Nano Lett. **2**, 369–373 (2002)

3.282 Y.P. Sun, W. Huang, Y. Lin, K. Fu, A. Kitaygorodskiy, L.A. Riddle, Y.J. Yu, D.L. Carroll: Soluble dendron-functionalized carbon nanotubes: Preparation, characterization, and properties, Chem. Mater. **13**, 2864–2869 (2001)

3.283 K. Fu, W. Huang, Y. Lin, L.A. Riddle, D.L. Carroll, Y.P. Sun: Defunctionalization of functionalized carbon nanotubes, Nano Lett. **1**, 439–441 (2001)

3.284 P.W. Chiu, G.S. Duesberg, U. Dettlaff-Weglikowska, S. Roth: Interconnection of carbon nanotubes by chemical functionalization, Appl. Phys. Lett. **80**, 3811–3813 (2002)

3.285 T. Fukushima, T. Aida: Ionic liquids for soft functional materials with carbon nanotubes, Chem. Eur. J. **13**, 5048–5058 (2007)

3.286 Y. Lei, C. Xiong, L. Dong, H. Guo, X. Su, J. Yao, Y. You, D. Tian, X. Shang: Ionic liquid of ultralong carbon nanotubes, Small **3**, 1889–1893 (2007)

3.287 E.T. Mickelson, C.B. Huffman, A.G. Rinzler, R.E. Smalley, R.H. Hauge, J.L. Margrave: Fluorination of single-wall carbon nanotubes, Chem. Phys. Lett. **296**, 188–194 (1998)

3.288 V.N. Khabashesku, W.E. Billups, J.L. Margrave: Fluorination of single-wall carbon nanotubes and

subsequent derivatization reactions, Acc. Chem. Res. **35**, 1087–1095 (2002)
3.289 P.J. Boul, J. Liu, E.T. Michelson, C.B. Huffman, L.M. Ericson, I.W. Chiang, K.A. Smith, D.T. Colbert, R.H. Hauge, J.L. Margrave, R.E. Smalley: Reversible side-wall functionalization of buckytubes, Chem. Phys. Lett. **310**, 367–372 (1999)
3.290 J.L. Bahr, J. Yang, D.V. Kosynkin, M.J. Bronikowski, R.E. Smalley, J.M. Tour: Functionalization of carbon nanotubes by electrochemical reduction of aryl diazonium salts: A bucky paper electrode, J. Am. Chem. Soc. **123**, 6536–6542 (2001)
3.291 M. Holzinger, O. Vostrowsky, A. Hirsch, F. Hennrich, M. Kappes, R. Weiss, F. Jellen: Sidewall functionalization of carbon nanotubes, Angew. Chem. Int. Ed. **40**, 4002–4005 (2001)
3.292 Y. Chen, R.C. Haddon, S. Fang, A.M. Rao, P.C. Eklund, W.H. Lee, E.C. Dickey, E.A. Grulke, J.C. Pendergrass, A. Chavan, B.E. Haley, R.E. Smalley: Chemical attachment of organic functional groups to single-walled carbon nanotube material, J. Mater. Res. **13**, 2423–2431 (1998)
3.293 C. Velasco-Santos, A.L. Martinez-Hernandez, M. Lozada-Cassou, A. Alvarez-Castillo, V.M. Castano: Chemical functionalization of carbon nanotubes through an organosilane, Nanotechnology **13**, 495–498 (2002)
3.294 A. Star, J.F. Stoddart, D. Steuerman, M. Diehl, A. Boukai, E.W. Wong, X. Yang, S.W. Chung, H. Choi, J.R. Heath: Preparation and properties of polymer-wrapped single-walled carbon nanotubes, Angew. Chem. Int. Ed. **41**, 1721–1725 (2002)
3.295 A. Pénicaud, P. Poulin, A. Derré, E. Anglaret, P. Petit: Spontaneous dissolution of a single-wall carbon nanotube salt, J. Am. Chem. Soc. **127**, 8–9 (2005)
3.296 R. Stevens, C. Nguyen, A. Cassel, L. Delzeit, M. Meyyappan, J. Han: Improved fabrication approach for carbon nanotube probe devices, Appl. Phys. Lett. **77**, 3453–3455 (2000)
3.297 J.H. Hafner, C.L. Cheung, A.T. Wooley, C.M. Lieber: Structural and functional imaging with carbon nanotube AFM probes, Progr. Biophys. Mol. Biol. **77**, 73–110 (2001)
3.298 S.S. Wong, E. Joselevich, A.T. Woodley, C.L. Cheung, C.M. Lieber: Covalently functionalized nanotubes as nanometre-size probes in chemistry and biology, Nature **394**, 52–55 (1998)
3.299 C.L. Cheung, J.H. Hafner, C.M. Lieber: Carbon nanotube atomic force microscopy tips: Direct growth by chemical vapor deposition and application to high-resolution imaging, Proc. Natl. Acad. Sci. USA **97**, 3809–3813 (2000)
3.300 W.A. de Heer, A. Châtelain, D. Ugarte: A carbon nanotube field-emission electron source, Science **270**, 1179–1180 (1995)
3.301 J.M. Bonard, J.P. Salvetat, T. Stockli, W.A. de Heer, L. Forro, A. Chatelâin: Field emission from single-wall carbon nanotube films, Appl. Phys. Lett. **73**, 918–920 (1998)
3.302 W. Zhu, C. Bower, O. Zhou, G. Kochanski, S. Jin: Large curent density from carbon nanotube field emitters, Appl. Phys. Lett. **75**, 873–875 (1999)
3.303 Y. Saito, R. Mizushima, T. Tanaka, K. Tohji, K. Uchida, M. Yumura, S. Uemura: Synthesis, structure, and field emission of carbon nanotubes, Fuller. Sci. Technol. **7**, 653–664 (1999)
3.304 J. Kong, N.R. Franklin, C. Zhou, M.G. Chapline, S. Peng, K. Cho, H. Dai: Nanotube molecular wire as chemical sensors, Science **287**, 622–625 (2000)
3.305 P.G. Collins, K. Bradley, M. Ishigami, A. Zettl: Extreme oxygen sensitivity of electronic properties of carbon nanotubes, Science **287**, 1801–1804 (2000)
3.306 H. Chang, J.D. Lee, S.M. Lee, Y.H. Lee: Adsorption of NH_3 and NO_2 molecules on carbon nanotubes, Appl. Phys. Lett. **79**, 3863–3865 (2001)
3.307 C. Cantalini, L. Valentini, L. Lozzi, I. Armentano, J.M. Kenny, S. Santucci: NO_2 gas sensitivity of carbon nanotubes obtained by plasma enhanced chemical vapor deposition, Sens. Actuators B **93**, 333–337 (2003)
3.308 J. Li, Y. Lu, Q. Ye, M. Cinke, J. Han, M. Meyyappan: Carbon nanotubes sensors for gas and organic vapor detection, Nano Lett. **3**, 929–933 (2003)
3.309 O.K. Varghese, P.D. Kichambre, D. Gong, K.G. Ong, E.C. Dickey, C.A. Grimes: Gas sensing characteristics of multi-wall carbon nanotubes, Sens. Actuators B **81**, 32–41 (2001)
3.310 K.G. Ong, K. Zeng, C.A. Grimes: A wireless, passive carbon nanotube-based gas sensor, IEEE Sens. J. **2**(2), 82–88 (2002)
3.311 J. Kong, M.G. Chapline, H. Dai: Functionalized carbon nanotubes for molecular hydrogen sensors, Adv. Mater. **13**, 1384–1386 (2001)
3.312 A. Modi, N. Koratkar, E. Lass, B. Wei, P.M. Ajayan: Miniaturized gas ionisation sensors using carbon nanotubes, Nature **424**, 171–174 (2003)
3.313 F. Rodriguez-Reinoso: The role of carbon materials in heterogeneous catalysis, Carbon **36**, 159–175 (1998)
3.314 E. Auer, A. Freund, J. Pietsch, T. Tacke: Carbon as support for industrial precious metal catalysts, Appl. Catal. A **173**, 259–271 (1998)
3.315 J.M. Planeix, N. Coustel, B. Coq, B. Botrons, P.S. Kumbhar, R. Dutartre, P. Geneste, P. Bernier, P.M. Ajayan: Application of carbon nanotubes as supports in heterogeneous catalysis, J. Am. Chem. Soc. **116**, 7935–7936 (1994)
3.316 P. Serp, M. Corrias, P. Kalck: Carbon nanotubes and nanofibers in catalysis, Appl. Catal. A **253**, 337–358 (2003)
3.317 K.P. De Jong, J.W. Geus: Carbon nanofibers: catalytic synthesis and applications, Catal. Rev. **42**, 481–510 (2000)

3.318 N.F. Goldshleger: Fullerene and fullerene-based materials in catalysis, Fuller. Sci. Technol. **9**, 255–280 (2001)

3.319 X. Pan, Z. Fan, W. Chen, Y. Ding, H. Luo, X. Bao: Enhanced ethanol production inside carbon-nanotube reactors containing catalytic particles, Nat. Mater. **6**, 507–511 (2007)

3.320 M.F.R. Pereira, J.L. Figueiredo, J.J.M. Órfão, P. Serp, P. Kalck, Y. Kihn: Catalytic activity of carbon nanotubes in the oxidative dehydrogenation of ethylbenzene, Carbon **42**, 2807–2813 (2004)

3.321 G. Mestl, N.I. Maksimova, N. Keller, V.V. Roddatis, R. Schlögl: Carbon nanofilaments in heterogeneous catalysis: An industrial application for new carbon materials?, Angew. Chem. Int. Ed. Engl. **40**, 2066–2068 (2001)

3.322 N. Muradov: Catalysis of methane decomposition over elemental carbon, Catal. Commun. **2**, 89–94 (2001)

3.323 J.E. Fischer, A.T. Johnson: Electronic properties of carbon nanotubes, Curr. Opin. Solid State Mater. Sci. **4**, 28–33 (1999)

3.324 M. Menon, A.N. Andriotis, G.E. Froudakis: Curvature dependence of the metal catalyst atom interaction with carbon nanotubes walls, Chem. Phys. Lett. **320**, 425–434 (2000)

3.325 N. Ishigami, H. Ago, Y. Motoyama, M. Takasaki, M. Shinagawa, K. Takahashi, T. Ikuta, M. Tsuji: Microreactor utilizing a vertically-aligned carbon nanotube array grown inside the channels, Chem. Commun., 1626 (2007)

3.326 G.G. Wildgoose, C.E. Banks, R.G. Compton: Metal nanoparticles and related materials supported on carbon nanotubes: methods and applications, Small **2**, 182–193 (2006)

3.327 T. Kyotani, S. Nakazaki, W.-H. Xu, A. Tomita: Chemical modification of the inner walls of carbon nanotubes by HNO_3 oxidation, Carbon **39**, 782–785 (2001)

3.328 Z.J. Liu, Z.Y. Yuan, W. Zhou, L.M. Peng, Z. Xu: Co/carbon nanotubes monometallic system: The effects of oxidation by nitric acid, PhysChemChemPhys **3**, 2518–2521 (2001)

3.329 R. Giordano, P. Serp, P. Kalck, Y. Kihn, J. Schreiber, C. Marhic, J.-L. Duvail: Preparation of rhodium supported on carbon canotubes catalysts via surface mediated organometallic reaction, Eur. J. Inorg. Chem. **2003**, 610–617 (2003)

3.330 A. Carrillo, J.A. Swartz, J.M. Gamba, R.S. Kane, N. Chakrapani, B. Wei, P.M. Ajayan: Noncovalent functionalization of graphite and carbon nanotubes with polymer multilayers and gold nanoparticles, Nano Lett. **3**, 1437–1440 (2003)

3.331 Z. Liu, X. Lin, J.Y. Lee, W. Zhang, M. Han, L.M. Gan: Preparation and characterization of platinum-based electrocatalysts on multiwalled carbon nanotubes for proton exchange membrane fuel cells, Langmuir **18**, 4054–4060 (2002)

3.332 H.-B. Chen, J.D. Lin, Y. Cai, X.Y. Wang, J. Yi, J. Wang, G. Wei, Y.Z. Lin, D.W. Liao: Novel multi-walled nanotube-supported and alkali-promoted Ru catalysts for ammonia synthesis under atmospheric pressure, Appl. Surf. Sci. **180**, 328–335 (2001)

3.333 Y. Zhang, H.B. Zhang, G.D. Lin, P. Chen, Y.Z. Yuan, K.R. Tsai: Preparation, characterization and catalytic hydroformylation properties of carbon nanotubes-supported Rh-phosphine catalyst, Appl. Catal. A **187**, 213–224 (1999)

3.334 M.S. Dresselhaus, K.A. Williams, P.C. Eklund: Hydrogen adsorption in carbon materials, Mater. Res. Soc. Bull. **24**, 45–50 (1999)

3.335 H.-M. Cheng, Q.-H. Yang, C. Liu: Hydrogen storage in carbon nanotubes, Carbon **39**, 1447–1454 (2001)

3.336 G.G. Tibbetts, G.P. Meisner, C.H. Olk: Hydrogen storage capacity of carbon nanotubes, filaments, and vapor-grown fibers, Carbon **39**, 2291–2301 (2001)

3.337 F.L. Darkrim, P. Malbrunot, G.P. Tartaglia: Review of hydrogen storage adsorption in carbon nanotubes, Int. J. Hydrogen Energy **27**, 193–202 (2002)

3.338 G.E. Froudakis: Hydrogen interaction with carbon nanotubes: a review of ab initio studies, J. Phys. Condens. Matter **14**, R453–R465 (2002)

3.339 M. Hirscher, M. Becher: Hydrogen storage in carbon nanotubes, J. Nanosci. Nanotechnol. **3**(1/2), 3–17 (2003)

3.340 P. Kowalczyk, R. Hołyst, M. Terrones, H. Terrones: Hydrogen storage in nanoporous carbon materials: myth and facts, PhysChemChemPhys **9**(15), 1786–1792 (2007)

3.341 C. Park, P.E. Anderson, C.D. Tan, R. Hidalgo, N. Rodriguez: Further studies of the interaction of hydrogen with graphite nanofibers, J. Phys. Chem. B **103**, 10572–10581 (1999)

3.342 S.M. Lee, H.Y. Lee: Hydrogen storage in single-walled carbon nanotubes, Appl. Phys. Lett. **76**, 2877–2879 (2000)

3.343 X. Zhang, D. Cao, J. Chen: Hydrogen adsorption storage on single-walled carbon nanotube arrays by a combination of classical potential and density functional theory, J. Phys. Chem. B **107**, 4942–4950 (2003)

3.344 H.M. Cheng, G.P. Pez, A.C. Cooper: Mechanism of hydrogen sorption in single-walled carbon nanotubes, J. Am. Chem. Soc. **123**, 5845–5846 (2001)

3.345 C.-H. Chen, C.-C. Huang: Hydrogen storage by KOH-modified multi-walled carbon nanotubes, Int. J. Hydrogen Energy **32**, 237–246 (2007)

3.346 M.A. de la Casa-Lillo, F. Lamari-Darkrim, D. Cazorla-Amoros, A. Linares-Solano: Hydrogen storage in activated carbons and activated carbon fibers, J. Phys. Chem. B **106**, 10930–10934 (2002)

3.347 P. Marinelli, R. Pellenq, J. Conard: H stocké dans les carbones un site légèrement métastable, Natl. Conf. Mater., Tours (2002), AF-14-020

3.348 G. Mpourmpakis, G.E. Froudakis, G.P. Lithoxoos, J. Samios: Effect of curvature and chirality for hy-

3.408 E. Flahaut, A. Peigney, C. Laurent, C. Marlière, F. Chastel, A. Rousset: Carbon nanotube-metal-oxide nanocomposites: Microstructure, electrical conductivity and mechanical properties, Acta Mater. **48**, 3803–3812 (2000)

3.409 J.W. An, D.H. You, D.S. Lim: Tribological properties of hot-pressed alumina-CNT composites, Wear **255**, 677–681 (2003)

3.410 J. Ning, J. Zhang, Y. Pan, J. Guo: Surfactants assisted processing of carbon nanotube-reinforced SiO_2 matrix composites, Ceram. Int. **30**, 63–67 (2004)

3.411 Q. Huang, L. Gao: Manufacture and electrical properties of multiwalled carbon nanotube/$BaTiO_3$ nanocomposite ceramics, J. Mater. Chem. **14**, 2536–2541 (2004)

3.412 J. Fan, D. Zhao, M. Wu, Z. Xu, J. Song: Preparation and microstructure of multi-wall carbon nanotubes-toughened Al_2O_3 composite, J. Am. Ceram. Soc. **89**, 750–753 (2006)

3.413 A. Peigney, S. Rul, F. Lefevre-Schlick, C. Laurent: Densification during hot-pressing of carbon nanotube metal-ceramic composites, J. Eur. Ceram. Soc. **27**, 2183–2193 (2007)

3.414 J. Sun, L. Gao, W. Li: Colloidal processing of carbon nanotube/alumina composites, Chem. Mater. **14**, 5169–5172 (2002)

3.415 G.D. Zhan, J.D. Kuntz, J. Wan, A.K. Mukherjee: Single-wall carbon nanotubes as attractive toughening agents in alumina-based composites, Nat. Mater. **2**, 38–42 (2003)

3.416 S.I. Cha, K.T. Kim, K.H. Lee, C.B. Mo, S.H. Hong: Strengthening and toughening of carbon nanotube reinforced alumina nanocomposite fabricated by molecular level mixing process, Scr. Mater. **53**, 793–797 (2005)

3.417 C.B. Mo, S.I. Cha, K.T. Kim, K.H. Lee, S.H. Hong: Fabrication of carbon nanotube reinforced alumina matrix nanocomposite by sol-gel process, Mater. Sci. Eng. A **395**, 124–128 (2005)

3.418 X. Wang, N.P. Padture, H. Tanaka: Contact-damage-resistant ceramic/single-wall carbon nanotubes and ceramic/graphite composites, Nat. Mater. **3**, 539–544 (2004)

3.419 W.A. Curtin, B.W. Sheldon: CNT-reinforced ceramics and metals, Mater. Today **7**, 44–49 (2004)

3.420 Z. Xia, L. Riester, W.A. Curtin, H. Li, B.W. Sheldon, J. Liang, B. Chang, J.M. Xu: Direct observation of toughening mechanisms in carbon nanotube ceramic matrix composites, Acta Mater. **52**, 931–944 (2004)

3.421 D.S. Lim, J.W. An, H.J. Lee: Effect of carbon nanotube addition on the tribological behavior of carbon/carbon composites, Wear **252**, 512–517 (2002)

3.422 D.-S. Lim, D.-H. You, H.-J. Choi, S.-H. Lim, H. Jang: Effect of CNT distribution on tribological behavior of alumina-CNT composites, Wear **259**, 539–544 (2005)

3.423 Z.H. Xia, J. Lou, W.A. Curtin: A multiscale experiment on the tribological of aligned carbon nanotube/ceramic composites, Scr. Mater. **58**, 223–226 (2008)

3.424 G.-D. Zhan, J.D. Kuntz, H. Wang, C.-M. Wang, A.K. Mukherjee: Anisotropic thermal properties of single-wall-carbon-nanotube-reinforced nanoceramics, Philos. Mag. Lett. **84**, 419–423 (2004)

3.425 Q. Huang, L. Gao, Y. Liu, J. Sun: Sintering and thermal properties of multiwalled carbon nanotube-$BaTiO_3$ composites, J. Mater. Chem. **15**, 1995–2001 (2005)

3.426 G.-D. Zhan, J.D. Kuntz, J.E. Garay, A.K. Mukherjee: Electrical properties of nanoceramics reinforced with ropes of single-walled carbon nanotubes, Appl. Phys. Lett. **83**, 1228–1230 (2003)

3.427 S. Rul, F. Lefevre-Schlick, E. Capria, C. Laurent, A. Peigney: Percolation of single-walled carbon nanotubes in ceramic matrix nanocomposites, Acta Mater. **52**, 1061–1067 (2004)

3.428 S.-L. Shi, J. Liang: Electronic transport properties of multiwall carbon nanotubes/yttria-stabilized zirconia composites, J. Appl. Phys. **101**, 023708–5 (2007)

3.429 A. Peigney, E. Flahaut, C. Laurent, F. Chastel, A. Rousset: Aligned carbon nanotubes in ceramic-matrix nanocomposites prepared by high-temperature extrusion, Chem. Phys. Lett. **352**, 20–25 (2002)

3.430 G.-D. Zhan, J.D. Kuntz, A.K. Mukherjee, P. Zhu, K. Koumoto: Thermoelectric properties of carbon nanotube/ceramic nanocomposites, Scr. Mater. **54**, 77–82 (2006)

3.431 P.M. Ajayan, O. Stephan, C. Colliex, D. Trauth: Aligned carbon nanotube arrays formed by cutting a polymer resin-nanotube composite, Science **265**, 1212–1214 (1994)

3.432 J.N. Coleman, U. Khan, Y.K. Gun'ko: Mechanical reinforcement of polymers using carbon nanotubes, Adv. Mater. **18**, 689–706 (2006)

3.433 R. Haggenmueller, H.H. Gommans, A.G. Rinzler, J.E. Fischer, K.I. Winey: Aligned single-wall carbon nanotubes in composites by melt processing methods, Chem. Phys. Lett. **330**, 219–225 (2000)

3.434 L.S. Schadler, S.C. Giannaris, P.M. Ajayan: Load transfer in carbon nanotube epoxy composites, Appl. Phys. Lett. **73**, 3842–3844 (1998)

3.435 S.J.V. Frankland, A. Caglar, D.W. Brenner, M. Griebel: Molecular simulation of the influence of chemical cross-links on the shear strength of carbon nanotube-polymer interfaces, J. Phys. Chem. B **106**, 3046–3048 (2002)

3.436 H.D. Wagner: Nanotube-polymer adhesion: A mechanics approach, Chem. Phys. Lett. **361**, 57–61 (2002)

3.437 P.M. Ajayan, L.S. Schadler, C. Giannaris, A. Rubio: Single-walled carbon nanotube-polymer composites: Strength and weakness, Adv. Mater. **12**, 750–753 (2000)

3.438 X. Gong, J. Liu, S. Baskaran, R.D. Voise, J.S. Young: Surfactant-assisted processing of carbon nano-

tube/polymer composites, Chem. Mater. **12**, 1049–1052 (2000)
3.439 E.T. Thostenson, W.Z. Li, D.Z. Wang, Z.F. Ren, T.W. Chou: Carbon nanotube/carbon fiber hybrid multiscale composites, J. Appl. Phys. **91**, 6034–6037 (2002)
3.440 F.H. Gojny, M.H.G. Wichmann, U. Kopke, B. Fiedler, K. Schulte: Carbon nanotube-reinforced epoxy-composites: enhanced stiffness and fracture toughness at low nanotube content, Compos. Sci. Technol. **64**, 2363–2371 (2004)
3.441 F.H. Gojny, M.H.G. Wichmann, B. Fiedler, K. Schulte: Influence of different carbon nanotubes on the mechanical properties of epoxy matrix composites – A comparative study, Compos. Sci. Tech. **65**, 2300–2313 (2005)
3.442 H. Rajoria, N. Jalili: Passive vibration damping enhancement using carbon nanotube-epoxy reinforced composites, Compos. Sci. Tech. **65**, 2079–2093 (2005)
3.443 M.J. Biercuk, M.C. Llaguno, M. Radosavljevic, J.K. Hyun, A.T. Johnson, J.E. Fischer: Carbon nanotube composites for thermal management, Appl. Phys. Lett. **80**, 2767–2769 (2002)
3.444 F.H. Gojny, K. Schulte: Functionalisation effect on the thermo-mechanical behaviour of multi-wall carbon nanotube/epoxy-composites, Compos. Sci. Technol. **64**, 2303–2308 (2004)
3.445 G. Pecastaings, P. Delhaes, A. Derre, H. Saadaoui, F. Carmona, S. Cui: Role of interfacial effects in carbon nanotube/epoxy nanocomposite behavior, J. Nanosci. Nanotechnol. **4**, 838–843 (2004)
3.446 S. Barrau, P. Demont, A. Peigney, C. Laurent, C. Lacabanne: Effect of palmitic acid on the electrical conductivity of carbon nanotubes-polyepoxy composite, Macromolecules **36**, 9678–9680 (2003)
3.447 S. Barrau, P. Demont, A. Peigney, C. Laurent, C. Lacabanne: DC and AC conductivity of carbon nanotubes-polyepoxy composites, Macromolecules **36**, 5187–5194 (2003)
3.448 J. Sandler, M.S.P. Shaffer, T. Prasse, W. Bauhofer, K. Schulte, A.H. Windle: Development of a dispersion process for carbon nanotubes in an epoxy matrix and the resulting electrical properties, Polymer **40**, 5967–5971 (1999)
3.449 Z. Jin, K.P. Pramoda, G. Xu, S.H. Goh: Dynamic mechanical behavior of melt-processed multi-walled carbon nanotube/poly(methyl methacrylate) composites, Chem. Phys. Lett. **337**, 43–47 (2001)
3.450 Z. Jin, K.P. Pramoda, S.H. Goh, G. Xu: Poly(vinylidene fluoride)-assisted melt-blending of multi-walled carbon nanotube/poly(methyl methacrylate) composites, Mater. Res. Bull. **37**, 271–278 (2002)
3.451 C.A. Cooper, D. Ravich, D. Lips, J. Mayer, H.D. Wagner: Distribution and alignment of carbon nanotubes and nanofibrils in a polymer matrix, Compos. Sci. Technol. **62**, 1105–1112 (2002)
3.452 J.M. Benoit, B. Corraze, S. Lefrant, W.J. Blau, P. Bernier, O. Chauvet: Transport properties of PMMA-carbon nanotubes composites, Synth. Met. **121**, 1215–1216 (2001)
3.453 J.M. Benoit, B. Corraze, O. Chauvet: Localization, Coulomb interactions, and electrical heating in single-wall carbon nanotubes/polymer composites, Phys. Rev. B **65**, 241405/1–241405/4 (2002)
3.454 F. Du, R.C. Scogna, W. Zhou, S. Brand, J.E. Fischer, K.I. Winey: Nanotube networks in polymer nanocomposites: Rheology and electrical conductivity, Macromolecules **37**, 9048–9055 (2004)
3.455 T. Kashiwagi, F. Du, K.I. Winey, K.M. Groth, J.R. Shields, R.H. Harris Jr., J.F. Douglas: Flammability properties of PMMA-single walled carbon nanotube nanocomposites, Polym. Mater. Sci. Eng. **91**, 90–91 (2004)
3.456 B. Vigolo, A. Pénicaud, C. Coulon, C. Sauder, R. Pailler, C. Journet, P. Bernier, P. Poulin: Macroscopic fibers and ribbons of oriented carbon nanotubes, Science **290**, 1331–1334 (2000)
3.457 B. Vigolo, P. Poulin, M. Lucas, P. Launois, P. Bernier: Improved structure and properties of single-wall carbon nanotube spun fibers, Appl. Phys. Lett. **11**, 1210–1212 (2002)
3.458 P. Poulin, B. Vigolo, P. Launois: Films and fibers of oriented single wall nanotubes, Carbon **40**, 1741–1749 (2002)
3.459 K. Jiang, Q. Li, S. Fan: Spinning continuous carbon nanotube yarn, Nature **419**, 801 (2002)
3.460 M. Zhang, K.R. Atkinson, R.H. Baughman: Multifunctional carbon nanotube yarns by downsizing an ancient technology, Science **306**, 1356–1361 (2004)
3.461 J. Steinmetz, M. Glerup, M. Paillet, P. Bernier, M. Holzinger: Production of pure nanotube fibers using a modified wet-spinning method, Carbon **43**, 2397–2400 (2005)
3.462 A.B. Dalton, S. Collins, E. Munoz, J.M. Razal, V.H. Ebron, J.P. Ferraris, J.N. Coleman, B.G. Kim, R.H. Baughman: Super-tough carbon-nanotube fibers, Nature **423**, 703 (2003)
3.463 M.S.P. Shaffer, A.H. Windle: Fabrication and characterization of carbon nanotube/poly(vinyl alcohol) composites, Adv. Mater. **11**, 937–941 (1999)
3.464 L. Jin, C. Bower, O. Zhou: Alignment of carbon nanotubes in a polymer matrix by mechanical stretching, Appl. Phys. Lett. **73**, 1197–1199 (1998)
3.465 H.D. Wagner, O. Lourie, Y. Feldman, R. Tenne: Stress-induced fragmentation of multiwall carbon nanotubes in a polymer matrix, Appl. Phys. Lett. **72**, 188–190 (1998)
3.466 H.D. Wagner, O. Lourie, X.F. Zhou: Macrofragmentation and microfragmentation phenomena in composite materials, Compos. Part A **30**, 59–66 (1998)
3.467 J.R. Wood, Q. Zhao, H.D. Wagner: Orientation of carbon nanotubes in polymers and its detection by

Raman spectroscopy, Compos. Part A **32**, 391–399 (2001)
3.468 Q. Zhao, J.R. Wood, H.D. Wagner: Using carbon nanotubes to detect polymer transitions, J. Polym. Sci. B **39**, 1492–1495 (2001)
3.469 M. Cochet, W.K. Maser, A.M. Benito, M.A. Callejas, M.T. Martinesz, J.M. Benoit, J. Schreiber, O. Chauvet: Synthesis of a new polyaniline/nanotube composite: In-situ polymerisation and charge transfer through site-selective interaction, Chem. Commun., 1450–1451 (2001)
3.470 D. Qian, E.C. Dickey, R. Andrews, T. Rantell: Load transfer and deformation mechanisms in carbon nanotube-polystyrene composites, Appl. Phys. Lett. **76**, 2868–2870 (2000)
3.471 V. Datsyuk, C. Guerret-Piecourt, S. Dagreou, L. Billon, J.-C. Dupin, E. Flahaut, A. Peigney, C. Laurent: Double walled carbon nanotube/polymer composites via in-situ nitroxide mediated polymerisation of amphiphilic block copolymers, Carbon **43**, 873–876 (2005)
3.472 R. Blake, Y.K. Gun'ko, J. Coleman, M. Cadek, A. Fonseca, J.B. Nagy, W.J. Blau: A generic organometallic approach toward ultra-strong carbon nanotube polymer composites, J. Am. Chem. Soc. **126**, 10226–10227 (2004)
3.473 T. Kashiwagi, E. Grulke, J. Hilding, K. Groth, R. Harris, K. Butler, J. Shields, S. Kharchenko, J. Douglas: Thermal and flammability properties of polypropylene/carbon nanotube nanocomposites, Polymer **45**, 4227–4239 (2004)
3.474 C. Wei, D. Srivastava, K. Cho: Thermal expansion and diffusion coefficients of carbon nanotube-polymer composites, Los Alamos Nat. Lab., Preprint Archive, Condensed Matter (archiv:cond-mat/0203349), 1–11 (2002)
3.475 J.C. Grunlan, M.V. Bannon, A.R. Mehrabi: Latex-based, single-walled nanotube composites: processing and electrical conductivity, Polym. Prepr. **45**, 154–155 (2004)
3.476 J.C. Grunlan, A.R. Mehrabi, M.V. Bannon, J.L. Bahr: Water-based single-walled-nanotube-filled polymer composite with an exceptionally low percolation threshold, Adv. Mater. (Weinheim) **16**, 150–153 (2004)
3.477 C. Pirlot, I. Willems, A. Fonseca, J.B. Nagy, J. Delhalle: Preparation and characterization of carbon nanotube/polyacrylonitrile composites, Adv. Eng. Mater. **4**, 109–114 (2002)
3.478 H. Lam, H. Ye, Y. Gogotsi, F. Ko: Structure and properties of electrospun single-walled carbon nanotubes reinforced nanocomposite fibrils by co-electrospinning, Polym. Prepr. **45**, 124–125 (2004)
3.479 L. Cao, H. Chen, M. Wang, J. Sun, X. Zhang, F. Kong: Photoconductivity study of modified carbon nanotube/oxotitanium phthalocyanine composites, J. Phys. Chem. B **106**, 8971–8975 (2002)
3.480 I. Musa, M. Baxendale, G.A.J. Amaratunga, W. Eccleston: Properties of regular poly(3-octylthiophene)/multi-wall carbon nanotube composites, Synth. Met. **102**, 1250 (1999)
3.481 E. Kymakis, I. Alexandou, G.A.J. Amaratunga: Single-walled carbon nanotube-polymer composites: Electrical, optical and structural investigation, Synth. Met. **127**, 59–62 (2002)
3.482 K. Yoshino, H. Kajii, H. Araki, T. Sonoda, H. Take, S. Lee: Electrical and optical properties of conducting polymer-fullerene and conducting polymer-carbon nanotube composites, Fuller. Sci. Technol. **7**, 695–711 (1999)
3.483 S.A. Curran, P.M. Ajayan, W.J. Blau, D.L. Carroll, J.N. Coleman, A.B. Dalton, A.P. Davey, A. Drury, B. McCarthy, S. Maier, A. Strevens: A composite from poly(*m*-phenylenevinylene-co-2,5-dioctoxy-*p*-phenylenevinylene) and carbon nanotubes. A novel material for molecular optoelectronics, Adv. Mater. **10**, 1091–1093 (1998)
3.484 P. Fournet, D.F. O'Brien, J.N. Coleman, H.H. Horhold, W.J. Blau: A carbon nanotube composite as an electron transport layer for M3EH-PPV based light-emitting diodes, Synth. Met. **121**, 1683–1684 (2001)
3.485 H.S. Woo, R. Czerw, S. Webster, D.L. Carroll, J. Ballato, A.E. Strevens, D. O'Brien, W.J. Blau: Hole blocking in carbon nanotube-polymer composite organic light-emitting diodes based on poly(*m*-phenylene vinylene-co-2,5-dioctoxy-*p*-phenylene vinylene), Appl. Phys. Lett. **77**, 1393–1395 (2000)
3.486 H.S. Woo, R. Czerw, S. Webster, D.L. Carroll, J.W. Park, J.H. Lee: Organic light emitting diodes fabricated with single wall carbon nanotubes dispersed in a hole conducting buffer: The role of carbon nanotubes in a hole conducting polymer, Synth. Met. **116**, 369–372 (2001)
3.487 H. Ago, K. Petritsch, M.S.P. Shaffer, A.H. Windle, R.H. Friend: Composites of carbon nanotubes and conjugated polymers for photovoltaic devices, Adv. Mater. **11**, 1281–1285 (1999)
3.488 B. Maruyama, K. Alam: Carbon nanotubes and nanofibers in composite materials, SAMPE Journal **38**, 59–70 (2002)
3.489 P. Lambin, A. Fonseca, J.P. Vigneron, J. B'Nagy, A.A. Lucas: Structural and electronic properties of bent carbon nanotubes, Chem. Phys. Lett. **245**, 85–89 (1995)
3.490 L. Chico, V.H. Crespi, L.X. Benedict, S.G. Louie, M.L. Cohen: Pure carbon nanoscale devices: Nanotube heterojunctions, Phys. Rev. Lett. **76**, 971–974 (1996)
3.491 Z. Yao, H.W.C. Postma, L. Balents, C. Dekker: Carbon nanotube intramolecular junctions, Nature **402**, 273–276 (1999)
3.492 S.J. Tans, A.R.M. Verschueren, C. Dekker: Room temperature transistor based on single carbon nanotube, Nature **393**, 49–52 (1998)

3.493 R. Martel, T. Schmidt, H.R. Shea, T. Hertel, P. Avouris: Single and multi-wall carbon nanotube field effect transistors, Appl. Phys. Lett. **73**, 2447–2449 (1998)

3.494 V. Derycke, R. Martel, J. Appenzeller, P. Avouris: Carbon nanotube inter- and intramolecular logic gates, Nano Lett. **1**, 453–456 (2001)

3.495 P. Kim, C.M. Lieber: Nanotube nanotweezers, Science **286**, 2148–2150 (1999)

3.496 P.G. Collins, M.S. Arnold, P. Avouris: Engineering carbon nanotubes using electrical breakdown, Science **292**, 706–709 (2001)

3.497 A.P. Graham, G.S. Duesberg, W. Hoenlein, F. Kreupl, M. Liebau, R. Martin, B. Rajasekharan, W. Pamler, R. Seidel, W. Steinhoegl, E. Unger: How do carbon nanotubes fit into the semiconductor roadmap?, Appl. Phys. A **80**, 1141–1151 (2005)

3.498 R.H. Baughman, C. Changxing, A.A. Zakhidov, Z. Iqbal, J.N. Barisci, G.M. Spinks, G.G. Wallace, A. Mazzoldi, D. de Rossi, A.G. Rinzler, O. Jaschinki, S. Roth, M. Kertesz: Carbon nanotubes actuators, Science **284**, 1340–1344 (1999)

3.499 Y. Gao, Y. Bando: Carbon nanothermometer containing gallium, Nature **415**, 599 (2002)

3.500 C. Niu, E.K. Sichel, R. Hoch, D. Moy, H. Tennent: High power electro-chemical capacitors based on carbon nanotube electrodes, Appl. Phys. Lett. **70**, 1480–1482 (1997)

3.501 E. Frackowiak, F. Béguin: Electrochemical storage of energy in carbon nanotubes and nanostructured carbons, Carbon **40**, 1775–1787 (2002)

3.502 C. Portet, P.L. Taberna, P. Simon, E. Flahaut: Influence of carbon nanotubes addition on carbon–carbon supercapacitor performances in organic electrolyte, J. Power. Sources **139**, 371–378 (2005)

3.503 E. Frackowiak, K. Jurewicz, K. Szostak, S. Delpeux, F. Béguin: Nanotubular materials as electrodes for supercapacitors, Fuel Process. Technol. **77**, 213–219 (2002)

3.504 G. Lota, E. Frackowiak, J. Mittal, M. Monthioux: High performance supercapacitor from chromium oxide-nanotubes based electrodes, Chem. Phys. Lett. **434**, 73–77 (2007)

3.505 R. Hurt, M. Monthioux, A. Kane (Eds.): Toxicology of carbon nanomaterials, Carbon **44**(6), 1028–1033 (2006), Special issue

3.506 C. Salvador-Morales, E. Flahaut, E. Sim, J. Sloan, M.L.H. Green, R.B. Sim: Complement activation and protein adsorption by carbon nanotubes, Mol. Immun. **43**, 193–201 (2006)

3.507 C. Salvador-Morales, P. Townsend, E. Flahaut, C. Vénien-Bryan, A. Vlandas, M.L.H. Green, R.B. Sim: Binding of pulmonary surfactant proteins to carbon nanotubes; potential for damage to lung immune defence mechanisms, Carbon **45**, 607–617 (2007)

4. Nanowires

Mildred S. Dresselhaus, Yu-Ming Lin, Oded Rabin, Marcie R. Black, Jing Kong, Gene Dresselhaus

This chapter provides an overview of recent research on inorganic nanowires, particularly metallic and semiconducting nanowires. Nanowires are one-dimensional, anisotropic structures, small in diameter, and large in surface-to-volume ratio. Thus, their physical properties are different than those of structures of different scale and dimensionality. While the study of nanowires is particularly challenging, scientists have made immense progress in both developing synthetic methodologies for the fabrication of nanowires, and developing instrumentation for their characterization. The chapter is divided into three main sections: Sect. 4.1 the synthesis, Sect. 4.2 the characterization and physical properties, and Sect. 4.3 the applications of nanowires. Yet, the reader will discover many links that make these aspects of nanoscience intimately interdepent.

Nanowires are attracting much interest from those seeking to apply nanotechnology and (especially) those investigating nanoscience. Nanowires, unlike other low-dimensional systems, have two quantum-confined directions but one unconfined direction available for electrical conduction. This allows nanowires to be used in applications where electrical conduction, rather than tunneling transport, is required. Because of their unique density of electronic states, in the limit of small diameters nanowires are expected to exhibit significantly different optical, electrical and magnetic properties to their bulk 3-D crystalline counterparts. Increased surface area, very high density of electronic states and joint density of states near the energies of their van Hove singularities, enhanced exciton binding energy, diameter-dependent bandgap, and increased surface scattering for electrons and phonons are just some of the ways in which nanowires differ from their corresponding bulk materials. Yet the sizes of nanowires are typically large enough (> 1 nm in the quantum-confined direction) to result in local crystal structures that are closely related to their parent materials, allowing theoretical predictions about their properties to be made based on knowledge of their bulk properties.

Not only do nanowires exhibit many properties that are similar to, and others that are distinctly different from, those of their bulk counterparts, nanowires also have the advantage from an applications standpoint in that some of the materials parameters critical for certain properties can be independently controlled in nanowires but not in their bulk counterparts. Certain properties can also be enhanced nonlinearly in small-diameter nanowires, by exploiting the singular aspects of the 1-D electronic density of states.


image
not
available

study of nanostructures [4.75]. Mesoporous molecular sieves [4.76], termed MCM-41, possess hexagonally-packed pores with very small channel diameters which can be varied between 2 and 10 nm. Conducting organic filaments have been fabricated in the nanochannels of MCM-41 [4.77]. Recently, the DNA molecule has also been used as a template for growing nanometer-sized wires [4.3].

Diblock copolymers, polymers that consist of two chain segments different properties, have also been utilized as templates for nanowire growth. When two components are immiscible in each other, phase segregation occurs, and depending on their volume ratio, spheres, cylinders and lamellae may self-assemble. To form self-assembled arrays of nanopores, copolymers composed of polystyrene and polymethylmethacrylate [P(S-b-MMA)] [4.79] were used. By applying an electric field while the copolymer was heated above the glass transition temperature of the two constituent polymers, the self-assembled cylinders of PMMA could be aligned with their main axis perpendicular to the film. Selective removal of the PMMA component afforded the preparation of 14 nm diameter ordered pore arrays with a packing density of 1.9×10^{11} cm^{-3}.

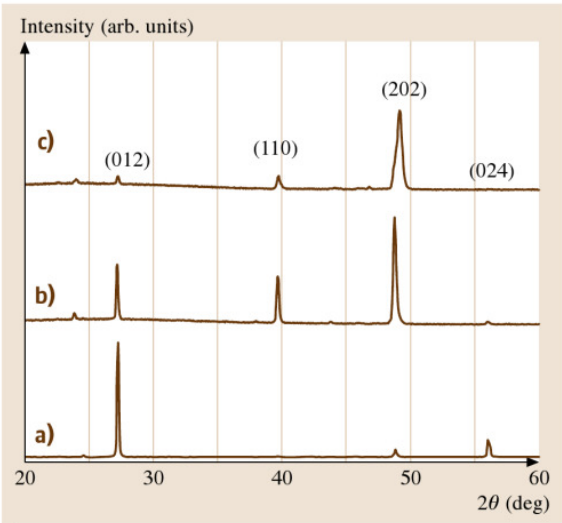

Fig. 4.2a–c XRD patterns of bismuth/anodic alumina nanocomposites with average bismuth wire diameters of (**a**) 40 nm, (**b**) 52 nm, and (**c**) 95 nm [4.78]. The Miller indices corresponding to the lattice planes of bulk Bi are indicated above the individual *peaks*. The majority of the Bi nanowires are oriented along the $[10\bar{1}1]$ and $[01\bar{1}2]$ directions for $d_W \geq 60$ nm and $d_W \leq 50$ nm, respectively (after [4.13,78]). The existence of more than one dominant orientation in the 52 nm Bi nanowires is attributed to the transitional behavior of *intermediate*-diameter nanowires as the preferential growth orientation is shifted from $[10\bar{1}1]$ to $[01\bar{1}2]$ with decreasing d_W

Nanowire Template-Assisted Growth by Pressure Injection

The pressure injection technique is often employed for fabricating highly crystalline nanowires from a low-melting point material and when using porous templates with robust mechanical strength. In the high-pressure injection method, the nanowires are formed by pressure-injecting the desired material in liquid form into the evacuated pores of the template. Due to the heating and pressurization processes, the templates used for the pressure injection method must be chemically stable and be able to maintain their structural integrity at high temperatures and at high pressures. Anodic aluminum oxide films and nanochannel glass are two typical materials used as templates in conjunction with the pressure injection filling technique. Metal nanowires (Bi, In, Sn, and Al) and semiconductor nanowires (Se, Te, GaSb, and Bi_2Te_3) have been fabricated in anodic aluminum oxide templates using this method [4.12,46,78].

The pressure P required to overcome the surface tension for the liquid material to fill the pores with a diameter d_W is determined by the Washburn equation [4.80]

$$d_W = -4\gamma \cos\theta / P \,, \tag{4.1}$$

where γ is the surface tension of the liquid, and θ is the contact angle between the liquid and the template. To reduce the required pressure and to maximize the filling factor, some surfactants are used to decrease the surface tension and the contact angle. For example, the introduction of Cu into the Bi melt can facilitate filling the pores in the anodic alumina template with liquid Bi and can increase the number of nanowires that are formed [4.13]. However, some of the surfactants might cause contamination problems and should therefore be avoided. Nanowires produced by the pressure injection technique usually possess high crystallinity and a preferred crystal orientation along the wire axis. For example, Fig. 4.2 shows the x-ray diffraction (XRD) patterns of Bi nanowire arrays of three different wire diameters with an injection pressure of ≈ 5000 psi [4.78], showing that the major ($> 80\%$) crystal orientation of the wire axes in the 95 and 40 nm diameter Bi nanowire arrays are, respectively, normal to the (202) and (012) lattice planes,

which are denoted by $[10\bar{1}1]$ and $[01\bar{1}2]$ when using a hexagonal unit cell, suggesting a wire diameter-dependent crystal growth direction. On the other hand, 30 nm Bi nanowires produced using a much higher pressure of $> 20\,000$ psi show a different crystal orientation of (001) along the wire axis [4.14], indicating that the preferred crystal orientation may also depend on the applied pressure, with the most dense packing direction along the wire axis for the highest applied pressure.

Electrochemical Deposition

The electrochemical deposition technique has attracted increasing attention as a versatile method for fabricating nanowires in templates. Traditionally, electrochemistry has been used to grow thin films on conducting surfaces. Since electrochemical growth is usually controllable in the direction normal to the substrate surface, this method can be readily extended to fabricate 1-D or 0-D nanostructures, if the deposition is confined within the pores of an appropriate template. In the electrochemical methods, a thin conducting metal film is first coated on one side of the porous membrane to serve as the cathode for electroplating. The length of the deposited nanowires can be controlled by varying the duration of the electroplating process. This method has been used to synthesize a wide variety of nanowires, such as metals (Bi [4.9, 74]; Co [4.81, 82]; Fe [4.25, 83]; Cu [4.73, 84]; Ni [4.39, 81]; Ag [4.85]; Au [4.5]); conducting polymers [4.9, 61]; superconductors (Pb [4.86]); semiconductors (CdS [4.19]); and even superlattice nanowires with A/B constituents (such as Cu/Co [4.73, 84]) have been synthesized electrochemically (Table 4.1).

In the electrochemical deposition process, the chosen template has to be chemically stable in the electrolyte during the electrolysis process. Cracks and defects in the templates are detrimental to the nanowire growth, since the deposition processes primarily occur in the more accessible cracks, leaving most of the nanopores unfilled. Particle track-etched mica films or polymer membranes are typical templates used in simple DC electrolysis. To use anodic aluminum oxide films in the DC electrochemical deposition, the insulating barrier layer which separates the pores from the bottom aluminum substrate has to be removed, and a metal film is then evaporated onto the back of the template membrane [4.87]. Compound nanowire arrays, such as Bi_2Te_3, have been fabricated in alumina templates with a high filling factor using the DC electrochemical deposition [4.16]. Figure 4.3a,b, respectively, shows the top view and the axial cross-sectional SEM images of a Bi_2Te_3 nanowire array [4.16]. The light areas are associated with Bi_2Te_3 nanowires, the dark regions denote empty pores, and the surrounding gray matrix is alumina.

Surfactants are also used with electrochemical deposition when necessary. For example, when using templates derived from PMMA/PS diblock copolymers, a methanol surfactant is used to facilitate pore filling [4.79], thereby achieving a $\approx 100\%$ filling factor.

It is also possible to employ an ac electrodeposition method in anodic alumina templates without the removal of the barrier layer, by utilizing the rectifying properties of the oxide barrier. In ac electrochemical deposition, although the applied voltage is sinusoidal and symmetric, the current is greater during the cathodic half-cycles, making deposition dominant over the stripping, which occurs in the subsequent anodic half-cycles. Since no rectification occurs at defect sites, the deposition and stripping rates are equal, and no material is deposited. Hence, the difficulties associated with cracks are avoided. In this fashion, metals, such as Co [4.82] and Fe [4.25, 83], and semiconductors, such as CdS [4.19], have been deposited into the pores of anodic aluminum oxide templates without removing the barrier layer.

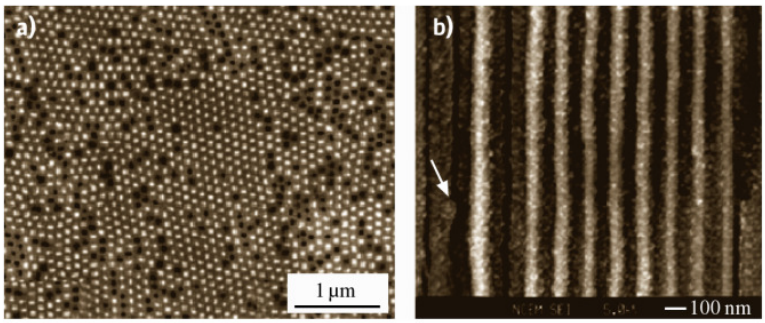

Fig. 4.3 (a) SEM image of a Bi_2Te_3 nanowire array in cross section showing a relatively high pore filling factor. (b) SEM image of a Bi_2Te_3 nanowire array composite along the wire axis (after [4.16])

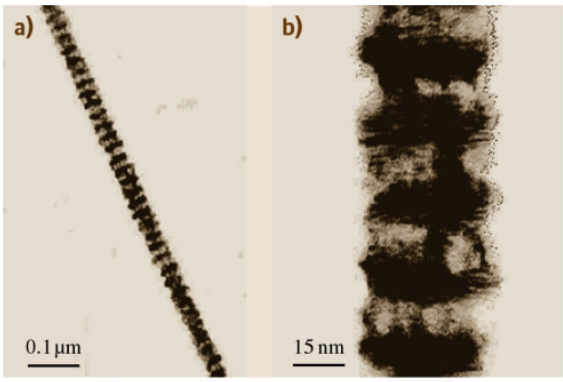

Fig. 4.4 (**a**) TEM image of a single Co(10 nm)/Cu(10 nm) multilayered nanowire. (**b**) A selected region of the sample at high magnification (after [4.84])

In contrast to nanowires synthesized by the pressure injection method, nanowires fabricated by the electrochemical process are usually polycrystalline, with no preferred crystal orientations, as observed by XRD studies. However, some exceptions exist. For example, polycrystalline CdS nanowires, fabricated by an ac electrodeposition method in anodic alumina templates [4.19], possibly have a preferred wire growth orientation along the *c*-axis. In addition, *Xu* et al. have prepared a number of single-crystal II–VI semiconductor nanowires, including CdS, CdSe and CdTe, by DC electrochemical deposition in anodic alumina templates with a nonaqueous electrolyte [4.18, 22]. Furthermore, single-crystal Pb nanowires were formed by pulse electrodeposition under overpotential conditions, but no specific crystal orientation along the wire axis was observed [4.86]. The use of pulse currents is believed to be advantageous for the growth of crystalline wires because the metal ions in the solution can be regenerated between the electrical pulses and therefore uniform deposition conditions can be produced for each deposition pulse. Similarly, single-crystal Ag nanowires were fabricated by pulsed electrodeposition [4.4].

One advantage of the electrochemical deposition technique is the possibility of fabricating multilayered structures within nanowires. By varying the cathodic potentials in the electrolyte, which contains two different kinds of ions, different metal layers can be controllably deposited. Co/Cu multilayered nanowires have been synthesized in this way [4.73, 84]. Figure 4.4 shows TEM images of a single Co/Cu nanowire which is about 40 nm in diameter [4.84]. The light bands represent Co-rich regions and the dark bands represent Cu-rich layers. This electrodeposition method provides a low-cost approach to preparing multilayered 1-D nanostructures.

Vapor Deposition

Vapor deposition of nanowires includes physical vapor deposition (PVD) [4.8], chemical vapor deposition (CVD) [4.29], and metallo-organic chemical vapor deposition (MOCVD) [4.32]. Like electrochemical deposition, vapor deposition is usually capable of preparing smaller-diameter (≤ 20 nm) nanowires than pressure injection methods, since it does not rely on the high pressure and the surface tension involved to insert the material into the pores.

In the physical vapor deposition technique, the material to be filled is first heated to produce a vapor, which is then introduced through the pores of the template and cooled to solidify. Using a specially designed experimental setup [4.8], nearly single-crystal Bi nanowires in anodic aluminum templates with pore diameters as small as 7 nm have been synthesized, and these Bi nanowires were found to possess a preferred crystal growth orientation along the wire axis, similar to the Bi nanowires prepared by pressure injection [4.8, 13].

Compound materials that result from two reacting gases have also be prepared by the chemical vapor deposition (CVD) technique. For example, single-crystal GaN nanowires have been synthesized in anodic alumina templates through a gas reaction of Ga_2O vapor with a flowing ammonia atmosphere [4.28, 29]. A different liquid/gas phase approach has been used to prepare polycrystalline GaAs and InAs nanowires in a nanochannel glass array [4.32]. In this method, the nanochannels are filled with one liquid precursor (such as Me_3Ga or Et_3In) via a capillary effect and the nanowires are formed within the template by reactions between the liquid precursor and the other gas reactant (such as AsH_3).

4.1.2 VLS Method for Nanowire Synthesis

Some of the recent successful syntheses of semiconductor nanowires are based on the so-called vapor–liquid–solid (VLS) mechanism of anisotropic crystal growth. This mechanism was first proposed for the growth of single crystal silicon whiskers 100 nm to hundreds of micrometer in diameter [4.88]. The proposed growth mechanism (Fig. 4.5) involves the absorption of source material from the gas phase into a liquid droplet of catalyst (a molten particle of gold on a silicon substrate in the original work [4.88]). Upon supersaturation of the liquid alloy, a nucleation event generates a solid

precipitate of the source material. This seed serves as a preferred site for further deposition of material at the interface of the liquid droplet, promoting the elongation of the seed into a nanowire or a whisker, and suppressing further nucleation events on the same catalyst. Since the liquid droplet catalyzes the incorporation of material from the gas source to the growing crystal, the deposit grows anisotropically as a whisker whose diameter is dictated by the diameter of the liquid alloy droplet. The nanowires thus obtained are of high purity, except for the end containing the solidified catalyst as an alloy particle (Figs. 4.5 and 4.6a). Real-time observations of the alloying, nucleation, and elongation steps in the growth of germanium nanowires from gold nanoclusters by the VLS method were recorded by in situ TEM [4.89].

Reduction of the average wire diameter to the nanometer scale requires the generation of nanosized catalyst droplets. However, due to the balance between the liquid-vapor surface free energy and the free energy of condensation, the size of a liquid droplet, in equilibrium with its vapor, is usually limited to the micrometer range. This obstacle has been overcome in recent years by several new methodologies:

1. Advances in the synthesis of metal nanoclusters have made monodispersed nanoparticles commercially available. These can be dispersed on a solid substrate in high dilution so that when the temperature is raised above the melting point, the liquid clusters do not aggregate [4.47].
2. Alternatively, metal islands of nanoscale sizes can self-form when a strained thin layer is grown or heat-treated on a nonepitaxial substrate [4.34].

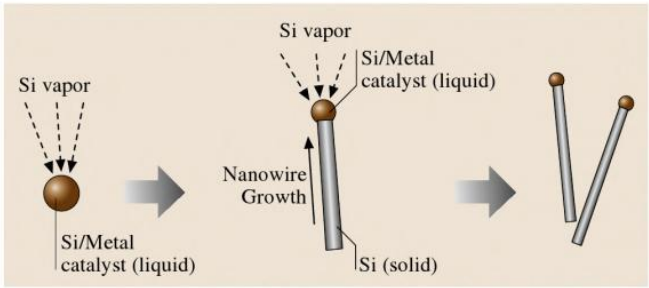

Fig. 4.5 Schematic diagram illustrating the growth of silicon nanowires by the VLS mechanism

3. Laser-assisted catalytic VLS growth is a method used to generate nanowires under nonequilibrium conditions. Using laser ablation of a target containing both the catalyst and the source materials, a plasma is generated from which catalyst nanoclusters nucleate as the plasma cools down. Single crystal nanowires grow as long as the particle remains liquid [4.48].
4. Interestingly, by optimizing the material properties of the catalyst-nanowire system, conditions can be achieved for which nanocrystals nucleate in a liquid catalyst pool supersaturated with the nanowire material, migrate to the surface due to a large surface tension, and continue growing as nanowires perpendicular to the liquid surface [4.50]. In this case, supersaturated nanodroplets are sustained on the outer end of the nanowire due to the low solubility of the nanowire material in the liquid [4.91].

A wide variety of elemental, binary and compound semiconductor nanowires has been synthesized

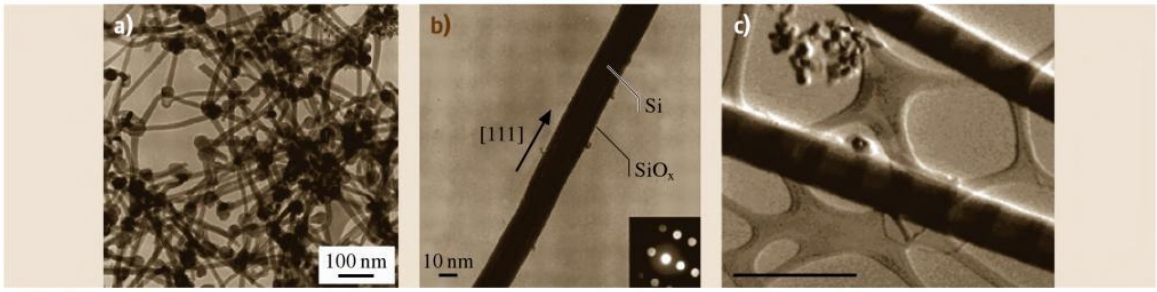

Fig. 4.6 (**a**) TEM images of Si nanowires produced after laser-ablating a $Si_{0.9}Fe_{0.1}$ target. The *dark spheres* with a slightly larger diameter than the wires are solidified catalyst clusters (after [4.48]). (**b**) Diffraction contrast TEM image of a Si nanowire. The crystalline Si core appears *darker* than the amorphous oxide surface layer. The *inset* shows the convergent beam electron diffraction pattern recorded perpendicular to the wire axis, confirming the nanowire crystallinity (after [4.48]). (**c**) STEM image of $Si/Si_{1-x}Ge_x$ superlattice nanowires in the bright field mode. The scale bar is 500 nm (after [4.90])

via the VLS method, and relatively good control over the nanowire diameter and diameter distribution has been achieved. Researchers are currently focusing their attention on the controlled variation of the materials properties along the nanowire axis. In this context, researchers have modified the VLS synthesis apparatus to generate compositionally-modulated nanowires. GaAs/GaP-modulated nanowires have been synthesized by alternately ablating targets of the corresponding materials in the presence of gold nanoparticles [4.92]. p-Si/n-Si nanowires were grown by chemical vapor deposition from alternating gaseous mixtures containing the appropriate dopant [4.92]. $Si/Si_{1-x}Ge_x$ nanowires were grown by combining silicon from a gaseous source with germanium from a periodically ablated target (Fig. 4.6c) [4.90]. NiSi-Si nanowires have been successfully synthesized which directly incorporate a nanowire metal contact into active nanowire devices [4.93]. Finally, using an ultrahigh vacuum chamber and molecular beams, InAs/InP nanowires with atomically sharp interfaces were obtained [4.94]. These compositionally-modulated nanowires are expected to exhibit exciting electronic, photonic, and thermoelectric properties.

Interestingly, silicon and germanium nanowires grown by the VLS method consist of a crystalline core coated with a relatively thick amorphous oxide layer (2–3 nm) (Fig. 4.6b). These layers are too thick to be the result of ambient oxidation, and it has been shown that these oxides play an important role in the nanowire growth process [4.49, 95]. Silicon oxides were found to serve as a special and highly selective catalyst that significantly enhances the yield of Si nanowires without the need for metal catalyst particles [4.49, 95, 96]. A similar yield enhancement was also found in the synthesis of Ge nanowires from the laser ablation of Ge powder mixed with GeO_2 [4.35]. The Si and Ge nanowires produced from these metal-free targets generally grow along the [112] crystal direction [4.97], and have the benefit that no catalyst clusters are found on either ends of the nanowires. Based on these observations and other TEM studies [4.35, 95, 97], an oxide-enhanced nanowire growth mechanism different from the classical VLS mechanism was proposed, where no metal catalyst is required during the laser ablation-assisted synthesis [4.95]. It is postulated that the nanowire growth is dependent on the presence of SiO (or GeO) vapor, which decomposes in the nanowire tip region into both Si (or Ge), which is incorporated into the crystalline phase, and SiO_2 (or GeO_2), which contributes to the outer coating. The initial nucleation

Fig. 4.7 TEM image showing the two major morphologies of Si nanowires prepared by the oxide-assisted growth method (after [4.95]). Notice the absence of metal particles when compared to Fig. 4.6a. The *arrow* points at an oxide-linked chain of Si nanoparticles

events generate oxide-coated spherical nanocrystals. The [112] crystal faces have the fastest growth rate, and therefore the nanocrystals soon begin elongating along this direction to form one-dimensional structures. The Si_mO or Ge_mO ($m > 1$) layer on the nanowire tips may be in or at temperatures near their molten states, catalyzing the incorporation of gas molecules in a directional fashion [4.97]. Besides nanowires with smooth walls, a second morphology of chains of unoriented nanocrystals linked by oxide necks is frequently observed (indicated by an arrow in Fig. 4.7). In addition, it was found by STM studies that about 1% of the wires consist of a regular array of two alternating segments, 10 and 5 nm in length, respectively [4.98]. The segments, whose junctions form an angle of 30°, are probably a result of alternating growth along different crystallographic orientations [4.98]. Branched and hyperbranched Si nanowire structures have also been synthesized by *Whang* et al. [4.99].

4.1.3 Other Synthesis Methods

In this section we review several other general procedures available for the synthesis of a variety of nanowires. We focus on *bottom-up* approaches, which afford many kinds of nanowires in large numbers, and

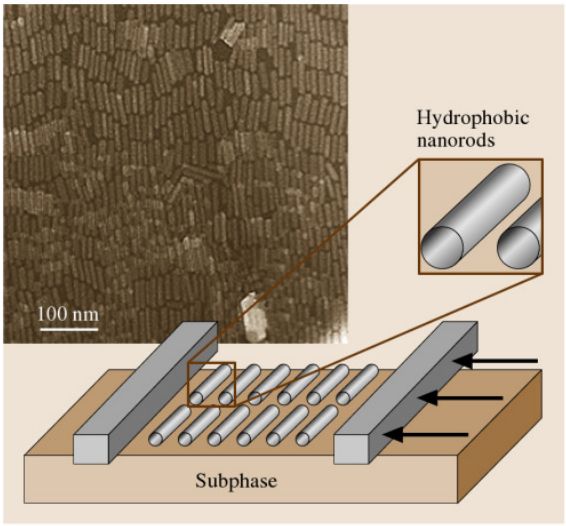

Fig. 4.10 A TEM image of a smectic phase of a $BaCrO_4$ nanorod film (*left inset*) achieved by the Langmuir–Blodgett technique, as depicted by the illustration (after [4.113])

In this process, a tetrahedral quantum dot core is first grown, and then the conditions are modified to induce one-dimensional growth of a nanowire from each one of the facets of the tetrahedron. A similar process produced high-symmetry In_2O_3/ZnO hierarchical nanostructures. From a mixture of heat-treated In_2O_3, ZnO, and graphite powders, faceted In_2O_3 nanowires were first obtained, on which oriented shorter ZnO nanowires were crystallized [4.107]. Brushlike structures were obtained as a mixture of 11 structures of different symmetries. For example, two, four, or six rows of ZnO nanorods could be found on different core nanowires, depending on the crystallographic orientation of the main axis of the core nanowire, as shown in Fig. 4.9. Comblike structures made entirely of ZnO were also reported [4.54].

Controlling the position of a nanowire in the growth process is important for preparing devices or test structures containing nanowires, especially when it involves a large array of nanowires. Post-synthesis methods to align and position nanowires include microfluidic channels [4.114], Langmuir–Blodgett assemblies [4.113], and electric field-assisted assembly [4.115]. The first method involves the orientation of the nanowires by the liquid flow direction when a nanowire solution is injected into a microfluidic channel assembly and by the interaction of the nanowires with the side walls of the channel. The second method involves the alignment of nanowires at a liquid–gas or liquid–liquid interface by the application of compressive forces on the interface (Fig. 4.10). The aligned nanowire films can then be transferred onto a substrate and lithography methods can be used to define interconnects. This allows the nanowires to be organized with a controlled alignment and spacing over large areas. Using this method, centimeter-scale arrays containing thousands of single silicon nanowire field-effect transistors with high performance could be assembled to make large-scale nanowire circuits and devices [4.99, 116]. The third technique is based on dielectrophoretic forces that pull polarizable nanowires toward regions of high field strength. The nanowires align between two isolated electrodes which are capacitatively coupled to a pair of buried electrodes biased with an AC voltage. Once a nanowire shorts the electrodes, the electric field is eliminated, preventing more nanowires from depositing. The above techniques have been successfully used to prepare electronic circuitry and optical devices out of nanowires (Sects. 4.3.1 and 4.3.3). Alternatively, alignment and positioning of the nanowires can be specified and controlled during their growth by the proper design of the synthesis method. For example, ZnO nanowires prepared by the VLS method were grown into an array in which both their position on the substrate and their growth direction and orientation were controlled [4.54]. The nanowire growth region was defined by patterning the gold film, which serves as a catalyst for the ZnO nanowire growth, employing soft-lithography, e-beam lithography, or photolithography. The orientation of the nanowires was achieved by selecting a substrate with a lattice structure matching that of the nanowire material to facilitate the epitaxial growth. These conditions result in an array of nanowire posts at predetermined positions, all vertically aligned with the same crystal growth orientation (Fig. 4.11). Similar rational GaN nanowire arrays have been synthesized epitaxially on (100)$LiAlO_2$ and (111)MgO single-crystal substrates. In addition, control over the crystallographic growth directions of nanowires was achieved by lattice-matching to different substrates. For example, GaN nanowires on (100)$LiAlO_2$ substrates grow oriented along the [110] direction, whereas (111)MgO substrates result in the growth of GaN nanowires with an [001] orientation, due to the different lattice-matching constraints [4.117]. A similar structure could be obtained by the template-mediated electrochemical synthesis of nanowires (Sect. 4.1.1), particularly if anodic alumina with its parallel and ordered channels is used. The control over the location

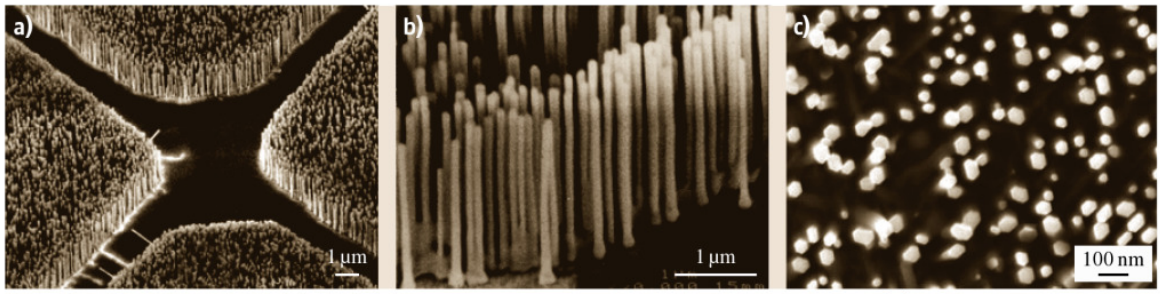

Fig. 4.11a–c SEM images of ZnO nanowire arrays grown on a sapphire substrate, where (**a**) shows patterned growth, (**b**) shows a higher resolution image of the parallel alignment of the nanowires, and (**c**) shows the faceted side-walls and the hexagonal cross section of the nanowires. For nanowire growth, the sapphire substrates were coated with a 1.0–3.5 nm thick patterned layer of Au as the catalyst, using a TEM grid as the shadow mask. These nanowires have been used for nanowire laser applications (after [4.122])

of the nucleation of nanowires in the electrochemical deposition is determined by the pore positions and the back-electrode geometry. The pore positions can be precisely controlled by imprint lithography [4.118]. By growing the template on a patterned conductive substrate that serves as a back-electrode [4.119–121] different materials can be deposited in the pores at different regions of the template.

4.2 Characterization and Physical Properties of Nanowires

In this section we review the structure and properties of nanowires and their interrelationship. The discovery and investigation of nanostructures were spurred on by advances in various characterization and microscopy techniques that enabled material characterization to take place at smaller and smaller length scales, reaching length scales down to individual atoms. For applications, characterizing the structural properties of nanowires is especially important, so that a reproducible relationship between their desired functionality and their geometrical and structural characteristics can be established. Due to the enhanced surface-to-volume ratio in nanowires, their properties may depend sensitively on their surface conditions and geometrical configurations. Even nanowires made of the same material may possess dissimilar properties due to differences in their crystal phase, crystalline size, surface conditions, and aspect ratios, which depend on the synthesis methods and conditions used in their preparation.

4.2.1 Structural Characterization

Structural and geometric factors play an important role in determining the various attributes of nanowires, such as their electrical, optical and magnetic properties. Therefore, various novel tools have been developed and employed to obtain this important structural information at the nanoscale. At the micrometer scale, optical techniques are extensively used for imaging structural features. Since the sizes of nanowires are usually comparable to or, in most cases, much smaller than the wavelength of visible light, traditional optical microscopy techniques are usually limited when characterizing the morphology and surface features of nanowires. Therefore, electron microscopy techniques play a more dominant role at the nanoscale. Since electrons interact more strongly than photons, electron microscopy is particularly sensitive relative to x-rays for the analysis of tiny samples.

In this section we review and give examples of how scanning electron microscopy, transmission electron microscopy, scanning probe spectroscopies, and diffraction techniques are used to characterize the structures of nanowires. To provide the necessary basis for developing reliable structure–property relations, multiple characterization tools are applied to the same samples.

Scanning Electron Microscopy

SEM usually produces images down to length scales of ≈ 10 nm and provides valuable information regarding the structural arrangement, spatial distribution, wire density, and geometrical features of the nanowires. The examples of SEM micrographs shown in Figs. 4.1 and 4.3 indicate that structural features at the 10 nm to

10 μm length scales can be probed, providing information on the size, size distribution, shapes, spatial distributions, density, nanowire alignment, filling factors, granularity, etc.. As another example, Fig. 4.11a shows an SEM image of ZnO nanowire arrays grown on a sapphire substrate [4.122], which provides evidence for the nonuniform spatial distribution of the nanowires on the substrate, which was attained by patterning the catalyst film to define high-density growth regions and nanowire-free regions. Figure 4.11b, showing a higher magnification of the same system, indicates that these ZnO nanowires grow perpendicular to the substrate, are well-aligned with approximately equal wire lengths, and have wire diameters in the range $20 \leq d_W \leq 150$ nm. The SEM micrograph in Fig. 4.11c provides further information about the surface of the nanowires, showing it to be well-faceted, forming a hexagonal cross section, indicative of nanowire growth along the ⟨0001⟩ direction. Both the uniformity of the nanowire size, their alignment perpendicular to the substrate, and their uniform growth direction, as suggested by the SEM data, are linked to the good epitaxial interface between the (0001) plane of the ZnO nanowire and the (110) plane of the sapphire substrate. (The crystal structures of ZnO and sapphire are essentially incommensurate, with the exception that the *a*-axis of ZnO and the *c*-axis of sapphire are related almost exactly by a factor of 4, with a mismatch of less than 0.08% at room temperature [4.122].) The well-faceted nature of these nanowires has important implications for their lasing action (Sect. 4.3.2). Figure 4.12 shows an SEM image of GaN nanowires synthesized by a laser-assisted catalytic growth method [4.30], indicating a random spatial orientation of the nanowire axes and a wide diameter distribution for these nanowires, in contrast to the ZnO wires in Fig. 4.11 and to arrays of well-aligned nanowires prepared by template-assisted growth (Fig. 4.3).

Transmission Electron Microscopy

TEM and high-resolution transmission electron microscopy (HRTEM) are powerful imaging tools for studying nanowires at the atomic scale, and they usually provide more detailed geometrical features than are seen in SEM images. TEM studies also yield information regarding the crystal structure, crystal quality, grain size, and crystal orientation of the nanowire axis. When operating in the diffraction mode, selected area electron diffraction (SAED) patterns can be made to determine the crystal structures of nanowires. As an example, the TEM images in Fig. 4.13 show four different morphologies for Si nanowires prepared by the laser ablation of a Si target [4.123]: (a) spring-shaped; (b) fishbone-shaped (indicated by solid arrow) and frogs egg-shaped (indicated by the hollow arrow), (c) pearl-shaped, while (d) shows the poly-sites of nanowire nucleation. The crystal quality of nanowires is revealed from high-resolution TEM images with atomic resolution, along with selected area electron diffraction (SAED) patterns. For example, Fig. 4.14 shows a TEM image of one of the GaN nanowires from Fig. 4.12, indicating single crystallinity and showing (100) lattice planes, thus indicating the growth direction of the nanowire. This information is supplemented by the corresponding electron diffraction pattern in the upper right. A more comprehensive review of the application of TEM for growth orientation indexing and crystal defect characterization in nanowires is available elsewhere [4.124].

The high resolution of the TEM also permits the surface structures of the nanowires to be studied. In many cases, the nanowires are sheathed with a native oxide layer, or an amorphous oxide layer that forms during the growth process. This can be seen in Fig. 4.6b for silicon nanowires and in Fig. 4.15 for germanium nanowires [4.35], showing a mass–thickness contrast TEM image and a selected-area electron diffraction pattern of a Ge nanowire. The main TEM image shows that these Ge nanowires possess an amorphous GeO_2 sheath with a crystalline Ge core that is oriented in the [211] direction.

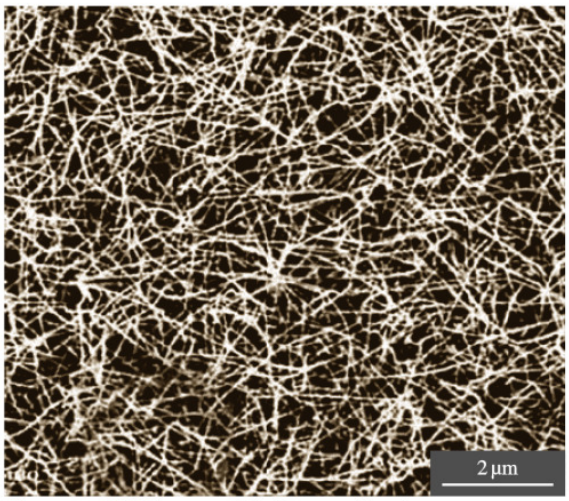

Fig. 4.12 SEM image of GaN nanowires in a mat arrangement synthesized by laser-assisted catalytic growth. The nanowires have diameters and lengths on the order of 10 nm and 10 μm, respectively (after [4.30])

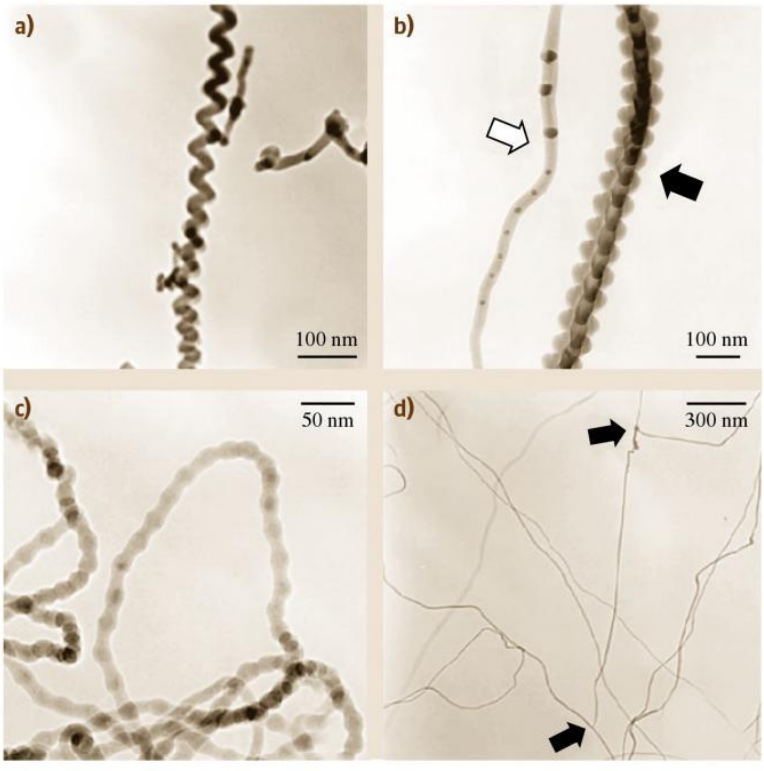

Fig. 4.13a–d TEM morphologies of four special forms of Si nanowires synthesized by the laser ablation of a Si powder target. **(a)** A spring-shaped Si nanowire; **(b)** fishbone-shaped (indicated by a *solid arrow*) and frogs egg-shaped (indicated by a *hollow arrow*) Si nanowires; and **(c)** pearl-shaped nanowires, while **(d)** shows polysites for the nucleation of silicon nanowires (indicated by *arrows*) (after [4.123])

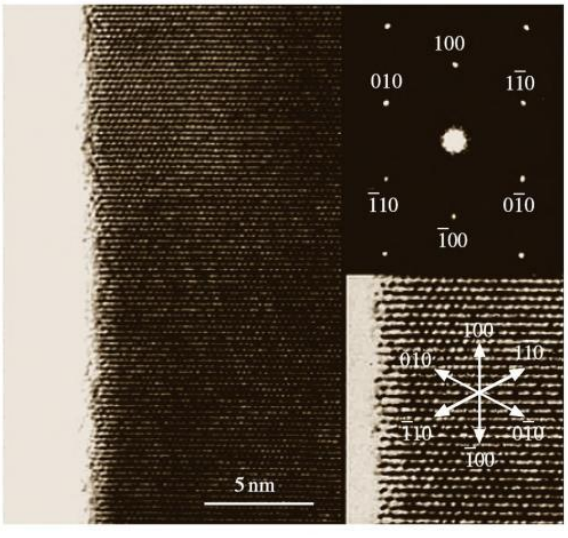

Fig. 4.14 Lattice-resolved high-resolution TEM image of one GaN nanowire (*left*) showing that (100) lattice planes are visible perpendicular to the wire axis. The electron diffraction pattern (*top right*) was recorded along the [001] zone axis. A lattice-resolved TEM image (*lower right*) highlights the continuity of the lattice up to the nanowire edge, where a thin native oxide layer is found. The directions of various crystallographic planes are indicated in the *lower right figure* (after [4.30]) ▶

Dynamical processes of the surface layer of nanowires can be studied in-situ using an environmental TEM chamber, which allows TEM observations to be made while different gases are introduced or as the sample is heat-treated at various temperatures, as illustrated in Fig. 4.16. The figure shows high-resolution TEM images of a Bi nanowire with an oxide coating and the effect of a dynamic oxide removal process carried out within the environmental chamber of the TEM [4.125]. The amorphous bismuth-oxide layer coating the nanowire (Fig. 4.16a) is removed by exposure to hydrogen gas within the environmental chamber of the TEM, as indicated in Fig. 4.16b.

By coupling the powerful imaging capabilities of TEM with other characterization tools, such as an electron energy loss spectrometer (EELS) or an energy dispersive x-ray spectrometer (EDS) within the

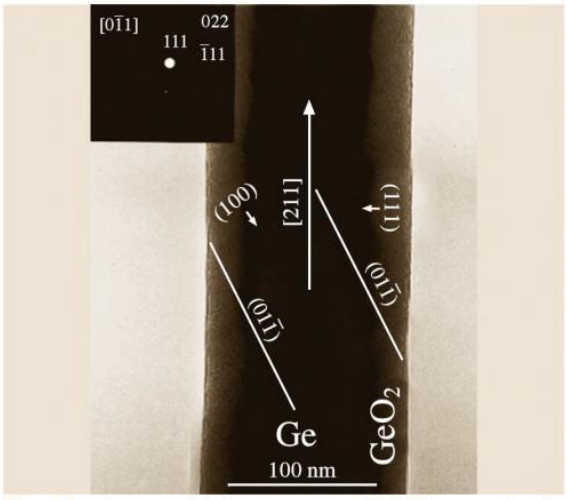

Fig. 4.15 A mass–thickness contrast TEM image of a Ge nanowire taken along the [0$\bar{1}$1] zone axis and a selected-area electron diffraction pattern (*upper left inset*) (after [4.35]). The Ge nanowires were synthesized by laser ablation of a mixture of Ge and GeO_2 powder. The core of the Ge nanowire is crystalline, while the surface GeO_2 is amorphous

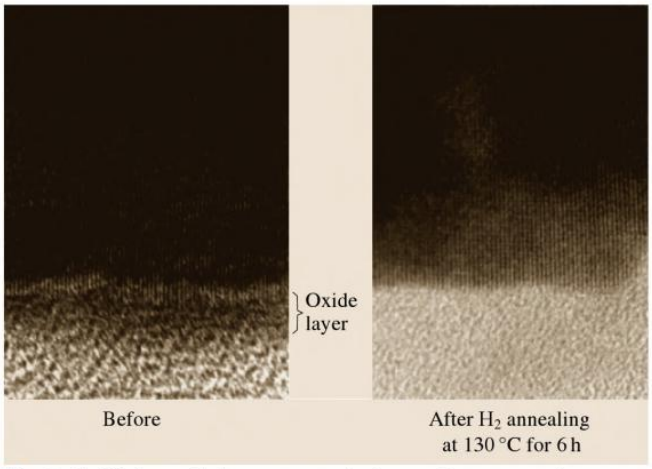

Fig. 4.16 High-resolution transmission electron microscope (HRTEM) image of a Bi nanowire (*left*) before and (*right*) after annealing in hydrogen gas at 130 °C for 6 h within the environmental chamber of the HRTEM instrument to remove the oxide surface layer (after [4.125])

TEM instrument, additional properties of the nanowires can be probed with high spatial resolution. With the EELS technique, the energy and momentum of the incident and scattered electrons are measured in an inelastic electron scattering process to provide information on the energy and momentum of the excitations in the nanowire sample. Figure 4.17 shows the dependence on nanowire diameter of the electron energy loss spectra of Bi nanowires. The spectra were taken from the center of the nanowire, and the shift in the energy of the peak position (Fig. 4.17) indicates the effect of the nanowire diameter on the plasmon frequency in the nanowires. The results show that there are changes in the electronic structure of the Bi nanowires as the wire diameter decreases [4.126]. Such changes in electronic structure as a function of nanowire diameter are also observed in their transport (Sect. 4.2.2) and optical (Sect. 4.2.3) properties, and are related to quantum confinement effects.

EDS measures the energy and intensity distribution of x-rays generated by the impact of the electron beam on the surface of the sample. The elemental composition within the probed area can be determined to a high degree of precision. The technique was particularly useful for the compositional characterization of superlattice nanowires [4.90] and core–shell nanowires [4.111] (Sect. 4.1.2).

Scanning Tunneling Probes

Several scanning probe techniques, such as scanning tunneling microscopy (STM) [4.127], electric

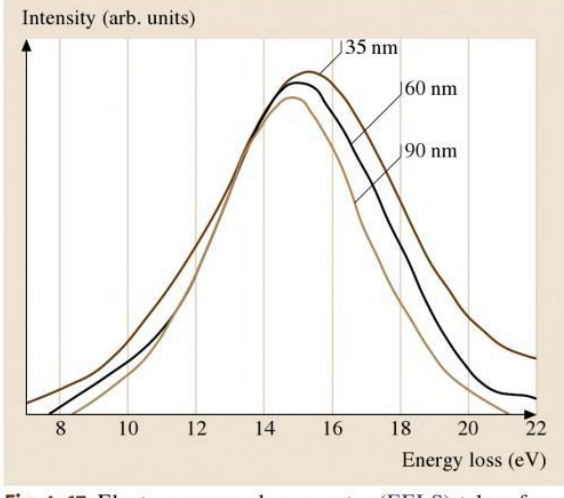

Fig. 4.17 Electron energy loss spectra (EELS) taken from the centers of bismuth nanowires with diameters of 35, 60 and 90 nm. The shift in the volume plasmon peaks is due to the effect of wire diameter on the electronic structure (after [4.126])

ermometer has been demonstrated using a 10 nm liquid gallium filled-carbon nanotube, showing an expansion coefficient that is linear in temperature and identical to the bulk value [4.132].

A different behavior was observed in free-standing copper nanowires [4.134]. In this system, there is little interaction between the nanowire surface and the surroundings, and the nanowire is not confined in its diameter, as in the case of the sheathed nanowires. Thermal treatment of the free-standing nanowires leads to their fragmentation into a linear array of metal spheres. Thinner nanowires were more vulnerable than thicker nanowires to the thermal treatment, showing constrictions and segmentation at lower temperatures. Analysis of the temperature response of the nanowires indicates that the nanowire segmentation is a result of the Rayleigh instability, starting with oscillatory perturbations of the nanowire diameter, leading to long cylindrical segments, that become more separated and more spherical at higher temperatures. These observations indicate that annealing and melting are dominated by the surface diffusion of atoms on the entire surface of the nanowire (versus tip-initiated melting).

4.2.3 Transport Properties

The study of electrical transport properties of nanowires is important for nanowire characterization, electronic device applications, and the investigation of unusual transport phenomena arising from one-dimensional quantum effects. Important factors that determine the transport properties of nanowires include the wire diameter, (important for both classical and quantum size effects), material composition, surface conditions, crystal quality, and the crystallographic orientation along the wire axis for materials with anisotropic material parameters, such as the effective mass tensor, the Fermi surface, or the carrier mobility.

Electronic transport phenomena in low-dimensional systems can be roughly divided into two categories: ballistic transport and diffusive transport. Ballistic transport phenomena occur when the electrons can travel across the nanowire without any scattering. In this case, the conduction is mainly determined by the contacts between the nanowire and the external circuit, and the conductance is quantized into an integral number of universal conductance units $G_0 = 2e^2/h$ [4.135, 136]. Ballistic transport phenomena are usually observed in very short quantum wires, such as those produced using mechanically controlled break junctions (MCBJ) [4.137, 138] where the electron mean free path is much longer than the wire length and the conduction is a pure quantum phenomenon. To observe ballistic transport, the thermal energy must also obey the relation $k_B T \ll \varepsilon_j - \varepsilon_{j-1}$, where $\varepsilon_j - \varepsilon_{j-1}$ is the energy separation between subband levels j and $j-1$. On the other hand, for nanowires with lengths much larger than the carrier mean free path, the electrons (or holes) undergo numerous scattering events when they travel along the wire. In this case, the transport is in the diffusive regime, and the conduction is dominated by carrier scattering within the wires, due to phonons (lattice vibrations), boundary scattering, lattice and other structural defects, and impurity atoms.

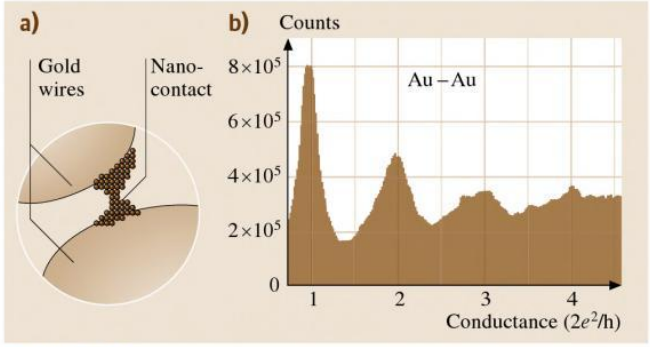

Fig. 4.21 (**a**) Schematic representation of the last stages of the contact breakage process (after [4.133]). (**b**) Histogram of conductance values built with 18 000 gold contact breakage experiments in air at room temperature, showing conductance peaks at integral values of G_0. In this experiment the gold electrodes approach and separate at 89 000 Å/s (after [4.133])

Conductance Quantization in Metallic Nanowires

The ballistic transport of 1-D systems has been extensively studied since the discovery of quantized conductance in 1-D systems in 1988 [4.135, 136]. The phenomena of conductance quantization occur when the diameter of the nanowire is comparable to the electron Fermi wavelength, which is on the order of 0.5 nm for most metals [4.139]. Most conductance quantization experiments up to the present were performed by bringing together and separating two metal electrodes. As the two metal electrodes are slowly separated, a nanocontact is formed before it breaks completely (Fig. 4.21a), and conductance in integral multiple values of G_0 is observed through these nanocontacts. Figure 4.21b shows the conductance histogram built with 18 000 contact breakage curves between two gold electrodes at room temperature [4.133], with the electrode sep-

aration up to ≈ 1.8 nm. The conductance quantization behavior is found to be independent of the contact material, and has been observed in various metals, such as Au [4.133], Ag, Na, Cu [4.140], and Hg [4.141]. For semimetals such as Bi, conductance quantization has also been observed for electrode separations as long as 100 nm at 4 K because of the long Fermi wavelength (≈ 26 nm) [4.139], indicating that the conductance quantization may be due to the existence of well-defined quantum states localized at a constriction instead of resulting from the atom rearrangement as the electrodes separate. Since conductance quantization is only observed in breaking contacts, or for very narrow and very short nanowires, most nanowires of practical interest (possessing lengths of several micrometer) lie in the diffusive transport regime, where the carrier scattering is significant and should be considered.

I–V Characterization of Semiconducting Nanowires

The electronic transport behavior of nanowires may be categorized based on the relative magnitudes of three length scales: carrier mean free path ℓ_W, the de Broglie wavelength of electrons λ_e, and the wire diameter d_W. For wire diameters much larger than the carrier mean free path ($d_W \gg \ell_W$), the nanowires exhibit transport properties similar to bulk materials, which are independent of the wire diameter, since the scattering due to the wire boundary is negligible compared to other scattering mechanisms. For wire diameters comparable to or smaller than the carrier mean free path ($d_W \approx \ell_W$ or $d_W < \ell_W$), but still much larger than the de Broglie wavelength of the electrons ($d_W \gg \lambda_e$), the transport in nanowires is in the classical finite size regime, where the band structure of the nanowire is still similar to that of bulk, while the scattering events at the wire boundary alter their transport behavior. For wire diameters comparable to the electronic wavelength $d_W \approx \lambda_e$, the electronic density of states is altered dramatically and quantum subbands are formed due to the quantum confinement effect at the wire boundary. In this regime, the transport properties are further influenced by the change in the band structure. Therefore, transport properties for nanowires in the classical finite size and quantum size regimes are highly diameter-dependent.

Researchers have investigated the transport properties of various semiconducting nanowires and have demonstrated their potential for diverse electronic devices, such as for p-n diodes [4.142, 143], field effect transistors [4.142], memory cells, and switches [4.144] (Sect. 4.3.1). So far, the nanowires studied in this context have usually been made from conventional semiconducting materials, such as group IV and III–V compound semiconductors, via the VLS growth method (Sect. 4.1.2), and their nanowire properties have been compared to their well-established bulk properties. Interestingly, the physical principles for describing bulk semiconductor devices also hold for devices based on these semiconducting nanowires with wire diameters of tens of nanometers. For example, Fig. 4.22 shows the current–voltage (I–V) behavior of a 4-by-1 crossed p-Si/n-GaN junction array at room temperature [4.142]. The long horizontal wire in the figure is a p-Si nanowire (10–25 nm in diameter) and the four short vertical wires are n-GaN nanowires (10–30 nm in diameter). Each of the four nanoscale cross points independently forms a p-n junction with current rectification behavior, as shown by the I–V curves in Fig. 4.22, and the junction behavior (for example the turn-on voltage) can be controlled by varying the oxide coating on these nanowires [4.142].

Huang et al. have demonstrated nanowire junction diodes with a high turn-on voltage (≈ 5 V) by increasing the oxide thickness at the junctions. The high turn-on voltage enables the use of the junction in

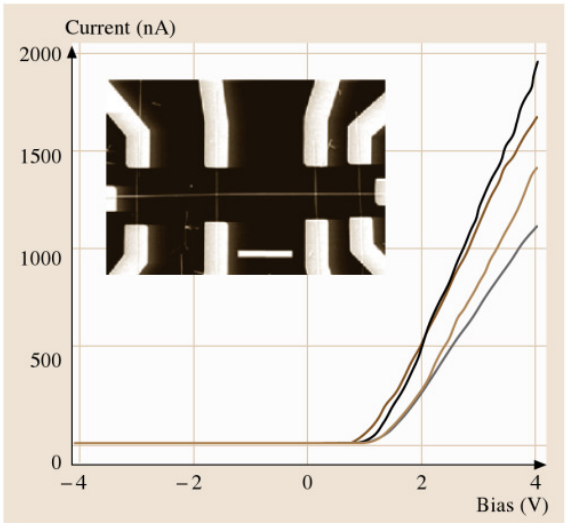

Fig. 4.22 I–V behavior for a 4(p) by 1(n) crossed p-Si/n-GaN junction array shown in the *inset*. The *four curves* represent the I–V response for each of the four junctions, showing similar current rectifying characteristics in each case. The length scale bar between the two *middle junctions* is 2 μm (after [4.142]). The p-Si and n-GaN nanowires are 10–25 and 10–30 nm in diameter, respectively

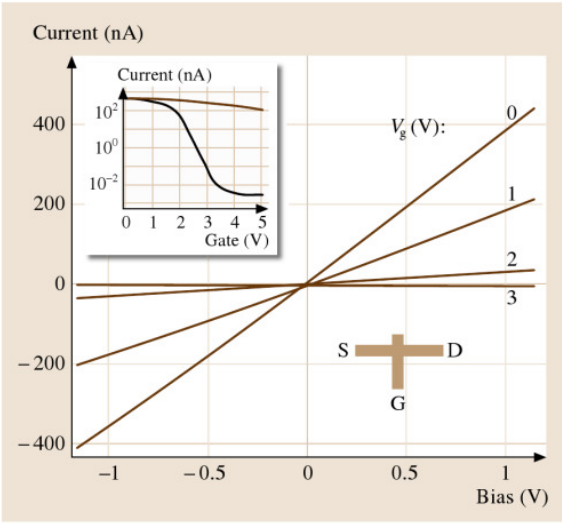

Fig. 4.23 Gate-dependent I–V characteristics of a crossed nanowire field-effect transistor (FET). The n-GaN nanowire is used as the nanogate, with the gate voltage indicated (0, 1, 2, and 3 V). The *inset* shows the current versus V_{gate} for a nanowire gate (*lower curve*) and for a global back-gate (*top curve*) when the bias voltage is set to 1 V (after [4.142])

a nanoscale FET, as shown in Fig. 4.23 [4.142] where I–V data for a p-Si nanowire are presented, for which the n-GaN nanowire with a thick oxide coating is used as a nanogate. By varying the nanogate voltage, the conductance of the p-Si nanowire can be changed by more than a factor of 10^5 (lower curve in the inset), whereas the conductance changes by only a factor of 10 when a global back-gate is used (top curve in the inset of Fig. 4.23). This behavior may be due to the thin gate dielectric between the crossed nanowires and the better control of the local carrier density through a nanogate. Based on the gate-dependent I–V data from these p-Si nanowires, it is found that the mobility of the holes in the p-Si nanowires may be higher than that for bulk p-Si, although further investigation is required for complete understanding.

Because of the enhanced surface-to-volume ratios of nanowires, their transport behavior may be modified by changing their surface conditions. For example, researchers have found that by coating n-InP nanowires with a layer of redox molecules, such as cobalt phthalocyanine, the conductance of the InP nanowires may change by orders of magnitude upon altering the charge state of the redox molecules to provide bistable nanoscale switches [4.144]. The resistance (or conductance) of some nanowires (such as Pd nanowires) is also very sensitive to the presence of certain gases (e.g., H_2) [4.145,146], and this property may be utilized for sensor applications to provide improved sensitivity compared to conventional sensors based on bulk material (Sect. 4.3.4).

Although it remains unclear how the size effect may influence the transport properties and device performance of semiconducting nanowires, many of the larger diameter semiconducting nanowires are expected to be described by classical physics, since their quantization energies $\hbar^2/(2m_e d_W^2)$ are usually smaller than the thermal energy $k_B T$. By comparing the quantization energy with the thermal energy, the critical wire diameter below which quantum confinement effects become significant is estimated to be 1 nm for Si nanowires at room temperature, which is much smaller than the sizes of many of the semiconducting nanowires that have been investigated so far. By using material systems with much smaller effective carrier masses m_e (such as bismuth), the critical diameter for which such quantum effects can be observed is increased, thereby facilitating the study of quantum confinement effects. It is for this reason that the bismuth nanowire system has been studied so extensively. Furthermore, since the crystal structure and lattice constants of bismuth nanowires are the same as for 3-D crystalline bismuth, it is possible to carry out detailed model calculations to guide and to interpret transport and optical experiments on bismuth nanowires. For these reasons, bismuth can be considered a model system for studying 1-D effects in nanowires.

Temperature-Dependent Resistance Measurements

Although nanowires with electronic properties similar to their bulk counterparts are promising for constructing nanodevices based on well-established knowledge of their bulk counterparts, it is expected that quantum size effects in nanowires will likely be utilized to generate new phenomena absent in bulk materials, and thus provide enhanced performance and novel functionality for certain applications. In this context, the transport properties of bismuth (Bi) nanowires have been extensively studied, both theoretically [4.147] and experimentally [4.8, 10, 78, 148–150] because of their promise for enhanced thermoelectric performance. Transport studies of ferromagnetic nanowire arrays, such as Ni or Fe, have also received much attention because of their potential for high-density magnetic storage applications [4.151].

The very small electron effective mass components and the long carrier mean free paths in Bi facilitate the study of quantum size effects in the transport properties of nanowires. Quantum size effects are expected to become significant in bismuth nanowires with diameters smaller than 50 nm [4.147], and the fabrication of crystalline nanowires with this diameter range is relatively easy.

Figure 4.24a shows the T dependence of the resistance $R(T)$ for Bi nanowires ($7 \leq d_W < 200$ nm) synthesized by vapor deposition and pressure injection [4.8], illustrating the quantum effects in their temperature-dependent resistance. In Fig. 4.24a, the $R(T)$ behavior of Bi nanowires is dramatically different from that of bulk Bi, and is highly sensitive to the wire diameter. Interestingly, the $R(T)$ curves in Fig. 4.24a show a nonmonotonic trend for large-diameter (70 and 200 nm) nanowires, although $R(T)$ becomes monotonic with T for small-diameter (≤ 48 nm) nanowires. This dramatic change in the behavior of $R(T)$ as a function of d_W is attributed to a unique semimetal–semiconductor transition phenomena in Bi [4.78], induced by quantum size effects. Bi is a semimetal in bulk form, in which the T-point valence band overlaps with the L-point conduction band by 38 meV at 77 K. As the wire diameter decreases, the lowest conduction subband increases in energy and the highest valence subband decreases in energy. Model calculations predict that the band overlap should vanish in Bi nanowires (with their wire axes along the trigonal direction) at a wire diameter ≈ 50 nm [4.147].

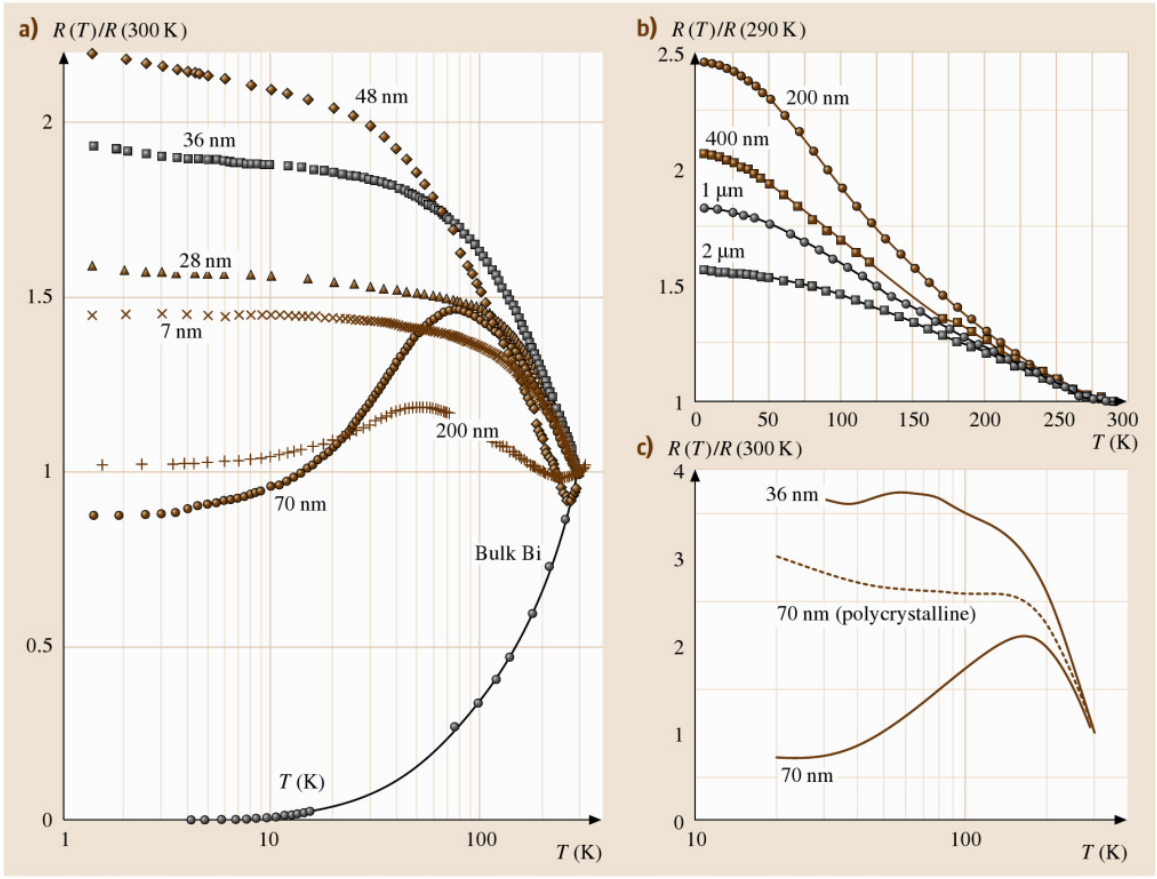

Fig. 4.24 (**a**) Measured temperature dependence of the resistance $R(T)$ normalized to the room temperature (300 K) resistance for bismuth nanowire arrays of various wire diameters d_W (after [4.8]). (**b**) $R(T)/R(290\,\text{K})$ for bismuth wires of larger d_W and lower mobility (after [4.10]). (**c**) Calculated $R(T)/R(300\,\text{K})$ of 36 and 70 nm bismuth nanowires. The *dashed curve* refers to a 70 nm polycrystalline wire with increased boundary scattering (after [4.78])

The resistance of Bi nanowires is determined by two competing factors: the carrier density that increases with T, and the carrier mobility that decreases with T. The nonmonotonic $R(T)$ for large-diameter Bi nanowires is due to a smaller carrier concentration variation at low temperature ($\leq 100\,\mathrm{K}$) in semimetals, so that the electrical resistance is dominated by the mobility factor in this temperature range. Based on the semi-classical transport model and the established band structure of Bi nanowires, the calculated $R(T)/R(300\,\mathrm{K})$ for 36 and 70 nm Bi nanowires is shown by the solid curves in Fig. 4.24c to illustrate different $R(T)$ trends for semiconducting and semimetallic nanowires, respectively [4.78]. The curves in Fig. 4.24c exhibit trends consistent with experimental results. The condition for the semimetal–semiconductor transition in Bi nanowires can be experimentally determined, as shown by the measured resistance ratio $R(10\,\mathrm{K})/R(100\,\mathrm{K})$ of Bi nanowires as a function of wire diameter [4.152] in Fig. 4.25. The maximum in the resistance ratio $R(10\,\mathrm{K})/R(100\,\mathrm{K})$ at $d_\mathrm{W} \approx 48\,\mathrm{nm}$ indicates the wire diameter for the transition of Bi nanowires from a semimetallic phase to a semiconducting phase. The semimetal–semiconductor transition and the semiconducting phase in Bi nanowires are examples of new transport phenomena resulting from low dimensionality that are absent in the bulk 3-D phase, and these phenomena further increase the possible benefits from the properties of nanowires for desired applications (Sect. 4.3.2).

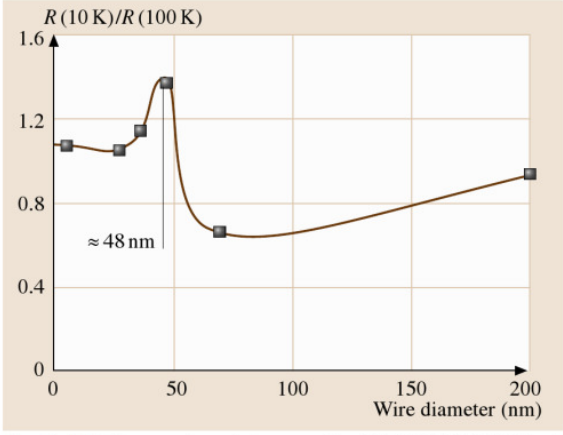

Fig. 4.25 Measured resistance ratio $R(10\,\mathrm{K})/R(100\,\mathrm{K})$ of Bi nanowire array as a function of diameter. The *peak* indicates the transition from a semimetallic phase to a semiconducting phase as the wire diameter decreases (after [4.153])

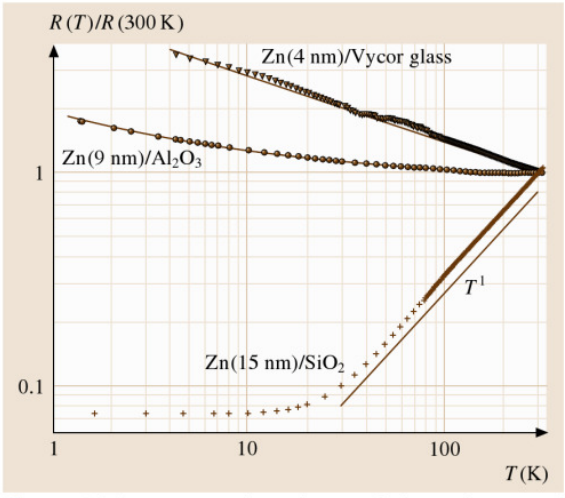

Fig. 4.26 Temperature dependence of the resistance of Zn nanowires synthesized by vapor deposition in various porous templates (after [4.52]). The data are given as *points*, the *full lines* are fits to a T^1 law for 15 nm diameter Zn nanowires in an SiO_2 template, denoted by Zn/SiO_2. Fits to a combined T^1 and $T^{-1/2}$ law were made for the smaller nanowire diameter composite samples denoted by Zn (9 nm)/Al_2O_3 and Zn 4 nm/Vycor glass

It should be noted that good crystal quality is essential for observing the quantum size effect in nanowires, as shown by the $R(T)$ plots in Fig. 4.24a. For example, Fig. 4.24b shows the normalized $R(T)$ measurements of Bi nanowires with larger diameters (200 nm–2 μm) prepared by electrochemical deposition [4.10], and these nanowires possess monotonic $R(T)$ behaviors, quite different from those of the corresponding nanowire diameters shown in Fig. 4.24a. The absence of the resistance maximum in Fig. 4.24b is due to the lower crystalline quality for nanowires prepared by electrochemical deposition, which tends to produce polycrystalline nanowires with a much lower carrier mobility. This monotonic $R(T)$ for semimetallic Bi nanowires with a higher defect level is also confirmed by theoretical calculations, as shown by the dashed curve in Fig. 4.24c for 70 nm wires with increased grain boundary scattering [4.154].

The theoretical model developed for Bi nanowires not only provides good agreement with experimental results, but it also plays an essential role in understanding the influence of the quantum size effect, the boundary scattering, and the crystal quality on their electrical properties. While the electronic density of states may be significantly altered due to quantum confinement

fined by the nanowire boundary (the 1-D regime), and above which the wavefunction is confined by the magnetic field (the 3-D regime). The physical basis for this phenomenon is associated with confinement of a single magnetic flux quantum within the nanowire cross section [4.150]. This phenomenon, though independent of temperature, is observed for $T \leq 5\,\mathrm{K}$, since the phase breaking length has to be larger than the wire diameter. This calculated field strength B_c indicated in Fig. 4.28 by vertical lines for the appropriate nanowire diameters, provides a good fit to the steplike features in these MR curves.

The Shubnikov–de Haas (SdH) quantum oscillatory effect, which results from the passage of the quantized Landau levels through the Fermi energy as the field strength varies, should, in principle, provide the most direct measurement of the Fermi energy and carrier density. For example, *Heremans* et al. have demonstrated that SdH oscillations can be observed in Bi nanowire samples with diameters down to 200 nm [4.159], and they have demonstrated that Te doping can be used to raise the Fermi energy in Bi nanowires. Such information on the Fermi energy is important because, for certain applications based on nanowires, it is necessary to place the Fermi energy near a subband edge where the density of states has a sharp feature. However, due to the unusual 1-D geometry of nanowires, other characterization techniques that are commonly used in bulk materials to determine the Fermi energy and the carrier concentration (such as Hall measurement) cannot be applied to nanowire systems. The observation of the SdH oscillatory effect requires crystal samples of very high quality which allow carriers to execute a complete cyclotron orbit in the nanowire before they are scattered. For small nanowire diameters, large magnetic fields are required to produce cyclotron radii smaller than the wire radius. For some nanowire systems, all Landau levels may have passed through the Fermi level at such a high field strength, and in such a case, no oscillations can be observed. The localization effect may also prevent the observation of SdH oscillations for very small diameter ($\leq 10\,\mathrm{nm}$) nanowires. Observing SdH oscillations in highly doped samples (as may be required for certain applications) may be difficult because impurity scattering reduces the mean free path, requiring high $\boldsymbol{B}$ fields to satisfy the requirement that carriers complete a cyclotron orbit prior to scattering. Therefore, although SdH oscillations provide the most direct method of measuring the Fermi energy and carrier density of nanowire samples, this technique may, however, not work for small-diameter nanowires, nor for nanowires that are heavily doped.

Thermoelectric Properties

Nanowires are predicted to hold great promise for thermoelectric applications [4.147, 160], due to their novel band structure compared to their bulk counterparts and the expected reduction in thermal conductivity associated with enhanced boundary scattering (see below). Due to the sharp density of states at the 1-D subband edges (where the van Hove singularities occur), nanowires are expected to exhibit enhanced Seebeck coefficients compared to their bulk counterparts. Since the Seebeck coefficient measurement is intrinsically independent of the number of nanowires contributing to the signal, the measurements on nanowire arrays of uniform wire diameter are, in principle, as informative as single-wire measurements. The major challenge with measuring the Seebeck coefficients of nanowires lies in the design of tiny temperature probes to accurately determine the temperature difference across the nanowire. Figure 4.29a shows the schematic experimental setup for the Seebeck coefficient measurement of nanowire arrays [4.161], where two thermocouples are placed on both faces of a nanowire array and a heater is attached to one face of the array to generate a temperature gradient along the nanowire axis. Ideally, the size of the thermocouples should be much smaller than the thickness of the nanowire array template (i. e. the nanowire length) to minimize error. However, due to the thinness of most templates ($\leq 50\,\mu\mathrm{m}$) and the large size of commercially-available thermocouples ($\approx 12\,\mu\mathrm{m}$), the measured Seebeck coefficient values are usually underestimated.

The thermoelectric properties of Bi nanowire systems have been investigated extensively because of their potential as good thermoelectric materials. Figure 4.29b shows the measured Seebeck coefficients $S(T)$ as a function of temperature for nanowire arrays with diameters of 40 and 65 nm and different isoelectronic Sb alloy concentrations [4.154], and $S(T)$ results for bulk Bi are shown (solid curve) for comparison. Thermopower enhancement is observed in Fig. 4.29b as the wire diameter decreases and as the Sb content increases, which is attributed to the semimetal–semiconductor transition induced by quantum confinement and to Sb alloying effects in $Bi_{1-x}Sb_x$ nanowires. *Heremans* et al. have observed a substantial increase in the thermopower of Bi nanowires as the wire diameter decreases further, as shown in Fig. 4.30a for Bi(15 nm)/silica and Bi(9 nm)/alumina nanocom-

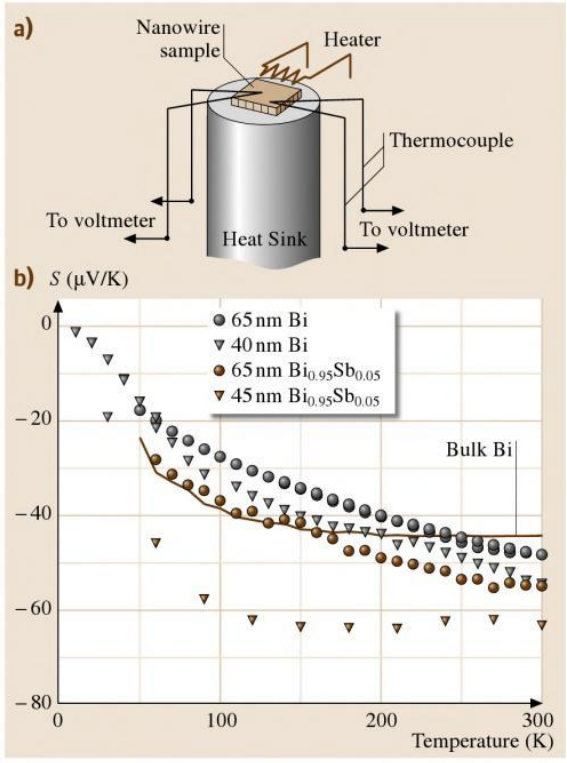

Fig. 4.29 (**a**) Experimental setup for the measurement of the Seebeck coefficient in nanowire arrays (after [4.161]). (**b**) Measured Seebeck coefficient as a function of temperature for Bi (○, ▽) and $Bi_{0.95}Sb_{0.05}$ (●, ▼) nanowires with different diameters. The *solid curve* denotes the Seebeck coefficient for bulk Bi (after [4.154]) ▶

posites [4.52]. The enhancement is due to the sharp density of states near the Fermi energy in a 1-D system. Although the samples in Fig. 4.30a also possess very high electrical resistance ($\sim$ GΩ), the results for the Bi(9 nm)/alumina samples show that the Seebeck coefficient can be enhanced by almost 1000 times relative to bulk material. However, for Bi nanowires with very small diameters ($\approx$ 4 nm), the localization effect becomes dominant, which compromises the thermopower enhancement. Therefore, for Bi nanowires, the optimal wire diameter range for the largest thermopower enhancement is found to be between 4 and 15 nm [4.52].

The effect of the nanowire diameter on the thermopower of nanowires has also been observed in Zn nanowires [4.52]. Figure 4.30b shows the Seebeck coefficient of Zn(9 nm)/alumina and Zn(4 nm)/Vycor glass nanocomposites, also exhibiting enhanced thermopower as the wire diameter decreases. It is found that while 9 nm Zn nanowires still exhibit metallic behavior,

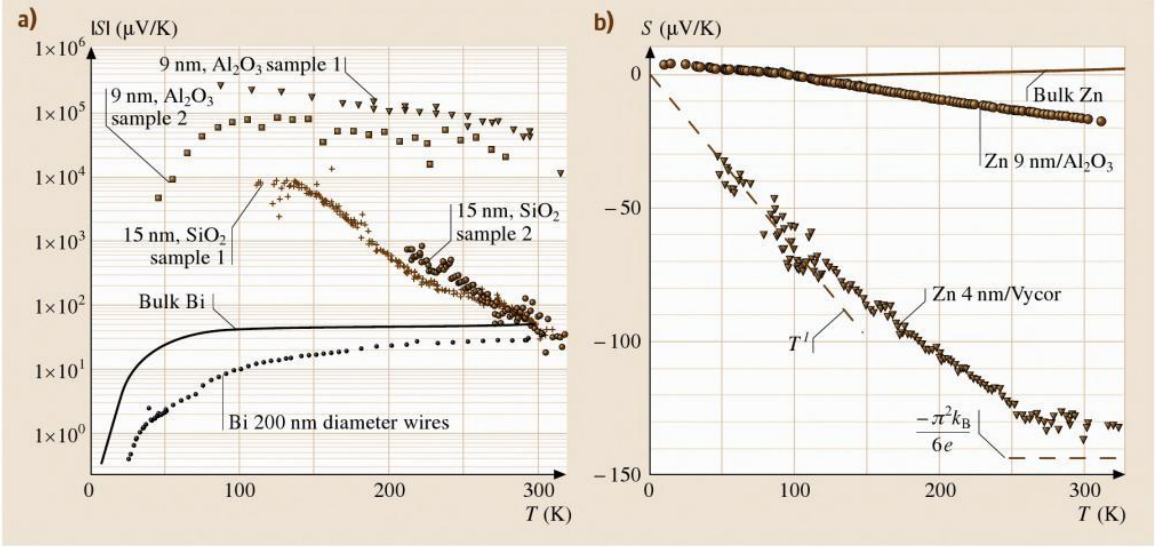

Fig. 4.30 (**a**) Absolute value of the Seebeck coefficient of two Bi(15 nm)/silica and two Bi(9 nm)/alumina nanocomposite samples, in comparison to bulk Bi and 200 nm Bi nanowires in the pores of alumina templates (after [4.52]). The *full line* on top part of the figure is a fit to a T^{-1} law. The Seebeck coefficient of the Bi(9 nm)/alumina composite is positive; the rest are negative. (**b**) The Seebeck coefficient of Zn(9 nm)/Al_2O_3 and Zn(4 nm)/Vycor glass nanocomposite samples in comparison to bulk Zn (after [4.52])

the thermopower of 4 nm Zn nanowires shows a different temperature dependence, which may be due to the 1-D localization effect, although further investigation is required for definitive identification of the conduction mechanism in such small nanowires.

Quantum Wire Superlattices

The studies on superlattice nanowires, which possess a periodic modulation in their materials composition along the wire axis, have attracted much attention recently because of their promise in various applications, such as thermoelectrics (Sect. 4.3.2) [4.90, 162], nanobarcodes (Sect. 4.3.3) [4.110], nanolasers (Sect. 4.3.3) [4.92], one-dimensional waveguides, and resonant tunneling diodes [4.94, 163]. Figure 4.31a shows a schematic structure of a superlattice nanowire consisting of interlaced quantum dots of two different materials, as denoted by A and B. Various techniques have been developed to synthesize superlattice nanowire structures with different interface conditions, as mentioned in Sects. 4.1.1 and 4.1.2.

In this superlattice (SL) nanowire structure, the electronic transport along the wire axis is made possible by the tunneling between adjacent quantum dots, while the uniqueness of each quantum dot and its 0-D characteristic behavior is maintained by the energy difference of the conduction or valence bands between quantum dots of different materials (Fig. 4.31b), which provides some amount of quantum confinement. Recently, *Björk* et al. have observed interesting nonlinear I–V characteristics with a negative differential resistance in one-dimensional heterogeneous structures made of InAs and InP, where InP serves as the potential barrier [4.94, 163]. The nonlinear I–V behavior is associated with the double barrier resonant tunneling process in one-dimensional structures, demonstrating that transport phenomena occur in superlattice nanowires via tunneling and the possibility of controlling the electronic band structure of the SL nanowires by carefully selecting the constituent materials. This new kind of structure is especially attractive for thermoelectric applications, because the interfaces between the nanodots can reduce the lattice thermal conductivity by blocking the phonon conduction along the wire axis, while electrical conduction may be sustained and even benefit from the unusual electronic band structures due to the periodic potential perturbation. For example, Fig. 4.32 shows the calculated dimensionless thermoelectric figure of merit $ZT = S^2\sigma T/\kappa$ (Sect. 4.3.2) where κ is the total thermal conductivity (including both the lattice and electronic contributions) of 10 nm diameter PbS/PbSe superlattice nanowires as a function of the segment length. A higher thermoelectric performance than for $PbSe_{0.5}S_{0.5}$ alloy nanowires can be achieved for a 10 nm diameter superlattice nanowire with segment lengths ≤ 7 nm. However, the localization effect, which may become important for very short segment lengths, may jeopardize this enhancement in the ZT of superlattice nanowires [4.153].

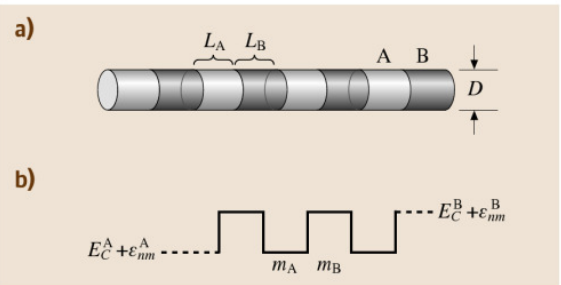

Fig. 4.31 (a) Schematic diagram of superlattice (segmented) nanowires consisting of interlaced nanodots A and B of the indicated length and wire diameter. (b) Schematic potential profile of the subbands in the superlattice nanowire (after [4.162])

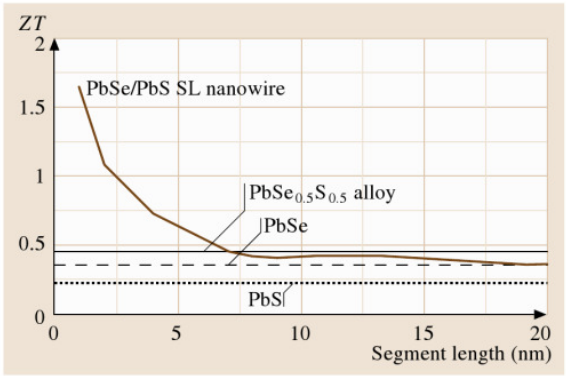

Fig. 4.32 Optimal ZT calculated as a function of segment length for 10 nm diameter PbSe/PbS nanowires at 77 K, where *optimal* refers to the placement of the Fermi level to optimize ZT. The optimal ZT for 10 nm diameter PbSe, PbS, and $PbSe_{0.5}S_{0.5}$ nanowires are 0.33, 0.22, and 0.48, respectively (after [4.153])

Thermal Conductivity of Nanowires

Experimental measurements of the temperature dependence of the thermal conductivity $\kappa(T)$ of individual suspended nanowires have been carried out on study the dependence of $\kappa(T)$ on wire diameter. In this context,

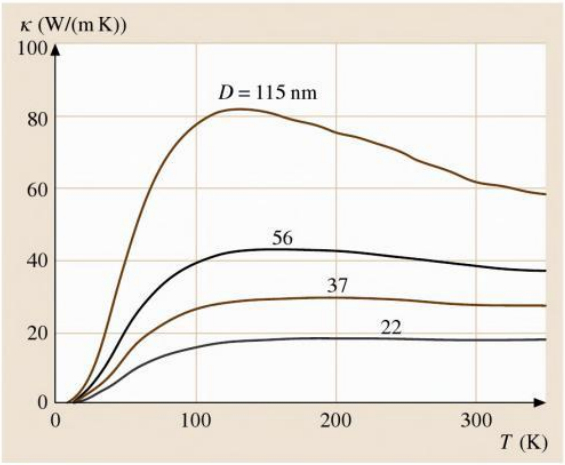

Fig. 4.33 Predicted thermal conductivities of Si nanowires of various diameters (after [4.168])

measurements have been made on nanowires down to only 22 nm in diameter [4.164]. Such measurements are very challenging and are now possible due to technological development in the micro- and nanofabrication of miniature thermal sensors, and the use of nanometer-size thermal scanning probes [4.128, 165, 166]. The experiments show that the thermal conductivity of small homogeneous nanowires may be more than one order of magnitude smaller than in the bulk, due mainly to strong boundary scattering effects [4.167]. Phonon confinement effects may eventually become important in nanowires with even smaller diameters. Measurements on mats of nanowires (Fig. 4.12) do not generally give reliable results because the contact thermal resistance between adjacent nanowires tends to be high, which is in part due to the thin surface oxide coating which most nanowires have. This surface oxide coating may also be important for thermal conductivity measurements on individual suspended nanowires because of the relative importance of phonon scattering at the lateral walls of the nanowire.

The most extensive experimental thermal conductivity measurements have been done on Si nanowires [4.164], where $\kappa(T)$ measurements have been made on nanowires in the diameter range $22 \leq d_W \leq 115$ nm. The results show a large decrease in the peak of $\kappa(T)$, associated with Umklapp processes as d_W decreases, indicating a growing importance of boundary scattering and a corresponding decreasing importance of phonon–phonon scattering. At the smallest wire diameter of 22 nm, a linear $\kappa(T)$ dependence is found experimentally, consistent with a linear T dependence of the specific heat for a 1-D system, and a temperature-independent mean free path and velocity of sound. Further insights are obtained through studies of the thermal conductivity of Si/SiGe superlattice nanowires [4.170].

Model calculations for $\kappa(T)$ based on a radiative heat transfer model have been carried out for Si nanowires [4.168]. These results show that the predicted $\kappa(T)$ behavior for Si nanowires is similar to that observed experimentally in the range of $37 \leq d_W \leq 115$ nm regarding both the functional form of $\kappa(T)$ and the magnitude of the relative decrease in the maximum thermal conductivity κ_{max} as a function of d_W. However, the model calculations predict

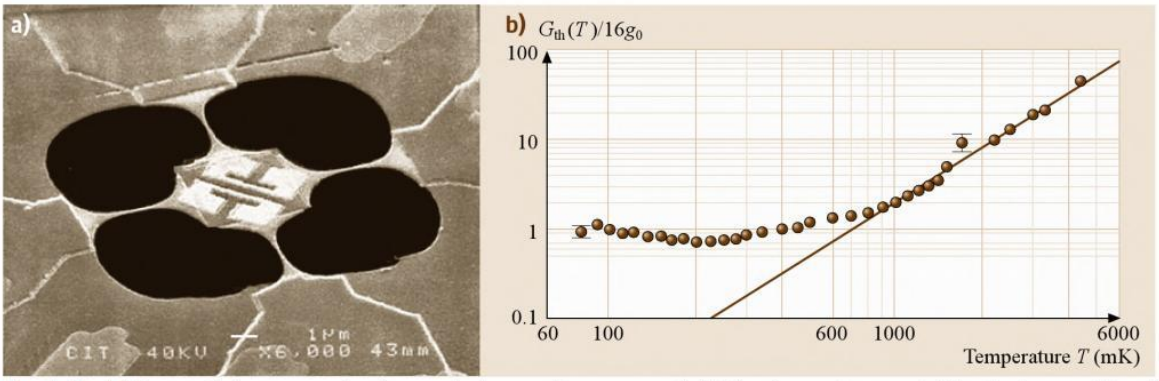

Fig. 4.34 (**a**) Suspended mesoscopic phonon device used to measure ballistic phonon transport. The device consists of an $4 \times 4\,\mu m^2$ *phonon cavity* (*center*) connected to four Si_3N_4 membranes, 60 nm thick and less than 200 nm wide. The two bright *C*-shaped objects on the phonon cavity are thin film heating and sensing Cr/Au resistors, whereas the *dark regions* are empty space. (**b**) Log–log plot of the temperature dependence of the thermal conductance G_0 of the structure in (**a**) normalized to $16g_0$ (see text) (after [4.169])

a substantially larger magnitude for $\kappa(T)$ (by 50% or more) than is observed experimentally. Furthermore, the model calculations (Fig. 4.34) do not reproduce the experimentally observed linear T dependence for the 22 nm nanowires, but rather predict a 3-D behavior for both the density of states and the specific heat in 22 nm nanowires [4.168, 171, 172].

Thermal conductance measurements on GaAs nanowires below 6 K show a power law dependence, but the T dependence becomes somewhat less pronounced below ≈ 2.5 K [4.165]. This deviation from the power law temperature dependence led to a more detailed study of the quantum limit for the thermal conductance. To carry out these more detailed experiments, a mesoscopic phonon resonator and waveguide device were constructed that included four ≈ 200 nm wide and 85 nm thick silicon nitride nanowirelike nanoconstrictions (Fig. 4.33a), and this was used to establish the quantized thermal conductance limit of $g_0 = \pi^2 k_B^2 T/(3h)$ (Fig. 4.33b) for ballistic phonon transport [4.169, 173]. For temperatures above 0.8 K, the thermal conductance in Fig. 4.33b follows a T^3 law, but as T is further reduced, a transition to a linear T dependence is observed, consistent with a phonon mean free path of ≈ 1 μm, and a thermal conductance value approaching $16g_0$, corresponding to four massless phonon modes per channel and four channels in their phonon waveguide structure (Fig. 4.33a). Ballistic phonon transport occurs when the thermal phonon wavelength (380 nm for the experimental structure) is somewhat greater than the width of the phonon waveguide at the waveguide constriction.

4.2.4 Optical Properties

Optical methods provide an easy and sensitive tool for measuring the electronic structures of nanowires, since optical measurements require minimal sample preparation (for example, contacts are not required) and the measurements are sensitive to quantum effects. Optical spectra of 1-D systems, such as carbon nanotubes, often show intense features at specific energies near singularities in the joint density of states that are formed under strong quantum confinement conditions. A variety of optical techniques have shown that the properties of nanowires are different to those of their bulk counterparts, and this section of the review focuses on these differences in the optical properties of nanowires.

Although optical properties have been shown to provide an extremely important tool for characterizing nanowires, the interpretation of these measurements is not always straightforward. The wavelength of light used to probe the sample is usually smaller than the wire length, but larger than the wire diameter. Hence, the probe light used in an optical measurement cannot be focused solely onto the wire, and the wire and the substrate on which the wire rests (or host material, if the wires are embedded in a template) are probed simultaneously. For measurements, such as photoluminescence (PL), if the substrate does not luminescence or absorb in the frequency range of the measurements, PL measures the luminescence of the nanowires directly and the substrate can be ignored. However, in reflection and transmission measurements, even a nonabsorbing substrate can modify the measured spectra of nanowires.

In this section we discuss the determination of the dielectric function for nanowires in the context of effective medium theories. We then discuss various optical techniques with appropriate examples that sensitively differentiate nanowire properties from those also found in the parent bulk material, placing particular emphasis on electronic quantum confinement effects. Finally, phonon confinement effects are reviewed.

The Dielectric Function

In this subsection, we review the use of effective medium theory as a method to handle the optical properties of nanowires whose diameters are typically smaller than the wavelength of light, noting that observable optical properties of materials can be related to the complex dielectric function [4.174, 175]. Effective medium theories [4.176, 177] can be applied to model the nanowire and substrate as one continuous composite with a single complex dielectric function $(\epsilon_1 + i\epsilon_2)$, where the real and imaginary parts of the dielectric function ϵ_1 and ϵ_2 are related to the index of refraction (n) and the absorption coefficient (K) by the relation $\epsilon_1 + i\epsilon_2 = (n + iK)^2$. Since photons at visible or infrared wavelengths *see* a dielectric function for the composite nanowire array/substrate system that is different from that of the nanowire itself, the optical transmission and reflection are different from what they would be if the light were focused only on the nanowire. One commonly observed consequence of effective medium theory is the shift in the plasma frequency in accordance with the percentage of nanowire material that is contained in the composite [4.178]. The plasma resonance occurs when $\epsilon_1(\omega)$ becomes zero, and the plasma frequency of the nanowire composite will shift to lower (higher) energies when the magnitude of the dielectric function of the host materials is larger (smaller) than that of the nanowire.

harmonic polarization tensor are found to be enhanced in nanowires while others are suppressed as the wire diameter is decreased, and such effects could be of interest for device applications. The authors also showed that the second-order nonlinearities are mostly wavelength-independent for $\lambda < 400\,\text{nm}$, which is in the transparent regime for ZnO, below the onset of band gap absorption, and this observation is also of interest for device applications.

Reflectivity and transmission measurements have also been used to study the effects of quantum confinement and surface effects on the low-energy indirect transition in bismuth nanowires [4.189]. *Black* et al. investigated an intense and sharp absorption peak in bismuth nanowires, which is not observed in bulk bismuth. The energy position E_p of this strong absorption peak increases with decreasing diameter. However, the rate of increase in energy with decreasing diameter $|\partial E_p/\partial d_W|$ is an order of magnitude less than that predicted for either a direct interband transition or for intersubband transitions in bismuth nanowires. On the other hand, the magnitude of $|\partial E_p/\partial d_W|$ agrees well with that predicted for an indirect L-point valence to T-point valence band transition (Fig. 4.37). Since both the initial and final states for the indirect L–T point valence band transition downshift in energy as the wire diameter d_W is decreased, the shift in the absorption peak results from a difference between the effective masses and not from the actual value of either of the masses. Hence the diameter dependence of the absorption peak energy is an order of magnitude less for a valence to valence band indirect transition than for a direct interband L-point transition. Furthermore, the band-tracking effect for the indirect transition gives rise to a large value for the joint density of states, thus accounting for the high intensity of this feature. The enhancement in the absorption resulting from this indirect transition may arise from a gradient in the dielectric function, which is large at the bismuth–air or bismuth–alumina interfaces, or from the relaxation of momentum conservation rules in nanosystems. It should be noted that, in contrast to the surface effect for bulk samples, the whole nanowire contributes to the optical absorption due to the spatial variation in the dielectric function, since the penetration depth is larger than or comparable to the wire diameter. In addition, the intensity can be quite signif-

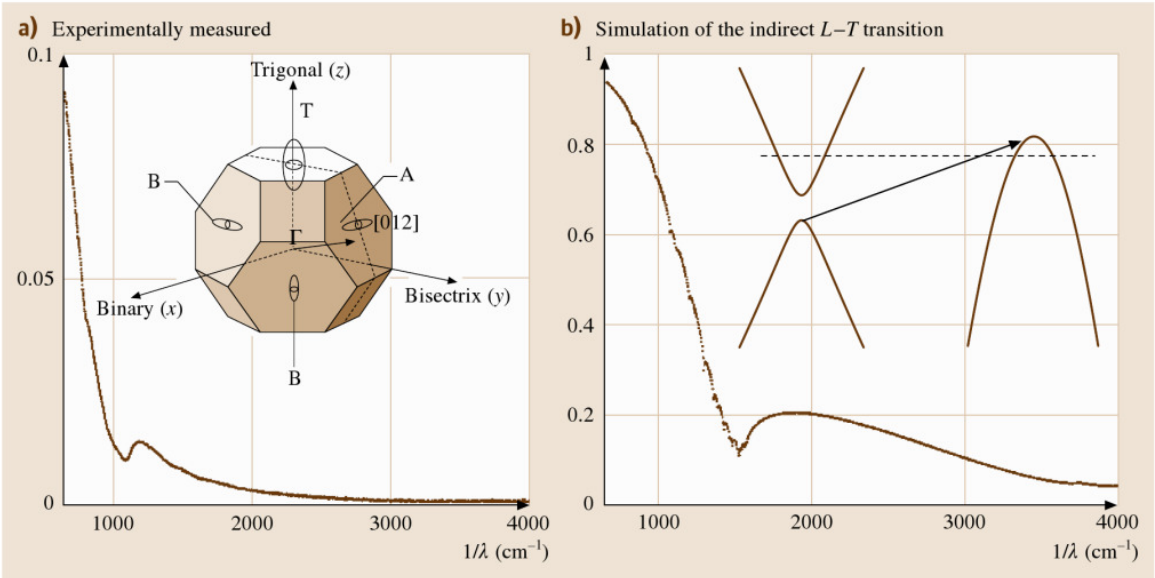

Fig. 4.37 **(a)** The measured optical transmission spectra as a function of wavenumber $(1/\lambda)$ of a $\approx 45\,\text{nm}$ diameter bismuth nanowire array. **(b)** The simulated optical transmission spectrum resulting from an indirect transition of an L-point electron to a T-point valence subband state. The *insert* in **(a)** shows the bismuth Brillouin zone, and the locations of the T-point hole and the three L-point electron pockets, including the nondegenerate A, and the doubly-degenerate B pockets. The *insert* in **(b)** shows the indirect L–T point electronic transition induced by a photon with an energy equal to the energy difference between the initial and final states minus the phonon energy (about $100\,\text{cm}^{-1}$) needed to satisfy conservation of energy in a Stokes process (after [4.188])

icant because there are abundant initial state electrons, final state holes, and appropriate phonons for making an indirect L–T point valence band transition at room temperature. Interestingly, the polarization dependence of this absorption peak is such that the strong absorption is present when the electric field is perpendicular to the wire axis, but is absent when the electric field is parallel to the wire axis, contrary to a traditional polarizer, such as a carbon nanotube where the optical E field is polarized by the nanotube itself and is aligned along the carbon nanotube axis. The observed polarization dependence for bismuth nanowires is consistent with a surface-induced effect that increases the coupling between the L-point and T-point bands throughout the full volume of the nanowire. Figure 4.37 shows the experimentally observed transmission spectrum in bismuth nanowires of ≈ 45 nm diameter (a), and the simulated optical transmission from an indirect transition in bismuth nanowires of ≈ 45 nm diameter is also shown for comparison in (b). The indirect L–T point valence band transition mechanism [4.188] is also consistent with observations of the effect on the optical spectra of a decrease in the nanowire diameter and of n-type doping of bismuth nanowires with Te.

Phonon Confinement Effects

Phonons in nanowires are spatially confined by the nanowire cross-sectional area, crystalline boundaries and surface disorder. These finite size effects give rise to phonon confinement, causing an uncertainty in the phonon wavevector which typically gives rise to a frequency shift and lineshape broadening. Since zone center phonons tend to correspond to maxima in the phonon dispersion curves, the inclusion of contributions from a broader range of phonon wave vectors results in both a downshift in frequency and an asymmetric broadening of the Raman line, which develops a low frequency tail. These phonon confinement effects have been theoretically predicted [4.191, 192] and experimentally observed in GaN [4.190], as shown in Fig. 4.38 for GaN nanowires with diameters in the range 10–50 nm. The application of these theoretical models indicates that broadening effects should be noticeable as the wire diameter in GaN nanowires decreases to ≈ 20 nm. When the wire diameter decreases further to ≈ 10 nm, the frequency downshift and asymmetric Raman line broadening effects should become

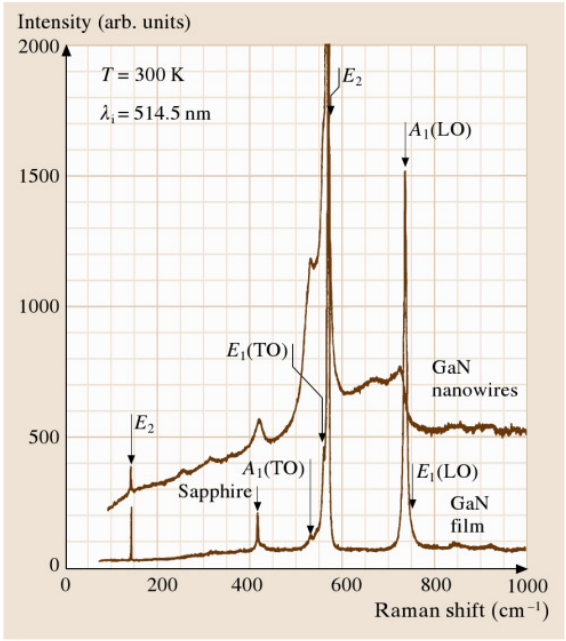

Fig. 4.38 Room-temperature Raman scattering spectra of GaN nanowires and of a 5 μm thick GaN epilayer film with green (514.5 nm) laser excitation. The Raman scattering response was obtained by dividing the measured spectra by the Bose–Einstein thermal factor [4.190]

observable in the Raman spectra for the GaN nanowires but are not found in the corresponding spectra for bulk GaN.

The experimental spectra in Fig. 4.38 show the four $A_1 + E_1 + 2E_2$ modes expected from symmetry considerations for bulk GaN crystals. Two types of quantum confinement effects are observed. The first type is the observation of the downshift and the asymmetric broadening effects discussed above. Observations of such downshifts and asymmetric broadening have also been recently reported in 7 nm diameter Si nanowires [4.193]. A second type of confinement effect found in Fig. 4.38 for GaN nanowires is the appearance of additional Raman features not found in the corresponding bulk spectra and associated with combination modes, and a zone boundary mode. Resonant enhancement effects were also observed for the A_1(LO) phonon at 728 cm^{-1} (Fig. 4.38) at higher laser excitation energies [4.190].

4.3 Applications

In the preceding sections we have reviewed many of the central characteristics that make nanowires in some cases similar to and in some cases very different from their parent materials. We have also shown that some properties are diameter-dependent, and these properties are therefore tunable during synthesis. Thus, it is of great interest to find applications that could benefit in unprecedented ways from both the unique and tunable properties of nanowires and the small sizes of these nanostructures, especially in the miniaturization of conventional devices. As the synthetic methods for the production of nanowires are maturing (Sect. 4.1) and nanowires can be made in reproducible and cost-effective ways, it is only a matter of time before applications will be seriously explored. This is a timely development, as the semiconductor industry will soon be reaching what seems to be its limit in feature size reduction, and approaching a classical-to-quantum size transition. At the same time, the field of biotechnology is expanding through the availability of tremendous genome information and innovative screening assays. Since nanowires are similar in size to the shrinking electronic components and to cellular biomolecules, it is only natural for nanowires to be good candidates for applications in these fields. Commercialization of nanowire devices, however, will require reliable mass production, effective assembly techniques and quality control methods.

In this section, applications of nanowires to electronics (Sect. 4.3.1), thermoelectrics (Sect. 4.3.2), optics (Sect. 4.3.3), chemical and biochemical sensing (Sect. 4.3.4), and magnetic media (Sect. 4.3.5) are discussed.

4.3.1 Electrical Applications

The microelectronics industry continues to face technological (in lithography for example) and economic challenges as the device feature size is decreased, especially below 100 nm. The self-assembly of nanowires might present a way to construct unconventional devices that do not rely on improvements in photolithography and, therefore, do not necessarily imply increasing fabrication costs. Devices made from nanowires have several advantages over those made by photolithography. A variety of approaches have been devised to organize nanowires via self-assembly (Sect. 4.1.4), thus eliminating the need for the expensive lithographic techniques normally required to produce devices the size of typical nanowires that are discussed in this review. In addition, unlike traditional silicon processing, different semiconductors can be used simultaneously in nanowire devices to produce diverse functionalities. Not only can wires of different materials be combined, but a single wire can be made of different materials. For example, junctions of GaAs and GaP show rectifying behavior [4.92], thus demonstrating that good electronic interfaces between two different semiconductors can be achieved in the synthesis of multicomponent nanowires. Transistors made from nanowires could also hold advantages due to their unique morphology. For example, in bulk field effect transistors (FETs), the depletion layer formed below the source and drain region results in a source–drain capacitance which limits the operation speed. However, in nanowires, the conductor is surrounded by an oxide and thus the depletion layer cannot be formed. Thus, depending on the device design, the source–drain capacitance in nanowires could be greatly minimized and possibly eliminated.

Device functionalities common in conventional semiconductor technologies, such as p-n junction diodes [4.142], field-effect transistors [4.144], logic gates [4.142], and light-emitting diodes [4.92, 194], have been recently demonstrated in nanowires, showing their promise as building blocks that could be used to construct complex integrated circuits by employing the *bottom-up* paradigm. Several approaches have been investigated to form nanowire diodes (Sect. 4.2.2). For example, Schottky diodes can be formed by contacting a GaN nanowire with Al electrodes [4.143]. Furthermore, p-n junction diodes can be formed at the crossing of two nanowires, such as the crossing of n- and p-type InP nanowires doped by Te and Zn, respectively [4.194], or Si nanowires doped by phosphorus (n-type) and boron (p-type) [4.195]. In addition to the crossing of two distinctive nanowires, heterogeneous junctions have also been constructed inside a single wire, either along the wire axis in the form of a nanowire superlattice [4.92], or perpendicular to the wire axis by forming a core–shell structure of silicon and germanium [4.111]. These various nanowire junctions not only possess the current rectifying properties (Fig. 4.22) expected of bulk semiconductor devices, but they also exhibit electroluminescence (EL) that may be interesting for optoelectronic applications, as shown in Fig. 4.39 for the electroluminescence of a crossed junction of n- and p-type InP nanowires [4.194] (Sect. 4.3.3).

In addition to the two-terminal nanowire devices, such as the p-n junctions described above, it is found that the conductance of a semiconductor nanowire can be significantly modified by applying voltage at a third gate terminal, implying the utilization of nanowires in field effect transistors (FETs). This gate terminal can either be the substrate [4.30, 196–199], a separate metal contact located close to the nanowire [4.200], or another nanowire with a thick oxide coating in the crossed nanowire junction configuration [4.142]. The operating principles of these nanowire-based FETs are discussed in Sect. 4.2.2. Various logic devices performing basic logic functions have been demonstrated using nanowire junctions [4.142], as shown in Fig. 4.40 for the OR and AND logic gates constructed from 2-by-1 and 1-by-3 nanowire p-n junctions, respectively. By functionalizing nanowires with redox-active molecules to store charge, nanowire FETs were demonstrated with two-level [4.144] and with eight-level [4.201] memory effects, which may be used for nonvolatile memory or as switches. In another advance, In_2O_3 nanowire FETs with high-k dielectric material were demonstrated, and substantially enhanced performance was obtained due to the highly efficient coupling of the gate [4.202]. A vertical FET with a surrounding gate geometry has also been demonstrated, which has the potential for high-density nanoscale memory and logic devices [4.203].

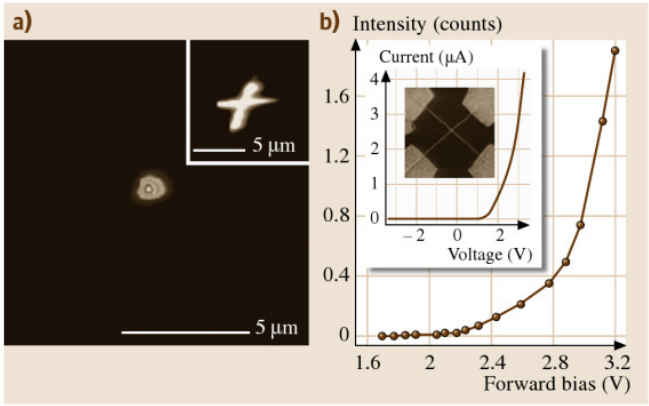

Fig. 4.39a,b Optoelectrical characterization of a crossed nanowire junction formed between 65 nm n-type and 68 nm p-type InP nanowires. **(a)** Electroluminescence (EL) image of the light emitted from a forward-biased nanowire p-n junction at 2.5 V. *Inset*, photoluminescence (PL) image of the junction. **(b)** EL intensity as a function of operation voltage. *Inset*, the SEM image and the I–V characteristics of the junction (after [4.194]). The scale bar in the *inset* is 5 μm

Nanowires have also been proposed for applications associated with electron field emission [4.204], such as flat panel displays, because of their small diameter and large curvature at the nanowire tip, which may reduce the threshold voltage for electron emission [4.205]. In

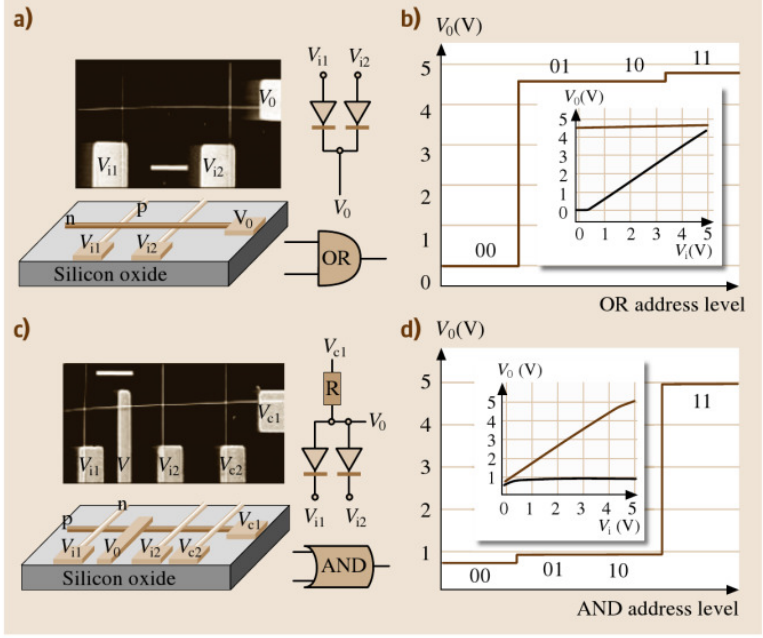

Fig. 4.40a–d Nanowire logic gates: **(a)** Schematic of logic OR gate constructed from a 2 (p-Si) by 1 (n-GaN) crossed nanowire junction. The *inset* shows the SEM image (scale bar: 1 μm) of an assembled OR gate and the symbolic electronic circuit. **(b)** The output voltage of the circuit in (**a**) versus the four possible logic address level inputs: (0,0); (0,1); (1,0); (1,1), where logic 0 input is 0 V and logic 1 is 5 V (same for below). **(c)** Schematic of logic AND gate constructed from a 1 (p-Si) by 3 (n-GaN) crossed nanowire junction. The *inset* shows the SEM image (scale bar: 1 μm) of an assembled AND gate and the symbolic electronic circuit. **(d)** The output voltage of the circuit in (**c**) versus the four possible logic address level inputs (after [4.142])

this regard, the demonstration of very high field emission currents from the sharp tip (≈ 10 nm radius) of a Si cone [4.204], from carbon nanotubes [4.206], from Si nanowires inside a carbon nanotube [4.207], and from Co nanowires [4.208], has stimulated interest in this potential area of application for nanowires.

The concept of constructing electronic devices based on nanowires has already been demonstrated, and the next step for electronic applications would be to devise a feasible method for integration and mass production. We expect that, in order to maintain the growing rate of device density and functionality in the existing electronic industry, new kinds of complementary electronic devices will emerge from this *bottom-up* scheme for nanowire electronics, different from what has been produced by the traditional *top-down* approach pursued by conventional electronics.

4.3.2 Thermoelectric Applications

One proposed application for nanowires is for thermoelectric cooling and for the conversion between thermal and electrical energy [4.171, 209]. The efficiency of a thermoelectric device is measured in terms of a dimensionless figure of merit ZT, where Z is defined as

$$Z = \frac{\sigma S^2}{\kappa}, \tag{4.2}$$

where σ is the electrical conductivity, S is the Seebeck coefficient, κ is the thermal conductivity, and T is the temperature. In order to achieve a high ZT and therefore efficient thermoelectric performance, a high electrical conductivity, a hugh Seebeck coefficient and a low thermal conductivity are required. In 3-D systems, the electronic contribution to κ is proportional to σ in accordance with the Wiedemann–Franz law, and normally materials with high S have a low σ. Hence an increase in the electrical conductivity (for example by electron donor doping) results in an adverse variation in both the Seebeck coefficient (decreasing) and the thermal conductivity (increasing). These two trade-offs set the upper limit for increasing ZT in bulk materials, with the maximum ZT remaining ≈ 1 at room temperature for the 1960–1995 time frame.

The high electronic density of states in quantum-confined structures is proposed as a promising possibility to bypass the Seebeck/electrical conductivity trade-off and to control each thermoelectric-related variable independently, thereby allowing for increased electrical conductivity, relatively low thermal conductivity, and a large Seebeck coefficient simultaneously [4.210]. For example, Figs. 4.29 and 4.30a in Sect. 4.2.3 show an enhanced in S for bismuth and bismuth-antimony nanowires as the wire diameter decreases. In addition to alleviating the undesired connections between σ, S and the electronic contribution to the thermal conductivity, nanowires also have the advantage that the phonon contribution to the thermal conductivity is greatly reduced because of boundary scattering (Sect. 4.2), thereby achieving a high ZT. Figure 4.41a shows the theoretical values for ZT versus sample size for both bismuth thin films (2-D) and nanowires (1-D) in the quantum-confined regime, exhibiting a rapidly increasing ZT as the quantum size effect becomes more and more important [4.210]. In addition, the quantum size effect in nanowires can be combined with other parameters to tailor the band structure and electronic transport behavior (for instance, Sb alloying in Bi) to further optimize ZT. For example, Fig. 4.41b shows the predicted ZT for p-type $Bi_{1-x}Sb_x$ alloy nanowires as a function of wire diameter and Sb content x [4.211]. The occurrence of a local ZT maxima in the vicinity of $x \approx 0.13$ and $d_W \approx 45$ nm is due to the coalescence of ten valence bands in the nanowire and the resulting unusual high density of states for holes, which is a phenomenon absent in bulk $Bi_{1-x}Sb_x$ alloys. For nanowires with very small diameters, it is speculated that localization effects will eventually limit the enhancement of ZT. However, in bismuth nanowires, localization effects are not significant for wires with diameters larger than 9 nm [4.52]. In addition to 1-D nanowires, ZT values as high as ≈ 2 have also been experimentally demonstrated in macroscopic samples containing PbSe quantum dots (0-D) [4.212] and stacked 2-D films [4.167].

Although the application of nanowires to thermoelectrics appears very promising, these materials are still in the research phase of the development cycle and are far from being commercialized. One challenge for thermoelectric devices based on nanowires lies in finding a suitable host material that will not reduce ZT too much due to the unwanted heat conduction through the host material. Therefore, the host material should have a low thermal conductivity and occupy a volume percentage in the composite material that is as low as possible, while still providing the quantum confinement and the support for the nanowires.

4.3.3 Optical Applications

Nanowires also hold promise for optical applications. One-dimensional systems exhibit a singularity in their joint density of states, allowing quantum effects in

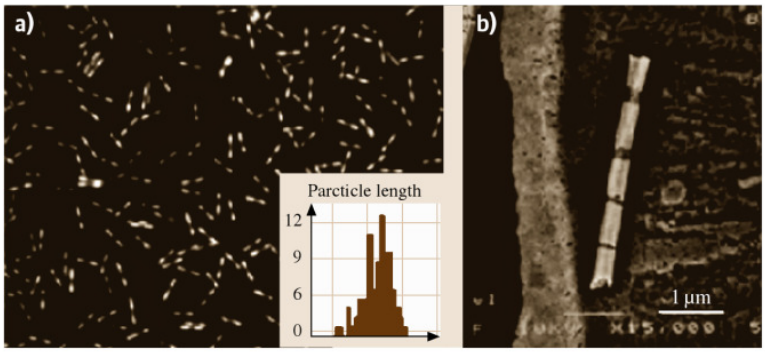

Fig. 4.43 (**a**) An optical image of many short bar-coded Au-Ag-Au-Au wires and (**b**) an FE-SEM image of an Au/Ag barcoded wire with multiple strips of varying length. The *insert* in (**a**) shows a histogram of the particle lengths for 106 particles in this image (after [4.110])

limit, and not by synthesis limitations, and thus can be as small as 145 nm. Figure 4.43a shows an optical image of many Au-Ag-Au-Ag barcoded wires, where the silver segments show higher reflectivity. Figure 4.43b is a backscattering mode FE-SEM image of a single nanowire, highlighting the composition and segment length variations along the nanowire.

Both the large surface area and the high conductivity along the length of a nanowire are favorable for its use in inorganic–organic solar cells [4.225], which offer promise from a manufacturing and cost-effectiveness standpoint. In a hybrid nanocrystal–organic solar cell, the incident light forms bound electron–hole pairs (excitons) in both the inorganic nanocrystal and in the surrounding organic medium. These excitons diffuse to the inorganic–organic interface and disassociate to form an electron and a hole. Since conjugated polymers usually have poor electron mobilities, the inorganic phase is chosen to have a higher electron affinity than the organic phase so that the organic phase carries the holes and the semiconductor carries the electrons. The separated electrons and holes drift to the external electrodes through the inorganic and organic materials, respectively. However, only those excitons formed within an exciton diffusion length from an interface can disassociate before recombining, and therefore the distance between the dissociation sites limits the efficiency of a solar cell. A solar cell prepared from a composite of CdSe nanorods inside poly(3-ethylthiophene) [4.225] yielded monochromatic power efficiencies of 6.9% and power conversion efficiencies of 1.7% under A.M. 1.5 illumination (equal to solar irradiance through 1.5 times the air mass of the Earth at direct normal incidence). The nanorods provide a large surface area with good chemical bonding to the polymer for efficient charge transfer and exciton dissociation. Furthermore, they provide a good conduction path for the electrons to reach the electrode. Their enhanced absorption coefficient and their tunable bandgap are also characteristics that can be used to enhance the energy conversion efficiency of solar cells.

4.3.4 Chemical and Biochemical Sensing Devices

Sensors for chemical and biochemical substances with nanowires as the sensing probe are a very attractive application area. Nanowire sensors will potentially be smaller, more sensitive, demand less power, and react faster than their macroscopic counterparts. Arrays of nanowire sensors could, in principle, achieve nanometer-scale spatial resolution and therefore provide accurate real-time information regarding not only the concentration of a specific analyte but also its spatial distribution. Such arrays could be very useful, for example, for dynamic studies on the effects of chemical gradients on biological cells. The operation of sensors made with nanowires, nanotubes, or nanocontacts is based mostly on the reversible change in the conductance of the nanostructure upon absorption of the agent to be detected, but other detection methods, such as mechanical and optical detection, are conceptually plausible. The increased sensitivity and faster response time of nanowires are a result of the large surface-to-volume ratio and the small cross section available for conduction channels. In the bulk, on the other hand, the abundance of charges can effectively shield external fields, and the abundance of material can afford many alternative conduction channels. Therefore, a stronger chemical stimulus and longer response time are necessary to observe changes in the physical properties of a 3-D sensor in comparison to a nanowire.

It is often necessary to modify the surface of the nanowires to achieve a strong interaction with the analytes that need to be detected. Surface modifications utilize the self-assembly, chemisorption or chemical re-

activity of selected organic molecules and polymers towards metal and oxide surfaces. Examples include: thiols on gold, isocyanides on platinum, and siloxanes on silica. These surface coatings regulate the binding and chemical reactivity of other molecules towards the nanowire in a predictable manner [4.226].

Cui et al. placed silicon nanowires made by the VLS method (Sect. 4.1.2) between two metal electrodes and modified the silicon oxide coating of the wire through the addition of molecules that are sensitive to the analyte to be detected [4.227]. For example, a pH sensor was made by covalently linking an amine-containing silane to the surface of the nanowire. Variations in the pH of the solution into which the nanowire was immersed caused protonation and deprotonation of the $-NH_2$ and the $-SiOH$ groups on the surface of the nanowire. The variation in surface charge density regulates the conductance of the nanowire; due to the p-type characteristics of a silicon wire, the conductance increases with the addition of negative surface charge. The combined acid and base behavior of the surface groups results in an approximately linear dependence of the conductance on pH in the pH range 2 to 9, thus leading to a direct readout pH meter. This same type of approach was used for the detection of the binding of biomolecules, such as streptavidin using biotin-modified nanowires (Fig. 4.44). This nanowire-based device has high sensitivity and could detect streptavidin binding down to a concentration of 10 pM (10^{-12} mol). Subsequent results demonstrated the capabilities of these functionalized Si nanowire sensors as DNA sensors down to the femtomolar range [4.228]. The chemical detection devices were made in a field effect transistor geometry, so that the back-gate potential could be used to regulate the conductance in conjugation with the chemical detection and to provide a real-time direct read-out [4.227]. The extension of this device to detect multiple analytes using multiple nanowires, each sensitized to a different analyte, could provide for fast, sensitive, and in situ screening procedures.

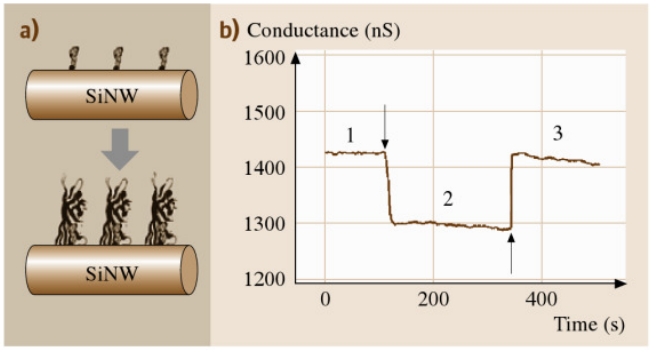

Fig. 4.44 (a) Streptavidin molecules bind to a silicon nanowire functionalized with biotin. The binding of streptavidin to biotin causes the nanowire to change its resistance. (b) The conductance of a biotin-modified silicon nanowire exposed to streptavidin in a buffer solution (regions 1 and 3) and with the introduction of a solution of antibiotin monoclonal antibody (region 2) (after [4.227])

A similar approach was used by *Favier* et al., who made a nanosensor for the detection of hydrogen from of an array of palladium nanowires between two metal contacts [4.44]. They demonstrated that nanogaps were present in their nanowire structure, and upon absorption of H_2 and formation of Pd hydride, the nanogap structure would close and improve the electrical contact, thereby increasing the conductance of the nanowire array. The response time of these sensors was 75 ms, and they could operate in the range 0.5–5% H_2 before saturation occurred.

4.3.5 Magnetic Applications

It has been demonstrated that arrays of single-domain magnetic nanowires can be prepared with controlled nanowire diameter and length, aligned along a common direction and arranged in a close-packed ordered array (Sect. 4.1), and that the magnetic properties (coercivity, remanence and dipolar magnetic interwire interaction) can be controlled to achieve a variety of magnetic applications [4.40, 79].

The most interesting of these applications is for magnetic storage, where the large nanowire aspect ratio (length/diameter) is advantageous for preventing the onset of the *superparamagnetic* limit at which the magnetization direction in the magnetic grains can be reversed by the thermal energy $k_B T$, thereby resulting in loss of recorded data in the magnetic recording medium. The magnetic energy in a grain can be increased by increasing either the volume or the anisotropy of the grain. If the volume is increased, the particle size increases, so the resolution is decreased. For spherical magnetized grains, the superparamagnetic limit at room temperature is reached at 70 Gbit/in^2. In nanowires, the anisotropy is very large and yet the wire diameters are small, so that the magnetostatic switching energy can easily be above the thermal energy while the spatial resolution is large. For magnetic data storage applications, a large aspect ratio is needed for the nanowires in order to maintain a high coercivity, and a sufficient separation between nanowires is needed to suppress interwire magnetic dipolar coupling. Thus

nanowires can form stable and highly dense magnetic memory arrays with packing densities in excess of 10^{11} wires/cm^2.

The onset of superparamagnetism can be prevented in the single-domain magnetic nanowire arrays that have already been fabricated using either porous alumina templates to make Ni nanowires with 35 nm diameters [4.40] or diblock copolymer templates [4.79] to make Co nanowires, with mean diameters of 14 nm and 100% filling of the template pores (Sect. 4.1.1). The ordered magnetic nanowire arrays that have already been demonstrated offer the exciting promise of systems permitting 10^{12} bits/in^2 data storage.

4.4 Concluding Remarks

In this chapter, we reviewed the synthesis, characterization and physical properties of nanowires, placing particular emphasis on nanowire properties that differ from those of the bulk counterparts and potential applications that might result from the special structures and properties of nanowires.

We have shown that the newly emerging field of nanowire research has developed very rapidly over the past few years, driven by the development of a variety of complementary nanowire synthesis methods and effective tools for measuring nanowire structure and properties (Sects. 4.1 and 4.2). At present, much of the progress is at the demonstration-of-concept level, with many gaps in knowledge remaining to be elucidated, theoretical models to be developed, and new nanowire systems to be explored. Having demonstrated that many of the most interesting discoveries to date relate to nanowire properties not present in their bulk material counterparts, we can expect future research emphasis to be increasingly focused on smaller diameter nanowires, where new unexplored physical phenomena related to quantum confinement effects are more likely to be found. We can also expect the development of applications to follow, some coming sooner and others later. Many promising applications are now at the early demonstration stage (Sect. 4.3), but are moving ahead rapidly because of their promise of new functionality, not previously available, in the fields of electronics, optoelectronics, biotechnology, magnetics, and energy conversion and generation, among others. Many exciting challenges remain in advancing both the nanoscience and the nanotechnological promise already demonstrated by the nanowire research described in this review.

References

4.1 R.P. Feynman: There's plenty of room at the bottom, Caltech Eng. Sci. **23**, 22 (1960)

4.2 Y. Mao, S.S. Wong: General, room-temperature method for the synthesis of isolated as well as arrays of single-crystalline ABO_4-type nanorods, J. Am. Chem. Soc. **126**, 15245–15252 (2004)

4.3 E. Braun, Y. Eichen, U. Sivan, G. Ben-Yoseph: DNA-templated assembly and electrode attachment of a conducting silver wire, Nature **391**, 775–778 (1998)

4.4 G. Sauer, G. Brehm, S. Schneider, K. Nielsch, R.B. Wehrspohn, J. Choi, H. Hofmeister, U. Gösele: Highly ordered monocrystalline silver nanowire arrays, J. Appl. Phys. **91**, 3243–3247 (2002)

4.5 G.L. Hornyak, C.J. Patrissi, C.M. Martin: Fabrication, characterization and optical properties of gold nanoparticle/porous alumina composites: The non-scattering Maxwell–Garnett limit, J. Phys. Chem. B **101**, 1548–1555 (1997)

4.6 X.Y. Zhang, L.D. Zhang, Y. Lei, L.X. Zhao, Y.Q. Mao: Fabrication and characterization of highly ordered Au nanowire arrays, J. Mater. Chem. **11**, 1732–1734 (2001)

4.7 Y.-T. Cheng, A.M. Weiner, C.A. Wong, M.P. Balogh, M.J. Lukitsch: Stress-induced growth of bismuth nanowires, Appl. Phys. Lett. **81**, 3248–3250 (2002)

4.8 J. Heremans, C.M. Thrush, Y.-M. Lin, S. Cronin, Z. Zhang, M.S. Dresselhaus, J.F. Mansfield: Bismuth nanowire arrays: Synthesis, galvanomagnetic properties, Phys. Rev. B **61**, 2921–2930 (2000)

4.9 L. Piraux, S. Dubois, J.L. Duvail, A. Radulescu, S. Demoustier-Champagne, E. Ferain, R. Legras: Fabrication and properties of organic, metal nanocylinders in nanoporous membranes, J. Mater. Res. **14**, 3042–3050 (1999)

4.10 K. Hong, F.Y. Yang, K. Liu, D.H. Reich, P.C. Searson, C.L. Chien, F.F. Balakirev, G.S. Boebinger: Giant positive magnetoresistance of Bi nanowire arrays in high magnetic fields, J. Appl. Phys. **85**, 6184–6186 (1999)

4.11 A.J. Yin, J. Li, W. Jian, A.J. Bennett, J.M. Xu: Fabrication of highly ordered metallic nanowire arrays by electrodeposition, Appl. Phys. Lett. **79**, 1039–1041 (2001)

4.12 Z. Zhang, J.Y. Ying, M.S. Dresselhaus: Bismuth quantum-wire arrays fabricated by a vacuum melting and pressure injection process, J. Mater. Res. **13**, 1745–1748 (1998)

4.13 Z. Zhang, D. Gekhtman, M.S. Dresselhaus, J.Y. Ying: Processing and characterization of single-crystalline ultrafine bismuth nanowires, Chem. Mater. **11**, 1659–1665 (1999)

4.14 T.E. Huber, M.J. Graf, P. Constant: Processing and characterization of high-conductance bismuth wire array composites, J. Mater. Res. **15**, 1816–1821 (2000)

4.15 L. Li, G. Li, Y. Zhang, Y. Yang, L. Zhang: Pulsed electrodeposition of large-area, ordered $Bi_{1-x}Sb_x$ nanowire arrays from aqueous solutions, J. Phys. Chem. B **108**, 19380–19383 (2004)

4.16 M.S. Sander, A.L. Prieto, R. Gronsky, T. Sands, A.M. Stacy: Fabrication of high-density, high aspect ratio, large-area bismuth telluride nanowire arrays by electrodeposition into porous anodic alumina templates, Adv. Mater. **14**, 665–667 (2002)

4.17 M. Chen, Y. Xie, J. Lu, Y.J. Xiong, S.Y. Zhang, Y.T. Qian, X.M. Liu: Synthesis of rod-, twinrod-, and tetrapod-shaped CdS nanocrystals using a highly oriented solvothermal recrystallization technique, J. Mater. Chem. **12**, 748–753 (2002)

4.18 D. Xu, Y. Xu, D. Chen, G. Guo, L. Gui, Y. Tang: Preparation of CdS single-crystal nanowires by electrochemically induced deposition, Adv. Mater. **12**, 520–522 (2000)

4.19 D. Routkevitch, T. Bigioni, M. Moskovits, J.M. Xu: Electrochemical fabrication of CdS nanowire arrays in porous anodic aluminum oxide templates, J. Phys. Chem. **100**, 14037–14047 (1996)

4.20 L. Manna, E.C. Scher, A.P. Alivisatos: Synthesis of soluble and processable rod-, arrow-, teardrop-, and tetrapod-shaped CdSe nanocrystals, J. Am. Chem. Soc. **122**, 12700–12706 (2000)

4.21 D. Routkevitch, A.A. Tager, J. Haruyama, D. Al-Mawlawi, M. Moskovits, J.M. Xu: Nonlithographic nano-wire arrays: fabrication, physics, and device applications, IEEE Trans. Electron. Dev. **43**, 1646–1658 (1996)

4.22 D.S. Xu, D.P. Chen, Y.J. Xu, X.S. Shi, G.L. Guo, L.L. Gui, Y.Q. Tang: Preparation of II–VI group semiconductor nanowire arrays by dc electrochemical deposition in porous aluminum oxide templates, Pure Appl. Chem. **72**, 127–135 (2000)

4.23 R. Adelung, F. Ernst, A. Scott, M. Tabib-Azar, L. Kipp, M. Skibowski, S. Hollensteiner, E. Spiecker, W. Jäger, S. Gunst, A. Klein, W. Jägermann, V. Zaporojtchenko, F. Faupel: Self-assembled nanowire networks by deposition of copper onto layered-crystal surfaces, Adv. Mater. **14**, 1056–1061 (2002)

4.24 T. Gao, G.W. Meng, J. Zhang, Y.W. Wang, C.H. Liang, J.C. Fan, L.D. Zhang: Template synthesis of single-crystal Cu nanowire arrays by electrodeposition, Appl. Phys. A **73**, 251–254 (2001)

4.25 D. Al-Mawlawi, N. Coombs, M. Moskovits: Magnetic-properties of Fe deposited into anodic aluminum-oxide pores as a function of particle-size, J. Appl. Phys. **70**, 4421–4425 (1991)

4.26 F. Li, R.M. Metzger: Activation volume of α-Fe particles in alumite films, J. Appl. Phys. **81**, 3806–3808 (1997)

4.27 A. Sugawara, T. Coyle, G.G. Hembree, M.R. Scheinfein: Self-organized Fe nanowire arrays prepared by shadow deposition on NaCl(110) templates, Appl. Phys. Lett. **70**, 1043–1045 (1997)

4.28 G.S. Cheng, L.D. Zhang, Y. Zhu, G.T. Fei, L. Li, C.M. Mo, Y.Q. Mao: Large-scale synthesis of single crystalline gallium nitride nanowires, Appl. Phys. Lett. **75**, 2455–2457 (1999)

4.29 G.S. Cheng, L.D. Zhang, S.H. Chen, Y. Li, L. Li, X.G. Zhu, Y. Zhu, G.T. Fei, Y.Q. Mao: Ordered nanostructure of single-crystalline GaN nanowires in a honeycomb structure of anodic alumina, J. Mater. Res. **15**, 347–350 (2000)

4.30 Y. Huang, X. Duan, Y. Cui, C.M. Lieber: Gallium nitride nanowire nanodevices, Nano Lett. **2**, 101–104 (2002)

4.31 X. Duan, C.M. Lieber: Laser-assisted catalytic growth of single crystal GaN nanowires, J. Am. Chem. Soc. **122**, 188–189 (2000)

4.32 A.D. Berry, R.J. Tonucci, M. Fatemi: Fabrication of GaAs, InAs wires in nanochannel glass, Appl. Phys. Lett. **69**, 2846–2848 (1996)

4.33 J.R. Heath, F.K. LeGoues: A liquid solution synthesis of single-crystal germanium quantum wires, Chem. Phys. Lett. **208**, 263–268 (1993)

4.34 Y. Wu, P. Yang: Germanium nanowire growth via simple vapor transport, Chem. Mater. **12**, 605–607 (2000)

4.35 Y.F. Zhang, Y.H. Tang, N. Wang, C.S. Lee, I. Bello, S.T. Lee: Germanium nanowires sheathed with an oxide layer, Phys. Rev. B **61**, 4518–4521 (2000)

4.36 S.J. May, J.-G. Zheng, B.W. Wessels, L.J. Lauhon: Dendritic nanowire growth mediated by a self-assembled catalyst, Adv. Mater. **17**, 598–602 (2005)

4.37 S. Han, C. Li, Z. Liu, B. Lei, D. Zhang, W. Jin, X. Liu, T. Tang, C. Zhou: Transition metal oxide core-shell nanowires: Generic synthesis and transport studies, Nano Lett. **4**, 1241–1246 (2004)

4.38 M.P. Zach, K.H. Ng, R.M. Penner: Molybdenum nanowires by electrodeposition, Science **290**, 2120–2123 (2000)

4.39 L. Sun, P.C. Searson, L. Chien: Electrochemical deposition of nickel nanowire arrays in single-crystal mica films, Appl. Phys. Lett. **74**, 2803–2805 (1999)

4.40 K. Nielsch, R. Wehrspohn, S. Fischer, H. Kronmüller, J. Barthel, J. Kirschner, U. Gösele: Magnetic properties of 100 nm nickel nanowire arrays obtained from

ordered porous alumina templates, MRS Symp. Proc. **636**, D1.9–1–D1.9–6 (2001)
4.41 Y. Wang, X. Jiang, T. Herricks, Y. Xia: Single crystalline nanowires of lead: Large-scale synthesis, mechanistic studies, and transport measurements, J. Phys. Chem. B **108**, 8631–8640 (2004)
4.42 E. Lifshitz, M. Bashouti, V. Kloper, A. Kigel, M.S. Eisen, S. Berger: Synthesis and characterization of PbSe quantum wires, multipods, quantum rods, cubes, Nano Lett. **3**, 857–862 (2003)
4.43 W. Lu, P. Gao, W.B. Jian, Z.L. Wang, J. Fang: Perfect orientation ordered in-situ one-dimensional self-assembly of Mn-doped PbSe nanocrystals, J. Am. Chem. Soc. **126**, 14816–14821 (2004)
4.44 F. Favier, E.C. Walter, M.P. Zach, T. Benter, R.M. Penner: Hydrogen sensors and switches from electrodeposited palladium mesowire arrays, Science **293**, 2227–2231 (2001)
4.45 B. Gates, B. Mayers, B. Cattle, Y. Xia: Synthesis, characterization of uniform nanowires of trigonal selenium, Adv. Funct. Mater. **12**, 219–227 (2002)
4.46 C.A. Huber, T.E. Huber, M. Sadoqi, J.A. Lubin, S. Manalis, C.B. Prater: Nanowire array composites, Science **263**, 800–802 (1994)
4.47 Y. Cui, L.J. Lauhon, M.S. Gudiksen, J. Wang, C.M. Lieber: Diameter-controlled synthesis of single crystal silicon nanowires, Appl. Phys. Lett. **78**, 2214–2216 (2001)
4.48 A.M. Morales, C.M. Lieber: A laser ablation method for the synthesis of crystalline semiconductor nanowires, Science **279**, 208–211 (1998)
4.49 N. Wang, Y.F. Zhang, Y.H. Tang, C.S. Lee, S.T. Lee: SiO_2-enhanced synthesis of Si nanowires by laser ablation, Appl. Phys. Lett. **73**, 3902–3904 (1998)
4.50 M.K. Sunkara, S. Sharma, R. Miranda, G. Lian, E.C. Dickey: Bulk synthesis of silicon nanowires using a low-temperature vapor-liquid-solid method, Appl. Phys. Lett. **79**, 1546–1548 (2001)
4.51 S. Vaddiraju, H. Chandrasekaran, M.K. Sunkara: Vapor phase synthesis of tungsten nanowires, J. Am. Chem. Soc. **125**, 10792–10793 (2003)
4.52 J.P. Heremans, C.M. Thrush, D.T. Morelli, M.-C. Wu: Thermoelectric power of bismuth nanocomposites, Phys. Rev. Lett. **88**, 216801–1–216801–4 (2002)
4.53 Y. Li, G.S. Cheng, L.D. Zhang: Fabrication of highly ordered ZnO nanowire arrays in anodic alumina membranes, J. Mater. Res. **15**, 2305–2308 (2000)
4.54 P. Yang, H. Yan, S. Mao, R. Russo, J. Johnson, R. Saykally, N. Morris, J. Pham, R. He, H.-J. Choi: Controlled growth of ZnO nanowires and their optical properties, Adv. Funct. Mater. **12**, 323–331 (2002)
4.55 M.J. Zheng, L.D. Zhang, G.H. Li, W.Z. Shen: Fabrication and optical properties of large-scale uniform zinc oxide nanowire arrays by one-step electrochemical deposition technique, Chem. Phys. Lett. **363**, 123–128 (2002)
4.56 M.S. Dresselhaus, Y.-M. Lin, O. Rabin, A. Jorio, A.G. Souza Filho, M.A. Pimenta, R. Saito, G.G. Samsonidze, G. Dresselhaus: Nanowires and nanotubes, Mater. Sci. Eng. C **23**, 129–140 (2003), also in: Current trends in nanotechnologies: From materials to systems, Eur. Mater. Res. Soc. Symp. Proc., Vol. 140, ed. by W. Jantsch, H. Grimmeiss, G. Marietta (Elsevier, Amsterdam 2002)
4.57 R. Saito, G. Dresselhaus, M.S. Dresselhaus: *Physical Properties of Carbon Nanotubes* (Imperial College Press, London 1998)
4.58 M.S. Dresselhaus, G. Dresselhaus, P. Avouris: Carbon nanotubes: Synthesis, structure, properties and applications, Springer Ser. Top. Appl. Phys. **80**, 1–447 (2001)
4.59 R.C. Haddon: Special issue on carbon nanotubes, Acc. Chem. Res. **35**, 997–1113 (2002)
4.60 Y.-M. Lin, X. Sun, S. Cronin, Z. Zhang, J.Y. Ying, M.S. Dresselhaus: Fabrication, transport properties of Te-doped bismuth nanowire arrays. In: *Molecular Electronics: MRS Symposium Proceedings*, Vol. 582, ed. by S.T. Pantelides, M.A. Reed, J. Murday, A. Aviran (Materials Research Society Press, Pittsburgh 2000) pp. 1–6, Chap. H10.3
4.61 C.R. Martin: Nanomaterials: A membrane-based synthetic approach, Science **266**, 1961–1966 (1994)
4.62 G.A. Ozin: Nanochemistry: synthesis in diminishing dimensions, Adv. Mater. **4**, 612–649 (1992)
4.63 R.J. Tonucci, B.L. Justus, A.J. Campillo, C.E. Ford: Nanochannel array glass, Science **258**, 783–785 (1992)
4.64 J.Y. Ying: Nanoporous systems and templates, Sci. Spec. **18**, 56–63 (1999)
4.65 J.W. Diggle, T.C. Downie, C.W. Goulding: Anodic oxide films on aluminum, Chem. Rev. **69**, 365–405 (1969)
4.66 J.P. O'Sullivan, G.C. Wood: The morphology and mechanism of formation of porous anodic films on aluminum, Proc. R. Soc. Lond. A **317**, 511–543 (1970)
4.67 A.P. Li, F. Müller, A. Birner, K. Neilsch, U. Gösele: Hexagonal pore arrays with a 50–420nm interpore distance formed by self-organization in anodic alumina, J. Appl. Phys. **84**, 6023–6026 (1998)
4.68 J.P. Sullivan, G.C. Wood: The morphology, mechanism of formation of porous anodic films on aluminum, Proc. R. Soc. Lond. A **317**, 511–543 (1970)
4.69 O. Jessensky, F. Müller, U. Gösele: Self-organized formation of hexagonal pore arrays in anodic alumina, Appl. Phys. Lett. **72**, 1173–1175 (1998)
4.70 F. Li, L. Zhang, R.M. Metzger: On the growth of highly ordered pores in anodized aluminum oxide, Chem. Mater. **10**, 2470–2480 (1998)
4.71 H. Masuda, M. Satoh: Fabrication of gold nanodot array using anodic porous alumina as an evaporation mask, Jpn. J. Appl. Phys. **35**, L126–L129 (1996)
4.72 E. Ferain, R. Legras: Track-etched membrane – dynamics of pore formation, Nucl. Instrum. Methods B **84**, 331–336 (1993)

4.135 D.A. Wharam, T.J. Thornton, R. Newbury, M. Pepper, H. Ahmed, J.E.F. Frost, D.G. Hasko, D.C. Peacock, D.A. Ritchie, G.A.C. Jones: One-dimensional transport and the quantization of the ballistic resistance, J. Phys. C **21**, L209–L214 (1988)
4.136 B.J. van Wees, H. van Houten, C.W.J. Beenakker, J.G. Williamson, L.P. Kouvenhoven, D. van der Marel, C.T. Foxon: Quantized conductance of point contacts in a two-dimensional electron gas, Phys. Rev. Lett. **60**, 848–850 (1988)
4.137 C.J. Muller, J.M. van Ruitenbeek, L.J. deJongh: Conductance and supercurrent discontinuities in atomic-scale metallic constrictions of variable width, Phys. Rev. Lett. **69**, 140–143 (1992)
4.138 C.J. Muller, J.M. Krans, T.N. Todorov, M.A. Reed: Quantization effects in the conductance of metallic contacts at room temperature, Phys. Rev. B **53**, 1022–1025 (1996)
4.139 J.L. Costa-Krämer, N. Garcia, H. Olin: Conductance quantization in bismuth nanowires at 4 K, Phys. Rev. Lett. **78**, 4990–4993 (1997)
4.140 C.Z. Li, H.X. He, A. Bogozi, J.S. Bunch, N.J. Tao: Molecular detection based on conductance quantization of nanowires, Appl. Phys. Lett. **76**, 1333–1335 (2000)
4.141 J.L. Costa-Krämer, N. Garcia, P. Garcia-Mochales, P.A. Serena, M.I. Marques, A. Correia: Conductance quantization in nanowires formed between micro and macroscopic metallic electrodes, Phys. Rev. B **55**, 5416–5424 (1997)
4.142 Y. Huang, X. Duan, Y. Cui, L.J. Lauhon, K.-H. Kim, C.M. Lieber: Logic gates and computation from assembled nanowire building blocks, Science **294**, 1313–1317 (2001)
4.143 J.-R. Kim, H. Oh, H.M. So, J.-J. Kim, J. Kim, C.J. Lee, S.C. Lyu: Schottky diodes based on a single GaN nanowire, Nanotechnology **13**, 701–704 (2002)
4.144 X. Duan, Y. Huang, C.M. Lieber: Nonvolatile memory and programmable logic from molecule-gated nanowires, Nano Lett. **2**, 487–490 (2002)
4.145 E.C. Walter, R.M. Penner, H. Liu, K.H. Ng, M.P. Zach, F. Favier: Sensors from electrodeposited metal nanowires, Surf. Interface Anal. **34**, 409–412 (2002)
4.146 E.C. Walter, K.H. Ng, M.P. Zach, R.M. Penner, F. Favier: Electronic devices from electrodeposited metal nanowires, Microelectron. Eng. **61/62**, 555–561 (2002)
4.147 Y.-M. Lin, X. Sun, M.S. Dresselhaus: Theoretical investigation of thermoelectric transport properties of cylindrical Bi nanowires, Phys. Rev. B **62**, 4610–4623 (2000)
4.148 K. Liu, C.L. Chien, P.C. Searson: Finite-size effects in bismuth nanowires, Phys. Rev. B **58**, R14681–R14684 (1998)
4.149 Z. Zhang, X. Sun, M.S. Dresselhaus, J.Y. Ying, J. Heremans: Magnetotransport investigations of ultrafine single-crystalline bismuth nanowire arrays, Appl. Phys. Lett. **73**, 1589–1591 (1998)
4.150 J. Heremans, C.M. Thrush, Z. Zhang, X. Sun, M.S. Dresselhaus, J.Y. Ying, D.T. Morelli: Magnetoresistance of bismuth nanowire arrays: A possible transition from one-dimensional to three-dimensional localization, Phys. Rev. B **58**, R10091–R10095 (1998)
4.151 L. Sun, P.C. Searson, C.L. Chien: Finite-size effects in nickel nanowire arrays, Phys. Rev. B **61**, R6463–R6466 (2000)
4.152 Y.-M. Lin, S.B. Cronin, O. Rabin, J.Y. Ying, M.S. Dresselhaus: Transport properties and observation of semimetal-semiconductor transition in Bi-based nanowires. In: *Quantum Confined Semiconductor Nanostructures: MRS Symposium Proceedings, Boston*, Vol. 737-C, ed. by J.M. Buriak, D.D.M. Wayner, F. Priolo, B. White, V. Klimov, L. Tsybeskov (Materials Research Society Press, Pittsburgh 2003) p. F3.14
4.153 Y.-M. Lin, M.S. Dresselhaus: Transport properties of superlattice nanowires and their potential for thermoelectric applications. In: *Quantum Confined Semiconductor Nanostructures: MRS Symposium Proceedings, Boston*, Vol. 737-C, ed. by J.M. Buriak, D.D.M. Wayner, F. Priolo, B. White, V. Klimov, L. Tsybeskov (Materials Research Society Press, Pittsburgh 2003) p. F8.18
4.154 Y.-M. Lin, O. Rabin, S.B. Cronin, J.Y. Ying, M.S. Dresselhaus: Semimetal-semiconductor transition in $Bi_{1-x}Sb_x$ alloy nanowires and their thermoelectric properties, Appl. Phys. Lett. **81**, 2403–2405 (2002)
4.155 J. Heremans, C.M. Thrush, Y.-M. Lin, S.B. Cronin, M.S. Dresselhaus: Transport properties of antimony nanowires, Phys. Rev. B **63**, 085406-1–085406-8 (2001)
4.156 Y.-M. Lin, S.B. Cronin, O. Rabin, J.Y. Ying, M.S. Dresselhaus: Transport properties of $Bi_{1-x}Sb_x$ alloy nanowires synthesized by pressure injection, Appl. Phys. Lett. **79**, 677–679 (2001)
4.157 Z. Zhang, X. Sun, M.S. Dresselhaus, J.Y. Ying, J. Heremans: Electronic transport properties of single crystal bismuth nanowire arrays, Phys. Rev. B **61**, 4850–4861 (2000)
4.158 D.E. Beutler, N. Giordano: Localization and electron-electron interaction effects in thin Bi wires and films, Phys. Rev. B **38**, 8–19 (1988)
4.159 J. Heremans, C.M. Thrush: Thermoelectric power of bismuth nanowires, Phys. Rev. B **59**, 12579–12583 (1999)
4.160 L.D. Hicks, M.S. Dresselhaus: Thermoelectric figure of merit of a one-dimensional conductor, Phys. Rev. B **47**, 16631–16634 (1993)
4.161 Y.-M. Lin, S.B. Cronin, O. Rabin, J. Heremans, M.S. Dresselhaus, J.Y. Ying: Transport properties of Bi-related nanowire systems. In: *Anisotropic Nanoparticles: Synthesis, Characterization and Applications: MRS Symposium Proceedings, Boston,*

Vol. 635, ed. by S. Stranick, P.C. Searson, L.A. Lyon, C. Keating (Materials Research Society Press, Pittsburgh 2001) pp. C4301–C4306
4.162 Y.-M. Lin, M.S. Dresselhaus: Thermoelectric properties of superlattice nanowires, Phys. Rev. B **68**, 075304 (2003)
4.163 M.T. Björk, B.J. Ohlsson, C. Thelander, A.I. Persson, K. Deppert, L.R. Wallenberg, L. Samuelson: Nanowire resonant tunneling diodes, Appl. Phys. Lett. **81**, 4458–4460 (2002)
4.164 D. Li, Y. Wu, P. Kim, L. Shi, P. Yang, A. Majumdar: Thermal conductivity of individual silicon nanowires, Appl. Phys. Lett. **83**, 2934–2936 (2003)
4.165 T.S. Tighe, J.M. Worlock, M.L. Roukes: Direct thermal conductance measurements on suspended monocrystalline nanostructures, Appl. Phys. Lett. **70**, 2687–2689 (1997)
4.166 S.T. Huxtable, A.R. Abramson, C.-L. Tien, A. Majumdar, C. LaBounty, X. Fan, G. Zeng, J.E. Bowers, A. Shakouri, E.T. Croke: Thermal conductivity of Si/SiGe and SiGe/SiGe superlattices, Appl. Phys. Lett. **80**, 1737–1739 (2002)
4.167 R. Venkatasubramanian, E. Siivola, T. Colpitts, B. O'Quinn: Thin-film thermoelectric devices with high room-temperature figures of merit, Nature **413**, 597–602 (2001)
4.168 C. Dames, G. Chen: Modeling the thermal conductivity of a SiGe segmented nanowire, 21st Int. Conf. Thermoelectr. Proc. ICT '02, Long Beach (IEEE, Piscataway 2002) pp. 317–320
4.169 K. Schwab, J.L. Arlett, J.M. Worlock, M.L. Roukes: Thermal conductance through discrete quantum channels, Physica E **9**, 60–68 (2001)
4.170 D. Li, Y. Wu, R. Fan, P. Yang, A. Majumdar: Thermal conductivity of Si/SiGe superlattice nanowires, Appl. Phys. Lett. **83**, 3186–3188 (2003)
4.171 G. Chen, M.S. Dresselhaus, G. Dresselhaus, J.-P. Fleurial, T. Caillat: Recent developments in thermoelectric materials, Int. Mater. Rev. **48**, 45–66 (2003)
4.172 C. Dames, G. Chen: Theoretical phonon thermal conductivity of Si-Ge superlattice nanowires, J. Appl. Phys. **95**, 682–693 (2004)
4.173 K. Schwab, E.A. Henriksen, J.M. Worlock, M.L. Roukes: Measurement of the quantum of thermal conductance, Nature **404**, 974–977 (2000)
4.174 M. Cardona: *Light Scattering in Solids* (Springer, Berlin Heidelberg 1982)
4.175 P.Y. Yu, M. Cardona: *Fundamentals of Semiconductors* (Springer, Berlin Heidelberg 1995), Chap. 7
4.176 J.C.M. Garnett: Colours in metal glasses, in metallic films, and in metallic solutions, Philos. Trans. R. Soc. Lond. A **205**, 237–288 (1906)
4.177 D.E. Aspnes: Optical properties of thin films, Thin Solid Films **89**, 249–262 (1982)
4.178 U. Kreibig, L. Genzel: Optical absorption of small metallic particles, Surf. Sci. **156**, 678–700 (1985)
4.179 M.R. Black, Y.-M. Lin, S.B. Cronin, O. Rabin, M.S. Dresselhaus: Infrared absorption in bismuth nanowires resulting from quantum confinement, Phys. Rev. B **65**, 195417–1–195417–9 (2002)
4.180 M.W. Lee, H.Z. Twu, C.-C. Chen, C.H. Chen: Optical characterization of wurtzite gallium nitride nanowires, Appl. Phys. Lett. **79**, 3693–3695 (2001)
4.181 D.M. Lyons, K.M. Ryan, M.A. Morris, J.D. Holmes: Tailoring the optical properties of silicon nanowire arrays through strain, Nano Lett. **2**, 811–816 (2002)
4.182 M.S. Gudiksen, J. Wang, C.M. Lieber: Size-depent photoluminescence from single indium phosphide nanowires, J. Phys. Chem. B **106**, 4036–4039 (2002)
4.183 J.C. Johnson, H. Yan, R.D. Schaller, L.H. Haber, R.J. Saykally, P. Yang: Single nanowire lasers, J. Phys. Chem. B **105**, 11387–11390 (2001)
4.184 S. Blom, L.Y. Gorelik, M. Jonson, R.I. Shekhter, A.G. Scherbakov, E.N. Bogachek, U. Landman: Magneto-optics of electronic transport in nanowires, Phys. Rev. B **58**, 16305–16314 (1998)
4.185 J.P. Pierce, E.W. Plummer, J. Shen: Ferromagnetism in cobalt-iron alloy nanowire arrays on w(110), Appl. Phys. Lett. **81**, 1890–1892 (2002)
4.186 S. Melle, J.L. Menendez, G. Armelles, D. Navas, M. Vazquez, K. Nielsch, R.B. Wehrsphon, U. Gösele: Magneto-optical properties of nickel nanowire arrays, Appl. Phys. Lett. **83**, 4547–4549 (2003)
4.187 J.C. Johnson, H. Yan, R.D. Schaller, P.B. Petersen, P. Yang, R.J. Saykally: Near-field imaging of nonlinear optical mixing in single zinc oxide nanowires, Nano Lett. **2**, 279–283 (2002)
4.188 M.R. Black, Y.-M. Lin, S.B. Cronin, M.S. Dresselhaus: Using optical measurements to improve electronic models of bismuth nanowires, 21st Int. Conf. Thermoelectr. Proc. ICT '02, Long Beach, ed. by T. Caillat, J. Snyder (IEEE, Piscataway 2002) pp. 253–256
4.189 M.R. Black, P.L. Hagelstein, S.B. Cronin, Y.-M. Lin, M.S. Dresselhaus: Optical absorption from an indirect transition in bismuth nanowires, Phys. Rev. B **68**, 235417 (2003)
4.190 H.-L. Liu, C.-C. Chen, C.-T. Chia, C.-C. Yeh, C.-H. Chen, M.-Y. Yu, S. Keller, S.P. DenBaars: Infrared and Raman-scattering studies in single-crystalline GaN nanowires, Chem. Phys. Lett. **345**, 245–251 (2001)
4.191 H. Richter, Z.P. Wang, L. Ley: The one phonon Raman-spectrum in microcrystalline silicon, Solid State Commun. **39**, 625–629 (1981)
4.192 I.H. Campbell, P.M. Fauchet: The effects of microcrystal size and shape on the one phonon Raman-spectra of crystalline semiconductors, Solid State Commun. **58**, 739–741 (1986)
4.193 R. Gupta, Q. Xiong, C.K. Adu, U.J. Kim, P.C. Eklund: Laser-induced Fano resonance scattering in silicon nanowires, Nano Lett. **3**, 627–631 (2003)
4.194 X. Duan, Y. Huang, Y. Cui, J. Wang, C.M. Lieber: Indium phosphide nanowires as building blocks

for nanoscale electronic and optoelectronic devices, Nature **409**, 66–69 (2001)
4.195 Y. Cui, C.M. Lieber: Functional nanoscale electronic devices assembled using silicon nanowire building blocks, Science **291**, 851–853 (2001)
4.196 Y. Cui, X. Duan, J. Hu, C.M. Lieber: Doping and electrical transport in silicon nanowires, J. Phys. Chem. B **104**, 101–104 (2000)
4.197 G.F. Zheng, W. Lu, S. Jin, C.M. Lieber: Synthesis and fabrication of high-performance n-type silicon nanowire transistors, Adv. Mater. **16**, 1890–1891 (2004)
4.198 J. Goldberger, D.J. Sirbuly, M. Law, P. Yang: ZnO nanowire transistors, J. Phys. Chem. B **109**, 9–14 (2005)
4.199 D.H. Kang, J.H. Ko, E. Bae, J. Hyun, W.J. Park, B.K. Kim, J.J. Kim, C.J. Lee: Ambient air effects on electrical characteristics of gap nanowire transistors, J. Appl. Phys. **96**, 7574–7577 (2004)
4.200 S.-W. Chung, J.-Y. Yu, J.R. Heath: Silicon nanowire devices, Appl. Phys. Lett. **76**, 2068–2070 (2000)
4.201 C. Li, W. Fan, B. Lei, D. Zhang, S. Han, T. Tang, X. Liu, Z. Liu, S. Asano, M. Meyyappan, J. Han, C. Zhou: Multilevel memory based on molecular devices, Appl. Phys. Lett. **84**, 1949–1951 (2004)
4.202 B. Lei, C. Li, D.Q. Zhang, Q.F. Zhou, K. Shung, C.W. Zhou: Nanowire transistors with ferroelectric gate dielectrics: Enhanced performance and memory effects, Appl. Phys. Lett. **84**, 4553–4555 (2004)
4.203 H.T. Ng, J. Han, T. Yamada, P. Nguyen, Y.P. Chen, M. Meyyappan: Single crystal nanowire vertical surround-gate field-effect transistor, Nano Lett. **4**, 1247–1252 (2004)
4.204 M. Ding, H. Kim, A.I. Akinwande: Observation of valence band electron emission from n-type silicon field emitter arrays, Appl. Phys. Lett. **75**, 823–825 (1999)
4.205 F.C.K. Au, K.W. Wong, Y.H. Tang, Y.F. Zhang, I. Bello, S.T. Lee: Electron field emission from silicon nanowires, Appl. Phys. Lett. **75**, 1700–1702 (1999)
4.206 P.M. Ajayan, O.Z. Zhou: Applications of carbon nanotubes. In: *Carbon Nanotubes: Synthesis, Structure, Properties and Applications*, Springer Ser. Top. Appl. Phys., Vol. 80, ed. by M.S. Dresselhaus, G. Dresselhaus, P. Avouris (Springer, Berlin Heidelberg 2001) pp. 391–425
4.207 M. Lu, M.K. Li, Z.J. Zhang, H.L. Li: Synthesis of carbon nanotubes/si nanowires core-sheath structure arrays and their field emission properties, Appl. Surf. Sci. **218**, 196–202 (2003)
4.208 L. Vila, P. Vincent, L. Dauginet-DePra, G. Pirio, E. Minoux, L. Gangloff, S. Demoustier-Champagne, N. Sarazin, E. Ferain, R. Legras, L. Piraux, P. Legagneux: Growth and field-emission properties of vertically aligned cobalt nanowire arrays, Nano Lett. **4**, 521–524 (2004)
4.209 G. Dresselhaus, M.S. Dresselhaus, Z. Zhang, X. Sun, J. Ying, G. Chen: Modeling thermoelectric behavior in Bi nano-wires, 17th Int. Conf. Thermoelectr. Proc. ICT'98, Nagoya, ed. by K. Koumoto (IEEE, Piscataway 1998) pp. 43–46
4.210 L.D. Hicks, M.S. Dresselhaus: The effect of quantum well structures on the thermoelectric figure of merit, Phys. Rev. B **47**, 12727–12731 (1993)
4.211 O. Rabin, Y.-M. Lin, M.S. Dresselhaus: Anomalously high thermoelectric figure of merit in $Bi_{1-x}Sb_x$ nanowires by carrier pocket alignment, Appl. Phys. Lett. **79**, 81–83 (2001)
4.212 T.C. Harman, P.J. Taylor, M.P. Walsh, B.E. LaForge: Quantum dot superlattice thermoelectric materials and devices, Science **297**, 2229–2232 (2002)
4.213 X. Duan, Y. Huang, R. Agarwal, C.M. Lieber: Single-nanowire electrically driven lasers, Nature **421**, 241 (2003)
4.214 F. Qian, Y. Li, S. Gradecak, D.L. Wang, C.J. Barrelet, C.M. Lieber: Gallium nitride-based nanowire radial heterostructures for nanophotonics, Nano Lett. **4**, 1975–1979 (2004)
4.215 V. Dneprovskii, E. Zhukov, V. Karavanskii, V. Poborchii, I. Salamatini: Nonlinear optical properties of semiconductor quantum wires, Superlattice. Microst. **23**(6), 1217–1221 (1998)
4.216 J.C. Johnson, K.P. Knutsen, H. Yan, M. Law, Y. Zhang, P. Yang, R.J. Saykally: Ultrafast carrier dynamics in single ZnO nanowire and nanoribbon lasers, Nano Lett. **4**, 197–204 (2004)
4.217 J.X. Ding, J.A. Zapien, W.W. Chen, Y. Lifshitz, S.T. Lee, X.M. Meng: Lasing in ZnS nanowires grown on anodic aluminum oxide templates, Appl. Phys. Lett. **85**, 2361 (2004)
4.218 J.C. Johnson, H.-J. Choi, K.P. Knutsen, R.D. Schaller, P. Yang, R.J. Saykally: Single gallium nitride nanowire lasers, Nat. Mater. **1**, 106–110 (2002)
4.219 H.J. Choi, J.C. Johnson, R. He, S.K. Lee, F. Kim, P. Pauzauskie, J. Goldberger, R.J. Saykally, P. Yang: Self-organized GaN quantum wire UV lasers, J. Phys. Chem. B **107**, 8721–8725 (2003)
4.220 C.J. Barrelet, A.B. Greytak, C.M. Lieber: Nanowire photonic circuit elements, Nano Lett. **4**, 1981–1985 (2004)
4.221 M. Law, D.J. Sirbuly, J.C. Johnson, J. Goldberger, R.J. Saykally, P. Yang: Ultralong nanoribbon waveguides for sub-wavelength photonics integration, Science **305**, 1269–1273 (2004)
4.222 H. Kind, H. Yan, B. Messer, M. Law, P. Yang: Nanowire ultraviolet photodetectors and optical switches, Adv. Mater. **14**, 158–160 (2002)
4.223 B.M.I. van der Zande, M.R. Böhmer, L.G.J. Fokkink, C. Schöneberger: Colloidal dispersions of gold rods: synthesis and optical properties, Langmuir **16**, 451–458 (2000)
4.224 B.M.I. van der Zande, G.J.M. Koper, H.N.W. Lekkerkerker: Alignment of rod-shaped gold particles by

electric fields, J. Phys. Chem. B **103**, 5754–5760 (1999)
4.225 W.U. Huynh, J.J. Dittmer, A.P. Alivisatos: Hybrid nanorod–polymer solar cells, Science **295**, 2425–2427 (2002)
4.226 L.A. Bauer, N.S. Birenbaum, G.J. Meyer: Biological applications of high aspect ratio nanoparticles, J. Mater. Chem. **14**, 517–526 (2004)
4.227 Y. Cui, Q. Wei, H. Park, C. Lieber: Nanowire nanosensors for highly sensitive and selective detection of biological and chemical species, Science **293**, 1289–1292 (2001)
4.228 J. Hahm, C. Lieber: Direct ultra-sensitive electrical detection of DNA and DNA sequence variations using nanowire nanosensors, Nano Lett. **4**, 51–54 (2004)

5. Template-Based Synthesis of Nanorod or Nanowire Arrays

Huamei (Mary) Shang, Guozhong Cao

This chapter introduces the fundamentals of and various technical approaches developed for template-based synthesis of nanorod arrays. After a brief introduction to various concepts associated with the growth of nanorods, nanowires and nanobelts, the chapter focuses mainly on the most widely used and well established techniques for the template-based growth of nanorod arrays: electrochemical deposition, electrophoretic deposition, template filling via capillary force and centrifugation, and chemical conversion. In each section, the relevant fundamentals are first introduced, and then examples are given to illustrate the specific details of each technique.

Syntheses, characterizations and applications of nanowires, nanorods, nanotubes and nanobelts (also often referred to as one-dimensional nanostructures) are significant areas of current endeavor in nanotechnology. Many techniques have been developed in these areas, and our understanding of the field has been significantly enhanced [5.1–5]. The field is still evolving rapidly with new synthesis methods and new nanowires or nanorods reported in the literature. Evaporation–condensation growth has been successfully applied to the synthesis of various oxide nanowires and nanorods. Similarly, the dissolution–condensation method has been widely used for the synthesis of various metallic nanowires from solutions. The vapor–liquid–solid (VLS) growth method is a highly versatile approach; various elementary and compound semiconductor nanowires have been synthesized using this method [5.6]. Template-based growth of nanowires or nanorods is an even more versatile method for various materials. Substrate ledge or step-induced growth of nanowires or nanorods has also been investigated intensively [5.7]. Except for VLS and template-based growth, most of the above-mentioned methods result in randomly oriented nanowires or nanorods (commonly in the form of powder). The VLS method provides the ability to grow well oriented nanorods or nanowires directly attached to substrates, and is therefore often advantageous for characterization and applications; however, catalysts are required to form a liquid capsule at the advancing surface during growth at elevated temperatures. In addition, the possible incorporation of catalyst into nanowires and the difficulty removing such capsules from the tips of nanowires or nanorods are two disadvantages of this technique. Template-based growth often suffers from the polycrystalline nature of the resultant nanowires and nanorods, in addition to the dif-

the energy level of a vacant molecular orbital in the electrolyte, electrons will transfer from the electrode to the solution and the electrolyte will be reduced, as shown in Fig. 5.1a [5.24]. On the other hand, if the electrode potential is lower than the energy level of an occupied molecular orbital in the electrolyte, the electrons will transfer from the electrolyte to the electrode, resulting in electrolyte oxidation, as illustrated in Fig. 5.1b [5.24]. These reactions stop when equilibrium is achieved.

When an external electric field is applied between two dissimilar electrodes, charged species flow from one electrode to the other, and electrochemical reactions occur at both electrodes. This process, called electrolysis, converts electrical energy to chemical potential.

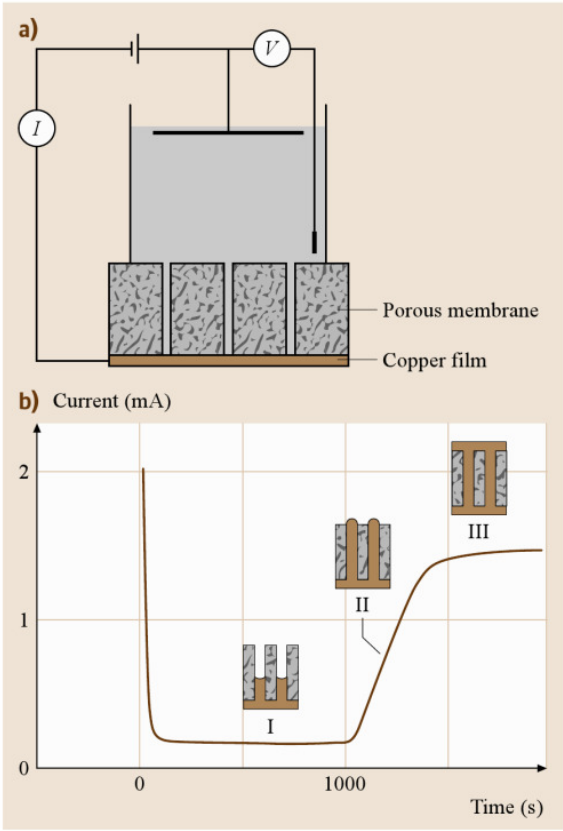

Fig. 5.2a,b Common experimental setup for the template-based growth of nanowires using electrochemical deposition. (**a**) Schematic illustration of the arrangement of the electrodes for nanowire deposition. (**b**) Current–time curve for electrodeposition of Ni into a polycarbonate membrane with 60 nm diameter pores at −1.0 V. *Insets* depict the different stages of the electrodeposition (after [5.26])

The system used to perform electrolysis is called an electrolytic cell. In this cell, the electrode connected to the positive side of the power supply, termed the *anode*, is where an oxidation reaction takes place, whereas the electrode connected to the negative side of the power supply, the *cathode*, is where a reduction reaction proceeds, accompanied by deposition. Therefore, electrolytic deposition is also called cathode deposition, but it is most commonly referred to as electrochemical deposition or electrodeposition.

5.2.1 Metals

The growth of nanowires of conductive materials in an electric field is a self-propagating process [5.27]. Once the small rods form, the electric field and the density of current lines between the tips of nanowires and the opposing electrode are greater than that between two electrodes, due to the shorter distances between the nanowires and the electrodes. This ensures that the species being deposited is constantly attracted preferentially to the nanowire tips, resulting in continued growth. To better control the morphology and size, templates containing channels in the desired shape are used to guide the growth of nanowires. Figure 5.2 illustrates a common setup used for the template-based growth of nanowires [5.26]. The template is attached to the cathode, which is brought into contact with the deposition solution. The anode is placed in the deposition solution, parallel to the cathode. When an electric field is applied, cations diffuse through the channels and deposit on the cathode, resulting in the growth of nanowires inside the template. This figure also shows the current density at different stages of deposition when a constant electric field is applied. The current does not change significantly until the pores are completely filled, at which point the current increases rapidly due to improved contact with the electrolyte solution. The current saturates once the template surface is completely covered. This approach has yielded nanowires made from different metals, including Ni, Co, Cu and Au, with nominal pore diameters of between 10 and 200 nm. The nanowires were found to be true replicas of the pores [5.28]. *Possin* [5.11] prepared various metallic nanowires using radiation track-etched mica. Likewise, *Williams* and *Giordano* [5.29] produced silver nanowires with diameters of less than 10 nm. *Whitney* et al. [5.26] fabricated arrays of nickel and cobalt nanowires, also using PC templates. Single crystal bismuth nanowires have been grown in AAM using pulsed electrodeposition and Fig. 5.3 shows SEM and TEM images

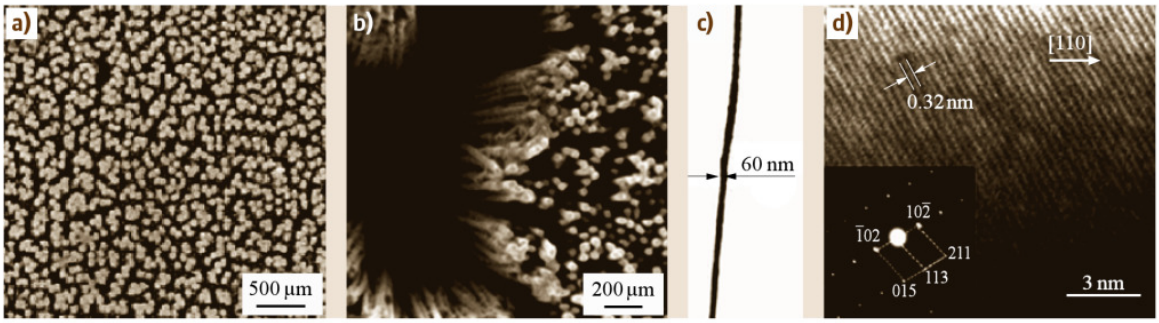

Fig. 5.3a–d SEM images of Bi nanowire arrays: (**a**) top view, (**b**) tilt view. (**c**) TEM image of a typical Bi single nanowire. (**d**) HRTEM image of a typical Bi single nanowire. The *inset* is the corresponding ED pattern (after [5.30])

of the bismuth nanowires [5.30]. Single crystal copper and lead nanowires were prepared by DC electrodeposition and pulse electrodeposition, respectively [5.31,32]. The growth of single crystal lead nanowires required a greater departure from equilibrium conditions (greater overpotential) compared to the conditions required for polycrystalline ones.

Hollow metal tubules can also be prepared [5.33, 34]. In this case the pore walls of the template are chemically modified by anchoring organic silane molecules so that the metal will preferentially deposit onto the pore walls instead of the bottom electrode. For example, the porous surface of an anodic alumina template was first covered with cyanosilanes; subsequent electrochemical deposition resulted in the growth of gold tubules [5.35]. An electroless electrolysis process has also been investigated for the growth of nanowires and nanorods [5.16, 33, 36]. Electroless deposition is actually a chemical deposition process and it involves the use of a chemical agent to coat a material onto the template surface [5.37]. The main differences between electrochemical deposition and electroless deposition are that the deposition begins at the bottom electrode and the deposited materials must be electrically conductive in the former. The electroless method does not require the deposited materials to be electrically conductive, and the deposition starts from the pore wall and proceeds inwardly. Therefore, in general, electrochemical deposition results in the formation of *solid* nanorods or nanowires of conductive materials, whereas electroless deposition often results in hollow fibrils or nanotubules. For electrochemical deposition, the length of nanowires or nanorods can be controlled by the deposition time, whereas in electroless deposition the length of the nanotubules is solely dependent on the length of the deposition channels or pores. Variation of deposition time would result in a different wall thickness of nanotubules. An increase in deposition time leads to a thick wall, but sometimes the hollow tubule morphology persists even after prolonged deposition.

Although many research groups have reported on the growth of uniformly sized nanorods and nanowires on PC template membranes, *Schönenberger* et al. [5.38] reported that the channels of carbonate membranes were not always uniform in diameter. They grew Ni, Co, Cu, and Au nanowires using polycarbonate membranes with nominal pore diameters of between 10 and 200 nm by an electrolysis method. From both a potentiostatic study of the growth process and a SEM analysis of nanowire morphology, they concluded that the pores were generally not cylindrical with a constant cross section, but instead were rather cigarlike. For pores with a nominal diameter of 80 nm, the middle section of the pores was wider by up to a factor of 3.

5.2.2 Semiconductors

Semiconductor nanowire and nanorod arrays have been synthesized using AAM templates, such as CdSe and CdTe [5.39]. The synthesis of nanowire arrays of bismuth telluride (Bi_2Te_3) provide a good example of the synthesis of compound nanowire arrays by electrochemical deposition. Bi_2Te_3 is of special interest as a thermoelectric material and Bi_2Te_3 nanowire arrays are believed to offer high figures of merit for thermal-electrical energy conversion [5.40, 41]. Both polycrystalline and single crystal Bi_2Te_3 nanowire arrays have been grown by electrochemical deposition inside anodic alumina membranes [5.42, 43]. *Sander* and coworkers [5.42] fabricated Bi_2Te_3 nanowire arrays with diameters as small as ≈ 25 nm from a solution of 0.075 M Bi and 0.1 M Te in 1 M HNO_3 by electrochemical deposition at -0.46 V versus a Hg/Hg_2SO_4

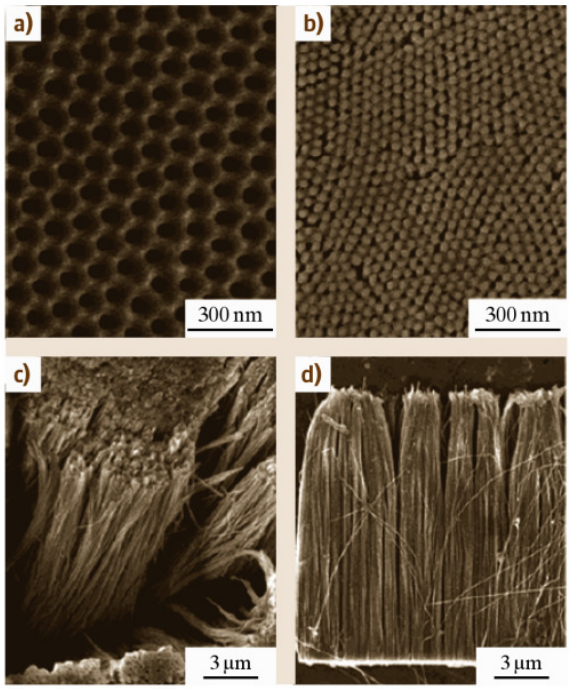

Fig. 5.4a–d SEM photographs of AAM template and Bi_2Te_3 nanowire arrays. **(a)** A typical SEM photograph of AAM. **(b)** Surface view of Bi_2Te_3 nanowire array (eroding time: 5 min). **(c)** Surface view of Bi_2Te_3 nanowire array (eroding time: 15 min). **(d)** Cross-sectional view of Bi_2Te_3 nanowire array (eroding time: 15 min) (after [5.43])

reference electrode. The resultant Bi_2Te_3 nanowire arrays are polycrystalline in nature, and subsequent melting-recrystallization failed to produce single crystal Bi_2Te_3 nanowires. More recently, single crystal Bi_2Te_3 nanowire arrays have been grown from a solution consisted of 0.035 M $Bi(NO_3)_3{\cdot}5H_2O$ and 0.05 M $HTeO_2^+$; the latter was prepared by dissolving Te powder in 5 M HNO_3 by electrochemical deposition. Figure 5.4a shows a typical SEM image of AAM. Both Fig. 5.4b and Fig. 5.4c are surface view of Bi_2Te_3 nanowire array with different eroding time, Fig. 5.4b is 5 min and Fig. 5.4c is 15 min. Figure 5.4d is cross-sectional view of Bi_2Te_3 nanowire array. Figure 5.5 shows TEM image of a cross section of a Bi_2Te_3 nanowire array and an XRD spectrum showing its crystal orientation, respectively. High-resolution TEM and electron diffraction, together with XRD, revealed that [110] is the preferred growth direction of Bi_2Te_3 nanowires. Single crystal nanowire or nanorod arrays can also be made by carefully controlling the initial deposition [5.44]. Similarly, large area Sb_2Te_3 nanowire arrays have also been successfully grown by template-based electrochemical deposition, but the nanowires grown are polycrystalline and show no clear preferred growth direction [5.45].

5.2.3 Conductive Polymers

Electrochemical deposition has also been explored for the synthesis of conductive polymer nanowire and nanorod arrays [5.46]. Conductive polymers have great potential for plastic electronics and sensor applications [5.47, 48]. For example, *Schönenberger* et al. [5.38] have made conductive polyporrole nanowires in PC membranes. Nanotubes are commonly observed for polymer materials, as shown in Fig. 5.6 [5.49], in contrast to *solid* metal nanorods or nanowires. It seems that deposition or solidification of polymers inside template pores starts at the surface and proceeds inwardly. *Martin* [5.50] proposed that this phenomenon was caused by the electrostatic attraction between the growing polycationic polymer and the anionic sites along the pore walls of the polycarbonate membrane. In addition, although the monomers are soluble, the polymerized form is insoluble. Hence there is a solvophobic component leading to deposition at the surface of the pores [5.51,52]. In the final stage, the diffusion of monomers through the inner pores becomes retarded and monomers inside the pores are quickly depleted. The deposition of polymer inside the inner pores stops.

Liang et al. [5.53] reported a direct electrochemical synthesis of oriented nanowires of polyaniline (PANI) – a conducting polymer with a conjugated backbone due to phenyl and amine groups – from solutions using no templates. The experimental design is based on the idea that, in theory, the rate of electropolymerization (or nanowire growth) is related to the current density. Therefore, it is possible to control the nucleation and the polymerization rate simply by adjusting the current density. The synthesis involves electropolymerization of aniline ($C_6H_5NH_2$) and in situ electrodeposition, resulting in nanowire growth.

5.2.4 Oxides

Similar to metals, semiconductors and conductive polymers, some oxide nanorod arrays can be grown directly from solution by electrochemical deposition. For example, V_2O_5 nanorod arrays have been grown on ITO substrate from $VOSO_4$ aqueous solution with VO^{2+} as the growth species [5.54]. At the interface between the

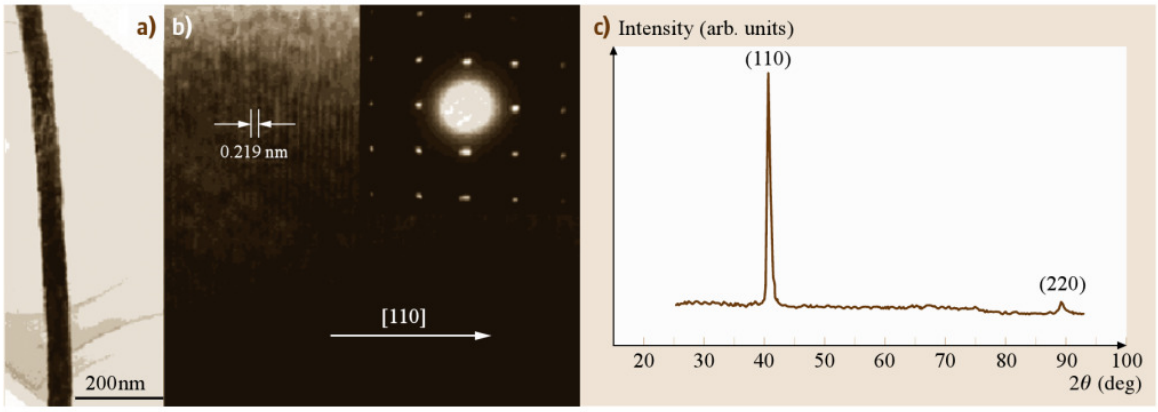

Fig. 5.5a–c TEM images and XRD pattern of a single Bi_2Te_3 nanowire. (**a**) TEM image and (**b**) HRTEM image of the same nanowire. The *inset* is the corresponding ED pattern. (**c**) XRD pattern of Bi_2Te_3 nanowire array (electrodeposition time: 5 min) (after [5.43])

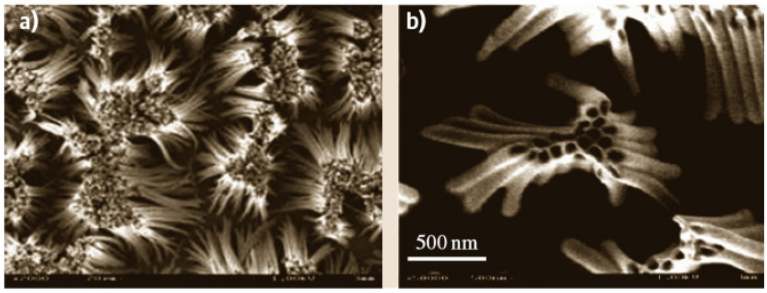

Fig. 5.6a,b SEM images of polymer nanotubes (after [5.49])

electrode (and therefore the subsequent growth surface) and the electrolyte solution, the ionic cluster (VO^{2+}) is oxidized and solid V_2O_5 is deposited through the following reaction

$$2VO^{2+} + 3H_2O \rightarrow V_2O_5 + 6H^+ + 2e^- \,. \qquad (5.2)$$

A reduction reaction takes place at the counter electrode

$$2H^+ + 2e^- \rightarrow H_2(g) \,. \qquad (5.3)$$

It is obvious that the pH and the concentration of VO^{2+} clusters in the vicinity of the growth surface shift away from that in the bulk solution; both the pH and the VO^{2+} concentration decrease.

ZnO nanowire arrays were fabricated by a one-step electrochemical deposition technique based on an ordered nanoporous alumina membrane [5.55]. The ZnO nanowire array is uniformly assembled into the nanochannels of an anodic alumina membrane and consists of single crystal particles.

5.3 Electrophoretic Deposition

The electrophoretic deposition technique has been widely explored, particularly for the deposition of ceramic and organoceramic materials onto a cathode from colloidal dispersions [5.56–58]. Electrophoretic deposition differs from electrochemical deposition in several aspects. First, the material deposited in the electrophoretic deposition method does not need to be electrically conductive. Second, nanosized particles in colloidal dispersions are typically stabilized by electrostatic or electrosteric mechanisms. As discussed in the previous section, when dispersed in a polar solvent or an electrolyte solution, the surface of a nanoparticle develops an electrical charge via one or more of the following mechanisms: (1) preferential dissolution, (2) deposition of charges or charged species, (3) preferential reduction or oxidation, and (4) physical adsorption of charged

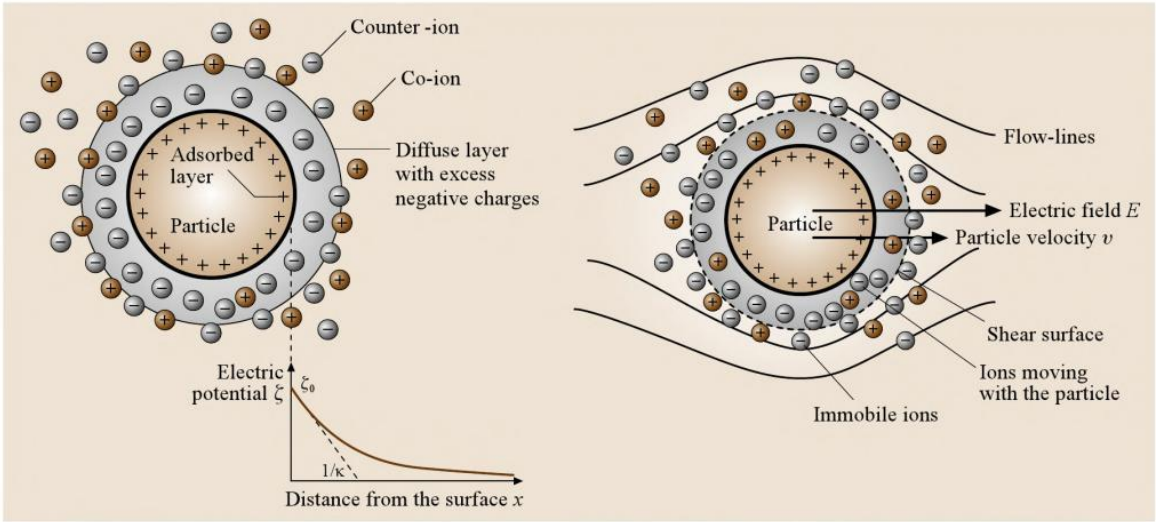

Fig. 5.7 Schematic illustrating electrical double layer structure and the electric potential near the solid surface with both the Stern and Gouy layers indicated. Surface charge is assumed to be positive (after [5.59])

species such as polymers. A combination of electrostatic forces, Brownian motion and osmotic forces results in the formation of a *double layer structure*, schematically illustrated in Fig. 5.7. The figure depicts a positively charged particle surface, the concentration profiles of negative ions (counterions) and positive ions (surface charge-determining ions), and the electric potential profile. The concentration of counterions gradually decreases with distance from the particle surface, whereas that of charge-determining ions increases. As a result, the electric potential decreases with distance. Near the particle surface, the electric potential decreases linearly, in the region known as the Stern layer. Outside of the Stern layer, the decrease follows an exponential relationship. The region between the Stern layer and the point where the electric potential equals zero is called the diffusion layer. Taken together, the Stern layer and diffusion layer is known as the double layer structure in the classical theory of electrostatic stabilization.

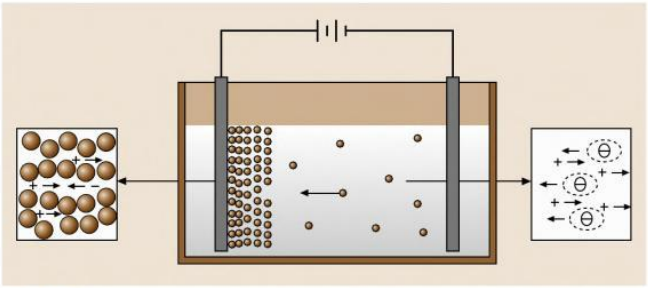

Fig. 5.8 Schematic showing electrophoresis. Upon application of an external electric field to a colloidal system or a sol, the charged nanoparticles or nanoclusters are set in motion (after [5.1])

Upon the application of an external electric field, charged particles are set in motion, as schematically illustrated in Fig. 5.8 [5.59]. This type of motion is referred to as electrophoresis. When a charged particle moves, some of the solvent or solution surrounding the particle will also move with it, since part of the solvent or solution is tightly bound to the particle. The plane that separates the tightly bound liquid layer from the rest of the liquid is called the *slip plane* (Fig. 5.7). The electric potential at the slip plane is known as the *zeta potential*, which is an important parameter when determining the stability and transport of a colloidal dispersion or a sol. A zeta potential of more than about 25 mV is typically required to stabilize a system [5.60]. The zeta potential ζ around a spherical particle can be described using the relation [5.61]

$$\zeta = \frac{Q}{4\pi\varepsilon_r a\,(1+\kappa a)}$$

with

$$\kappa = \left(\frac{e^2 \sum n_i z_i^2}{\varepsilon_r \varepsilon_0 k_B T}\right)^{1/2}, \qquad (5.4)$$

where Q is the charge on the particle, a is the radius of the particle out to the shear plane, ε_r is the relative dielectric constant of the medium, and n_i and z_i are the

The formation of single crystal nanorods from solutions by pH change-induced surface condensation has been proven by TEM analyses, including high-resolution imaging showing the lattice fringes and electron diffraction. The growth of single crystal nanorods by pH change-induced surface condensation is attributed to evolution selection growth, which is briefly summarized below. The initial heterogeneous nucleation or deposition onto the substrate surface results in the formation of nuclei with random orientations. The subsequent growth of various facets of a nucleus is dependent on the surface energy, and varies significantly from one facet to another [5.74]. For one-dimensional growth, such as film growth, only the highest growth rate with a direction perpendicular to the growth surface will be able to continue to grow. The nuclei with the fastest growth direction perpendicular to the growth surface will grow larger, while nuclei with slower growth rates will eventually cease to grow. Such a growth mechanism results in the formation of columnar structured films where all of the grains have the same crystal orientation (known as textured films) [5.75, 76]. In the case of nanorod growth inside a pore channel, such evolution selection growth is likely to lead to the formation of a single crystal nanorod or a bundle of single crystal nanorods per pore channel. Figure 5.10 shows typical TEM micrographs and selected-area electron diffraction patterns of V_2O_5 nanorods. It is well known that [010] (the *b*-axis) is the fastest growth direction for a V_2O_5 crystal [5.77, 78], which would explain why single crystal vanadium nanorods or a bundle of single crystal nanorods grow along the *b*-axis.

5.3.3 Single Crystal Oxide Nanorod Arrays Grown by Homoepitaxial Aggregation

Single crystal nanorods can also be grown directly by conventional electrophoretic deposition. However, several requirements must be met for such growth. First, the nanoclusters or particles in the sol must have a crystalline structure extended to the surface. Second, the deposition of nanoclusters on the growth surface must have a certain degree of reversibility so that the nanoclusters can rotate or reposition prior to their irreversible incorporation into the growth surface. Thirdly, the deposition rate must be slow enough to permit sufficient time for the nanoclusters to rotate or reposition. Lastly, the surfaces of the nanoclusters must be free of strongly attached alien chemical species. Although precise control of all these parameters remains a challenge, the growth of single crystal nanorods through homoepitaxial aggregation of nanocrystals has been demonstrated [5.79, 80]. The formation of single crystalline vanadium pentoxide nanorods by template-based sol electrophoretic deposition can be attributed to homoepitaxial aggregation of crystalline nanoparticles. Thermodynamically it is favorable for the crystalline nanoparticles to aggregate epitaxially; this growth behavior and mechanism is well documented in the literature [5.81, 82]. In this growth mechanism, an initial weak interaction between two nanoparticles allows rotation and migration relative to each other. Obviously, homoepitaxial aggregation is a competitive process and porous structure is expected to form through this homoepitaxial aggregation (as schematically illustrated in Fig. 5.11). Vanadium oxide particles present in a typ-

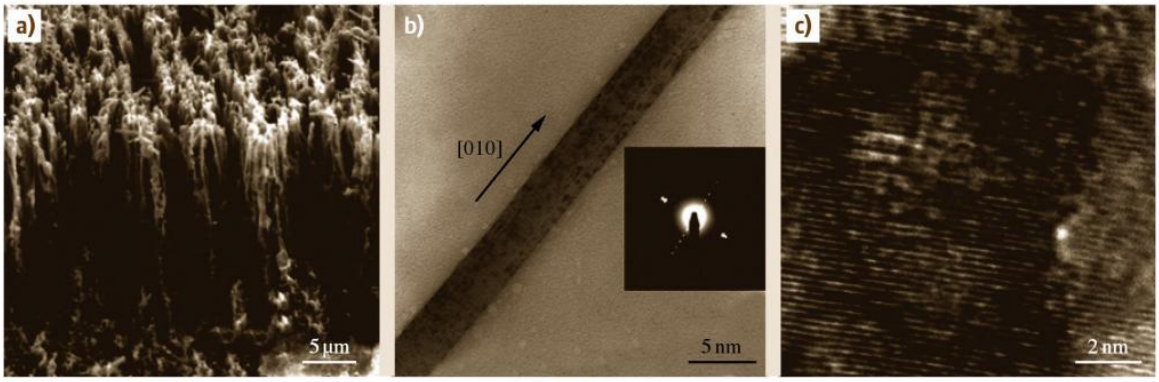

Fig. 5.10 (**a**) SEM image of V_2O_5 nanorod arrays on an ITO substrate grown in a 200 nm carbonate membrane by sol electrophoretic deposition; (**b**) TEM image of a V_2O_5 nanorod with its electron diffraction pattern; (**c**) high-resolution TEM image of the V_2O_5 nanorod showing the lattice fringes (after [5.54])

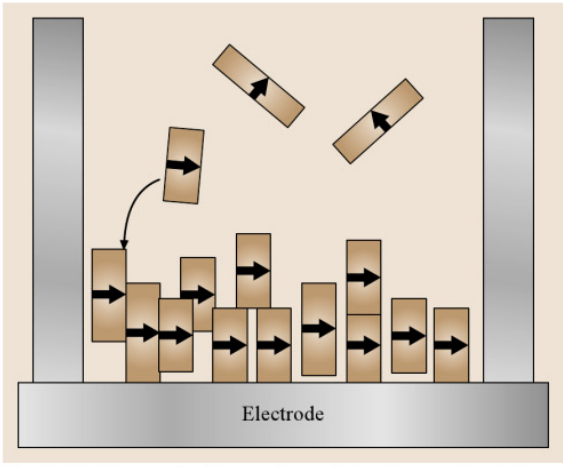

Fig. 5.11 Schematic illustration of the homoepitaxial aggregation growth mechanism of single-crystalline nanorods (after [5.54])

ical sol are known to easily form ordered crystalline structure [5.83], so it is reasonable to expect that homoepitaxial aggregation of vanadium nanocrystals from sol results in the formation of single crystal nanorods. Single crystal nanorods formed in this way are likely to undergo significant shrinkage when fired at high temperatures due to its original porous nature; 50% lateral shrinkage has been observed in vanadium pentoxide nanorods formed by this method. In addition, it might be possible that the electric field and the internal surfaces of the pore channels play significant roles in the orientation of the nanorods, as suggested in the literature [5.84, 85].

5.3.4 Nanowires and Nanotubes of Fullerenes and Metallofullerenes

Electrophoretic deposition in combination with template-based growth has also been successfully explored in the formation of nanowires and nanotubes of carbon fullerenes, such as C_{60} [5.86], or metallofullerenes, such as $Sc@C_{82}(I)$ [5.87]. Typical experiments include the purification or isolation of the fullerenes or metallofullerenes required using multiple-step liquid chromatography and dispersion of the fullerenes in a mixed solvent of acetonitrile/toluene in a ratio of 7 : 1. The electrolyte solution has a relatively low concentration of fullerenes (35 μM) and metallofullerenes (40 μM), and the electrophoretic deposition takes place with an externally applied electric field of 100–150 V with a distance of 5 mm between the two electrodes. Both nanorods and nanotubes of fullerenes or metallofullerenes can form and it is believed that initial deposition occurs along the pore surface. A short deposition time results in the formation of nanotubes, whereas extended deposition leads to the formation of solid nanorods. These nanorods possess either crystalline or amorphous structure.

5.4 Template Filling

Directly filling a template with a liquid mixture precursor is the most straightforward and versatile method for preparing nanowire or nanorod arrays. The drawback of this approach is that it is difficult to ensure complete filling of the template pores. Both nanorods and nanotubules can be obtained depending on the interfacial adhesion and the solidification modes. If the adhesion between the pore walls and the filling material is weak, or if solidification starts at the center (or from one end of the pore, or uniformly throughout the rods), solid nanorods are likely to form. If the adhesion is strong, or if the solidification starts at the interfaces and proceeds inwardly, hollow nanotubules are likely to form.

5.4.1 Colloidal Dispersion (Sol) Filling

Martin and coworkers [5.73, 88] have studied the formation of various oxide nanorods and nanotubules by simply filling the templates with colloidal dispersions (Fig. 5.12). Nanorod arrays of a mesoporous material (SBA-15) were recently synthesized by filling an ordered porous alumina membrane with sol containing surfactant (Pluronic P123) [5.89]. Colloidal dispersions were prepared using appropriate sol–gel processing techniques. The template was placed in a stable sol for various periods of time. The capillary force drives the sol into the pores if the sol has good wettability for the template. After the pores were filled with sol, the template was withdrawn from the sol and dried. The sample was fired at elevated temperatures to remove the template and to densify the sol–gel-derived green nanorods.

A sol typically consists of a large volume fraction of solvent, up to 90% or higher. Although the capillary force may ensure complete filling of the pores with the suspension, the amount of solid occupying the pore space is small. Upon drying and subsequent fir-

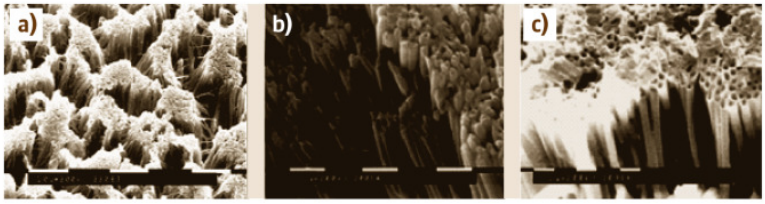

Fig. 5.12a–c SEM micrographs of oxide nanorods created by filling the templates with sol–gels: **(a)** ZnO, **(b)** TiO_2 and **(c)** hollow nanotube (after [5.73])

ing processes, significant shrinkage would be expected. However, the actual shrinkage observed is small when compared with the pore size. These results indicate that an (unknown) mechanism is acting to enrich the concentration of solid inside the pores. One possible mechanism could be the diffusion of solvent through the membrane, leading to the enrichment of solid on the internal surfaces of the template pores, similar to what happens during ceramic slip casting [5.90]. Figure 5.12a is a top view of ZnO nanotubules array, Fig. 5.12b is TiO_2 nanotubules array, Fig. 5.12c is hollow nantube array. The observed formation of nanotubules (in Fig. 5.12 [5.73]) may imply that this process is indeed present. However, considering the fact that the templates were typically emerged into sol for just a few minutes, diffusion through the membrane and enrichment of the solid inside the pores must be rather rapid processes. It was also noticed that the nanorods made by template filling are commonly polycrystalline or amorphous, although single crystal TiO_2 nanorods were sometimes observed for nanorods smaller than 20 nm [5.73].

5.4.2 Melt and Solution Filling

Metallic nanowires can also be synthesized by filling a template with molten metals [5.91]. One example is the preparation of bismuth nanowires using pressure injection of molten bismuth into the nanochannels of an anodic alumina template [5.92]. The anodic alumina template was degassed and immersed in the liquid bismuth at 325 °C ($T_m = 271.5$ °C for Bi), and then high pressure Ar gas of ≈ 300 bar was applied in order to inject liquid Bi into the nanochannels of the template for 5 h. Bi nanowires with diameters of 13–110 nm and large aspect ratios (of up to several hundred) have been obtained. Individual nanowires are believed to be single-crystal. When exposed to air, bismuth nanowires are readily oxidized. An amorphous oxide layer ≈ 4 nm in thickness was observed after 48 h. After 4 weeks, the bismuth nanowires were completely oxidized. Nanowires of other metals, such as In, Sn and Al, and the semiconductors Se, Te, GaSb, and Bi_2Te_3, were also prepared by injecting molten liquid into anodic alumina templates [5.93].

Polymeric fibrils have been made by filling the template pores with a monomer solution containing the desired monomer and a polymerization reagent, followed by in situ polymerization [5.14, 94–97]. The polymer preferentially nucleates and grows on the pore walls, resulting in tubules at short deposition times.

Metal, oxide and semiconductor nanowires have recently been synthesized using self-assembled mesoporous silica as the template. For example, *Han* et al. [5.98] have synthesized Au, Ag and Pt nanowires in mesoporous silica templates. The mesoporous templates were first filled with aqueous solutions of the corresponding metal salts (such as $HAuCl_4$). After drying and treatment with CH_2Cl_2, the samples were reduced under H_2 flow to form metallic nanowires. *Liu* et al. [5.99] carefully studied the interface between these nanowires and the matrix using high-resolution electron microscopy and electron energy loss spectroscopy techniques. A sharp interface only exists between noble metal nanowires and the matrix. For magnetic nickel oxide, a core–shell nanorod structure containing a nickel oxide core and a thin nickel silicate shell was observed. The magnetic properties of the templated nickel oxide were found to be significantly different from nickel oxide nanopowders due to the alignment of the nanorods. In another study, *Chen* et al. filled the pores of a mesoporous silica template with an aqueous solution of Cd and Mn salts, dried the sample, and reacted it with H_2S gas to convert it to (Cd,Mn)S [5.100].

5.4.3 Centrifugation

Filling the template with nanoclusters via centrifugation forces is another inexpensive method for mass producing nanorod arrays. Figure 5.13 shows SEM images of lead zirconate titanate (PZT) nanorod arrays with uniform sizes and unidirectional alignment [5.101]. These nanorod arrays were grown in polycarbonate membrane from PZT sol by centrifugation at 1500 rpm for 60 min. The samples were attached to silica glass

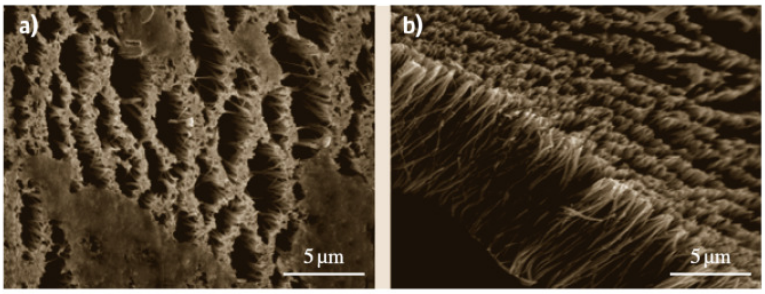

Fig. 5.13a,b SEM images of the top view (*left*) and side view (*right*) of lead zirconate titanate (PZT) nanorod arrays grown in polycarbonate membrane from PZT sol by centrifugation at 1500 rpm for 60 min. Samples were attached to silica glass and fired at 650 °C in air for 60 min (after [5.101])

and fired at 650 °C in air for 60 min. Nanorod arrays of other oxides (silica and titania) were prepared. The advantages of centrifugation include its applicability to any colloidal dispersion system, including those consisting of electrolyte-sensitive nanoclusters or molecules.

5.5 Converting from Reactive Templates

Nanorods or nanowires can also be synthesized using consumable templates, although the resultant nanowires and nanorods are generally not ordered to form aligned arrays. Nanowires of compounds can be prepared using a template-directed reaction. First nanowires or nanorods of one constituent element are prepared, and then these are reacted with chemicals containing the other element desired in order to form the final product. *Gates* et al. [5.102] converted single crystalline trigonal selenium nanowires into single crystalline nanowires of Ag_2Se by reacting Se nanowires with aqueous $AgNO_3$ solutions at room temperature. Nanorods can also be synthesized by reacting volatile metal halides or oxide species with carbon nanotubes to form solid carbide nanorods with diameters of between 2 and 30 nm and lengths of up to 20 µm [5.103]. ZnO nanowires were prepared by oxidizing metallic zinc nanowires [5.104]. Hollow nanotubules of MoS_2 ≈ 30 µm long and 50 nm in external diameter with wall thicknesses of 10 nm were prepared by filling a solution mixture of the molecular precursors, $(NH_4)_2MoS_4$ and $(NH_4)_2Mo_3S_{13}$, into the pores of alumina membrane templates. Then the template filled with the molecular precursors was heated to an elevated temperature and the molecular precursors were thermally decomposed into MoS_2 [5.105]. Certain polymers and proteins were also used to direct the growth of nanowires of metals or semiconductors. For example, *Braun* et al. [5.106] reported a two-step procedure using DNA as a template for the vectorial growth of a silver nanorods 12 µm in length and 100 nm in diameter. CdS nanowires were prepared by polymer-controlled growth [5.107]. For the synthesis of CdS nanowires, cadmium ions were well distributed in a polyacrylamide matrix. The Cd^{2+}-containing polymer was treated with thiourea (NH_2CSNH_2) solvothermally in ethylenediamine at 170 °C, resulting in degradation of polyacrylamide. Single crystal CdS nanowires 40 nm in diameter and up to 100 µm in length were obtained with preferential [001] orientations.

5.6 Summary and Concluding Remarks

This chapter provides a brief summary of the fundamentals of and techniques used for the template-based synthesis of nanowire or nanorod arrays. Examples were used to illustrate the growth of each nanorod material made with each technique. The literature associated with this field is overwhelming and is expanding very rapidly. This chapter is by no means comprehensive in its coverage of the relevant literature. Four groups of template-based synthesis methods have been reviewed and discussed in detail. Electrochemical deposition or electrodeposition is the method used to grow electrically conductive or semiconductive materials, such as metals, semiconductors, and conductive polymers and oxides. Electrophoretic deposition from

colloidal dispersion is the method used to synthesize dielectric nanorods and nanowires. Template filling is conceptually straightforward, although complete filling is often very difficult. Converting reactive templates is a method used to achieve both nanorod arrays and randomly oriented nanowires or nanorods, and it is often combined with other synthetic methods.

This chapter has focused on the growth of solid nanorod and nanowire arrays by template-based synthesis; however, the use of template-based synthesis to synthesize nanotubes, and in particular nanotube arrays, has received increasing attention [5.108]. One of the greatest advantages using template-based synthesis to grow of nanotubes and nanotube arrays is the independent control of the lengths, diameters, and the wall thicknesses of the nanotubes available. While the lengths and the diameters of the resultant nanotubes are dependent on the templates used for the synthesis, the wall thicknesses of the nanotubes can be readily controlled through the duration of growth. Another great advantage of the template-based synthesis of nanotubes is the possibility of multilayered hollow nanotube or solid nanocable structures. For example, Ni@$V_2O_5{\cdot}nH_2O$ nanocable arrays have been synthesized by a two-step approach [5.109]. First, Ni nanorod arrays were grown in a PC template by electrochemical deposition, and then the PC template was removed by pyrolysis, followed by sol electrophoretic deposition of $V_2O_5{\cdot}nH_2O$ on the surfaces of the Ni nanorod arrays. It is obvious that there is a lot of scope for more research into template-based syntheses of nanorod, nanotube and nanocable arrays, and their applications.

References

5.1 G.Z. Cao: *Nanostructures and Nanomaterials: Synthesis, Properties and Applications* (Imperial College, London 2004)

5.2 Z.L. Wang: *Nanowires and Nanobelts: Materials, Properties and Devices, Nanowires and Nonobelts of Functional Materials*, Vol. 2 (Kluwer, Boston 2003)

5.3 Y. Xia, P. Yang, Y. Sun, Y. Wu, Y. Yin, F. Kim, H. Yan: One-dimensional nanostructures: Synthesis, characterization and applications, Adv. Mater. **15**, 353–389 (2003)

5.4 A. Huczko: Template-based synthesis of nanomaterials, Appl. Phys. A **70**, 365–376 (2000)

5.5 C. Burda, X. Chen, R. Narayanan, M.A. El-Sayed: Chemistry and properties of nanocrystals of different shapes, Chem. Rev. **105**, 1025–1102 (2005)

5.6 X. Duan, C.M. Lieber: General synthesis of compound semiconductor nanowires, Adv. Mater. **12**, 298–302 (2000)

5.7 M.P. Zach, K.H. Ng, R.M. Penner: Molybdenum nanowires by electrodeposition, Science **290**, 2120–2123 (2000)

5.8 R.C. Furneaux, W.R. Rigby, A.P. Davidson: The formation of controlled-porosity membranes from anodically oxidized aluminium, Nature **337**, 147–149 (1989)

5.9 R.L. Fleisher, P.B. Price, R.M. Walker: *Nuclear Tracks in Solids* (Univ. of California Press, Berkeley 1975)

5.10 R.J. Tonucci, B.L. Justus, A.J. Campillo, C.E. Ford: Nanochannel array glass, Science **258**, 783–787 (1992)

5.11 G.E. Possin: A method for forming very small diameter wires, Rev. Sci. Instrum. **41**, 772–774 (1970)

5.12 C. Wu, T. Bein: Conducting polyaniline filaments in a mesoporous channel host, Science **264**, 1757–1759 (1994)

5.13 S. Fan, M.G. Chapline, N.R. Franklin, T.W. Tombler, A.M. Cassell, H. Dai: Self-oriented regular arrays of carbon nanotubes and their field emission properties, Science **283**, 512–514 (1999)

5.14 P. Enzel, J.J. Zoller, T. Bein: Intrazeolite assembly and pyrolysis of polyacrylonitrile, J. Chem. Soc. Chem. Commun. **8**, 633–635 (1992)

5.15 C. Guerret-Piecourt, Y. Le Bouar, A. Loiseau, H. Pascard: Relation between metal electronic structure and morphology of metal compounds inside carbon nanotubes, Nature **372**, 761–765 (1994)

5.16 P.M. Ajayan, O. Stephan, P. Redlich, C. Colliex: Carbon nanotubes as removable templates for metal oxide nanocomposites, nanostructures, Nature **375**, 564–567 (1995)

5.17 M. Knez, A.M. Bittner, F. Boes, C. Wege, H. Jeske, E. Maiâ, K. Kern: Biotemplate synthesis of 3-nm nickel and cobalt nanowires, Nano Lett. **3**, 1079–1082 (2003)

5.18 R. Gasparac, P. Kohli, M.O.M.L. Trofin, C.R. Martin: Template synthesis of nano test tubes, Nano Lett. **4**, 513–516 (2004)

5.19 C.F. Monson, A.T. Woolley: DNA-templated construction of copper nanowires, Nano Lett. **3**, 359–363 (2003)

5.20 Y. Weizmann, F. Patolsky, I. Popov, I. Willner: Telomerase-generated templates for the growing of metal nanowires, Nano Lett. **4**, 787–792 (2004)

5.21 A. Despic, V.P. Parkhuitik: *Modern Aspects of Electrochemistry*, Vol. 20 (Plenum, New York 1989)

5.22 D. Al Mawiawi, N. Coombs, M. Moskovits: Magnetic properties of Fe deposited into anodic aluminum oxide pores as a function of particle size, J. Appl. Phys. **70**, 4421–4425 (1991)

5.23 C.A. Foss, M.J. Tierney, C.R. Martin: Template-synthesis of infrared-transparent metal microcylin-

5.93 E.G. Wolff, T.D. Coskren: Growth, morphology of magnesium oxide whiskers, J. Am. Ceram. Soc. **48**, 279–285 (1965)
5.94 W. Liang, C.R. Martin: Template-synthesized polyacetylene fibrils show enhanced supermolecular order, J. Am. Chem. Soc. **112**, 9666–9668 (1990)
5.95 S.M. Marinakos, L.C. Brousseau III, A. Jones, D.L. Feldheim: Template synthesis of one-dimensional Au, Au-poly(pyrrole) and poly(pyrrole) nanoparticle arrays, Chem. Mater. **10**, 1214–1219 (1998)
5.96 H.D. Sun, Z.K. Tang, J. Chen, G. Li: Polarized Raman spectra of single-wall carbon nanotubes monodispersed in channels of $AlPO_4$-5 single crystals, Solid State Commun. **109**, 365–369 (1999)
5.97 Z. Cai, J. Lei, W. Liang, V. Menon, C.R. Martin: Molecular and supermolecular origins of enhanced electronic conductivity in template-synthesized polyheterocyclic fibrils. 1. Supermolecular effects, Chem. Mater. **3**, 960–967 (1991)
5.98 Y.J. Han, J.M. Kim, G.D. Stucky: Preparation of noble metal nanowires using hexagonal mesoporous silica SBA-15, Chem. Mater. **12**, 2068–2069 (2000)
5.99 J. Liu, G.E. Fryxell, M. Qian, L.-Q. Wang, Y. Wang: Interfacial chemistry in self-assembled nanoscale materials with structural ordering, Pure Appl. Chem. **72**, 269–279 (2000)
5.100 L. Chen, P.J. Klar, W. Heimbrodt, F. Brieler, M. Fröba: Towards ordered arrays of magnetic semiconductor quantum wires, Appl. Phys. Lett. **76**, 3531–3533 (2000)
5.101 T. Wen, J. Zhang, T.P. Chou, S.J. Limmer, G.Z. Cao: Template-based growth of oxide nanorod arrays by centrifugation, J. Sol-Gel Sci. Tech. **33**, 193–200 (2005)
5.102 B. Gates, Y. Wu, Y. Yin, P. Yang, Y. Xia: Single-crystalline nanowires of Ag_2Se can be synthesized by templating against nanowires of trigonal Se, J. Am. Chem. Soc. **123**, 11500–11501 (2001)
5.103 E.W. Wong, B.W. Maynor, L.D. Burns, C.M. Lieber: Growth of metal carbide nanotubes, nanorods, Chem. Mater. **8**, 2041–2046 (1996)
5.104 Y. Li, G.S. Cheng, L.D. Zhang: Fabrication of highly ordered ZnO nanowire arrays in anodic alumina membranes, J. Mater. Res. **15**, 2305–2308 (2000)
5.105 C.M. Zelenski, P.K. Dorhout: The template synthesis of monodisperse microscale nanofibers, nanotubules of MoS_2, J. Am. Chem. Soc. **120**, 734–742 (1998)
5.106 E. Braun, Y. Eichen, U. Sivan, G. Ben-Yoseph: DNA-templated assembly and electrode attachment of a conducting silver wire, Nature **391**, 775–778 (1998)
5.107 J. Zhan, X. Yang, D. Wang, S. Li, Y. Xie, Y. Xia, Y. Qian: Polymer-controlled growth of CdS nanowires, Adv. Mater. **12**, 1348–1351 (2000)
5.108 Y. Wang, K. Takahashi, H.M. Shang, G.Z. Cao: Synthesis, electrochemical properties of vanadium pentoxide nanotube arrays, J. Phys. Chem. **B109**, 3085–3088 (2005)
5.109 K. Takahashi, Y. Wang, G.Z. Cao: Ni-$V_2O_5 \cdot n\,H_2O$ core-shell nanocable arrays for enhanced electrochemical intercalation, J. Phys. Chem. B **109**, 48–51 (2005)

6. Templated Self-Assembly of Particles

Tobias Kraus, Heiko Wolf

Nanoparticles are frequently immobilized on substrates to use them as functional elements. In the resulting layer, the particles are accessible, so that their useful properties can be exploited, but their positions are fixed, so that their behavior is stable and reproducible. Frequently, the particles' positions have to be well defined. Templated assembly can position particles even in the low-nanometer size regime, and it can do so efficiently for many particles in parallel. Thus, nanoparticles become building blocks, capable of forming complex superstructures.

Templated assembly is based on a simple idea: particles are brought to a surface that has binding sites which strongly interact with the particles. Ideally, the particles adsorb solely at the predefined binding sites, thus creating the desired arrangement. In reality, it is often a challenge to reach good yields, high precision, and good specificity, in particular for very small particles. Since the method is very general, particles of various materials such as oxides, metals, semiconductors, and polymers can be arranged for applications ranging from microelectronics to optics and biochemistry.

Solid particles with sub-μm diameters are intriguing objects. They have a well-defined surface which is large compared with their volume, so that they interact strongly with their environment. At the same time, particles are clearly defined entities which can be mixed, purified, modified, and arranged into larger structures. This combination has made them popular in fields ranging from biology (where they carry analyte-binding molecules) to semiconductor fabrication (where they confine electrons) [6.1].

It is tempting to try and use such particles as nanoscale building blocks to create functional devices, be their function electronic, mechanical or chemical. There are two prerequisites: first, particles with narrow size distribution and well-defined structures and surfaces have to be available from different materials in sufficient quantities. Second, these particles have to be arranged such that they provide the desired functionality. Templated particle assembly is one way to do so. A template defines the particle arrangement in advance according to the designer's wishes.

Producing particles of sufficient quality to be used as building blocks is not necessarily simple, but it can be done efficiently. Chemical methods are known to produce particles from very small clusters (with diameters in the low nanometer regime), various shapes of sin-

gle crystals with diameters from 10 to about 100 nm, and larger particles with diameters up to micrometers. Some syntheses produce particles that are rather monodisperse, the best methods reaching coefficients of variation below 3%. This is still worse than, say, the relative size distribution of bricks in most buildings, but good enough for the particle to arrange spontaneously into ordered supercrystals [6.2]. The particles can be simple crystals or complex structures with a shell that differs from the core, for example, to protect the surface of the core [6.3]. Chemical methods readily produce such core–shell structures which would be exceedingly complicated to make using conventional methods.

As for their arrangement, particles down to about 100 μm in diameter are routinely handled using conventional pick-and-place techniques, a method widely used in industrial processes. Such serial methods become very time consuming at smaller scales, and they fail in the sub-μm regime, where adhesion forces render the simple maneuver of *putting down* a particle very challenging [6.4]. In this size range, particles are dominated by Brownian motion. They move randomly in their suspensions, and alternative assembly methods become necessary for their placement. Templated particle assembly is such an alternative strategy, based on a predefined surface that carries the information on the final particle placement. It can produce a variety of particle arrangements in parallel and over large areas (with typical lateral dimensions up to 10^6 particle diameters).

Templated assembly utilizes the strong interactions of particles with interfaces and their tendency to produce dense packings to create predictable arrangements on a patterned surface. Since the desirable arrangement depends on the desired material properties, it is an advantage of templated assembly to give the user great flexibility in attainable particle arrangements.

There are rather different motivations for the use of well-defined particle arrangements. If single-particle properties are to be exploited (for example, their small size, large surface-to-volume ratio or optical properties), it is often critical to know in advance the exact particle positions. Particles are then commonly arranged into spaced arrays, possibly with alignment marks. In a biological assay, for example, a fluorescence reader can find the individual particles in a regular array according to their position and record their optical properties to gain information on an analyte that had come into contact with the particles [6.5]. Similarly, if particles are used as memory elements [6.6], they need to be electrically addressed – a task that is greatly simplified if their positions are well known in advance.

Interacting particles can exhibit collective properties that depend on their relative arrangement. In the field of metamaterials, for example, the activity of many particles with sizes well below the wavelength of an incident electromagnetic wave leads to unusual far-field behavior [6.7]. From afar, the bulk metamaterial appears to have, for example, a negative refractive index. Optical metamaterials also include photonic crystals, which exhibit a photonic bandgap much like the electronic bandgap of semiconductors due to a periodic potential caused by regular crystals of spherical, diffracting particles. Templated assembly can create such dense structures with well-defined boundaries, and it can influence the packing itself by imposing a desired geometry on the first layer.

More complex structures, possibly including more than one particle type, offer even more complex functionalities. One popular target is *smart materials*, which react to a stimulus in a coherent and useful way. Much like the electronic properties of a semiconductor microchip lead to extremely complex electronic behavior, patterned materials formed from arranged particles might exhibit useful mechanical, thermal or other properties. Another application of such complex structures (which are hard to produce) is anticounterfeiting, where an object is protected by a small particle structure with a unique property that can be detected.

Templated assembly is, of course, competing with more traditional means of micro- and nanofabrication, as covered in other chapters of this Handbook. Templated assembly is advantageous in that it takes advantage of the chemically produced small dimensions of nanoparticles, and it is more general than traditional methods in that it can process a wide variety of available colloids. The actual assembly process can be rather simple and compatible with continuous processing, even under ambient conditions. The most challenging prerequisite is usually the template, which has to be fabricated to provide sufficient definition of the assembled structure.

A process that arranges particles into a regular structure without any template is often called *self-assembly*. Here, the information on the arrangement is not contained in a template but in the properties of the particles themselves. The problem of *programming* the assembly process is thus shifted to the particles, which have to be chosen (or modified) such that they assemble into

a certain structure. This is not an easy task, and there are few examples so far of rational materials design using engineered particles. A template, on the other hand, can be defined using classical top-down methods, which provide great flexibility.

Still, templates become hard to fabricate if the particles are small and high patterning resolution is required. A combination of self-assembly and templated assembly is then useful: boundaries are defined by the template, but additional effects such as particle–particle, particle–surface or particle–solvent interactions lead to a predictable particle arrangement inside the boundaries.

We will limit ourselves here to processes with surface-bound templates and disregard supramolecular assembly, although molecular cages might also be regarded as templates. Likewise, biomineralization processes which can be templated using certain surfaces will not be covered here. The main focus is on sub-μm particles that are hard to place using any other method but can be assembled with high quality by means of templated assembly processes.

Even today, larger particles (between ≈ 1 and 100 μm) are assembled using templated assembly methods, mostly from slurries in an approach called *fluidic assembly* [6.8]. Illumina, Inc. arranges 3 μm-diameter glass beads functionalized with short DNA strands into a regular grid, which can then be used for DNA sequencing. Alien Technology Corporation holds several patents covering the integration of semiconductor pieces into polymers and other carriers, which today it mainly uses for the production of radiofrequency identification (RFID) chips, in which small electronic radiofrequency components are mounted on a paper or polymer label which is attached to an item for wireless identification. Similar methods for much smaller particles are currently being developed, but have not yet been applied industrially.

The challenges that occur when going down in particle size are mostly due to the greater influence of Brownian motion, which disturbs any order formed; strong adhesion to surfaces, which increases unspecific adsorption and makes pick-and-place difficult; and the problem of process control as the particles become harder to resolve with conventional optical methods.

In addition, the dimensions of the targeted nanostructured materials are often comparable to those produced with larger particles, but the number of particles involved is now very much higher (scaling inversely with the particle volume). Even assembly methods with very high yields are therefore bound to produce defects, which might hinder the function of the material. In some interesting applications (such as optical metamaterials), the absolute placement accuracies required to create a discernible optical effect are strict. Templated assembly is in principle able to provide such accuracies – even for many particles – and we will discuss its prerequisites in the next section.

6.1 The Assembly Process

Templated particle assembly involves particle adsorption on surfaces, and the well-developed ideas from adsorption theory (treated in many monographs and reviews) also hold for the case of templated assembly. While in many classical adsorption processes adsorption occurs at unpredictable positions, often until the entire surface is covered, the goal of a templated assembly process is the arrangement of particles with great precision and specificity. In this chapter, we will review some concepts that are less prominent in the adsorption literature. A useful metaphor of the directed assembly process is the energy landscape, which we will introduce here and frequently use to illustrate effects of interaction lengths, particle mobility, time scales, and other features of assembly methods.

6.1.1 Energy and Length Scales

A driving force that brings a colloidal object to a defined position and holds it there has to overcome Brownian motion. This constitutes the minimum requirement for the design of a templated assembly process. In the absence of a driving force, the particle will deviate from its original position r_0 according to

$$\frac{1}{3}\left\langle (r - r_0)^2 \right\rangle = \frac{k_\mathrm{B} T}{6\pi a \eta} t = 2Dt \,, \tag{6.1}$$

depending on the temperature T, the particle diameter a, the viscosity of the surrounding fluid η, the time t, and Boltzmann's constant k_B [6.9]. Thus, when averaging over a very large number of particles, a 10 nm-diameter particle in water would move about 51 μm in 60 s.

Table 6.1 Interactions that can drive particle assembly processes

Interaction	Typical range (order of magnitude)
Covalent	0.1 nm
van der Waals	1 nm
Coulomb (electrostatic)	1 nm (polar)–100 nm (apolar)
Hydrophobic	1 nm
Capillary	1 mm

The goal of an assembly process is to overcome this random, diffusional motion (with an energy scale of $k_B T$ and characterized by the diffusion coefficient D) by a bias that induces drift so that the probability of finding a particle at the desired position is markedly increased. Particles are then held in place until the system is quenched in some way, for example, by exchanging its environment.

In order to arrange the particles, templated assembly processes use potentials with minima at the particles' target positions. Such potential wells can be defined using various particle–surface interactions, some of which are listed in Table 6.1. These interactions act over different lengths, have different strengths, and form minima with different geometries, all of which can influence the assembly process.

Let us consider a particle that is moving in a fluid in the vicinity of a surface with *binding sites*, that is, features that interact with the particle more strongly than does the rest of the surface. The particle is mobile and moves randomly due to thermal excitation. Figure 6.1 illustrates this situation: depending on its position, the free energy of the particle will change as the interaction with the binding sites changes. If there is a gradient present, a directing force will act on the particle and bias its random motion towards an energy minimum. This *energy landscape*, formed by the superposition of the interaction, governs the particle's motion.

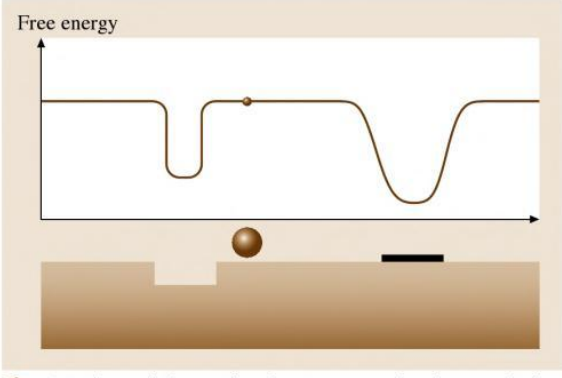

Fig. 6.1 A particle moving in an energy landscape during templated assembly. Its trajectory depends on the shape of the potential wells created by the binding sites, which also influence yield and accuracy of assembly

Some interactions are strong but short-ranged, for example, covalent bonds. In the energy landscape picture shown in Fig. 6.1, they will resemble a steep well into which the particle falls and from which it can hardly escape. On the other hand, the particle can be in close proximity to such steep wells and still not feel their presence. More precisely, the probability distribution of its presence will only be affected locally. When the particle is trapped inside the well, and if the entrapment can be reasonably modeled using a harmonic oscillator, its deviations from the minimum at $x = 0$ equals [6.10]

$$\left\langle x^2 \right\rangle = \frac{k_B T}{m\omega_0^2} \tag{6.2}$$

for a particle with mass m that is bound as in a harmonic oscillator with a frequency $\omega = \sqrt{k/m}$, the square root of the spring constant over the particle mass. Thus, a steep potential minimum can trap a particle with high accuracy: if the oscillator has a frequency of 1 GHz, a 10 nm particle of gold will deviate by less than a nanometer. The prototypical example of such a strong binding site is a topographical hole from which the particle cannot escape. The walls provide very steep exclusion potentials. Much less steep, but affecting a larger volume, is the well formed by an electrostatic field. In practice, even if the theoretical assembly accuracy of such an electrostatic binding site is limited, it often provides very good results. Other factors turn out to be critical as well – in particular the minimal achievable size of the binding sites and the yield of assembly. An assembled particle can simply block a binding site geometrically by not letting any other particle sufficiently close to the site, but it can also neutralize its charge (at least partially) and therefore hinder the adsorption of additional particles. Such changes in the energy landscape due to adsorption are often critical for the specificity and kinetics of the assembly.

Some of the most relevant interactions in directed assembly processes are summarized in Table 6.1. The exact shapes of the energy landscape caused by a particular interaction potential depend critically on the binding-site geometry, while the interaction lengths depend mainly on the used materials, solvents, and surfactants. Electrostatic interactions in suspensions are

If particles readily desorb from binding sites, an equilibrium situation will finally develop. The yield will then never reach unity, and its value will fluctuate over time.

6.1.3 Large Binding Sites

Consider a particle that hits a binding site with area A. If the particle gets sufficiently close to the site and if its interaction with the site is sufficiently large to overcome Brownian motion, the particle will be adsorbed. When we have a large number of such binding sites, particles will be randomly arranged inside the various A, so that the precision of arrangement is limited by the minimum size that (a) the template patterning can produce and (b) allows for sufficiently rapid particle assembly.

If, on the other hand, a funneling effect of the kind discussed above is present, the distribution of the particles might be biased towards a certain part of A. Then, the width of the position distribution is the result of the competition between a stochastic force (Brownian in general) and the directing force.

If the area A is large enough to accommodate multiple particles, particles can either arrange into random submonolayers or into ordered dense layers. The first case, particle adsorption on strongly adsorbing surfaces, is described reasonably well by the random sequential adsorption (RSA) model, which predicts a random particle distribution. Adsorption ceases when there is no space left in the binding area that could accommodate an additional particle. The final packing density is called the *jamming limit*, which can be numerically found to be $\theta_\infty \approx 0.547$ for two-dimensional, circular particles [6.16]. Random sequential adsorption is the subject of numerous reviews, which also discuss its application to anisotropic particle such as rods [6.17, 18].

The RSA model accurately describes many molecular adsorption problems, in particular the adsorption of proteins on surfaces. It does not cover processes that result in dense ordered arrangements, for example, self-assembled monolayers (SAM). In contrast to the RSA model, the molecules that constitute a SAM retain some mobility even after they are adsorbed on the surface. They interact with other molecules even before they adsorb, and they interact with the underlying metal film. Larger particles sometimes behave similarly. The rearrangement of particles in an evaporating liquid film due to capillary forces is a well-known example.

When dense ordered packings are desired, the particle–surface interaction has to be appropriate to avoid RSA-like adsorption. It turns out [6.19] that, by tuning the strength of the interaction, particle arrangements between well-ordered layers and randomly distributed submonolayers can be obtained.

6.1.4 Thermodynamics, Kinetics, and Statistics

Diffusion constants scale inversely with the particle radius. The diffusion constants of nanoparticles are therefore much smaller than those of molecules. A 100 nm-diameter sphere moving in water will exhibit a diffusion constant D of approximately $10^{-12}\,\mathrm{m}^2/\mathrm{s}$. Diffusion-limited processes with particles are thus slow, equilibrium situations can often not be reached in observable times, and the kinetics of the assembly process influences the assembly results. From an energy landscape point of view, it is not sufficient to provide a well-defined minimum in an appropriate position; the pathway to this minimum also has to be taken into account.

Most real template–particle systems will have complex energy landscapes with a variety of secondary minima and kinetic traps. A well-known example is a chemically functionalized surface onto parts of which particles should bind specifically. In practice, one finds unspecific deposition and a certain degree of particle accumulation, both caused typically by unspecific van der Waals-type attractions. Countermeasures include stirring, which increases particle mobility and keeps them from settling in secondary minima; rapid processing, which decreases the number of undesired particle collisions and thus the probability of reaching such a minimum; and washing, which removes weakly bound particles.

There is one limitation, however, that cannot be overcome by such mobility-increasing measures. When the number of particles in the volume affected by a binding site is small, the probability of finding at least one particle inside this volume will be small too. In the simple Poisson model of the situation, a volume V would contain a certain number n of particles with probability

$$W(n) = \mathrm{e}^{-\nu}\frac{\nu^n}{n!}\,, \tag{6.7}$$

where υ is the average number of particles in the volume, $\nu = Vc$ in the homogenous case. The probability of finding at least a single particle in this volume is therefore smaller than

$$W(n \geq 1) \leq \sum_{n=1}^{\infty} W(n) = 1 - \mathrm{e}^{-\nu}\,, \tag{6.8}$$

and the particle concentration has to be above

$$c_c \geq -\frac{\ln(1-\gamma)}{V} \tag{6.9}$$

to guarantee a certain probability γ for a particle to be present. This limits the yield in assembly methods which only capture particles during a short period of time from the volume V: when there is no particle present, none can be assembled. When we regard a large number of binding sites and require a certain minimum yield, say, 90%, the colloid concentration at the binding sites therefore has to be at least $c = 2.3/V$, independent of any further process details. This concentration can be provided either by an overall larger colloid concentration or (often more practical) by an additional, long-range force that acts on many particles, much like a funnel again. Electrostatic or hydrodynamic forces can increase the particle concentration locally, for example, at a three-phase boundary line, and enable sufficient assembly yields. We will see how this is done experimentally in the next section.

6.2 Classes of Directed Particle Assembly

There are many options and examples of how to assemble particles and small objects into templates. Depending on the synthesis and the material of the particles, and especially on the medium in which the particles are supplied, different strategies can be applied. Furthermore, the material of the target substrate can determine the assembly method to be used.

Nanoparticles can be synthesized and held in the gas phase by a carrier gas as an aerosol. At this point, they can be assembled directly from the gas phase onto a template (Fig. 6.3a). As a dry powder, nanoparticles tend to agglomerate into larger clusters due to strong van der Waals interactions, thus making it almost impossible to arrange patterns of individual particles. Therefore, submicron-sized particles are often delivered as suspensions in a liquid medium, especially when they were synthesized in liquid phase. Usually, nanoparticles are easier to stabilize in liquid, and particle agglomeration is prevented by surface chemicals creating a surface charge or by the addition of surfactants.

For assembly from the liquid phase we differentiate two cases: assembly from the bulk liquid onto the solid template (Fig. 6.3b) or assembly at the solid–liquid–gas boundary, i. e., at the meniscus of a liquid front moving over the substrate (Fig. 6.3c). In the following subsection we will illustrate the different assembly strategies with some instructive examples.

6.2.1 Assembly from the Gas Phase

Particles can be assembled from the gas phase into a pattern by localized surface charges on a substrate, as in xerography. Here however, the fabricated patterns are considerably smaller than in a copier or a laser printer. The *latent image* of charges is produced in a thin-film electret by contacting a nanopatterned electrode with the target substrate [6.20, 21]. The electret material can be a polymer (poly(methylmethacrylate) PMMA or a fluorocarbon layer) or SiO_2. The flexible patterned electrode is made from a patterned silicone elastomer (polydimethylsiloxane PDMS) with a thin conductive gold layer evaporated on top [6.20] or from thin patterned silicon on top of a flat PDMS sheet [6.22]. The flexible electrode is brought into direct contact with the electret and the charge image is produced by an electrical pulse. Charge patterns can also be produced by sequentially writing with a conducting atomic force microscopy (AFM) tip [6.23], although in these exam-

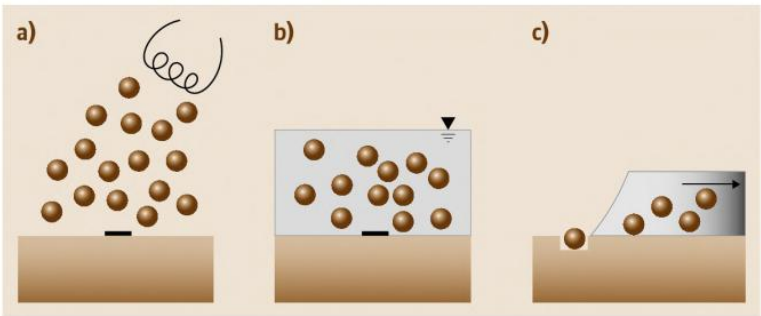

Fig. 6.3a–c Particles can be assembled from different media: they can be synthesized in a vacuum (or a gas) and directly assembled from the gas phase (**a**). Most commonly used are colloidal suspensions, from which particles are assembled at the liquid–solid interface (**b**). Alternatively, the particles can be assembled at the gas–liquid–solid boundary where strong capillary and confinement forces act on them (**c**)

ples the nanoparticles (NPs) were then adsorbed from the liquid phase (see the next section). The charge patterns are reported to be stable for more than 1 week in air [6.23]. Nanoparticle preparation is performed by an evaporative process in a tube furnace, by electrospray or in a plasma system [6.24]. Nanoparticles that have been synthesized in a wet chemical process can be used if they can be aerosolized without agglomerating. An interesting aspect is the combination of gas-phase particle synthesis with particle sorting methods, directly before the particles are assembled [6.25]. Almost monodisperse particle streams with few 10 nm-diameter nanoparticles can be prepared in this way. For the actual assembly, the nanoparticles have to be accelerated towards the target surface by an external field in a particle assembly module. Assembly of nanosized patterns from particles with a narrow size distribution can be achieved in this way.

Templates with an additional material contrast can improve the accuracy of particle assembly from the gas phase [6.24, 25]. The template is prepared from a patterned photoresist on a silicon substrate. In addition to the aerosol of charged nanoparticles, a stream of equally charged ions is introduced into the assembly chamber (Fig. 6.4). The ions are very mobile and fast compared with the nanoparticles and charge the resist structures on the substrate. The electric field of the charged resist pattern guides the nanoparticles into the areas of free silicon substrate. The additional ions improve the contrast between deposition in desired and undesired areas of the template (Fig. 6.5). By controlling the amount of ions it is possible to create and control a funneling effect which focuses the nanoparticles into structures much smaller than the actual template pattern. Among the smallest structures that have been realized by this method are 35 nm features assembled from 10 nm Ag nanoparticles in 200 nm holes (Fig. 6.6) [6.25]. In the majority of these assemblies, multiple nanoparticles are deposited into one assembly site and it is difficult if not impossible to assemble single nanoparticles with high yield.

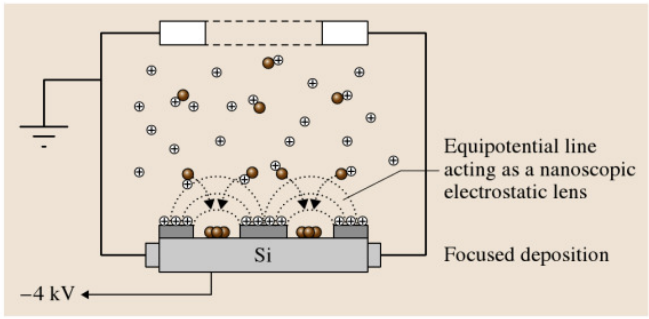

Fig. 6.4 Schematic setup for the assembly of nanoparticles from the gas phase in an electric field and with additional ions in the gas (after [6.25], © Macmillan 2006)

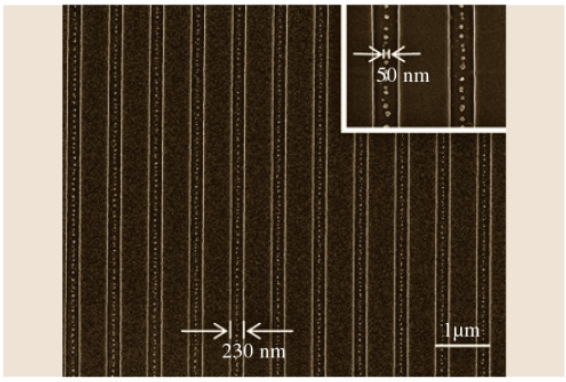

Fig. 6.5 Ag particles (10 nm) assembled in 230 nm-wide lines. The inset shows the funneling effect which reduces the actual width of the assembled particle lines to only 50 nm. The scale bar corresponds to 1 μm (after [6.25], © Macmillan 2006)

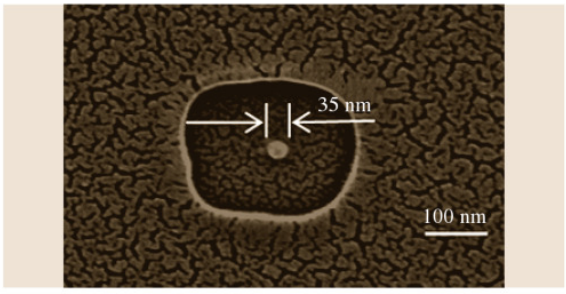

Fig. 6.6 Ag particles (10 nm) assembled in a 230 nm-wide hole. The funneling effect reduces the size of the actual assembly to only 35 nm. The scale bar corresponds to 100 nm (after [6.25], © Macmillan 2006)

6.2.2 Assembly in the Liquid Phase

In the majority of examples of templated assembly, particles are deposited from the liquid phase onto a solid template surface. Here, we want to differentiate assembly from the bulk liquid and assembly from the liquid at the liquid–solid–gas boundary (Sect. 6.2.3). For assembly directly from the liquid phase, a great variety of interactions such as electrostatic forces [6.26], capillary forces [6.27], formation of covalent bonds [6.28], specific recognition between biomolecules [6.29], supramolecular interac-

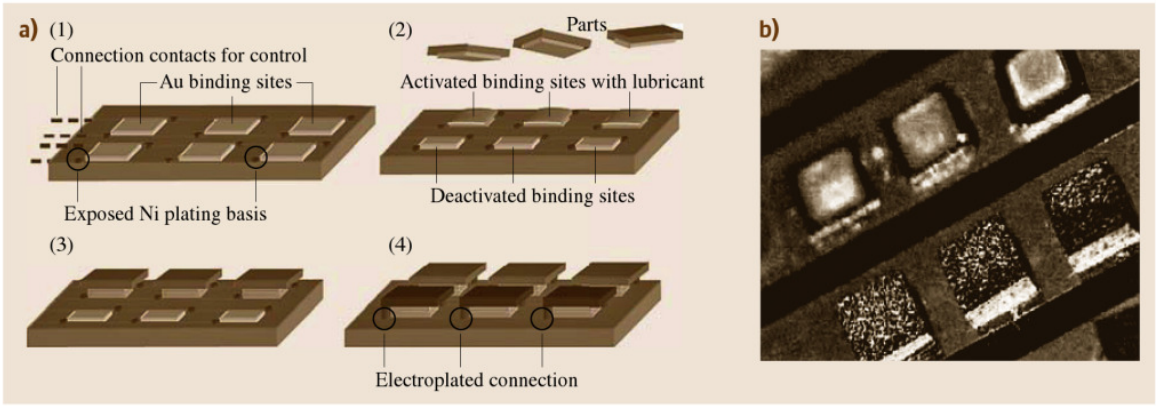

Fig. 6.7a,b Schematic description of the multibatch assembly process (1–4) with SAM-covered binding sites that can be deactivated selectively (**a**). A two-batch assembly result fabricated according to the scheme (**b**) (after [6.32], © IOP 2003)

tions [6.30], and form factor [6.8, 31] have been used. Also, electric fields can be applied to direct the particles or nanoobjects towards the targeted adsorption sites.

Wetting Contrast

For larger particles and objects, ranging from millimeters down to several tens of micrometers, wetting contrast in combination with capillary forces is applied for the assembly [6.27, 32, 33]. Topographic three-dimensional (3-D) features on the template may support the assembly in addition and introduce selectivity in a multicomponent assembly [6.34]. The template has hydrophobic assembly sites which can be selectively covered by a layer of adhesive or solder. The objects to be assembled are agitated in a fluid. In the simplest case – when a low-melting solder or a liquid organic adhesive is used – the fluid is water [6.35]. When higher temperatures are necessary to melt the solder, ethylene glycol [6.33, 34] can be used as a fluid. The suspended objects selectively adhere to the solder or adhesive when they come into contact. Objects to be assembled may also have a combination of hydrophilic and hydrophobic faces, which makes them adsorb with a preferred side or orientation. The strong capillary forces of the solder or adhesive guide the assembled objects into the desired orientation. The geometry of the adsorption sites and of the attached surfaces play a crucial role in this last step because local energy minima might freeze the assembled objects into undesired orientations on the template if the binding sites are not designed carefully.

Böhringer and coworkers devised a method in which hydrophobic assembly sites can be selectively switched off and reactivated later for a second assembly step (Fig. 6.7) [6.32,36]. In this way, different objects or particles can be assembled onto the same template sequentially. For this purpose, the assembly sites consist of gold electrodes which are covered by a hydrophobic alkanethiol SAM. The alkanethiol SAM can be electrochemically removed from individual electrodes in a selective manner. When dipped into an adhesive, only the hydrophobic SAM-covered sites of the template are wetted and covered with an adhesive layer. In the subsequent assembly step, only the adhesive-covered sites are active and can grab an object from solution. After the first particle assembly, all vacant electrodes can be modified with a SAM, simply by dipping into an alkanethiol solution, and the process can begin again.

Electrostatic Nanoparticle Adsorption

In liquid suspensions, particles are usually stabilized by surface charges. These surface charges prevent the particles from agglomerating and can be exploited to guide the particles by electrostatic interaction to adsorption sites of opposite charge. The template needs to display a contrast in surface charge. This can be achieved by microcontact printing of SAMs with charged endgroups [6.11, 37]. The pattern contrast can be further enhanced through layer-by-layer (LBL) adsorption of polyelectrolyte multilayers onto the printed monolayers [6.26,38]. Microcontact printing of a polyelectrolyte pattern onto LBL multilayers also results in a pattern of different surface charge on the template [6.39]. Other methods based on nanoimprint lithography (NIL) and subsequent monolayer formation have been described as well (Sect. 6.3) [6.40].

On such charged SAM patterns, oppositely charged 10 μm-diameter gold discs adsorbed selectively onto sites of opposite charge [6.37]. The Au discs were modified by thiol monolayers to control their surface charge. Once the discs have adsorbed onto the surface of the template, there is no more mobility. The discs are fixed to their initial adsorption site. This lack of mobility prevents ordering in the layer of adsorbed discs. For the formation of an ordered monolayer a certain mobility of the discs on the template surface would be required. The same observation is made with smaller particles being adsorbed electrostatically. The adhesion forces are too strong to allow for any mobility of the particles on the surface. Thus, a well-ordered and densely packed layer of particles is inhibited. Well-defined arrays of particles can only be achieved when a single particle or a small number of particles per site are adsorbed. This was demonstrated for particles a few microns in diameter [6.26]. For smaller particles in the nanometer regime this is a very challenging task.

Polar solvents (water, alcohol) are usually necessary to stabilize the colloidal suspension of charged particles. However, additional ions in water have to be avoided since the surface charges of the template are more effectively screened with higher ionic strength in the solvent [6.37].

Sagiv and coworkers fabricated charged adsorption sites by means of writing with a conductive AFM into a self-assembled silane monolayer [6.41]. The otherwise inert monolayer is activated by the charged AFM tip, and functionalized molecules can be coupled onto the patterned areas (Fig. 6.8). The added molecules

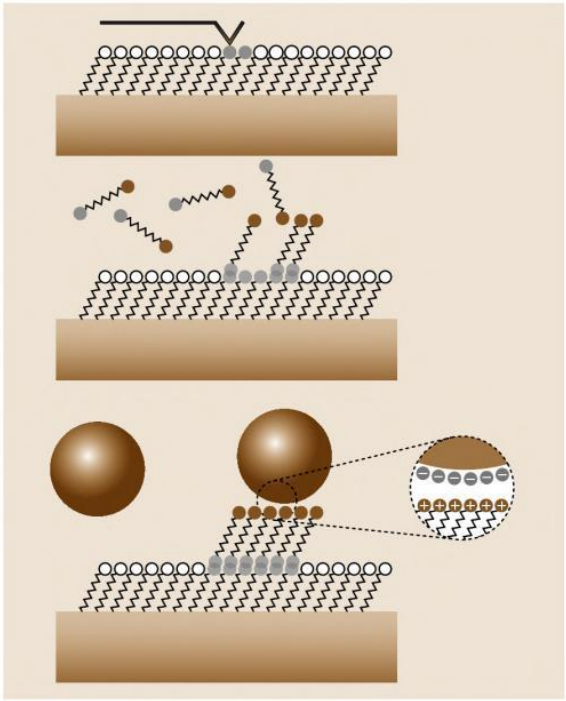

Fig. 6.8 Schematic representation of the modification of SAMs by AFM and subsequent bilayer formation to create assembly sites for selective adsorption of nanoparticles (after [6.41], © American Chemical Society)

can either carry a positive charge to attract negatively charged nanoparticles (Fig. 6.9) or carry a thiol group which binds to gold nanoparticles [6.28]. The latter

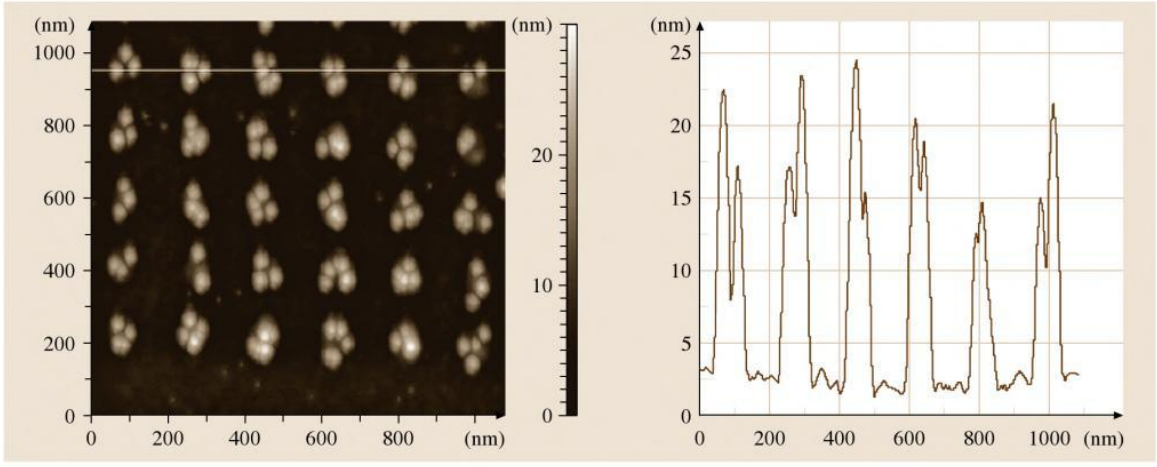

Fig. 6.9 Au particles (17 nm) assembled on amino-terminated bilayer templates (after [6.41], © American Chemical Society 2004)

A very versatile variant of dielectrophoretic assembly was demonstrated by *Chiou* and coworkers [6.53]. They fabricated an assembly setup with rewritable electrode patterns on a photoconductive surface. Simply by projecting an image through a microscope lens, they could define their electrode pattern for dielectrophoretic assembly of 4.5 μm latex beads.

When NPs are assembled from aqueous suspensions, drying is always a critical step where strong capillary forces of the drying droplet may act on the assembled particles and destroy or alter the assembled pattern. On the other hand, the strength and directing capacity of capillary forces may be exploited to control the assembly of nanoparticles very accurately, as shown in the next section.

6.2.3 Assembly at Gas–Liquid Interfaces

At the phase boundary between a colloidal suspension, the template, and the surrounding air, very strong capillary forces may act, depending on the solvent composition used. In many microelectromechanical systems (MEMS) those capillary forces are detrimental to the fabricated microstructures and drying is a very critical step in MEMS fabrication. However, those strong directing forces can be exploited very well for the assembly of particles onto a template.

When the meniscus of an aqueous particle suspension gets pinned on a surface it deposits the particles at the phase boundary in monolayers and multilayers onto the substrate. Convective flow of water transports even more particles towards the edge of the drop, thus forming the well-known coffee-stain-like patterns [6.57]. When the convective flow of water towards the meniscus can be controlled, it is possible to assemble particle monolayers or multilayers in a reproducible manner [6.56, 58]. Particles can even be assembled in spaced arrays when the meniscus only gets pinned at some specific locations on an otherwise smooth and nonwetting substrate. Such pinning locations can be formed by geometric features on the substrate, by a pattern of wetting spots, or by spots of increased particle–substrate interaction. Many researchers have exploited this mechanism for templated particle assembly with different setups (Fig. 6.13).

In most examples of this kind of assembly, the particles are dispersed in an aqueous colloidal suspension. Often, these suspensions contain surfactants to further stabilize the colloids and prevent them from agglomeration and precipitation. When the meniscus of such a particle suspension sweeps over a flat nonwetting surface, no particles are left on the substrate. The meniscus acts like a doctor blade, moving the particles over the surface. At geometrical features on the substrate such as a hole or the step of a raised structure, the water meniscus gets pinned and capillary forces can drive particles into holes or corners.

In the simplest experimental setup, a drop of colloidal suspension is left drying on a topographically

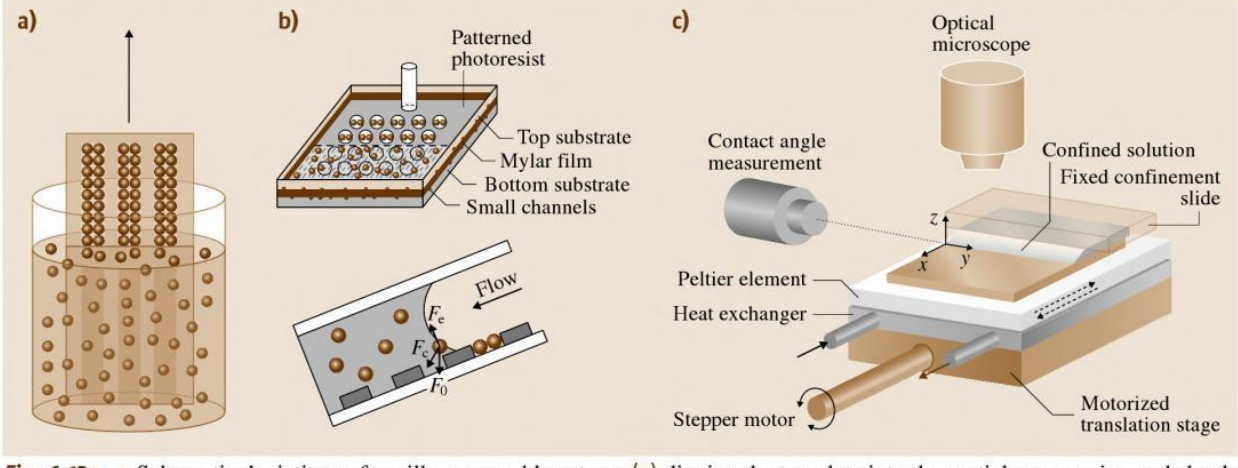

Fig. 6.13a–c Schematic depictions of capillary assembly setups: (**a**) dipping the template into the particle suspension and slowly pulling it out (after [6.54], © Wiley-VCH 2005); (**b**) assembly in a fluidic cell with a constant flow of particle suspension (after [6.55], © American Chemical Society 2001); (**c**) assembly on a motorized stage with controllable assembly speed and temperature (after [6.56], © American Chemical Society 2007)

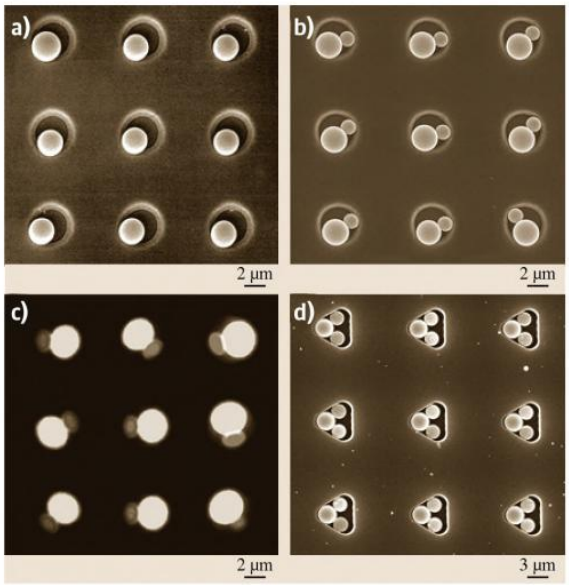

Fig. 6.14a–d Images of particles of different sizes assembled into holes with the device illustrated in Fig. 6.13b (after [6.55], © American Chemical Society 2001)

patterned template. As water evaporates the meniscus of the drop sweeps over the template and deposits particles into geometric features on the template. Here, there is only minimal control of the yield and evolution of the deposition process. At the start of the process, a low concentration of particles will be present at the meniscus. Then, with increasing evaporation, more particles are driven to the edge of the drop with the flux of water, and the assembly yield will increase. Finally, as the particle concentration in the drying drop reaches higher values, particles start to agglomerate and deposit in large aggregates. Thus, this simple method only supplies a relative small fraction of the template area with the desired assembly result.

Better assembly yield is achieved by placing the template (almost) vertically into a container of the colloidal suspension (Fig. 6.13a) [6.60]. As the solvent slowly evaporates, the meniscus moves over the template and deposits the particles in a controlled manner. Particles as small as 2 nm in diameter have been successfully assembled into template features of several 10 nm by this method [6.60]. Still, there is no direct control of particle concentration during the assembly and little possibility to react to changing parameters. Better control can be gained by pulling the template in a controlled manner out of the flask of colloidal suspension [6.54, 61].

Xia and coworkers designed a fluidic cell where the colloidal solution is sandwiched between the template and a cover slide (Fig. 6.13b) [6.55, 62]. A thin frame of Mylar film defines the distance between template and cover slide and controls the flow rate at which the dispersion flows through the cell. Depending on the ratio of particle diameter and template geometry, very regular and reproducible arrangements of particles in the assembly sites ranging from pairs to tetrahedral packings can be achieved [6.55]. When the assembly procedure is repeated with a second batch of smaller particles, assemblies of pairs of different particles in the same adsorption site are possible (Fig. 6.14) [6.55].

With a tool that controls colloid temperature and speed of meniscus movement, and allows direct observation of the assembly process through an optical

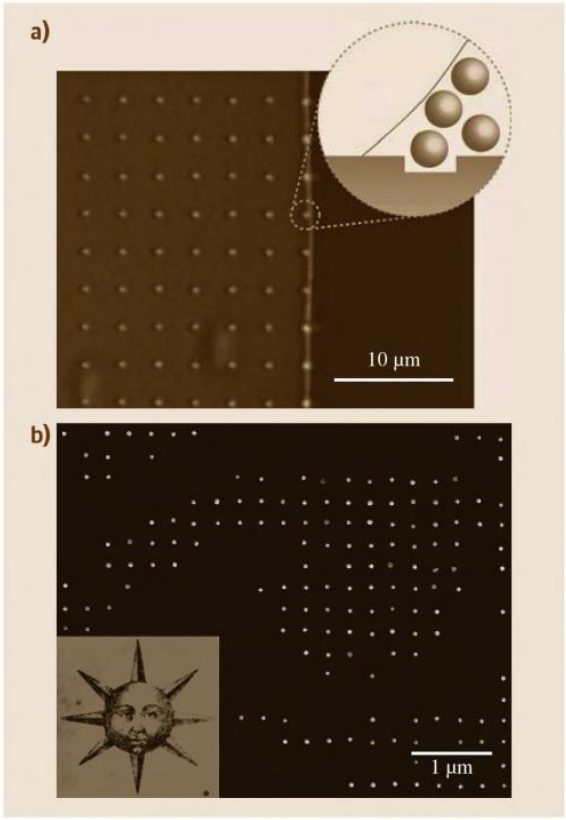

Fig. 6.15a,b Optical micrograph of the assembly of 60 nm Au particles into 3 μm-spaced holes. The bright accumulation zone is clearly visible. (**a**) Optical micrograph (inset) and SEM image of 60 nm Au particles assembled in a setup as illustrated in Fig. 6.13c and transferred to a silicon wafer (after [6.59], © Macmillan 2007)

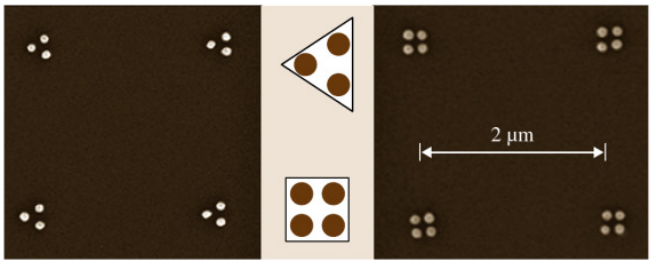

Fig. 6.16 SEM images of isolated 100 nm Au particles after removal of the template. The arrangement of the nanoparticles is determined by the geometry of the template (schematically depicted *in the middle*) (after [6.63], © American Institute of Physics 2006)

microscope, immediate response to changing conditions during assembly is possible (Fig. 6.13c) [6.56]. The template is mounted horizontally on a computer-controlled movable stage with a heatable vacuum chuck, and the colloidal suspension is sandwiched between the template and a glass slide. Observation of the assembly process from above reveals that for good yields a high concentration of particles is required at the meniscus. Particles are transported towards the meniscus by the flux of water in the same direction. As the temperature is increased, the evaporation at the meniscus increases. This causes an even greater flux of water and particles towards the meniscus. Lowering the temperature reduces the water flux and allows the particles to diffuse away from this so-called accumulation zone into the bulk solution. Consequently, assembly yield drops dramatically. Upon renewed increase of temperature and particle flux, the accumulation zone is reestablished and assembly reaches high yields again (Fig. 6.15).

The templates used in this kind of assembly method mostly have topographical (3-D) features that capture the particles. Also, templates which only rely on a chemical contrast have been described [6.54, 61]. The particle trapping relies on electrostatic interactions in this case and many of the adsorption sites also capture particles from the bulk solution [6.19], as described in the previous section. Thus, in the case of templates with chemical patterns, there is a combination of trapping mechanisms. Often, areas prepared for particle adsorption carry a hydrophilic surface functionality which causes lower contact angles in these areas and particle trapping in a mechanism closer to convective assembly.

Combinations of geometrical trapping and wetting contrast are possible too. With a well-designed balance of geometrical features and wetting contrast, it is even possible to control nanoparticle placement within the adsorption site [6.63]. When the adsorption site is large enough, particles are dragged into its corners and thus well-separated particle assemblies in a triangular or quadratic arrangement can be achieved (Fig. 6.16). This can be regarded as a kind of hierarchical assembly, where the assembly mechanism helps to form a substructure with features smaller than those of the actual template.

6.3 Templates

The template carries the positional information on particle arrangement. In most templates used today, there is a simple relation between the position of a binding site and the final particle position. The binding site might be larger than the particle's footprint or differ from its shape; it might accommodate just a single particle or a large number of particles. When working with very small particles, its shape might be irregular due to the limited resolution of the patterning process. The assembly process translates this geometry into a particle arrangement, as discussed in Sect. 6.1. Still, the relation between template and particle position is simple: there has to be a feature on the template exactly where a particle is intended to be placed. Thus, the patterning technique used to make the template has to define the particle locations with an accuracy that is within the range of the particle's dimensions.

Some assembly processes are more complex. A particle might only be deposited on one side of a binding site, only in its center (even if there is enough space for multiple particles around it) or multiple particles might fill a larger binding site with a regular structure. This can be desirable: the fabrication of the template is usually easier if the critical dimensions do not have to be identical to the particle's diameter. In the ideal case, the template pattern would be easy to fabricate but define the desired assembly of very small particles unambiguously, whereupon the assembly process would translate it into a very high-resolution energy landscape for the particles to occupy. If the desired arrangement is very complex, the template will generally have to be rather complex too, but most practical arrangements are highly repetitive and modular, and could be encoded efficiently.

Many assembly templates are fabricated by means of top-down micro- and nanofabrication. The patterns are usually designed in a computer, transferred to a mask (often via electron-beam or laser direct writing), and converted to chemical or topographical patterns on the template surface. The typical resolution limit for templates formed using typical ultraviolet (UV) lithography is around 1 μm, although smaller structures are achievable if artifacts are acceptable. Smaller structures can be written using electron-beam (e-beam) lithography. While photomasks for UV photolithography (produced in large e-beam writers) are readily available commercially, sub-μm e-beam patterns in other materials are less common, and the sequential nature of e-beam writing makes the patterning of large areas time consuming and costly. Electron-beam patterning is very flexible, however, and is widely used for research purposes.

If the primary patterning method is costly, replication techniques are useful both to produce multiple templates from one primary pattern and to cover larger areas with a repeated pattern. For patterns below the optical diffraction limit, molding and printing are popular methods. The primary structure is used either to imprint a polymer layer at increased temperature and under pressure (nanoimprint lithography) or to shape a liquid prepolymer while it is curing (molding, UV imprint lithography, and others). Although some top-down methods directly produce chemical patterns, for example, by oxidizing UV-sensitive monolayers in photolithography or with an e-beam, the most common product is a topographical pattern. Soft lithography is a route both to replicate such a pattern and to convert it to chemical contrast: a silicone prepolymer mixture is cured on the topographical pattern, cured to a solid rubber, and used as a stamp with the inverse pattern. This stamp can then print molecules on various surfaces, a process named microcontact printing.

Even e-beam writing is limited to minimum feature sizes in the range of tens of nanometers. Smaller structures can be formed using probe methods. For example, the tip of an atomic force microscope can mechanically remove (scratch) a monolayer or oxidize its functional groups locally. The resulting template cannot be replicated easily, which makes the process rather uneconomical, but it provides extremely high resolution, for example, for the arrangement of metal clusters in lines to investigate their conductivity.

An efficient alternative to e-beam writing for the patterning of larger areas is the use of interference lithography techniques. They only produce regular interference patterns, but they can do so over large areas in a single exposure step. If small structures are to be created, the radiation wavelength has to be low, its intensity high, and its coherence sufficient. An excellent source is synchrotron radiation. Larger patterns are straightforward to create using simple laser interference. Other efficient routes to certain template geometries include wrinkling patterns and step edges that form when crystals are cleaved along high-index planes. All these templates are limited to specific geometries and, thus, create specific particle arrangements.

6.3.1 Chemical Templates

Chemical templates display a pattern of selective surface chemistries with areas that prevent particle adsorption and others that support it. Additional geometrical features are not necessary per se but can be helpful to increase selectivity. A simple wetting contrast (e.g., hydrophilic patches on a hydrophobic substrates) can be sufficient to assemble colloidal particles at the three-phase boundary [6.61]. In this case, the hydrophilic spots have to be large enough ($> 25\,\mu m$) to cause a significant lowering of the receding contact angle and deposition of particles. Chemical patterns with features of several micrometers can be fabricated by optical lithography. After exposure and development of the photoresist on a Si/SiO_2 surface, the exposed substrate areas can be treated with a silane molecule. Upon removal of the remaining photoresist, a chemical pattern (bare Si/SiO_2 surface versus silane surface) is achieved. For higher-resolution features, nanoimprint lithography or e-beam lithography can be utilized to pattern a polymer resist layer. Again, the accessible substrate areas can then be patterned by a specific surface chemistry, and subsequent removal of the polymer resist provides the template. The areas of bare substrate may also be covered by a surface chemistry orthogonal to the first one (hydrophobic–hydrophilic, anionic–cationic) in order to increase assembly contrast [6.40]. Alternatively, the polymer resist might not be removed at all, thus providing an additional 3-D feature to support assembly onto the template [6.40].

Microcontact printing of organic monolayers is also a viable method for the fabrication of surface-chemical patterns on oxide or noble-metal surfaces. Depending on the quality of the stamp material and architecture, even sub-μm patterns are attainable [6.64].

Many examples of chemical templates do not only rely on a wetting contrast, but provide real adsorption sites for the particles. This can be achieved by pattern-

ing a charged molecule or a polyelectrolyte layer, which then attracts the particles by electrostatic forces or with specific supramolecular interactions [6.43, 54].

Self-assembled structures of block copolymers on surfaces can also act as a chemical template when nanoparticles selectively adsorb onto one block of the polymer [6.65].

6.3.2 Charges and Electrodes

Electric charge can be brought onto a surface by means of an electrode. This is the principle of xerography, which has been scaled down using electrically conductive AFM tips to write very small charged areas onto the surface of a dielectric. The charged regions attract particles, which then assemble on the written patterns [6.23]. Small tips (readily available in an AFM) enable high resolution to be attained, although the actual charge pattern can deviate from the intended design.

Actively driven electrodes are the most versatile option for electric-field templates. They require considerable effort in terms of interconnections and electrode design and one has to avoid particle attractions to the wiring, but they can be actively switched. What is more, AC potentials can be applied, so that dielectrophoresis takes place. Nanoparticles [6.66] and nanowires can thus be aligned with two electrodes and can then be connected [6.67]. The electric leads for both assembly electrodes and device interconnects (which can be identical) are fabricated using standard microfabrication techniques. If necessary, they can be combined with additional topographical features, for example, to improve alignment in the assembly of anisotropic particles [6.44].

Dielectrophoresis can also be driven by an external electromagnetic field that is projected onto an appropriate substrate [6.53]. The projected image, microscopically demagnified, causes the assembly forces. Such an image can be modulated and is far more flexible than patterned electrodes; it can even be time dependent to further optimize the assembly process. Its resolution is, however, diffraction limited.

6.3.3 Topographical Templates

Purely topographical templates guide particle assembly by geometrical exclusion and by modulating other forces, for example, capillary interactions. Geometrical confinement can be very precise – the particle cannot enter a template wall – but it is limited by template precision. Compared with electrodes or chemical patterns, topographical templates are simple in structure and fabrication and can be replicated via molding and imprinting techniques.

Topographical templates are used in convective [6.56] and capillary particle assembly [6.62], as an additional guide to the crystal structure in electrophoretic particle assembly [6.68], and as an additional guide in dielectrophoretic assembly [6.44]. In all these cases, the geometries are very simple: holes of uniform depth in an otherwise continuous layer. In most cases, the structures are formed in photoresist by standard UV lithography and used without further processing. If the resist sits on top of a wafer, it is simple to create an additional wetting contrast between the (polymer) top surface and the (silicon oxide) bottom surface of the template holes.

More complex geometries are required to precisely tune the forces in capillary assembly. Step edges, crosses, corner shapes, and other well-defined obstacles trap particles in reproducible arrangements. Such templates are harder to fabricate than holes. They can, however, be replicated in polymers, such as polydimethylsiloxane (PDMS). A single silicon master can then produce many (up to several hundred) single-use assembly templates.

Polymer molding is also the basis of the microfluidic ducts used as templates in the micromolding in capillaries (MIMIC) process. These channels, in which particles are arranged from a microfluidic flow, are first formed as lines in ultrathick resist and then replicated in PDMS. The soft silicone replica adheres to flat surfaces, forming channels into which the particle suspension is sucked by capillary forces.

6.3.4 Advanced Templates

More than one force can be involved in particle assembly, thus assembly templates can guide the assembly in more than one way. Advanced templates combine, for example, a long-range force caused by electrostatic or dielectrophoretic interactions with short-range interactions due to topography that provide high accuracy in the last moments of assembly [6.44]. An electrode array can be created on a flat substrate and a polymer resist patterned on top of the array, so that a hole in the shape of the particle remains. In a similar vein, a hydrophilic substrate can be coated with a hydrophobic resist, which creates a wetting difference that helps to capture a liquid volume in the binding site [6.60].

If one of the particle–template interactions is controllable (as is dielectrophoresis), such templates could

to produce large areas of identical patterns efficiently. Nanoimprint lithography, for example, can replicate a master many times and is even compatible with *roll-to-roll*-type fabrication, where long plastic sheets are continuously patterned by a rotating drum. As with molding, nanoimprint lithography is not an alternative to templated nanoparticle assembly, since it can only handle a very limited set of materials, but it is ideal for the production of templates.

Finally, the assembly processes themselves are constantly improving. Improved understanding of the interactions during assembly allows researchers to tune the interaction strengths and thereby engineer the energy landscape of the assembly process. Thus, both the stability of the original particles (for example, the colloidal suspension) and their behavior during assembly are optimized towards high yield. In addition, better control of the process parameters during assembly is now possible in modified versions of classical dip-coating setups. When combined with in situ analysis methods, yields and assembly qualities can be optimized by adjusting parameters such as temperature and template velocity.

Today, coatings containing nanoparticles are commonly applied using dip-coating, spin-coating or spray-coating techniques. Such methods are comparatively simple and compatible with a variety of relevant geometries. If templated assembly could be performed using the same deposition techniques, this would render it compatible with established technology and simplify its introduction into other processes. Alternatively, if specialized deposition techniques are required, or if the template cannot be applied to the substrate, assembly can be performed on a specialized template and the particles subsequently transferred onto the target surface. Together, these processes bridge the gap between particle assembly and current standard methods of fabrication. If particles are to be combined with, say, complementary metal–oxide–semiconductor (CMOS)-type components, the assembly and transfer precision has to be adequate to match the underlying structures. In most cases, short-range accuracy is governed by the assembly process and the precision of the template, while long-range order is influenced mainly by the template and the transfer process. All three may have to be optimized to meet the stringent requirements of semiconductor fabrication.

In addition to such improvements, the development of templated assembly processes for increasingly smaller particles with very high accuracy will continue. An important goal here is the assembly of particles well below 10 nm in diameter, which exhibit electronic quantum effects, with a precision that is sufficient to connect them electronically. Ideally, this would be possible on areas far above the square centimeters that have so far been demonstrated, if possible on standard 300 mm wafers. Finally, the assembly (and, if necessary, the transfer) should be compatible with different particle materials and substrates. A truly versatile process would accept any colloidal particle and thus be able to handle a very wide range of materials including oxides, semiconductors, metals, and polymers, amongst many others.

The ideal process would also handle very small particles. How small? We do not know at present. Gold-55 clusters that resemble molecules rather than particles have already been arranged using templated assembly processes, albeit with a precision far worse than the particle diameter [6.28]. Will it be possible at some point to arrange single atoms and molecules on a surface using a reasonably simple template? That such arrangements are stable and lead to interesting effects has already been demonstrated using high-vacuum scanning tunneling microscopy [6.74]. Whether templated assembly can provide a realistic route to such patterning with ultimate precision will remain an active topic of research for years to come.

References

6.1 A.N. Shipway, E. Katz, I. Willner: Nanoparticle arrays on surfaces for electronic, optical, and sensor applications, Chem. Phys. Chem. **1**(1), 18–52 (2000)

6.2 C.B. Murray, C.R. Kagan, M.G. Bawendi: Synthesis and characterization of monodisperse nanocrystals and close-packed nanocrystal assemblies, Annu. Rev. Mater. Sci. **30**, 545–610 (2000)

6.3 F. Caruso: Nanoengineering of particle surfaces, Adv. Mater. **13**(1), 11 (2001)

6.4 K. Molhave, T.M. Hansen, D.N. Madsen, P. Boggild: Towards pick-and-place assembly of nanostructures, J. Nanosci. Nanotechnol. **4**(3), 279–282 (2004)

6.5 P. Alivisatos: The use of nanocrystals in biological detection, Nat. Biotechnol. **22**(1), 47–52 (2004)

6.6 S. Paul, C. Pearson, A. Molloy, M.A. Cousins, M. Green, S. Kolliopoulou, P. Dimitrakis, P. Normand, D. Tsoukalas, M.C. Petty: Langmuir–Blodgett film deposition of metallic nanoparticles and their application to electronic memory structures, Nano Lett. **3**(4), 533–536 (2003)

6.7 J.D. Joannopoulos, S.G. Johnson, J.N. Winn, R.D. Meade: *Photonic Crystals: Molding the Flow of Light* (Princeton Univ. Press, Princeton 2008)

6.8 H.J.J. Yeh, J.S. Smith: Fluidic self-assembly for the integration of GaAs light-emitting-diodes on Si substrates, IEEE Photon. Technol. Lett. **6**(6), 706–708 (1994)

6.9 A. Einstein: The theory of the Brownian motion, Ann. Phys. **19**(2), 371–381 (1906)

6.10 R.M. Mazo: *Brownian Motion. Fluctuations, Dynamics, and Applications* (Clarendon, Oxford 2002)

6.11 J. Aizenberg, P.V. Braun, P. Wiltzius: Patterned colloidal deposition controlled by electrostatic and capillary forces, Phys. Rev. Lett. **84**(13), 2997–3000 (2000)

6.12 N.D. Denkov, O.D. Velev, P.A. Kralchevsky, I.B. Ivanov, H. Yoshimura, K. Nagayama: Mechanism of formation of 2-dimensional crystals from latex-particles on substrates, Langmuir **8**(12), 3183–3190 (1992)

6.13 S. Chandrasekhar: Stochastic problems in physics and astronomy, Rev. Mod. Phys. **15**(1), 1–89 (1943)

6.14 W.R. Russel, D.A. Saville, W.R. Schowalter: *Colloidal Dispersions* (Cambridge Univ. Press, Cambridge 1989)

6.15 J.M. Schurr: Role of diffusion in bimolecular solution kinetics, Biophys. J. **10**(8), 700–716 (1970)

6.16 J. Feder: Random sequential adsorption, J. Theor. Biol. **87**(2), 237–254 (1980)

6.17 J.W. Evans: Random and cooperative sequential adsorption, Rev. Mod. Phys. **65**(4), 1281–1329 (1993)

6.18 J. Talbot, G. Tarjus, P.R. Van Tassel, P. Viot: From car parking to protein adsorption: An overview of sequential adsorption processes, Colloids Surf. A **165**(1-3), 287–324 (2000)

6.19 X.Y. Ling, L. Malaquin, D.N. Reinhoudt, H. Wolf, J. Huskens: An in situ study of the adsorption behavior of functionalized particles on self-assembled monolayers via different chemical interactions, Langmuir **23**(20), 9990–9999 (2007)

6.20 H.O. Jacobs, A.R. Tao, A. Schwartz, D.H. Gracias, G.M. Whitesides: Fabrication of a cylindrical display by patterned assembly, Science **296**(5566), 323–325 (2002)

6.21 C.R. Barry, M.G. Steward, N.Z. Lwin, H.O. Jacobs: Printing nanoparticles from the liquid and gas phases using nanoxerography, Nanotechnology **14**(10), 1057–1063 (2003)

6.22 C.R. Barry, J. Gu, H.O. Jacobs: Charging process and coulomb-force-directed printing of nanoparticles with sub-100-nm lateral resolution, Nano Lett. **5**(10), 2078–2084 (2005)

6.23 P. Mesquida, A. Stemmer: Attaching silica nanoparticles from suspension onto surface charge patterns generated by a conductive atomic force microscope tip, Adv. Mater. **13**(18), 1395–1398 (2001)

6.24 C.R. Barry, H.O. Jacobs: Fringing field directed assembly of nanomaterials, Nano Lett. **6**(12), 2790–2796 (2006)

6.25 H. Kim, J. Kim, H.J. Yang, J. Suh, T. Kim, B.W. Han, S. Kim, D.S. Kim, P.V. Pikhitsa, M. Choi: Parallel patterning of nanoparticles via electrodynamic focusing of charged aerosols, Nat. Nanotechnol. **1**(2), 117–121 (2006)

6.26 I. Lee, H.P. Zheng, M.F. Rubner, P.T. Hammond: Controlled cluster size in patterned particle arrays via directed adsorption on confined surfaces, Adv. Mater. **14**(8), 572–577 (2002)

6.27 U. Srinivasan, D. Liepmann, R.T. Howe: Microstructure to substrate self-assembly using capillary forces, J. Microelectromech. Syst. **10**(1), 17–24 (2001)

6.28 S.T. Liu, R. Maoz, G. Schmid, J. Sagiv: Template guided self-assembly of [Au(55)] clusters on nanolithographically defined monolayer patterns, Nano Lett. **2**(10), 1055–1060 (2002)

6.29 J.D. Le, Y. Pinto, N.C. Seeman, K. Musier-Forsyth, T.A. Taton, R.A. Kiehl: DNA-templated self-assembly of metallic nanocomponent arrays on a surface, Nano Lett. **4**(12), 2343–2347 (2004)

6.30 P. Maury, M. Peter, O. Crespo-Biel, X.Y. Ling, D.N. Reinhoudt, J. Huskens: Patterning the molecular printboard: patterning cyclodextrin monolayers on silicon oxide using nanoimprint lithography and its application in 3-D multilayer nanostructuring, Nanotechnology **18**(4), 044007 (2007)

6.31 J.J. Talghader, J.K. Tu, J.S. Smith: Integration of fluidically self-assembled optoelectronic devices using a silicon-based process, IEEE Photon. Technol. Lett. **7**(11), 1321–1323 (1995)

6.32 K.F. Böhringer: Surface modification and modulation in microstructures: controlling protein adsorption, monolayer desorption and micro-self-assembly, J. Micromech. Microeng. **13**(4), S1–S10 (2003)

6.33 W. Zheng, H.O. Jacobs: Self-assembly process to integrate and connect semiconductor dies on surfaces with single-angular orientation and contact-pad registration, Adv. Mater. **18**(11), 1387 (2006)

6.34 S.A. Stauth, B.A. Parviz: Self-assembled single-crystal silicon circuits on plastic, Proc. Natl. Acad. Sci. USA **103**(38), 13922–13927 (2006)

6.35 H.O. Jacobs, A.R. Tao, A. Schwartz, D.H. Gracias, G.M. Whitesides: Fabrication of a cylindrical display by patterned assembly, Science **296**(5566), 323–325 (2002)

6.36 X.R. Xiong, Y. Hanein, J.D. Fang, Y.B. Wang, W.H. Wang, D.T. Schwartz, K.F. Böhringer: Controlled multibatch self-assembly of microdevices, J. Microelectromech. Syst. **12**(2), 117–127 (2003)

6.37 J. Tien, A. Terfort, G.M. Whitesides: Microfabrication through electrostatic self-assembly, Langmuir **13**(20), 5349–5355 (1997)

6.38 K.M. Chen, X.P. Jiang, L.C. Kimerling, P.T. Hammond: Selective self-organization of colloids on patterned polyelectrolyte templates, Langmuir **16**(20), 7825–7834 (2000)

6.39 H.P. Zheng, M.F. Rubner, P.T. Hammond: Particle assembly on patterned "plus/minus" polyelectrolyte surfaces via polymer-on-polymer stamping, Langmuir **18**(11), 4505–4510 (2002)

6.40 P. Maury, M. Peter, V. Mahalingam, D.N. Reinhoudt, J. Huskens: Patterned self-assembled monolayers on silicon oxide prepared by nanoimprint lithography and their applications in nanofabrication, Adv. Funct. Mater. **15**(3), 451–457 (2005)

6.41 S.T. Liu, R. Maoz, J. Sagiv: Planned nanostructures of colloidal gold via self-assembly on hierarchically assembled organic bilayer template patterns with in-situ generated terminal amino functionality, Nano Lett. **4**(5), 845–851 (2004)

6.42 Y.H. Kim, J. Park, P.J. Yoo, P.T. Hammond: Selective assembly of colloidal particles on a nanostructured template coated with polyclectrolyte multilayers, Adv. Mater. **19**(24), 4426 (2007)

6.43 X.Y. Ling, I.Y. Phang, D.N. Reinhoudt, G.J. Vancso, J. Huskens: Supramolecular layer-by-layer assembly of 3-D multicomponent nanostructures via multivalent molecular recognition, Int. J. Mol. Sci. **9**, 486–497 (2008)

6.44 M.W. Li, R.B. Bhiladvala, T.J. Morrow, J.A. Sioss, K.K. Lew, J.M. Redwing, C.D. Keating, T.S. Mayer: Bottom-up assembly of large-area nanowire resonator arrays, Nat. Nanotechnol. **3**(2), 88–92 (2008)

6.45 B. Kannan, R.P. Kulkarni, A. Majumdar: DNA-based programmed assembly of gold nanoparticles on lithographic patterns with extraordinary specificity, Nano Lett. **4**, 1521–1524 (2004)

6.46 H. Zhang, Z. Li, C.A. Mirkin: Dip-pen nanolithography-based methodology for preparing arrays of nanostructures functionalized with oligonucleotides, Adv. Mater. **14**, 1472–1474 (2002)

6.47 E. Winfree, F.R. Liu, L.A. Wenzler, N.C. Seeman: Design and self-assembly of two-dimensional DNA crystals, Nature **394**(6693), 539–544 (1998)

6.48 P.W.K. Rothemund: Folding DNA to create nanoscale shapes and patterns, Nature **440**(7082), 297–302 (2006)

6.49 J. Sharma, R. Chhabra, Y. Liu, Y. Ke, H. Yan: DNA-templated self-assembly of two-dimensional and periodical gold nanoparticle arrays, Angew. Chem. Int. Ed. **45**, 730–735 (2006)

6.50 I. Cheng, B. Wei, X. Zhang, Y. Wang, Y. Mi: Patterning of gold nanoparticles on DNA self-assembled scaffolds, Res. Lett. Nanotechnol. **2008**, 827174 (2008)

6.51 A. Kuzyk, B. Yurke, J.J. Toppari, V. Linko, P. Törmä: Dielectrophoretic trapping of DNA origami, Small **4**, 447–450 (2008)

6.52 M. Suzuki, T. Yasukawa, Y. Mase, D. Oyamatsu, H. Shiku, T. Matsue: Dielectrophoretic micropatterning with microparticle monolayers covalently linked to glass surfaces, Langmuir **20**, 11005–11011 (2004)

6.53 P.Y. Chiou, A.T. Ohta, M.C. Wu: Massively parallel manipulation of single cells and microparticles using optical images, Nature **436**(7049), 370–372 (2005)

6.54 P. Maury, M. Escalante, D.N. Reinhoudt, J. Huskens: Directed assembly of nanoparticles onto polymer-imprinted or chemically patterned templates fabricated by nanoimprint lithography, Adv. Mater. **17**(22), 2718–2723 (2005)

6.55 Y.D. Yin, Y. Lu, B. Gates, Y.N. Xia: Template-assisted self-assembly: A practical route to complex aggregates of monodispersed colloids with well-defined sizes, shapes, and structures, J. Am. Chem. Soc. **123**(36), 8718–8729 (2001)

6.56 L. Malaquin, T. Kraus, H. Schmid, E. Delamarche, H. Wolf: Controlled particle placement through convective and capillary assembly, Langmuir **23**, 11513–11521 (2007)

6.57 R.D. Deegan, O. Bakajin, T.F. Dupont, G. Huber, S.R. Nagel, T.A. Witten: Capillary flow as the cause of ring stains from dried liquid drops, Nature **389**(6653), 827–829 (1997)

6.58 B.G. Prevo, O.D. Velev: Controlled, rapid deposition of structured coatings from micro- and nanoparticle suspensions, Langmuir **20**(6), 2099–2107 (2004)

6.59 T. Kraus, L. Malaquin, H. Schmid, W. Riess, N.D. Spencer, H. Wolf: Nanoparticle printing with single-particle resolution, Nat. Nanotechnol. **2**, 570–576 (2007)

6.60 Y. Cui, M.T. Bjork, J.A. Liddle, C. Sonnichsen, B. Boussert, A.P. Alivisatos: Integration of colloidal nanocrystals into lithographically patterned devices, Nano Lett. **4**(6), 1093–1098 (2004)

6.61 C.A. Fustin, G. Glasser, H.W. Spiess, U. Jonas: Parameters influencing the templated growth of colloidal crystals on chemically patterned surfaces, Langmuir **20**, 9114–9123 (2004)

6.62 Y.N. Xia, Y.D. Yin, Y. Lu, J. McLellan: Template-assisted self-assembly of spherical colloids into complex and controllable structures, Adv. Funct. Mater. **13**(12), 907–918 (2003)

6.63 M.J. Gordon, D. Peyrade: Separation of colloidal nanoparticles using capillary immersion forces, Appl. Phys. Lett. **89**(5), 053112 (2006)

6.64 H. Schmid, B. Michel: Siloxane polymers for high-resolution, high-accuracy soft lithography, Macromolecules **33**(8), 3042–3049 (2000)

6.65 C. Minelli, C. Hinderling, H. Heinzelmann, R. Pugin, M. Liley: Micrometer-long gold nanowires fabricated using block copolymer templates, Langmuir **21**(16), 7080–7082 (2005)

6.66 O.D. Velev, E.W. Kaler: In situ assembly of colloidal particles into miniaturized biosensors, Langmuir **15**(11), 3693–3698 (1999)

6.67 P.A. Smith, C.D. Nordquist, T.N. Jackson, T.S. Mayer, B.R. Martin, J. Mbindyo, T.E. Mallouk: Electric-

field assisted assembly and alignment of metallic nanowires, Appl. Phys. Lett. **77**(9), 1399–1401 (2000)

6.68 N.V. Dziomkina, G.J. Vancso: Colloidal crystal assembly on topologically patterned templates, Soft Matter **1**(4), 265–279 (2005)

6.69 G. Markovich, C.P. Collier, J.R. Heath: Reversible metal-insulator transition in ordered metal nanocrystal monolayers observed by impedance spectroscopy, Phys. Rev. Lett. **80**(17), 3807–3810 (1998)

6.70 E. Kim, Y.N. Xia, G.M. Whitesides: Micromolding in capillaries: Applications in materials science, J. Am. Chem. Soc. **118**(24), 5722–5731 (1996)

6.71 Y. Lu, Y.D. Yin, B. Gates, Y.N. Xia: Growth of large crystals of monodispersed spherical colloids in fluidic cells fabricated using non-photolithographic methods, Langmuir **17**(20), 6344–6350 (2001)

6.72 I. Langmuir, V.J. Schaefer: Activities of urease and pepsin monolayers, J. Am. Chem. Soc. **60**, 1351–1360 (1938)

6.73 T. Kraus, L. Malaquin, E. Delamarche, H. Schmid, N.D. Spencer, H. Wolf: Closing the gap between self-assembly and microsystems using self-assembly, transfer, and integration of particles, Adv. Mater. **17**(20), 2438–2442 (2005)

6.74 F. Rosei, M. Schunack, Y. Naitoh, P. Jiang, A. Gourdon, E. Laegsgaard, I. Stensgaard, C. Joachim, F. Besenbacher: Properties of large organic molecules on metal surfaces, Prog. Surf. Sci. **71**(5–8), 95–146 (2003)

7. Three-Dimensional Nanostructure Fabrication by Focused Ion Beam Chemical Vapor Deposition

Shinji Matsui

In this chapter, we describe three-dimensional nanostructure fabrication using 30 keV Ga^+ focused ion beam chemical vapor deposition (FIB-CVD) and a *phenanthrene* ($C_{14}H_{10}$) source as a precursor. We also consider microstructure plastic art, which is a new field that has been made possible by microbeam technology, and we present examples of such art, including a *micro wine glass* with an external diameter of 2.75 µm and height of 12 µm. The film deposited during such a process is diamond-like amorphous carbon, which has a Young's modulus exceeding 600 GPa, appearing to make it highly desirable for various applications. The production of three-dimensional nanostructure is discussed. The fabrication of microcoils, nanoelectrostatic actuators, and 0.1 µm nanowiring – all potential components of nanomechanical systems – is explained. The chapter ends by describing the realization of nanoinjectors and nanomanipulators, novel nanotools for manipulation and analyzing subcellular organelles.

Electron beams (EBs) and focused ion beam (FIBs) have been used to fabricate various two-dimensional nanostructure devices such as single-electron transistors and metal–oxide–semiconductor (MOS) transistors with nanometer gate lengths. Ten-nanometer structures can be formed by using a commercially available EB or FIB system with 5–10 nm-diameter beams and high-resolution resist [7.1]. Two-dimensional nanostructure fabrication is therefore already an established process. There are various approaches to three-dimensional fabrication using a laser, an EB, or a FIB to perform chemical vapor deposition (CVD). FIB- and EB-CVD are superior to laser-CVD [7.2] in terms of spatial resolution and beam-scan control. *Koops* et al. demonstrated some applications such as an atomic force microscopy (AFM) tip and a field emitter that were realized using EB-CVD [7.3]. *Blauner* et al. demonstrated pillars and walls with high aspect ratios achieved using FIB-CVD [7.4].

The deposition rate of FIB-CVD is much higher than that of EB-CVD due to factors such as the difference in mass between an electron and an ion. Furthermore, the smaller penetration depth of ions compared with electrons makes it easier to create complicated three-dimensional nanostructures. For example, when we attempt to make a coil nanostructure with line width of 100 nm, 10–50 keV electrons pass through the ring of the coil and reach the substrate because of the large range of electrons (at least a few microns), which makes it difficult to create a coil nanostructure using EB-CVD. On the other hand, since the range of ions is a few tens of nanometers or less, the ions are deposited in-

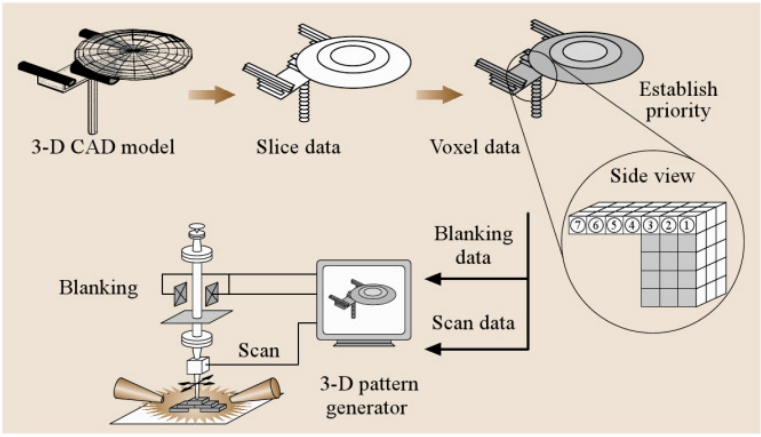

Fig. 7.5 Data flow of 3-D pattern-generating system for FIB-CVD

substrate and on a human hair as works of microstructure plastic art are shown in Figs. 7.2a and 7.3. A micro wine glass with an external diameter of 2.75 μm and a height of 12 μm was formed. The fabrication time was 600 s at a beam current of 16 pA. This beautiful micro wine glass shows the potential of the field of microstructure plastic art. A *micro Colosseum* and a *micro Leaning Tower of Pisa* were also fabricated on a Si substrate, as shown in Figs. 7.2c and 7.4.

Various microsystem parts have been fabricated using FIB-CVD. Figure 7.2b shows a microcoil with a coil diameter of 0.6 μm, a coil pitch of 0.7 μm, and a line width of 0.08 μm. The exposure time was 40 s at a beam current of 0.4 pA. The diameter, pitch, and height of the microcoil were 0.25, 0.20, and 3.8 μm, respectively. The exposure time was 60 s at a beam current of 0.4 pA. The results show that FIB-CVD is a highly promising technique for realizing parts of a microsystem, although their mechanical performance must be measured.

7.1.2 Three-Dimensional Pattern-Generating System

We used ion-beam-assisted deposition of a source gas to fabricate 3-D structures. The 3-D structure is built up as a multilayer structure. In the first step of this 3-D pattern-generating system, a 3-D model of the structure, designed using a 3-D computer-aided design (CAD) system (3-D DXF format), is needed. In this case we realized a structure shaped like a pendulum. The 3-D CAD model, which is a surface model, is cut into several slices, as shown in Fig. 7.5. The thickness of the slices depends upon the resolution in the z-direction (the vertical direction). The x- and y-coordinates of the slices are then used to create the scan data (voxel data). To fabricate the overhanging structure, the ion beam must irradiate the correct positions in the correct order. If the ion beam irradiates a voxel located in mid-air without a support layer, the ions intended for the voxel will be deposited on the substrate. Therefore,

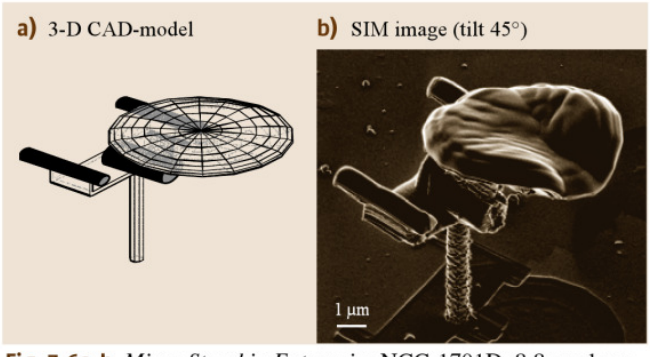

Fig. 7.6a,b *Micro Starship Enterprise* NCC-1701D, 8.8 μm long

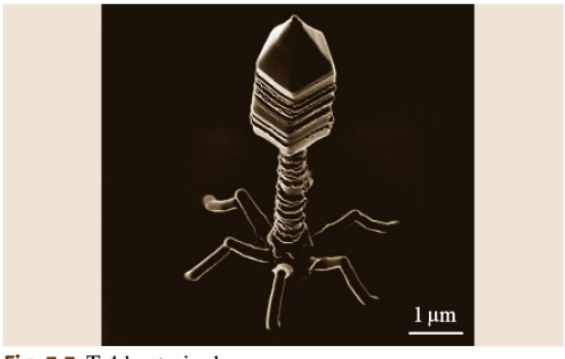

Fig. 7.7 T-4 bacteriophage

the sequence of irradiation is determined, as shown in Fig. 7.5.

The scan data and blanking signal therefore include the scan sequence, the dwell time, the interval time, and the irradiation pitch. These parameters are calculated from the beam diameter, xy-resolution, and z-resolution of fabrication. The z-resolution is proportional to the dwell time and inversely proportional to the square of the irradiation pitch. The scan data are passed to the beam deflector of the FIB-CVD, as are the blanking data. The blanking signal controls the dwell time and interval time of the ion beam.

Figure 7.6 shows a 3-D CAD model and an scanning ion microscope (SIM) image of the starship Enterprise NCC-1701D (from the television series Star Trek), which was fabricated by FIB-CVD at $10 \sim 20$ pA [7.8]. The nanospaceship is 8.8 μm long and was realized at about 1 : 100 000 000 scale on silicon substrate. The dwell time (t_d), interval time (t_i), irradiation pitch (p), and total process time (t_p), were 80 μs, 150 μs, 2.4 nm, and 2.5 h, respectively. The horizontal overhang structure was successfully fabricated.

Figure 7.7 shows a nano T4 bacteriophage, which is an artificial version of the virus fabricated by FIB-CVD on silicon surface. The size of the artificial nano T4 bacteriophage is about ten times that of the real virus.

7.2 Nanoelectromechanics

7.2.1 Measuring Young's Modulus

An evaluation of the mechanical characteristics of such nanostructures is needed for material physics. *Buks* and *Roukes* reported a simple but useful technique [7.9] for measuring the resonant frequencies of nanoscale objects using a scanning electron microscope (SEM). The secondary electron detector in the SEM can detect frequencies up to around 4 MHz, so the sample vibration is measured as the oscillatory output signal of the detector. *Buks* and *Roukes* used this technique to evaluate the Casimir attractive force between two parallel beams fabricated on a nanoscale. We evaluated the mechanical characteristics of DLC pillars in terms of the Young's modulus, determined using resonant vibration and the SEM monitoring technique [7.10, 11].

The system setup for monitoring mechanical vibration is shown in Fig. 7.8b. There were two ways of measuring the pillar vibrations. One is active measurement, where the mechanical vibration is induced by a thin piezoelectric device, 300 μm thick and 3 mm square. The piezo device was bonded to the sidewall of the SEM's sample holder with silver paste. The sample holder was designed to observe cross sections in the SEM (S5000, Hitachi) system. Therefore, the pillar's vibration was observed as a side-view image, as shown in Fig. 7.8a. The range of vibration frequencies involved was 10 kHz up to 2 MHz, which is much faster

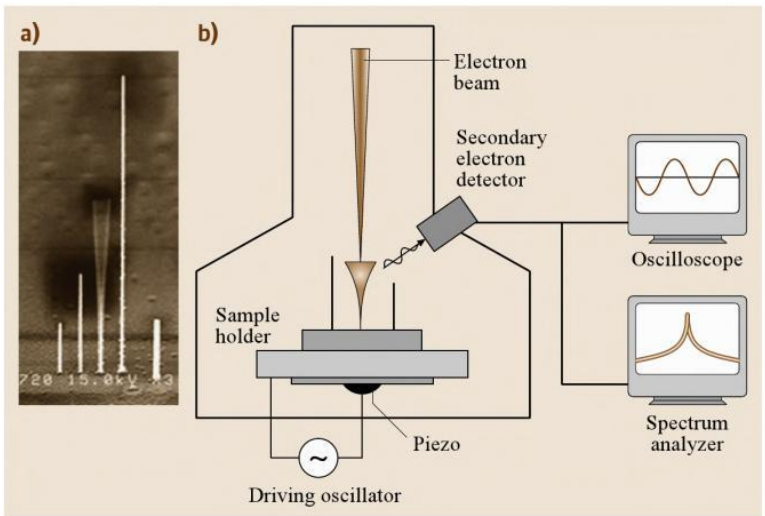

Fig. 7.8 (**a**) SEM image of the vibration. The resonant frequency was 1.21 MHz. (**b**) Schematic diagram of the vibration monitoring system

than the SEM raster scanning speed. Thus the resonant vibrations of the pillars can be taken as the trace of the pillar's vibration in the SEM image. The resonant frequency and amplitude were controlled by adjusting the power of the driving oscillator.

The other way to measure pillar vibrations is passive measurement using a spectrum analyzer (Agilent 4395A), where most of the vibration seemed to derive from environmental noise from rotary pumps and air conditioners. Some parts of the vibration result from spontaneous vibration associated with thermal excitations [7.9]. Because of the excitation and residual noise, the pillars on the SEM sample holder always vibrated at a fundamental frequency, even if noise isolation is enforced on the SEM system. The amplitude of these spontaneous vibrations was on the order of a few nanometers at the top of the pillar, and high-resolution SEM can easily detect it at a magnification of 300 000.

We arranged several pillars with varying diameters and lengths. The DLC pillars with the smallest diameter of 80 nm were grown using point irradiation. While we used two FIB systems for pillar fabrication, slight differences in the beam diameters of the two systems did not affect the diameters of the pillars. Larger-diameter pillars were fabricated using an area-limited raster scan mode. Raster scanning of a 160 nm^2 region produced a pillar with a cross section of about 240 nm^2, and a 400 nm^2 scan resulted in a pillar with a cross section of 480 nm^2. A typical SEM image taken during resonance is shown in Fig. 7.8a. The FIB-CVD pillars seemed very durable against mechanical vibration. This kind of measurement usually requires at least 30 min, including spectrum analysis and photo recording, but the pillars still survived without any change in resonance characteristics. This durability of the DLC pillars should be useful in nanomechanical applications.

The resonant frequency f of the pillar is defined by (7.1) for a pillar with a square cross section, and (7.2) for a circular cross section

$$f_{\text{square}} = \frac{a\beta^2}{2\pi L^2}\sqrt{\frac{E}{12\rho}}\,, \tag{7.1}$$

$$f_{\text{circular}} = \frac{a\beta^2}{2\pi L^2}\sqrt{\frac{E}{16\rho}}\,, \tag{7.2}$$

where a is the width of the square pillar or the diameter of the circular-shaped pillar, L is the length of the pillar, ρ is the density, and E is the Young's modulus. The coefficient β defines the resonant mode; $\beta = 1.875$ for the fundamental mode. We used (7.1) for pillars 240 and 480 nm wide, and (7.2) for pillars grown by point-beam irradiation. The relationship of the resonant frequency to the Young's modulus, which depends on the ratio of the pillar diameter to the squared length, is summarized in Fig. 7.9. All of the pillars evaluated in this figure were fabricated using the SMI9200 FIB system under rapid growth conditions. Typical growth rates were about 3–5 μm/min for the 100 nm-diameter and 240 μm-wide pillars, and 0.9 μm/min for the 480 nm-wide pillars. When calculating the data shown in Fig. 7.9, we assumed that the density of the DLC pillars was about 2.3 g/cm^3, which is almost identical to that of graphite and quartz. The slope of the line in Fig. 7.9 indicates the Young's modulus for each pillar. The Young's moduli of the pillars were distributed over a range from 65 to 140 GPa, which is almost identical to that of normal metals. Wider pillars tended to have larger Young's moduli.

We found that the stiffness increases significantly as the local gas pressure decreases, as shown in Fig. 7.10. While the absolute value of the local gas pressure at the beam point is very difficult to determine, we found that the growth rate can be a useful parameter for describing the dependence of Young's modulus on pressure. All data points indicated in Fig. 7.10 were obtained from pillars grown using point irradiation. Therefore, the pillar diameters did vary slightly from 100 nm but not by more than 5%. A relatively low gas pressure, with good uniformity, was obtained by using a single gas nozzle and gas reflector. We used a cleaved side-wall of an Si tip as the gas reflector, which was placed 10–50 μm away from the beam point so as to face the gas nozzle. The growth rate was controlled by changing the distance to the wall. While there is a large distribu-

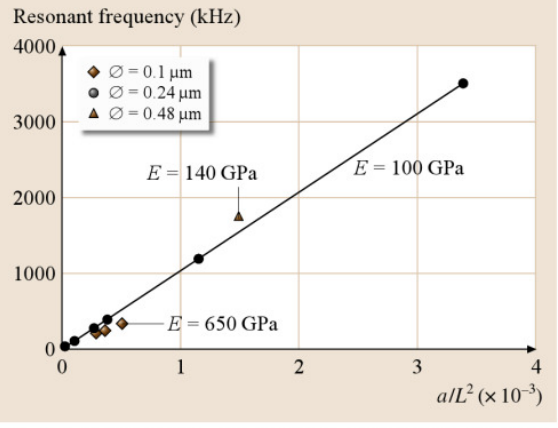

Fig. 7.9 Dependence of resonant frequency on pillar length

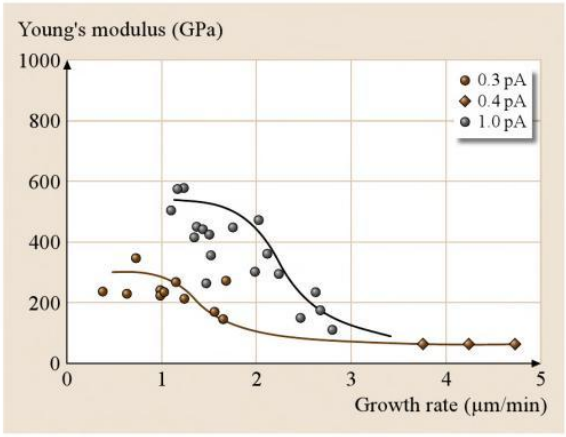

Fig. 7.10 Dependence of Young's modulus on growth rate

tion of data points, the stiffness of the pillar tended to become stiffer as the growth rate decreased. The two curves in Fig. 7.10 represent data points obtained for a beam current of 0.3 and 1 pA, respectively. Both curves show the same tendency; the saturated upper levels of the Young's modulus are different for each ion current at low gas pressure (low growth rate). It should be noted that some of the pillars' Young's moduli exceeded 600 GPa, which is of the same order as that of tungsten carbide. In addition, these estimations assume a pillar density of 2.3 g/cm^3, but a finite amount of Ga was incorporated with the pillar growth. If the calculation takes the increase in pillar density due to the Ga concentration into account, the Young's modulus exceeds 800 GPa. Such a high Young's modulus reaches that of carbon nanotubes and natural diamond crystals. We think that this high Young's modulus is due to surface modification caused by the direct ion impact.

In contrast, when the gas pressure was high enough to achieve a growth rate of more than 3 μm/min, the pillars became soft but the change in the Young's modulus was small. The uniformity of the Young's modulus (as seen in Fig. 7.9) presumably results from the fact that the growth occurred in this insensitive region, where the low levels of source gas limit pillar growth.

7.2.2 Free-Space Nanowiring

All experiments were carried out in a commercially available FIB system (SMI9200: SII NanoTechnology Inc.) using a beam of 30 kV Ga^+ ions. The beam was focused to a spot size of 7 nm at a beam current of 0.4 pA, and it was incident perpendicular to the surface. The pattern drawing system (CPG-1000: Crestec Co., Tokyo) was added to the FIB apparatus to draw any patterns. Using the CPG, it is possible to control beam scan parameters such as scanning speed, xy-direction, and blanking of the beam, and so 3-D free space nanowiring can be performed [7.12].

Figure 7.11 illustrates the free-space nanowiring fabrication process using both FIB-CVD and CPG. When *phenanthrene* ($C_{14}H_{10}$) gas or tungsten hexacarbonyl ($W(CO)_6$) gas, which is a reactive organic gas, is evaporated from a heated container and injected into the vacuum chamber by a nozzle located 300 μm above the sample surface at an angle of about 45° with respect to surface, the gas density of the $C_{14}H_{10}$ or $W(CO)_6$ molecules increases on the substrate near the gas nozzle. The nozzle system creates a local high-pressure region over the surface. The base pressure of the sample chamber is 2×10^{-5} Pa and the chamber pressure upon introducing $C_{14}H_{10}$ and $W(CO)_6$ as a source gas was 1×10^{-4} and 1.5×10^{-3} Pa, respectively. If a Ga^+

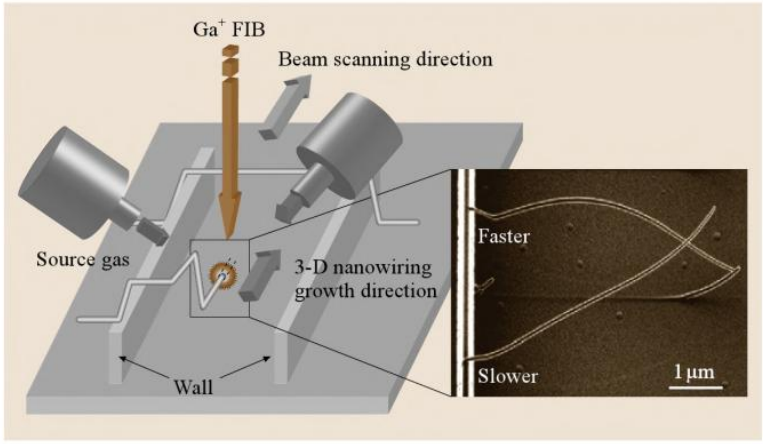

Fig. 7.11 Fabrication of DLC free-space wiring using both FIB-CVD and CPG

ion beam is irradiated onto the substrate, $C_{14}H_{10}$ or $W(CO)_6$ molecules adsorbed on the substrate surface are decomposed, and carbon (C) is mainly deposited onto the surface of the substrate. The direction of deposition growth can be controlling through the scanning direction of the beam. The material deposited using $C_{14}H_{10}$ gas was diamond-like carbon, as confirmed by Raman spectra, and it had a very large Young's modulus of 600 GPa [7.7, 10].

After the two walls shown in Fig. 7.11 were formed, free-space nanowiring was performed by adjusting the beam scanning speed. The ion beam used was a 30 kV Ga^+ FIB, and the irradiation current was 0.8–2.3 pA. The x- and y-scanning directions and the beam scanning speed were controlled by the CPG. The height in the z-direction was proportional to the irradiation time. Deposition is made to occur horizontally by scanning the beam at a certain fixed speed in a plane. However, if the beam scanning speed is faster than the nanowiring growth speed, it grows downward or drops; conversely, if the scanning speed is too slow, the deposition grows slanting upward. Therefore, it is very important to control the beam scanning speed carefully when growing a nanowire horizontally. It turns out that the optimal beam scanning speed to realize a nanowire growing horizontally, using two $C_{14}H_{10}$ gas guns, was about 190 nm/s. The expected pattern resolution archived using FIB-CVD is around 80 nm, because both the primary Ga^+ ion and secondary-electron scattering occur over distances of around 20 nm [7.10, 13].

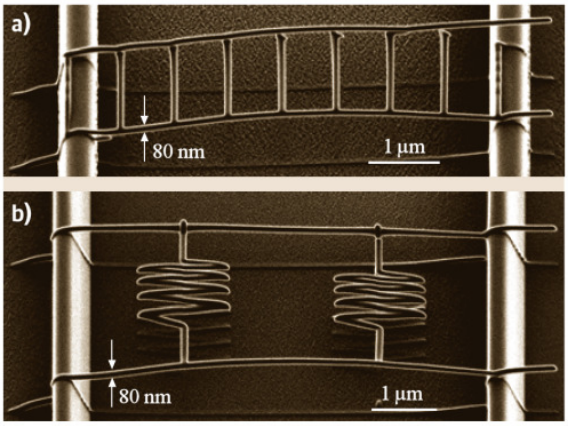

Fig. 7.12 (a) DLC free-space wiring with a bridge shape. (b) DLC free-space wiring with parallel resistances

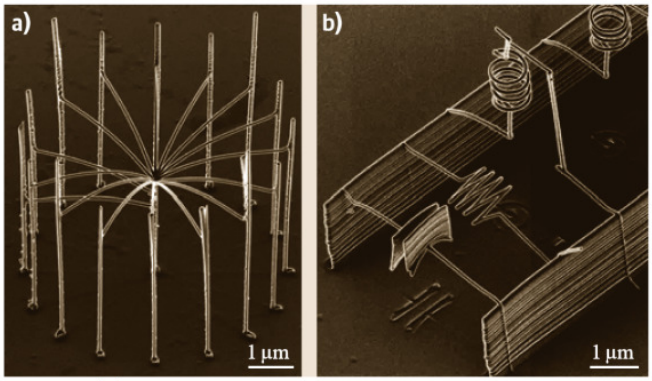

Fig. 7.13 (a) Radial DLC free-space wiring grown in 16 directions from the center. (b) Scanning ion microscope (SIM) micrograph of inductance (L), resistance (R), and capacitor (C) structure

Figures 7.12 and 7.13 show examples of free-space nanowiring fabricated by FIB-CVD and CPG. All of the structures shown were fabricated using $C_{14}H_{10}$ as a precursor gas.

Figure 7.12a shows nanobridge free-space wiring. The growth time was 1.8 min and the wiring width was 80 nm. Figure 7.12b shows free-space nanowires with parallel resistances. The growth time was 2.8 min, and the wiring width was also 80 nm.

Figure 7.13a shows free-space nanowiring grown in 16 directions from the center. Figure 7.13b shows a scanning ion microscope (SIM) image of an inductor (L), a resistor (R), and a capacitor (C) in a parallel circuit structure with free-space nanowiring. A coiled structure was fabricated by circle-scanning of the Ga^+ FIB. The growth times of the L, R, and C structures were about 6, 2, and 12 min, and all the nanowiring is about 110 nm wide. From these structures, one can see that it is possible to fabricate nanowiring at an arbitrary position using FIB-CVD and CPG. These results also indicate that various circuit structures can be formed by combining L, C, and R.

The free-space wiring structures were observed using 200 keV TEM. The analyzed area was 20 nm in diameter. Figure 7.14a,b shows TEM images of DLC free-space wiring and a pillar. It became clear from these energy-dispersive x-ray (EDX) measurements that the dark part (A) of Fig. 7.14a corresponds to the Ga core, while the outside part (B) of Fig. 7.14a corresponds to amorphous carbon. This free-space wiring therefore consists of amorphous carbon with a Ga core. The center position of the Ga core is actually located below the center of the wiring. However, in the case of the DLC pillar, the Ga core is located at the center of the pillar. To investigate the difference between these core positions, the Ga core distribution in free-space wiring was observed in detail by TEM. The center position of the Ga core was about 70 nm from the top, which was

a 0.2 μm-thick SiO_2-on-Si substrate by an electron-beam lithography and lift-off process. After that, a coil and free-space nanowiring were fabricated onto the Au electrode to form a switch function using nanowiring fabrication technology with FIB-CVD and CPG. The coil structure was fabricated by scanning a Ga^+ beam in a circle at fixed speed in $C_{14}H_{10}$ ambiance gas. An electric charge (positive or negative) was applied to the coil, and the reverse electric charge was applied to the nanowiring. The coil extended upward when a voltage was applied, because these was now an electrical repulsive force between each loop of the coil. At the same time, the coil and the nanowiring gravitated toward one another, because they had opposite charges. This attraction caused the coil to contact with the nanowiring when a certain threshold voltage was reached.

Next, we evaluated the switch function by measuring the current that flowed when the coil and the nanowiring were in contact. Figure 7.18b,c shows SIM micrographs of the nanomechanical switch before and after applying a voltage. These micrographs indicate that the coil and nanowiring make contact when a voltage is applied to the coil. At the same time, I–V measurements of the nanomechanical switch were carried out, as shown in Fig. 7.19a. The current was plotted against the applied voltage at room temperature, and from this graph, it was apparent that the current begins to flow at a threshold voltage of 17.6 V. At this point, the electrical resistance and the resistivity of the nanomechanical switch are about 250 MΩ and 11 Ω cm, respectively. We measured the I–V characteristics for ten nanomechanical switches. The threshold voltage was around 20 V in each case. The switching function was confirmed by performing on/off operations at an applied voltage of 30 V, as shown in Fig. 7.19b. A pulsed current of about 170 nA was detected for this applied voltage.

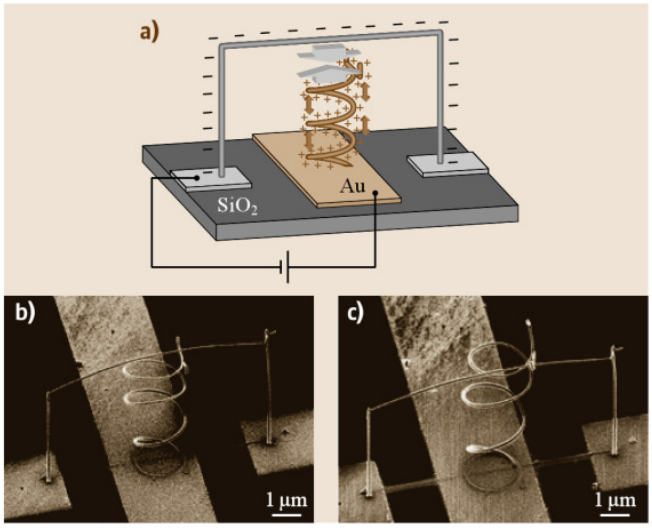

Fig. 7.18 (**a**) Principle of movement of nanomechanical switch. SIM micrographs of nanomechanical switch: (**b**) before applying voltage and (**c**) after applying voltage

7.2.4 Nanoelectrostatic Actuator

The fabrication process of 3-D nanoelectrostatic actuators (and manipulators) is very simple [7.16]. Figure 7.20 shows the fabrication process. First, a glass capillary (GD-1: Narishige Co., East meadow, NY) was pulled using a micropipette puller (PC-10: Narishige Co.). The dimensions of the glass capillary were 90 mm in length and 1 mm in diameter. Using this process,

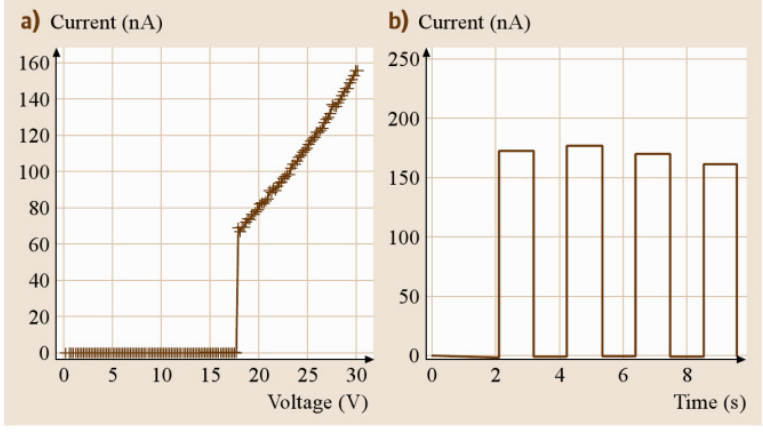

Fig. 7.19 (**a**) I–V curve for the nanomechanical switch. (**b**) Pulsed current to on/off operation for the nanomechanical switch at an applied voltage of 30 V

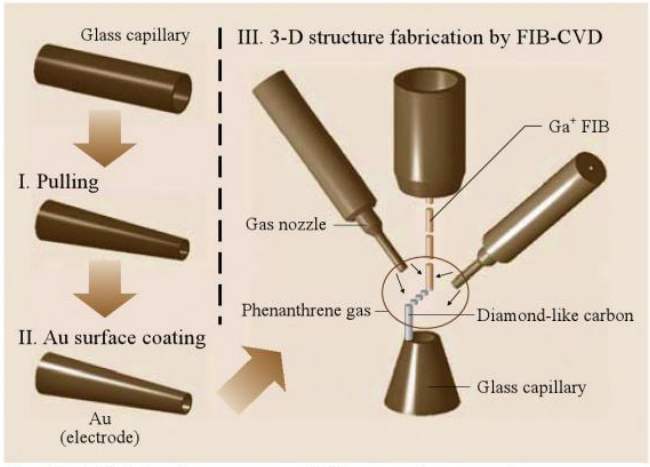

Fig. 7.20 Fabrication process of 3-D nanoelectrostatic actuators

we obtained a glass capillary tip with a 1 μm diameter. Next, we coated the glass capillary surface with Au by direct-current (DC) sputtering. The Au thickness was ≈ 30 nm. This Au coating serves as the electrode that controls the actuator and manipulator. Then, the 3-D nanoelectrostatic actuators and manipulators were fabricated by FIB-CVD. This process was carried out in a commercially available FIB system (SIM9200: SII NanoTechnology Inc.) with a Ga^+ ion beam operating at 30 keV. FIB-CVD was carried out using a *phenanthrene* ($C_{14}H_{10}$) precursor as the source material. The beam diameter was about 7 nm. The inner diameter of each nozzle was 0.3 mm. The *phenanthrene* gas pressure during growth was typically 5×10^{-5} Pa in the specimen chamber. The Ga^+ ion beam was controlled by transmitting CAD data on the arbitrary structures to the FIB system.

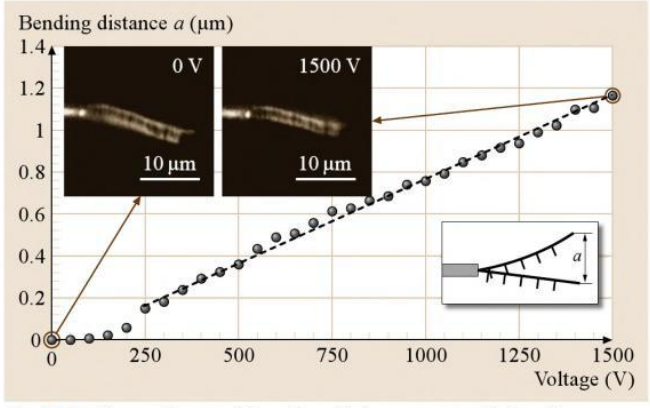

Fig. 7.22 Dependence of bending distance on applied voltage

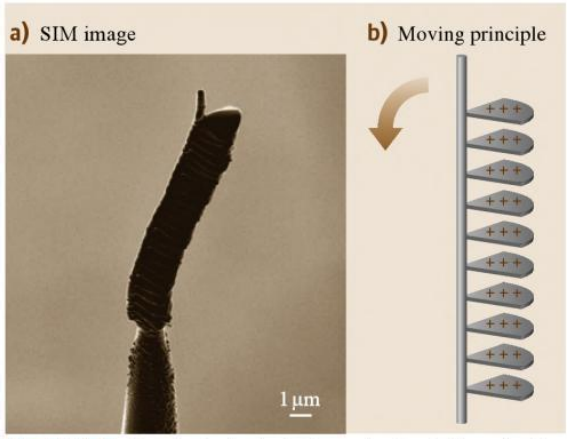

Fig. 7.21a,b Laminated pleats-type electrostatic actuator. **(a)** SIM image of a laminated pleats-type electrostatic actuator fabricated on the tip of a Au-coated glass capillary. **(b)** Illustration of moving principle of the actuator

A laminated pleats-type electrostatic actuator was fabricated by FIB-CVD. Figure 7.21a shows an SIM image of a laminated pleats-type electrostatic actuator fabricated at 7 pA and 60 min exposure time. Figure 7.21b shows the principle behind the movement of this actuator. The driving force is the repulsive force due to the accumulation of electric charge. This electric charge can be stored in the pleats structures of the actuator by applying a voltage across the glass capillary. The pillar structure of this actuator bends due to charge repulsion, as shown in Fig. 7.21b. Figure 7.22 shows the dependence of the bending distance on the

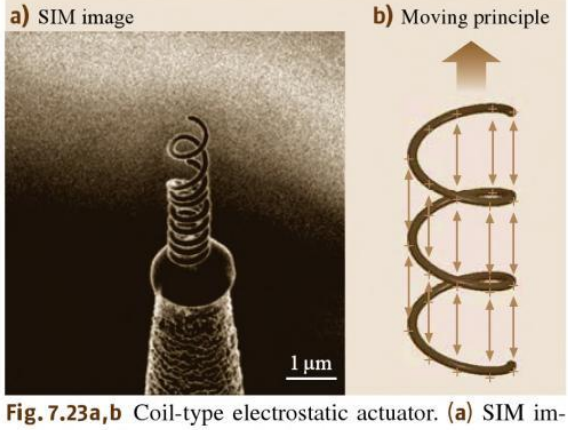

Fig. 7.23a,b Coil-type electrostatic actuator. **(a)** SIM image of a coil-type electrostatic actuator fabricated on the tip of a Au-coated glass capillary. **(b)** Illustration of moving principle for the actuator

applied voltage. The bending distance is defined as the distance a in the inset of Fig. 7.22. The bending rate of this laminated pleats-type electrostatic actuator was about 0.7 nm/V.

A coil-type electrostatic actuator was fabricated by FIB-CVD. Figure 7.23a shows an SIM image of a coil-type electrostatic actuator fabricated at 7 pA and 10 min of exposure time. Figure 7.23b shows the principle behind the movement of this actuator, which is very simple. The driving force is the repulsive force induced by electric charge accumulation; the electric charge can be stored in this coil structure by applying a voltage across the glass capillary. This coil structure expands and contracts due to charge repulsion, as shown in Fig. 7.23b. Figure 7.24 shows the dependence of the coil expansion on the applied voltage. The length of the expansion is the distance a in the inset of Fig. 7.24. The result revealed that the expansion could be controlled in the applied voltage range from 0 to 500 V.

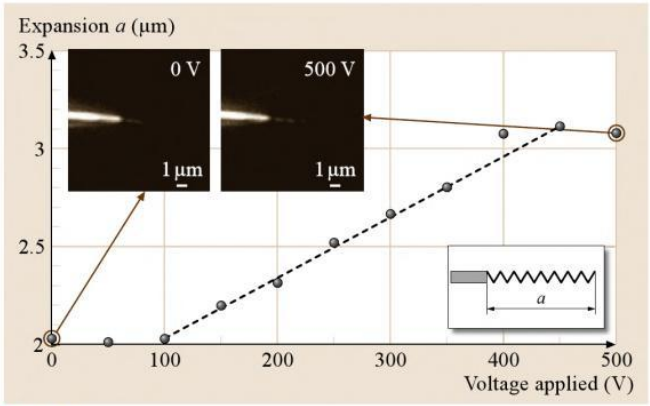

Fig. 7.24 Dependence of coil expansion on applied voltage

7.3 Nanooptics: Brilliant Blue Observation from a *Morpho* Butterfly Scale Quasistructure

The *Morpho* butterfly has brilliant blue wings, and the source of this intense color has been an interesting topic of debate for a long time. Due to an intriguing optical phenomenon, the scales reflect interfered brilliant blue color for any angle of incidence of white light. This color is called a structural color, meaning that it is not caused by pigment reflection [7.17]. When we observed the scales with a scanning electron microscope (SEM) (Fig. 7.25a), we found three-dimensional (3-D) nanostructures 2 μm in height, 0.7 μm in width, and with a 0.22 μm grating pitch on the scales. These nanostructures cause a similar optical phenomenon to the iridescence produced by a jewel beetle.

We duplicated the *Morpho* butterfly scale quasistructure with a commercially available FIB system (SMI9200: SII Nanotechnology Inc.) using a Ga^+ ion beam operating at 30 kV [7.18]. The beam diameter was about 7 nm at 0.4 pA. The FIB-CVD was performed using *phenanthrene* ($C_{14}H_{10}$) as a precursor.

In this experiment, we used a computer-controlled pattern generator, which converted 3-D computer-aided design (CAD) data into a scanning signal, which was passed to an FIB scanning apparatus in order to fabricate a 3-D mold [7.8]. The scattering range of the Ga primary ions is about 20 nm, and the range of the secondary electrons induced by the Ga ion beam is about 20 nm, so the expected pattern resolution of the FIB-CVD is about 80 nm.

Figure 7.25b shows an SIM image of the *Morpho* butterfly quasistructure fabricated by FIB-CVD using 3-

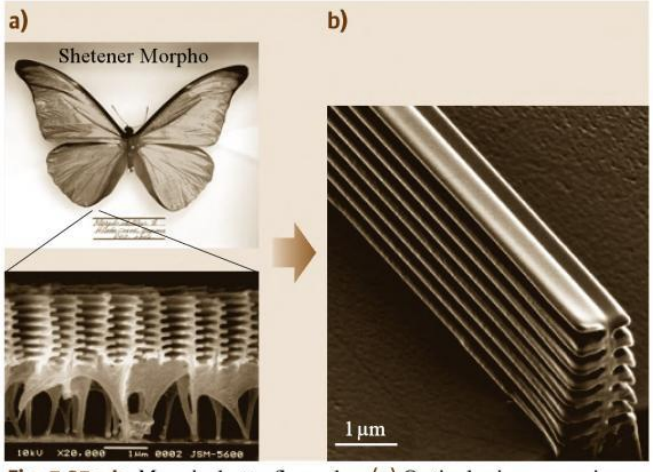

Fig. 7.25a,b *Morpho* butterfly scales. **(a)** Optical microscope image showing top view of *Morpho* butterfly. SEM image showing a cross-sectional view of *Morpho* butterfly scales. **(b)** SIM image showing inclined view of *Morpho* butterfly scale quasistructure fabricated by FIB-CVD

D CAD data. This result demonstrates that FIB-CVD can be used to fabricate the quasistructure.

We measured the reflection intensities from *Morpho* butterfly scales and the *Morpho* butterfly scale quasistructure optically; white light from a halogen lamp was directed onto a sample with angles of incidence ranging from 5° to 45°. The reflection was concentrated by an optical microscope and analyzed using a commercially available photonic multichannel spectral analyzer system (PMA-11: Hamamatsu Photonics K.K., Hamamatsu City, Japan). The intensity of light incident from the halogen lamp had a peak at a wavelength close to 630 nm.

The *Morpho* butterfly scale quasistructure was made of DLC. The reflectivity and transmittance of a 200 nm-thick DLC film deposited by FIB-CVD, measured by the optical measurement system at a wavelength close to 440 nm (the reflection peak wavelength of the *Morpho* butterfly), were 30% and 60%, respectively. Therefore, the measured data indicated that the DLC film had high reflectivity near 440 nm, which is important for the fabrication of an accurate *Morpho* butterfly scale quasistructure.

We measured the reflection intensities of the *Morpho* butterfly scales and the quasistructure with an optical measurement system, and compared their characteristics. Figure 7.26a,b shows the reflection intensities from *Morpho* butterfly scales and the quasistructure, respectively. Both gave a peak intensity near 440 nm and showed very similar reflection intensity spectra for various angles of incidence.

We have thus successfully demonstrated that a *Morpho* butterfly scale quasistructure fabricated using FIB-CVD can give almost the same optical characteristics as real *Morpho* butterfly scales.

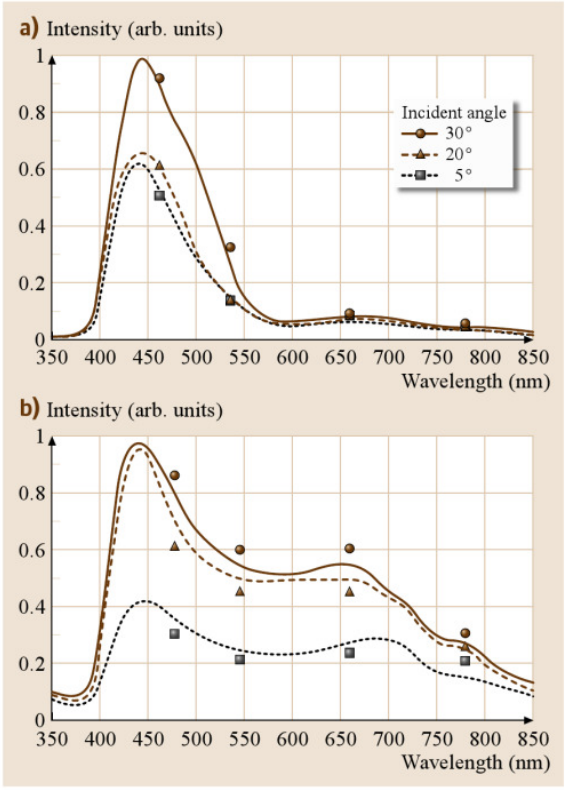

Fig. 7.26a,b Intensity curves of the reflection spectra for: (**a**) *Morpho* butterfly scales, (**b**) *Morpho* butterfly scale quasistructure

7.4 Nanobiology

7.4.1 Nanoinjector

Three-dimensional nanostructures on a glass capillary have a number of useful applications, such as manipulators and sensors in various microstructures. We have demonstrated the fabrication of a nozzle nanostructure on a glass capillary for a bioinjector using 30 keV Ga^+ focused ion beam assisted deposition with a precursor of phenanthrene vapor and etching [7.19]. It has been demonstrated that nozzle nanostructures of various shapes and sizes can be successfully fabricated. An inner tip diameter of 30 nm on a glass capillary and a tip shape with an inclined angle have been realized. We reported that diamond-like carbon (DLC) pillars grown by FIB-CVD with a precursor of *phenanthrene* vapor have very large Young's moduli, exceeding 600 GPa, which potentially makes them useful for various applications [7.10]. These characteristics are applicable to the fabrication of various biological devices.

In one experiment, nozzle nanostructure fabrication for biological nanoinjector research was studied. The tip diameters of conventional bioinjectors are greater than 100 nm and the tip shapes cannot be controlled. A bio-nanoinjector with various nanostructures on the top of a glass capillary has the following potential applications (shown in Fig. 7.27):

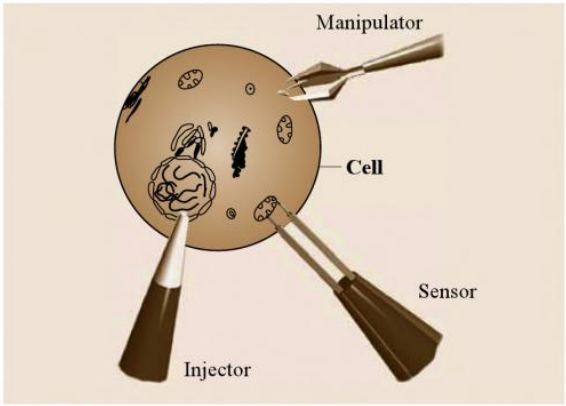

Fig. 7.27 Potential uses for a bionanoinjector

1. Injection of various reagents into a specific organelle in a cell
2. Selective manipulation of a specific organelle outside of a cell by using the nanoinjector as an aspirator
3. Reducing the mechanical stress produced when operating in the cell by controlling the shape and size of the bionanoinjector
4. Measurement of the electric potential of a cell, an organelle, and an ion channel exiting on a membrane, by fabricating an electrode

Thus far, 3-D nanostructure fabrications on a glass capillary have not been reported. We present nozzle nanostructure fabrication on a glass capillary by FIB-CVD and etching in order to confirm the possibility of bionanoinjector fabrication.

The nozzle structures of the nanoinjector were fabricated using a function generator (Wave Factory: NF Electronic Instruments, Yokohama, Japan). Conventional microinjectors are fabricated by pulling a glass capillary (GD-1: Narishige Co.) using a micropipette puller (PC-10: Narishige Co.). The glass capillary was 90 mm in length and 1 mm in diameter.

Conventionally, the tip shape of a microinjector made by pulling a glass capillary, and which is used as an injector into a cell, is controlled by applying mechanical grinding (or not). However, the reliability of this technique for controlling tip shape is very poor and requires experienced workers.

A bionanoinjector tip was fabricated on a glass capillary by FIB-CVD, as shown in Fig. 7.28a–c. First, FIB etching made the tip surface of the glass capillary smooth. Then, a nozzle structure was fabricated at the tip by FIB-CVD. Figure 7.28a shows the surface of a chip smoothed at 120 pA and after 30 s exposure time by FIB etching, with inner hole diameter of 870 nm. A nozzle structure fabricated by FIB-CVD with inner hole diameter of 220 nm is shown in Fig. 7.28b. Figure 7.28c shows a cross section of Fig. 7.28b. These results demonstrate that a bionanoinjector could be successfully fabricated by 3-D nanostructure fabrication using FIB-CVD. The bionanoinjector was used to inject dye into a egg cell (*Ciona intestinalis*) as shown in Fig. 7.29.

7.4.2 Nanomanipulator

An electrostatic 3-D nanomanipulator that can manipulate nanoparts and operate on cells has been developed by FIB-CVD. This 3-D nanomanipulator has four fingers so that it can manipulate a variety of shapes. To move the nanomanipulator, electric charge is accumulated in the structure by applying voltage to the four-fingered structure, and electric charge repulsion causes them to move. Furthermore, we succeeded in catching a microsphere (made from polystyrene latex) with a diameter of 1 μm using this 3-D nanomanipulator with four fingers [7.20].

The glass capillary (GD-1; Narishige Co.) was pulled using a micropipette puller (PC-10; Narishige Co.). A tip diameter of about 1.0 μm could be obtained using this process. Then, the glass capillary surface was coated with Au in order to fabricate an electrode for

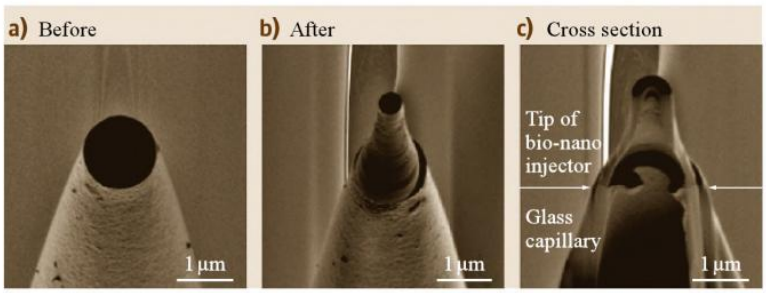

Fig. 7.28a–c SIM images of a bionanoinjector fabricated on a glass capillary by FIB-CVD. (**a**) Before FIB-CVD, (**b**) after FIB-CVD, and (**c**) cross section of (**b**)

7.5 Summary

Three-dimensional nanostructure fabrication using 30 keV Ga^+ FIB-CVD and a *phenanthrene* ($C_{14}H_{10}$) source as a precursor has been demonstrated. The film deposited on a silicon substrate was characterized using a transmission microscope and Raman spectra. This characterization indicated that the deposited film is diamond-like amorphous carbon, which has attracted attention due to its hardness, chemical inertness, and optical transparency. Its large Young's modulus, which exceeds 600 GPa, makes it highly desirable for various applications. A nanoelectrostatic actuator and 0.1 μm nanowiring were fabricated and evaluated as parts of nanomechanical system. Furthermore, a nanoinjector and nanomanipulator were fabricated as novel nanotools for manipulation and analysis of subcellular organelles. These results demonstrate that FIB-CVD is one of the key technologies needed to make 3-D nanodevices that can be used in the field of electronics, mechanics, optics, and biology.

References

7.1 S. Matsui: Nanostructure fabrication using electron beam and its application to nanometer devices, Proc. IEEE **85**, 629 (1997)

7.2 O. Lehmann, F. Foulon, M. Stuke: Surface and three-dimensional processing by laser chemical vapor deposition, NATO ASI Ser. Appl. Sci. **265**, 91 (1994)

7.3 H.W. Koops, J. Kretz, M. Rudolph, M. Weber, G. Dahm, K.L. Lee: Characterization and application of materials grown by electron-beam-induced deposition, Jpn. J. Appl. Phys. **33**, 7099 (1994)

7.4 A. Wagner, J.P. Levin, J.L. Mauer, P.G. Blauner, S.J. Kirch, P. Long: X-ray mask repair with focused ion beams, J. Vac. Sci. Technol. B **8**, 1557 (1990)

7.5 I. Utke, P. Hoffmann, B. Dwir, K. Leifer, E. Kapon, P. Doppelt: Focused electron beam induced deposition of gold, J. Vac. Sci. Technol. B **18**, 3168 (2000)

7.6 A.J. DeMarco, J. Melngailis: Lateral growth of focused ion beam deposited platinum for stencil mask repair, J. Vac. Sci. Technol. B **17**, 3154 (1999)

7.7 S. Matsui, T. Kaito, J. Fujita, M. Komuro, K. Kanda, Y. Haruyama: Three-dimensional nanostructure fabrication by focused-ion-beam chemical vapor deposition, J. Vac. Sci. Technol. B **18**, 3181 (2000)

7.8 T. Hoshino, K. Watanabe, R. Kometani, T. Morita, K. Kanda, Y. Haruyama, T. Kaito, J. Fujita, M. Ishida, Y. Ochiai, S. Matsui: Development of three-dimensional pattern-generating system for focused-ion-beam chemical-vapor deposition, J. Vac. Sci. Technol. B **21**, 2732 (2003)

7.9 E. Buks, M.L. Roukes: Stiction, adhesion energy, and the Casimir effect in micromechanical systems, Phys. Rev. B **63**, 033402 (2001)

7.10 J. Fujita, M. Ishida, T. Sakamoto, Y. Ochiai, T. Kaito, S. Matsui: Observation and characteristics of mechanical vibration in three-dimensional nanostructures and pillars grown by focused ion beam chemical vapor deposition, J. Vac. Sci. Technol. B **19**, 2834 (2001)

7.11 M. Ishida, J. Fujita, Y. Ochiai: Density estimation for amorphous carbon nanopillars grown by focused ion beam assisted chemical vapor deposition, J. Vac. Sci. Technol. B **20**, 2784 (2002)

7.12 T. Morita, R. Kometani, K. Watanabe, K. Kanda, Y. Haruyama, T. Hoshino, K. Kondo, T. Kaito, T. Ichihashi, J. Fujita, M. Ishida, Y. Ochiai, T. Tajima, S. Matsui: Free-space-wiring fabrication in nano-space by focused-ion-beam chemical vapor deposition, J. Vac. Sci. Technol. B **21**, 2737 (2003)

7.13 J. Fujita, M. Ishida, Y. Ochiai, T. Ichihashi, T. Kaito, S. Matsui: Graphitization of Fe-doped amorphous carbon pillars grown by focused ion-beam-induced chemical-vapor deposition, J. Vac. Sci. Technol. B **20**, 2686 (2002)

7.14 K. Nakamatsu, K. Yamamoto, T. Hirayama, S. Matsui: Fabrication of fine electron biprism filament by free-space-nanowiring technique of focused-ion-beam + chemical vapor deposition for accurate off-axis electron holography, Appl. Phys. Express **1**, 117004 (2008)

7.15 T. Morita, K. Nakamatsu, K. Kanda, Y. Haruyama, K. Kondo, T. Hoshino, T. Kaito, J. Fujita, T. Ichihashi, M. Ishida, Y. Ochiai, T. Tajima, S. Matsui: Nanomechanical switch fabrication by focused-ion-beam chemical vapor deposition, J. Vac. Sci. Technol. B **22**, 3137 (2004)

7.16 R. Kometani, T. Hoshino, K. Kondo, K. Kanda, Y. Haruyama, T. Kaito, J. Fujita, M. Ishida, Y. Ochiai, S. Matsui: Characteristics of nano-electrostatic actuator fabricated by focused ion beam chemical vapor deposition, Jpn. J. Appl. Phys. **43**, 7187 (2004)

7.17 P. Vukusic, J.R. Sambles: Photonic structures in biology, Nature **424**, 852 (2003)

7.18 K. Watanabe, T. Hoshino, K. Kanda, Y. Haruyama, S. Matsui: Brilliant blue observation from a *Morpho-butterfly*-scale quasi-structure, Jpn. J. Appl. Phys. **44**, L48 (2005)

7.19 R. Kometani, T. Morita, K. Watanabe, K. Kanda, Y. Haruyama, T. Kaito, J. Fujita, M. Ishida, Y. Ochiai, S. Matsui: Nozzle-nanostructure fabrication on glass capillary by focused-ion-beam chemical vapor deposition and etching, Jpn. J. Appl. Phys. **42**, 4107 (2003)

7.20 R. Kometani, T. Hoshino, K. Kondo, K. Kanda, Y. Haruyama, T. Kaito, J. Fujita, M. Ishida, Y. Ochiai, S. Matsui: Performance of nanomanipulator fabricated on glass capillary by focused-ion-beam chemical vapor deposition, J. Vac. Sci. Technol. B **23**, 298 (2005)

7.21 S. Akita, Y. Nakayama, S. Mizooka, Y. Takano, T. Okawa, K.Y. Miyatake, S. Yamanaka, M. Tsuji, T. Nosaka: Nanotweezers consisting of carbon nanotubes operating in an atomic force microscope, Appl. Phys. Lett. **79**, 1691 (2001)

7.22 R. Kometani, T. Hoshino, K. Kanda, Y. Haruyama, T. Kaito, J. Fujita, M. Ishida, Y. Ochiai, S. Matsui: Three-dimensional high-performance nanotools fabricated using focused-ion-beam chemical-vapor-deposition, Nucl. Instrum. Methods Phys. Res. B **232**, 362 (2005)

8. Introduction to Micro-/Nanofabrication

Babak Ziaie, Antonio Baldi, Massood Z. Atashbar

This chapter outlines and discusses important micro- and nanofabrication techniques. We start with the most basic methods borrowed from the integrated circuit (IC) industry, such as thin-film deposition, lithography and etching, and then move on to look at microelectromechanical systems (MEMS) and nanofabrication technologies. We cover a broad range of dimensions, from the micron to the nanometer scale. Although most of the current research is geared towards the nanodomain, a good understanding of top-down methods for fabricating micron-sized objects can aid our understanding of this research. Due to space constraints, we focus here on the most important technologies; in the microdomain these include surface, bulk, and high-aspect-ratio micromachining; in the nanodomain we concentrate on e-beam lithography, epitaxial growth, template manufacturing, and self-assembly. MEMS technology is maturing rapidly, with some new technologies displacing older ones that have proven to be unsuited to manufacture on a commercial scale. However, the jury is still out on methods used in the nanodomain, although it appears that bottom-up methods are the most feasible, and these will have a major impact in a variety of application areas such as biology, medicine, environmental monitoring, and nanoelectronics.

Recent innovations in the area of micro/nanofabrication have created a unique opportunity for manufacturing structures in the nm–mm range. The available six orders of magnitude dimensional span can be used to fabricate novel electronic, optical, magnetic, mechanical, and chemical/biological devices with applications ranging from sensors to computation and control. In this chapter, we will introduce major micro/nanofabrication techniques currently used to fabricate structures from the nm to several hundred μm range. We will mainly focus on the most important and widely used techniques and will not discuss specialized methods. After a brief introduction to basic microfabrication, we will discuss MEMS fabrication techniques used to build microstructures down to about 1 μm in dimensions. Following this, we will discuss several top-down and bottom-up nanofabrication methods not discussed in other chapters of this Handbook.

8.1 Basic Microfabrication Techniques

Most micro/nanofabrication techniques have their roots in the standard fabrication methods developed for the semiconductor industry [8.1–3]. Therefore, a clear understanding of these techniques is necessary for anyone starting to embark on a research and development path in the micro/nano area. In this section, we will discuss the major microfabrication methods used most frequently in the manufacturing of micro/nanostructures. Some of these techniques such as thin-film deposition and etching are common between the micro/nano and very large-scale integration (VLSI) microchip fabrication disciplines. However, several other techniques which are more specific to the micro/nanofabrication area will also be discussed in this section.

8.1.1 Lithography

Lithography is the technique used to transfer a computer-generated pattern onto a substrate (silicon, glass, GaAs, etc.). This pattern is subsequently used to etch an underlying thin film (oxide, nitride, etc.) for various purposes (doping, etching, etc.). Although photolithography, i. e., lithography using an ultraviolet (UV) light source, is by far the most widely used lithography technique in the microelectronic fabrication, electron-beam (e-beam) and x-ray lithography are two other alternatives which have attracted considerable attention in the MEMS and nanofabrication areas. We will discuss photolithography in this section and postpone discussion of e-beam and x-ray techniques to subsequent sections dealing with MEMS and nanofabrication.

The starting point subsequent to the creation of the computer layout for a specific fabrication sequence is the generation of a photomask. This involves a sequence of photographic processes (using optical or e-beam pattern generators), which results in a glass plate having the desired pattern in the form of a thin ($\approx 100\,\text{nm}$) chromium layer. Following the generation of the photomask, the lithography process can proceed as shown in Fig. 8.1. This sequence demonstrates the pattern transfer onto a substrate coated with silicon dioxide; however, the same technique is applicable to other materials. After depositing the desired material on the substrate, the photolithography process starts with spin-coating the substrate with a photoresist. This is a polymeric photosensitive material which can be spun onto the wafer in liquid from (usually an adhesion promoter such as hexamethyldisilazane HMDS is used prior to the application of the resist). The spinning speed and photoresist viscosity will determine the final resist thickness, which is typically in the range $0.5–2.5\,\mu\text{m}$. Two different kinds of photoresist are available: positive and negative. With positive resist, UV-exposed areas will be dissolved in the subsequent development stage, whereas with negative photoresist, the exposed areas will remain intact after UV development. Due to its better performance with regard to process control in small geometries, positive resist is the most extensively used in the VLSI processes. After spinning the photoresist onto the wafer, the substrate is soft-baked (5–30 min at 60–100 °C) in order to remove the solvents from the resist and improve adhesion. Subsequently, the mask is aligned to the wafer and the photoresist is exposed to a UV source.

Depending on the separation between the mask and the wafer three different exposure systems are available:

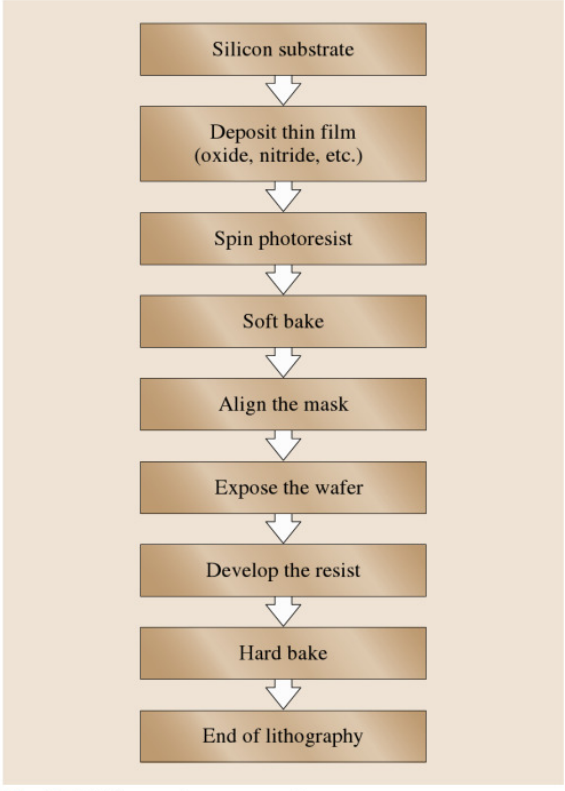

Fig. 8.1 Lithography process flow

1. Contact
2. Proximity
3. Projection

Although contact printing gives better resolution compared with the proximity technique, the constant contact of the mask with the photoresist reduces the process yield and can damage the mask. Projection printing uses a dual-lens optical system to project the mask image onto the wafer. Since only one die at a time can be exposed, this requires a step-and-repeat system to cover the whole wafer area. Projection printing is by far the most widely used system in microfabrication and can yield superior resolutions compared with the contact and proximity methods. The exposure source for photolithography depends on the resolution. Above 0.25 μm minimum line width, a high-pressure mercury lamp is adequate (436 nm g-line and 365 nm i-line). However, between 0.25 and 0.13 μm, deep-UV sources such as excimer lasers (248 nm KrF and 193 nm ArF) are required. Although there has been extensive competition for the below-0.13 μm regime (including e-beam and x-ray), extreme UV (EUV) with wavelength of 10–14 nm seems to be the preferred technique, although major technical challenges still remain [8.4]. Immersion lithography (i. e., using a liquid in the space between the lens and substrate in order to increase the numerical aperture), a recent innovation, has allowed the minimum feature size to be reduced to 32 nm without the requirement for EUV sources [8.5].

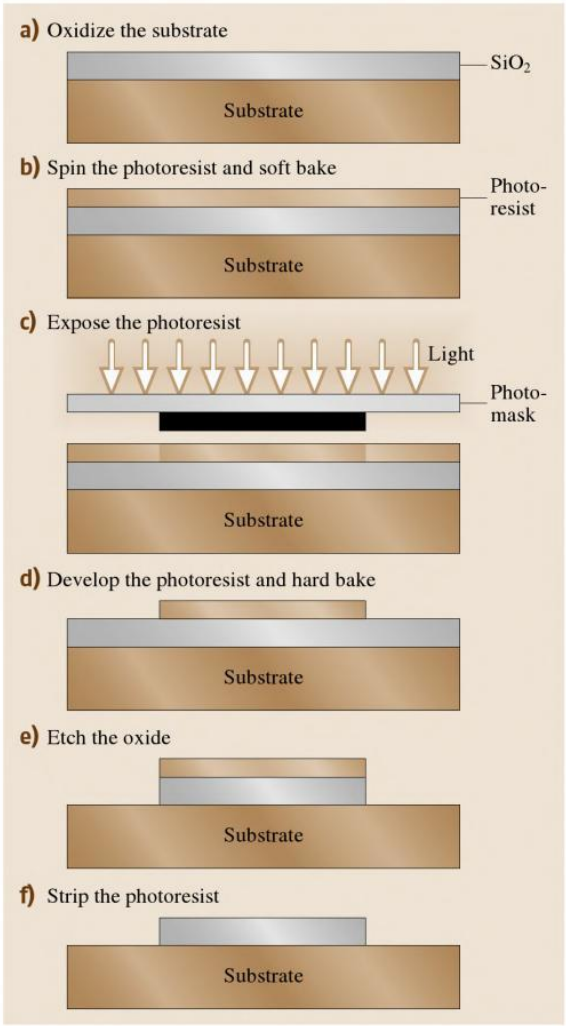

Fig. 8.2a–f Schematic drawing of the photolithographic steps with a positive PR

After exposure, the photoresist is developed in a process similar to the development of photographic films. The resist is subsequently hard-baked (20–30 min at 120–180 °C) in order to further improve adhesion. The hard-bake step concludes the photolithography sequence by creating the desired pattern on the wafer. Next, the underlying thin film is etched and the photoresist is stripped using acetone or other organic removal solvents. Figure 8.2 shows a schematic of the photolithography steps with a positive photoresist.

8.1.2 Thin-Film Deposition and Doping

Thin-film deposition and doping are extensively used in micro/nanofabrication technologies. Most fabricated micro/nanostructures contain materials other than that of the substrate, which are obtained by various deposition techniques or by modification of the substrate. Following is a list of a few typical applications for the deposited and/or doped materials used in micro/nanofabrication, which gives an idea of the required properties:

- Mechanical structure
- Electrical isolation
- Electrical connection
- Sensing or actuating
- Mask for etching and doping
- Support or mold during deposition of other materials (sacrificial materials)
- Passivation

Most of the deposited thin films have properties different from those of their corresponding *bulk* forms (for example, metals shows higher resistivities in thin-film

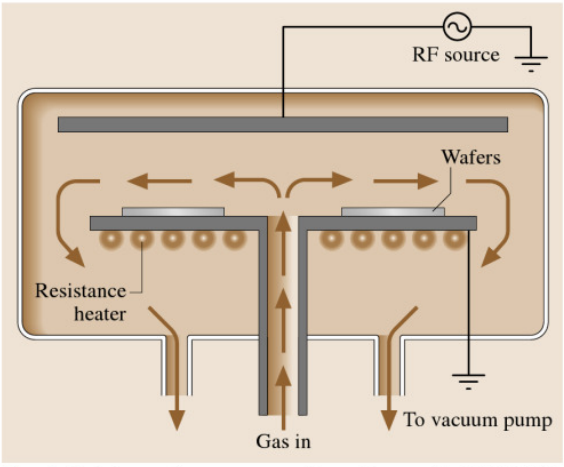

Fig. 8.6 Schematic representation of a typical PECVD system

nitride, and amorphous silicon. Conformality is good for low-aspect-ratio structures, but becomes very poor for deep trenches (20% of the surface thickness inside through-wafer holes with an aspect ratio of 10). Stress depends on deposition parameters and can be either compressive or tensile. PECVD nitrides are typically nonstoichiometric (Si_xN_y) and are much less resistant to etchants in masking applications.

Another interesting type of CVD is epitaxial growth. In this process, a single-crystalline material is grown as an extension of the crystal structure of the substrate. It is possible to grow dissimilar materials if the crystal structures are somehow similar (lattice matched). Silicon-on-sapphire (SoS) substrates and some heterostructures are fabricated in this way. However, most common in microfabrication is the growth of silicon on another silicon substrate. Of particular interest for the formation of microstructures is selective epitaxial growth. In this process the silicon crystal is allowed to grow only in windows patterned on a masking material. Many CVD techniques have been used to produce epitaxial growth. The most common for silicon is thermal chemical vapor deposition or vapor-phase epitaxy (VPE). Metalorganic chemical vapor deposition (MOCVD) and molecular-beam epitaxy (MBE) are the most common for growing high-quality III–V compound layers with nearly atomic abrupt interfaces. The former uses vapors of organic compounds with group III atoms such as trimethylgallium ($Ga(CH_3)_3$) and group V hydrides such as AsH_3 in a CVD chamber with fast gas switching capabilities. The latter typically uses molecular beams from thermally evaporated elemental sources aiming at the substrate in an ultrahigh-vacuum chamber. In this case, rapid on/off control of the beams is achieved by using shutters in front of the sources. Finally, it should be mentioned that many metals (molybdenum, tantalum, titanium, and tungsten) can also be deposited using LPCVD. These are attractive for their low resistivities and their ability to form silicides with silicon. Due to its application in new interconnect technologies, copper CVD is an active area of research.

Physical Vapor Deposition (Evaporation and Sputtering)

In physical deposition systems the material to be deposited is transported from a source to the wafers, both being in the same chamber. Two physical principles are used to do this: evaporation and sputtering.

In evaporation, the source is placed in a small container with tapered walls, called the crucible, and is heated up to a temperature where evaporation occurs. Various techniques are utilized to reach the high temperatures needed, including the induction of high currents with coils wound around the crucible and the bombardment of the material surface with an electron beam (e-beam evaporators). This process is mainly used to deposit metals, although dielectrics can also be evaporated. In a typical system the crucible is located at the bottom of a vacuum chamber whereas the wafers are placed lining the dome-shaped ceiling of the chamber (Fig. 8.7). The main characteristic of this process is very poor step coverage, including shadow effects as illustrated in Fig. 8.8. As will be explained in subsequent

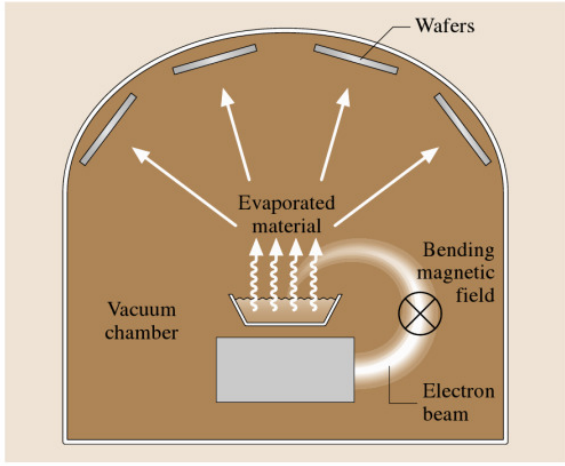

Fig. 8.7 Schematic representation of an e-beam deposition system

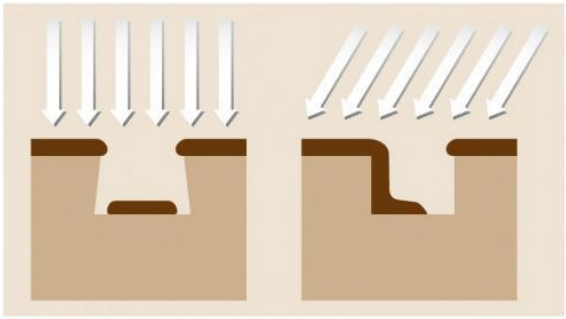

Fig. 8.8 Shadow effects observed in evaporated films. *Arrows* show the trajectory of the material atoms being deposited

sections, some microfabrication techniques utilize these effects to pattern the deposited layer. One way to improve the step coverage is by rotating and/or heating the wafers during deposition.

In sputtering, a target of the material to be deposited is bombarded with high-energy inert ions (usually argon). The outcome of the bombardment is that individual atoms or clusters are removed from the surface and ejected towards the wafer. The physical nature of this process allows its use with virtually any existing material. Examples of interesting materials for microfabrication that are frequently sputtered include metals, dielectrics, alloys (such as shape memory alloys), and all kinds of compounds (for example, piezoelectric lead zirconate titanate (PZT)). The inert ions bombarding the target are produced in direct-current (DC) or RF plasma. In a simple parallel-plate system the top electrode is the target and the wafers are placed horizontally on top of the bottom electrode. In spite of its lower deposition rate, step coverage in sputtering is much better than in evaporation. However, the films obtained with this deposition process are nonconformal. Figure 8.9 illustrates successive sputtering profiles in a trench.

Both evaporation and sputtering systems are often able to deposit more than one material simultaneously or sequentially. This capability is very useful to obtain alloys and multilayer films (e.g., multilayer magnetic recording heads are sputtered). For certain low-reactivity metals such as Au and Pt the previous deposition of a thin layer of another metal is needed to improve adhesion. Ti and Cr are two frequently used adhesion promoters. Stress in evaporated or sputtered layers is typically tensile. The deposition rates are much higher than for most CVD techniques. However, due to stress accumulation and cracking, thickness beyond 2 μm is rarely deposited with these processes.

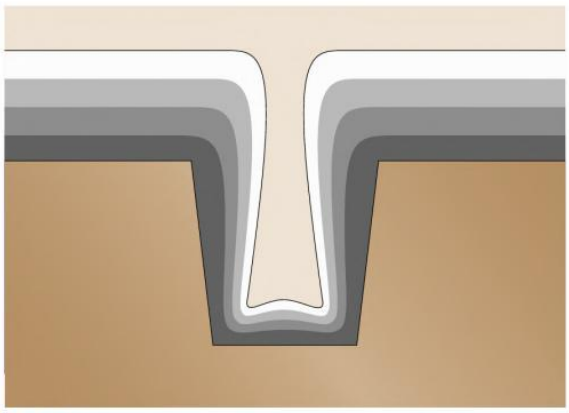

Fig. 8.9 Typical cross section evolution of a trench while being filled with sputter deposition

For thicker deposition a technique described in the next section is sometimes used.

Electroplating

Electroplating (or electrodeposition) is a process typically used to obtain thick (tens of μm) metal structures. The sample to be electroplated is introduced into a solution containing a reducible form of the ion of the desired metal and is maintained at a negative potential (cathode) relative to a counterelectrode (anode). The ions are reduced at the sample surface and the insoluble metal atoms are incorporated into the surface. As an example, copper electrodeposition is frequently done in copper sulfide-based solutions. The reaction taking place at the surface is $Cu^{2+} + 2e^- \rightarrow Cu_{(s)}$. Recommended current densities for electrodeposition processes are on the order of $5-100\,mA/cm^2$.

As can be deduced from the process mechanism, the surface to be electroplated has to be electrically conductive, and preferably of the same material as the deposited one if good adhesion is desired. In order to electrodeposit metals on top of an insulator (the most frequent case) a thin film of the same metal, called the seed layer, is previously deposited on the surface. Masking of the seed layer with a resist permits selective electroplating of the patterned areas. Figure 8.10 illustrates a typical sequence of the steps required to obtain isolated metal structures.

Pulsed Laser and Atomic Layer Deposition

Pulsed laser and atomic layer deposition techniques have attracted a considerable amount of attention recently. These two techniques offer several unique advantages compared with other thin-film deposition

the relaxation of the internal (compressive or tensile) stress during the release step. Otherwise the structures will clamp themselves to the walls of the template and their retrieval will not be possible. Any material that can be conformally deposited and yet not damaged during the HF release step is suitable for the structural layer. Structures made of polysilicon, nitride, and electroless nickel [8.50] have been reported. Nickel can only be deposited in combination with polysilicon since a conductive surface is needed for the deposition to occur. After deposition of structural materials a blanket etch (poly-Si or nitride) or a mechanical lapping (nickel) is performed to remove the excess materials from the surface. Finally, a 49% HF with surfactant is used to dissolve the sacrificial layers. The process can be repeated many times using the same template, thus considerably lowering fabrication costs. Figure 8.40 shows an SEM photograph of a microactuator fabricated using the HEXSIL process.

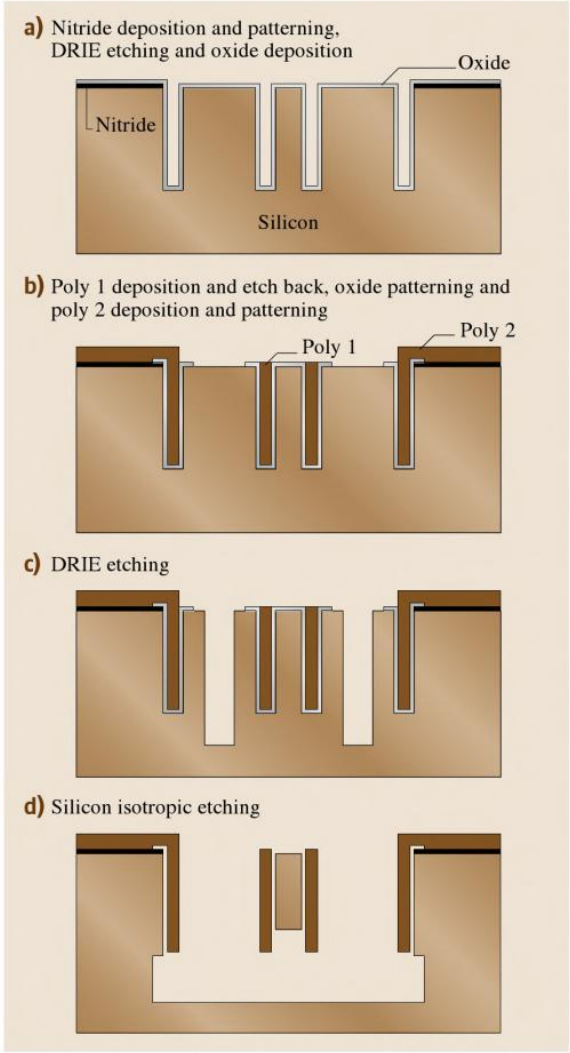

Fig. 8.41a–d HARPSS process flow: (**a**) nitride deposition and patterning, DRIE etching and oxide deposition, (**b**) poly 1 deposition and etch back, oxide patterning, and poly 2 deposition and patterning, (**c**) DRIE etching, and (**d**) silicon isotropic etching

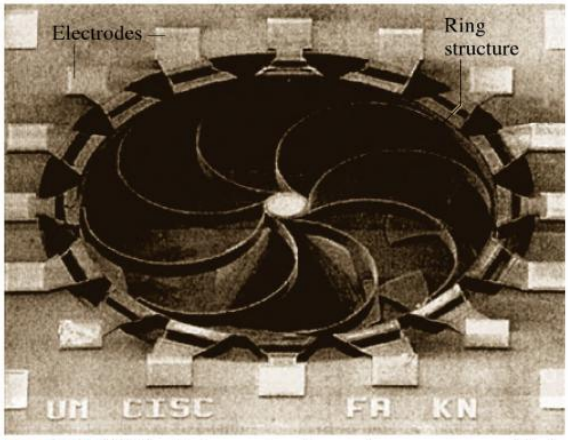

Fig. 8.42 SEM photograph of a microgyroscope fabricated using the HARPSS process (after [8.51])

HARPSS

The high-aspect-ratio combined poly- and single-crystal silicon (HARPSS) technology is another technique capable of producing high-aspect-ratio electrically isolated polycrystalline and single-crystal silicon microstructures with capacitive air gaps ranging from submicrometer to tens of micrometers [8.52]. The structures, tens to hundreds of micrometers thick, are defined by trenches etched with DRIE and filled with oxide and poly layers. The release of the microstructures is done at the end by means of a directional silicon etch followed by an isotropic etch. The small vertical gaps and thick structures possible with this technology find application in the fabrication of a variety of MEMS devices, particularly inertial sensors [8.53] and RF beam resonators [8.54]. Figure 8.41 shows the process flow in a cross section of a single-crystal silicon beam resonator. The HARPSS process starts with deposition and patterning of a silicon nitride layer that will be used to isolate the poly structure's connection pads from the substrate. High-aspect-ratio trenches ($\approx 5\,\mu$m wide) are then etched into the substrate using a DRIE etch. Next,